MICROANALYTICAL APPROACHES TO THE STUDY OF HYDROTHERMAL ALTERATION IN EPITHERMAL AND OROGENIC AU-AG DEPOSITS IN NEWFOUNDLAND

By

Carlos Arbiol González

A thesis submitted to the School of Graduate Studies
in partial fulfillment of the requirements for the degree of

Doctor of Philosophy

Department of Earth Sciences

Memorial University

May 2022

St. John's, Newfoundland and Labrador

Abstract

The Island of Newfoundland (Canada) is an amalgamation of terranes defining the northernmost extent of the Appalachian orogen in North America. A subset of these terranes host epithermal and orogenic gold occurrences of Neoproterozoic and Silurian-Devonian age, respectively. Well-preserved examples of high- and low- sulfidation epithermal gold mineralization and associated phyllosilicate-rich alteration occur in the Neoproterozoic portion of the Avalon Zone. High-sulfidation epithermal occurrences, including the Hickey´s Pond prospect and the Hope Brook deposit, are characterized by the phyllosilicates Fe muscovite ($2M_1$ polytypism), paragonite, Al clinochlore (ripidolite with *IIb* polytypism), pyrophyllite, kaolinite group minerals, and mixed layer clay phases, which formed at relatively high temperatures (200-300 ºC). Low-sulfidation epithermal occurrences, such as the Heritage prospect, feature a phyllosilicate assemblage defined by Fe-Mg muscovite (high Tschermak substitution and $2M_2$ polytypism), Al clinochlore (brunsvigite with *IIb* polytypism), and mixed layered clay phases, which formed at lower temperatures (100-200 ºC). Raman microspectroscopy proved highly effective in characterizing alunite group minerals (alunite and natroalunite endmembers), pyrophyllite, white mica (muscovite/paragonite and phengite), and Fe-Mg chlorite (clinochlore and chamosite end-members) in these examples. The sensitivity of the white mica Raman band between 1000 cm^{-1} and 1150 cm^{-1} to changes in Si^{4+} and Al^{3+} in tetrahedral coordination revealed that compositional variations due to Tschermak substitution (muscovite-paragonite versus phengite(celadonite)) can be effectively detected by Raman microspectroscopy. The position of the main chlorite Si-O-Si Raman band shifts from >680 cm^{-1} for Mg-rich chlorite to <670 cm^{-1} for Fe-rich chlorite, permitting the estimation of the Fe^{2+} content in chlorite. The Baie Verte Peninsula

(Dunnage Zone) hosts abundant orogenic gold mineralization with formation of hydrothermal rutile at distances of 10s of m from the auriferous veins. The distal-to-proximal evolution of Fe-Ti phases consists of (Ti)-magnetite - ilmenite - titanite - rutile, showing a progression from Fe- to Ti-rich phases. Vein-proximal rutile from the essentially barren Animal Pond prospect contains high concentrations of Fe and Mn, while vein-proximal rutile from the auriferous Stog'er Tight and Argyle deposits contains higher concentrations of Nb, Ta, Sn, and, in particular, Sb (80-100 ppm). The Fe-Mn-poor, Sb-rich composition of rutile formed proximal to auriferous veins has potential application to gold exploration in the Baie Verte region and elsewhere.

General Summary

The island of Newfoundland is made of rocks formed in a wide variety of geological environments (volcanic arcs, sedimentary basins, magmatic intrusions, metamorphic terranes, etc.), which have been compressed together in a mountain-building process (known as orogenesis) that gave rise to the North American Appalachians. Some of these geological environments contain valuable minerals and metals, including gold deposits formed at shallow depths due to heat-driven fluid migration in volcanic arc settings ("epithermal gold-silver deposits") and those formed at greater depth due to metamorphic fluid migration through the crust in orogenic terranes ("orogenic gold deposits"). Together with gold, "alteration" minerals such as mica, chlorite, alunite, and clays formed due to the interaction of these hot fluids with the surrounding rocks. By studying these minerals with microanalytical techniques (scanning electron microscopy, electron probe microanalysis, Raman microspectroscopy, secondary ion mass spectrometry), it is possible to distinguish compositional features of the alteration that occur over a wide area, and can be linked to the presence of more localized gold mineralization, therefore aiding in the exploration for gold deposits. The epithermal gold-silver occurrences studied in this thesis are characterized by phyllosilicates ("sheet silicates") such as Fe muscovite, Fe-Mg muscovite, paragonite, Al clinochlore, pyrophyllite, kaolinite group minerals, and mixed layer clay phases, which formed at temperatures between 100 and 300 ºC. Raman microspectroscopy was shown to be very effective in identifying and characterizing the compositions of alunite group minerals (alunite and natroalunite endmembers), pyrophyllite, white mica (muscovite/paragonite and phengite), and Fe-Mg chlorite (clinochlore and chamosite end-members). The Baie Verte Peninsula (Northern Newfoundland) hosts numerous orogenic gold deposits with wide alteration envelopes rich in Fe-

Ti minerals like rutile. Rutile with high Fe and Mn contents is generally associated with gold-barren veins. Conversely, rutile shows high concentrations of Nb, Sn, Sb, and Ta in association with gold-bearing veins. These characteristics can be applied to assess rutile in rocks, or in heavy minerals separated from glacial till samples, to help locate gold-bearing orogenic veins.

Acknowledgements

The present Ph.D. Thesis is mainly the result of countless days in dark labs together with priceless discussions and input from many individuals.

First and foremost, I would like to express my gratitude to my thesis supervisor, Dr. Graham Layne, for his valuable guidance, advice, and academic and personal support. His broad knowledge on ore deposits and his strong drive for innovating science has inspired me through this process and it is reflected in this thesis. Thank you for your mentorship, trust, and for putting things back into perspective when I thought I was stuck. This thesis, and all the opportunities that have come from it, would not have been possible without your support at all levels. Through the years, I have certainly gone through several personal situations, and I will never forget how accommodating you have always been for me, particularly during my last years of Ph.D. from Ottawa and Quebec City.

I would like to thank Dr. Stephen Piercey for all his help and enthusiasm while conducting research on orogenic gold deposits in Newfoundland. I am also grateful to him for allowing me to acquire spectral data with a Terraspec Pro at his lab.

I would also like to acknowledge the essential contribution of Dr. Branimir Šegvić to this thesis. To start, I would not have done this Ph.D. without your motivation and drive to pursue a Ph.D. degree after my masters at the Université de Genève, where we met and worked together. You were not only an essential part of my success during my masters, but also gave me the opportunity to work with you during my Ph.D. Thank you for accommodating me at Texas Tech University, for the access to your excellent facilities, for the countless hours of training on various techniques, and your dedication during data acquisition and interpretation. Keep inspiring young scientists like me.

I am grateful to Dr. John Jamieson for being part of my supervisory committee and for the valuable courses he taught me at MUN. And I want to thank Dr. John Hanchar for granting me access to his lab for cathodoluminescence analyses and for always being happy to help me.

Data acquisition as well as logistics for this research would not have been possible without the help of countless staff at Memorial University of Newfoundland: Glenn Piercey, Dylan Goudie, Wanda Aylward, Matt Crocker, Keir Hiscock, Amanda Langille, Diane Guzzwell, Michelle Miskell, Jane O'Neil, Danyelle Drodge, Sharon Deemer, and Darren Smith.

Fieldwork and sampling would not have been possible without the collaboration of *Puddle Pond Resources* and *Anaconda Mining,* which provided logistical support and access to mines, prospects, and properties, and sampling. In particular, I would like to thank Greg Woodland and Carly Mueller for their assistance and help in the field.

There are several organizations and companies that financially supported this research and deserve to be acknowledged here. First, I would like to thank the *Society of Economic Geologists (SEG) Foundation, Inc.*, and the *Newmont Mining Corporation* for supporting initial field work and sample preparation through a *Student Research Grant (SRG)* received in 2017. Secondly, I want to thank the *Society for Geology Applied to Mineral Deposits (SGA)* for granting economic support to attend and present part of this research at the *Goldschmidt Conference 2019* in Barcelona (Spain). Finally, I would like to express my gratitude to MITACS and their representative at MUN Niraj Shukla, for presenting me with a *Globalink Research Award* in 2019. The funding received allowed me to travel and undertake research with Dr. Branimir Šegvić at *Texas Tech University* in Lubbock (Texas, USA) during the months of February, March, and April 2020.

Moreover, I would like to thank the support I received over the years by my friends, roommates, officemates, and fellow graduate students. In particular, I'd like to thank my friends back home, Teresa Palma, David Artiaga, David Arias, and Mariel García, my roommate, landlord, and dear friend Jerry Dick, my good friends Ariadni Georgatou and Nabil Shawwa, my Newfoundland friends Bruce Knox and Andrew O'Dea, mis amigos latinos Natalia Vivas, Coni Safatle, and Tomás Araya (and their beautiful children, Mateo and Victoria), my officemates Pierre Groulier, Ethan Matchinski, Dilanka Athukorala, and Mackenzie Patrick, and my fellow graduate students Laura Mateo, Dorota Pietruszka, Maria Kotsi, and Dennis Sánchez Mora.

This PhD Thesis is dedicated to my family: my parents Mari and Roberto, my brother David, and my grand-mother María. I particularly want to dedicate this thesis to my grand-father Sixto, who passed away in February 2020 and was a very inspiring and positive man. Through the hardship of living abroad and missing all of you every day, you have remained my rock and my main source of support and love. This is *for* you, *because* of you, and *thanks* to you.

Table of Contents

1. Chapter 1: Introduction 1

2. Chapter 2: Characteristics and genesis of phyllosilicate hydrothermal mineral assemblages from Neoproterozoic epithermal Au-Ag mineralization of the Avalon Zone of Newfoundland, Canada 53

List of Figures

List of Tables

List of Abbreviations

Å: Angstrom

AOT: Annieopsquotch Oceanic Tract

a.p.f.u.: Atom per formula unit

ɑ: activity

BSE: Back-Scattered Electron

BVBL: Baie Verte - Brompton Line

BVOT: Baie Verte Oceanic Tract

CA-TIMS: Chemical Abrasion Thermal Ionization Mass Spectrometry

cm: centimeter

cm^{-1}: Raman wavelength

CRE: Cosmic Ray Events

°C: Degree Celsius

DF: Dover Fault

DZ(e): Exploits subzone

DZ(n): Notre Dame subzone

EDS: Energy Dispersive Spectroscopy

EG: Ethylene glycol

EPMA: Electron Probe Microanalysis

Fe#: Iron number

FTR: Fourier Transform Raman

g/t: Grams per ton

HB: Hope Brook high-sulfidation deposit

HBF: Hermitage Bay Fault

HE: Heritage low-sulfidation prospect

HP: Hickey’s Pond high-sulfidation prospect

HSED: High-sulfidation epithermal deposits

HSS: High-sulfidation system

I18: Inoue et al. (2018) geothermometer

IOCG: Iron oxide copper-gold deposit

ISED: Intermediate-sulfidation epithermal deposits

KM87: Kranidiotis and MacLean (1987) geothermometer

kV: kilovolt

LBOT: Lushs Bight Oceanic Tract

LOD: Limit of Detection

LOI: Loss on ignition

LSED: Low-sulfidation epithermal deposits

LSS: Low-sulfidation system

m: meter

Ma: Mega Annum (Latin), million years

mA: milliampere

mm: millimeter

Mt: Million tones

nA: nanoampere

nm: nanometer

P: Pressure

ppb: parts per billion

ppm: parts per million

REE: Rare Earth Elements

RIL: Red Indian Line

RIR: Reference Intensity Ratio

s: second

SEM: Scanning Electron Microscope

SIMS: Secondary Ion Mass Spectrometry

s.s.: sensu stricto

SWIR: Short Wave Infrared

T: Temperature

T-O-T: Tetrahedral - Octahedral - Tetrahedral

Vis-NIR-SWIR: Visible - Near Infrared - Short Wave Infrared

VMS: Volcanogenic Massive Sulfide deposit

WDS: Wavelength Dispersive Spectrometry

wt.%: weight percent

XRD: X-Ray Diffraction

μm: micron

Mineral Abbreviations:

Ab: Albite

Alu: Alunite

Cal: Calcite

Chl: Chlorite

Clc: Clinochlore

C-Sme: Chlorite-smectite mixed layer

Gn: Galena

Hm: Hematite

Ilm: Ilmenite

I-Sme: Illite-smectite mixed layer

K-Alu: Potassium alunite (i.e., alunite end-member)

Kfs: K-feldspar

Kln: Kaolinite

Mag: Magnetite

Mca: Mica

Mnz: Monazite

Ms: Muscovite

Na-Alu: Sodium alunite (i.e., natroalunite end-member)

Pg: Paragonite

Pl: Plagioclase

Prl: Pyrophyllite

Py: Pyrite

Qtz: Quartz

Rt: Rutile

Ser: Sericite

Sme: Smectite

Sp: Sphalerite

Ttn: Titanite

Zrn: Zircon

List of Appendices

Co-Authorship Statement

This research was first designed by Dr. Graham Layne (MUN), with further input from Dr. Stephen Piercey (MUN) and Dr. Branimir Šegvić (Texas Tech University; TTU). The thesis author was mainly responsible of the research presented here, including fieldwork, sample collection and preparation, and acquisition of analytical data by multiple techniques. Fieldwork was carried out with the assistance of Dr. Graham Layne, Dr. Stephen Piercey, Greg Woodland, and Carly Mueller, with property access granted by *Puddle Pond Resources Inc.* and *Anaconda Mining*. Sample preparation was accomplished by the thesis author, with the help of Matt Crocker (MUN), Glenn Piercey (CREAIT – MUN), and Dylan Goudie (CREAIT – MUN). Scanning electron microscopy (SEM) and electron probe microanalyses (EPMA) analyses were possible thanks to the assistance of Dylan Goudie (CREAIT – MUN) and Wanda Aylward (TERRA – MUN), respectively. Visible – near-infrared – short-wave infrared (Vis-NIR-SWIR) spectroscopy was possible thanks to the assistance of Dr. Stephen Piercey. Access to the Raman spectroscopes at the Department of Chemistry at MUN was enabled by Dr. Erika Merschrod (MUN), with assistance from Lucas Stewart, Liam Whelan, and Silvana Rodrigues Pereira. Dr. Branimir Šegvić (TTU) was vital in granting access and assistance during clay separation, X-ray diffraction (XRD) data acquisition, modeling by Sybilla software, and data interpretation, as was Giovanni Zanoni. Secondary ion mass spectrometry (SIMS) analyses were performed by Dr. Graham Layne and Glenn Piercey (MUN).

Editing of this thesis was primarily carried out by Dr. Graham Layne, with further editing by Dr. Branimir Šegvić (Chapter 2) and the thesis committee members Dr. Stephen Piercey and Dr. John Jamieson, as well as the thesis examiners (to be determined).

Chapter 2 has been published in *Applied Clay Sciences* (DOI: 10.1016/j.clay.2020.105960) and is co-authored by Graham Layne, Giovanni Zanoni, and Branimir Šegvić. Dr. Graham Layne provided guidance during the writing of the paper, as well as final edits. Dr. Branimir Šegvić aided during preparation of clay separate samples, XRD data acquisition, mineral modelling, interpretation, and edits. Mr. Giovanni Zanoni helped during preparation of clay separate samples and XRD data acquisition. The paper was reviewed by two anonymous reviewers and edited by journal editor Prof. Alberto López Galindo.

Chapter 3 has been published in *Applied Spectroscopy* (DOI: 10.1177/00037028211047869) and is co-authored by Graham Layne, who provided guidance during the writing of the paper, as well as final edits. The paper was reviewed by two anonymous reviewers and edited by journal editor Dr. Sergei Kazarian.

Chapter 4 is expected to be submitted for publication to *Canadian Mineralogist* and is co-authored by Graham Layne and Stephen Piercey. Dr. Graham Layne acquired SIMS data and provided guidance during the writing of the paper, as well as during final edits. Dr. Stephen Piercey provided details on the geological setting, as well as input in the discussion and final edits.

Chapter 1: Introduction

The Island of Newfoundland (Canada) is an amalgamation of terranes that define the northernmost extent of the Appalachian orogen in North America (Williams, 1979). Some of these terranes present an important economic potential, given the multiple occurrences of both epithermal and orogenic gold deposits of Neoproterozoic and Silurian-Devonian age, respectively. In view of the relevance of gold in the global market, the exploration interest towards new hydrothermal gold deposits is ever increasing. As a result, exploration efforts are now focusing on areas traditionally considered devoid of gold mineralization, notably in the case of epithermal deposits, as well as on the development of new geochemical vectors to help narrow prospective areas for hydrothermal gold mineralization. This thesis examines well-preserved examples of i) Neoproterozoic epithermal Au-Ag mineralization from the Avalon Zone of Newfoundland and, ii) Orogenic Au deposits of Silurian age from the Baie Verte (Pointe Rousse) district.

The research was directed at both providing new insights into hydrothermal alteration processes in gold systems and developing techniques for using the mineralogical, spectral, and geochemical characteristics of alteration minerals in defining exploration vectors towards gold mineralization. Key research questions in this investigation included: (1) Can alteration minerals be more precisely characterized with the combination of multiple analytical techniques? (2) What are the mineralogical and geochemical signatures of hydrothermal alteration minerals genetically associated with precious metals in epithermal and orogenic ore systems? (3) Can a more accurate characterization of hydrothermal alteration provide new exploration vectors in the prospection for gold mineralization?

For the epithermal examples, the study emphasizes the use of combined and complementary analytical approaches – particularly microanalytical techniques – to characterizing alteration minerals. Raman spectroscopy, reflectance spectroscopy, X-ray diffractometry, and electron probe microanalysis are applied to phyllosilicate (and related) alteration minerals to: i) characterize variations within and between alteration zones; and ii) explore possible application to exploration vectoring for the definition and development of this deposit type.

For the orogenic deposits, this thesis presents a study of compositional and textural variation in hydrothermal rutile from fertile and relatively barren orogenic vein systems. Scanning electron microscopy, electron probe microanalysis, and secondary ion mass spectrometry are applied to develop a profile of rutile geochemistry that has significant potential to discriminate rutile related to Au delivery events, in veins or in till samples.

This thesis is the result of research efforts towards the understanding of hydrothermal alteration in precious metal systems in order to help vector towards the discovery of new mineralized occurrences. Therefore, new petrological, spectral, and geochemical data from various epithermal and orogenic gold systems in Newfoundland are reported herein.

1.1. Overview of Epithermal and Orogenic Gold Systems

Hydrothermal gold deposits, predominantly those occurring in epithermal and orogenic environments (Fig. 1.1a), account for about 65% of recent global gold production (Frimmel, 2008). The most recent publication that enumerates global gold production by deposit type is Frimmel (2008), who reports that orogenic (plus intrusion-related) and epithermal deposits supply 31% and 13% of the recent global gold production, respectively (Fig. 1.1b). These two deposit types are characterized by the common occurrence of hydrothermal alteration formed during the interaction of hydrothermal fluids with the wall rocks. This complex process induces mineralogical and geochemical changes to the original rock. The study of hydrothermal alteration provides an effective approach for investigating the geochemical processes involved during fluid-rock interaction, and can be used as a proxy for targeting exploration (Bierlein & Crowe, 2000; Goldfarb et al., 2005).

The term “epithermal” was first introduced by Lindgren (1933) to characterize the shallow ore-forming hydrothermal environment developed in volcanic arc settings that host Au, Ag, base metals, Hg, Sb, S, kaolinite, alunite, and silica deposits (Fig. 1.2). According to the same author, depths of between 50 m and 1,500 m and temperatures ranging from 50°C to 200°C were perceived as favorable for the generation of epithermal deposits. More recent fluid inclusion studies of epithermal deposits indicate temperatures of between 150°C and 300°C (Hedenquist et al., 2000).

The epithermal environment contains two contrasting end-member styles of hydrothermal system. The end-member styles show different ore and gangue assemblages, as well as contrasting alteration minerals, which reflect both the chemistry and evolution of the hydrothermal fluids. Different classifications have been proposed during the last decades based on diverse geological characteristics of the deposits: acid and alkaline (based on fluid pH; Sillitoe, 1977), acid sulfate and adularia-sericite (based on gangue mineralogy; Heald et al., 1987), high sulfur and low sulfur (based on the relative quantity of sulfide minerals; Bonham, 1986), alunite-kaolinite and adularia-sericite (based on alteration minerals; Berger and Henley, 1989), and high-sulfidation and low-sulfidation (based on the T-fS_2 stability of the constituent sulfide minerals; Hedenquist, 1987). The lattermost terminology is now most widely used to refer to these sub-types in the epithermal environment.

High-sulfidation epithermal deposits (HSED) are associated with quartz ± alunite ± pyrophyllite ± dickite ± kaolinite alteration genetically related to highly acidic magmatic-hydrothermal fluids, and contain Au ± Cu ± Ag mineralization (Simmons et al., 2005 and references therein; Fig. 1.2). Ore minerals include native gold, electrum, enargite, luzonite, covellite, tetrahedrite, and tennantite (Simmons et al., 2005 and references therein). The hydrothermal alteration of the host rocks develops in a concentric pattern, with a vuggy silica (i.e., residual silica due to intense leaching of rocks by highly acidic fluids) core that sharply changes to quartz-alunite, pyrophyllite, kaolinite/dickite, and an outer halo of propylitic alteration (Arribas, 1995 and references therein). The ore is commonly disseminated and hosted in the leached silica-rich core of the system, also known as lithocap (Arribas, 1995; Hedenquist et al., 2000). Geological and geochemical evidence often suggests a multistage genesis of HSED, with an early lithocap formation hosting and promoting subsequent mineralization (e.g., Arribas, 1995; Simmons et al., 2005). These two stages are part of the dynamic evolution of a magmatic-hydrothermal system, and are devoid of sharp transitions (Arribas, 1995).

Upon the shallow emplacement of a water-rich and oxidized magma, the exsolution of a single-phase magmatic fluid takes place, but it may undergo phase separation during ascent to the epithermal environment, with the formation of a brine and a vapor-rich phase (Hedenquist et al., 2000; Heinrich et al., 2004; Heinrich, 2005; Williams-Jones and Heinrich, 2005; Richards, 2011). The magmatic brine becomes enriched in metals, whilst the vapor is enriched in volatiles and will ascend to the epithermal environment, where it will condense into a liquid and mix with groundwater, fostering the formation of highly acidic fluids through the disproportionation of SO_2 (Arribas, 1995; Hedenquist et al., 2000). The disproportionation of SO_2 forms H_2SO_4 and either native S (under oxidizing, lower temperature and high total sulfur contents; Kusakabe et al., 2000; McDermott et al., 2015) or H_2S (under reducing, high temperature and low total sulfur contents; Kusakabe et al., 2000; McDermott et al., 2015), and causes extensive hydrothermal alteration and intense leaching of the host rocks (Arribas, 1995; Hedenquist et al., 2000). With time, the magma crystallization front contracts to greater depths due to the progressive crystallization of the shallow intrusion (Heinrich et al., 2004; Sillitoe, 2010), and the exsolved fluids are forced to interact with a larger volume of rock, resulting in a more reduced and lower temperature fluid capable of transporting metals such as Au in the form of bisulfide complexes to the epithermal environment (Heinrich et al., 2004). The mixing of such fluid with groundwater induces further cooling and increases its sulfidation state through the cooling-induced formation of H^+ following: $4H_2SO_{3(aq)} = H_2S_{(aq)} + 3H_2SO_{4(aq)} = H_2S_{(aq)} + 3H^+ + 3HSO_4^-$ (Einaudi et al., 2003). This high-sulfidation fluid is responsible for the commonly observed Cu mineralization (Sillitoe, 2010), after which it evolves to an intermediate-sulfidation fluid and produces the Au mineralization (Einaudi et al., 2003). These deposits develop in close spatial and genetic relation to volcanic activity (Fig. 1.2), indicating their proximal formation to the magmatic-hydrothermal fluid source (Simmons et al., 2005 and references therein).

Low-sulfidation epithermal deposits (LSED), on the other hand, present distinctly different ore and alteration assemblages, characterized by Ag ± Au ± Pb ± Zn and quartz ± adularia ± calcite ± illite, respectively (Simmons et al., 2005 and references therein; Fig. 1.2). Ore minerals include electrum, native Ag, acanthite, Ag sulfosalts and selenides, Au-Ag tellurides, galena, sphalerite, and minor chalcopyrite (Hedenquist et al., 2000). Hydrothermal alteration zoning is common, with a deep propylitic alteration grading to illite-carbonate, and quartz-adularia-illite alteration close to the orebodies. The ore is most often vein-hosted, reflecting a clear structural control on the mineralization (Hedenquist et al., 2000). In contrast to HSED, LSED mineralization occurs at a greater lateral distance (5-6 km) from the causative intrusion. This reflects the convective movement of original acidic and oxidizing exsolved magmatic fluids through the host rocks, consequent mixing with groundwater − causing the fluids to become more reducing, with neutral pH (Hedenquist et al., 2000 and references therein). Low-sulfidation epithermal deposits fluids are capable of transporting metals, notably Au, in bisulfide complexes, which can be deposited in shallow depths by various mechanisms (cooling, depressurization, changes in oxygen and sulfur fugacity; Zhu et al., 2011 and references therein), the most notably of which is boiling (Hedenquist et al., 2000). Modern analogues are the geothermal systems developed in plutonic-volcanic terranes in distal settings from the magmatic-hydrothermal fluid source (e.g., Broadlands-Ohaaki geothermal field, New Zealand; Simmons et al., 2005; Fig. 1.2).

Intermediate-sulfidation epithermal deposits (ISED) were defined by Hedenquist et al. (2000) in order to include those low-sulfidation epithermal mineralizations with an intermediate sulfidation-state assemblage (pyrite, tetrahedrite/tennantite, chalcopyrite, low-Fe sphalerite). They contain Ag ± Zn-Pb-Cu ores, together with Mn-bearing carbonates, rhodonite, and quartz (Sillitoe, 2010). These lode mineralizations generally occur in close spatial relation to HSED (Hedenquist et al., 2000; Sillitoe, 2010).

Orogenic gold deposits, also referred to as *mesothermal*, *lode-gold*, or *greenstone-hosted quartz-carbonate vein* deposits, are commonly formed synchronously with major accretionary or collisional orogenic episodes that produce considerable volumes of hydrothermal fluids, which may precipitate gold at intermediate-to-deep crustal levels (up to 15-20 km deep) in shear and fracture zones (Groves et al., 1998; Goldfarb et al., 2005; Phillips & Powell, 2010; Pitcairn et al., 2014, 2015; Goldfarb & Groves, 2015; Groves et al., 2019; Fig. 1.1a). They are usually hosted by deformed and hydrothermally-altered metamorphic rocks characterized by amphibolite to greenschist metamorphic facies and alteration assemblages that feature carbonates (calcite, ankerite, siderite, dolomite), sericite (fine-grained white mica; and, less frequently, green di-octahedral micas such as fuchsite (chromium-rich) and roscoelite (vanadium-rich)), chlorite (commonly Fe-rich), albite, tourmaline, scheelite, pyrite, hematite, and magnetite (Dubé and Gosselin, 2007 and references therein). Proximal alteration is typically characterized by white mica, chlorite, albite, carbonate, and pyrite, grading to distal areas characterized by the presence of magnetite, chlorite, and carbonate (Dubé and Gosselin, 2007 and references therein). Economic mineralization occurs most frequently as native gold, auriferous pyrite, auriferous pyrrhotite, and auriferous chalcopyrite, either located in the vein itself or in the directly surrounding host rock (Groves et al., 1998). The mineralization is structurally controlled, mainly occurring in second-order brittle-ductile shear zones and faults that act as splays off major crustal-scale structures (Groves et al., 1998; Dubé and Gosselin, 2007). The geometry of hydrothermal-related structures is widely variable, from stockwork and hydrothermal breccia veins, to fault-fill geometries. Other common features of orogenic gold deposits are the occurrence of vein formation and mineralization after peak metamorphism during orogenesis, structural control governed by differences in the rheology and competency contrast between host rocks, thermal equilibrium between the ore fluid and the surrounding host rocks, and precipitation of gold during retrograde P-T conditions close to the brittle – ductile transition (Goldfarb and Groves, 2015 and references therein).

The model of formation for orogenic gold deposits has evolved in the last decades. Some early magmatic-hydrothermal models involved the generation of orogenic gold deposits through the emplacement of granitic intrusions and the exsolution of magmatic-hydrothermal fluids that were responsible for the gold mineralization (Mueller, 1992; Walshe et al., 2003; Bath et al., 2013; Fig. 1.3). However, these intrusion-related models are in contrast to those involving the generation of metamorphic fluids derived from the dehydration of crustal rocks during prograde metamorphism resulted from orogenic events (Kerrich and Fyfe, 1981; Groves et al., 1987; Fig. 1.3). And even though the general orogenic-metamorphic model stands today as the most widely supported by geochemical data and accepted by the scientific community, some relevant advances in the details of this model have been made in recent years. For example, Goldfarb and Groves (2015) and Groves et al. (2019) proposed the devolatilization of subducted oceanic slabs and related Au-bearing sulfide-rich sedimentary sequences as the source of both fluids and gold. Such fluids, rich in H_2O and CO_2 and characterized by having low-salinity and neutral pH, are mobilized through the mantle wedge and through the crust by major structures such as faults and shear zones, all the while transporting gold as sulfide or bisulfide complexes to higher crustal levels. Gold precipitation takes place in late stages of the orogenesis (post peak metamorphism) through the destabilization of gold-sulfide complexes, either by changes in oxygen fugacity (oxidation), and/or sulfidation of Fe-rich host rocks (formation of pyrite, or other sulfide minerals, decreases the activity of HS^-) (Goldfarb and Groves, 2015; Groves et al., 2019).

Despite the economic importance of epithermal and orogenic gold deposits, some of the processes related to the genesis of hydrothermal alteration are still poorly understood. Major knowledge gaps include: (1) exact timing between successive or overlapping episodes of hydrothermal alteration and Au-Ag mineralization; (2) detailed mineralogical characterization of the hydrothermal alteration spatially and genetically associated with the Au-Ag mineralization event(s); (3) underutilization of the currently available analytical methods for the precise identification of fine-grained hydrothermal alteration minerals and their microscale analysis; (4) underdevelopment of exploration vectors based on geochemical signatures of alteration minerals; and (5) lack of well-defined signatures allowing discrimination between mineralized and barren hydrothermally altered rocks.

1.2. Objectives and Research Questions

The design of this study was to undertake a detailed characterization of the hydrothermal alteration associated with precious metal mineralization in examples of epithermal and orogenic gold occurrences from the Burin and Baie Verte districts of Newfoundland (Canada). The research was directed at both providing new insights into hydrothermal alteration processes in gold systems and developing techniques for using the characteristics of alteration minerals in defining exploration vectors towards gold mineralization.

As previously stated, key research questions in this investigation included: (1) Can alteration minerals be more precisely characterized with the combination of multiple analytical techniques? (2) What are the mineralogical and geochemical signatures of hydrothermal alteration minerals genetically associated with precious metals in epithermal and orogenic ore systems? (3) Can a more accurate characterization of hydrothermal alteration provide new exploration vectors in the prospection for gold mineralization?

The study was structured in two separate blocks, each of them with its own goals, approaches, and challenges.

***Spectral and geochemical characterization of hydrothermal alteration in epithermal systems*:**

The first part of the thesis (Chapters 2 and 3) addresses the development and application of microanalytical techniques for the study of hydrothermal alteration in high- and low-sulfidation epithermal systems, using exemplar deposits in Newfoundland. In tandem with Raman microspectroscopy, EPMA, reflectance spectroscopy, and X-ray diffraction (XRD) techniques were used to identify and describe hydrothermal alteration minerals, with an emphasis on phyllosilicates.

Specific objectives included: (1) provide further details on the understanding and characterization of Raman spectral features of key hydrothermal alteration minerals in epithermal systems; (2) correlate changes in phyllosilicate composition (specifically solid solution variations) to changes in spectral features; (3) investigate the reliability and resolution of the spectral results at various scales by comparing macro- and micro-analytical spectroscopic techniques; (4) characterize compositional differences between phyllosilicates with regards to space and relative time of formation; and (5) provide new insights into specific processes involved in metal precipitation (e.g., boiling and mixing in Au-Ag systems), and their relative timing with respect to other alteration and mineralization, as well as the physicochemical characteristics of ore-forming fluids.

Challenges during this portion of the study included sample purification and preparation, instrumentation setting and calibration, with special focus on the removal of fluorescence effects during Raman spectral acquisition, interpretation of spectral features, and distinction between particular alteration and mineralization events.

***Geochemical characterization of rutile and other Fe-Ti alteration phases in orogenic gold deposits*:**

This portion of the study (Chapter 4) focussed on the geochemical characterization of rutile and other Ti-Fe phases in orogenic gold systems from the Baie Verte Peninsula of Newfoundland.

Individual objectives included: (1) precise determination of the mineralogy and evolution of Fe-Ti phases in orogenic systems, from the distal to the most proximal to the mineralization; (2) geochemical characterization of rutile through the combination of electron probe microanalysis (EMPA) and secondary-ion mass spectrometry (SIMS); and (3) definition of new exploration vectors towards mineralized orogenic systems in the Baie Verte region of Newfoundland based on the geochemical signature of rutile related to Au mineralization.

Challenges during this process involved the correct distinction of Fe-Ti phases and their evolution with increasing hydrothermal activity, as well as the obtention of good SIMS analyses of rutile, given its occasional fine-grained nature and great number of micro-inclusions.

1.3. Geological Setting

The main orogenic event resulting from the closure of the Iapetus and Rheic oceans and the consequent continental collision between Laurussia and Gondwana to form the supercontinent Pangaea between 325 and 260 Ma (Carboniferous – Permian) is, in North America, known as the Appalachian or Alleghenian Orogeny (i.e., Variscan or Hercynian Orogeny in Europe; Hatcher, 2010; Williams, 1979). The Appalachian accretionary orogen is mainly the result of this orogenic event, formed through a complete Wilson cycle that started with the breakup of the supercontinent Rodinia during the Neoproterozoic (Hatcher, 2010).

1.3.1. The Appalachian orogen in Newfoundland

Based on tectonostratigraphic, lithological, faunal, geophysical, magmatic, and metamorphic criteria, Williams (1979) divided the Canadian segment of the Appalachian Orogen into five zones: Humber, Dunnage, Gander, Avalon, and Meguma. These distinct zones represent the Laurentian continental margin (Humber Zone), vestiges of island arcs and oceanic crust of the Iapetus Ocean (Dunnage Zone), and several peri-Gondwanan continental terranes (Gander, Avalon, and Meguma Zones; Williams, 1979). The geologically distinct Gander, Avalon, and Meguma zones are considered to be part of different peri-Gondwanan microcontinents: Ganderia, Avalonia, and Meguma, respectively (Hatcher, 2010; Hibbard et al., 2007; Fig. 1.4). A fourth major continental block known as Carolinia has been recognized in the southern Appalachians of North America (Hibbard et al., 2007; Fig. 1.4).

On the island of Newfoundland, the Appalachians are represented by the presence of the Humber, Dunnage, Gander, and Avalon zones (Fig. 1.5). The Humber Zone consists of Grenvillian basement (i.e., rock units affected by the Grenville orogeny during the mid-late Mesoproterozoic and associated with the assembly of the supercontinent Rodinia; Tollo et al., 2004) covered by rift, continental margin, and foreland basin units belonging to Laurentia prior to the formation of the Appalachians. The tectonic boundary between the Humber Zone and the Dunnage Zone is known as the Baie Verte – Brompton Line (BVBL; Fig. 1.5), and it is defined by the presence of an ophiolitic belt (Williams, 1979).

The Dunnage Zone is subdivided into the Notre Dame and the Exploits subzones (Fig. 1.5; Williams et al., 1988). The Notre Dame subzone presents vestiges of peri-Laurentian island arcs and Iapetus oceanic crust (Willner et al., 2014). The Exploits subzone is considered to be part of the microcontinent Ganderia (van Staal et al., 1996; Fig. 1.5). The subzones are separated by the Red Indian Line (RIL; Fig. 1.5), which delineate the main suture of the closing of the Iapetus Ocean (Williams et al., 1988; Willner et al., 2014).

The Gander Zone, together with the Exploits subzone, represents the Ganderia microcontinent (van Staal et al., 1996), which is characterized by polydeformed and metamorphosed magmatic arc rocks covered by a pelitic sequence (Williams et al., 1988). The tectonic boundary between the Gander Zone and the Avalon Zone is marked by the Dover – Hermitage Bay fault (DF and HBF; Fig. 1.5).

The Avalon Zone comprises several Neoproterozoic – Cambrian volcanic arcs and related volcano-sedimentary sequences covered by shale-rich sedimentary rocks and represents the type-area of the peri-Gondwanan Avalonia microcontinent (Williams et al., 1988; Willner et al., 2014).

1.3.2. The Avalon Zone

The geology of the Avalon Zone in Newfoundland comprises several Neoproterozoic volcanic arcs and related volcano-sedimentary sequences, covered by shale-rich sedimentary rocks (Williams, 1979). These volcanic arcs record the tectonic and magmatic evolution of the microcontinent Avalonia, one of the peri-Gondwanan terranes that played a major role in the formation of the Appalachian Orogen, which consisted of the following major events (O'Brien et al., 1983; 1996): (1) Early 760-660 Ma arc magmatism and the accretion of Avalonia to Gondwana; (2) Peak 635-570 Ma arc magmatism; (3) Major 570-550 Ma continental extension; (4) Late Neoproterozoic - Early Cambrian stable continental platform formation; (5) Ordovician rifting of Avalonia from Gondwana; and (6) Late Silurian - Early Devonian accretion of Avalonia to Laurentia.

The Late Neoproterozoic (635-570 Ma) peak arc magmatism is characterized by lithologically diverse, submarine to subaerial, calc-alkaline to tholeiitic, volcanic rocks intruded by calc-alkaline plutonic complexes (O'Brien et al., 1994; 1996). Thick marine sedimentary successions formed during this period, originating in basins adjacent to the magmatic arcs (Dec et al., 1992).

1.3.2.1. Geology of the Burin Peninsula

The Burin Peninsula, located in the southwestern region of the Avalon Zone (Fig. 1.5), is characterized by extensive units of arc-related volcanic, volcaniclastic, and sedimentary rocks of Neoproterozoic age, which are intruded by Late Neoproterozoic – Paleozoic magmatic suites (O'Brien et al., 1996; Sparkes and Dunning, 2014). Stratigraphically, the Burin Peninsula is divided in three main units: the Marystown Group, the Musgravetown Group, and the Long Harbour Group (O'Brien et al., 1996; Fig. 1.6).

The 590-570 Ma Marystown Group is the most extensive volcanic unit outcropping in the Burin Peninsula, and comprises felsic and mafic subaerial lava flows and pyroclastic deposits of calc-alkaline and tholeiitic composition (O'Brien et al., 1996; 1998; 1999). These rocks are affected by regional metamorphism, with a widespread greenschist facies alteration (O'Brien et al., 1996), although deformation is generally mild. This unit is intruded by several coeval plutonic bodies of Late Neoproterozoic age that form a NNE-SSW oriented plutonic belt (O'Brien et al., 1999; Fig. 1.6). The plutonic bodies comprise granite, granodiorite, diorite, and gabbro, with the largest intrusion being the 577±3 Ma Swift Current Granite (O'Brien et al., 1998; Fig. 1.6). The western margin of the Marystown Group is characterized by the presence of clastic and epiclastic sediments belonging to the Grandy's Pond Arenite Belt, which defines the limit between the volcanic rocks of the Marystown Group and those associated with the Long Harbour Group (O'Brien et al., 1996).

The 570 Ma Musgravetown Group comprises an early deposition of alluvial sedimentary rocks followed by subaerial bimodal volcanics of alkaline affiliation and a late deposition of shallow marine siliciclastic rocks, describing a transition sequence from a subaerial to a shallow marine depositional environment (O'Brien et al., 1996; 1999).

The 570-550 Ma Long Harbour Group is made of an alternating succession of subaerial bimodal volcanic rocks and siliciclastic sedimentary rocks (O'Brien et al., 1996). This unit is intruded by felsic plutons of Late Neoproterozoic age and alkaline to peralkaline affiliation (O'Brien et al., 1996; Fig. 1.6).

1.3.2.2. Epithermal gold mineralization of the Burin Peninsula and Hermitage Flexure

The potential for epithermal gold mineralization in the Burin Peninsula emerged after the discovery of the Hickey's Pond high-sulfidation occurrence (Fig. 1.6) in the early 1980s. Low-sulfidation epithermal systems were only explicitly recognized after the discovery of the Big Easy prospect in the late 1990s and the Heritage prospect in 2011 (Sparkes, 2012). The Hope Brook high-sulfidation epithermal gold deposit occurs in the southwestern part of the Avalon Zone and represents the only epithermal deposit in the Avalon Zone mined to date (Dubé et al., 1995).

High- and low-sulfidation epithermal gold occurrences in the Burin Peninsula region are hosted by Neoproterozoic volcanic rocks belonging to the Marystown, Musgravetown, and Long Harbour Groups (O'Brien et al., 1998; 1999; Sparkes, 2012; Sparkes and Dunning, 2014; Fig. 1.6). Due to their shallow crustal environment of formation, epithermal deposits of Neoproterozoic age are relatively uncommon globally. The presence of sedimentary sequences of marine, deltaic, and alluvial character overlying the volcanic rocks, together with the tectonic evolution of the microcontinent Avalonia, played a crucial role in the exceptional preservation of such epithermal systems (Sparkes et al., 2005).

High-sulfidation epithermal gold occurrences in the Burin Peninsula are hosted within an extensive NE-SW belt of advanced argillic alteration, known as the Hickey's Pond − Point Rosie alteration belt (O'Brien et al., 1999), which can be traced intermittently for more than 100 km. This alteration belt is characterized by advanced argillic alteration minerals; pyrophyllite, alunite, hematite, and vuggy silica. Recognized high-sulfidation epithermal systems in the Burin Peninsula include Hickey's Pond, Monkstown Road, Tower, and Stewart, all hosted in volcanic and volcaniclastic rocks belonging to the Marystown Group (Fig. 1.6). General regional descriptive studies have been carried out on these occurrences (Huard and Driscoll, 1986; O'Brien et al., 1997, 1998, 1999; Sparkes et al., 2005, 2016; Sparkes, 2012; Sparkes and Dunning, 2014; Ferguson, 2017).

The best described high-sulfidation epithermal deposit in the Burin Peninsula is Hickey's Pond, given its well-developed zonation in surface exposure. It is hosted in highly deformed, greenschist-grade pyroclastic rocks affected by the Hickey's Brook Fault, which has juxtaposed the host rock sequence with the 577±3 Ma Swift Current Granite (O'Brien et al., 1998; Fig. 1.7). The prospect is characterized by a core of massive silicic alteration with discontinuous zones of vuggy silica (zone A, Fig. 1.7) containing anomalous Au contents (between 0.3 g/t Au and 1.1 g/t Au; O'Brien et al., 1999), but locally returning Bonanza-grade assays of up to 60.4 g/t Au (Sparkes et al., 2016). Together with quartz, variable amounts of alunite and pyrite are commonly observed in this zone. Disseminated pyrite in zone A (Fig. 1.7) is reported to contain inclusions of tennantite, enargite, bornite, chalcopyrite, covellite, chalcocite, Ag and Au tellurides and selenides, native Te, and native Au (Sparkes et al., 2016). The massive silicic core is surrounded by a narrow envelope of advanced argillic alteration dominated by quartz, alunite, pyrite, and rutile (zones B1 and B2, Fig. 1.7). Mineralization in this zone occurs as native gold associated with the pyrite and alunite (Sparkes et al., 2016). At the northeastern end of the massive silica core, a hydrothermal quartz-hematite breccia is developed (zone G, Fig. 1.7). It is characterized by rounded and angular quartz-alunite-pyrophyllite clasts in a specular hematite matrix. Native gold is associated with the hematite-rich matrix, and gold values of up to 5.4 g/t Au have been documented (Huard, 1989). An extensive zone of schistose quartz-alunite-pyrite alteration surrounds zones A, B, and G (zone C, Fig. 1.7). Banded quartz-hematite-alunite alteration occurs interlayered within the unit, where values of up to 2.36 g/t Au have been recorded (O'Brien et al., 1999). This alteration envelope gradually changes to a zone of quartz-alunite-lazulite alteration (zones D and E, Fig. 1.7), and then an outermost zone of schistose quartz-sericite (zone F, Fig. 1.7), which represents the most distal alteration zone of the hydrothermal system. Hydrothermal zircon U-Pb dating from the advanced argillic alteration zone by chemical abrasion - thermal ionization mass spectrometry (CA-TIMS) provided a maximum age limit for the mineralization event at Hickey's Pond of 586±3 Ma (Sparkes et al., 2016).

In contrast, low-sulfidation epithermal systems on the Burin Peninsula appear as more isolated occurrences, largely distal from the Hickey's Pond - Point Rosie epithermal alteration belt (Fig. 1.6). Most of the known systems are characterized by crustiform and colloform textures in quartz and cryptocrystalline silica (i.e., chalcedony), as well as platy calcite, indicative of boiling processes and formation in very shallow (<2 km) environments (Ferguson, 2017). The Heritage prospect, located in the southern tip of the peninsula (Fig. 1.6), is hosted by volcanic rocks belonging to the Marystown Group (Fig. 1.6), whereas the Big Easy system is hosted by epiclastic sediments of the Musgravetown Group (Fig. 1.6).

The Heritage prospect is hosted by andesitic lapilli and crystal tuffs belonging to the Marystown Group and altered by a pervasive envelope of hydrothermal silicification. The prospect is characterized by outer silica ± mica ± chlorite alteration assemblage and an inner silica ± illite ± chlorite ± chalcedony assemblage. Within the hydrothermally-altered rocks, hydrothermal quartz breccias of cockade style, together with multiple generations of silica-quartz-adularia veining dominate the system. Quartz-chalcedony banding and blading textures are commonly observed in portions of veins, the latter being associated with boiling processes. Gold-Ag mineralization is developed as inclusions of chalcopyrite, galena, acanthite, sphalerite, arsenopyrite, and native Ag in pyrite (Ferguson, 2017), which is the most abundant sulfide in the property and occurs disseminated both within the silicified host rocks and in the veins. More pronounced Au-Ag mineralization is usually associated with lower pyrite contents. Further, Au-Ag mineralization is distinguished by ginguro-style bands characterized by native silver, acanthite, naumannite, chalcopyrite, galena, and sphalerite, in close genetic association with calcite and quartz blading, indicating precious metal deposition due to fluid boiling (Ferguson, 2017).

The Hope Brook gold deposit is a high-sulfidation epithermal deposit located within the distal Hermitage Flexure of the Avalon Zone. Geologically, the area primarily comprises the Neoproterozoic Cinq Cerf Gneiss, and its coeval cover sequences, namely the Whittle Hill Sandstone and the Third Pond Tuff (O'Brien et al., 1991; Dubé et al., 1995). These units are intruded by the Neoproterozoic Roti Intrusive Suite and the Sill-Dyke Complex, as well as by post-mineralization Paleozoic intrusions and their related cover sequences (Dunning and O'Brien, 1989; O'Brien et al., 1991; Dubé et al., 1995). Intense deformation during the Silurian resulted in the Cinq Cerf fault zone, which has juxtaposed the Whittle Hill Sandstone and the Third Pond Tuff with the La Poile Group cover rocks (Dubé et al., 1995). The deposit is hosted in extensively altered sandstones, greywackes, siltstones, argillites, and conglomerates of Neoproterozoic age belonging to the Whittle Hill Sandstone, as well as mafic volcaniclastic rocks from the Sill-Dyke Complex. The altered rocks are crosscut by both pre- and post-mineralization porphyry dykes, which has allowed precise U-Pb dating of the mineralization event (578-574 Ma; Dubé et al., 1995). The deposit is modified by the Cinq Cerf fault zone, which post-dates the hydrothermal alteration and gold mineralization events (Dubé et al., 1995). As a result, the deposit occurs in the hanging wall of the fault and locally presents strong deformation. Mineralization, in the form of native Au, is contained in an assemblage of pyrite, chalcopyrite, and bornite, with lesser amounts of tennantite and enargite (Dubé et al., 1995).

Table 1.1 summarizes the major geological characteristics of the main epithermal deposits and occurrences in the Avalon Zone of Newfoundland.

1.3.3. The Humber and Dunnage Zones

Both the Humber and the western Dunnage zones are intimately involved in the geological and tectonic evolution of the eastern Appalachians in Newfoundland, as they represent the eastern Laurentian continental margin and the different oceanic environments of the Iapetus Ocean, respectively (van Staal and Barr, 2012). These terranes collided in a series of accretionary events defining the Taconic Orogeny (van Staal et al., 2007).

The Humber Zone is characterized by a Mesoproterozoic Grenvillian crystalline basement overlain by deformed Neoproterozoic - Ordovician passive margin sequences, which are the result of the opening of the Iapetus Ocean (van Staal and Barr, 2012).

The Notre Dame subzone of the Dunnage Zone presents the remnants of several peri-Laurentian terranes, including the Lushs Bight Oceanic Tract (LBOT), the Baie Verte Oceanic Tract (BVOT), the Annieopsquotch Oceanic Tract (AOT), the Dashwoods microcontinent, and the Notre Dame Magmatic Arc (van Staal and Barr, 2012). The BVOT represents the vestiges of an oceanic tract known as the *Humber* or *Taconic Seaway* that developed in the Iapetus Ocean in close proximity to Laurentia (Waldron and van Staal, 2001).

1.3.3.1. Geology of the Baie Verte Peninsula

The Baie Verte Peninsula is located on the north coast of Newfoundland (Fig. 1.8) and straddles the geological boundary between the western Humber Zone (continental margin of Laurentia) and the eastern Notre Dame subzone of the Dunnage Zone (oceanic rocks formed in the Iapetus Ocean in close proximity to Laurentia; Williams 1979; Fig. 1.8), which is defined by the Baie Verte Line (northern extension of the Baie Verte - Brompton Line; Figs. 1.5 and 1.8). This complex tectonic boundary is characterized by poly-phase shear zones and faults that separate oceanic and mantle-derived rocks from the Laurentian continental margin (Castonguay et al., 2014).

The Humber Zone comprises migmatitic gneisses of the East Pond Metamorphic Suite, representing the Grenvillian basement, and the overlying Mesoproterozoic - Early Paleozoic Fleur de Lys Supergroup rocks (Fig. 1.8), interpreted to be derived from the eastern continental margin of Laurentia (Hibbard, 1983). The Fleur de Lys Supergroup consists of metamorphosed and polydeformed clastic sedimentary rocks, including psammites, pelites, marbles, schists, and amphibolites (Hibbard, 1983).

The Dunnage Zone in the Baie Verte Peninsula is made of several supra-subduction zone ophiolitic complexes belonging to the BVOT and their volcano-sedimentary cover sequences (Fig. 1.8), including: (1) the Betts Cove Complex; (2) the Pacquet Harbour Group; (3) the Point Rousse Complex; and (4) the Advocate Complex.

The oceanic complexes defining the BVOT are intruded by several Late Ordovician - Early Silurian granitoid plutons (Fig. 1.8), including the ca. 445-433 Ma Burlington plutonic suite, the ca. 429 Ma Cape Brulé porphyry, the ca. 427 Ma Dunamagon granite, the ca. 428 Ma Wild Cove Pond Igneous Suite, and the ca. 423 Ma Trap Pond pluton (Hibbard, 1983; Fig. 1.8). Equivalent Silurian volcanic products are represented in the bimodal volcanic rocks of the Cape St. John Group and the Micmac Lake Group (Skulski et al., 2009; Fig. 1.8).

1.3.3.2. Orogenic gold occurrences and previous work

The Baie Verte Peninsula is a long-lived mining district, and hosts multiple base and precious metal deposits, including volcanogenic massive sulfide (VMS) deposits and orogenic gold occurrences (Fig. 1.8).

The potential for orogenic gold mineralization has been historically recognized in the cover sequences of the ophiolitic rocks of the BVOT, with the small Goldenville deposit representing one of the first gold producers on the island of Newfoundland (Skulski et al., 2009; Fig. 1.8). Exploration in the 1970s and 1980s lead to the discovery of numerous and diverse gold-bearing occurrences, with vein deposits featuring chlorite-carbonate-quartz-pyrite-albite alteration (e.g., Pine Cove, Stog'er Tight; Skulski et al., 2009; Fig. 1.8), replacement-style stratiform vein zones associated with quartz-albite-carbonate alteration of iron formation (e.g., Nugget Pond; Skulski et al., 2009; Fig. 1.8), and classic quartz veins with gold and base metals (e.g., Deer Cove; Skulski et al., 2009; Fig. 1.8).

The tectonostratigraphy of the various rock packages that serve as hosts for orogenic gold on the Baie Verte Peninsula was reported by Skulski et al. (2010), whereas the general geological overview of individual gold deposits was summarized by Evans (2004). Details of the hydrothermal alteration of the deposits, their geochemical variations, and spatial distribution have been the subject of recent studies (Ramezani, 1992; Ramezani et al., 2000; Ybarra, 2019; Pawlukiewicz, 2020).

The Pine Cove deposit has been the main larger-scale orogenic gold operation in Newfoundland since the beginning of mining and production in 2011. A recent study by Ybarra (2019) focussed on a detailed description and geochemical characterization of hydrothermal alteration at Pine Cove. The Pine Cove deposit is hosted in Fe-Ti basalts and gabbro sills and ore mineralization consists of inclusions of Au in fractured pyrite. Mineralized quartz veins were emplaced in areas where strong rheological contrasts were encountered (especially lithological contacts between rigid gabbro sills and the surrounding ductile volcano-sedimentary rocks) during the Silurian (Salinic) orogenic event (Skulski et al., 2010; Kerr and Selby, 2012). Dating using Re-Os in pyrite from Pine Cove by Kerr and Selby (2012) implied model ages of 420±7 Ma.

Alteration zoning is characterized by a proximal sericite-rutile-chlorite-calcite assemblage, followed by an intermediate carbonate-chlorite assemblage and a distal alteration with epidote-titanite-chlorite-calcite (Ybarra, 2019). Gold deposition was provoked by the sulfidation of Fe-rich lithologies, which produced the precipitation of pyrite and the destabilization of the bisulfide complex carrying the gold in the fluid (Skulski et al, 2010; Ybarra, 2019). Ybarra (2019) also defined potential exploration vectors based on spectroscopic and geochemical features of white mica. White mica composition and short-wave infrared (SWIR) spectroscopic features change across the alteration zones. Proximal alteration is characterized by pure muscovite (K-rich, high-Al) with Al-OH SWIR wavelength between 2195 nm and 2202 nm. Intermediate alteration contains paragonitic muscovite (higher Na, high-Al), with Al-OH wavelengths commonly below 2200 nm. Finally, distal alteration assemblages are characterized by a phengitic composition white mica (high Fe+Mg, Al-poor), with Al-OH wavelengths higher than 2205 nm.

The Stog'er Tight deposit is hosted in a shear zone transecting gabbro sills emplaced in a volcanic sequence. As in the case of Pine Cove, gold mineralization occurs as inclusions of native Au in fractured pyrite within quartz veins, or in the immediate wall rock (Ramezani, 1992; Ramezani et al., 2000). Gold deposition also occurred due to sulfidation of Fe-rich wall rocks (Ramezani, 1992; Ramezani et al., 2000). Hydrothermal alteration at Stog'er Tight presents an asymmetric zonation, with the footwall and hanging wall of the gabbroic sill displaying a somewhat different alteration distribution (Ramezani, 1992; Ramezani et al., 2000). These alteration zones, from most distal through most proximal to the mineralization, are: (1) chlorite-calcite; (2) sericite-ankerite (only developed in the hanging wall); (3) chlorite-magnetite (only developed in the footwall); and (4) red albite-pyrite-gold (Ramezani, 1992; Ramezani et al., 2000; Fig. 1.9). Uranium-Pb dating of hydrothermal zircon in gold-bearing veins yielded an age of 420±5 Ma for the mineralization event (Ramezani, 1992; Ramezani et al., 2000), which is in agreement with the recent Re-Os dating in pyrite of 411±7 Ma (Kerr and Selby, 2012).

Additional orogenic gold occurrences include the Argyle deposit, currently in development stages for mining by Anaconda Mining Inc., and located about 10 km west of the town of Ming's Bight. Soil geochemistry and airborne magnetic surveys carried out between 2012 and 2014 highlighted anomalous gold in soils, coincident with magnetic lows (Anaconda Mining Inc.). Further trenching in 2014 and 2015 exposed strongly altered mafic igneous rocks (mainly gabbro) with disseminated pyrite and crosscutting quartz veins. High-grade gold mineralization has been detected in grab and channel samples, with grades up to 3.75 g/t Au. Further exploration since 2016 has included diamond drilling, with over to 5,900 meters of drill core recovered from 61 holes, to define and delineate the ore zone (Anaconda Mining Inc.). Current estimates include an indicated resource of 543,000 t of ore, with an average grade of 2.19 g/t Au, and inferred resources of 517,000 t at 1.82 g/t Au (Anaconda Mining Inc., Technical report NI 43-101, 2018). The Argyle deposit is hosted in a tholeiitic gabbro sill intruding volcanoclastic rocks of the Lower Ordovician Snooks Arm Group. Mineralization occurs as inclusions of native Au in pyrite. Hydrothermal alteration presents a distinct zonation with proximal sericite-quartz-ankerite ± albite-chlorite-rutile-pyrite that grades into an intermediate chlorite-epidote-albite-calcite ± ankerite-rutile-hematite-sericite-pyrite zone and then a distal assemblage consisting of chlorite-calcite-rutile ± epidote-albite (Pawlukiewicz, 2020).

The Animal Pond prospect is located approximately 2 km northeast of the Pine Cove orogenic Au deposit and consists of a 42 m wide zone of altered gabbro with quartz stockwork veining with anomalous Au content (Anaconda Mining Inc.). Hydrothermal alteration in the gabbro is characterized by chlorite and epidote, with minor amounts of pyrite, sericite, carbonate, and albite (Anaconda Mining Inc.). The core of the system is featured by zones of quartz stockwork, with pyrite and gold (Anaconda Mining Inc.). Pervasively altered gabbro around stockwork areas consists of chlorite, epidote, ankerite, albite, pyrite, and gold (Anaconda Mining Inc.). Limited gold mineralization is hosted as inclusions in pyrite occurring in association with quartz veins and breccias (Anaconda Mining Inc.). Unmineralized gabbro shows hydrothermal alteration consisting of chlorite and epidote (Anaconda Mining Inc.).

As previously stated, orogenic gold occurrences in the Baie Verte Peninsula present different mineralization styles and associated hydrothermal alterations. Table 1.2 summarizes the main geological characteristics of the main orogenic gold deposits and occurrences in the Baie Verte peninsula of Newfoundland.

1.4. Research Methodology

This research project contained a strong laboratory component and investigated the application of a broad range of different and innovative methodologies. The rock sample set was both assembled from archived collections, and supplemented by new collection in the field.

1.4.1. Field work

The first field campaign was conducted in June 2017 in the Burin Peninsula area, where several high- and low-sulfidation epithermal occurrences were visited. Rock samples of both outcrops and core (where available) were collected, covering various alteration styles and mineralization. Main sampling was directed towards the well-documented Hickey's Pond high-sulfidation epithermal system and the currently active Heritage low-sulfidation epithermal prospect (Puddle Pond Resources). A suite of additional samples from the Hickey's Pond deposit were provided by the Geological Survey of Newfoundland in 2019, and by Sarah Ferguson, a Memorial graduate student who collected samples and studied various mineral deposits in the Burin Peninsula for her M.Sc. thesis project. Additional samples from the Heritage prospect were obtained from Greg Woodland, who's M.Sc. research is focussed on the Heritage prospect. A total of 12 samples from Hickey's Pond and 30 samples from Heritage were assembled for study.

Samples from the Hope Brook high-sulfidation epithermal deposit (n=14) were obtained from an archived sample collection at Memorial University.

The second field campaign took place in June 2019 in the Baie Verte Peninsula, where various orogenic gold occurrences were studied and sampled. Fieldwork focussed on understanding the regional and local geology of the Baie Verte area, as well as gaining broad familiarity with common stratigraphic units and mineralized host rocks. Ninety samples were collected from four different drill holes that were made accessible by Anaconda Mining. These holes penetrated three different orogenic gold occurrences: the barren Animal Pond prospect, the Au mineralized Argyle prospect, and the Stog'er Tight mine.

1.4.2. Analytical methods

Petrography: Ninety-two polished thin sections were prepared at *Vancouver Petrographics* or pulled from archives of previous studies, and 80 polished mounts (25 mm diameter) were fabricated at Memorial University (CREAIT MAF Facility). These sections were studied by both transmitted and reflected light microscopy in order to characterize the ore, gangue, and alteration minerals, and their assemblages, textures, and paragenesis. Scanning Electron Microscopy (SEM), with an FEI Quanta 650 FEG equipped with Back Scattered Electron (BSE) and Energy Dispersive X-Ray Spectroscopy (EDS) detectors (CREAIT MAF Facility, Memorial University), was used to refine petrological observations and mineral identification at the microscale, as well as for imaging documentation of alteration phases spatially and genetically associated with precious metals.

Bulk-rock and microanalytical mineral spectroscopy: Visible – near-infrared – short-wave infrared spectroscopy (VIS-NIR-SWIR) was performed on hand samples to identify and spectrally characterize alteration at the macroscale. The instrument used was a Terraspec Pro, which consists of a light probe (with an analyzing area of 2 cm of diameter) attached to a spectrometer module, and is equipped with several diffraction gratings and photosensitive arrays that allow the acquisition of signal in the visible (VIS; 390-750 nm), near-infrared (NIR; 750-1300 nm), and short-wave infrared (SWIR; 1300-2500 nm) regions. Raman microspectroscopy on the polished rock mounts was carried out using two instruments: a Renishaw InVia micro-spectrometer equipped with an 830-nm diode laser coupled to an optical microscope, and a Renishaw InVia micro-spectrometer equipped with a 633-nm He-Ne excitation laser (Department of Chemistry, Memorial University). Raman spectra were subsequently processed with the CrystalSleuth software (The RRUFF Project) for background noise and cosmic ray events (CRE) removal.

Mineral chemistry: Electron probe microanalyses (EPMA) using a JEOL JXA 8230 TERRA instrument (CREAIT Terra Facility, Memorial University) were performed on hydrothermal alteration minerals in order to: (i) characterize their chemical composition in major elements; (ii) detect and define any chemical variations; and (iii) report chemical differences between distinct generations or populations of alteration minerals. Secondary ion mass spectrometry (SIMS) analyses were performed on rutile from the orogenic gold examples using a Cameca IMS 4f SIMS instrument (CREAIT MAF Facility, Memorial University).

Mineral diffraction: X-ray diffraction (XRD) analysis of powdered bulk rock and clay mounts was carried out at the Department of Geosciences of Texas Tech University (Lubbock, TX, USA) with a Bruker D8 Advance diffractometer with CuKα radiation, including a LYNXEYE SSD160 detector to enable ultra-fast diffraction measurement and electronic suppression of fluorescence and beta radiations. The interpretation was done using Bruker EVA software and comparison against the PDF4 database issued by the International Centre for Diffraction Data.

Mineral modeling: To achieve a high-precision identification and characterization of XRD spectra, the modelling software Sybilla™ (Drits and Sakharov, 1976) was utilized. The modelling includes a trial-and-error procedure that provides optimal clay mineral structural and probability parameters to obtain the best fit between experimental and calculated patterns and of the intensities of the 00l reflections for each of the clay-fraction phases present in a given sample. For mixed-layer minerals, the number, nature, and stacking sequence of different compositional layers were taken as modifiable values (e.g., Uzarowicz et al., 2011; Šegvić et al., 2016). A semi-quantitative mineral composition of each clay fraction was also estimated from fitted spectra.

1.5. Structure of the Thesis

This thesis consists of five separate Chapters, three of them in manuscript format, plus supplementary Appendices. *Chapter 1* (this Chapter) provides an introduction and background information for the thesis. *Chapters 2* through *4* correspond to individual papers in manuscript form, published, in review, or planned for submission in the near future. Finally, *Chapter 5* provides a summary of the main results and conclusions reported in this thesis.

Chapter 2 is titled “Characteristics and genesis of phyllosilicate hydrothermal assemblages from Neoproterozoic epithermal Au-Ag mineralization of the Avalon Zone of Newfoundland, Canada”, by authors Carlos Arbiol, Graham D. Layne, Giovanni Zanoni, and Branimir Šegvić, and is published in *Applied Clay Science Vol. 202 (2021) Article 105960*. This chapter demonstrates the practicality of the study of hydrothermal phyllosilicates in hydrothermal systems by multiple complementary techniques, to obtain temporal and chemical information on hydrothermal and mineralizing events.

Chapter 3 is titled “Raman spectroscopy coupled with reflectance spectroscopy as a tool for the characterization of key hydrothermal alteration minerals in epithermal Au-Ag systems: utility and implications for mineral exploration”, by authors Carlos Arbiol and Graham D. Layne, and is published in *Applied Spectroscopy Vol. 75, Issue 12 (2021) p. 1475-1496*. This paper focusses on the documentation and interpretation of Raman spectra of the important phyllosilicate minerals found in epithermal systems, supplemented by, and compared to, reflectance spectroscopy.

Chapter 4 is titled “Geochemical signature of hydrothermal rutile related to orogenic gold mineralization in the Baie Verte region of Newfoundland, Canada, and its application to exploration” and it is planned for submission to *Canadian Mineralogist* by authors Carlos Arbiol, Graham D. Layne, and Stephen J. Piercey. This chapter focuses on detailed chemical characterization of rutile in terms of major, minor, and trace elements, from orogenic gold deposits in the Baie Verte (Point Rousse) District of Newfoundland, and how rutile chemistry can be correlated to Au mineralization events.

Chapter 5 is a summary of the findings and conclusions presented in the previous chapters, with discussion of new and remaining questions and suggested directions for future research.

1.6. References

Anaconda Mining Inc. https://www.anacondamining.com (Accessed: 18 October 2019).

Anaconda Mining Inc. Technical Report NI 43-101: Mineral resource and mineral reserve update on the Point Rousse project Baie Verte, Newfoundland and Labrador, Canada. Prepared by: Cullen, M. Pitman, C., Coperland, D., McNeill, P., Slepcev, G. February 22, 2018.

Arribas, A., 1995. Characteristics of high-sulfidation epithermal deposits, and their relation to magmatic fluid. Mineralogical Association of Canada Short Course 23, 419-454.

Bath, A.B., Walshe, J.L., Cloutier, J., Verrall, M., Cleverley, J.S., Pownceby, M.I., Macrae, C.M., Wilson, N.C., Tunjic, J., Nortje, G.S., and Robinson, P. (2013. Biotite and apatite as tools for tracking pathways of oxidized fluids in the Archean East Repulse gold deposit, Australia. Economic Geology 108, 667-690. https://doi.org/10.2113/econgeo.108.4.667

Berger, B.R. and Henley, R.W., 1989. Advances in the understanding of epithermal gold-silver deposits, with special reference to the western United States. Economic Geology Monograph 6, 405-423. https://doi.org/10.5382/Mono.06.32

Bierlein, F.P. & Crowe, D.E., 2000. Phanerozoic Orogenic Lode Gold Deposits. In Gold in 2000 (S.G. Hagemann & P.E. Brown, eds.). Reviews in Economic Geology 13, 103–140. https://doi.org/10.5382/Rev.13.03

Bonham, H.F., 1986. Models for volcanic-hosted epithermal precious metal deposits: A review: Volcanism, hydrothermal systems and related mineralization, 5th International

Volcanological Congress, University of Auckland, Auckland, New Zealand, Proceedings, 13-17.

Castonguay, S., van Staal, C.R., Joyce, N., Skulski, T., and Hibbard, J.P., 2014. Taconic metamorphism preserved in the Baie Verte Peninsula, Newfoundland Appalachians: Geochronological evidence for ophiolite obduction and subduction and exhumation of the leading edge of the Laurentian (Humber) margin during closure of the Taconic Seaway. Geoscience Canada 41, 459-482. https://doi.org/10.12789/geocanj.2014.41.055

Dec, T., O'Brien, S.J., and Knight, I., 1992. Late Precambrian volcaniclastic deposits of the Avalonian Eastport Basin (Newfoundland Appalachians): Petrofacies, detrital clinopyroxene geochemistry and paleotectonic implications. Precambrian Research 59, 243-262. https://doi.org/10.1016/0301-9268(92)90059-W

Drits, V.A. and Sakharov, B.A., 1976. X-ray Structural Analysis of Mixed-layer Minerals. Nauka, Moscow, Russian Federation.

Dubé, B., Dunning, G., Lauzière, K., 1995. Geology of the Hope Brook Mine, Newfoundland, Canada: A preserved Late Proterozoic high-sulfidation epithermal gold deposit and its implications for exploration. Economic Geology 93, 405-436. https://doi.org/10.2113/gsecongeo.93.4.405

Dubé, B. and Gosselin, P., 2007. Greenstone-hosted quartz-carbonate vein deposits. In Goodfellow, W.D., ed.: Mineral Deposits of Canada: A Synthesis of Major Deposit-Types, District Metallogeny, the Evolution of Geological Provinces, and Exploration Methods. Geological Association of Canada, Mineral Deposits Division, Special Publication 5, 49-73.

Dunning, G. and O'Brien, S.J., 1989. Late Proterozoic-Early Paleozoic crust in the Hermitage flexure, Newfoundland Appalachians: U-Pb ages and tectonic significance. Geology 17, 548-551. https://doi.org/10.1130/0091-7613(1989)017<0548:LPEPCI>2.3.CO;2

Einaudi, M.T., Hedenquist, J.W., and Inan, E.E., 2003. Sulfidation state of fluids in active and extinct hydrothermal systems: Transitions from porphyry to epithermal environments. Society of Economic Geologists Special Publication 10, 285-313. https://doi.org/10.5382/SP.10.15

Evans, D.T.W., 2004. Epigenetic gold occurrences, Baie Verte Peninsula (NTS 12H/09, 16 and 12I/01), Newfoundland. Government of Newfoundland and Labrador, Department of Natural Resources, Geological Survey. Mineral Resources Report 11, 157 pp.

Ferguson, S.A., 2017. Late Neoproterozoic epithermal-style Au mineralization of the Burin Peninsula, Newfoundland: U-Pb geochronology and deposit characteristics. Unpublished Master Thesis. Department of Earth Sciences, Memorial University of Newfoundland, 393 pp.

Frimmel, H.E., 2008. Earth’s continental crustal gold endowment. Earth and Planetary Science Letters 267(1), 45-55. https://doi.org/10.1016/j.epsl.2007.11.022

Goldfarb, R.J., Baker, T., Dubé, B., Groves, D.I., Hart, C.J.R., & Gosselin, P., 2005. Distribution, Character, and Genesis of Gold Deposits in Metamorphic Terranes. Economic Geology 100th Anniversary Volume, 407–450. https://doi.org/10.5382/AV100.14

Goldfarb, R.J. and Groves, D.I., 2015. Orogenic Gold: Common or evolving fluid and metal sources through time. Lithos 233, 2-16. https://doi.org/10.1016/j.lithos.2015.07.011

Groves, D.I., Phillips, G.N., Ho, S.E., Houstoun, S.M., and Standing, C.A., 1987. Craton-scale distribution of Archean greenstone gold deposits – predictive capacity of the metamorphic model. Economic Geology 82(8), 2045-2058. https://doi.org/10.2113/gsecongeo.82.8.2045

Groves, D.I., Goldfarb, R.J., Gebre-Mariam, M., Hagemann, S.G., and Robert, F., 1998. Orogenic gold deposits: a proposed classification in the context of their crustal distribution and relationship to other gold deposit types. Ore Geology Reviews 13(1-5), 7-27. https://doi.org/10.1016/S0169-1368(97)00012-7

Groves, D.I., Santosh, M., Deng, J., Wang, Q., Yang, L., and Zhang, L., 2019. A holistic model for the origin of orogenic gold deposits and its implications for exploration. Mineralium Deposita 55, 275-292. https://doi.org/10.1007/s00126-019-00877-5

Hatcher, R.D., 2010. The Appalachian orogen: A brief summary. In Tollo, R.P., Bartholomew, M.J., Hibbard, J.P., and Karabinos, P.M., eds.: From Rodinia to Pangea: The Lithotectonic Record of the Appalachian Region. Geological Society of America Memoir 206, 1-19. https://doi.org/10.1130/2010.1206(01)

Heald, P., Hayba, D.O., and Foley, N.K., 1987. Comparative anatomy of volcanic-hosted epithermal deposits: Acid-sulfate and adularia-sericite types. Economic Geology 82(1), 1-26. https://doi.org/10.2113/gsecongeo.82.1.1

Hedenquist, J.W., 1987. Mineralization associated with volcanic-related hydrothermal systems in the Circum-Pacific basin. Transactions of the Fourth Circum-Pacific Conference on Energy and Mineral Resources Conference, Singapore, American Association of Petroleum Geologists, 513-524.

Hedenquist, J.W., Arribas, A., and Gonzalez-Urien, E., 2000. Exploration for epithermal gold deposits. Economic Geology Reviews 13, 245-277. https://doi.org/10.5382/Rev.13.07

Heinrich, C.A., 2005. The physical and chemical evolution of low- to medium-salinity magmatic fluids at the porphyry to epithermal transition: a thermodynamic study. Mineralium Deposita 39, 864-889. https://doi.org/10.1007/s00126-004-0461-9

Heinrich, C.A., Driesner, T., Stefánsson, A., and Seward, T.M., 2004. Magmatic vapor contraction and the transport of gold from the porphyry environment to epithermal ore deposits. Geology 32(9), 761-764. https://doi.org/10.1130/G20629.1

Hibbard, J., 1983. Geology of the Baie Verte Peninsula, Newfoundland. Mineral Development Division Department of Mines and Energy, Government of Newfoundland and Labrador, Memoir 2, 279 pp.

Hibbard, J.P., van Staal, C.R., and Miller, B.V., 2007. Links among Carolinia, Avalonia, and Ganderia in the Appalachian peri-Gondwanan realm. In Sears, J.W., Harms, T.A., and Evenchick, C.A., eds.: Whence the Mountains? Inquiries into the Evolution of Orogenic Systems. Geological Society of America Special Paper 433, 291-311. https://doi.org/10.1130/2007.2433(14)

Huard, A., 1989. Epithermal alteration and gold mineralization in Late Precambrian volcanic rocks on the northern Burin Peninsula, southeastern Newfoundland, Canada. Unpublished M.Sc. thesis, Memorial University of Newfoundland, St. John's, Newfoundland, 273 pp.

Huard, A. and O'Driscoll, C., 1986. Epithermal gold mineralization in late Precambrian volcanic rocks on the Burin Peninsula. Current Research, Newfoundland Department of Mines and Energy, Mineral Development Division, Report 86-1, 65-78.

Kerr, A. and Selby, A., 2012. The timing of epigenetic gold mineralization on the Baie Verte Peninsula, Newfoundland, Canada: new evidence from Re-Os pyrite geochronology. Mineralium Deposita 47, 325-337. https://doi.org/10.1007/s00126-011-0375-2

Kerrich, R. and Fyfe, W.S., 1981. The gold–carbonate association: source of CO_2, and CO_2 fixation reactions in Archaean lode deposits. Chemical Geology 33(1-4), 265-294. https://doi.org/10.1016/0009-2541(81)90104-2

Kusukabe, M., Komoda, Y., Takano, B., Abiko, T., 2000. Sulfur isotopic effects in the disproportionation reaction of sulfur dioxide in hydrothermal fluids: implications of the $\delta^{34}S$ variations of dissolved bisulfate and elemental sulfur from active crater lakes. Journal of

Volcanology and Geothermal Research 97(1-4), 287-307. https://doi.org/10.1016/S0377-0273(99)00161-4

Lindgren, W., 1933. Mineral Deposits. New York, McGraw-Hill, 4th ed., 930 pp.

McDermott, J.M., Ono, S., Tivey, M.K., Seewald, J.S., Shanks III, W.C., Solow, A.R., 2015. Identification of sulfur sources and isotopic equilibria in submarine hot-springs using multiple sulfur isotopes. Geochimica et Cosmochimica Acta 160, 169-187. https://doi.org/10.1016/j.gca.2015.02.016

Moore, D.M. and Reynolds, R.C., 1997. X-Ray Diffraction and the Identification and Analysis of Clay Minerals, 2nd ed. Oxford University Press.

Mueller, A.G., 1992. Petrogenesis of amphibole–biotite–calcite–plagioclase alteration and laminated gold–silver quartz veins in four Archean shear zones of the Norseman district, Western Australia. Canadian Journal of Earth Sciences 29(3), 388-417. https://doi.org/10.1139/e92-036

O’Brien, S.J., Wardle, R.J., and King, A.F., 1983. The Avalon Zone: A Pan-African terrane in the Appalachian Orogen of Canada. Geological Journal 18(3), 195-222. https://doi.org/10.1002/gj.3350180302

O’Brien, B.H., O’Brien, S.J., and Dunning, G.R., 1991. Silurian cover, Late Precambrian-Early Ordovician basement, and the chronology of Silurian orogenesis in the Hermitage flexure (Newfoundland Appalachians). American Journal of Science 291(8), 760-799. https://doi.org/10.2475/ajs.291.8.760

O’Brien, S.J., Tucker, R.D., and O’Driscoll, C.F., 1994. Neoproterozoic basement-cover relationships and the tectono-magmatic record of the Avalon Zone on the Hermitage Peninsula and environs, Newfoundland: New perspectives in the Appalachian-Caledonian Orogen. Geological Association of Canada Nuna Conference, Program and Abstracts, 21-22.

O'Brien, S.J., O'Brien, B.H., Dunning, G.R., and Tucker, R.D., 1996. Late Neoproterozoic Avalonian and related peri-Gondwanan rocks of the Newfoundland Appalachians. In Nance, R. D., and Thompson, M. D., eds.: Avalonian and Related Peri-Gondwanan Terranes of the Circum–North Atlantic: Boulder, Colorado. Geological Society of America Special Paper 304, 9-28. https://doi.org/10.1130/0-8137-2304-3.9

O'Brien, S.J., King, A.F., and O'Driscoll, C.F., 1997. Late Neoproterozoic geology of the central Avalon Peninsula, Newfoundland, with an overview of mineralization and hydrothermal alteration. Current Research, Newfoundland Department of Mines and Energy, Geological Survey, Report 97-1, 257-282.

O'Brien, S.J., Dubé, B., O'Driscoll, C.F., and Mills, J., 1998. Geological setting of gold mineralization and related hydrothermal alteration in Late Neoproterozoic (Post -640 Ma) Avalonian rocs of Newfoundland, with a review of the coeval gold deposits elsewhere in the Appalachian Avalonian Belt. In Current Research. Newfoundland Department of Mines and Energy, Geological Survey, Report 98-1, 93-124.

O'Brien, S.J., Dubé, B., and O'Driscoll, C.F., 1999. High-sulphidation, epithermal-style hydrothermal systems in Late Neoproterozoic Avalonian rocks on the Burin Peninsula, Newfoundland: Implications for gold exploration. In Current Research. Newfoundland Department of Mines and Energy, Geological Survey, Report 99-1, 275-296.

Pawlukiewicz, M., 2020. Hydrothermal reconstruction and lithogeochemistry of the Argyle Orogenic Gold Deposit, Baie Verte, Newfoundland. Unpublished Master Thesis. Department of Earth Sciences, Memorial University of Newfoundland, 426 pp.

Phillips, G.N. & Powell, R., 2010. Formation of gold deposits: a metamorphic devolatilization model. Journal of Metamorphic Geology 28(6), 689–718. https://doi.org/10.1111/j.1525-1314.2010.00887.x

Pitcairn, I.K., Craw, D., & Teagle, D.A.H., 2014. The gold conveyor belt: Large-scale gold mobility in an active orogen. Ore Geology Reviews 62, 129–142. https://doi.org/10.1016/j.oregeorev.2014.03.006

Pitcairn, I.K., Craw, D., & Teagle, D.A.H., 2015. Metabasalts as sources of metals in orogenic gold deposits. Mineralium Deposita 50, 373–390. https://doi.org/10.1007/s00126-014-0547-y

Ramezani, J., 1992. The geology, geochemistry and U-Pb geochronology of the Stog'er Tight Gold Prospect, Baie Verte Peninsula, Newfoundland. Unpublished Master Thesis. Department of Earth Sciences, Memorial University of Newfoundland, 312 pp.

Ramezani, J., Dunning, G.R., and Wilson, M.R., 2000. Geologic setting, geochemistry of alteration, and U-Pb age of hydrothermal zircon from the Silurian Stog'er Tight gold prospect, Newfoundland Appalachians, Canada. Exploration Mining Geology 9(3-4), 171-188. https://doi.org/10.2113/0090171

Richards, J.P., 2011. Magmatic to hydrothermal metal fluxes in convergent and collided margins. Ore Geology Reviews 40(1), 1-26. https://doi.org/10.1016/j.oregeorev.2011.05.006

Robb, L., 2005. Introduction to ore-forming processes. Blackwell Publishing, 373 pp.

Šegvić, B., Benvenuti, A., Moscariello, A., 2016. Illite-Smectite-Rich Clay Parageneses from Quaternary Tunnel Valley Sediments of the Dutch Southern North Sea – Mineral Origin and Paleoenvironment Implications. Clays and Clay Minerals 64(5), 608-627. https://doi.org/10.1346/000986016820500438

Sillitoe, R.H., 1977. Metallic mineralization affiliated to subaerial volcanism: A review. In: Volcanic processes in ore-genesis: London, Institution of Mining and Metallurgy and Geological Society, 99–116. https://doi.org/10.1144/GSL.SP.1977.007.01.13

Sillitoe, R.H., 2010. Porphyry copper systems. Economic Geology 105(1), 3-41. https://doi.org/10.2113/gsecongeo.105.1.3

Simmons, S.F., White, N.C., and John, D.A., 2005. Geological characteristics of epithermal precious and base metal deposits. Economic Geology 100th Anniversary Volume, 485-522. https://doi.org/10.5382/AV100.16

Skulski, T., Castonguay, S., van Staal, C., Rogers, N., McNicoll, V., Kerr, A., and Escayola, M., 2009. Baie Verte Peninsula: An evolving geological story. Geological Association of Canada, Newfoundland and Labrador Section, Annual Fall Field Trip Guide, 76 pp.

Skulski, T., Castonguay, S., McNicoll, V., van Staal, C., Kidd, W., Rogers, N., Morris, W., Ugalde, H., Slavinski, H., Spicer, W., and Moussallam, Y., 2010. Tectonostratigraphy of the Baie Verte oceanic tract and its ophiolite cover sequence on the Baie Verte Peninsula. Current Research, Newfoundland and Labrador, Department of Natural Resources, Geological Survey, Report 10-1, 315-337.

Sparkes, G.W., 2012. New developments concerning epithermal alteration and related mineralization along the western margin of the Avalon zone, Newfoundland. In Current Research. Newfoundland and Labrador Department of Natural Resources, Geological Survey, Report 12-1, 103-120.

Sparkes, G.W. and Dunning, G.R., 2014. Late Neoproterozoic epithermal alteration and mineralization in the western Avalon zone: A summary of mineralogical investigations and new U/Pb geochronological results. In Current Research. Newfoundland and Labrador Department of Natural Resources, Geological Survey, Report 14-1, 99-128.

Sparkes, G.W., O'Brien, S.J., Dunning, G.R. and Dubé, B., 2005. U–Pb geochronological constraints on the timing of magmatism, epithermal alteration and low-sulphidation gold mineralization, eastern Avalon Zone, Newfoundland. In Current Research. Newfoundland Department of Mines and Energy, Geological Survey, Report 05-1, 115-130.

Sparkes, G.W., Ferguson, S.A., Layne, G.D., Dunning, G.R., O'Brien, S.J., and Langille, A., 2016. The nature and timing of Neoproterozoic high-sulfidation gold mineralization from the Newfoundland Avalon zone: Insights from new U-Pb ages, ore petrography, and spectral data from the Hickey's Pond prospect. In Current Research. Newfoundland and Labrador Department of Natural Resources, Geological Survey, Report 16-1, 91-116.

Tollo, R.P., Corriveau, L., McLelland, J., and Bartholomew, M.J., 2004. Proterozoic tectonic evolution of the Grenville orogen in North America: An introduction. In Tollo, R.P., Corriveau, L., McLelland, J., and Bartholomew, M.J., eds.: Proterozoic tectonic evolution of the Grenville orogen in North America: Boulder, Colorado. Geological Society of America Memoir 197, 1-18. https://doi.org/10.1130/MEM197

Uzarowicz, Ł., Skiba, S., Skiba, M., Šegvić, B., 2011. Clay-Mineral Formation in Soils Developed in the Weathering Zone of Pyrite-Bearing Schists: A Case Study from the Abandoned Pyrite Mine in Wieœciszowice, Lower Silesia, SW Poland. Clays and Clay Minerals 59(6), 581–594. https://doi.org/10.1346/CCMN.2011.0590604

van Staal, C.R. and Barr, S.M., 2012. Lithospheric architecture and tectonic evolution of the Canadian Appalachians and associated Atlantic margin. Chapter 2 in J.A. Percival, F.A. Cook, and R.M. Clowes, eds.: Tectonic Styles in Canada: the LITHOPROBE Perspective. Geological Association of Canada, Special Paper 49, 41-95.

van Staal, C.R., Sullivan, R.W., and Whalen, J.B., 1996. Provenance and tectonic history of the Gander Margin in the Caledonian/Appalachian Orogen: Implications for the origin and assembly of Avalonia. In Nance, R.D., and Thompson, M.D., eds.: Avalonian and related peri-Gondwanan terranes of the Circum-North Atlantic. Geological Society of America Special Papers 304, 347-367. https://doi.org/10.1130/0-8137-2304-3.347

van Staal, C.R., Whalen, J.B., McNicoll, V.J., Pehrsson, S., Lissenberg, C.J., Zagorevski, A., van Breemen, O., and Jenner, G.A., 2007. The Notre Dame arc and the Taconic orogeny in Newfoundland. In Hatcher, R.D., Jr., Carlson, M.P., McBride, J.H., and Martínez Catalán, J.R., eds.: 4-D Framework of Continental Crust. Geological Society of America Memoir 200, 511-552. https://doi.org/10.1130/2007.1200(26)

Waldron, J.W.F. and van Staal, C.R., 2001. Taconian orogeny and the accretion of the Dashwoods block: A peri-Laurentian microcontinent in the Iapetus Ocean. Geological Society of America 29(9), 881-814. https://doi.org/10.1130/0091-7613(2001)029<0811:TOATAO>2.0.CO;2

Walshe, J.L., Halley, S.W., Hall, G.A., and Kitto, P., 2003. Contrasting fluid systems, chemical gradients and controls on large-tonnage, high-grade Au deposits, Eastern Goldfields Province, Yilgarn Craton, Western Australia. In Mineral Exploration and Sustainable Development, 7th Biennial SGA Meeting, Athens, 827–830.

Williams, H., 1979. Appalachian Orogen in Canada. Canadian Journal of Earth Sciences 16(3), 792-807. https://doi.org/10.1139/e79-070

Williams, P.F., Elliott, C.G., and Lafrance, B.D., 1988. Structural geology and mélanges of eastern Notre Dame Bay, Newfoundland. Geological Association of Canada, Annual Meeting, St. John's, Newfoundland, Field Trip Guidebook, Trip B2, 99 pp.

Williams-Jones, A.E. and Heinrich, C.A., 2005. Vapor transport of metals and the formation of magmatic-hydrothermal ore deposits. Economic Geology 100(7), 1287-1312. https://doi.org/10.2113/gsecongeo.100.7.1287Willner, A.P., Gerdes, A., Massonne, H.J., van Staal, C.R., and Zagorevski, A., 2014. Crustal evolution of the northeast Laurentian margin and the peri-Gondwanan microcontinent Ganderia prior to and during closure of the Iapetus

Ocean: Detrital zircon U-Pb and Hf isotope evidence from Newfoundland. Geoscience Canada 41(3), 345-364. https://doi.org/10.12789/geocanj.2014.41.046

Ybarra, S., 2019. Hydrothermal alteration and lithogeochemistry of the Pine Cove orogenic gold deposit, Baie Verte Peninsula, Newfoundland, Canada. Unpublished Master Thesis. Department of Earth Sciences, Memorial University of Newfoundland, 172 pp.

Zhu, Y., An, F., Tan, J., 2011. Geochemistry of hydrothermal gold deposits: A review. Geoscience Frontiers 2(3), 367-374. https://doi.org/10.1016/j.gsf.2011.05.006

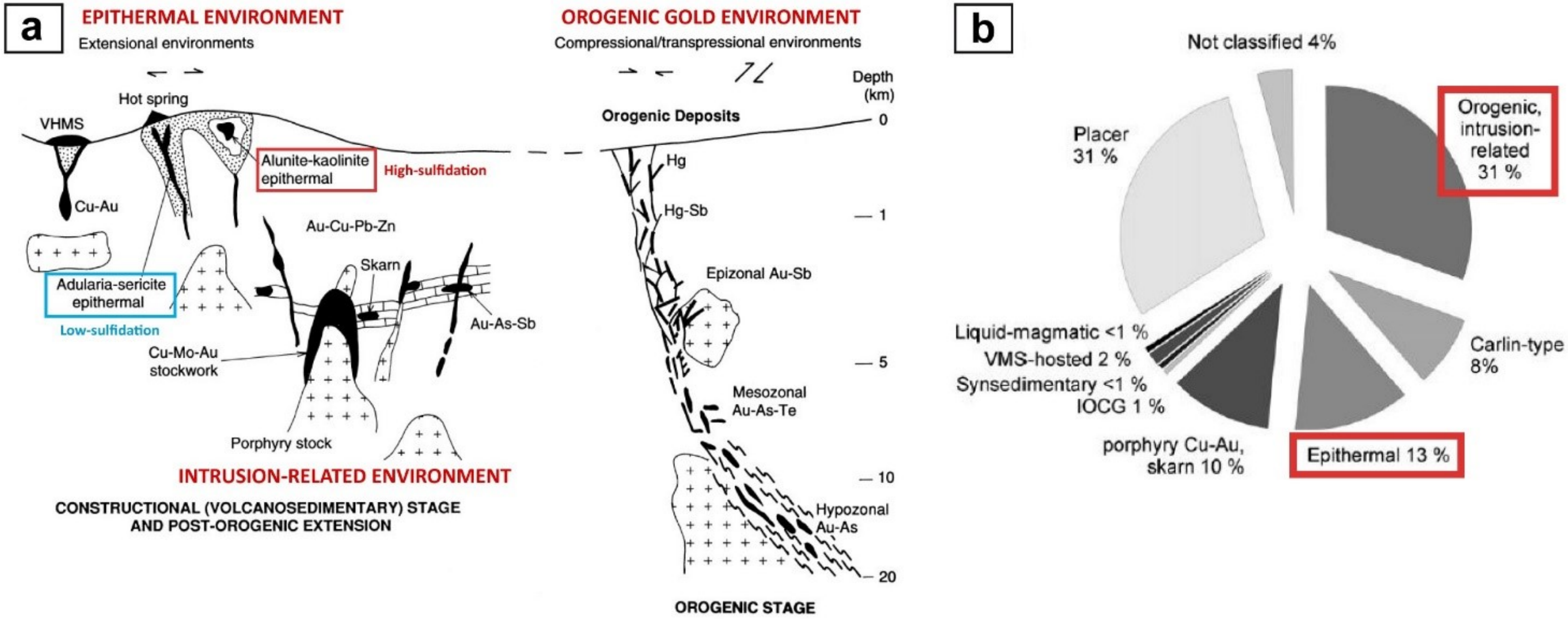

Figure 1.1: (a) Different types of gold deposits and their environment of formation (Modified from Groves et al., 1998); (b) Relative significance of different gold deposits in recent (1984-2006) global production (Modified from Frimmel, 2008). Figure 1.1a corresponds to Figure 2 from Groves et al. (1998). Figure 1.1b corresponds to Figure 2a from Frimmel (2008). Reproduced with permission from Elsevier (Appendix 1).

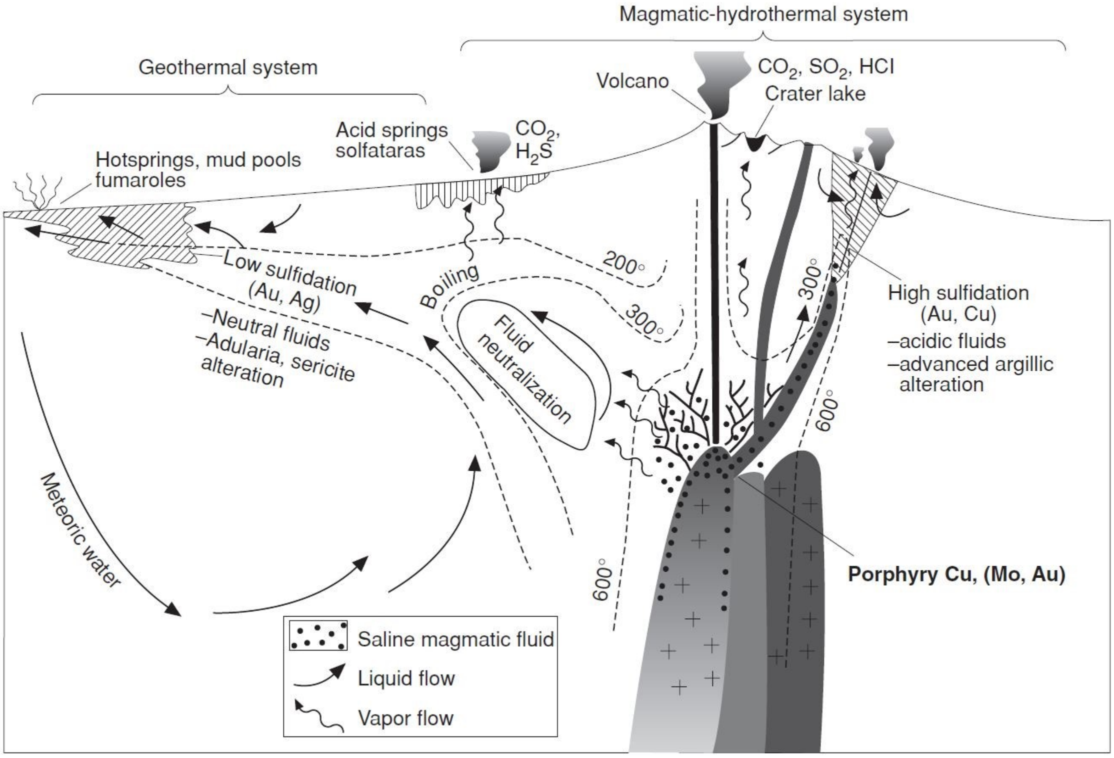

Figure 1.2: Conceptual model for the two types of hydrothermal systems commonly associated to volcanic arcs, and showing the relation between magmatism, fluid paths, and epithermal mineralizations (Robb, 2005). Figure 2.22 from Robb (2005). Reproduced with permission from John Wiley and Sons (Appendix 1).

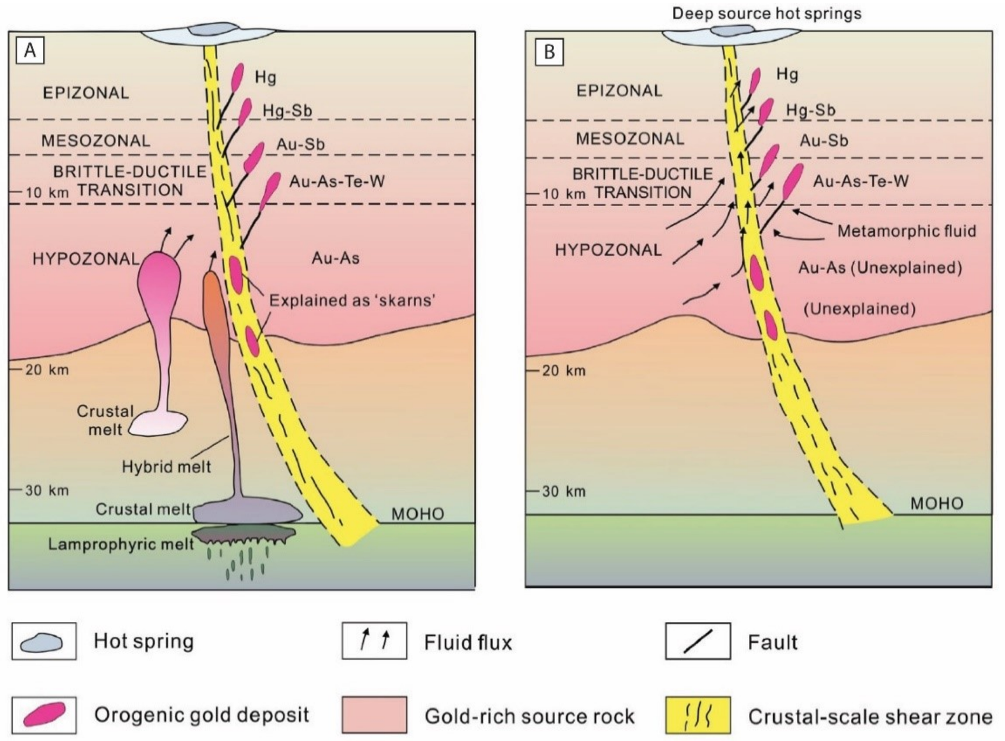

Figure 1.3: Conceptual model for the two major genetic models for orogenic gold mineralization (Modified from Groves et al., 2019). Figure 1 from Groves et al. (2019). Reproduced with permission from Springer Nature (Appendix 1).

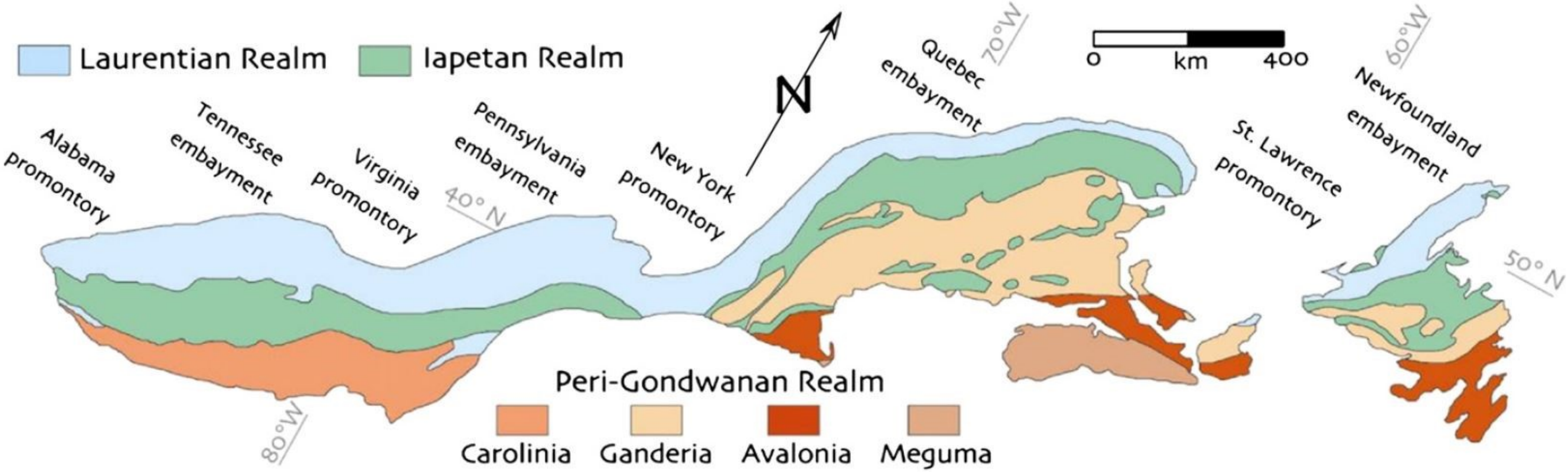

Figure 1.4: Peri-Gondwanan microcontinents of the North America Appalachians (Modified from Hibbard et al., 2007 and Murphy et al., 2010). Figure 2 from Murphy et al. (2010). Reproduced with permission from Elsevier (Appendix 1)..

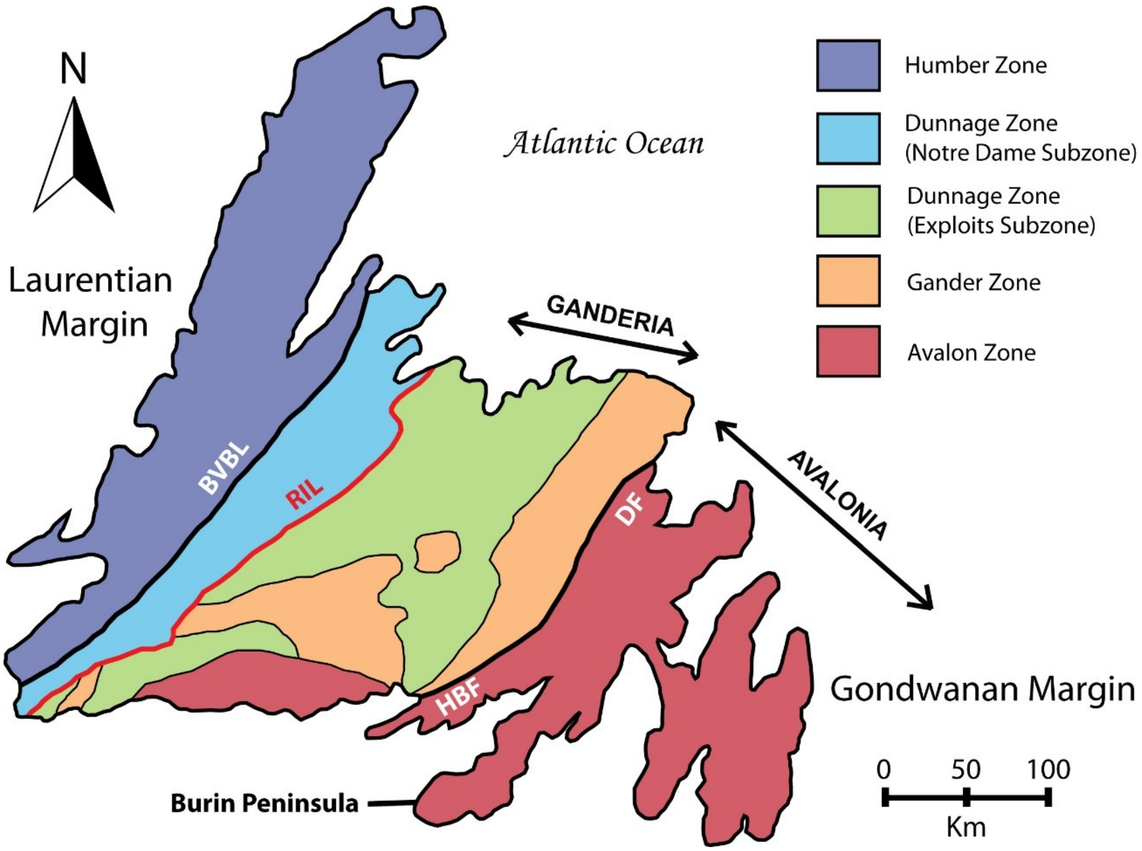

Figure 1.5: Tectonostratigraphic zones of the Appalachian orogen on the island of Newfoundland (Modified from O'Brien et al., 1996 and Skulski et al., 2010). Abbreviations: BVBL: Baie Verte – Brompton Line; HBF: Hermitage Bay fault; DF: Dover fault; RIL: Red Indian Line.

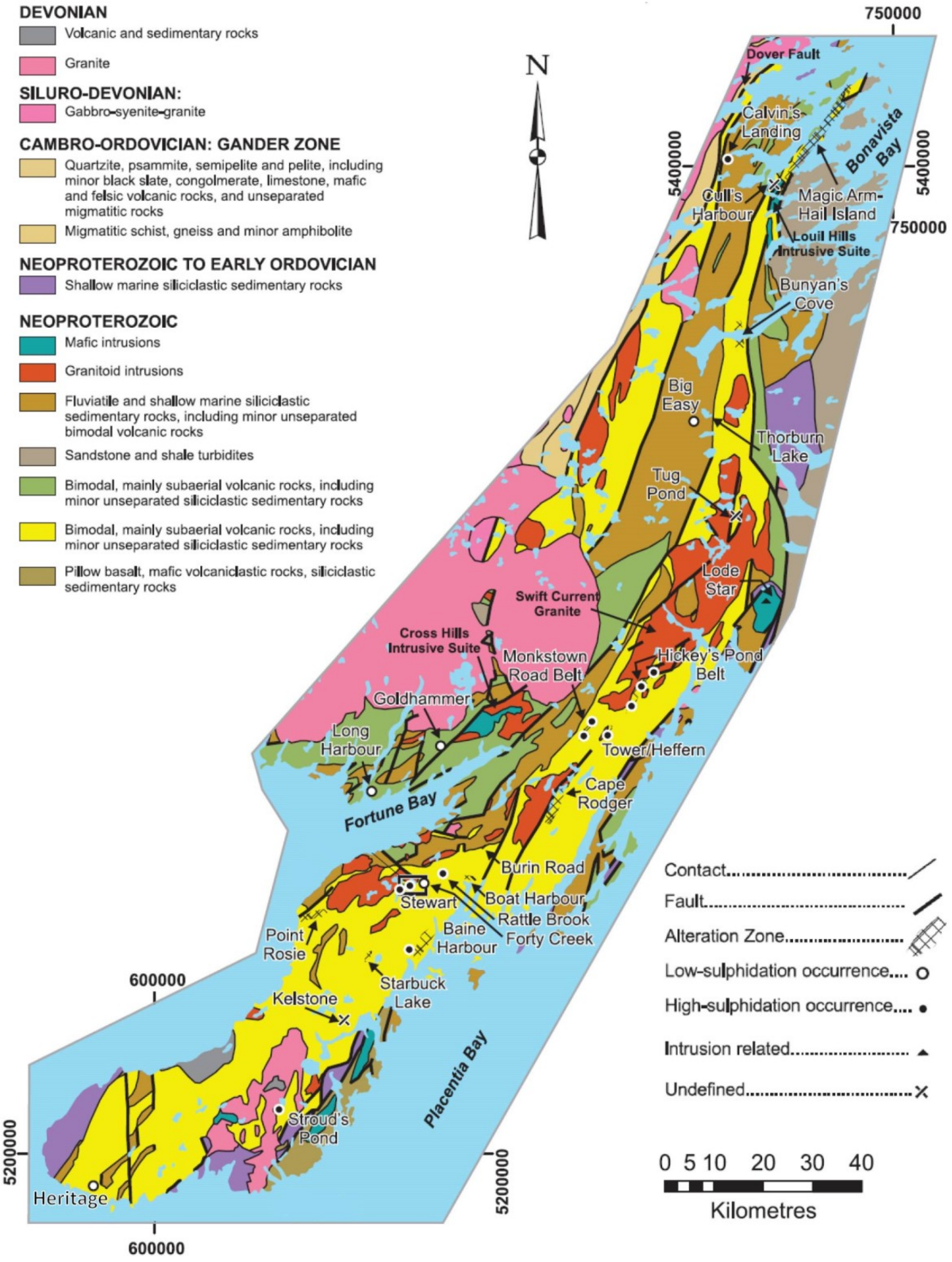

Figure 1.6: Geological map of the Burin Peninsula region (western Avalon Zone, Fig. 1.5) with the location of epithermal occurrences (Modified from Sparkes and Dunning, 2014). Figure 1 from O'Brien et al. (1996). Reproduced with permission from the Government of Newfoundland and Labrador (Appendix 1).

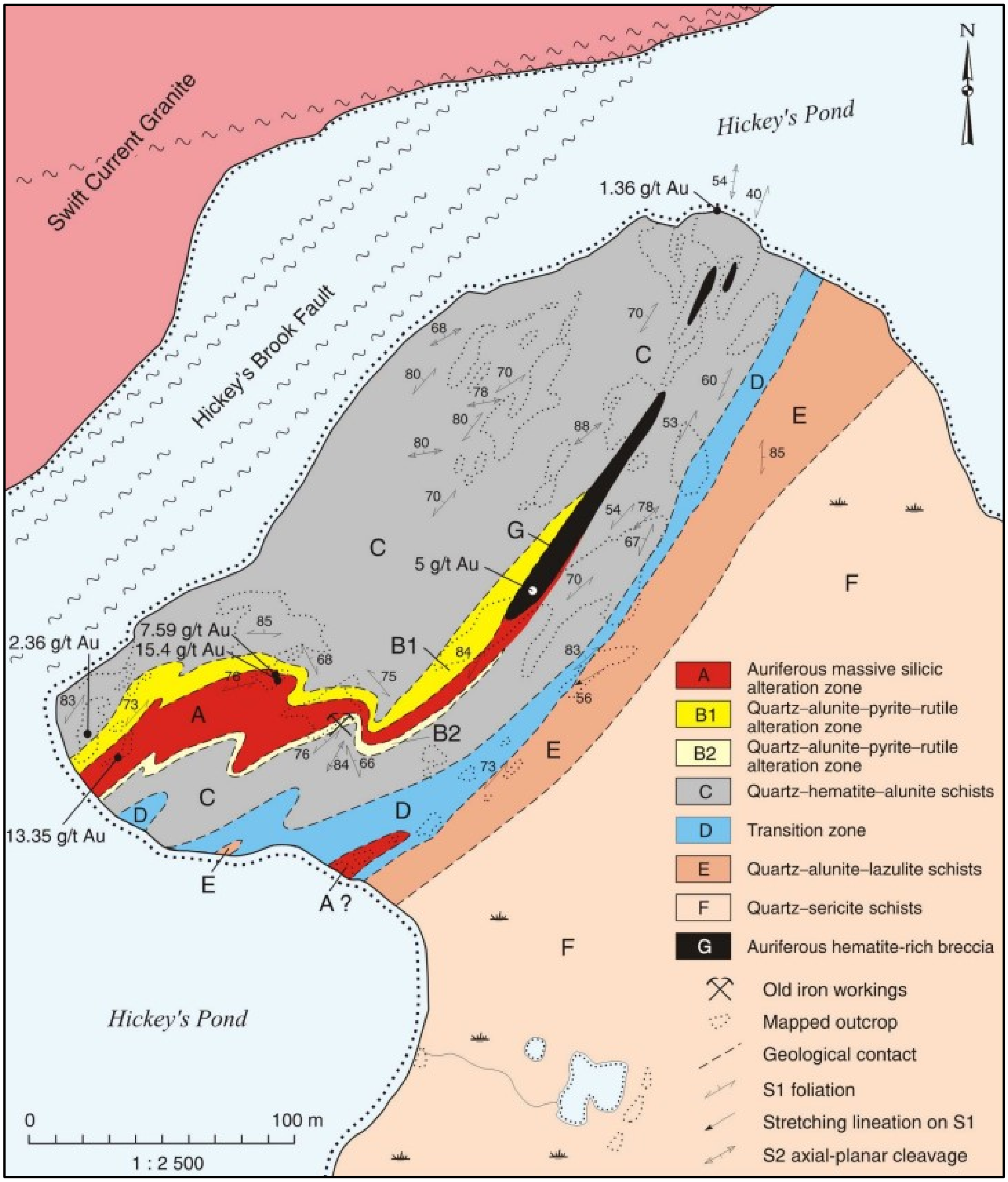

Figure 1.7: Hydrothermal alteration zones at the Hickey's Pond prospect (O'Brien et al., 1999). Figure 4 from O'Brien et al. (1999). Reproduced with permission from the Government of Newfoundland and Labrador (Appendix 1).

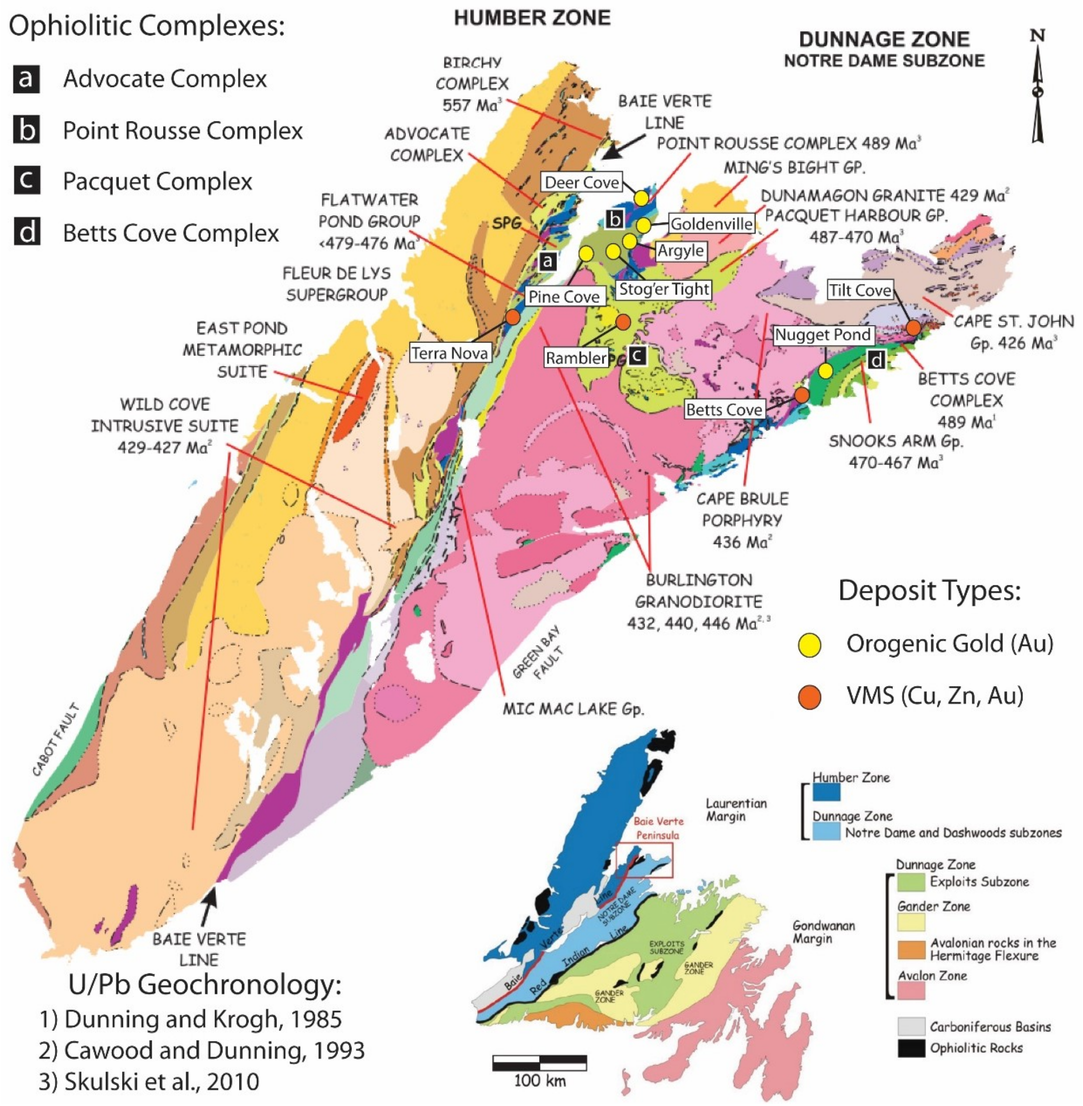

Figure 1.8: Geology of the Baie Verte Peninsula, with location of major mineral occurrences (Modified from Skulski et al., 2010). Figure 1 from Skulski et al (2010). Reproduced with permission from the Government of Newfoundland and Labrador (Appendix 1).

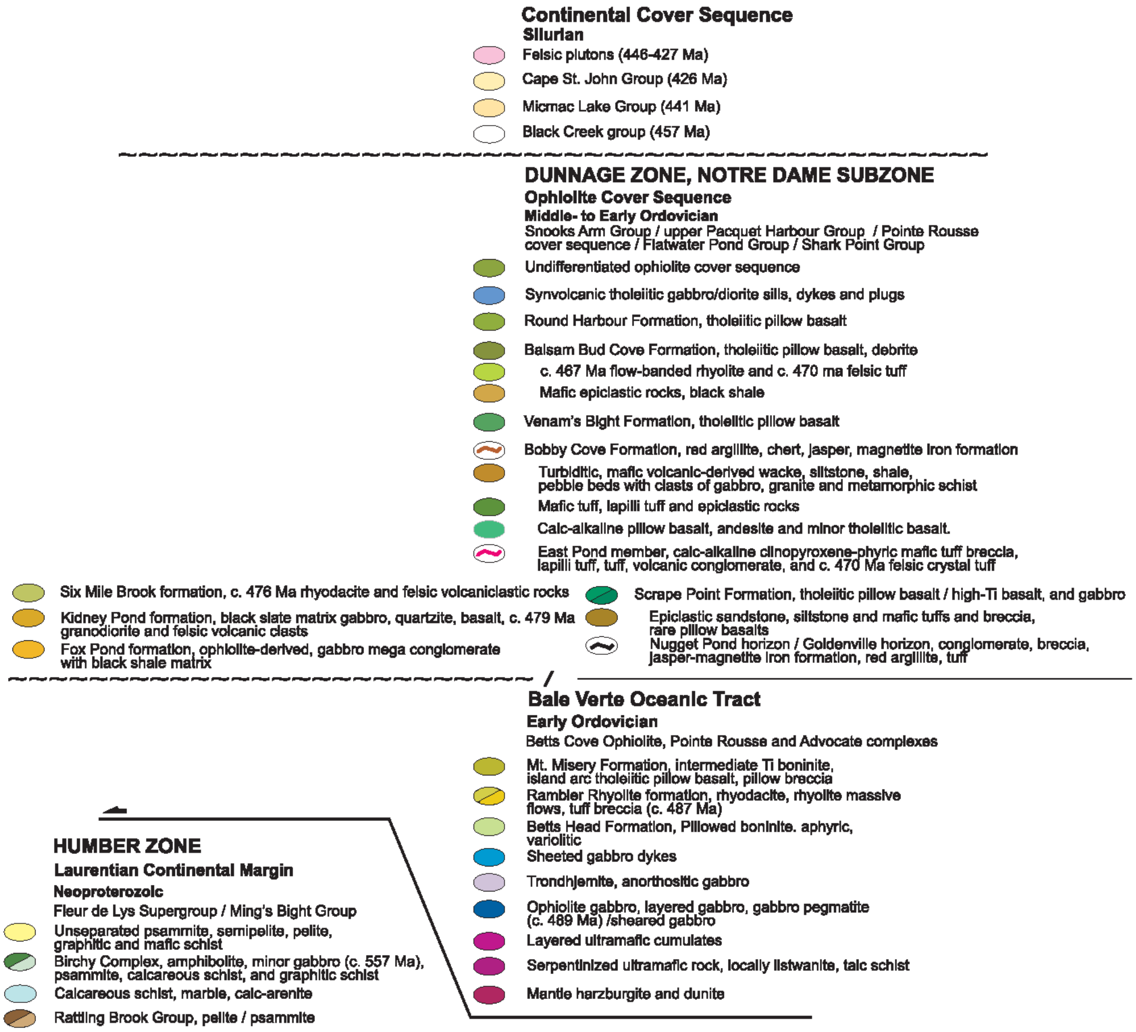

Figure 1.8 (continuation): Legend of the various tectonostratigraphic units from Figure 10 (Skulski et al., 2010). Figure 1 from Skulski et al (2010). Reproduced with permission from the Government of Newfoundland and Labrador (Appendix 1).

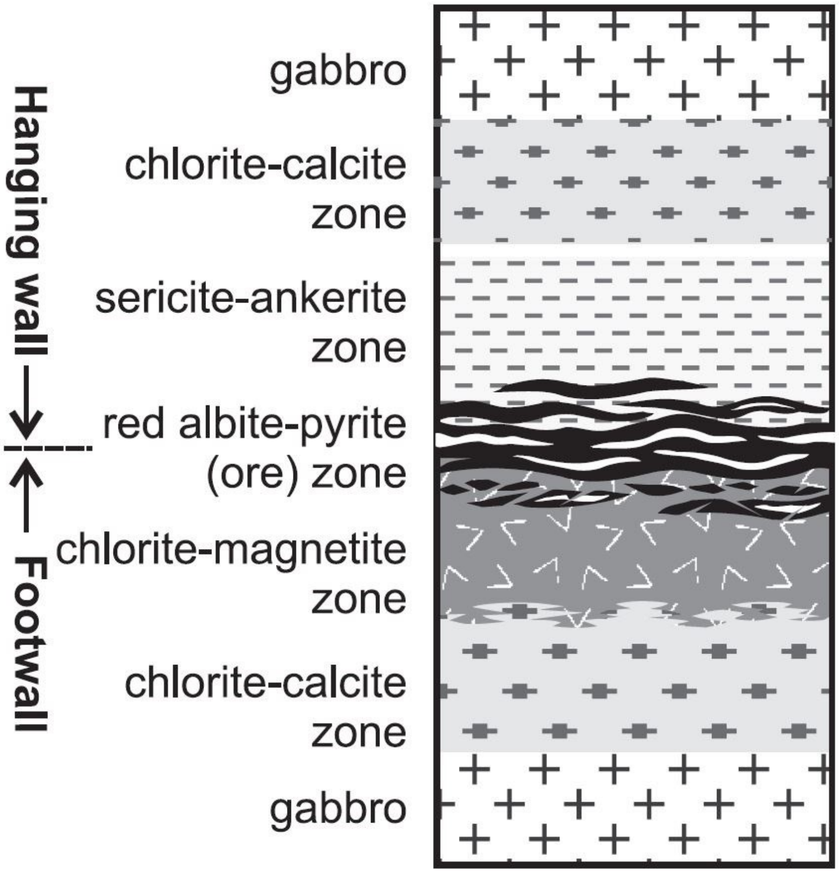

Figure 1.9: Schematic cross-section of the Stog'er Tight showing the distribution of alteration and mineralization (Ramezani et al., 2000). Figure 3b from Ramezani et al (2000). Reproduced with permission from the Canadian Institute of Mining, Metallurgy and Petroleum (Appendix 1).

Table 1.1: Main geological characteristics of selected epithermal deposits in Newfoundland. Data from: Dubé et al., 1995; Sparkes et al., 2016; Ferguson, 2017.

Epithermal Deposits	Hickey's Pond	Hope Brook	Heritage	Big Easy
Deposit Type	High-sulfidation	High-sulfidation	Low-sulfidation	Low-sulfidation
Age	< 586 Ma	578 - 574 Ma	< 574 Ma	585 - 565 Ma
Tonnage	Unkown	11.2 Mt	Aproximately 1 Mt proven	Unkown
Average Grade	Up to 60.4 g/t	2.5 g/t Au	Up to 117 g/t Au Up to 2769 g/t Ag	Up to 6.05 g/t Au Up to 174 g/t Ag
Host Rocks	Felsic and mafic pyroclastics	Sandstones, greywackes, silstones, argillites, conglomerates, and mafic volcaniclastics	Andesitic volcaniclastics	Sandstones and conglomerates
Hydrothermal Alterations	Vuggy silica, advanced argillig alteration, phyllic alteration	Silicic alteration, advanced argillic alteration	Phyllic alteration	Argillic alteration
Alteration Mineralogy	Pyrophyllite, quartz, hematite, alunite, dickite, muscovite, topaz, diaspore, pyrite, sericite	Pyrophyllite, kaolinite, andalusite, sericite, paragonite, diaspore, alunite, quartz, rutile, pyrite	White micas (phengite, illite), quartz, adularia	Illite, smectite, adularia, quartz
Regional Metamorphism	Greenschist facies	Greenschist facies	Greenschist facies	Greenschist facies
Metamorphic Assemblage	Biotite, Chlorite, epidote, pyrite	Biotite, Chlorite, epidote, pyrite	Biotite, Chlorite, epidote, pyrite	Biotite, Chlorite, epidote, pyrite
Mineralization Style	Disseminated and breccia	Disseminated and vein networks	Disseminated and ginguro-style bands	Disseminated and ginguro-style bands
Ore Mineralogy	Tennantite, enargite, bornite, chalcopyrite, covellite, chalcocite, Ag and Au tellurides and selenides, native Au	Chalcopyrite, bornite, tennantite, galena, enargite, native Au, calaverite, aikinite	Chalcopyrite, galena, acanthite, sphalerite, native Ag, hessite, acanthite, naumannite, stibnite	Ag tellurides and selenides, electrum, acanthite, native Ag, freibergite, naumannite
Gangue Mineralogy	Quartz, pyrite, specularite	Quartz, pyrite	Quartz, calcite, calcedony, adularia	Quartz, calcite, calcedony, adularia

Table 1.2: Main geological characteristics of selected orogenic gold deposits in Newfoundland. Data from: Evans, 2004; Ramezani et al., 2000; Kerr and Selby, 2012; Pawlukiewicz, 2020.

Orogenic Gold Deposits	**Pine Cove**	**Stog'er Tight**	**Argyle**
Age	420 ± 7 Ma	420 ± 5 Ma	Unknown
Tonnage	2.3 Mt proven	350,000 t inferred	543,000 t proven 517,000 t inferred
Average Grade	2.76 g/t Au	4.5 g/t Au	2.19 g/t Au 1.82 g/t Au
Host Rocks	Volcanic rocks, gabbro, and hematitic arenites	Gabbroic sill intruding pyroclastic and volcaniclastic rocks	Tholeiitic Gabbro sill intruding volcaniclastic rocks
Hydrothermal Alterations	Silicification, chloritization, oxidation	Silicification, chloritization, seritization, albitization	silicification, chloritization, seritization, oxidation, albitization
Alteration Mineralogy	Iron carbonate (ankerite), albite, pyrite, quartz,	Chlorite, calcite, red albite, pyrite, magnetite, ankerite, sericite	Chlorite, calcite, rutile, epidote, albite, ankerite, hematite, sericite, pyrite
Regional Metamorphism	Greenschist facies	Greenschist facies	Greenschist facies
Metamorphic Assemblage	Biotite, Chlorite, epidote, pyrite	Biotite, Chlorite, epidote, pyrite	Chlorite, epidote, pyrite
Mineralization Style	Veins and disseminated	Disseminated	Veins and disseminated
Ore Mineralogy	Native Au in pyrite	Native Au in pyrite	Native Au in pyrite, Au in calaverite, Au in arsenopyrite, Au in chalcopyrite
Gangue Mineralogy	Pyrite, quartz, carbonates	Pyrite, quartz, carbonates, zircon, albite	Pyrite, quartz, albite, carbonates, rutile, apatite

Chapter 2: Characteristics and genesis of phyllosilicate hydrothermal mineral assemblages from Neoproterozoic epithermal Au-Ag mineralization of the Avalon Zone of Newfoundland, Canada

2.1. Abstract

The Avalon Zone hosts well-preserved examples of high- and low-sulfidation epithermal Au-Ag mineralization and associated phyllosilicate alteration. Using examples from the Hope Brook and Hickey's Pond high-sulfidation systems (HSS) and the Heritage low-sulfidation system (LSS), this study presents new data on the mineralogical and chemical characterization of phyllosilicates associated with epithermal Au-Ag deposits. Electron probe microanalysis and X-ray diffraction studies revealed that the HSS examples contain Fe muscovite $((K_{0.62-0.79}Na_{0.10-0.37}Ca_{0.00-0.01})Al_{1.31-1.72}(Mg_{0.01-0.08}Fe_{0.05-0.19})(Al_{1.00-1.24}Si_{2.76-3.00}O_{10})(OH)_2)$, paragonite $((K_{0.05-0.30}Na_{0.78-1.02}Ca_{0.00-0.01})Al_{1.66-1.84}(Mg_{0.00-0.01}Fe_{0.02-0.04})(Al_{1.01-1.11}Si_{2.89-2.99}O_{10})(OH)_2)$, Al clinochlore $((Mg_{2.42-2.65}Fe_{1.62-1.78})(Si_{2.57-2.69}Al_{1.31-1.43}O_{10})(OH)_8)$, pyrophyllite, kaolinite group minerals, illite-smectite (I-Sme) and chlorite-smectite (C-Sme). Conversely, the LSS examples contain Fe-Mg muscovite $((K_{0.44-0.76}Na_{0.00-0.02}Ca_{0.00-0.01})Al_{1.55-1.82}(Mg_{0.17-0.31}Fe_{0.05-0.12})(Al_{0.55-0.71}Si_{3.29-3.45}O_{10})(OH)_2)$, Al clinochlore $((Mg_{2.17-2.56}Fe_{1.59-2.01})(Si_{2.71-2.92}Al_{1.08-1.29}O_{10})(OH)_8)$, and I-Sme and C-Sme intermediates. Chlorite geothermometry indicated that HSS and LSS assemblages crystallized at average temperatures of 261 ºC and 145 ºC, respectively. Mica and chlorite from HSS and LSS are defined by Tschermak substitution and high-temperature polytypism ($2M_1$ and *IIb,* respectively). In the HSS examples, one or more pulses of hot, acidic fluid reacted with host rocks, generating an envelope of advanced argillic alteration (Fe-Ms, Kln, Pg, Prl) around a vuggy silica core. This is bounded by a zone of argillic alteration (Fe-Ms, Kln), with sericitic/chloritic

alterations (Fe-Ms, Al-Clc) developed in distal parts of the systems. In the LSS, near-neutral hydrothermal fluids led to the formation of broad phyllic/chloritic zones (Fe-Mg Ms and Al-Clc). A low temperature overprint with *1M* mica, *Ib* clinochlore ($(Mg_{2.48-2.74}Fe_{1.58-1.73})(Si_{3.05-3.15}Al_{0.85-0.95}O_{10})(OH)_8$), kaolinite, and Sme-poor I-Sme and C-Sme is attributed to late waning stage hydrothermal activity and/or weathering. A close paragenetic link was established between Fe-Mg muscovite and Ag mineralization at Heritage, as well as between Fe-Mg muscovite and bladed calcite, suggesting boiling as the ore precipitation mechanism. The present study provides guidance on how phyllosilicate assemblages have the potential to discern HSS versus LSS mineralization during early prospection in terranes with limited exposure, and to contribute to the reconstruction of their hydrothermal record.

2.2. Introduction

Epithermal ore deposits that are rich in Au-Ag and accessory base metals represent a significant precious metals source, accounting for about 13% of known Au production (past and present) and resources (Frimmel, 2008; Lipson, 2014; Frimmel, 2018). The volcanic and volcaniclastic rocks of intermediate composition that commonly host epithermal Au-Ag deposits are characterized by widespread hydrothermal alteration associated with the mineralization (Sillitoe, 1993; Arribas, 1995; Hedenquist et al., 2000; Simmons et al., 2005). This alteration is dominated by phyllosilicates (chlorite, mica, pyrophyllite, smectite, mixed-layer clay minerals), sulfates (alunite, natroalunite), carbonates (calcite, ankerite, siderite), oxides (magnetite, hematite), and some other characteristic silicates (adularia, K-feldspar, quartz). The formation of alteration phases records physicochemical variations in the mineralizing fluid across the epithermal environment (i.e., temperature, oxygen fugacity, sulfur fugacity), which can result in distinct alteration zones useful for vectoring towards valuable mineralization during exploration campaigns (White and Hedenquist, 1990; Hedenquist et al., 2000; Hedenquist, 2015). In consequence, through the comprehensive study of the mineralogy, chemistry, and spatial distribution of phyllosilicates, critical information on hydrothermal processes and ore genesis may be gathered, facilitating mineral exploration endeavors (White and Hedenquist, 1995).

The Island of Newfoundland (eastern Canada) is a combination of distinct geological terranes that constitute the northern end of the Appalachian orogen in North America (Williams, 1979). The Avalon Zone is the easternmost of those terranes, and consists of Neoproterozoic - Cambrian volcanic arcs and their related volcano-sedimentary sequences (Williams, 1979). This terrane is endowed with multiple occurrences of well-preserved high- and low-sulfidation Au-Ag epithermal mineralization of Neoproterozoic age, mainly occurring on the Avalon and Burin Peninsulas. Mineral exploration activity in the Burin Peninsula area during the last decades has included epithermal Au-Ag occurrences at Hickey's Pond prospect (high-sulfidation; Huard and O'Driscoll, 1986; O'Brien et al., 1998; 1999), Big Easy prospect (low-sulfidation; Dimmell, 2012; Clarke, 2013), and Heritage prospect (low-sulfidation; Ferguson, 2017). To date, the Hope Brook high-sulfidation epithermal deposit, southwestern Newfoundland, is the only historically mined epithermal deposit in the Avalon Zone (11.2 Mt. of ore at 4.54 g/t Au, total estimated Cu content of 13,500 t; McKenzie, 1986).

Despite the fact that phyllosilicates are a major constituent of alteration in epithermal deposits, and hydrothermal deposits in general, research focusing on detailed characterization of their mineralogy and composition in this context is sparse (Tillick et al., 2001; Yan et al., 2001; Carrillo-Rosúa et al., 2009; Simpson and Mauk, 2011). However, research of this type has potential to contribute to the understanding of the genesis of hydrothermal alteration and hydrothermal ore deposits, with the added prospect of revealing mineralogical and geochemical information useful for improving success in mineral exploration (e.g., porphyry Cu environment: Wilkinson et al., 2015; skarn environment: Zhang et al., 2020). The present study characterizes the morphological, mineralogical, and chemical characteristics of key hydrothermal alteration phyllosilicates in examples of epithermal Au-Ag deposits. It involved integrated use of optical microscopy, X-ray diffractometry (XRD), electron probe microanalysis (EPMA), and scanning electron microscopy coupled with both back-scattered electron imaging (SEM-BSE) and energy dispersive x-ray spectrometry (SEM-EDS). The modeling of XRD patterns was utilized in order to precisely identify the sheet silicates in selected samples.

A principal objective of this study was to characterize the hydrothermal phyllosilicates occurring in exemplar Au-Ag epithermal systems, and to provide insight into how they may be used for reconstruction of hydrothermal events and associated alteration processes. Epithermal systems are herein discussed based on the distinct end-member genetic environments (i.e., high- and low-sulfidation epithermal systems, HSS and LSS hereafter), which allows for a better understanding of their inherent phyllosilicate mineralogy, geochemistry, and the hydrothermal processes responsible for their formation.

2.3. Geological Setting

The Island of Newfoundland (eastern Canada; Fig. 2.1) is an amalgamation of various terranes defining the northern end of the Appalachian orogen in North America (Williams, 1979). One of these terranes, the Avalon Zone, contains Neoproterozoic - Cambrian volcanic arcs and related volcano-sedimentary sequences (Williams, 1979). The Avalon Zone represents the exotic micro-continent of Avalonia, which accreted to the North American part of Laurentia during the Silurian orogeny (O’Brien et al., 1996). Several HSS and LSS of Neoproterozoic age are hosted in the Avalon Zone, as well as in analogous penecontemporaneous terranes in the Carolina Slate Belt in the United States (O'Brien et al., 1998; Hibbard et al., 2007). Epithermal mineralizations of Proterozoic and Paleozoic age are uncommon given their shallow environment of formation (<1 km depth; Lindgren, 1933; Hedenquist, 1987; White and Hedenquist, 1995). There are, however, an increasing number of epithermal deposits documented in terranes of such age, including the Paleoproterozoic Enåsen high-sulfidation epithermal deposit in Sweden (Hallberg, 1994), the Neoproterozoic Hope Brook high-sulfidation epithermal deposit in Newfoundland (Dubé et al., 1995), and the Paleozoic Temora high-sulfidation epithermal deposit in southeastern Australia (Thompson et al., 1986). The recognition of epithermal-style mineralization in Paleozoic and Proterozoic terranes underlines their underestimated preservation potential in the geological record (Sillitoe, 1993; Arribas, 1995; Hedenquist et al., 2000; Simmons et al., 2005). In the Avalon Zone, the most significant epithermal occurrences are located in the Burin Peninsula (southern Newfoundland), with the exception of the Hope Brook high-sulfidation epithermal deposit, which is located in a more south-western part of the island (Fig. 2.1). The Burin Peninsula is characterized by extensive units of arc-related volcanic, volcaniclastic, and sedimentary rocks of Neoproterozoic age, which are intruded by Late Neoproterozoic - Paleozoic magmatic suites (O'Brien et al., 1996; Sparkes and Dunning, 2014; Fig. 2.1). Stratigraphically, the Neoproterozoic rocks of the Burin Peninsula are divided into three main units: the Marystown, the Musgravetown, and the Long Harbour Groups (O'Brien et al., 1996; Fig. 2.1). The 590-570 Ma Marystown Group is the most extensive volcanic unit and consists of felsic and mafic subaerial lava flows and pyroclastic deposits of calc-alkaline and tholeiitic affinity (O'Brien et al., 1996; 1998; 1999). These rocks are affected by widespread lower-greenschist facies regional metamorphism (O'Brien et al., 1996).

High-sulfidation occurrences in the Burin Peninsula region form an extensive belt of advanced argillic alteration, known as the Hickey's Pond - Point Rosie alteration belt (O'Brien et al., 1999). The Hickey's Pond HSS is hosted in highly deformed, greenschist-grade pyroclastic rocks affected by the Hickey's Brook Fault, which has juxtaposed the 577 ± 3 Ma Swift Current Granite with the hydrothermally-altered rocks (O'Brien et al., 1998). The prospect is characterized by a core of massive vuggy silicic alteration containing anomalous Au contents (between 0.3 and 1.1 g/t; O'Brien et al., 1999), locally of up to 60.4 g/t Au (Sparkes et al., 2016). The silicic alteration commonly contains disseminated pyrite, which accommodates inclusions of tennantite, enargite, bornite, chalcopyrite, covellite, chalcocite, Ag and Au tellurides and selenides, native Te, and native Au (Sparkes et al., 2016).

A number of LSS are also recognized in the Burin Peninsula region (Fig. 2.1). These systems are characterized by bladed, crustiform, and colloform textures of both quartz and chalcedony. The Heritage prospect, located near the southern tip of the peninsula (Fig. 2.1), is hosted by andesitic lapilli and crystal tuffs of the Marystown Group. The locus of epithermal mineralization is marked by a broad envelope of pervasive silicification. Within this envelope, hydrothermal quartz breccias of cockade style, and multiple generations of silica-quartz-adularia veining with quartz-chalcedony banding and blading textures dominate the system. The Au-Ag mineralization includes an assemblage of acanthite and native Ag, with chalcopyrite, galena, sphalerite, and minor arsenopyrite (Ferguson, 2017).

The Hope Brook gold deposit is a HSS located within the distal Hermitage Flexure of the Avalon Zone (Fig. 2.1). Geologically the area primarily comprises the Neoproterozoic Cinq Cerf Gneiss, and its coeval cover sequences, namely the Whittle Hill Sandstone and the Third Pond Tuff (O'Brien et al., 1991; Dubé et al., 1995). These units are intruded by the Neoproterozoic Roti Intrusive Suite and the Sill-Dyke Complex, as well as by post-mineralization Paleozoic intrusions (Fig. 2.1a) and their related cover sequences (Dunning and O'Brien, 1989; O'Brien et al., 1991; Dubé et al., 1995; Fig. 2.1a). Intense deformation during the Silurian resulted in the Cinq Cerf fault zone, which has juxtaposed the Whittle Hill Sandstone and the Third Pond Tuff with the La Poile Group cover rocks (Dubé et al., 1995). The deposit is hosted in extensively altered sandstones, greywackes, siltstones, argillites, and conglomerates of Neoproterozoic age belonging to the Whittle Hill Sandstone (Fig. 2.1), as well as mafic volcaniclastic rocks from the Sill-Dyke Complex (Fig. 2.1). The altered rocks are crosscut by both pre- and post-mineralization porphyry dykes (Sill-Dyke Complex; Fig. 2.1), which has allowed precise U-Pb dating of the mineralization event (578-574 Ma; Dubé et al., 1995). The deposit is modified by the Cinq Cerf fault zone (Fig. 2.1), which post-dates the hydrothermal alteration and gold mineralization events (Dubé et al., 1995). As a result, the deposit occurs in the hanging wall of the fault and locally presents strong deformation. Mineralization, in the form of native Au, is contained in an assemblage of pyrite, chalcopyrite, and bornite, with lesser amounts of tennantite and enargite (Dubé et al., 1995).

Finally, Neoproterozoic volcanic rocks hosting the HSS and LSS deposits are intercalated with, and overlain by thick sequences of marine, deltaic and fluviatile siliciclastic rocks whose deposition and subsequent rapid burial played a pivotal role in the preservation of the underlying epithermal systems studied herein (Sparkes et al., 2005). The subsequent Paleozoic deformation gave rise to the Appalachian orogeny, which caused a regional low-grade metamorphic overprint that did not obliterate epithermal systems in the Avalon Zone (O’Brien et al., 1999).

2.4. Materials and Methods

Samples were obtained from both surface locations and archival drill core, with particular focus on the sampling of phyllosilicate-rich material (Table 2.1). Petrographic thin sections were studied by both transmitted and reflected light microscopy in order to pre-characterize the phyllosilicate mineralogy, assemblages, textures, and paragenesis. Scanning electron microscopy

(SEM) was employed to refine petrological observations and mineral identification at the microscale, including semi-quantitative elemental analyses. This was accomplished using both the backscattered electron (BSE) imaging and energy dispersive x-ray spectrometry (EDS) capabilities of the FEI MLA 650FEG instrument in the CREAIT MAF Facility (Memorial University).

X-ray powder diffraction (XRD) was performed on both the global sample and clay particle fraction. For whole-rock measurements, the sample preparation included initial material powdering in an agate mortar. The whole-rock powder was back-loaded into plastic deep-well XRD sample holders (Bruker C79298A3244D88/D89) in order to avoid any preferential orientation of phyllosilicates. To ensure a uniform cation exchange, clay fractions separated by centrifugation were saturated with Mg using a solution of 10 ml of approximately 4 M $MgCl_2$. The solution was then rinsed and cleaned using a Millipore membrane filter and a vacuum filtration device. The resulting clay particles were put into solution again in distilled water. This clay-rich solution was subsequently dropped with a pipette into circular glass wells and left to air dry in order for the clay particles to deposit in a preferential orientation to acquire stronger clay XRD peaks for easier identification and interpretation. The final clay fraction sample was loaded into an XRD sample holder. The measurements were undertaken in air-dried (AD) conditions and after ethylene-glycol (EG) saturation at the Geosciences Clay Laboratory of Texas Tech University using a Bruker D8 Advance diffractometer. This instrument features a horizontal goniometer axis and synchronized rotation of both the X-ray source and detector arms. Measurement consisted of a step scan in the Bragg-Brentano geometry with CuKa radiation (40 kV and 40 mA). Sample mounts were scanned for 1.8 s per 0.02°, from 3° to 70° 2θ and from 3° to 30° 2θ for the whole rock and the clay fraction samples, respectively. XRD spectrum interpretation was accomplished using Bruker EVA's software and comparison against the PDF4 database issued by the International Centre for Diffraction Data (ICDD). X-ray diffraction spectra of clay minerals were interpreted following the recommendations of Moore and Reynolds (1997) and Środoń (2006). Based on diagnostic *hkl* reflections, polytypes of mica (Bailey, 1980a; Grathoff and Moore, 1996), chlorite (Bailey, 1980a), and pyrophyllite (Brindley and Wardle, 1970) were determined. To characterize the mixed-layer clay minerals, type of chlorite, and 10 Å species (phyllosilicate phases with an interlayer space of 10 Å, such as muscovite or illite), clay mineral XRD patterns were modeled using the Sybilla© (Drits and Sakharov, 1976) software package. The modeling included a trial-and-error procedure that provided optimal clay-mineral structural and probability parameters to obtain the best fit between experimental and calculated patterns, and the intensities of the 00l reflections for each of the clay phases present. For mixed-layer minerals, the number, nature, and stacking sequence of different compositional layers were taken as modifiable values (e.g., Uzarowicz et al., 2012; Zanoni et al., 2016). The reference intensity ratio (RIR), which scales all known ratios to a common reference (Zhou et al., 2018), was used to determine the abundances of mineral phases present. The whole set of XRD spectra of the global sample and clay fraction (both air-dry and after ethylene-glycol saturation) is reported in Appendix 2.

Electron probe microanalysis (EPMA) was performed with a JEOL JXA 8230 TERRA Superprobe (JEOL Ltd., Akishima, Japan) equipped for wavelength dispersive x-ray spectrometry, at the CREAIT Terra Facility (Memorial University). Operating parameters included an accelerating voltage of 15 kV, a 20 nA beam current, and a 5 µm beam size. The following elements were analyzed: Si, Al, Ca, K, Na, Mg, Fe, Mn, Cr, Ti, and V. Counting times of 20 to 30 s on peak and 10 s on background on both sides of the peak were used for major and minor elements. For K and Na, the counting times were reduced to 10 s and 5 s on peak and backgrounds, respectively, and these elements were run first in the counting sequence to mitigate the effects of alkali migration under the electron beam. Limits of detection (LOD) were calculated as the minimum concentration required to produce count rates three times higher than the square root of the measured background (i.e., 3σ; 99% degree of confidence at the lower detection limit). Raw data were corrected for matrix effects using the PAP algorithm (Pouchou and Pichoir, 1984, 1985) as implemented by JEOL software. Natural oxides (corundum, spinel, hematite, and rutile) and silicates (albite, orthoclase, anorthite, and wollastonite) were used for calibration. The whole set of EPMA data for white mica and chlorite, as well as instrument parameters and standard materials, is reported in Appendix 3.

For the calculation of mica formulae, all Fe was assumed to be Fe(II). Iron, Mg, and Ti were assumed to be octahedral, while Al was assumed to be tetrahedral up to Si + Al = 4 atoms per 11 oxygens, with the remaining Al assigned to octahedral sites. In the case of chlorite, all Fe was treated as Fe(II) and Al was considered to be tetrahedral up to Si + Al = 4, atoms per 14 oxygens, with the remaining Al assigned to octahedral sites. All transition metals, and Mg, were assumed to be allocated to 2:1 (or brucite) octahedral positions. For the purpose of kaolinite formula calculation, all Fe was assigned as Fe(III).

Two different chlorite geothermometers have been utilized in this contribution: the empirical geothermometer proposed by Kranidiotis and MacLean (1987) and the semi-empirical geothermometer of Inoue et al. (2018). The former is based on the original chlorite geothermometer of Cathelineau and Nieva (1985), and refined by Cathelineau (1988), and takes into account the content of tetrahedral Al in the structure of Al-rich Mg-Fe chlorite, which was found to be temperature dependent according to: $T\ (^{\circ}C) = 106 * Al(IV) + 18$ (Cathelineau and Nieva, 1985). Considering the effect of Fe#, Kranidiotis and MacLean (1987) introduced a correction for Al(IV): $Al(IV)_{corrected} = Al(IV) + 0.7 * Fe/(Fe + Mg)$. The absolute accuracy of empirical geothermometers has been widely questioned (De Caritat et al., 1993; Vidal et al., 2006; 2016) and therefore, the geothermometer of Kranidiotis and MacLean (1987) has been used only tentatively, to explore potential differences between the empirical and semi-empirical chlorite thermometers applied in hydrothermal systems. The semi-empirical chlorite geothermometer of Inoue et al. (2018) is the result of the combination of the semi-empirical geothermometer of Inoue et al. (2009) and the empirical geothermometer of Walshe (1986). Considering the range of available semi-empirical geothermometers (e.g., Bourdelle et al., 2013; Lanari et al., 2014), that of Inoue et al. (2018) has been used herein because it was initially developed for application to hydrothermal systems (Inoue et al., 2009) and assumes equilibrium of quartz-chlorite-water[1]. Ideally, the $Fe^{3+}/\Sigma Fe$ should be obtained or estimated, as required for the application of most semi-empirical geothermometers. However, the Inoue et al. (2018) geothermometer does permit the calculation of chlorite formation temperatures assuming that $\Sigma Fe = Fe^{2+}$, which is the approach followed in this contribution.

2.5. Results

2.5.1. Optical petrography and XRD bulk-rock mineralogy

Globally, quartz and phyllosilicates, particularly fine-grained white mica and chlorite, are the predominant phases in the samples examined. “White mica” refers generally to a group of light-colored phyllosilicate minerals such as muscovite, paragonite, margarite, and celadonite (e.g., Parry et al., 1984).

At Hope Brook, samples from archival drill core show a high intensity of hydrothermal alteration, predominated by fine-grained quartz, fine-grained white mica, chlorite, and pyrite (Fig. 2.2a,b). Kaolinite was observed in one of the studied samples, and it occurs filling pockets in the host rock (Fig. 2.2c).

---

[1] The equilibrium of quartz-chlorite-water is made on the assumption of SiO_2 saturation (activity of quartz equal to 1), which implies that the application of this geothermometer is restricted to quartz-bearing mineral assemblages (Bourdelle, 2021)

At Hickey's Pond, quartz, alunite, Fe-oxides (mainly hematite), and rutile were observed in the massive silicic core of the system (Fig. 2.2d,e,f). Vuggy silica develops locally here, in close association with Fe-oxides. Alunite occurs disseminated throughout the rock (Fig. 2.2d,f). Hematite displays colloform and boxwork textures, indicating that it is the result of the alteration (oxidation) of primary sulfides, most probably pyrite (Pires et al., 2020). An argillic alteration zone characterized by quartz, alunite, pyrite, and rutile surrounds the massive silica core. White mica is occasionally observed, defining the schistosity of the host rocks, and alunite crystals occur concentrated on schistosity planes (Fig. 2.2d,f). Within this alteration zone, a 1 m wide vein is observed, characterized by coarse-grained quartz, specular hematite, alunite, and white mica (Fig. 2.2e). Beyond the argillic alteration zone, an outer hydrothermal alteration zone is characterized by alunite and hematite disseminated in quartz-mica schists.

The mineralogy at Heritage is dominated by quartz and fine-grained white mica and chlorite (Fig. 2.2g,h,i), which are indicative of silicification and associated phyllic/chloritic hydrothermal alteration. Calcite-bearing veins are a common feature. Sulfide mineralization is characterized mainly by pyrite, with minor sphalerite, galena, and chalcopyrite, in close association with phyllosilicates, particularly white mica.

The global fraction XRD mineralogy and mineral proportions of all studied samples are presented in Table 2.2. As a whole, samples are rich in quartz (27.8-98.8 %), with pyrite (up to 25.5 %) as the main sulfide, and white mica (up to 32%) and chlorite (up to 55 %) as the main phyllosilicates. However, clear mineralogical differences are apparent between the HSS and LSS. The XRD patterns of the Hope Brook and Hickey's Pond HSS show a ubiquitous presence of quartz, rutile, muscovite (0.9-32.0 %), and kaolinite (0.2-2.5 %), with the sporadic occurrence of natroalunite, hematite, chlorite, and pyrophyllite (10 % in sample HB-9). In addition to muscovite, paragonite is fairly abundant at Hope Brook (up to 20.5 %). The greater amount of pyrite at Hope

Brook (up to 25.5 %) in comparison to Hickey's Pond (2 % in sample HP-3) is related to the higher overall sulfide content of analyzed samples in the former HSS. The high acidity and intensity of alteration typical of HSS is reflected by the prevalent occurrence of quartz and rutile, which are the only non-phyllosilicate minerals routinely present in substantial quantity at Hope Brook. Conversely, the mineralogy of the Heritage LSS is characterized by the dominance of muscovite and chlorite, with some minor illite-smectite and chlorite-smectite, as well as the occurrence of kaolinite in a single sample (HE-23-3R). In addition, K-feldspar (likely orthoclase) is prevalent in most samples (1-13 %, as is the low-temperature hydrothermally-formed potassic feldspar adularia (up to 30%). Given the neutral nature of hydrothermal fluids in LSS (Hedenquist et al., 2000), carbonates are widely present at Heritage. The absence of alunite, natroalunite, and pyrophyllite at Heritage is expected, since those phases are commonly formed by hot, oxidizing, and very acidic hydrothermal fluids more likely associated with HSS (Arribas, 1995; Simmons et al., 2005).

2.5.2. XRD clay fraction mineralogy and electron microbeam (SEM, EPMA) characterization

Hydrothermally-altered rocks analyzed in this study are characterized by phyllosilicate assemblages consisting of variable proportions of 10 Å minerals, chlorite-group minerals, kaolinite group minerals, pyrophyllite, as well as mixed-layer illite-smectite, paragonite-smectite, and chlorite-smectite.

Exemplar XRD spectra for the deposits studied are presented in Figure 2.3. Mineral proportions of various phyllosilicates were calculated and are reported in Table 2.2. Table 2.3 compiles the Sybilla© parameters of modeled phyllosilicates and mixed-layered phases. In most samples, white mica, mixed-layer intermediates, and chlorite are the main phases determined by XRD and further refined by Sybilla© modeling (Fig. 2.3). There is, however, a clear distinction in phyllosilicate distribution between the HSS and LSS. Specifically, the HSS deposits (i.e., Hope Brook and Hickey's Pond) are characterized by the presence of kaolinite group minerals and pyrophyllite (Table 2.2), while these phases were not detected in the LSS example (Heritage; Table 2.2).

Paragonite with minor smectite interlayers is characteristic of Hope Brook, commonly occurring associated with white mica and illite-smectite (Table 2.3). Chlorite and chlorite-smectite are present both in Hope Brook (HSS) and Heritage (LSS), but were not detected in Hickey's Pond (HSS) (Table 2.3).

A detailed description of phyllosilicate mineralogy and composition from all three deposits is provided in the text below – based on XRD identification and spectral modeling (Fig. 2.3; Table 2.3), as well as the microbeam imaging of phyllosilicate morphology (SEM; Figs. 2.4 and 2.5) and elemental determinations (EMPA; Tables 2.4, 2.5, and 2.6; Figs. 2.6 and 2.7).

2.5.2.1. 10 Å phases

Micaceous 10 Å phases were defined by their characteristic d_{001} basal peaks between 9.5 Å and 10.0 Å. Consistent with such practice is the notation on the ordered mixed-layer I-Sme with less than 5% of smectite, which in this contribution has been considered as pure mica (Table 2.3). Dioctahedral white mica from the muscovite-paragonite series, marked by Na^+ and K^+ substitution in the interlayer space, has been identified in all deposits (Fig. 2.3; Table 2.3). Muscovite occurs in all three deposits, while paragonite occurs solely at Hope Brook. Expandable weathering products, such as smectite-poor I-Sme and/or P-Sme (Table 2.3), were regularly observed in association with mica. Distinction between muscovite and paragonite is based on their d_{001} at 9.8-10.0 Å and 9.5-9.6 Å, respectively (Fig. 2.3a, b).

Mica from these samples belong to the *$2M_1$* polytype, as evidenced by the characteristics *hkl* reflections at 4.29 Å, 4.09 Å, 3.88 Å, 3.72 Å, 3.49 Å, 3.20 Å, 2.98 Å, 2.86 Å, and 2.79 Å. In some samples, the *$2M_1$* polytype is accompanied by other diagnostic peaks, likely related to the *$2M_2$* polytype (Brigatti et al., 2005) and indicative of increased Mg and Fe contents along the Tschermak substitution vector (e.g., phengitic muscovite, celadonite), which results in a reduced dimensional difference between the larger *trans*-oriented *M1* site and smaller *cis*-oriented *M2* octahedral site (Brigatti et al., 2005). In several samples where spectral modeling indicated the presence of I-Sme (Table 2.3), the *1M* mica polytype also occurs (Table 2.2).

Based on the occupancy of the octahedral layer, mica analyzed in this contribution lies within the muscovite-(celadonite) series of Tischendorf et al. (2007) (Fig. 2.6a). Subsidiary nomenclature of K-rich true mica herein will follow the recommendations of Tischendorf et al. (2007) whereby element prefixes are used to denote impure mica varieties (e.g., "Fe-bearing muscovite"). The SEM and EPMA investigation identified four different morphological and compositional varieties of mica: (1) Paragonite (-Muscovite) at Hope Brook; (2) Fe muscovite at Hope Brook; (3) Fe muscovite at Hickey's Pond; and (4) Fe-Mg muscovite at Heritage. These phases are documented by means of BSE imagery (Fig. 2.4) and phase composition data (Table 2.4; Fig. 2.6).

(1) Paragonite (-Muscovite) at Hope Brook

At Hope Brook, mica readily forms thick platy crystals of up to 60 µm in size that are oriented following the schistosity/foliation of the host rock (Fig. 2.4a,b,c). In some areas, mica is intergrown with chlorite, forming mica-chlorite stacks (Fig. 2.4b). Mica crystals are compositionally zoned (Fig. 2.4c), with a core enriched in Na (6.60-8.64 wt.% Na_2O, 0.78-1.02 Na a.p.f.u.; Table 2.4) and minor amounts of K (0.63-3.83 wt.% K_2O, 0.05-0.30 K a.p.f.u.; Table 2.4) and Fe (0.38-0.88 wt.% FeO, 0.02-0.04 Fe a.p.f.u.; Table 2.4), which is consistent with paragonite

(Fig. 2.6b). Characterization as paragonite is also consistent with the XRD analyses (Fig. 2.3). The outer zones of mica crystals show an enrichment in K (7.66-9.94 wt.% K_2O, 0.62-0.77 K a.p.f.u.; Table 2.4), with minor amounts of Na (1.31-3.00 wt.% Na_2O, 0.15-0.37 Na a.p.f.u.; Table 2.4) and Fe (1.40-2.53 wt.% FeO, 0.07-0.13 Fe a.p.f.u.; Table 2.4), consistent with a muscovitic composition (Fig. 2.6b). In both cases, the Ca content is insignificant (<0.01 Ca a.p.f.u.; Table 2.4; Fig. 2.6b), and the (Na + K + Ca) is generally <1 a.p.f.u. (Table 2.4), indicating that the interlayer exchange is mainly controlled by K^+ and Na^+ substitutions. Aluminum is enriched in paragonite (39.00-40.74 wt.% Al_2O_3, 2.77-2.92 Al a.p.f.u.) compared to muscovite (Table 2.4), and Si is within the same range in both paragonite (47.65-49.13 wt.% SiO_2, 2.89-2.99 Si a.p.f.u.; Table 2.4; Fig. 2.6c) and muscovite (Table 2.4).

(2) Fe muscovite at Hope Brook

Muscovite referred above and found in association with paragonite at Hope Brook deposit is classified as Fe muscovite (Table 2.4; Fig. 2.6a). It is characterized by comparatively lower Al_2O_3 content (33.82-37.60 wt.% Al_2O_3, 2.40-2.73 Al a.p.f.u.; Table 2.4) while SiO_2 is in the same range as paragonite (45.72-49.31 wt.% SiO_2, 2.86-3.00 Si a.p.f.u.; Table 2.4; Fig. 2.6c). The octahedral Mg content is somewhat lower than in the phase of analogue composition reported in the Hickey's Pond HSS (Table 2.4; Fig. 2.6c, d).

(3) Fe muscovite at Hickey's Pond

Iron muscovite in Hickey's Pond is sparse, but occurs within hydrothermal veins along with alunite, quartz, hematite, and rutile. Iron muscovite is coarse-grained, of up to 500 µm, and forms veinlets oriented within the broader vein geometry (Fig. 2.4d). Iron muscovite shows higher contents of Mg and Fe than paragonite at Hope Brook (Fig. 2.6d). This latter observation indicates the role of the Tschermak substitution, where Fe muscovite represents a higher degree of substitution of Al(IV) + (Al + Fe^{3+})(VI) by (Fe^{2+} + Mg) + Si than paragonite (Fig. 2.6c). The composition of Fe muscovite at Hickey's Pond is, as expected, predominated by Si, Al, and K, with minor amounts of Fe and Na. Potassium is the main interlayer cation (9.55-10.19 wt.% K_2O, 0.74-0.79 K a.p.f.u.; Table 2.4; Fig. 2.6b), with 0.86-1.38 wt.% Na_2O (0.10-0.16 Na a.p.f.u.; Table 2.4; Fig. 2.6b) and 0.01-0.10 wt.% CaO (0.0007-0.0065 Ca a.p.f.u.; Table 2.4; Fig. 2.6b).

(4) Fe-Mg muscovite at Heritage

At the Heritage LSS, Fe-Mg muscovite generally occurs in the form of fine-grained agglomerations, occasionally associated with chlorite (Fig. 2.4e). The space between bladed calcite crystals (formed during boiling of hydrothermal fluids; Etoh et al., 2002), is also commonly occupied by fine-grained Fe-Mg muscovite (Fig. 2.4f). Further, a close spatial relationship has been observed between Fe-Mg muscovite and sulfides, including Ag-sulfides (i.e., acanthite; Fig. 2.4g). The interlayer space of Fe-Mg muscovite is dominated by K^+ (8.47-9.68 wt.% K_2O, 0.67-0.76 K a.p.f.u.; Table 2.4; Fig. 2.6b) with minor amounts of Na^+ (0.03-0.19 wt.% Na_2O, 0.003-0.023 Na a.p.f.u.; Table 2.4; Fig. 2.6b) and Ca^+ (0.02-0.21 wt.% CaO, 0.001-0.014 Ca a.p.f.u.; Table 2.4; Fig. 2.6b). In addition, SiO_2 and MgO contents are high (53.03-56.01 wt.% SiO_2, 3.29-3.45 Si a.p.f.u.; 1.80-3.23 wt.% MgO; 0.17-0.31 Mg a.p.f.u.; Table 2.4) while Al_2O_3 content is lower (29.12-32.44 wt.% Al_2O_3, 2.11-2.37 Al a.p.f.u.; Table 2.4) and FeO content is generally > 1 wt.% (0.92-2.29 wt.% FeO, 0.05-0.12 Fe a.p.f.u.; Table 2.4; Fig. 2.6d). The reported Si, Mg, and Al contents are all consistent with the Tschermak (phengitic) substitution (Fig. 2.6c), and define a muscovite composition quite distinct from the HSS deposits, and lying between the "Mus s.s." and "Mg muscovite" fields of Tischendorf et al. (2007) (Fig. 2.6a).

2.5.2.2. Mixed-layer illite-smectite

Expandable mixed-layer illite-smectite with a substantial Sme content was first recognized following glycolation of samples, as indicated by the migration of the I-Sme 001 basal peak from

9.8-10.0 Å to 10.3-10.4 Å (criteria after Reynolds and Hower, 1970). The precise nature of I-Sme species was determined by XRD spectra modeling, which resulted in the characterization of one ordered (R1 I-Sme) and one disordered (R0 I-Sme) mixed-layer species at Hickey's Pond (Table 2.3). Both phases were defined by their 001 basal peak at 10.1 Å, having slightly different Sme abundances (Table 2.3). The presence of illite-smectite with such a low smectite content at Hickey's Pond likely stems from surficial weathering of mica (e.g., Rafiei and Kennedy, 2019). In the case of Heritage, two distinct disordered R0 I-Sme were documented (Table 2.3), one with the 001 basal peak at 10.0 Å and the other one with a 001 peak at ~13.5 Å.

2.5.2.3. Chlorite

X-ray diffraction peaks of chlorite, though somewhat overlapped by those of kaolinite, were distinguishable as basal peaks at ~14.1 Å, ~7.1 Å, ~4.7 Å, and ~3.5 Å (Fig. 2.3).

At Heritage, chlorite is defined by a strong d_{001} peak at ~14.10 Å and d_{002} at ~7.07 Å (Fig. 2.3e,f). At Hope Brook chlorite presents two distinct XRD patterns, with one showing peak positions analogous to the Heritage chlorite, and the other characterized by a shift of the d_{002} peak to ~6.96 Å (Fig. 2.3a,b). Chlorite from the Heritage LSS has a relatively uniform 001/002 intensity ratio of ~0.3, while chlorite from the Hope Brook HSS shows a significantly lower 001/002 ratio of ~0.08. The peak positions of the chlorite 00l reflections, as well as the intensity ratios of its odd and even peaks, are generally consistent with classification as clinochlore (001/002 ~0.3) at Heritage and Fe-rich clinochlore (001/002 ~0.08) at Hope Brook. However, the reduced *d* values of the Hope Brook chlorite (Fig. 2.3) are likely related to tetrahedral substitution of Si by Al, which concomitantly decreases both the d_{001} and the size of the diffraction domain (Walshe, 1986). This provides an alternative explanation for lower intensity ratios (001/002) in Hope Brook chlorite, as the effect of Fe scattering of X-rays is exercised over a comparatively smaller unit cell. This reasoning is line with XRD spectral modeling where the species utilized to model chlorite reflections feature a similar content of octahedral Fe (~1 a.p.f.u.; Table 2.3). The R1 C-Sme, with ~5% of smectite layers, has been identified in sample HB-14 (Table 2.3), consistent with cycles of post peak-hydrothermal activity as described by Sugimori et al. (2008).

In this contribution, chlorite polytypes *IIb* and *Ib* ($\beta = 97^{\circ}$ or 90°) were determined based on the diagnostic reflections recommended by Bailey (1980a). Both polytypes were present in sample HB-14 (Table 2.2), the only sample with sufficient amounts of chlorite to allow for polytype determination. Polytype *IIb* is the high-temperature chlorite polytype stable at temperatures above 200 ºC (Walker, 1993), and observed occurring in equilibrium with $2M_1$ mica (Walker, 1993) as is the case in this study. Conversely, polytype *Ib* is usually observed forming at comparatively lower temperatures (Hayes, 1970) and, as in the case of *1M* mica, is often attributed to low-temperature hydrothermal or weathering processes. Analogous to mica, the nomenclature of chlorite is further refined by introducing element prefixes (e.g., Al clinochlore stands for Al-rich clinochlore). The microbeam characterization of hydrothermal chlorite revealed the presence of three distinct textural and chemical varieties of chlorite: (1) Al clinochlore at Hope Brook; (2) Al-Mn clinochlore at Heritage; and (3) Clinochlore at Heritage (Figs. 2.4 and 2.7; Table 2.5).

(1) Al clinochlore at Hope Brook

Chlorite at Hope Brook occurs as coarse crystals (up to 70 µm) disseminated throughout the wall rock. It is also found associated with mica in the form of veins filled by mica-chlorite stacks (Fig. 2.4a,b). No chemical zonation was observed in high contrast BSE images (Fig. 2.4b). Chemically, chlorite is Al-rich, with up to 24.22 wt.% Al_2O_3 (2.97 Al a.p.f.u.; Table 2.5) and up to 26.32 wt.% SiO_2 (2.69 Si a.p.f.u.; Table 2.5). Magnesium and Fe contents were determined to be between 15.56 and 17.40 wt.% MgO (2.42-2.65 Mg a.p.f.u.) and between 18.79 and 20.30 wt.% FeO (1.62-1.78 Fe a.p.f.u.), respectively (Table 2.5), with Fe# values between 0.38 and 0.42.

Manganese content is consistently below 0.4 wt.% MnO (<0.04 Mn a.p.f.u.; Table 2.5). Chlorite from Hope Brook belongs to Type I trioctahedral Mg-Fe chlorite (Fig. 2.7a), as defined by Zane and Weiss (1998), being further categorized as Al clinochlore. Considering the elevated content of tetrahedral Al and analogous components of octahedral Mg and Fe, chlorite from Hope Brook may be further defined as ripidolite (Fig. 2.7b).

(2) Al-Mn clinochlore at Heritage

At Heritage, two distinct textural and compositional varieties of chlorite have been identified. The first occurs either in the form of fine-grained replacement of previous phases (Fig. 2.4h) or within mica-chlorite stacks (Fig. 2.4e). This variety of chlorite has Al and Si contents in the range of 18.75-22.87 wt.% Al_2O_3 (2.40-2.77 Al a.p.f.u.) and 25.75-29.93 wt.% SiO_2 (2.70-2.92 Si a.p.f.u.), respectively (Table 2.5). Iron content ranges between 18.76 and 22.83 wt.% FeO (1.60-2.01 Fe a.p.f.u.; Table 2.5), whereas Mg content ranges between 13.81 and 17.30 wt.% MgO (2.17-2.56 Mg a.p.f.u.; Table 2.5). The Mn content reaches up to 4.39 wt.% MnO (0.38 Mn a.p.f.u.; Table 2.5). Following the same classification scheme as for Hope Brook, this chlorite is classified as Type I trioctahedral Mg-Fe chlorite (Zane and Weiss, 1998), specifically Al-rich Mg-chlorite (clinochlore, Fig. 2.7a), even though it accommodates comparatively less octahedral Al, which would permit its further classification as brunsvigite (Fig. 2.7b). The most distinctive geochemical signature of this type of chlorite is the elevated content of Mn (up to 0.38 a.p.f.u.; Table 2.5). It is consequently classified, for further discussion herein, as Al-Mn clinochlore.

(3) Clinochlore at Heritage

The second variety of chlorite at Heritage occurs as radial aggregates of platy crystals commonly found in pockets within the wall rock (Fig. 2.4i). Chlorite with this texture is defined by the following major element chemistry: 28.60-32.83 wt.% SiO_2 (3.05-3.15 Si a.p.f.u.; Table 2.5), 17.38-19.02 wt.% Al_2O_3 (2.12-2.21 Al a.p.f.u.; Table 2.5), 15.43-19.01 wt.% MgO (2.48-2.74

Mg a.p.f.u.; Table 2.5), and 18.44-21.09 wt.% FeO (1.58-1.74 Fe a.p.f.u.; Table 2.5). Manganese content does not exceed 1 wt.% (<0.08 Mn a.p.f.u.; Table 2.5). This chlorite has the lowest Al content of all chlorite analyzed in this study, and is classified as Type I Mg-Fe trioctahedral chlorite of clinochlore composition (Zane and Weiss, 1998; Fig. 2.7a). With respect to the tetrahedral Al and the Fe# this chlorite shows a transitional composition between brunsvigite and diabantite (Fig. 2.7a).

Figure 2.7b illustrates the relationship between chlorite chemistry and polytypism, where Al clinochlore samples (ripidolite at Hope Brook and brunsvigite at Heritage) plot in the field of polytype *IIb*. Conversely, clinochlore (brunsvigite-diabantite) samples from Heritage fall within the field of polytype *Ib* (Fig. 2.7b). Taking into account the polytypism information presented above, this observation implies a clear relationship between high content of tetrahedral Al in chlorite and higher formation temperatures. Such a relationship is consistent with the process of Tschermak substitution in chlorite, where Al substitutes for Si in tetrahedral position at higher temperatures according to $Si^{4+}(IV) + (Fe^{2+}, Mg^{2+})(VI) = Al^{3+}(IV) + Al^{3+}(VI)$ (Walshe, 1986; Fig. 2.7c).

2.5.2.4. Mixed-layer chlorite-smectite

The broad first and second basal peaks of chlorite observed under air-dried conditions, which tend to get narrower upon glycolation, indicate the presence of mixed-layer chlorite-smectite in the Heritage LSS (Table 2.3). This is corroborated by Sybilla© modeling which returned an R0 C-Sme with up to 50% of smectite component that best fitted the broadenings indicative for C-Sme (Fig. 2.3e,f). Chlorite-smectite, analogous to I-Sme, in this hydrothermal environment is likely a result of post-epithermal transformations of high-temperature hydrothermal chlorite (Inoue, 1995).

2.5.2.5. Kaolinite group

Kaolinite group minerals occur as accessory clays in the studied epithermal systems (Table 2.2), with characteristic peaks at d_{001} at 7.18 Å and d_{002} at 3.58 Å (Fig. 2.3b,c,d). To precisely confirm the presence of kaolinite group minerals, spectral modeling was deemed necessary, given the partial overlap of 001 and 002 *hkl* reflections of kaolinite with 002 and 004 of chlorite and C-Sme. Sybilla© modeling strongly suggested a substantial presence of kaolinite group minerals, particularly at Hope Brook HSS and Hickey's Pond HSS (Table 2.3). The positions of kaolinite peaks were found immutable in response to glycolation treatment, which excluded the presence of mixed-layer kaolinite-smectite in the samples analyzed. Microbeam characterization of Hope Brook samples with SEM revealed kaolinite filling open spaces in the form of randomly oriented well-shaped platy crystals of 10 μm to 15 μm in size (Fig. 2.4j,k). Chemically, Si content varies between 44.87 and 46.87 wt.% SiO_2 (1.83-1.98 Si a.p.f.u.; Table 2.6), Al content is found to be between 37.54 and 39.57 wt.% Al_2O_3 (1.79-2.01 Al a.p.f.u.; Table 2.6), and Fe is reported to range between 0.07 and 0.30 wt.% Fe_2O_3 (0.002-0.010 Fe a.p.f.u.; Table 2.6) – all values that lie in the range of stoichiometric kaolinite.

2.5.2.6. Pyrophyllite

Pyrophyllite was identified in both HSS examined in this study (Figs. 2.3c and 2.4l; Table 2.2). Two polytypes of pyrophyllite were identified following the inspection of diffraction data – pyrophyllite-2*M* and pyrophyllite-1T_c. The former is the most abundant variety of pyrophyllite in the sample set, while the latter occurs solely as an accessory phase at Hope Brook. Pyrophyllite-2*M* denotes a somewhat disordered two-layer monoclinic pyrophyllite polytype, which is commonly encountered in natural samples (Kogure et al., 2006). It has diffraction peaks at ~9.1 Å, ~4.6 Å, and ~3.0 Å, which corresponds to d_{002}, d_{004}, and d_{006}, respectively. Pyrophyllite-1T_c is a one-layer triclinic pyrophyllite polytype that forms at higher temperatures compared to pyrophyllite-2*M* (Kogure et al., 2006). Characteristic XRD peaks of pyrophyllite-1T_c polytype occur at ~9.2 Å, ~4.4 Å, and ~4.0 Å, which corresponds to d_{001}, d_{110}, and $d_{0\text{-}21}$, respectively.

2.5.3. Chlorite geothermometry

The empirical geothermometer of Kranidiotis and MacLean (1987; KM87 hereafter) and the semi-empirical geothermometer of Inoue et al. (2018; I18 hereafter) were applied to compositional data determined for chlorite samples. Al clinochlore (ripidolite) from Hope Brook consistently yielded the highest temperatures, with ranges of 181-197 ºC (KM87; Table 2.5; Fig. 2.8a) and 201-297 ºC (I18; Table 2.5, Fig. 2.8b). At Heritage, two distinct populations can be distinguished, which are precisely related to the two distinct compositions of chlorite reported from this location. Based on the KM87 geothermometer, Al-Mn clinochlore (brunsvigite) shows temperatures between 160 and 189 ºC (Table 2.5; Fig. 2.8a), and clinochlore (brunsvigite-diabantite) yielded the lowest temperatures of all analyzed chlorite, with a range of 133-143 ºC (Table 2.5; Fig. 2.8a). Geothermometric calculations using the I18 geothermometer for these same samples returned formation temperatures of Al-Mn clinochlore (brunsvigite) of 108-192 ºC (Table 2.5; Fig. 2.8b), and temperatures of 91-126 ºC for clinochlore (brunsvigite-diabantite) (Table 2.5; Fig. 2.8b).

2.6. Discussion

2.6.1. Origin of phyllosilicates and significance for epithermal systems

Mica from all three epithermal systems studied shows a predominance of interlayer K^+ in comparison to Na^+ and Ca^{2+} (< 0.367 Na a.p.f.u and < 0.014 Ca a.p.f.u.; Table 2.4). In both HSS, the predominant K-mica is classified as Fe muscovite (Fig. 2.6a; Table 2.4).

At Hope Brook, an additional mica, with a major paragonitic (Na) component, has been reported (Table 2.4; Figs. 2.3a,b and 2.6b; Table 2.3). Further, a clear textural observation documenting the replacement or overgrowth of paragonite by Fe muscovite was apparent, with paragonite occurring in the core of large mica crystals (up to 60 μm) while Fe muscovite manifests along mineral rims (Fig. 2.4c). This explains the ~30% muscovitic component (~ 0.299 K a.p.f.u.) in the average paragonite (Table 2.4). Paragonite as a hydrothermal phase is uncommon in porphyry-epithermal systems (Jiang and Peacor, 1993). It has, however, been described in the Asarel porphyry copper deposit in association with kaolinite, fine-grained white mica, quartz, pyrite, alunite, pyrophyllite, and diaspore (Hikov, 2014), which is an assemblage typical for HSS advanced argillic alteration (Sillitoe, 1993; Arribas, 1995; Hedenquist et al., 2000; Simmons et al., 2005). Sequential high-temperature hydrothermal episodes of mica deposition may explain the textural relationship of the two compositions. In this scenario, the first episode is responsible for the formation of paragonite, while the second reflects a change in the composition of hydrothermal solutions, leading to the overgrowth and/or replacement of Na by K mica (Fig. 2.4c). The formation of paragonite in hydrothermal and metamorphic environments is, however, not necessarily related simply to high levels of Na in the host rock or hydrothermal fluids, but to low Na/(Na + Al) and K/(K + Al) in host rocks (Árkai et al., 2008). Indeed, high-Al magmatic-hydrothermal activity favors the formation of paragonite (Merriman, 2005). Such circumstances are consistent with the normal progression of hydrothermal alteration in HSS (Arribas, 1995). Initially, high-temperature/low-pH fluids cause an extreme leaching of mobile elements, while the less mobile Al is enriched in the residue (Sillitoe, 1993; Arribas, 1995; Hedenquist et al., 2000; Simmons et al., 2005; Árkai et al., 2008). Mica precipitated as an overprint on the residuum would thus tend to be paragonitic under these physicochemical conditions. Progressive cooling and lateral dispersion of hydrothermal fluid will eventually allow for an increase in pH, which in turn creates an environment rich in alkalis that support the precipitation of K mica over paragonite (Árkai et al., 2008). According to Árkai et al. (2008), paragonite can form under epizonal conditions of pressure and temperature related to low Na/(Na + Al) and K(K + Al) ratios, and an enrichment of both K and Na in the system will favor the formation of muscovite and not paragonite.

A different hydrothermal history has unfolded at the Heritage LSS, where Fe-Mg muscovite occurs as the main phyllosilicate (Fig. 2.6a; Table 2.4). In this case Fe-Mg muscovite presents a phengitic composition with lower Al content (Table 2.4). The chemistry of Fe-Mg muscovite is essentially controlled by the Tschermak exchange reaction (Fig. 2.6c), related to lower values of $a\mathrm{K}^+$ and/or neutral pH. Such conditions result from a durable buffering of K-rich hydrothermal fluids by igneous host rocks (Gaillard et al., 2018).

Chlorite at Hope Brook HSS and Heritage LSS show contrasting textures and compositions, which also reflect the physicochemical differences in their formation environments (Yoneda and Maeda, 2008; Wang et al., 2018). In the XRD pattern of chlorite from Hope Brook, a second basal reflection is over-pronounced while the first line is only weak or absent (Figs. 2.3a,b and 2.7d). Such a pattern is usually attributed to Fe-rich chamosite (Moore and Reynolds, 1997; Beaufort et al., 2015). However, a thorough microbeam investigation showed that chlorite at Hope Brook is Al clinochlore of ripidolitic composition (Fig. 2.7a,b). The basal reflection characteristics are thus attributed to a temperature dependent increase of Al content in chlorite (De Caritat et al., 1993), which in turn leads to the significant reduction of the d_{001} diffraction line (Walshe, 1986).

Several authors have reported an extremely broad range of Fe# chlorite values from various active and fossil hydrothermal systems (volcanic-hosted massive sulfide deposits, Kranidiotis and MacLean 1987, Sánchez España et al., 2000; active hydrothermal vents in mid-ocean ridges, Saccocia and Gillis, 1995; stratabound Cu deposits, Zaccarini et al., 2003; HSS, Carrillo-Rosúa et al., 2009). However, the Fe# of chlorite from both Hope Brook and Heritage fits a narrow range – between 0.37 and 0.48 (Fig. 2.7b). Higher Fe# is found in Al-Mn clinochlore at Heritage (0.39-0.48) and Al clinochlore at Hope Brook (0.38-0.42), while a lower Fe# is reported in clinochlore from Heritage (0.37-0.41). Physicochemical properties of the parent hydrothermal fluids explain the differences in chlorite composition – with high values of Fe# and octahedral Al (high Tschermak substitution) normally interpreted as an indication of elevated crystallization temperatures (e.g., Deer et al., 1966), and therefore more prevalent in chlorite from HSS.

Chlorite geothermometry has been applied to a wide variety of geological environments, to studies including metamorphic petrology, sedimentary petrology, and hydrothermal alteration (De Caritat et al., 1993). The lattermost application is closely linked to the study of mineralization of hydrothermal origin. The absolute errors in temperatures calculated from any published chlorite geothermometer are difficult or impossible to calculate. However, estimated temperatures calculated from chlorite geothermometers may be a useful additional datum in characterizing and comparing phyllosilicates from different hydrothermal environments. Consequently, we have applied chlorite geothermometry in this study in context of comparison to temperature information derived from crystallochemical composition and textures of phyllosilicates, and from generalized models for the different ore deposit types examined herein.

For the purpose of comparison, we have presented temperatures calculated using the empirical geothermometer proposed by Kranidiotis and MacLean (1987) and the semi-empirical geothermometer of Inoue et al. (2018). As noted in Materials and Methods (above), the latter geothermometer was initially developed for application to hydrothermal systems (Inoue et al., 2009).

In the Hope Brook HSS, temperatures of 180-200 ºC (KM87) and 201-297 ºC (I18) were returned by chlorite geothermometry of the Al clinochlore (ripidolite; Table 2.5; Fig. 2.8). In this deposit, coeval crystallization of chlorite and mica has been suggested given their textural relationship in the form of mica-chlorite stacks (Fig. 2.4a,b). Their common origin here is interpreted as deriving from the high-temperature hydrothermal alteration of igneous biotite in the host rocks (Jiang and Peacor, 1993). Therefore, high-temperature ripidolite at Hope Brook is of hydrothermal origin, but was most likely formed in the distal parts of the hydrothermal system during late stages of hydrothermal activity. There is a considerable difference in chlorite formation temperatures obtained by the KM87 and the I18 geothermometers when applied to the Hope Brook HSS (up to ~100 ºC; Table 2.5; Fig. 2.8). At Heritage, chlorite geothermometry returned temperatures of 133-189 ºC (KM87; Table 2.5; Fig. 2.8a) and 91-192 ºC (I18; Table 2.5; Fig. 2.8b), which are on average 20-40 ºC (KM87) and 70-100 ºC (I18) lower than those reported for Al clinochlore at Hope Brook, respectively. Conversely, the occurrence of adularia and K mica as hydrothermal products in LSS (Heritage) indicates formation temperatures of ~250 ºC at near-neutral pH conditions (Barton et al., 1977), while precious metal deposition is described at temperatures generally < 250 ºC in other studies of LSS (Simmons and Browne; 2000; John et al., 2003; Rivai et al., 2019). Aluminum-Mn clinochlore at Heritage is interpreted as a high-temperature chlorite, given its composition (Al-Mn-rich), and its calculated temperature of formation (160-189 ºC KM87; 108-192 ºC I18), with its origin related to the phyllic and propylitic alterations that characterize the prospect. The application of both chlorite geothermometers to LSS does not result in significant discrepancies in resulting formation temperatures, in contrast to the results obtained for HSS. As observed in Figure 2.8, the I18 geothermometer appears to act more effectively at discriminating between relative chlorite formation temperatures from the HSS and LSS examples, with the maximum estimated temperature in Heritage samples (192 ºC) being more than 100 ºC lower than that for Hope Brook samples (297 ºC). This is attributed to the fact that the KM87 thermometer relies on the content of Al(IV), Fe^{2+}, and Mg (Kranidiotis and MacLean, 1987), whilst the I18 considers Si, Al(IV), Al(VI), Fe, Mg, as well as the octahedral vacancies (Inoue et al., 2018). The latter is based on the ratio of end-member activities (clinochlore, daphnite, Fe-amesite, Mg-amesite, Fe-sudoite, Mg-sudoite) and takes into account the three main substitutions in chlorite (Fe-Mg substitution; Tschermak substitution; di/trioctahedral substitution). These parameters are more sensitive to the changes in the environment of formation, thus providing a more accurate estimation of chlorite formation temperatures (Vidal et al., 2016), with particular application to hydrothermal systems (Inoue et al., 2009). In addition, there is a direct negative relationship apparent between octahedral chlorite vacancies and formation temperatures (Table 2.5), which relates to the higher contents of Fe^{3+} in low-temperature chlorite (Vidal et al., 2016).

An alternative, metamorphic origin of Al-rich chlorite due to regional greenschist-grade metamorphic overprint of Avalonian rocks (Williams, 1979; O'Brien et al., 1996) is not supported by our data. Later regional metamorphism in the Avalon Zone was characterized by temperatures of 350-450 ºC (Miyashiro, 1994; Bucher, 2005), which are at least 50-100 ºC higher than the highest geothermometric temperature obtained from chlorite in this contribution (Table 2.5). Further, metamorphic chlorite commonly shows an Al content below 20 wt.% Al_2O_3 (Schmidt et al., 1997; Šegvić et al., 2016) as opposed to the high Al content in chlorite described at Hope Brook (~24 wt.% Al_2O_3; Table 2.5) and Heritage (~19-22 wt.% Al_2O_3; Table 2.5). Finally, there is evidence for cogenetic precipitation of mica and chlorite in stacks at Hope Brook and Heritage (Fig. 2.4a,b,e), which strongly argues in favor of a hydrothermal origin for both phases (Jiang and Peacor, 1993).

Mineralogical, textural, and compositional indications of various post-peak hydrothermal events (waning stage low-temperature hydrothermal activity, metamorphic overprint, and/or weathering) are commonplace in the studied epithermal systems. Thus, the omnipresent minor content of smectite in mica (Table 2.3; Fig. 2.3) may be related to surface or shallow subsurface weathering (Çelik et al., 1999). This interpretation is supported by the occurrence of *1M* mica attributable to the weathering of hydrothermal $2M_1$ mica (Martin-Garcia et al., 1997; Wilson, 2004). The same holds true for the minor smectite component in chlorite at Hope Brook and Heritage (Table 2.3). In addition to its smectite content, clinochlore (brunsvigite-diabantite) at Heritage is characterized by (i) lower Al content (~17-19 wt.% Al_2O_3; Table 2.5; Fig. 2.7b,c), (ii) lower temperature of formation (133-143 ºC KM87; 91-126 ºC I18; Table 2.5; Fig. 2.8), and (iii) peculiar radial texture in open space (Fig. 2.4i). This type of chlorite belongs to the low-temperature *Ib* polytype (Fig. 2.7b) and may be attributed to late-stage low-temperature hydrothermal processes (Moore and Reynolds, 1997). Kaolinite is another low-temperature phase in Hope Brook as suggested by (i) its occurrence filling open space pockets (Fig. 2.4j,k), (ii) 10-15 µm size of randomly oriented crystallites (Fig. 2.4k), and (iii) chemical composition showing limited Al substitution by Fe (Table 2.6). The minimal extent of such isomorphic substitution in this kaolinite (< 0.01 a.p.f.u. Fe; Table 2.6) reflects the low-pressure (near surface) and low-temperature conditions of its formation (Hu et al., 2011).

Regional greenschist metamorphism affected hydrothermal rocks during the Late Ordovician to Early Silurian (O'Brien et al., 1996), following the orogenesis resulting from the collision of the Avalonia microcontinent with Laurentia (Hibbard et al., 2007; Murphy et al., 2010).

The intensity of metamorphism was likely insufficient to recrystallize the pre-existing hydrothermal assemblages. This event is however documented regionally through the formation of ambient metamorphic chlorite and epidote in the neighboring host rocks (O'Brien et al., 1996).

2.6.2. Phyllosilicate-based hydrothermal record of epithermal systems and potential for ore genesis

The mineralogy and geochemistry of phyllosilicates may contribute to reconstruction of the hydrothermal record of the studied epithermal systems (Fig. 2.9). At Hickey's Pond there is a clear hydrothermal alteration zonation that develops from the vuggy silica core of the system outwards, which reflects the cooling and reaction path of the parent hydrothermal fluids (Sillitoe, 1993; Arribas, 1995; Hedenquist et al., 2000; Simmons et al., 2005). Negligible phyllosilicate content and an absence of feldspars were observed in the vuggy silica core of the system due to the extreme leaching of the volcanic host rock produced by the hot, oxidizing, and acidic hydrothermal fluid (Sillitoe, 1993; Arribas, 1995; Hedenquist et al., 2000). With the lateral dispersion, cooling, and pH buffering of the fluid, the physicochemical conditions became favorable for the formation of phyllosilicates in surrounding zones. Thus, outward from the massive silicic core, there is an advanced argillic alteration zone comprised of quartz, alunite, pyrite, and rutile, as well as pyrophyllite, kaolinite group minerals, and minor Fe muscovite (Fig. 2.9). The presence of pyrophyllite, and presumed high-temperature kaolinite group polymorphs (i.e., dickite and nacrite), indicate temperatures below 300 ºC (Zhu et al., 2011; Fig 7). Further outwards, an argillic alteration zone is characterized by quartz, hematite, and alunite, accompanied by Fe muscovite and kaolinite group minerals, suggesting that temperatures diminished to ~200 ºC (Seedorf et al., 2005; Fig. 2.9). In the most distal zone of the system sampled, phyllic alteration is mainly defined by quartz and fine-grained white mica (Fig. 2.9). Chlorite was not detected in the outcrop sample set studied from

Hickey's Pond, but it has been reported at depth (drill core) by visible - near infrared - short-wave infrared (Vis-NIR-SWIR) spectroscopy (Sparkes et al., 2016), corresponding to the distal phyllic/propylitic alteration zone.

At Hope Brook HSS, a similar hydrothermal record as the one described for the Hickey's Pond HSS can be inferred. Due to greater variability in host rock lithology, and a wider areal extent of the alteration, as well as the post-hydrothermal tectonic history in the area, alteration zones are not as well defined and laterally continuous as in the case of Hickey's Pond. Various now disconnected zones of massive silicic alteration with vuggy quartz and pyrite trace original discharge zones for hydrothermal fluids into the epithermal environment. Immediately surrounding those silica-rich zones, advanced argillic alteration envelopes are formed, with characteristic pyrophyllite and kaolinite group minerals as well as white mica (Fig. 2.9). The crystals of white mica have cores of paragonite (Fig. 2.4c) implicitly formed at peak hydrothermal temperatures. Their Fe muscovite rims likely formed at lower temperatures during the progressive cooling of the epithermal system (Fig. 2.9). Towards the outermost parts of the system, Fe muscovite and Al clinochlore become the prevalent hydrothermal phyllosilicates (Fig. 2.9). The general absence of feldspars is attributed to the complete obliteration of volcanic feldspars during extremely acidic hydrothermal alteration (Sillitoe, 1993; Arribas, 1995; Hedenquist et al., 2000). Ore mineralization in form of native Au, Au-Ag sulfosalts, and sulfides tends to be restricted to within (or very near to) the massive silicic alteration core of both Hope Brook and Hickey's Pond, with minor mineralization in the surrounding advanced argillic alteration envelope (Sparkes and Dunning, 2014; Sparkes et al., 2016). This is a recurring theme in HSS, where mineralization occurs in the porous massive silicic core, concentrated in the pores of the vuggy silica (Sillitoe, 1993; Arribas, 1995; Hedenquist et al., 2000; Simmons et al., 2005). This has two main implications: (i) mineralization event(s) are not necessarily contemporaneous with phyllosilicate formation; and (ii) the characteristic phyllosilicates occurring in HSS alteration zones (pyrophyllite, kaolinite group minerals, smectite, illite, chlorite, etc.) give guidance as to the location of core zone(s) but may not be directly linked to the precipitation of ore mineralization.

The Heritage LSS features a hydrothermal phyllosilicate assemblage that consists of Fe-Mg muscovite and Al chlorite, with minor amounts of I-Sme and C-Sme (Table 2.3; Fig. 2.9). Bulk non-phyllosilicate mineralogy is consistent in all samples, with abundant quartz, carbonates, and K-feldspar. The XRD identification of K-feldspar, interpreted as relict from the host igneous wall rock, is indicative of the relatively less consumptive nature of hydrothermal alteration in LSS. Fe-Mg muscovite and Al clinochlore are both ubiquitous throughout the broad zone of hydrothermally altered rocks, with the latter being somewhat less abundant (Table 2.2). In this case the hydrothermal alteration zones are, therefore, better defined by key non-phyllosilicate phases that are the main constituents of the epithermal veins and breccias, as illustrated by the increased predominance of chalcedony and adularia in the center of the system and quartz towards the distal areas (Ferguson, 2017). Kaolinite has been detected in one sample accompanied by adularia, white mica, and chlorite (Table 2.2), and is therefore considered to be associated with the hydrothermal system core (Fig. 2.9). The co-precipitation of mica and chlorite at Heritage is explicit based on their textural relationships. Temperatures were estimated to lie between 160 and 189 ºC (KM87) and between 108 and 192 ºC (I18) for Al-Mn clinochlore (Fig. 2.8), which means that mica likely formed in this same temperature window. Furthermore, ore mineralization in the form of Ag sulfides (mainly acanthite) is closely spatially and texturally related to Fe-Mg muscovite (Figs. 2.4g and 2.5c,d), which strongly implies their contemporaneous precipitation. Boiling is indicated by the occurrence of bladed calcite (Fig. 2.6f), a common characteristic of LSS (Simmons and Christenson, 1994). The boiling of hydrothermal fluids is a core process for the deposition of precious metal mineralization (Au, Ag; Cooke and Simmons, 2000; Hedenquist et al., 2000). At

Heritage, the space between calcite blades is occupied by Fe-Mg muscovite (Fig. 2.6f), which indicates that mica crystallization is (pene)contemporaneous with boiling.

As evidenced in Figure 2.6, the range of muscovite compositions displayed by HSS versus LSS is quite distinct. This distinction may prove valuable in assessments at the prospection or early exploration stages, especially in poorly exposed terranes, where it is desirable to make an initial assessment as to which style of precious metals mineralization has been encountered (HSS vs LSS, with possible extension to orogenic deposit types). As observed at Hope Brook, the earlier paragonitic cores of muscovite may be an additional identifying characteristic of some HSS systems.

Exploration for epithermal systems has traditionally included mineralogical observation and enumeration of hydrothermal alteration zones (White and Hedenquist, 1990; Hedenquist et al., 2000; Hedenquist, 2015). Yet the depositional timing of the characteristic phyllosilicates occurring in high-sulfidation deposits (Fe muscovite, paragonite, Al clinochlore, pyrophyllite, kaolinite, smectite, mixed-layered phases, etc.) is often not simultaneous with the economic mineralization (Arribas, 1995), with precious metals often appearing to overprint pre-existing alteration (Fig. 2.5a,b). Further study of hydrothermal phyllosilicates in HSS should attempt to recognize and characterize the presence of phyllosilicates texturally related with ore minerals at the sub-micron scale, as these could provide valuable information on the physiochemical conditions of ore fluids, as well as on the precipitation mechanisms of Au in these systems. At Heritage, as previously stated, Fe-Mg muscovite occurs spatially linked to Ag mineralization (Figs. 2.4g and 2.5c,d), as well as in the space between calcite blades (Fig. 2.4f). This is interpreted as Fe-Mg muscovite being genetically linked to ore-forming fluids and precipitating in the same hydrothermal event as ore mineralization, probably through boiling processes. This interpretation has implications in exploration for LSS, where the presence of these more phengitic micas may provide a mappable indicator for the presence of epithermal Au-Ag mineralization.

2.7. Conclusions

i. The high-sulfidation systems studied are characterized by paragonite and Fe muscovite, whereas the low-sulfidation system is rich in Fe-Mg muscovite. The latter reflects a composition characterized by high Tschermak substitution (Al(IV) + (Al + Fe^{3+})(VI) by (Fe^{2+} + Mg) + Si)). Chlorite is Al clinochlore in all systems, but is richer in Al in HSS compared to LSS.

ii. Iron muscovite from HSS is a high-temperature phase (~200 ºC) as suggested by (a) the overprinting/replacement of Na by K rich mica, (b) prevalence of the $2M_1$ polytype, and (c) low Tschermak substitution. Conversely Fe-Mg muscovite from LSS has somewhat lower crystallization temperatures (< 200 ºC) as inferred from (a) its occurrence in the form of fine-grained aggregates, (b) prevalence of $2M_2$ polytype characteristic for (c) higher degrees of substitution along the Tschermak exchange vector.

iii. Aluminum clinochlore (ripidolite) from HSS is a high-temperature chlorite – returning 201-297 ºC (I18) from chlorite geothermometry – and as inferred from (a) the coarse vein crystals which evolve into chlorite-mica (Fe muscovite) stacks, (b) prevalence of the *IIb* polytype, and (c) Al-rich trioctahedral chemistry coupled with low Tschermak substitution. Al-Mn clinochlore (brunsvigite) from LSS is also a high-temperature chlorite, but with slightly lower formation temperatures – returning 108-192 ºC (I18) from chlorite geothermometry – and as inferred from (a) replacement textures, (b) prevalence of *IIb* polytype, (c) Al-rich trioctahedral chemistry coupled with low Tschermak substitution, and

(d) high Mn content. Clinochlore (brunsvigite to diabantite) from LSS is a low-temperature chlorite, returning 91-126 ºC (I18) from chlorite geothermometry, and as inferred from (a) characteristic radial aggregates formed in pockets within the wall rock, (b) prevalence of the *Ib* polytype, and (c) lower Al content and higher degrees of substitution along the Tschermak exchange vector.

iv. In the HSS examples studied, hydrothermal phyllosilicates are consistent with the progressive cooling and neutralization of initially hot and acidic magmatic-hydrothermal fluids, with the deposits displaying the following zonation: (a) massive silicic zone(s) (i.e., vuggy silica) with negligible phyllosilicate content, (b) advanced argillic alteration (pyrophyllite, kaolinite group minerals, and minor paragonite being replaced by Fe muscovite), (c) argillic alteration (Fe muscovite, kaolinite group minerals), and (d) sericitic and propylitic alterations (Fe muscovite and Al clinochlore). In the LSS example studied, the hydrothermal phyllosilicates are Fe-Mg muscovite and Al clinochlore, which are widespread throughout the broad zone of silicification that contains epithermal veins and breccias, and show no regular/concentric zonation patterns. Alteration zoning is, however, better defined by non-phyllosilicates, as reflected in bulk XRD data, with LSS showing a core rich in chalcedony and adularia, while quartz becomes more dominant in the distal part of the system.

v. Post-peak hydrothermal events include late low-temperature hydrothermal activity (the occurrence of clinochlore (brunsvigite to diabantite) and low-Fe kaolinite) and weathering (the occurrence of illite-smectite and chlorite-smectite intermediates with low smectite content).

vi. Detailed characterization of phyllosilicate mineralogy and composition proved useful in interpreting the hydrothermal record of epithermal systems in the Avalon terrane, and reflects the contrasting high- and low-sulfidation epithermal environments. The high- and low-sulfidation epithermal systems studied herein were related to the Neoproterozoic arc volcanism of the Avalonian microcontinent. High-sulfidation epithermal systems formed in close proximity to the causative magmatic intrusions from originally very acidic and oxidizing fluids which gave rise to the precipitation of pyrophyllite, kaolinite group minerals, paragonite, Fe muscovite, and Al clinochlore (ripidolite). Low-sulfidation epithermal systems originated in a distal setting from near neutral and reducing hydrothermal fluids, developing Fe-Mg muscovite and Al clinochlore (brunsvigite) as the main hydrothermal phyllosilicates. Post-peak hydrothermal events and weathering are characterized by the formation of readily discernible low-temperature chlorite, kaolinite, and mixed-layered phases. A subsequent Late Ordovician to Early Silurian Appalachian (lower-) greenschist metamorphic overprint was mild, and did not significantly alter the composition or mineralogy of the hydrothermal phyllosilicates analyzed from the epithermal systems.

2.8. Acknowledgements

Financial support for this research was provided by an NSERC Discovery Grant to GDL (RGPIN/005037-2017). A MITACS Globalink Research Award (IT15075 2019) enabled a productive research stay at Texas Tech University by CA. Further support was received by CA from the Society of Economic Geology Foundation and Newmont Mining Corporation (SEG Student Research Grant 2017). TTU Geoscience Clay Laboratory provided invaluable assistance with X-ray diffraction analyses. Gratitude goes to Dylan Goudie and Wanda Aylward for providing excellent microbeam conditions in the Memorial University CREAIT Facilities. We extend our appreciation to Puddle Pond Resources (Newfoundland, Canada) for access to the Heritage prospect, and to Greg Woodland for his assistance in selecting and collecting appropriate samples. The constructive reviews by two anonymous reviewers as well as the editorial handling by Prof. Alberto López Galindo contributed significantly to the manuscript quality.

2.9. References

Abd Elmola, A., Charpentier, D., Buatier, M., Lanari, P., Monié, P., 2017. Textural-chemical changes and deformation conditions registered by phyllosilicates in a fault zone (Pic de Port Vieux thrust, Pyrenees). Applied Clay Science 144, 88-103. https://doi.org/10.1016/j.clay.2017.05.008

Árkai, P., Livi, K.J.T., Horváth, P., 2008. Dioctahedral mixed K-Na-micas and paragonite in diagenetic to low-temperature metamorphic terranes: bulk rock chemical, thermodynamic and textural constraints. Central European Geology 51/4, 283-314. https://doi.org/10.1556/ceugeol.51.2008.4.1

Arribas, A., 1995. Characteristics of high-sulfidation epithermal deposits, and their relation to magmatic fluid. Mineralogical Association of Canada Short Course 23, 419-454.

Bailey, S.W., 1980a. Structures of layer silicates. In: Brindley, G.W., Brown, G., editors. Crystal structures of clay minerals and their X-ray identification, Monograph 5. London Mineralogical Society, 1-123. https://doi.org/10.1180/mono-5.1

Bailey, S.W., 1980b. Summary of recommendations of AIPEA nomenclature committee on clay minerals. American Mineralogist 65, 1-7.

Barton, P.B., Bethke, P.M., Roedder, E, 1977. Environment of ore deposition in the Creede mining district, San Juan Mountains, Colorado; Part III, Progress toward interpretation of the chemistry of the ore-forming fluid for the OH Vein. Economic Geology 72, 1-24. https://doi.org/10.2113/gsecongeo.72.1.1

Beaufort, D., Rigault, C., Billon, S., Billault, V., Inoue, A., Inoue, S., Patrier, P., 2015. Chlorite and chloritization processes through mixed-layer mineral series in low-temperature geological systems - a review. Clay Minerals 50, 497-523. https://doi.org/10.1180/claymin.2015.050.4.06

Bourdelle, F., 2021. Low-temperature chlorite geothermometry and related recent analytical advances: a review. Minerals 11(2), 130. https://doi.org/10.3390/min11020130

Bourdelle, F., Parra, T., Chopin, C., Beyssac, O., 2013. A new chlorite geothermometer for diagenetic to low-grade metamorphic conditions. Contributions to Mineralogy and Petrology 165, 723-735. https://doi.org/10.1007/s00410-012-0832-7

Brigatti, M.F., Malferrari, D., Poppi, M., Poppi, L., 2005. The $2M_1$ dioctahedral mica polytype: a crystal chemical study. Clays and Clay Minerals 53, 190-197. https://doi.org/10.1346/CCMN.2005.0530209

Brindley, G.W. and Wardle, R., 1970. Monoclinic and triclinic forms of pyrophyllite and pyrophyllite anhydride. The American Mineralogist 55, 1259-1272.

Bucher, K., 2005. Facies and Zones. In: Metamorphic Rocks. Encyclopedia of Geology, 402-409. https://doi.org/10.1016/B0-12-369396-9/00319-1

Carrillo-Rosúa, J., Morales-Ruano, S., Esteban-Arispe, I., Fenoll Hach-Alí, P., 2009. Significance of phyllosilicate mineralogy and mineral chemistry in an epithermal environment. Insights from the Palai-Islica Au-Cu deposit (Almería, SE Spain). Clays and Clay Minerals 57-1, 1-24. https://doi.org/10.1346/CCMN.2009.0570101

Cathelineau, M., 1988. Cation site occupancy in chlorites and illites as a function of temperature. Clay Minerals 23, 471-485. https://doi.org/10.1180/claymin.1988.023.4.13

Cathelineau, M. and Nieva, D., 1985. A chlorite solid solution geothermometer: The Los Azufres (Mexico) geothermal system. Contributions to Mineralogy and Petrology 91, 235-244. https://doi.org/10.1007/BF00413350

Çelik, M., Karakaya, N., Temel, A., 1999. Clay minerals in hydrothermally altered volcanic rocks, Eastern Pontides, Turkey. Clays and Clay Minerals 47, 708-717. https://doi.org/10.1346/CCMN.1999.0470604

Clarke, M., 2013. Host lithologies, breccia development, alteration and gold mineralization at the Big Easy Prospect. St. John's, NL: Memorial University of Newfoundland and Labrador.

Cooke, D.R. and Simmons, SF., 2000. Characteristics and genesis of epithermal gold deposits. Society of Economic Geologists, Reviews in Economic Geology 13, 221-244. https://doi.org/10.5382/Rev.13.06

Curtis, C.D.; Hughes, C.R.; Whiteman, J.A.; Whittle, C.K., 1985. Compositional variations within some sedimentary chlorites and some comments on their origin. Mineralogical Magazine 49, 375-386.

De Caritat, P., Hutcheon, I., Walshe, J.L., 1993. Chlorite geothermometry: a review. Clays and Clay Minerals 41, 219-239. https://doi.org/10.1346/CCMN.1993.0410210

Deer, W.A., Howie, R.A., Zussman, J., 1966. An introduction to the rock forming minerals. Longman Scientific and Technical, Essex (1966), 498 pp. https://doi.org/10.1180/DHZ

Dimmell, P., 2012. Report of 2012 Exploration (Prospecting, Stream Sediment Geochemistry, Airborne Geophysics, Diamond Drilling, Compilation,) on the Big Easy (BE) Property. St. John's, NL: Department of Natural Resources.

Drits, V.A. and Sakharov, B.A., 1976. X-ray Structural Analysis of Mixed-layer Minerals. Nauka, Moscow, Russian Federation.

Dubé, B., Dunning, G., Lauzière, K., 1995. Geology of the Hope Brook Mine, Newfoundland, Canada: A preserved Late Proterozoic high-sulfidation epithermal gold deposit and its implications for exploration. Economic Geology 93, 405-436. https://doi.org/10.2113/gsecongeo.93.4.405

Dunning, G. and O'Brien, S.J., 1989. Late Proterozoic-Early Paleozoic crust in the Hermitage flexure, Newfoundland Appalachians: U-Pb ages and tectonic significance. Geology 17, 548-551. https://doi.org/10.1130/0091-7613(1989)017<0548:LPEPCI>2.3.CO;2

Etoh, J., Izawa, E., Watanabe, K., Taguchi, S., Sekine, R., 2002. Bladed quartz and its relationship to gold mineralization in the Hishikari low-sulfidation epithermal gold deposit, Japan. Economic Geology 97, 1841-1851. https://doi.org/10.2113/gsecongeo.97.8.1841

Ferguson, S.A., 2017. Late Neoproterozoic epithermal-style Au mineralization of the Burin Peninsula, Newfoundland: U-Pb geochronology and deposit characteristics. Unpublished Master Thesis. Department of Earth Sciences, Memorial University of Newfoundland, 393 pp.

Foster, M.D., 1962. Interpretation of the composition and a classification of the chlorites. U.S. Geological Survey Professional Paper 414, 1-33.

Foster, M. D., 1969. Studies of celadonite and glauconite. U.S. Geological Survey Professional Paper 614-F, Shorter Contributions to General Geology, 117 pp.

Frimmel, H.E., 2008. Earth's continental crustal gold endowment. Earth and Planetary Science Letters 267(1), 45-55. https://doi.org/10.1016/j.epsl.2007.11.022

Frimmel, H.E., 2018. Episodic concentration of gold to ore grade through Earth's history. Earth-Science Reviews 180, 148-158. https://doi.org/10.1016/j.earscirev.2018.03.011

Gaillard, N., Williams-Jones, A.E., Clark, J.R., Lypaczewski, P., Salvi, S., Perrouty, S., Piette-Laurière, N., Guilmette, C., Linnen, R.L., 2018. Mica composition as a vector to gold mineralization: Deciphering hydrothermal and metamorphic effects in the Malartic district, Quebec. Ore Geology Reviews 95, 789-820. https://doi.org/10.1016/j.oregeorev.2018.02.009

Grathoff, G.H. and Moore, D.M., 1996. Illite polytype quantification using wildfire© calculated x-ray diffraction patterns. Clays and Clay Minerals 44, 835-842. https://doi.org/10.1346/CCMN.1996.0440615

Hallberg, A., 1994. The Enåsen gold deposit, central Sweden. Mineralium Deposita 29, 150-162. https://doi.org/10.1007/BF00191512

Hayes, J. B., 1970. Polytypism of chlorite in sedimentary rocks. Clays & Clay Minerals 18, 285-306.

Hedenquist, J.W., 1987. Mineralization associated with volcanic-related hydrothermal systems in the Circum-Pacific basin. Transactions of the Fourth Circum-Pacific Conference on Energy and Mineral Resources Conference, Singapore, American Association of Petroleum Geologists, 513-524.

Hedenquist, J.W., 2015. Recent developments in understanding of and exploration for epithermal deposits in volcanic arcs. PACRIM 2015 Congress Abstract, 1-6.

Hedenquist, J.W., Arribas, A., and Gonzalez-Urien, E., 2000. Exploration for epithermal gold deposits. Economic Geology Reviews 13, 245-277. https://doi.org/10.5382/Rev.13.07

Hibbard, J.P., van Staal, C.R., and Miller, B.V., 2007. Links among Carolinia, Avalonia, and Ganderia in the Appalachian peri-Gondwanan realm. In Sears, J.W., Harms, T.A., and Evenchick, C.A., eds.: Whence the Mountains? Inquiries into the Evolution of Orogenic Systems. Geological Society of America Special Paper 433, 291-311. https://doi.org/10.1130/2007.2433(14)

Hikov, A., 2014. Paragonite and paragonitic altered rocks from the Asarel porphyry copper deposit, central Srednogorie. Comptes rendus de l'Académie bulgare des sciences: sciences mathématiques et naturelles 67(8), 1119-1128.

Ho Ahn, J., Peacor, D.R., Essene, E.J., 1985. Coexisting paragonite-phengite in blueschist eclogite: a TEM study. American Mineralogist 70, 1193-1204.

Hoffer, E., 1978. On the “late” formation of paragonite and its breakdown in pelitic rocks of the southern Damara orogen (Namibia). Contributions to Mineralogy and Petrology 67, 209-219. https://doi.org/10.1007/BF01046577

Hu, Y., Ray, J.R., Jun, Y.-S., 2011. Biotite-Brine Interactions under Acidic Hydrothermal Conditions: Fibrous Illite, Goethite, and Kaolinite Formation and Biotite Surface Cracking. Environmental Science and Technology 45, 6175-6180. https://doi.org/10.1021/es200489y

Huard, A. and O’Driscoll, C., 1986. Epithermal gold mineralization in late Precambrian volcanic rocks on the Burin Peninsula. Current Research, Newfoundland Department of Mines and Energy, Mineral Development Division, Report 86-1, 65-78.

Inoue, A., 1995. Formation of Clay Minerals in Hydrothermal Environments. In: Velde, B. (Ed.), Origin and Mineralogy of Clays: Clays and the Environment. Springer, Berlin, Heidelberg, 268-329. https://doi.org/10.1007/978-3-662-12648-6_7

Inoue, A., Kurokawa, K., Hatta, T., 2009. Application of chlorite geothermometry to hydrothermal alteration in Toyoha Geothermal System, southwestern Hokkaido, Japan. Resource Geology 60, 52-70. https://doi.org/10.1111/j.1751-3928.2010.00114.x

Inoue, A., Inoué, S., Utada, M., 2018. Application of chlorite thermometry to estimation of formation temperature and redox conditions. Clay Minerals 53, 143-158. https://doi.org/10.1180/clm.2018.10

Jiang, W. and Peacor, D.R., 1993. Formation and modification of metastable intermediate sodium potassium mica paragonite, and muscovite in hydrothermally altered metabasites from northern Wales. American Mineralogist 78, 782-793.

John, D.A., Hofstra, A.H., Fleck, R.J., Brummer, J.E., Saderholm, E.C., 2003. Geologic setting and genesis of the Mule Canyon low-sulfidation epithermal gold-silver deposit, North-Central Nevada. Economic Geology 98, 425-463. http://dx.doi.org/10.2113/gsecongeo.98.2.425

Kogure, T., Jige, M., Kameda, J., Yamagishi, A., Miyawaki, R., Kitagawa, R., 2006. Stacking structures in pyrophyllite revealed by high-resolution transmission electron microscopy (HRTEM). American Mineralogist 91, 1293-1299. https://doi.org/10.2138/am.2006.1997

Kranidiotis, P. and MacLean, W.H., 1987. Systematics of chlorite at the Phelps Dodge massive sulfide deposit, Matagami, Quebec. Economic Geology 82, 1898-1911. https://doi.org/10.2113/gsecongeo.82.7.1898

Lanari, P., Wagner, T., Vidal, O., 2014. A thermodynamic model for di-trioctahedral chlorite from experimental and natural data in the system MgO-FeO-Al_2O_3-SiO_2-H_2O: applications to P-T sections and geothermometry. Contributions to Mineralogy and Petrology 167, 968. https://doi.org/10.1007/s00410-014-0968-8

Lindgren, W., 1933. Mineral Deposits. New York, McGraw-Hill, 4th ed., 930 pp.

Lipson, R., 2014. The promise and perils of porphyry deposits in the future gold production. SEG Newsletter 98, 1-21.

Martin-Garcia, J.M., Delgado, G., Sanchez-Maranon, M., Parraga, J.F., Delgado, R., 1997. Nature of dioctahedral micas in Spanish red soils. Clay Minerals 32, 107-121.

Maydagán, L., Franchini, M., Impiccini, A., Lentz, D., Patrier, P., Beaufort, D., 2018. Chlorite, white mica and clay minerals as proximity indicators to ore in the shallow porphyry environment of Quebrada de la Mina deposit, Argentina. Ore Geology Reviews 92, 297-317. https://doi.org/10.1016/j.oregeorev.2017.11.028

McKenzie, C.B., 1986. Geology and mineralization of the Chetwynd deposit, southwestern Newfoundland, Canada. In Macdonald, A.J., Gold ’86: Willowdale, Ontario, Konsult International, 137-148.

Merriman, R.J., 2005. Clay minerals and sedimentary basin history. European Journal of Mineralogy 17, 7-20. https://doi.org/10.1127/0935-1221/2005/0017-0007

Miyashiro, A., 1994. Metamorphic petrology, UCL Press, London, 404 pp.

Moore, D.M. and Reynolds, R.C., 1997. X-Ray Diffraction and the Identification and Analysis of Clay Minerals, 2nd ed. Oxford University Press.

Murphy, J.B., Keppie, J.D., Nance, R.D., and Dostal, J., 2010. Comparative evolution of the Iapetus and Rheic oceans: A North America perspective. Gondwana Research 17, 482-499. https://doi.org/10.1016/j.gr.2009.08.009

O’Brien, B.H., O’Brien, S.J., and Dunning, G.R., 1991. Silurian cover, Late Precambrian-Early Ordovician basement, and the chronology of Silurian orogenesis in the Hermitage flexure (Newfoundland Appalachians). American Journal of Science 291, 760-799.

O’Brien, S.J., O’Brien, B.H., Dunning, G.R., and Tucker, R.D., 1996. Late Neoproterozoic Avalonian and related peri-Gondwanan rocks of the Newfoundland Appalachians. In Nance, R. D., and Thompson, M. D., eds.: Avalonian and Related Peri-Gondwanan Terranes of the Circum-North Atlantic: Boulder, Colorado. Geological Society of America Special Paper 304, 9-28. https://doi.org/10.1130/0-8137-2304-3.9

O’Brien, S.J., Dubé, B., O’Driscoll, C.F., and Mills, J., 1998. Geological setting of gold mineralization and related hydrothermal alteration in Late Neoproterozoic (Post -640 Ma) Avalonian rocs of Newfoundland, with a review of the coeval gold deposits elsewhere in the

Appalachian Avalonian Belt. In Current Research. Newfoundland Department of Mines and Energy, Geological Survey, Report 98-1, 93-124.

O'Brien, S.J., Dubé, B., and O'Driscoll, C.F., 1999. High-sulphidation, epithermal-style hydrothermal systems in Late Neoproterozoic Avalonian rocks on the Burin Peninsula, Newfoundland: Implications for gold exploration. In Current Research. Newfoundland Department of Mines and Energy, Geological Survey, Report 99-1, 275-296.

Parry, W.T., Ballantyne, J.M., and Jacobs, D.C., 1984. Geochemistry of hydrothermal sericite from Roosevelt Hot Springs and the Tintic and Santa Rita porphyry copper systems. Economic Geology 79, 72-86. https://doi.org/10.2113/gsecongeo.79.1.72

Pires, G.L.C., Renac, C., Bongiolo, E.M., Neumann, R., 2020. Gossan mineralogy, textures, and gold enrichment over the Au (As, Bi, Ag) deposit in the Buracão Area (Brasília Fold Belt, Brazil): Implications for gold prospecting in weathering profiles. Journal of Geochemical Exploration 218, 106615. https://doi.org/10.1016/j.gexplo.2020.106615

Pouchou, J.L. and Pichoir, F., 1984. A new model for quantitative analyses. I. Application to the analysis of homogeneous samples. La Recherche Aérospatiale, 3, 13-38.

Pouchou, J.L. and Pichoir, F., 1985. ''PAP'' correction procedure for improved quantitative microanalysis. Pp. 104-106 in: Microbeam Analysis (J.T. Armstrong, editor). San Francisco Press, San Francisco, California, USA.

Rafiei, M., Kennedy, M., 2019. Weathering in a world without terrestrial life recorded in the Mesoproterozoic Velkerri Formation. Nature Communications 10, 3448. https://doi.org/10.1038/s41467-019-11421-4

Reynolds, R.C. and Hower, J., 1970. The Nature of Interlayering in Mixed-Layer Illite-Montmorillonites. Clays and Clay Minerals 18, 25-36. https://doi.org/10.1346/CCMN.1970.0180104

Rivai, T.A., Yonezu, K., Afrizal, S., Sanematsu, K., Kusumanto, D., Imai, A., Watanabe, K., 2019. A low-sulfidation epithermal mineralization in the River Reef Zone, the Poboya prospect, Central Sulawesi, Indonesia: vein textures, ore mineralogy, and fluid inclusions. Resource geology 69, 385-401. https://doi.org/10.1111/rge.12206

Saccocia, P.J. and Gillis, K.M., 1995. Hydrothermal upflow zones in the oceanic crust. Earth and Planetary Science Letters 136, 1-16. https://doi.org/10.1016/0012-821X(95)00155-5

Sánchez España, J., Velasco, F., and Yusta, I., 2000. Hydrothermal alteration of felsic volcanic rocks associated with massive sulphide deposition in the northern Iberian Pyrite Belt (SW Spain). Applied Geochemistry 15, 1265-1290. https://doi.org/10.1016/S0883-2927(99)00119-5

Schmidt, D., Schmidt, S.T, Mullis, J., Ferreiro Mählmann, R., Frey, M., 1997. Very low metamorphism of the Taveyanne formation of western Switzerland. Contributions to Mineralogy and Petrology 129, 385-403. https://doi.org/10.1007/s004100050344

Seedorff, E., Dilles, J.H., Proffett, J.M., Einaudi, M.T., Zurcher, L., Stavast, W.J.A., Johnson, D.A., Barton, M.D., 2005. Porphyry deposits: characteristics and origin of hypogene features. Economic Geology 100th Anniversary volume, 251-298. https://doi.org/10.5382/AV100.10

Šegvić, B., Lugović, B., Slovenec, D., Meyer, H.P., 2016. Mineralogy, petrology and geochemistry of amphibolites from the Kalnik Mt. (Sava Unit, North Croatia): Implications for the evolution of north-westernmost part of the Dinaric-Vardar branch of Mesozoic Tethys. Ofioliti 41, 35-58. https://doi.org/10.4454/ofioliti.v41i1.441

Sillitoe, R.H., 1993. Epithermal models: Genetic types, geometrical controls and shallow features. Geological Association of Canada Special Paper 40, 403-417.

Simmons, S.F. and Browne, P.R.L., 2000. Hydrothermal minerals and precious metals in the Broadlands-Ohaaki geothermal system: Implications for understanding low-sulfidation epithermal environments. Economic Geology 95, 971-999. https://doi.org/10.2113/gsecongeo.95.5.971

Simmons, S.F. and Christenson, B.W., 1994. Origins of calcite in a boiling geothermal system. American Journal of Science 294, 361-400. https://doi.org/10.2475/ajs.294.3.361

Simmons, S.F., White, N.C., and John, D.A., 2005. Geological characteristics of epithermal precious and base metal deposits. Economic Geology 100th Anniversary Volume, 485-522. https://doi.org/10.5382/AV100.16

Simpson, M.P. and Mauk, J.L., 2011. Hydrothermal alteration and veins at the epithermal Au-Ag deposits and prospects of the Waitekauri area, Hauraki Goldfield, New Zealand. Economic Geology 106, 945-973. https://doi.org/10.2113/econgeo.106.6.945

Sparkes, G.W., O'Brien, S.J., Dunning, G.R., Dubé., 2005. U-Pb geochronological constraints on the timing of magmatism, epithermal alteration and low-sulphidation gold mineralization, eastern Avalon Zone, Newfoundland. In: Current Research. Newfoundland and Labrador Department of Natural Resources, Geological Survey, Report 05-1, 115-130.

Sparkes, G.W. and Dunning, G.R., 2014. Late Neoproterozoic epithermal alteration and mineralization in the western Avalon zone: A summary of mineralogical investigations and new U/Pb geochronological results. In Current Research. Newfoundland and Labrador Department of Natural Resources, Geological Survey, Report 14-1, 99-128.

Sparkes, G.W., Ferguson, S.A., Layne, G.D., Dunning, G.R., O'Brien, S.J., and Langille, A., 2016. The nature and timing of Neoproterozoic high-sulfidation gold mineralization from the Newfoundland Avalon zone: Insights from new U-Pb ages, ore petrography, and spectral data from the Hickey's Pond prospect. In Current Research. Newfoundland and Labrador Department of Natural Resources, Geological Survey, Report 16-1, 91-116.

Środoń, J., 2006. Identification and quantitative analysis of clay minerals, in: Handbook of Clay Science. Elsevier Ltd., Amsterdam, 765-787. https://doi.org/10.1016/B978-0-08-098259-5.00004-4

Sugimori, H., Iwatsuki, T., Murakami, T., 2008. Chlorite and biotite weathering, Fe^{2+}-rich corrensite formation, and Fe behavior under low PO_2 conditions and their implication for Precambrian weathering. American Mineralogist 93, 1080-1089. https://doi.org/10.2138/am.2008.2663

Thompson, J.F.H., Lessman, J., Thompson, A.J.B., 1986. The Temora gold-silver deposit: a newly recognized style of high sulfur mineralization in the lower Paleozoic of Australia. Economic Geology 81, 732-738. https://doi.org/10.2113/gsecongeo.81.3.732

Tillick, D.A., Peacor, D.R., Mauk, J.L., 2001. Genesis of dioctahedral phyllosilicates during hydrothermal alteration of volcanic rocks: I. The Golden Cross epithermal ore deposit, New Zealand. Clays and Clay Minerals 49-2, 126-140. https://doi.org/10.1346/CCMN.2001.0490203

Tischendorf, G., Förster, H.J., Gottesmann, B., Rieder, M., 2007. True and brittle micas: composition and solid-solution series. Mineralogical Magazine 71 (3), 285-320. https://doi.org/10.1180/minmag.2007.071.3.285

Uzarowicz, Ł., Šegvić, B., Michalik, M., Bylina, P., 2012. The effect of hydrochemical conditions and pH of the environment on phyllosilicate transformations in the weathering zone of pyrite-bearing schists in Wieściszowice (SW Poland). Clay Minerals 47, 401-417. http://dx.doi.org/10.1180/claymin.2012.047.4.01

Vidal, O., De Andrade, V., Lewin, E., Muñoz, M., Parra, T., Pascarelli, S., 2006. P-T-deformation-Fe^{3+}/Fe^{2+} mapping at the thin section scale and comparison with XANES mapping: application to a garnet-bearing metapelite from the Sambagawa metamorphic belt (Japan).

Journal of Metamorphic Geology 24, 669-683. https://doi.org/10.1111/j.1525-1314.2006.00661.x

Vidal, O., Lanari, P., Muñoz, M., Bourdelle, F., De Andrade, V., 2016. Deciphering temperature, pressure and oxygen-activity conditions of chlorite formation. Clay Minerals 51, 615-633. https://doi.org/10.1180/claymin.2016.051.4.06

Walker, J.R., 1993. Chlorite polytype geothermometry. Clays and Clay Minerals 41, 260-267. https://doi.org/10.1346/CCMN.1993.0410212

Walshe, J.L., 1986. A six-component chlorite solid solution model and the conditions of chlorite formation in hydrothermal and geothermal systems. Economic Geology 81, 681-703. https://doi.org/10.2113/gsecongeo.81.3.681

Wang, Z., Chen, B., Yan, X., Li, S., 2018. Characteristics of hydrothermal chlorite from the Niujuan Ag-Au-Pb-Zn deposit in the north margin of NCC and implications for exploration tools for ore deposits. Ore Geology Reviews 101, 398-412. https://doi.org/10.1016/j.oregeorev.2018.08.003

White, N.C. and Hedenquist, J.W., 1990. Epithermal environments and styles of mineralization: variations and their causes, and guidelines for exploration. Journal of Geochemical Exploration 36, 445-474. https://doi.org/10.1016/0375-6742(90)90063-G

White, N.C. and Hedenquist, J.W., 1995. Epithermal gold deposits: styles, characteristics, and exploration. SEG Newsletter 23, 9-13.

Whitney, D.L. and Evans, B.W., 2010. Abbreviations for names of rock-forming minerals. American Mineralogist, 95, 185-187. https://doi.org/10.2138/am.2010.3371

Wilkinson, J.J., Chang, Z., Cooke, D.R., Baker, M.J., Wilkinson, C.C., Inglis, S., Chen, H., Gemmell, J.B., 2015. The chlorite proximitor: A new tool for detecting porphyry ore deposits. Journal of Geochemical Exploration 152, 10-26. https://doi.org/10.1016/j.gexplo.2015.01.005

Williams, H., 1979. Appalachian Orogen in Canada. Canadian Journal of Earth Sciences 16 (3), 792-807. https://doi.org/10.1139/e79-070

Wilson, M.J., 2004. Weathering of the primary rock-forming minerals: processes, products, and rates. Clay Minerals 39, 233-266. https://doi.org/10.1180/0009855043930133

Yan, Y., Tillick, D.A., Peacor, D.R., Simmons, S.F., 2001. Genesis of dioctahedral phyllosilicates during hydrothermal alteration of volcanic rocks: II. The Broadlands-Ohaaki hydrothermal system, New Zealand. Clays and Clay Minerals 49-2, 141-155. https://doi.org/10.1346/CCMN.2001.0490204

Yoneda, T. and Maeda, H., 2008. The Chemical Composition of Chlorites from Hydrothermal Ore Deposits and its Applicability to Geothermometers. Journal of MMIJ 124, 694-699. https://doi.org/10.2473/journalofmmij.124.694

Zaccarini, F., Garuti, G., Rossi, A., Carrillo Rosúa, F.J., Morales Ruano, S., and Fenoll Hach-Alí, P., 2003. Application of chlorite and fluid-inclusion geothermometry to vein and stratiform Fe-Cu-Zn sulphide deposits of the northern Apennine ophiolites (Emilia Romagna and Liguria, Italy). Atti Ticinensi di Scienze della Terra 9, 109-111.

Zane, A. and Weiss, Z., 1998. A procedure for classifying rock-forming chlorites based on microprobe data. Rendiconti Lincei 9, 51-56. https://doi.org/10.1007/BF02904455

Zanoni, G., Šegvić, B., Moscariello, A., 2016. Clay mineral diagenesis in Cretaceous clastic reservoirs from West African passive margins (the South Gabon Basin) and its impact on regional geology and basin evolution history. Applied Clay Science, 134, 186-209. https://doi.org/10.1016/j.clay.2016.09.032

Zhang, S., Xiao, B., Long, X., Chu, G., Cheng, J., Zhang, Y., Tian, J., Xu, G., 2020. Chlorite as an exploration indicator for concealed skarn mineralization: Perspective from the Tonglushan Cu-Au-Fe skarn deposit, Eastern China. Ore Geology Reviews 126, 1-14. https://doi.org/10.1016/j.oregeorev.2020.103778

Zhou, X., Liu, D., Bu, H., Deng, L., Liu, H., Yuan, P., Du, P., Song, H., 2018. XRD-based quantitative analysis of clay minerals using reference intensity ratios, mineral intensity factors, Rietveld, and full pattern summation methods: A critical review. Solid Earth Sciences 3, 16-29. https://doi.org/10.1016/j.sesci.2017.12.002

Zhu, Y., An, F., and Tan, J., 2011. Geochemistry of hydrothermal gold deposits: A review. Geoscience Frontiers 2, 367-374. https://doi.org/10.1016/j.gsf.2011.05.006

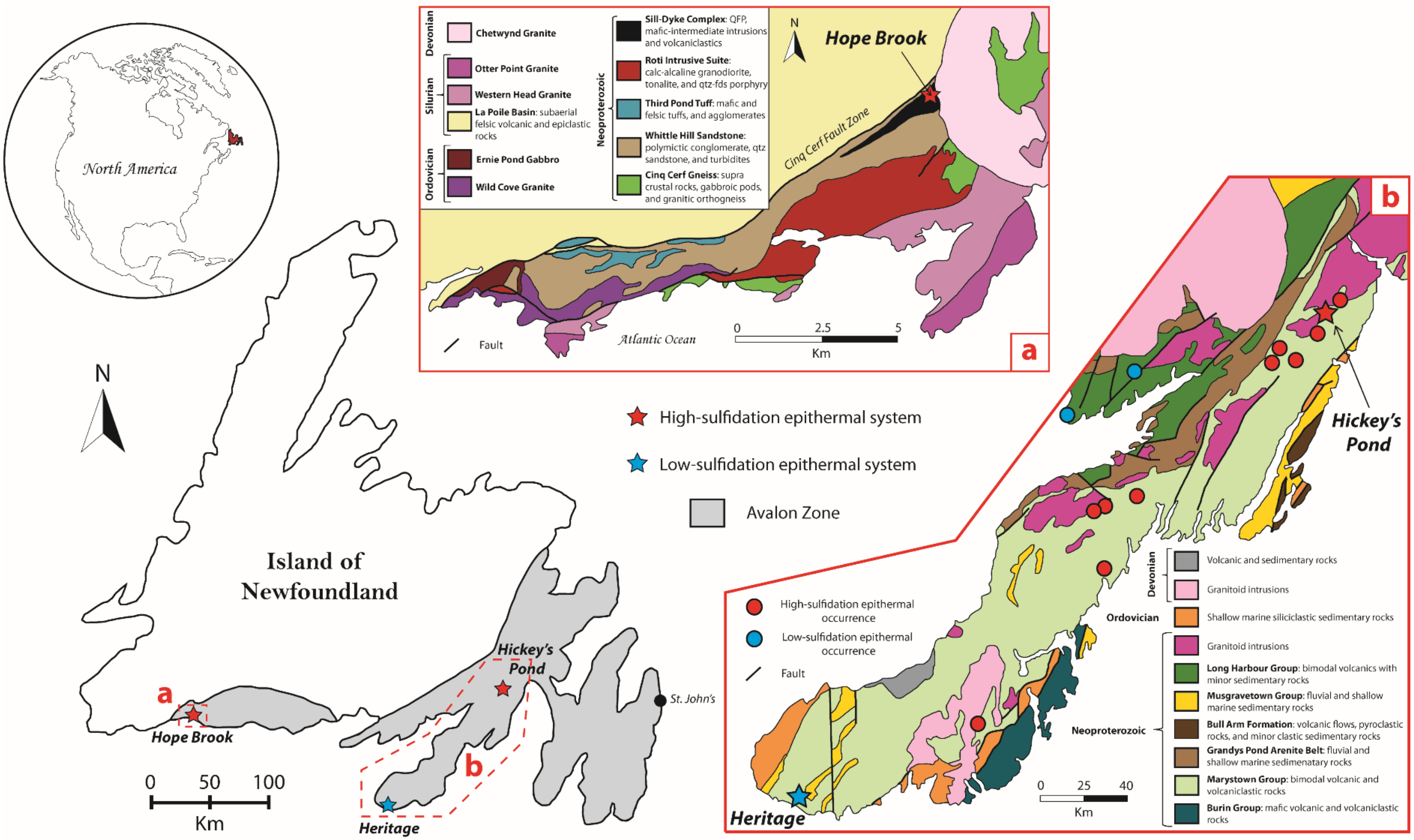

Figure 2.1: Geographical and geological setting of the studied areas in the Avalon Zone of Newfoundland (Newfoundland map modified after Sparkes and Dunning, 2014). (a) Location and geological setting of the Hope Brook high-sulfidation epithermal deposit (modified after Dubé et al., 1995). (b) Locations and geological setting of the Hickey's Pond high-sulfidation epithermal system and the Heritage low-sulfidation epithermal prospect (modified after O'Brien et al., 1999 and Sparkes and Dunning, 2014).

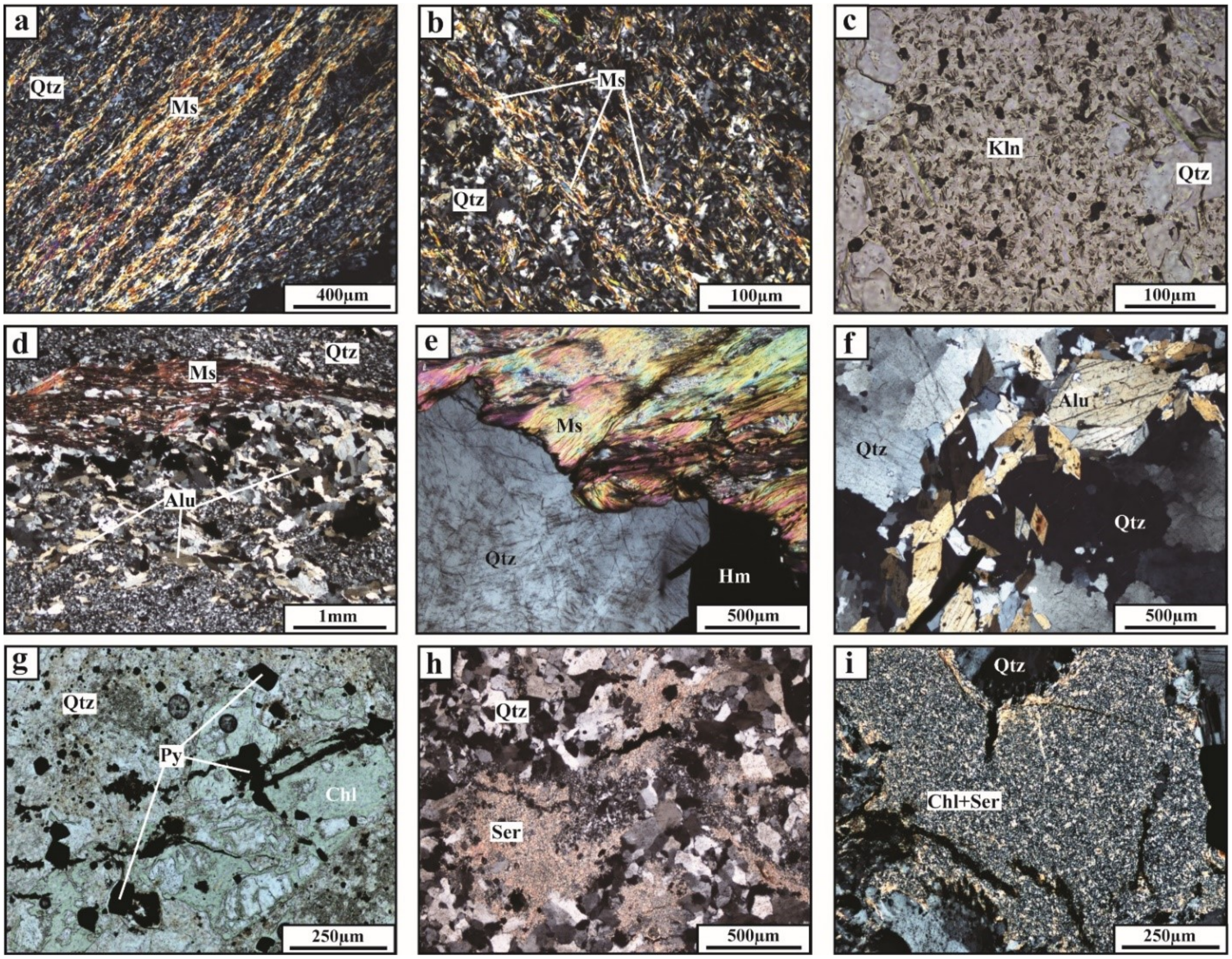

Figure 2.2: Optical petrography photomicrographs of the studied epithermal systems. (a) Hope Brook: Phyllic/sericitic alteration with mica veinlets in silica-rich rocks. (b) Hope Brook: Zoom of (a), with the detailed relationship between mica crystals and quartz. (c) Hope Brook: Kaolinite crystals developed in open space pocket in silicified rock. (d) Hickey's Pond: Quartz-alunite schist with mica. (e) Hickey's Pond: Coarse mica crystals in quartz-hematite vein. (f) Hickey's Pond: Quartz-alunite schist. (g) Heritage: chloritic alteration in quartz-pyrite silicified rock. (h) Heritage: Fine-grained white mica (phyllic/sericitic alteration) in silicified rock. (i) Heritage: Fine-grained chlorite and white mica in quartz-rich rock.

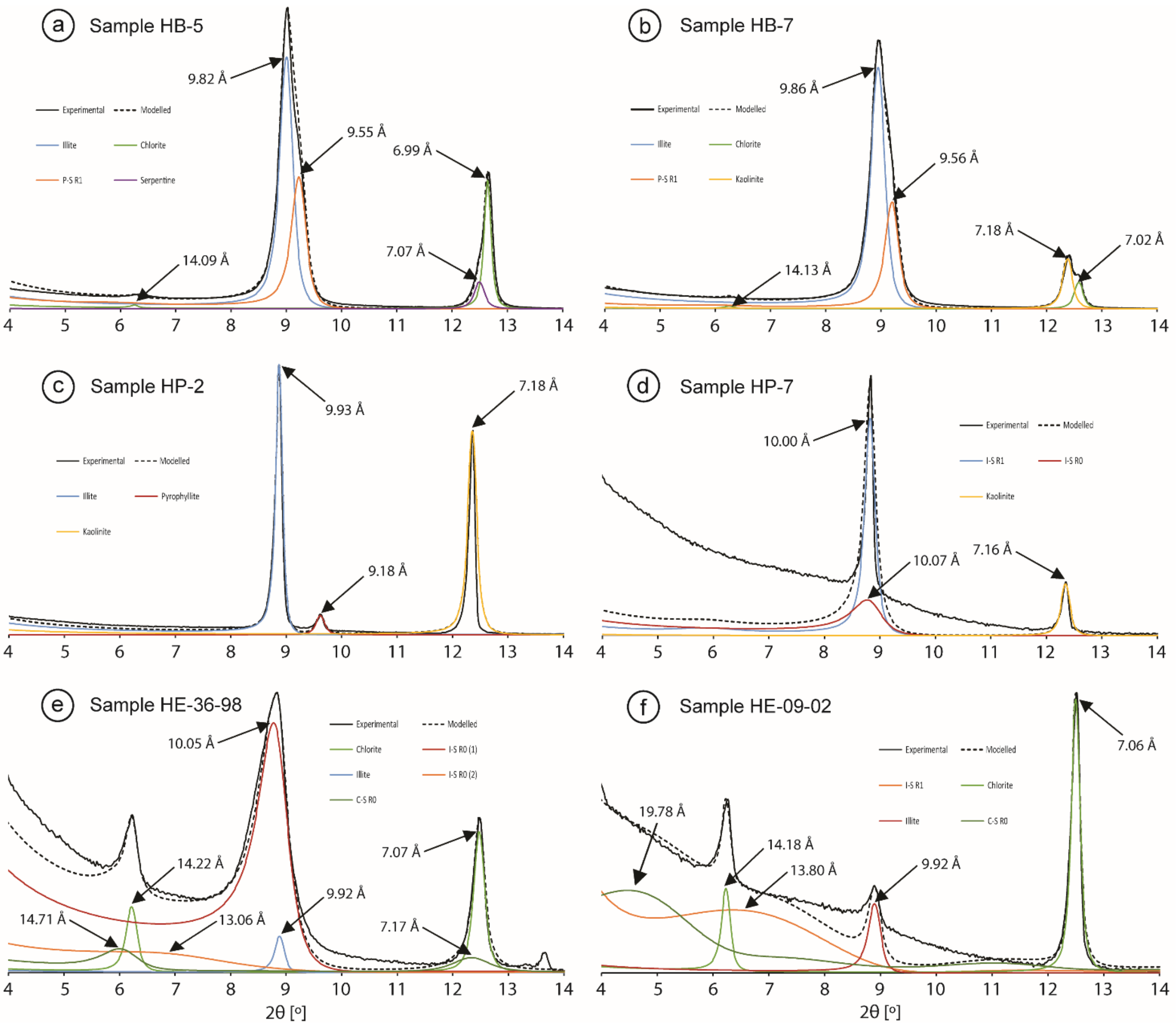

Figure 2.3: Comparison between experimental (continuous line) and Sybilla© modeled (dashed line) XRD pattern of representative phyllosilicate assemblages from the three studied epithermal systems. Abbreviations: HB = Hope Brook; HP = Hickey's Pond; HE = Heritage.

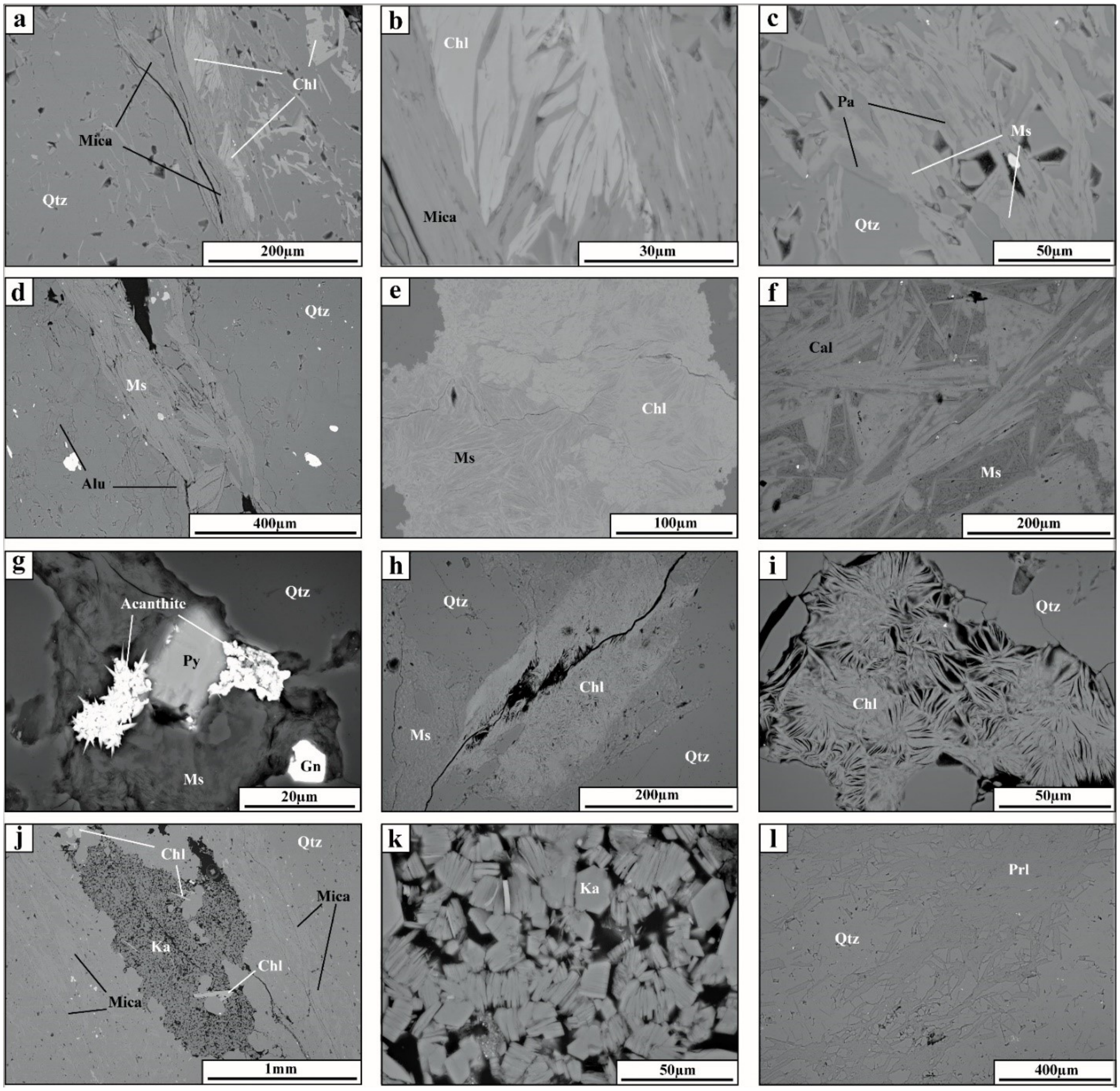

Figure 2.4: Backscattered electron (BSE) photomicrographs of selected phyllosilicate-rich samples from the three studied epithermal systems. (a) Hope Brook: quartz-mica schist with mica-chlorite stacks. (b) Hope Brook: zoom of mica-chlorite stacks of (a). (c) Hope Brook: mica crystals with cores enriched in Na and rims enriched in K. (d) Hickey's Pond: quartz-mica schist with alunite. (e) Heritage: relationship between mica and chlorite. (f) Heritage: bladed calcite with mica. (g) Heritage: sulfide mineralization in the form of acanthite, pyrite, and galena in close spatial relationship with mica in silica-rich rocks. (h) Heritage: relationship between mica and chlorite in phyllic altered rocks. (i) Heritage: radial aggregates of chlorite developed in open space pockets. (j) Hope Brook: kaolinite developed in open space pockets in mica-chlorite schist. (k) Hope Brook: zoom of (j). (l) Hope Brook: advanced argillic alteration characterized by quartz and pyrophyllite. Abbreviations: Qtz = quartz; Chl = chlorite; Ms = muscovite; Pa = paragonite; Alu = alunite; Cal = calcite; Py = pyrite; Ga = galena; Ka = kaolinite; Prl = pyrophyllite.

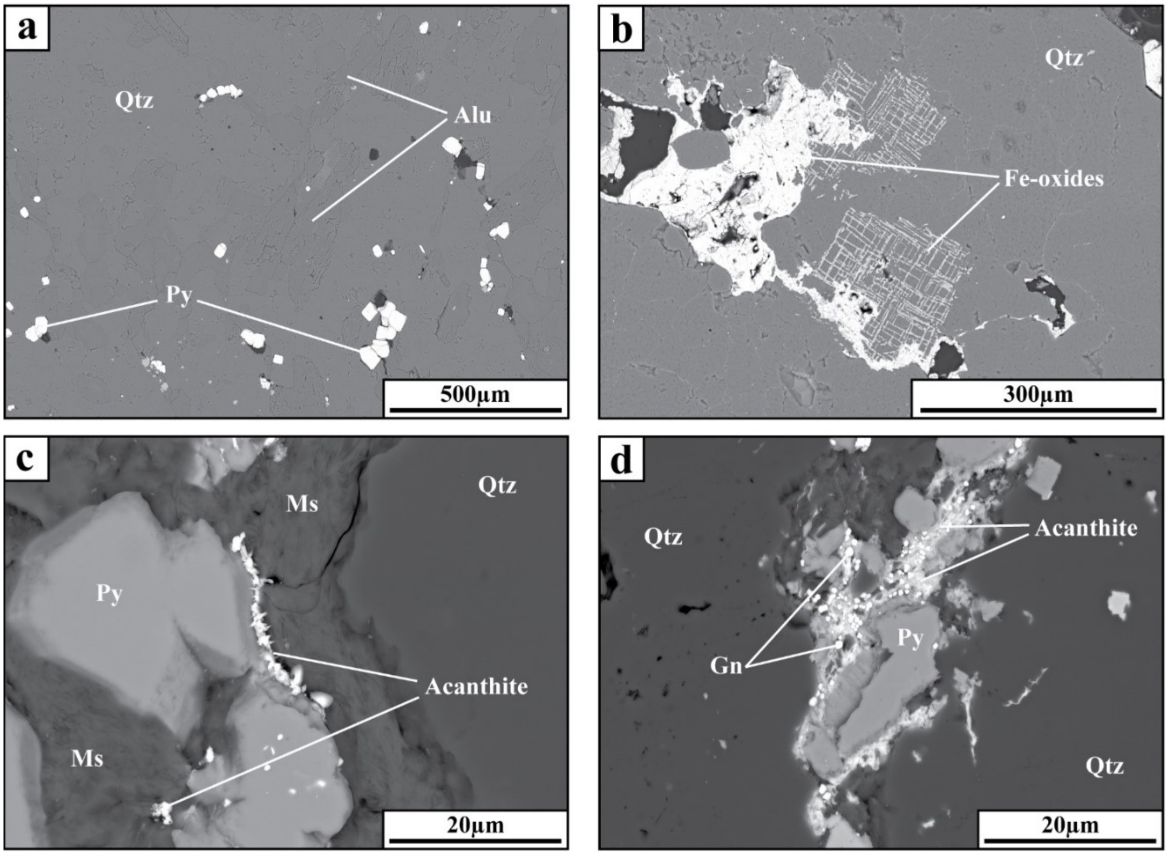

Figure 2.5: Backscattered electron (BSE) photomicrographs illustrating the relationship between alteration and mineralization in the studied epithermal systems. (a) Hope Brook: pyrite crystals developed filling open space vugs in quartz-alunite advanced argillic alteration zone. (b) Hickey's Pond: Fe-oxides in open space vugs inside the vuggy silica alteration zone. (c) Heritage: sulfide mineralization in the form of acanthite and pyrite in close spatial relationship with mica (Fe-Mg muscovite) in silica-rich rocks. (d) Heritage: sulfide mineralization in the form of acanthite, pyrite, and galena in close spatial relationship with mica (Fe-Mg muscovite) in silica-rich rocks.

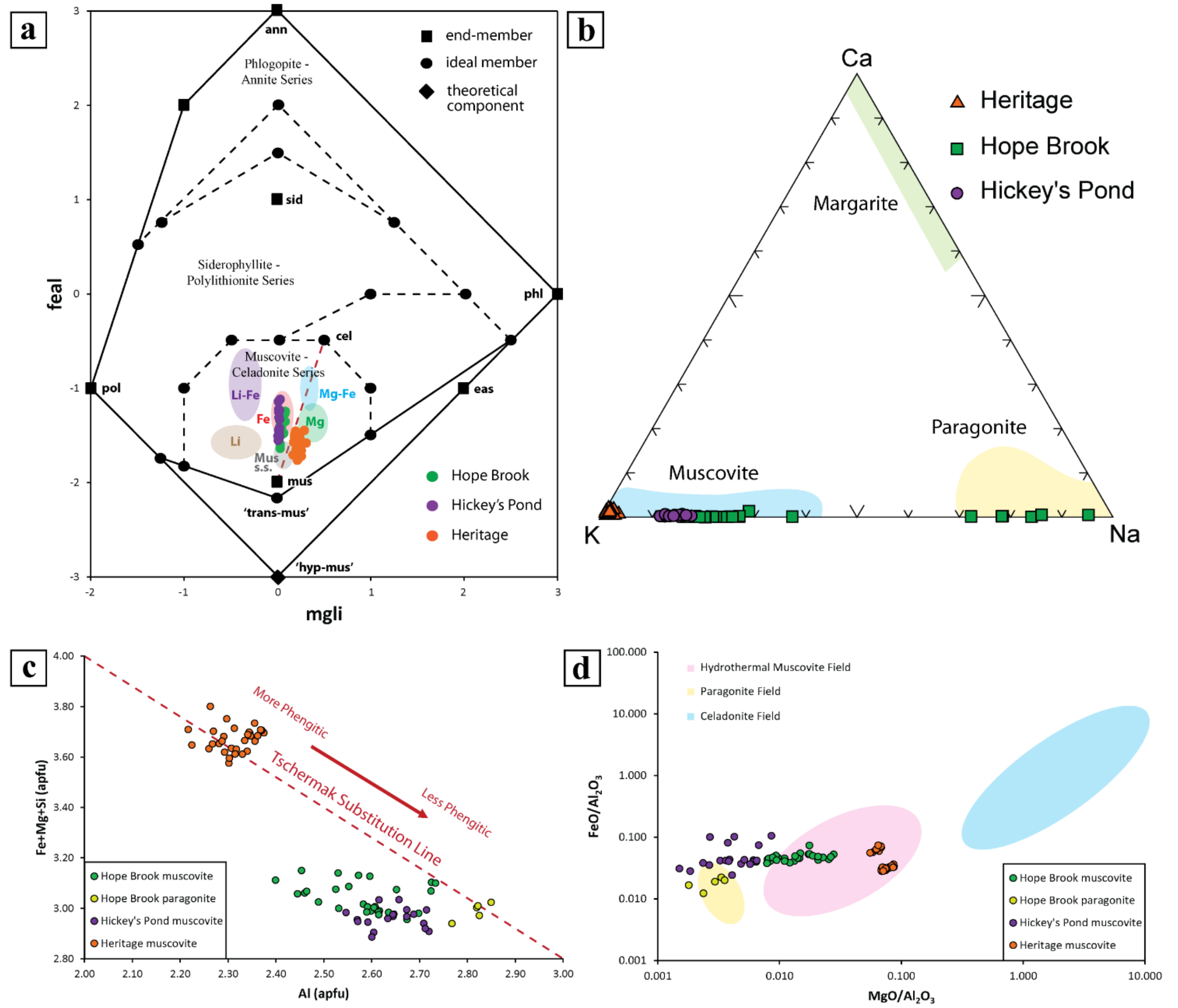

Figure 2.6: Chemical discrimination diagrams and plots for mica from the three analyzed epithermal systems. (a) mgli/feal diagram with indication of mica end-members, ideal end-members, and theoretical component, as well as prefixes that characterize mica varieties from the muscovite-celadonite series (mgli = Mg–Li; feal = (VIFetot+Mn+Ti)-VIAl; based on Tischendorf et al., 2007). (b) Interlayer K-Na-Ca triangular plot. (c) Al vs. Fe+Mg+Si (a.p.f.u.) binary diagram expressing the various degrees of Tschermak substitution of the different mica varieties. (d) FeO/Al_2O_3 vs. MgO/Al_2O_3 binary diagram (hydrothermal muscovite field from Maydagan et al., 2018; paragonite field from Ho Ahn et al., 1985, Hoffer, 1978, Deer et al., 1966; celadonite field from Foster, 1969).

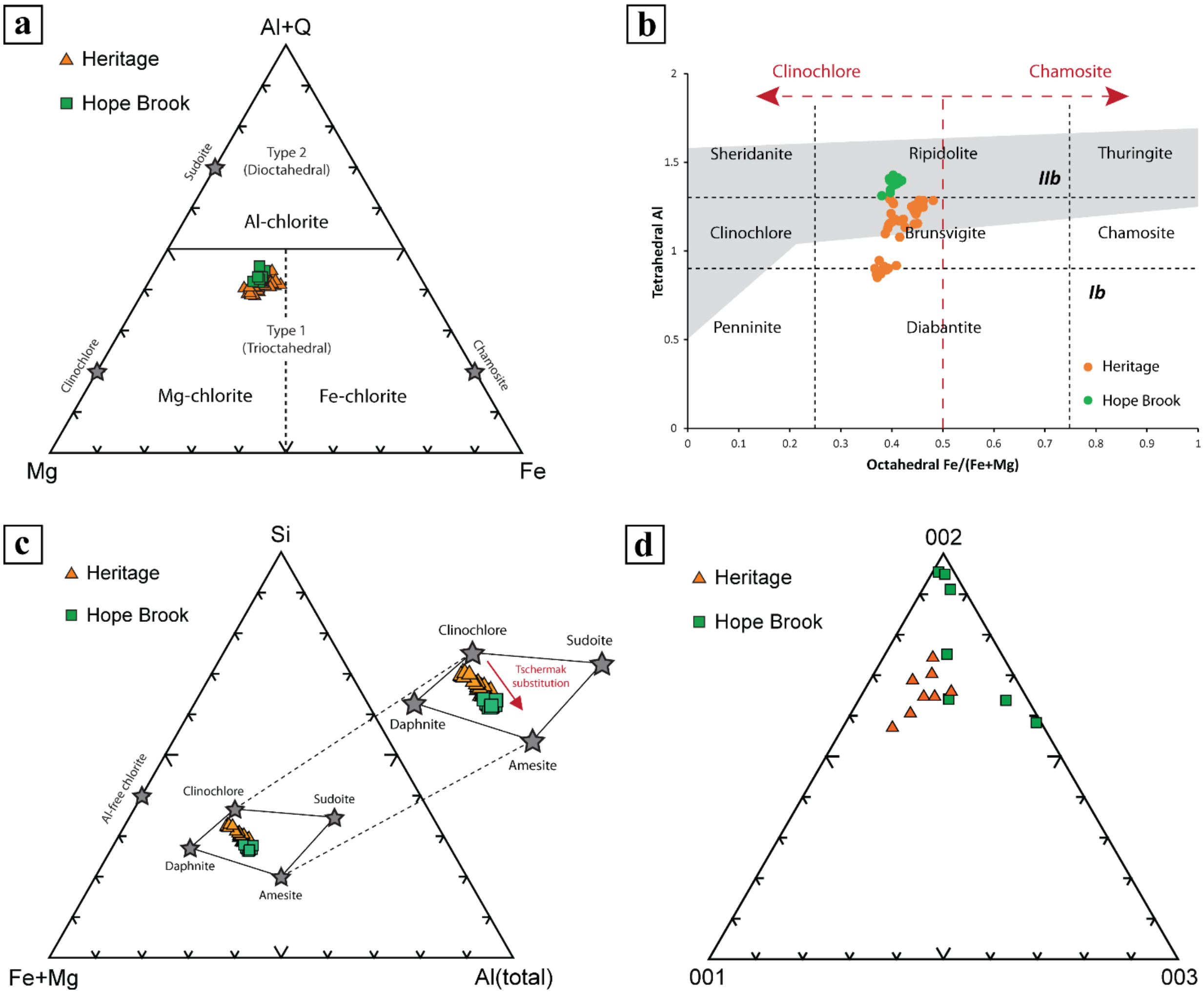

Figure 2.7: Chemical discrimination diagrams and plots for chlorite from the Hope Brook HSS and the Heritage LSS. (a) Compositional fields of chlorite (after Zane and Weiss, 1998). Type I chlorite is mostly Mg-Fe chlorite, depending on the dominant cation. Type II chlorite is mostly Al-chlorite. (b) Octahedral Fe/(Fe+Mg) vs. tetrahedral Al binary diagram with the different varieties of Fe-Mg chlorite (chlorite classification after Foster, 1962; clinochlore-chamosite boundary after Bailey, 1980b; IIb chlorite polytype area after Foster, 1962; Ib chlorite polytype area after Curtis et al., 1985). (c) Fe+Mg – Si – Al(total) ternary diagram (after Abd Elmola et al., 2017). (d) Ternary diagram of the 001, 002, and 003 XRD basal reflection peak intensity of analyzed chlorite.

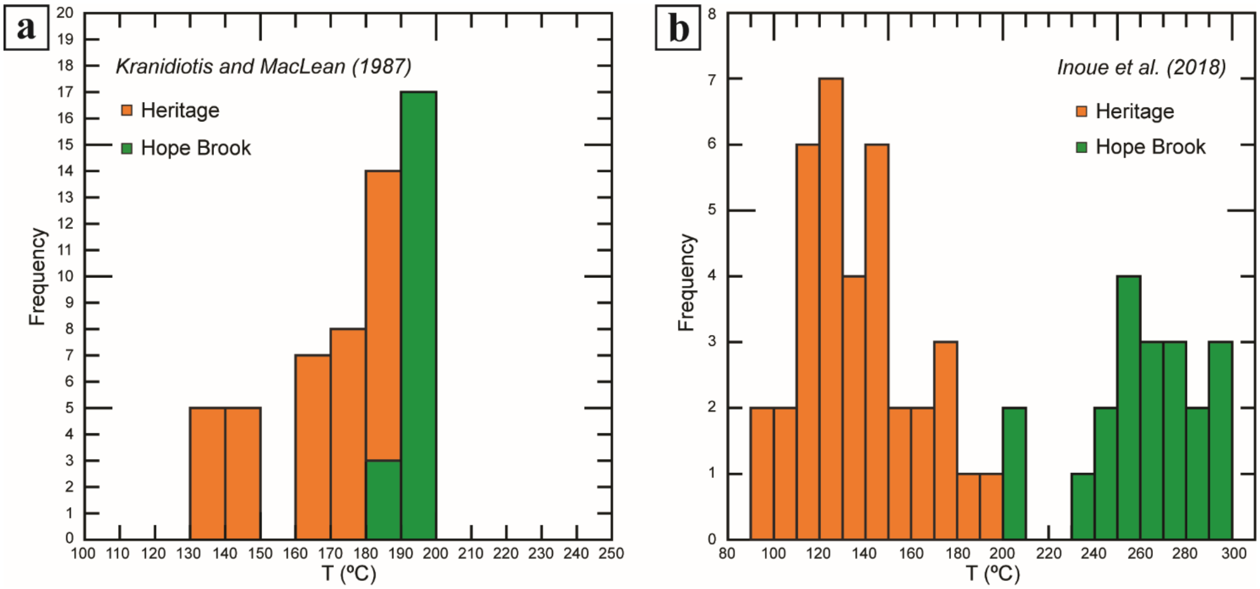

Figure 2.8: Frequency histogram of chlorite temperature obtained using (a) the Kranidiotis and MacLean (1987) empirical geothermometer and (b) the Inoue et al. (2018) semi-empirical geothermometer.

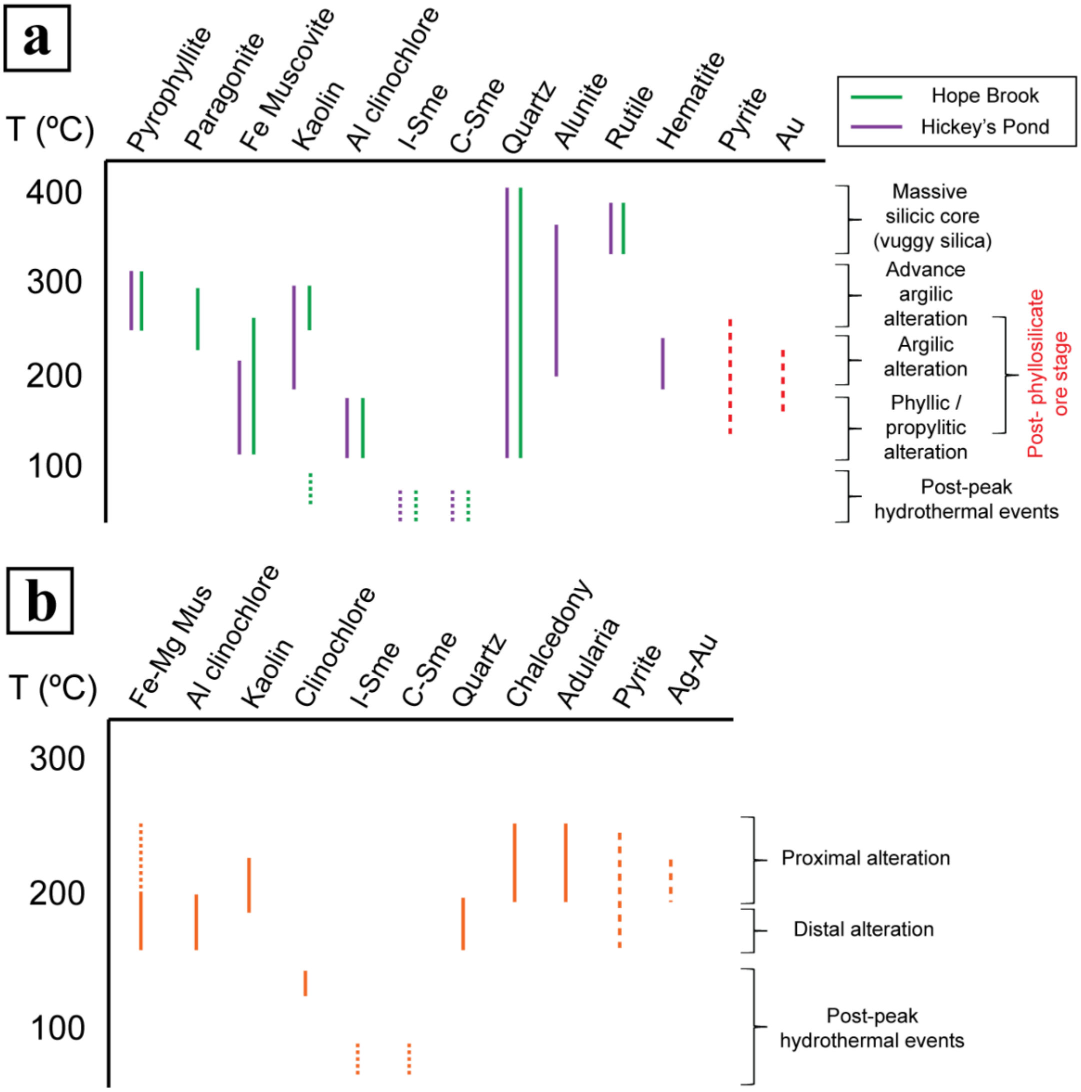

Figure 2.9: Reconstruction of hydrothermal events in the three studied epithermal systems based on phyllosilicate mineralogy, distribution, and genesis. Abbreviations: Mus = muscovite; I-Sme = illite-smectite; C-Sme = chlorite-smectite.

Table 2.1: List of samples analyzed from epithermal deposits/prospects in the Avalon Zone. Deposit type, drill core depth, short description, and analytical methods applied are reported for each sample.

Sample	Deposit / Prospect	Outcrop / Drill core	Core number	Depth (m)	Description	Applied methods
High-sulfidation epithermal systems						
HB-1	Hope Brook	Drill Core	HB12-100	47.60 – 54.90	Quartz-sericite-chlorite schist	OM, XRD, CL
HB-2	Hope Brook	Drill Core	HB12-100	82.20 – 102.10	Pyrite-silica breccia	OM, XRD, CL
HB-3	Hope Brook	Drill Core	HB12-100	122.70 – 134.50	Pyrite-silica breccia	OM, XRD
HB-4	Hope Brook	Drill Core	HB12-100	225.80 – 234.20	Quartz-sericite schist	OM, XRD, CL, CM
HB-5	Hope Brook	Drill Core	HB12-100	245.80 – 247.30	Quartz-sericite schist	OM, XRD, CL, CM
HB-6	Hope Brook	Drill Core	HB12-100	277.20 – 285.10	Quartz-sericite schist	OM, XRD, CL
HB-7	Hope Brook	Drill Core	HB12-100	288.00 – 294.40	Silicified breccia	OM, XRD, CL, CM
HB-8	Hope Brook	Drill Core	HB12-100	318.50 – 319.10	Vuggy silica zone	OM, XRD
HB-9	Hope Brook	Drill Core	HB12-100	329.80 – 336.80	Quartz-sericite-pyrophyllite schist	OM, XRD, CL
HB-10	Hope Brook	Drill Core	HB12-100	349.90 – 354.00	Vuggy silica zone	OM, XRD, CL
HB-11	Hope Brook	Drill Core	HB12-100	378.80 – 383.00	Massive silica zone	OM, XRD
HB-12	Hope Brook	Drill Core	HB12-100	392.50 – 394.20	Silicified breccia	OM, XRD
HB-13	Hope Brook	Drill Core	HB12-100	428.10 – 437.40	Quartz-sericite-chlorite schist	OM, XRD, CL
HB-14	Hope Brook	Drill Core	HB12-100	457.10 – 458.70	Quartz-sericite-chlorite schist	OM, XRD, CL, CM
HP-1	Hickey's Pond	Outcrop	-	-	Quartz-alunite schist	OM, XRD
HP-2	Hickey's Pond	Outcrop	-	-	Quartz-hematite-alunite schist	OM, XRD, CL, CM
HP-3	Hickey's Pond	Outcrop	-	-	Vuggy silica zone	OM, XRD, CL, CM
HP-4A	Hickey's Pond	Outcrop	-	-	Quartz-hematite vein	OM, XRD
HP-4B	Hickey's Pond	Outcrop	-	-	Quartz-hematite vein	OM, XRD, CL, CM
HP-5	Hickey's Pond	Outcrop	-	-	Quartz-alunite-pyrite schist	OM, XRD
HP-6	Hickey's Pond	Outcrop	-	-	Quartz-alunite-hematite vein	OM, XRD
HP-7	Hickey's Pond	Outcrop	-	-	Hematite-rich breccia	OM, XRD, CL, CM
Low-sulfidation epithermal systems						
HE32-25	Heritage	Drill Core	HE-32-16	25.18 – 25.35	Hematite-rich breccia	OM, XRD, CL
HE33-68	Heritage	Drill Core	HE-33-16	68.79 – 68.89	Hematite-oxide-rich breccia	OM, XRD
HE35-50	Heritage	Drill Core	HE-35-16	50-61 – 50.71	Silicified hydrothermal vein/breccia	OM, XRD, CL
HE36-98	Heritage	Drill Core	HE-36-16	98.33 – 98.42	Silica-illite hydrothermal breccia	OM, XRD, CL, CM
HE36-107	Heritage	Drill Core	HE-36-16	107.20 – 107.80	Chlorite-oxide-silica breccia	OM, XRD
HE47-23	Heritage	Drill Core	HE-47-16	22.90 – 23.00	Silicified hydrothermal vein/breccia	OM, XRD
HE47-26	Heritage	Drill Core	HE-47-16	25.90 – 26.00	Silicified hydrothermal vein	OM, XRD, CL
HE48-27	Heritage	Drill Core	HE-48-16	27.45 – 27.63	Silicified hydrothermal vein	OM, XRD
HE48-28	Heritage	Drill Core	HE-48-16	28.00 – 28.14	Silicified hydrothermal vein/breccia	OM, XRD, CL, CM
HE-02-03	Heritage	Drill Core	-	-	Quartz-carbonate-sulfide vein	XRD
HE-02-04	Heritage	Drill Core	-	-	Silicified hydrothermal vein	XRD
HE-03-03	Heritage	Drill Core	-	-	Quartz-adularia breccia	XRD
HE-05-03	Heritage	Drill Core	-	-	Quartz-carbonate vein/breccia	XRD
HE-05-15	Heritage	Drill Core	-	-	Quartz-chlorite vein	XRD, CL
HE-07-03	Heritage	Drill Core	-	-	Hematite-rich breccia	XRD, CL
HE-08-01	Heritage	Drill Core	-	-	Quartz-chlorite vein/breccia	XRD
HE-08-02	Heritage	Drill Core	-	-	Quartz-carbonate-chlorite vein	XRD
HE-08-03	Heritage	Drill Core	-	-	Quartz-chlorite vein/breccia	XRD
HE-09-01	Heritage	Drill Core	-	-	Silicified hydrothermal breccia	XRD
HE-09-02	Heritage	Drill Core	-	-	Quartz-chlorite vein/breccia	XRD, CL, CM
HE-22-1R	Heritage	Drill Core	-	-	Quartz-chlorite-sulfide vein	XRD
HE-23-1R	Heritage	Drill Core	-	-	Quartz-sericite-altered andesite	XRD
HE-23-2R	Heritage	Drill Core	-	-	Silicified hydrothermal breccia	XRD, CL
HE-23-3R	Heritage	Drill Core	-	-	Quartz-adularia breccia	XRD
HE-24-1R	Heritage	Drill Core	-	-	Quartz-chlorite vein/breccia	XRD, CL, CM

Abbreviations: OM = optical microscopy; XRD = X-ray diffraction; CL = clay mineral fractions; CM = clay mineral modeling.

Table 2.2: X-ray diffraction mineralogy and quantification abundances (in wt.%) of samples analyzed.

Sample	Qtz	Cal	Kfs	Pl	Adl	Alu	Nalu	Hem	Rt	Py	Sp	Gn	Ms	Pg	Chl	Kln	Prl	Mix	Ms polytype	Chl polytype
High-sulfidation epithermal systems																				
HB-1	45.5	1.5	-	19	-	-	-	-	0.5	-	-	-	32.0	-	1.5	-	-	-	$2M_1$	-
HB-2	74.0	-	-	-	-	-	-	-	0.5	25.5	-	-	-	-	-	-	-	-	-	-
HB-3	89.6	-	-	-	-	-	-	-	0.2	9.2	-	-	1.0	-	-	-	-	-	-	-
HB-4	65.6	-	-	-	-	-	-	-	0.9	-	-	-	25.0	6.5	1.5	0.5	-	-	$2M_1$	-
HB-5	90.4	-	-	-	-	-	-	-	0.4	0.9	-	-	6.0	2.0	-	0.3	-	-	$2M_1$	-
HB-6	63.9	-	-	-	-	-	-	-	1.0	5.0	-	-	22.5	6.5	0.2	0.9	-	-	$2M_1$	-
HB-7	70.6	-	-	-	-	-	-	-	0.9	1.0	-	-	20.5	6.0	0.3	0.7	-	-	$2M_1$	-
HB-8	89.2	-	-	-	-	-	-	-	0.3	7.5	-	-	3.0	-	-	-	-	-	$2M_1$	-
HB-9	84.3	-	-	-	-	-	-	-	0.2	1.5	-	-	2.0	0.5	-	1.5[1]	10.0	-	$2M_1$	-
HB-10	77.3	-	-	-	-	-	-	-	0.7	4.5	-	-	6.5	10.0	0.4	0.6	-	-	$2M_1$	-
HB-11	98.8	0.1	-	-	-	-	-	-	0.2	-	-	-	0.9	-	-	-	-	-	$2M_1$	-
HB-12	95.7	-	-	-	-	-	-	-	0.4	2.5	-	-	1.2	-	0.2	-	-	-	$2M_1$	-
HB-13	60.4	-	-	-	-	-	-	-	1.0	7.3	-	-	10.0	20.5	-	0.8	-	-	$2M_1$	-
HB-14	27.8	-	-	-	-	-	-	-	0.7	-	-	-	11.5	5.0	55.0	-	-	-	$2M_1$	*IIb + Ib*
HP-1	78.4	-	-	-	-	*	13.7	-	0.4	-	-	-	7.5	-	-	-	-	-	$2M_1$	-
HP-2	73.6	-	-	-	-	-	-	7.4	0.3	-	-	-	18.0	-	-	0.7	-	-	$2M_1$	-
HP-3	95.1	-	-	-	-	-	1.1	-	-	2.0	-	-	1.5	-	-	0.3	-	-	$2M_1$	-
HP-4A	85.3	-	-	-	-	-	5.0	2.0	0.2	-	-	-	7.0	-	-	0.5	-	-	$2M_1$	-
HP-4B	65.9	-	-	-	-	2.0	21.5	0.7	0.4	-	-	-	7.0	-	-	2.5	-	-	$2M_1$	-
HP-5	81.6	-	-	-	-	-	13.5	0.9	-	-	-	-	3.5	-	-	0.5	-	-	$2M_1$	-
HP-6	74.6	-	-	-	-	-	23.0	0.3	0.3	-	-	-	1.6	-	-	0.2	-	-	-	-
HP-7	79.8	-	-	-	-	-	14.0	0.7	0.2	-	-	-	5.0	-	-	0.3	-	-	-	-
Low-sulfidation epithermal system																				
HE-32-25	60.0	2.5	6.0	-	20.0	-	-	-	-	-	-	-	2.5	-	9.0	-	-	*	$2M_1 + 1M$	-
HE-33-68	37.0	-	10.0	-	30.0	-	-	-	-	-	-	-	5.0	-	18.0	-	-	-	-	-
HE-35-50	91.0	-	1.0	-	3.0	-	-	-	-	1.0	-	-	2.5	-	1.5	-	-	*	$2M_1 + 1M$	-
HE-36-98	84.0	8.0	1.0	-	2.5	-	-	-	-	1.0	-	-	1.5	-	2.0	-	-	*	-	-
HE-36-107	84.0	10.0	-	-	-	-	-	-	-	-	0.4	0.1	3.5	-	2.0	-	-	-	-	-
HE-47-23	88.6	-	2.0	-	-	-	-	-	-	2.5	-	-	6.5	-	0.4	-	-	-	$2M_1$	-
HE-47-26	90.2	5.0	-	-	-	-	-	-	-	0.8	-	-	1.5	-	2.5	-	-	-	-	-
HE-48-27	90.5	1.0	-	-	-	-	-	-	-	0.5	-	-	8.0	-	-	-	-	-	$2M_1$	-
HE-48-28	89.5	-	-	-	-	-	-	-	-	0.4	0.1	-	7.0	-	3.0	-	-	-	-	-
HE-02-03	41.9	41.0	8.5	-	4.0	-	-	-	-	0.8	0.5	-	2.5	-	0.8	-	-	-	$2M_1$	-
HE-02-04	70.0	4.5	-	-	-	-	-	-	-	-	3.0	0.5	22.0	-	-	-	-	-	$2M_1$	-
HE-03-03	69.5	0.5	13.5	-	5.0	-	-	-	-	4.5	-	-	7.0	-	-	-	-	-	$2M_1$	-
HE-05-03	37.9	18.5	10.0	-	19.0	-	-	-	-	2.6	-	-	7.0	-	5.0	-	-	-	$2M_1$	-
HE-05-Odd	47.5	2.5	3.0	-	1.0	-	-	-	-	15.0	-	-	26.5	-	4.5	-	-	*	$2M_1$	-
HE-07-03	83.3	-	1.5	-	*	-	-	-	-	0.7	-	-	13.0	-	1.5	-	-	-	$2M_1$	-
HE-08-01	87.5	-	-	-	-	-	-	-	-	-	-	-	9.5	-	3.0	-	-	-	$2M_1$	-
HE-08-02	98.0	-	-	-	-	-	-	-	-	-	-	-	1.5	-	0.5	-	-	-	$2M_1$	-
HE-08-03	79.3	-	3.0	-	4.0	-	-	-	-	4.5	-	-	8.5	-	0.7	-	-	-	$2M_1$	-
HE-09-01	89.0	-	-	-	-	-	-	-	-	1.5	-	-	6.0	-	3.5	-	-	-	$2M_1$	-
HE-09-02	87.3	8.0	-	-	-	-	-	-	-	-	0.2	-	2.0	-	2.5	-	-	*	-	-
HE-22-1R	92.9	0.7	-	-	-	-	-	-	-	-	0.3	0.1	3.5	-	2.5	-	-	-	$2M_1 + 1M$	-
HE-23-1R	79.5	-	6.0	-	5.0	-	-	-	-	2.0	-	-	5.0	-	2.5	-	-	-	$2M_1 + 1M$	-
HE-23-2R	83.5	0.5	5.5	-	2.0	-	-	-	-	3.5	-	-	5.0	-	-	-	-	*	$2M_1$	-
HE-23-3R	81.9	-	3.5	-	2.0	-	-	-	-	1.5	-	-	10.0	-	0.7	0.4	-	-	$2M_1$	-
HE-24-1R	90.4	0.3	2.5	-	1.0	-	-	-	-	1.5	-	-	3.5	-	0.8	-	-	*	$2M_1 + 1M$	-

Abbreviations: *Indicates phases believed to be present in sample but not unequivocally confirmed by XRD, "-"indicates phases/polytype not detected by XRD; Qtz = quartz. Cal = calcite; Kfs = K-feldspar; Plg = plagioclase; Adl = adularia; Alu = alunite; Nalu = natroalunite; Hem = hematite; Rt = rutile; Py = pyrite; Sp = sphalerite; Gn = galena; Ms. = muscovite; Pg = paragonite; Chl =chlorite; Kln = kaolinite group mineral; Prl = pyrophyllite; Mix = mix-layered sheet silicates. Mineral abbreviations after Whitney and Evans (2010).

[1] Indicates the presence of dickite from the kaolinite mineral group.

Table 2.3: Sybilla© parameters of main phyllosilicates and mixed-layered phases used for XRD pattern modelling of representative samples.

Mixed-layer phase/ Phase parameters	Sample	σ*	CSDS (layers)	Sme (%)	Chl (%)	Ill-Par (%)	Fe^{VI} (a.p.f.u.)	ICC (a.p.f.u.)
Illite / Muscovite	HB-4	52.70	26.74	-	-	-	1.52	1.50
	HB-5	80.00	19.72	-	-	-	3.72	1.50
	HB-7	12.00	18.55	-	-	-	2.44	1.50
	HB-14	12.00	18.16	-	-	-	0.88	1.50
	HP-2	18.38	37.27	-	-	-	0.28	1.73
	HP-3	80.00	33.76	-	-	-	0.80	1.74
	HP-4B	2.00	31.81	-	-	-	0.50	1.50
	HE-36-98	12.00	26.74	-	-	-	0.50	1.50
	HE-48-28	12.00	2.56	-	-	-	0.50	1.50
	HE-09-02	33.98	20.89	-	-	-	0.50	1.50
	HE-24-1R	12.00	24.79	-	-	-	0.24	1.50
Chlorite	HB-4	36.32	31.81	-	-	-	0.00	1.00
	HB-5	44.12	25.96	-	-	-	0.20	1.00
	HB-7	12.00	20.50	-	-	-	0.50	1.00
	HB-14	15.26	35.32	-	-	-	1.00	1.00
	HE-48-28	12.00	16.21	-	-	-	1.52	1.00
	HE-09-02	12.00	20.89	-	-	-	1.52	1.00
	HE-24-1R	69.86	20.11	-	-	-	0.48	1.00
Serpentine	HB-5	41.78	34.93	-	-	-	6.00	-
Kaolinite	HB-4	31.64	40.00	-	-	-	-	-
	HB-7	12.00	36.49	-	-	-	-	-
	HP-2	80.00	40.00	-	-	-	-	-
	HP-3	80.00	40.00	-	-	-	-	-
	HP-4B	35.54	33.37	-	-	-	-	-
	HP-7	48.80	40.00	-	-	-	-	-
Pyrophyllite	HP-2	12.00	32.59	-	-	-	-	-
R1 I-Sme	HP-3	42.56	16.95	8.00	-	92.00	0.50	1.50
	HP-7	80.00	28.84	3.00	-	97.00	1.80	1.50
	HE-48-28	12.00	13.18	3.00	-	97.00	0.50	1.50
	HE-09-02	12.00	1.87	3.00	-	97.00	0.50	1.50
	HE-24-1R	52.70	1.58	3.00	-	97.00	2.68	1.50
R0 I-Sme	HP-7	51.92	16.95	6.00	-	94.00	0.50	1.50
	HE-36-98 (1)	34.76	17.24	6.00	-	94.00	0.50	1.50
	HE-36-98 (2)	51.92	4.77	30.00	-	70.00	0.50	1.50
R1 P-Sme	HB-4	33.20	23.33	3.00	-	97.00	1.96	2.00
	HB-5	12.00	20.14	2.00	-	98.00	2.24	2.00
	HB-7	34.76	22.46	3.00	-	97.00	4.00	2.00
	HB-14	12.00	27.10	3.00	-	97.00	0.44	2.00
R1 C-Sme	HB-14	12.00	28.26	5.00	95.00	-	0.76	1.00
R0 C-Sme	HE-36-98	38.66	5.93	24.00	76.00	-	1.08	1.00
	HE-48-28	29.30	14.34	50.00	50.00	-	2.64	1.00
	HE-09-02	12.00	1.87	50.00	50.00	-	0.00	1.00

Abbreviations and symbols: σ* = orientation of particles on the mounted X-ray slide; CSDS = coherent scattering domain sizes expressed in layers; Sme (%), Chl (%) Sr (%), and Ill (%) = smectite, chlorite, serpentine, and illite content in the respective mixed-layered minerals (in %); I-Sme, P-Sme, and C-Sme = mixed-layered illite-smectite, paragonite-smectite, and chlorite-smectite; R = Reichweit (measure of order); Fe^{VI} = octahedral Fe in illite (I), paragonite (P), and chlorite (C); ICC = interlayer cation content expressed per full unit cell in illite (Ill), paragonite (Par), and chlorite (Chl).

Table 2.4: Selected electron microprobe analyses (in wt.%) of mica from the studied epithermal systems and respective structural formulas.

Deposit	HB	HB	HB	HB	HB	HB	HB	HB	HP	HP	HP	HP	HE	HE	HE	HE
Sample	HB-4	HB-4	HB-4	HB-4	HB-14	HB-14	HB-14	HB-14	HP-2	HP-2	HP-2	HP-2	HE-48-28	HE-48-28	HE-48-27	HE-48-26
No. anal.	6	11	17	19	8	10	14	15	1	9	15	19	9	10	6	6
SiO_2	48.61	48.22	48.37	48.04	48.25	47.34	49.13	47.65	48.20	47.33	47.41	45.72	53.26	53.93	54.68	54.47
TiO_2	0.05	0.08	0.04	0.06	0.08	0.08	0.03	0.02	0.04	0.02	0.02	0.04	-	-	-	0.03
Al_2O_3	34.74	35.67	39.54	39.00	36.96	37.60	39.72	40.74	37.03	37.26	37.46	36.13	29.99	31.16	31.00	31.65
Cr_2O_3	-	0.01	-	-	0.01	0.07	-	0.01	-	-	0.01	-	-	-	0.02	-
V_2O_3	-	0.02	0.01	0.03	0.07	0.09	0.05	0.03	0.05	0.04	0.01	0.02	0.09	0.07	0.05	0.07
FeO	1.53	1.96	0.66	0.74	1.82	1.51	0.49	0.38	1.57	1.38	1.53	2.95	1.55	1.03	1.13	0.92
MnO	-	-	-	-	0.01	-	0.01	-	0.03	-	0.02	-	0.17	0.06	0.09	0.08
MgO	0.88	0.53	0.07	0.12	0.50	0.24	0.09	0.03	0.23	0.18	0.14	0.14	3.23	2.70	2.67	2.17
CaO	-	0.01	0.02	0.05	0.04	0.01	0.08	0.08	0.03	0.09	0.07	0.04	0.03	0.04	0.05	0.10
Na_2O	1.55	1.77	7.45	6.94	1.36	2.06	7.12	8.64	0.89	0.91	1.12	0.99	0.04	0.11	0.15	0.07
K_2O	9.21	9.06	2.13	2.88	9.28	9.09	1.72	0.63	9.94	9.80	9.58	9.95	8.52	8.98	8.88	8.77
Cl	0.00	0.01	0.00	0.02	0.01	0.01	0.01	0.02	-	-	0.01	0.01	0.01	0.01	-	-
F	0.25	0.13	0.09	0.12	0.17	0.02	0.03	0.02	0.36	0.36	0.39	0.32	-	0.04	0.30	0.06
Total	96.73	97.41	98.36	97.93	98.48	98.11	98.46	98.23	98.20	97.21	97.62	96.16	96.89	98.09	98.90	98.35
Si	2.903	2.978	2.932	2.893	2.937	2.882	2.991	2.901	2.934	2.881	2.886	2.784	3.410	3.350	3.396	3.383
Ti	0.002	0.004	0.002	0.003	0.004	0.003	0.001	0.001	0.002	0.001	0.001	0.002	-	-	-	0.001
Al_{Total}	2.445	2.596	2.825	2.768	2.652	2.698	2.850	2.923	2.657	2.673	2.688	2.592	2.263	2.281	2.270	2.317
^{IV}Al	1.097	1.022	1.068	1.107	1.063	1.118	1.009	1.099	1.066	1.119	1.114	1.216	0.590	0.650	0.604	0.617
^{VI}Al	1.348	1.574	1.757	1.660	1.589	1.580	1.841	1.824	1.591	1.555	1.574	1.376	1.673	1.631	1.666	1.701
Cr	-	0.000	-	-	0.000	0.003	-	0.000	-	-	0.000	-	-	-	0.001	-
V	-	0.001	0.001	0.002	0.004	0.005	0.003	0.002	0.003	0.002	0.001	0.001	0.005	0.004	0.003	0.004
Fe^{2+}	0.077	0.101	0.033	0.037	0.093	0.077	0.025	0.019	0.080	0.070	0.078	0.150	0.083	0.053	0.059	0.048
Mn	-	-	-	-	0.001	-	0.000	-	0.001	-	0.001	-	0.009	0.003	0.005	0.004
Mg	0.078	0.049	0.006	0.010	0.045	0.022	0.009	0.003	0.021	0.016	0.013	0.012	0.308	0.250	0.248	0.201
Σ Oct.	1.506	1.729	1.800	1.713	1.735	1.691	1.878	1.849	1.697	1.645	1.669	1.541	2.079	1.942	1.981	1.958
Ca	-	0.001	0.001	0.003	0.003	0.001	0.005	0.005	0.002	0.006	0.005	0.003	0.002	0.003	0.003	0.007
Na	0.179	0.212	0.876	0.810	0.161	0.244	0.840	1.019	0.105	0.107	0.132	0.117	0.006	0.013	0.018	0.008
K	0.702	0.714	0.165	0.221	0.721	0.706	0.134	0.049	0.772	0.761	0.744	0.773	0.696	0.711	0.704	0.695
Σ Int.	0.881	0.926	1.042	1.034	0.884	0.950	0.979	1.073	0.879	0.874	0.881	0.893	0.704	0.728	0.725	0.710
Cl	0.000	0.001	0.000	0.002	0.001	0.001	0.001	0.002	-	-	0.001	0.001	0.001	0.001	-	-
F	0.048	0.026	0.017	0.022	0.032	0.004	0.007	0.004	0.065	0.066	0.070	0.059	-	0.008	0.054	0.011

Mica formulae calculated on basis of 11 oxygen atoms and all iron was considered as Fe^{2+}. Abbreviations: HB = Hope Brook high-sulfidation epithermal deposit; HP = Hickey's Pond high-sulfidation epithermal system; HE = Heritage low-sulfidation epithermal prospect. Calculated H_2O contents are reported in Appendix 3.

Table 2.5: Selected electron microprobe analyses (in wt.%) of chlorite and calculated structural formulas.

Deposit	HB	HB	HB	HB	HB	HB	HE	HE	HE	HE	HE	HE	HE	HE	HE	HE
Sample	HB-14	HB-14	HB-14	HB-14	HB-14	HB-14	HE47-26	HE47-26	HE48-27	HE48-27	HE48-27	HE48-28	HE48-28	HE48-28	HE36-107B	HE36-107B
No. anal.	1	4	8	13	17	20	6	8	1	7	10	1	5	8	4	9
SiO_2	25.02	25.17	24.85	24.93	25.04	25.04	30.75	30.73	26.42	27.01	26.26	26.56	26.09	28.19	28.59	29.04
TiO_2	23.67	23.78	23.67	24.12	24.22	23.89	17.92	18.47	21.60	22.05	22.27	21.55	21.58	20.89	20.85	20.41
Al_2O_3	0.08	0.06	0.05	0.02	0.06	0.03	-	0.01	-	-	-	0.02	0.01	-	0.02	0.02
Cr_2O_3	0.08	0.06	0.05	0.05	0.08	0.08	-	-	-	-	0.01	-	-	-	0.02	-
V_2O_3	0.04	0.04	0.04	0.06	0.05	0.05	0.08	0.04	0.02	0.02	0.03	0.08	0.04	0.03	0.02	0.03
FeO	19.64	20.30	20.29	20.04	20.30	19.39	20.29	19.64	20.73	20.70	22.08	19.68	19.27	19.21	19.73	19.33
MnO	0.38	0.32	0.30	0.25	0.28	0.32	0.69	0.82	3.33	3.06	3.24	3.86	3.99	3.17	3.36	3.26
MgO	16.79	16.63	16.04	15.56	16.28	16.65	17.83	18.33	14.28	14.36	14.43	16.42	16.49	16.47	17.05	17.17
CaO	0.01	0.01	0.00	0.03	0.00	0.03	0.33	0.62	0.08	0.06	0.03	0.03	0.02	0.04	0.06	0.06
Na_2O	0.03	0.03	0.02	0.07	0.05	0.09	0.04	0.08	0.02	0.02	0.03	0.07	0.03	0.03	-	-
K_2O	0.01	0.01	-	0.07	0.02	0.06	0.02	0.10	0.22	0.45	0.04	0.03	0.03	0.25	0.01	0.01
Cl	0.01	0.03	0.01	0.02	0.01	0.02	0.01	0.02	0.01	0.01	0.01	0.01	0.01	0.03	0.02	0.02
F	-	-	-	-	-	-	-	-	-	-	-	-	-	-	-	-
Total	85.60	86.37	85.14	85.08	86.23	85.51	87.83	88.75	86.58	87.64	88.26	88.14	87.37	88.07	89.52	89.12
Si	2.603	2.584	2.611	2.602	2.587	2.592	3.107	3.053	2.777	2.791	2.715	2.726	2.707	2.845	2.853	2.903
Al_{Total}	2.902	2.877	2.931	2.967	2.950	2.915	2.133	2.162	2.676	2.686	2.715	2.607	2.640	2.485	2.453	2.404
^{IV}Al	1.397	1.416	1.389	1.398	1.413	1.408	0.893	0.947	1.223	1.209	1.285	1.274	1.293	1.155	1.147	1.097
^{VI}Al	1.505	1.461	1.542	1.569	1.537	1.507	1.240	1.215	1.452	1.477	1.430	1.333	1.347	1.330	1.306	1.307
Ti	0.007	0.005	0.004	0.001	0.005	0.002	-	0.001	-	-	-	0.001	0.001	-	0.002	0.002
Cr	0.007	0.005	0.005	0.004	0.007	0.006	-	-	-	-	0.001	-	-	-	0.001	-
V	0.004	0.004	0.003	0.005	0.004	0.004	0.007	0.003	0.002	0.002	0.002	0.007	0.004	0.003	0.002	0.003
Fe^{2+}	1.708	1.743	1.783	1.750	1.755	1.679	1.714	1.632	1.822	1.789	1.909	1.689	1.672	1.622	1.647	1.616
Mn	0.034	0.028	0.027	0.022	0.025	0.028	0.059	0.069	0.297	0.268	0.284	0.335	0.350	0.271	0.284	0.276
Mg	2.603	2.545	2.512	2.422	2.508	2.570	2.685	2.715	2.237	2.212	2.224	2.513	2.550	2.478	2.537	2.559
Σ Oct.$_{(Fe+Mg+AlVI)}$	5.816	5.749	5.837	5.741	5.799	5.755	5.639	5.563	5.511	5.478	5.563	5.535	5.569	5.531	5.489	5.483
Σ Vac. Oct.	0.184	0.251	0.163	0.259	0.201	0.245	0.361	0.437	0.489	0.522	0.437	0.465	0.431	0.469	0.511	0.517
Ca	0.002	0.002	0.000	0.004	0.000	0.003	0.036	0.066	0.009	0.007	0.004	0.003	0.002	0.004	0.007	0.007
Na	0.006	0.007	0.004	0.014	0.011	0.018	0.009	0.015	0.004	0.005	0.007	0.013	0.006	0.007	-	-
K	0.001	0.002	-	0.010	0.002	0.008	0.002	0.013	0.030	0.060	0.005	0.004	0.004	0.032	0.001	0.001
Cl	0.002	0.005	0.001	0.003	0.002	0.004	0.002	0.004	0.001	0.002	0.002	0.002	0.001	0.005	0.004	0.003
F	-	-	-	-	-	-	-	-	-	-	-	-	-	-	-	-
Geothermometry (ºC)																
(1) Empirical	194	195	195	195	197	194	140	143	180	178	187	181	184	166	166	160
(2) Semi-empirical	281	253	293	247	277	254	123	110	147	138	171	158	169	116	125	116

Chlorite formulae calculated on basis of 14 oxygen atoms and all iron was considered as Fe^{2+}. (1) Empirical geothermometry calculation after Kranidiotis and MacLean (1987). (2) Semi-empirical geothermometry calculation after Inoue et al. (2018). Abbreviations: HB = Hope Brook high-sulfidation epithermal deposit; HE = Heritage low-sulfidation epithermal prospect. Calculated H_2O contents are reported in Appendix 3.

Table 2.6: Selected electron microprobe analyses (in wt.%) of kaolinite from the Hope Brook Deposit and respective structural formulas.

Deposit	HB	HB	HB	HB	HB	HB	HB	HB	HB	HB	HB	HB	HB	HB	HB	HB	HB	HB	HB	HB
Sample	HB-4	HB-4	HB-4	HB-4	HB-4	HB-4	HB-4	HB-4	HB-4	HB-4	HB-4	HB-4	HB-4	HB-4	HB-4	HB-4	HB-4	HB-4	HB-4	HB-4
No. anal.	1	2	3	4	5	6	7	8	9	10	11	12	13	14	15	16	17	18	19	20
SiO_2	46.46	45.31	45.79	46.10	46.87	45.90	45.10	45.97	46.11	45.98	46.20	45.96	45.79	45.63	46.27	45.16	44.87	46.60	46.02	45.72
TiO_2	-	-	-	-	0.01	0.02	0.01	0.01	0.01	-	0.01	-	0.02	-	-	-	0.01	-	-	0.01
Al_2O_3	39.47	37.84	38.37	39.57	38.80	39.24	39.01	39.57	39.30	39.15	39.11	39.43	38.92	38.61	39.57	38.37	37.54	39.50	39.37	39.39
Cr_2O_3	-	-	-	-	-	-	-	-	-	-	-	-	-	-	-	-	-	-	-	-
V_2O_3	-	-	-	-	-	-	-	-	-	-	-	-	-	-	-	-	-	-	-	-
Fe_2O_3	0.14	0.20	0.16	0.16	0.21	0.22	0.11	0.08	0.22	0.13	0.15	0.12	0.18	0.12	0.11	0.14	0.29	0.14	0.07	0.08
MnO	0.02	-	-	-	-	-	0.02	0.02	-	-	0.01	0.02	0.01	-	-	-	-	-	-	-
MgO	0.01	0.02	0.00	0.00	0.03	0.02	-	0.01	0.03	-	0.02	-	0.02	0.02	0.01	-	-	-	-	-
CaO	0.03	0.05	0.02	0.01	0.07	0.05	0.02	0.01	0.06	0.02	0.06	0.01	0.07	0.04	0.04	0.02	0.03	0.03	0.01	0.01
Na_2O	0.13	0.18	0.02	0.05	0.23	0.13	0.05	0.06	0.16	0.08	0.09	0.04	0.14	0.11	0.16	0.09	0.07	0.12	0.08	0.04
K_2O	0.08	0.14	0.02	0.03	0.20	0.10	0.02	0.03	0.08	0.04	0.07	0.01	0.08	0.06	0.09	0.07	0.03	0.07	0.03	0.01
Cl	0.03	0.07	0.01	0.01	0.07	0.02	0.02	0.01	0.04	0.02	0.04	0.01	0.05	0.04	0.03	0.04	0.02	0.02	0.02	0.01
F	0.08	0.10	0.05	0.04	0.20	-	0.05	0.03	0.09	0.02	0.15	0.05	0.10	0.10	0.13	0.03	0.08	-	0.02	-
Total	86.47	83.91	84.45	85.97	86.68	85.70	84.41	85.79	86.10	85.42	85.89	85.66	85.36	84.71	86.41	83.92	82.95	86.47	85.62	85.26
Si	1.909	1.881	1.958	1.948	1.830	1.965	1.931	1.958	1.892	1.963	1.863	1.944	1.889	1.898	1.873	1.940	1.926	1.978	1.961	1.977
Ti	-	-	-	-	0.000	0.001	0.000	0.000	0.000	-	0.000	-	0.001	-	-	-	0.000	-		0.000
Al_{Total}	1.911	1.852	1.933	1.970	1.786	1.980	1.969	1.986	1.900	1.970	1.859	1.965	1.893	1.893	1.888	1.943	1.899	1.976	1.977	2.007
^{IV}Al	0.091	0.119	0.042	0.052	0.170	0.035	0.069	0.042	0.108	0.037	0.137	0.056	0.111	0.102	0.127	0.060	0.074	0.022	0.039	0.023
^{VI}Al	1.819	1.733	1.891	1.918	1.616	1.945	1.900	1.944	1.792	1.932	1.723	1.909	1.782	1.792	1.761	1.883	1.825	1.954	1.937	1.984
Cr	-	-	-	-	-	-	-	-	-	-	-	-	-	-	-	-	-	-	-	-
V	-	-	-	-	-	-	-	-	-	-	-	-	-	-	-	-	-	-	-	-
Fe^{3+}	0.004	0.006	0.005	0.005	0.006	0.007	0.004	0.003	0.007	0.004	0.005	0.004	0.006	0.004	0.003	0.005	0.010	0.005	0.002	0.002
Mn	0.001	-	-	-	-	-	0.001	0.001	-	-	0.000	0.001	0.000	-	-	-	-	-	-	-
Mg	0.001	0.001	0.000	0.000	0.001	0.001	-	0.001	0.002	-	0.001	-	0.001	0.001	0.000	-	-	-	-	-
Σ Oct.	1.825	1.741	1.896	1.924	1.624	1.954	1.905	1.949	1.801	1.937	1.729	1.914	1.790	1.796	1.765	1.887	1.835	1.958	1.940	1.987
Ca	0.001	0.002	0.001	0.000	0.003	0.002	0.001	0.000	0.002	0.001	0.002	0.001	0.003	0.002	0.002	0.001	0.001	0.001	0.001	0.000
Na	0.011	0.015	0.002	0.004	0.017	0.011	0.004	0.005	0.012	0.007	0.007	0.003	0.011	0.009	0.013	0.008	0.006	0.010	0.007	0.004
K	0.004	0.007	0.001	0.002	0.010	0.006	0.001	0.001	0.004	0.002	0.004	0.001	0.004	0.003	0.005	0.004	0.002	0.004	0.001	0.001
Cl	0.002	0.005	0.001	0.001	0.005	0.002	0.001	0.001	0.003	0.002	0.003	0.001	0.003	0.002	0.002	0.003	0.002	0.002	0.001	0.001
F	0.011	0.013	0.007	0.006	0.024	-	0.007	0.004	0.012	0.003	0.019	0.006	0.012	0.013	0.017	0.004	0.011	-	0.003	-

Kaolinite formulae calculated on basis of 7 oxygen atoms and all iron was considered as Fe^{3+}. Abbreviations: HB = Hope Brook HSS. Calculated H_2O contents are reported in Appendix 3.

Chapter 3: Raman spectroscopy coupled with reflectance spectroscopy as a tool for the characterization of key hydrothermal alteration minerals in epithermal Au-Ag systems: utility and implications for mineral exploration

3.1. Abstract

Raman spectroscopy of fine-grained hydrothermal alteration minerals, and phyllosilicates in particular, presents certain challenges. However, given the increasingly widespread recognition of field portable visible - near infrared - short-wave infrared (Vis-NIR-SWIR) spectroscopy as a valuable tool in the mineral exploration industry, Raman microspectroscopy has promise as an approach for developing detailed complementary information on hydrothermal alteration phases in ore-forming systems. Here we present exemplar high-quality Raman and Vis-NIR-SWIR spectra of four key hydrothermal alteration minerals (pyrophyllite, white mica, chlorite, and alunite) that are common in precious metal epithermal systems, from deposits on the island of Newfoundland, Canada. The results reported here demonstrate that Raman microspectroscopy can accurately characterize pyrophyllite, white mica, chlorite, and alunite, and provide details on their compositional variation at the microscale. In particular, spectral differences in the 1000-1150 cm^{-1} white mica Raman band allows the distinction between low-Tschermak phases (muscovite, paragonite) and phases with higher degrees of Tschermak substitution (phengitic white mica composition). The peak position of the main chlorite Raman band shifts between 683 cm^{-1} for Mg-rich chlorite and 665 cm^{-1} for Fe-rich chlorite, and can be therefore used for semiquantitative estimation of the Fe^{2+} content in chlorite. Further, while Vis-NIR-SWIR macrospectroscopy allows the rapid identification of the overall composition of the most abundant hydrothermal alteration mineral in a given sample, Raman microspectroscopy provides an in-depth spectral and chemical

characterization of individual mineral grains – preserving the spatial and paragenetic context of each mineral and allowing for the distinction of chemical variation between (and within) different mineral grains. This is particularly useful in the case of alunite, white mica, and chlorite – minerals with extensive solid solution, where microscale characterization can grant information on the alteration zonation useful for mineral exploration and provide insight into mineral deposit genesis.

3.2. Introduction

Hydrothermal gold deposits contribute a noteworthy fraction of the world's gold endowment, with the epithermal deposit class contributing up to 13% of the global gold production (Frimmel, 2008). These deposits have widespread hydrothermal alteration that formed due to the interaction of hydrothermal fluids with the enclosing wall rocks, and the alteration mineral assemblages provide a record of the physicochemical characteristics of hydrothermal fluids (Arribas, 1995; Hedenquist et al., 1996; Hedenquist et al., 2000; Simmons et al., 2005). The study of hydrothermal alteration is, therefore, crucial for the understanding of the geochemical processes involved during fluid-rock interaction and can be used as a tool for exploration, since specific alteration assemblages may be related to significant ore-forming events (Arribas, 1995; Hedenquist et al., 1996; Hedenquist et al., 2000; Simmons et al., 2005). Hydrothermal alteration routinely involves the formation of new hydrous minerals, including various phyllosilicates (i.e., sheet silicates), and, in certain systems, sulfate minerals, such as alunite. Phyllosilicates are one of the most diverse and complex groups of silicates, but share the common features of being hydrous (H_2O and/or OH groups) and comprising parallel sheets of silicate tetrahedra and octahedra units (Deer et al., 1992; Bergaya and Lagaly, 2013). Characteristic phyllosilicates found in epithermal systems include pyrophyllite, the white mica group (including muscovite, phengite, and paragonite), trioctahedral chlorite group minerals (e.g., clinochlore, chamosite), illite, and smectite (Arribas, 1995; Hedenquist et al., 1996; Hedenquist et al., 2000; Simmons et al., 2005).

Epithermal deposits are formed at shallow depths in volcanic arc environments, where two contrasting end-member styles are defined: high- and low-sulfidation (Hedenquist, 1987). High-sulfidation epithermal Au ± Cu (± Ag) deposits are associated with quartz ± alunite ± pyrophyllite ± dickite ± kaolinite alteration assemblages genetically linked to highly acidic and oxidizing magmatic-hydrothermal fluids (Arribas, 1995; Hedenquist et al., 1996; Hedenquist et al., 2000; Simmons et al., 2005). The hydrothermal alteration of the host rocks commonly develops in a concentric pattern, with a core of vuggy silica (i.e., residual silica due to intense leaching of rocks by highly acidic fluids) that transitions sharply to quartz-alunite ± pyrophyllite ± kaolinite ± dickite, and then to an outer halo of propylitic (epidote + chlorite) alteration (Arribas, 1995). Low-sulfidation epithermal Ag-Au deposits contain vein and selvage alteration minerals formed from neutral and reducing hydrothermal fluids (Hedenquist et al., 2000; Simmons et al., 2005). Hydrothermal alteration zoning includes a highly quartz-altered (i.e., silicified) inner alteration zone characterized by the presence of chalcedony, sericite, adularia, and mixed layered illite-smectite (Hedenquist et al., 2000). This proximal alteration is most often surrounded by an outer alteration halo comprising chlorite, calcite, and epidote (Hedenquist et al., 2000). A third epithermal mineralization style, intermediate-sulfidation epithermal deposits, share many features with low-sulfidation epithermal deposits, but display an intermediate sulfidation-state assemblage indicated by minerals such as tetrahedrite/tennantite and low-Fe sphalerite (Hedenquist et al., 2000).

Multiple studies have focused on the mineralogical and chemical characterization of hydrothermal alteration in epithermal systems through a combination of optical microscopy, scanning electron microscopy (SEM), electron probe microanalysis (EPMA), and/or X-ray diffraction (XRD) (Arribas, 1995; Hedenquist, 1987; Hedenquist et al., 1996; Berger and Bethke, 1985; Cooke and Simmons, 2000; Arbiol et al., 2021). However, powder X-ray diffraction is a destructive technique, which does not preserve textural and paragenetic information, and the separation of fine-grained clay fraction minerals (mainly phyllosilicates) is a labour-intensive process that has only been implemented in a handful of hydrothermal alteration studies (e.g., Arbiol et al., 2021; Tillick et al., 2001; Yan et al., 2001; Inoue et al., 2004; Carrillo-Rosúa et al., 2009; Simpson and Mauk, 2011). In addition to the aforementioned techniques, visible - near infrared - short-wave infrared (Vis-NIR-SWIR) spectroscopy, and in particular the SWIR spectral range (1300-2500 nm), has been increasingly applied in mineral exploration and related research (Thompson et al., 1999; Kerr et al., 2011; Sparkes and Dunning, 2014; Wang et al., 2017; Neal et al., 2018), linked to the availability of field-portable instruments (e.g., PIMA, Terraspec). These latter devices allow the identification of major Vis-NIR-SWIR active hydrothermal alteration minerals at the centimeter scale with widespread application to deposit-scale mapping and core logging.

The more detailed examination of phyllosilicates using microspectroscopic techniques, such as Raman microspectroscopy, benchtop infrared spectroscopy, and Fourier transform Raman (FTR) spectroscopy, is not as frequently deployed (Tlili et al., 1989; Frost, 1995; 1997; Frost and Rintoul, 1996; Frost and Shurvell, 1997; Frost and Van Der Gaast, 1997; Farmer, 1998; Frost and Kloprogge, 2000; Frost et al., 2010). Consequently, there is a lack of information linking the rock-scale spectroscopic features of hydrothermal alteration assemblages with the mineral-scale chemical information accessible by microspectroscopic techniques. Traditionally, this has been attributed to the challenges of fine grain size and poor crystallinity of hydrothermal alteration minerals, as well as to the presence of substantial fluorescence effects due to impurities (e.g., organic compounds, nano-inclusions, presence of sulfides and oxides, high Fe content in the mineral of interest, etc.) that limit the quantification of weak Raman signals (White, 1974; Wang et al., 2015). In addition, the application of Raman microspectroscopy to the study of phyllosilicates has the added overhead of relatively complex mineral structures and widely variable chemical compositions within this group of minerals. It is only relatively recently that Raman spectral features of phyllosilicates have begun to be studied and understood (Wang et al., 2015; Bishop and Murad, 2004; Gates et al., 2017), supporting the forward use of Raman microspectroscopy for a wide range of potential applications in the study of hydrothermal ore deposits, planetary exploration (Bishop and Murad, 2004; Gillet et al., 2002; Hochleitner et al., 2004; Wang et al., 2004), environmental geochemistry (Saikia et al., 2016), and natural clay pigments in historical paintings (Košařová et al., 2013).

This paper presents the first integrated multi-scale spectroscopic study of key hydrothermal alteration minerals found in epithermal gold-silver systems and explores the significant potential of Raman spectroscopy in the study and characterization of phyllosilicates in hydrothermal ore systems in an effort to support the exploration and development of mineral deposits. The examples studied are from well-preserved epithermal precious metal deposits hosted in the late Neoproterozoic rocks of the Avalon Zone terrane in Newfoundland, eastern Canada (Fig. 3.1), including: (i) Hope Brook high-sulfidation epithermal deposit, (ii) Hickey's Pond high-sulfidation epithermal prospect, (iii) Heritage low-sulfidation epithermal prospect, (iv) Oval Pit pyrophyllite mine (barren high-sulfidation occurrence), and (v) Vinjer high-sulfidation epithermal prospect. The nature, textural characteristics, and compositional variations of the alteration minerals in these occurrences, in particular phyllosilicates, have been described by Arbiol et al. (2021).

The results reported in this contribution consist of: (i) high-quality Vis-NIR-SWIR and Raman spectra of key hydrothermal alteration minerals (alunite, pyrophyllite, white mica, and chlorite), (ii) characterization of the major spectral features of these minerals, their measurable compositional variations and their subsequent mineral classification, (iii) comparison between macro- and micro-analytical spectroscopic measurements, (iv) semi-quantitative links between Raman shift and chemical composition and, (v) implications for mineral exploration.

3.2.1. Overview of the mineral structure of key hydrothermal alteration minerals

Phyllosilicates are a group of silicates with a basic structure consisting of tetrahedra of SiO_4^{-4} (i.e., four oxygen atoms surrounding a silicon atom) forming parallel sheets with an intrinsic 2:5 ratio of Si:O (Millot, 1970; Bailey, 1980a; Deer et al., 1992; Velde, 1992; 1995; Meunier, 2005; Bergaya and Lagaly, 2013). The general formula of layered silicates is the following: $IM_{2-3}\square_{1-2}T_4O_{10}A_2$ (Bishop et al., 2008a). The interlayer space (I site) can be occupied by K^+, Na^+, Ca^{2+}, NH_4^+, Rb^+, Ba^{2+}, H_3O^+, a vacancy, or a brucite ($(Mg^{2+}, Fe^{2+})(OH)_6$) octahedral layer in chlorite (Bishop et al., 2008a). The vacancy (□ site) occurs in the octahedral layer. Aluminum (Al^{3+}) may substitute for Si^{4+} in the tetrahedral sites (T site). The A site is commonly OH, F, Cl, or O (Bishop et al., 2008a). Other cations (including Mg, Fe, Li, Mn, Zn, Cr, Ti, or Al) predominantly occupy 6-fold coordinated sites in octahedral layers (M site) that are bonded with the tetrahedral layers through the unshared apical oxygen atoms of the tetrahedral layer (each tetrahedron has one unshared apical oxygen) (Bergaya and Lagaly, 2013). Each octahedral layer is bonded to either one or two tetrahedral layers in this manner (1:1 or 2:1 phyllosilicates, respectively), with the alternative combination of two tetrahedral layers interlinked with two octahedral layers referred to as the 2:1+1 phyllosilicates (Bergaya and Lagaly, 2013). The number of cations in the octahedral layer can vary between 2 and 3, therefore defining *dioctahedral* (i.e., with 2/3 of sites in the octahedral layer filled by Al^{3+} or Fe^{3+}) and *trioctahedral* (i.e., all 3 sites in the octahedral layer filled by Mg^{2+}, Fe^{2+}, or other divalent cations) phyllosilicates, respectively (Millot, 1970; Velden 1992; 1995; Meunier, 2005). Hydroxyl (OH) groups are linked to two octahedral atoms in dioctahedral phyllosilicates and to three octahedral atoms in trioctahedral phyllosilicates (Bishop et al., 2008a). In addition to this defining di- and tri-octahedral substitution, other types of substitutions can occur in phyllosilicates. The most relevant are charge imbalance substitution, where the substitution of a cation with a different charge in either the tetrahedral or octahedral layer creates a charge imbalance and triggers a cation substitution in the other layer, and interlayer substitutions, where the substitution of a cation by another one of a different charge is compensated by the insertion of an ion between the unit layers of the structure of the phyllosilicate (Millot, 1970; Velden 1992; 1995; Meunier, 2005; Bergaya and Lagaly, 2013). All phyllosilicates are hydrated, containing hydroxyl (OH^-) groups within their structure. The hydrogen ions are linked to free oxygen anions in the octahedral layer, therefore forming hydroxyl groups and defining the octahedral sheet as hydrated (Velde, 1995). Depending on their structure, and specifically on their tetrahedral-octahedral layering, the number of hydroxyl ions per cation changes, decreasing with the increase of the thickness of the fundamental sheet structure (i.e., increase in the ratio of tetrahedral layers interlinked with octahedral layers) (Velde, 1992; 1995; Meunier, 2005). Water (H_2O) groups can also be absorbed in the interlayer space of low charge expanding phyllosilicate species, such as smectite.

Pyrophyllite is a simple 2:1 phyllosilicate, with a 9.6 Å thick unit layer structure made of one octahedral sheet sandwiched between two tetrahedral sheets (T-O-T stacking) and a mineral formula of $Al_2Si_4O_{10}(OH)_2$ (Millot, 1970; Bailey, 1980a; Deer et al., 1992; Velde, 1992; 1995; Meunier, 2005; Bergaya and Lagaly, 2013). This dioctahedral mineral has two-thirds of the octahedral sites filled with Al^{3+} (the remaining one-third of the octahedral sites being vacant) and does not display any substantial isomorphic substitution, while maintaining a neutral layer charge (Wardle and Brindley, 1972). The oxygen ions in OH groups form the apices of the SiO_4 tetrahedra (Wardle and Brindley, 1972).

White Mica in hydrothermal gold systems, and other altered rocks, is commonly referred to as *'sericite'*. The term sericite (from the Greek *seiroς* meaning "silken") reflects the fine-grained (and somewhat cryptic) nature of mica species and illite that result from hydrothermal alteration of previous minerals (e.g., feldspars) (Deer et al., 1992). White mica group minerals are dioctahedral 2:1 phyllosilicates with a 10 Å thick unit layer comprising one octahedral sheet sandwiched between two tetrahedral sheets (Millot, 1970; Bailey, 1980a; Deer et al., 1992; Velde, 1992; 1995; Meunier, 2005; Bergaya and Lagaly, 2013). Interlayer positions in the tetrahedral-octahedral-tetrahedral stacking are filled by K^+, Na^+, and/or Ca^{2+} (Millot, 1970; Bailey, 1980a; Deer et al., 1992; Velde, 1992; 1995; Meunier, 2005; Bishop et al., 2008a; Bergaya and Lagaly, 2013). The vast majority of hydrothermal micas are part of the muscovite-paragonite solid solution series, related to the interlayer substitution of K^+ by Na^+ (or vice versa) – including the K^+ end-member *muscovite*, $KAl_2(AlSi_3O_{10})(OH)_2$, and the Na^+ endmember *paragonite*, $NaAl_2(AlSi_3O_{10})(OH)_2$ (Millot, 1970; Bailey, 1980a; Deer et al., 1992; Velde, 1992; 1995; Meunier, 2005; Bergaya and Lagaly, 2013). However, ionic substitutions can take place in the octahedral layer as well, where Al^{3+}, Fe^{2+}, Fe^{3+}, and Mg^{2+} can be accommodated (Millot, 1970; Bailey, 1980a; Deer et al., 1992; Velde, 1992; 1995; Meunier, 2005; Bergaya and Lagaly, 2013). Consequently, there is a solid solution series between the Al end-member *muscovite* and the Fe-Mg endmember *celadonite*, $K(Mg,Fe^{2+})Fe^{3+}(Si_4O_{10})(OH)_2$ (Millot, 1970; Bailey, 1980a; Deer et al., 1992; Velde, 1992; 1995; Meunier, 2005; Bergaya and Lagaly, 2013). Intermediate compositions with variable Al^{3+} and Mg^{2+} in the octahedral site are referred to as *phengite*, $K(AlMg)_2(OH)_2(SiAl)_4O_{10}$ (Millot, 1970; Bailey, 1980a; Deer et al., 1992; Velde, 1992; 1995; Meunier, 2005; Bergaya and Lagaly, 2013), a non-International Mineralogical Association (IMA) approved term for this variety of muscovite.

Chlorite is a 2:1+1 phyllosilicate comprising a 14 Å thick unit layer structure made up of two octahedral sheets and two tetrahedral sheets, with the second octahedral layer not directly bonded to the T-O-T stacked subunit (Millot, 1970; Bailey, 1980a; Deer et al., 1992; Velde, 1992; 1995; Meunier, 2005; Bergaya and Lagaly, 2013). The octahedral sites are filled with Al^{3+}, Fe^{2+}, and Mg^{2+} (Millot, 1970; Bailey, 1980a; Deer et al., 1992; Velde, 1992; 1995; Meunier, 2005; Bergaya and Lagaly, 2013), cations that can also occupy the interlayer position between the T-O-T stacking (Bishop et al., 2008a). There are two main trioctahedral Fe-Mg endmembers that form a solid solution series within the chlorite group, and commonly occur in hydrothermal environments: The Mg endmember *clinochlore*, $Mg_5Al_2Si_3O_{10}(OH)_8$, and the Fe endmember *chamosite*, $Fe^{2+}{}_5Al_2Si_3O_{10}(OH)_8$ (Millot, 1970; Bailey, 1980a; Deer et al., 1992; Velde, 1992; 1995; Meunier, 2005; Bergaya and Lagaly, 2013). *Ripidolite* is the general term used for chlorite of intermediate composition in the clinochlore-chamosite series.

The alunite group is a non-phyllosilicate sulfate mineral group with trigonal crystal symmetry and a structure consisting of somewhat distorted sheets of $AlO_2(OH)_4$ octahedra linked by $SO_4{}^{2-}$ tetrahedra (one O atom bound to Al) (Stoffregen et al., 2000), with the following general formula: $AM_3(SO_4)_2(OH)$. The M site in the octahedral layer is occupied by Al^{3+} (Stoffregen et al., 2000; Bishop and Murad, 2005). The interlayer space between sulfate tetrahedra and aluminum octahedra (A site) is commonly occupied by K^+ or Na^+ (and less frequently Ca^{2+}. $NH_4{}^+$, Pb^+, Ag^+, or H_3O^+) defining an omnidirectional solid solution series. *Alunite*, $KAl_3(SO_4)_2(OH)_6$, is the K^+ endmember, *natroalunite*, $NaAl_3(SO_4)_2(OH)_6$, is the Na^+ endmember, *huangite*, $CaAl_6(SO_4)_4(OH)_{12}$, is the Ca^{2+} end-member, and *ammonioalunite*, $(NH)_4Al_3(SO_4)_2(OH)_6$, is the $NH_4{}^+$ end-member. For the more common alunite and natroalunite endmembers, the difference in both radii and charge/radius values between K^+ and Na^+ has an impact on the characteristic of their bonding with OH groups (Bishop and Murad, 2005).

3.3. Major macro- and micro-spectral features of key hydrothermal minerals

This section focuses on the description of the main Vis-NIR-SWIR and Raman spectral features of key hydrothermal minerals, their band assignments, and the chemical information they provide.

3.3.1. Vis-NIR-SWIR reflectance spectroscopy

Visible - infrared - short-wave infrared (Vis-NIR-SWIR) spectroscopy is based on the absorption of incident electromagnetic radiation of wavelengths between 350 nm and 2500 nm. The absorption of specific wavelengths by minerals is mainly due to molecular bond vibrations (rotation, bending, and stretching of bonds) excited by this incident electromagnetic radiation (Thompson et al., 1999; Bishop et al., 2008b). Bonds involving structural water (H_2O) and hydroxyl (OH) groups generate the most characteristic absorption features; in particular, cation-hydroxyl bonds (i.e., vibration of the OH bond in which the hydroxyl is linked to octahedrally coordinated atoms such as Al, Fe, and Mg; Thompson et al., 1999; Cuadros et al., 2016). Phyllosilicates are hydrated, and consequently generate strong absorption features that allow their distinction and characterization. In general, SWIR spectra of phyllosilicates display absorption features close to 1400 nm (OH bond), 1900 nm (H_2O bond), and additional, more variable, features close to 2200 nm (Al-OH bond), 2250 nm (Fe-OH bond), and 2330 nm (Mg-OH bond) (Kerr et al., 2011; Cuadros et al., 2016). Hydrous sulfates show a characteristic SO_4^{2-} absorption band at ~1800 nm and an OH absorption feature at ~1400 nm (Bishop and Murad, 2005). However, the shape and exact position of the characteristic absorption bands of each mineral are determined by various parameters (e.g., dioctahedral/trioctahedral phyllosilicate structure, cation size, charge, and electronegativity; Duke, 1994; Prieto et al., 1991) and thus provide information on the specific structure and composition of the mineral (Thompson et al., 1999; Kerr et al., 2011).

Pyrophyllite

As an aluminum-rich hydrous phyllosilicate, pyrophyllite shows a strong OH absorption band at 1398 nm and a main Al-OH band at 2168 nm (Fig. 3.2a). Secondary OH absorption bands close to 950 nm and 1230 nm, and secondary Al-OH absorption bands at 2090 nm and 2320 nm are also observed (Clark et al., 1990).

White mica

White mica exhibits dominant absorption features close to 1414 nm (OH), 1910 nm (H_2O), and 2200 nm (Al-OH) (Fig. 3.2a). Even though the presence of K^+ or Na^+ in the interlayer position of white mica does not affect the Al-OH bond length, the proportion of Al in octahedral coordination in muscovite, paragonite, and phengite is different, following the coupled octahedral-tetrahedral Tschermak substitution ($(Mg+Fe^{2+})+Si \leftrightarrow Al^{IV}+(Al,Fe^{3+})^{VI}$; Duke, 1994; Herrmann et al., 2001). The incorporation of Fe^{2+}, Fe^{3+}, Mg, and/or Al in the octahedral layer of white mica results in changes in the length of the Al(Fe,Mg)-OH bond, resulting in diagnostic shifts of the ~2200 nm absorption band that are causally related to changes in white mica composition. Muscovite shows this absorption feature between 2198 nm and 2210 nm (Fig. 3.2a), whereas paragonite (high proportion of octahedral Al) shows the same feature at lower wavelengths (<2198 nm; Fig. 3.2a) and phengite (low proportions of octahedral Al) shifts it to higher wavelengths (>2210 nm; Fig. 3.2a) (Herrmann et al., 2001). Discrimination between white mica and illite is only possible through the observation of the absorption features at ~1414 nm (OH) and ~1910 nm

(H_2O), which are significantly deeper in illite due to the presence of hydration water in the space between T-O-T layers (Kerr et al., 2011; Gates et al., 2017).

Chlorite

Trioctahedral chlorite from the clinochlore-chamosite solid solution series (i.e., Mg-Fe series) presents a clear common OH absorption band at ~1400 nm (Fig. 3.2a), with a weaker H_2O absorption band at 1900-2000 nm (Fig. 3.2a). In addition, SWIR absorption bands at ~2250 nm and ~2350 nm (Fig. 3.2a) are related to the Fe-OH and Mg-OH bond, respectively (Herrmann et al., 2001). Magnesium-rich and Fe-rich chlorite can be distinguished by their relative reflectance and a noticeable absorption shift between SWIR features. Clinochlore (Mg-chlorite) displays a distinct absorption band at ~2330 nm (Mg-OH bond; Fig. 3.2a) and a shallower absorption band at ~2250 nm (Fe-OH bond; Fig. 3.2a), consequent to the dominance of Mg^{2+} over Fe^{2+} in its structure (Clark et al., 1990; Herrmann et al., 2001). Chamosite (Fe-chlorite), on the other hand, exhibits a shift of the Mg-OH absorption feature to ~2356 nm (Fig. 3.2a), with the presence of a deeper and shifted Fe-OH absorption band at ~2260 nm (Fig. 3.2a; Prieto et al., 1991; Clark et al., 1990). The precise position of such peaks depends on the exact composition of the analyzed chlorite within the clinochlore-chamosite series (e.g., Fe-Mg composition of the octahedral sheet, composition of the brucite sheet in the interlayer zone, presence of Fe^{3+}, etc.), and peak positions intermediate between those reported for chlorite near-endmembers are most frequently observed (Herrmann et al., 2001).

Alunite

In the SWIR region, sulfates show a distinctive absorption feature at 1740-1800 nm (Fig. 3.2a) that is related to the SO_4^{2-} bond. In addition to this feature, two doublet absorption bands (i.e., peaks in close wavelength proximity that produce a double peak absorption feature) are observed at ~1430 nm and ~1470 nm (Fig. 3.2a), related to OH bonds (Clark et al., 1990). Absorption bands at ~2170 nm and ~2320 nm are attributed to Al-OH vibrations (Clark et al., 1990). Wavelength variations in the ~1470 nm band allow the distinction between K-rich alunite and Na-rich natroalunite (Thompson et al., 1999; Kerr et al., 2011). These spectral differences are due to the contrasting bond length/strength of K^+ and Na^+ linked to OH groups (Bishop and Murad, 2005). Specifically, an absorption band closer to 1470 nm is indicative of alunite, whereas an absorption approaching 1495 nm is indicative of natroalunite (Thompson et al., 1999; Kerr et al., 2011). This diagnostic variation is advantageous in exploration for high-sulfidation epithermal deposits since it can enable compositional discrimination between alunite minerals formed by hypogene and supergene processes (Arribas, 1995; Hedenquist et al., 2000).

3.3.2. Raman microspectroscopy

The major Raman peaks of a mineral derive from the chemical bonds with the highest degree of covalency, in particular, for the minerals discussed herein, Si-O in silicate tetrahedra, and SO_4 in sulfate groups (Wang et al., 2015; Gates et al., 2017). In the case of silicates and sulfates, the predominant Raman spectral signatures occur between 100 cm^{-1} and 1200 cm^{-1} (Fig. 3.2b), a wavelength range that is referred to as the spectral range of fundamental vibrations (Wang et al., 2015; Gates et al., 2017). Structural water (H_2O) and hydroxyl groups (OH) produce a set of peaks in the spectral range of >3000 cm^{-1} (Wang et al., 2015; Gates et al., 2017).

Phyllosilicates display characteristic Raman spectral features that are distinct from other silicate mineral groups (Fig. 3.2b). All phyllosilicates display major Raman peaks in the 600-750 cm^{-1} range, with a prominent Raman band consistently located close to 700 cm^{-1}, and a set of weak Raman peaks in the 800-1200 cm^{-1} and <600 cm^{-1} spectral ranges (Fig. 3.2b,c; Wang et al., 2015;

Gates et al., 2017). The 600-750 cm^{-1} peaks are associated with the Si-O-Si vibration mode. Peaks in the 800-1100 cm^{-1} range are due to the symmetric stretching vibration of Si-O bonds within the $(Si_xO_y)^{z-}$ unit, and the <600 cm^{-1} peaks are attributed to the breathing vibration mode of the T-O-T stacking sequence in the phyllosilicate structure (Wang et al., 2015; Gates et al., 2017). Hydroxyl groups (OH) foster sharp Raman peaks in the >3600 cm^{-1} region, and structural water (H_2O) shows broad and highly variable peaks in the 3000-3700 cm^{-1} spectral range (Wang et al., 2015; Gates et al., 2017). Based upon the position of the strongest Raman peak in the 600-750 cm^{-1} spectral range, dioctahedral (>700 cm^{-1}) and trioctahedral (<700 cm^{-1}) phyllosilicates can be readily distinguished (Wang et al., 2015; Gates et al., 2017). This is caused by the effect that the difference in length of the M-O bond between dioctahedral and trioctahedral phyllosilicates generates on the main Si-O-Si Raman band (Wang et al., 2015; Gates et al., 2017). More subtle shifts in specific Raman peak positions can be attributed to structural or chemical changes, in particular changes in cation site occupancy, which allows the accurate identification of a wide range of phyllosilicates and provides information on mineral compositions. For a more comprehensive overview of the Raman spectral features of phyllosilicates the reader is referred to Wang et al. (2015) and Gates et al. (2017).

Pyrophyllite

Raman spectra of pyrophyllite reported by Wang et al. (2015) feature peaks at 193 cm^{-1}, 260 cm^{-1}, 360 cm^{-1}, 470 cm^{-1}, 706 cm^{-1}, 958 cm^{-1}, and 1075 cm^{-1}. Figure 3.2c shows the spectrum of a natural pyrophyllite sample with prominent Raman peaks at 195 cm^{-1}, 262 cm^{-1} and 701 cm^{-1}. Even though the Raman bands of pyrophyllite were not attributed to specific bond vibrations by Wang et al. (2015), Gates et al. (2017) interpreted their vibration modes based on the scheme presented by Loh (1973), assigning the peak at 470 cm^{-1} to Si-O stretching modes, the peak at 958 cm^{-1} to Al_2-OH vibrations, and the peak at 1075 cm^{-1} to Al-OH planar bending. The hydroxyl groups in pyrophyllite produce an extremely sharp peak at 3670-3675 cm^{-1}, associated with the Al_2-OH stretching mode (Gates et al., 2017; Zhai et al., 2008; Farmer, 1974; Kloprogge and Frost, 1999; Wang et al., 2002; Lantenois et al., 2007). A second less common weak peak is located at 3647 cm^{-1}, and it has been interpreted as the result of structural distortion (Wang et al., 2015) or as being associated with the $AlFe^{3+}OH$ stretching mode (Prieto et al., 1991) occurring due to significant substitution of Al^{3+} by Fe^{3+} in the octahedral sheet (Gates et al., 2017; Zhai et al., 2008).

White mica

Differences in the Raman spectra of discrete white mica compositions are challenging to quantify, as the solid solutions involved cause only subtle peak shifts. Pure muscovite shows distinct Raman peaks close to 196 cm^{-1}, 263 cm^{-1}, 411 cm^{-1}, 702 cm^{-1}, and 3625 cm^{-1} (Fig. 3.2b,c; Wang et al., 2015). A characteristic feature of white mica in general is the presence of somewhat variable peaks on either side of the central phyllosilicate peak (at ~702 cm^{-1}), around 630-670 cm^{-1} and 750-760 cm^{-1} (Fig. 3.2b,c). According to Wang et al. (2015) and Gates et al. (2017), the exchange between Na^+ and K^+ in the interlayer position results in almost negligible shifts in Raman peak positions (<2-3 cm^{-1}), and therefore, discrimination between muscovite and paragonite through Raman spectroscopy is challenging. However, discrimination between pure muscovite and more phengitic compositions is possible, given variations in a characteristic spectral feature in the 1000-1150 cm^{-1} spectral range (Li et al., 2011). Muscovite presents a broad low-intensity peak at 1050 cm^{-1}, while phengite shows a shift of that peak towards 1115 cm^{-1} (Li et al., 2011). This Raman peak shift is related to the Si (vs. Al) content in tetrahedral coordination, where lower Si contents correspond to muscovite composition, and higher Si contents correspond to phengite (Li et al., 2011).

Chlorite

In the spectral range of fundamental vibrations, clinochlore presents Raman peaks at ~203 cm^{-1}, 357 cm^{-1}, 552 cm^{-1}, and 683 cm^{-1} (Fig. 3.2c; Wang et al., 2015). According to Wang et al. (2015), an increase in octahedral Fe in the chlorite structure has a measurable impact on its Raman spectra, with a noticeable downshift of the major phyllosilicate Raman peak to ~662 cm^{-1} for Fe-rich chlorite, as well as reduced intensity of the peak located at ~357 cm^{-1}. However, due to the lack of Raman spectral information on chamosite in the literature, further downshift of the central phyllosilicate peak due to the more complete substitution of Mg^{2+} by Fe^{2+} in the octahedral layer, together with other possible undocumented effects on spectra, cannot be excluded. In the 3400-3700 cm^{-1} region, chlorite usually presents three defined peaks related to OH vibrations, even though the exact peak positions are widely variable (Wang et al., 2015). In the clinochlore-chamosite series, these variations are most probably related to octahedral substitutions. Therefore, different proportions of Mg^{2+} and Fe^{2+} in the structure of chlorite may result in complex peak shifts in the 3400-3700 cm^{-1} region.

Alunite

Raman spectra of sulfates consistently feature a very intense Raman band between 970 cm^{-1} and 1050 cm^{-1}, associated with the S-O bond (Fig. 3.2b; Omori, 1968; Wang et al., 2006; Buzgar et al., 2009). For alunite-group minerals, this most intense band is located at 1024 cm^{-1}, and is attributed specifically to the SO_4 stretching mode of alunite (Lerouge et al., 2007; Maubec et al., 2012; Frost et al., 2006). Raman spectra of alunite are characterized by an additional set of peaks in the 1000-1200 cm^{-1} and 100-650 cm^{-1} spectral ranges (Fig. 3.2b), mainly associated with S-O, O-H, and Al-O bond vibrations (Lerouge et al., 2007). Less intense bands at ~390 cm^{-1} and ~650 cm^{-1} are assigned to SO_4 and Al-O stretching vibrations, respectively (Frost et al., 2006; Breitinger et al., 1997; Rudolph and Mason, 2001; Toumi and Tlili, 2008). When the dominant alkaline cation is Na^+ instead of K^+, shifts in both peak position and intensity are observed in the 1050-1200 cm^{-1} region, allowing the distinction between alunite and natroalunite. The alunite endmember presents secondary peaks at ~1077 cm^{-1}, ~1151 cm^{-1}, and ~1186 cm^{-1} (Omori, 1968), the latter peak being the most intense. The natroalunite endmember shows a significant shift of those peaks to ~1085 cm^{-1}, ~1163 cm^{-1}, and ~1183 cm^{-1} (Omori, 1968), with the peak at ~1085 cm^{-1} showing higher intensity. In the >3000 cm^{-1} spectral region, alunite is characterized by two major peaks, at 3480 cm^{-1} and 3508 cm^{-1}, derived from OH vibration modes, whereas natroalunite shows a shift of these peaks towards lower wavelengths and lower intensities (Maubec et al., 2012).

3.4. Geological setting of studied epithermal occurrences

The Avalon Zone is the easternmost terrane belonging to the Appalachian orogen in Newfoundland (Fig. 3.1; Williams, 1979). Geologically, this zone is characterized by Neoproterozoic volcanic arcs and related volcano-sedimentary sequences (Williams, 1979), which host abundant epithermal occurrences (Fig. 3.1; O´Brien et al., 1996; 1998). The Hickey's Pond high-sulfidation epithermal prospect and the Heritage low-sulfidation epithermal prospect are located in the Burin Peninsula (southern Newfoundland), currently the most prospective area for epithermal mineralization (O´Brien et al., 1998). The Burin Peninsula is geologically characterized by Neoproterozoic arc-related volcanic, volcaniclastic, and sedimentary rocks divided into three units: the Marystown, the Musgravetown, and the Long Harbour Groups (O´Brien et al., 1996). The Hickey's Pond and Heritage epithermal prospects are hosted in volcanic and volcaniclastic rocks from the 590-570 Ma Marystown Group (O´Brien et al., 1996). Rocks from the Avalon Zone have been affected by a mild lower-greenschist metamorphism and deformation during the

Paleozoic Appalachian orogeny, but the epithermal occurrences are generally well preserved due to their thick overlying sedimentary sequences and consequent rapid burial (O´Brien et al., 1999).

The Hickey's Pond high-sulfidation epithermal prospect is hosted in mildly deformed greenschist facies pyroclastic rocks. The hydrothermal alteration is characterized by a core of massive silicic alteration, with discontinuous zones of vuggy silica and variable amounts of alunite and pyrite (O´Brien et al., 1999). The massive silicic alteration is surrounded by advanced argillic alteration dominated by quartz, alunite, pyrite, and rutile, which gradually changes to quartz-alunite(-lazulite) alteration (O´Brien et al., 1999). The most distal outer alteration zone comprises quartz-sericite alteration (O´Brien et al., 1999).

The Heritage low-sulfidation epithermal prospect is hosted in pyroclastic andesite-basalt and rhyodacite porphyry. The distal hydrothermal alteration at Heritage is characterized by quartz, white mica, and chlorite, and the proximal hydrothermal alteration assemblage consists of quartz, chalcedony, calcite, illite, chlorite, and adularia.

The Hope Brook high-sulfidation epithermal deposit is a past-producing mine located in southern Newfoundland (Fig. 3.1) and hosted in altered and deformed sedimentary and mafic volcaniclastic rocks of the Whittle Hill Sandstone and Third Pond Tuff successions (Dubé et al., 1995). The host rocks display a hydrothermal alteration defined by extensive advanced argillic alteration with more confined massive silicic alteration at its core. The former is characterized by quartz-mica-pyrite-pyrophyllite, with minor kaolinite, andalusite, alunite, and rutile (Dubé et al., 1995).

The Vinjer prospect and the Oval Pit mine (Fig. 3.1) are two barren high-sulfidation epithermal systems located in the Avalon zone and contain extensive advanced argillic alteration zones with pyrophyllite. The Oval Pit mine actively produces pure pyrophyllite for diverse industrial applications.

3.5. Experimental

Materials and Preparation

Samples from the Hickey's Pond, Heritage, Vinjer, and Oval Pit epithermal occurrences were collected during a field campaign in June 2017. Samples from Hope Brook were selected from drill core archived in the Department of Earth Sciences at Memorial University. Table 3.1 presents the complete list of rock samples, their summary descriptions (ore deposit type, mineralogy) and analytical methods applied for the mineral(s) of interest in each sample. Arbiol et al. (2021) describes in detail the regional geology, epithermal characteristics, mineralogy, and chemistry of hydrothermal phases from the epithermal occurrences investigated in this study.

Preparation of rock samples for analysis consisted of cutting the sample with a fine kerf lapidary saw into small flat sided squares that fit within 25.4-mm diameter aluminum retaining rings. These rings were subsequently cast with two-component epoxide. The embedded samples were then polished using traditional lapidary procedures, with 7 steps (of descending polishing compound grit size) until a high-quality polished surface was achieved. Final polish was accomplished with a 0.25μm diamond polishing paste.

Vis-NIR-SWIR Reflectance Spectroscopy

Laboratory benchtop Vis-NIR-SWIR spectroscopy analyses were performed with the ASD Terraspec 2 Pro instrument (Department of Earth Sciences, Memorial University), which consists of a light probe (with an analyzing area of 2 cm diameter) attached to a spectrometer module and a control computer. The light reflected from the sample reaches the spectrometer module through a fiber optic cable. The Terraspec 2 Pro is equipped with several diffraction gratings and photosensitive arrays that allow the acquisition of signal in the visible (390-750 nm), near-infrared

(750-1300 nm), and short-wave infrared (1300-2500 nm) regions. The spectral resolution of the Terraspec Pro is approximately 2 nm. Calibration of the spectral response involved analysing a manufacturer-provided high-reflectance polished Spectralon (sintered polytetrafluoroethylene) disk that reflects uniformly across the spectrum, in order to eliminate atmosphere and background spectral effects. This step was followed by an internal standard consisting of a pure polished pyrophyllite sample to confirm optimal spectral response. Analysis of both the Spectralon disk and the pyrophyllite standard was performed prior to first analysis and between sets of 20 unknown sample measurements. Individual measurements took 20-60 s. Spectral analyses were performed in both hand sample (sawn drill core) and the polished rock mounts. Analyses were performed in a naturally sunlit room in order to avoid any artificial light interference. Sawn drill core surfaces generally produced more total reflectance than polished rock mounts, but the latter generally produced a superior spectral resolution. Reflectance spectra were collected with the RS^3 Spectral Acquisition software. A minimum of three analyses per sample were obtained to ensure the consistency and representativity of the spectral measurements. Acquired data was subsequently processed, hull quotient-corrected, and normalized with The Spectral Geologist (TSG; CSIRO, Australia) software. The wavelength, shape, and position of major absorption bands (Al-OH, Fe-OH, Mg-OH, H_2O, OH) were compared with the TSG reference library for initial mineral identification. The whole set of Vis-NIR-SWIR spectra of studied samples is reported in Appendix 4.

Raman Spectroscopy

Two similar instruments were used to obtain Raman spectra of polished rock mounts. Both were Renishaw inVia confocal micro-spectrometers coupled to an optical microscope with a charge-coupled device (CCD) camera to record Raman spectra (Department of Chemistry, Memorial University). One of the systems is equipped with a 633-nm He-Ne excitation laser, whereas the other uses an 830-nm diode laser source. The 830-nm-laser Renishaw inVia spectrometer uses a grating system that covers the Raman stokes shift from ~0 to 3000 cm^{-1}, with a spectral resolution of 1 cm^{-1}. The wattage of this laser system is 300 mW at 100% laser power. This instrument was the primary system used for the present study, given its speed and reliability. However, given its grating system, structural/hydration water spectra (both H_2O and OH group spectra occur in the 3000-3700 cm^{-1} region) could not be measured with this first Raman instrument. The 633-nm-laser Renishaw inVia spectrometer uses a grating system that covers the Raman stokes shift from ~0 cm^{-1} to 4000 cm^{-1}, with a spectral resolution of 1 cm^{-1}. The 633-nm-laser system has a wattage of 450 mW at 100% laser power and was used specifically to acquire Raman signatures of structural/hydration water. In both systems, calibration of the zero Raman shift was performed daily before spectrum acquisition and consisted of measuring and aligning the appropriate spectral peak of a pure silica disk to 520 cm^{-1}. Therefore, errors in peak position were minimized, and routinely consisted of less than ±1 cm^{-1}. Spectral acquisition was made using either a 20x or 50x microscope objective, resulting in a focussed laser spot of <20 μm diameter in both cases. Different combinations of laser power and exposure times were tested in order to minimize sample fluorescence and obtain the cleanest Raman spectra. For both instruments, best quality spectra were generally acquired using a reduced laser power of 50% to avoid mineral damage and an exposure time of 40 s for minerals in polished rock mounts. A minimum of three analyses per point were acquired to ensure the consistency and representativity of the spectral measurements. The whole set of Raman spectra of studied samples is reported in Appendix 5.

Instrument management, calibration, measurement characteristics, and Raman spectrum acquisition were executed with the Renishaw WiRE software package. Following acquisition, Raman spectra were processed with the CrystalSleuth software (The RRUFF Project), where background noise and cosmic ray events (CRE) were removed.

Appendix 5 also contains additional remarks on the selection of excitation wavelength for Raman Spectroscopy and effects related to the nature of samples.

Scanning Electron Microscopy (SEM)

Scanning electron microscopy (SEM), using a FEI MLA 650FEG instrument in the CREAIT MAF Facility (Memorial University), was used on carbon-coated polished rock samples to refine petrographic observations and mineral identification, as well as for qualitative analyses and documentation of hydrothermal alteration minerals before Raman spectroscopy. This was accomplished using both the backscattered electron (BSE) imaging and energy dispersive X-ray spectrometry (EDS) capabilities of the instrument. Analyses were performed at high vacuum, with an accelerating voltage of 15 kV and a sample current of 10 nA. Spectral analysis by EDS was performed using spots of 10 µm diameter and an acquisition time of 20 s.

Electron Probe Microanalysis (EPMA)

Electron probe microanalyses were carried out using the JEOL JXA-8230 SuperProbe instrument in the CREAIT Hibernia Electron Beam Facility (Memorial University) equipped with 5 wavelength dispersive spectrometers (WDS). All analyses were performed either on the polished rock samples (described above) or in polished petrographic thin sections prepared from the same sample. Samples were coated with a 20 nm (200 Å) thick carbon layer before analysis.

In the case of white mica and chlorite, the accelerating voltage was set to 15 kV, with a beam current of 20 nA and a 5 µm spot diameter. The following major elements were determined: Si, Al, Ca, K, Na, Mg, Fe, Mn, Cr, Ti, V, Cl, and F. Mineral formulae and molar proportions of white mica (based on the general structural formula $AD_2T_4O_{10}(OH)_2$) were calculated assuming: i) all Fe is Fe(II), ii) Fe, Mg, Ti, Mn, Cr, and V are in octahedral sites, iii) K, Na, and Ca are allocated in the interlayer position between TOT layers, iv) Al is tetrahedral up to Si + Al = 4 atoms per 11 oxygens, and v) any remaining Al is assigned to octahedral sites. For chlorite (structural formula $A_{5\text{-}6}T_4O_{10}(OH)_8$), the following assumptions were made: i) all Fe is Fe(II), ii) Fe, Mg, Ti, Mn, Cr, and V are allocated to the 2:1 (or brucite) octahedral positions, iii) Al is allocated in tetrahedral positions up to Si + Al = 4 atoms per 14 oxygens, and iv) any remaining Al is assigned to octahedral sites.

Alunite and pyrophyllite were measured with an accelerating voltage of 15 kV, and a beam current of 10 nA for alunite and 20 nA for pyrophyllite. The electron beam was defocussed to a 10 μm diameter to avoid crystal damage and reduce alkali element migration during analysis (Autefage and Couderc, 1980). The following elements were determined: Si, S, Al, K, Na, Mg, Fe, Ti, Ca, Mn, P, Ba, Cl, F, Sr, Ce, Cl, and F. Pyrophyllite mineral formulae ($D_2T_4O_{10}(OH)_2$) were calculated assuming: i) all Fe is Fe(III), ii) Fe, Mn, Mg, Ca, Na, K, and Ti are allocated to octahedral positions, iii) Al is allocated to tetrahedral positions up to Si + Al = 4 atoms per 11 oxygens, and iv) any remaining Al is assigned to octahedral sites. For alunite (based on the general structural formula $DG_3(TO_4)_2(OH)_6$), mineral formulae were calculated assuming: i) all Fe is Fe(III), ii) S, P, and Si are allocated to the T position, iii) Al and Fe^{3+} are allocated to the G position, iii) K, Na, Ca, Sr, Ba, Mg, Ti, Mn, and Ce are allocated to the D position.

For all analyses, counting times were 20-30 s on the optimum WDS peak for each of the major and minor elements analyzed and 10 s on background on both sides of the peak. For K and Na, the counting times were reduced to 10 s and 5 s on peak and backgrounds, respectively, and these elements were run first in the counting sequence to mitigate the effects of alkali migration under the electron beam. Limits of detection (LOD) were calculated as the minimum concentration required to produce count rates three times higher than the square root of the measured background (i.e., 3σ; 99% degree of confidence at the lower detection limit). Raw data were corrected for matrix effects using the PAP algorithm (Pouchou and Pichoir, 1984; 1985) as implemented by JEOL software. The standards used for EPMA acquisition consisted of a collection of synthetic and natural silicates, oxides, and sulfates commonly used for EPMA calibrations. The Astimex biotite standard (for white mica analyses) and Astimex chlorite standard (for chlorite, pyrophyllite, and alunite analyses) were measured at the beginning and end of each sample analyzed, as well for every 25-30 points of analysis as a secondary standard to ensure the consistency of the calibration of the electron probe instrument. For quality control, EPMA totals of <96 wt.% and >102 wt.% in white mica after recalculation were considered erroneous and discarded. For chlorite, pyrophyllite, and alunite, analyses were discarded if the initial EPMA total values did not lie between 84-87 wt.%, 94-98 wt.%, and 94-99 wt.%, respectively.

The whole set of EPMA data for pyrophyllite, white mica, chlorite, and alunite, as well as instrument parameters and standard materials, is reported in Appendix 3.

3.6. Results

3.6.1. Pyrophyllite

Pyrophyllite from the Vinjer prospect and the Oval Pit mine were analyzed in this study. Both occurrences show extensive and pervasive advanced argillic alteration zones, where pyrophyllite occurs as massive aggregates, routinely associated with minor amounts of quartz (Fig. 3.3a,b).

Visible - near infrared - short-wave infrared spectroscopy

Pyrophyllite samples from both the Vinjer prospect and the Oval Pit mine display an absorption band in the NIR spectrum at 950 nm, two major bands in the SWIR spectrum at 1394 nm and 2167 nm (Fig. 3.4a; Table 3.2), and secondary absorption bands at 1232 nm and close to 2320 nm (Fig. 3.4a). In addition to pyrophyllite absorption bands, bands close to 1414 nm, 1909 nm and 2208 nm (Fig. 3.4a; Table 3.2) indicate the presence of muscovite in these samples.

Raman spectral features

Raman spectra of pyrophyllite from Oval Pit and the Vinjer prospect show virtually the same five major peaks, at 193-194 cm^{-1}, 260-261 cm^{-1}, 360-362 cm^{-1}, 704-705 cm^{-1}, and 3673-3675 cm^{-1} (Fig. 3.4b; Table 3.3). The adjacent Raman band at 3647 cm^{-1} reported by Gates et al. (2017) and Zhai et al. (2008) is not resolved in Raman spectra of pyrophyllite obtained in this study (Fig. 3.4b; Table 3.3).

Mineral chemistry

Electron probe microanalyses of Oval Pit and Vinjer pyrophyllite suggest a generally homogeneous chemical composition. The largest compositional variation within the analyzed samples is observed in their SiO_2 and (Al_2O_3 + Fe_2O_3) contents, where lower SiO_2 compositions correlate with higher Al_2O_3 + Fe_2O_3 contents (Table 3.4). Total Fe^{3+} contents are low (0.005-0.010 Fe^{3+} a.p.f.u.; Table 3.4), in agreement with the absence of a detectable Raman band at 3647 cm^{-1} (Fig. 3.4b).

3.6.2. White mica/Sericite

At Heritage, white mica most frequently occurs in fine-grained agglomerations, as a replacement of protolith minerals (mainly feldspars), and is sometimes associated with chlorite (Fig. 3.3c). White mica is spatially associated with acanthite and/or native silver (Fig. 3.3.d), as well as occurring filling the space between bladed calcite crystals (a diagnostic feature indicating fluid boiling; Etoh et al., 2002).

At Hope Brook, white mica occurs as medium-grained crystals of up to 60 µm (Fig. 3.3e) that are occasionally intergrown with chlorite, giving rise to mica-chlorite stacks. Mica crystals are chemically zoned , with Na-rich cores and K-rich rims (Fig. 3.3e).

At Hickey's Pond, white mica mainly occurs as coarse-grained crystals (up to 500 µm) in a quartz-hematite-alunite-rutile vein, where it commonly develops in close spatial association with specular hematite.

Visible - near infrared - short-wave infrared spectroscopy

White mica at Heritage shows consistent absorption bands at 1410-1414 nm, 1906-1915 nm, and 2212-2218 nm (Fig. 3.5a; Table 3.2). The Al-OH related band located at 2212-2218 nm suggests phengite is the prevalent white mica species. In addition to phengite, smectite is also recognized in some Heritage samples, evidenced by the deeper absorption band at 1919-1929 nm and the presence of an H_2O band shoulder near 1460 nm in some of the acquired spectra (Fig. 3.5a; Table 3.2).

The Hope Brook samples contain white mica with absorption bands at 1409-1412 nm, 1908-1941 nm, and 2192-2201 nm (Fig. 3.5a). In this case, the position of the Al-OH band at 2192-2201 nm, together with the slight downshift of the water band to 1409-1412 nm, indicates the occurrence of paragonite.

White mica at Hickey's Pond could not be identified by Vis-NIR-SWIR spectroscopy, given the fact that it is closely intermixed with specular hematite and the dominant absorption bands observed, typical of Fe-oxide phases (~930 nm, ~1450 nm, ~1930 nm), obscure the spectral features of any associated white mica.

Raman spectral features

White mica from Heritage displays major Raman peaks at 191-202 cm^{-1}, 259-266 cm^{-1}, 412-429 cm^{-1}, 640-667 cm^{-1}, 702-706 cm^{-1}, 748-759 cm^{-1}, and 1082-1113 cm^{-1} (Fig. 3.5b; Table 3.3), with a single H_2O/OH vibration band at 3620-3632 cm^{-1} (Fig. 3.5b; Table 3.3). The Raman band at 1082-1113 cm^{-1} suggests that white mica at Heritage is close to phengite in composition.

White mica from Hope Brook has major Raman peaks at 197-201 cm^{-1}, 262-267 cm^{-1}, 403-411 cm^{-1}, 638-657 cm^{-1}, 701-704 cm^{-1}, 744-751 cm^{-1}, 1010-1065 cm^{-1}, and 3627 cm^{-1} (Fig. 3.5b; Table 3.3). The reported band positions are typical for muscovite-group mica with low degrees of Tschermak substitution.

Accurate, well resolved Raman spectra of white mica from Hickey's Pond were not possible to acquire due to strong fluorescence problems consequent to the presence of hematite (Fig. 3.5b).

Mineral chemistry

Electron probe microanalyses of white mica at Heritage confirmed they are part of the muscovite-celadonite solid solution series, containing high Si^{4+} and substantial Mg^{2+} (0.17-0.31 a.p.f.u.; Fig. 3.5c, Table 3.4) and Fe^{2+} (0.05-0.12 a.p.f.u.; Fig. 3.5c, Table 3.4), with a composition closer to phengite. This is in agreement with both spectroscopic techniques used in this study. In contrast, white mica at Hickey's Pond is muscovite in composition (Fig. 3.5c), being K-rich (0.74-0.79 a.p.f.u. K^{+}; Table 3.4) with minor amounts of Na^{+} (0.10-0.16 a.p.f.u.; Table 3.4). White mica at Hope Brook is chemically zoned, with cores of paragonite (0.78-1.02 a.p.f.u. Na^+ and 0.05-0.30 a.p.f.u K^+; Table 3.4) and muscovitic rims (0.15-0.37 a.p.f.u. Na^+ and 0.62-0.77 a.p.f.u. K^+; Table 3.4).

3.6.3. Chlorite

Chlorite at Heritage generally occurs pervasively as a fine-grained alteration of the groundmass of the intermediate pyroclastic and porphyritic volcanic rocks that host the deposit, as well as replacing volcanic phenocrysts. Chlorite is texturally associated with white mica (Fig. 3.3c).

Chlorite at Hope Brook occurs as fine-grained (15 μm) to medium-grained (70 μm) crystals with white mica and disseminated pyrite in highly deformed quartz-sericite-chlorite schists.

Visible - near infrared - short-wave infrared spectroscopy

Chlorite at Heritage is characterized by major absorption bands at 1410-1414 nm, 1907-1993 nm, 2240-2262 nm, and 2339-2352 nm (Fig. 3.6a; Table 3.2). Both the Mg-OH and the Fe-OH bands show positions lying between those reported for clinochlore and chamosite, suggesting an intermediate Fe-Mg composition of chlorite.

Chlorite from Hope Brook presents major absorption bands at 1408 nm, 1995 nm, 2255 nm, and 2346 nm (Fig. 3.6a; Table 3.2). As in the case of chlorite from Heritage, the Mg-OH and Fe-OH bands lie between those reported for the clinochlore and chamosite end-members, indicating an intermediate composition of chlorite.

Raman spectral features

Chlorite at Heritage is characterized by Raman peaks at 198-214 cm^{-1}, 357-373 cm^{-1}, 541-550 cm^{-1}, 658-675 cm^{-1}, 3420-3430 cm^{-1}, 3559-3574 cm^{-1}, and 3652-3670 cm^{-1} (Fig. 3.6b; Table

3.3). The evident downshift in the major Raman peak to 658-675 cm^{-1} (from the 683 cm^{-1} of Mg-rich chlorite) together with the very low intensity of the peak located at 357-373 cm^{-1} suggests an intermediate Fe-Mg composition of chlorite.

The acquisition of Raman spectra of chlorite from Hope Brook was particularly challenging, due to strong fluorescence effects attributed to the fine-grained nature of the chlorite and its association with disseminated pyrite. However, a small number of analyses yielded good Raman spectra, which is characterized by major bands at 201 cm^{-1}, 356 cm^{-1}, 546 cm^{-1}, 670 cm^{-1}, 3432 cm^{-1}, 3579 cm^{-1}, and 3653 cm^{-1} (Fig. 3.6b: Table 3.3). As in the case of chlorite from the Heritage prospect, the low wavelength of the main phyllosilicate Raman band at 670 cm^{-1} and the very low intensity of the 356 cm^{-1} peak indicate that chlorite at Hope Brook has an intermediate Fe-Mg composition.

Mineral chemistry

Representative chlorite EPMA analyses are compiled in Table 3.4 and Figure 3.6c. Chlorite from both the Heritage low-sulfidation epithermal prospect and the Hope Brook high-sulfidation epithermal deposit show intermediate compositions between the clinochlore and the chamosite endmembers, based on octahedral site occupancy (Fe/(Fe+Mg); Fig. 3.6c; Table 3.4). Chlorite at both Hope Brook and Heritage is substantially enriched with Fe^{2+} relative to the clinochlore field (1.62-1.78 a.p.f.u. Fe^{2+} and 1.59-2.01 a.p.f.u. Fe^{2+}, respectively; Fig. 3.6c; Table 3.4). At Heritage, the chlorite plots within the brunsvigite field (Fig. 3.6c). Chlorite from Hope Brook has a tetrahedral Al^{+3} content of $\geq$1.3 a.p.f.u. and plots within the ripidolite field (Fig. 3.6c).

3.6.4. Alunite

In this study, alunite was only recognized, either petrographically or spectroscopically, in samples from the Hickey's Pond high-sulfidation epithermal prospect. Here, it is abundant in most of the recognized hydrothermal alteration zones, occurring as coarse to fine-grained crystals disseminated in the altered wallrocks (Fig. 3.3f).

Visible - near infrared - short-wave infrared spectroscopy

Alunite at Hickey's Pond shows a compositionally diagnostic absorption band between 1490 nm and 1491 nm (Fig. 3.7a; Table 3.2), indicating the predominance of Na^+ over K^+ in the alunite structure and an essentially natroalunite composition. Additional absorption bands occur at 1434-1435 nm, 1763-1766 nm, 2165-2170 nm, 2212-2214 nm, and 2319-2323 nm (Fig. 3.7a; Table 3.2).

Raman spectral features

In the 100-1200 cm^{-1} spectral region, alunite from Hickey's Pond presents two clearly distinct Raman spectral styles. Both of them have characteristic Raman bands at 388-394 cm^{-1}, 515-518 cm^{-1}, 560-572 cm^{-1}, 651-656 cm^{-1}, 1024-1025 cm^{-1}, 1078-1086 cm^{-1}, 1160-1166 cm^{-1}, and 1181-1186 cm^{-1} (Fig. 3.7b; Table 3.3). However, they differ in the relative intensity of the bands at 651-656 cm^{-1}, 1078-1086 cm^{-1}, and 1181-1186 cm^{-1}. One of the spectral styles has a high-intensity Raman band at 1181-1186 cm^{-1}, as well as the presence of a low-intensity peak at 651-656 cm^{-1}, indicative of the alunite endmember (Fig. 3.7b; Table 3.3). The other spectral style contains higher intensity Raman bands at 652 cm^{-1} and 1078-1086 cm^{-1}, indicating the presence of natroalunite (Fig. 3.7b; Table 3.3).

Mineral chemistry

Electron probe microanalyses confirm the presence of chemical compositions intermediate to the end-members alunite and natroalunite (Fig. 3.7c; Table 3.4). Individual alunite crystals range from 0.10-0.53 a.p.f.u. K^+ and 0.18-0.51 a.p.f.u. Na^+ (Table 3.4), with common crystal chemical zonation from a core enriched in K^+ (alunite) to crystal rims enriched in Na^+ (natroalunite) (Fig. 3.3f).

3.7. Discussion

3.7.1. Comparison between Vis-NIR-SWIR and Raman spectroscopic identification and characterization of hydrothermal alteration

Visible - near infrared - short-wave infrared spectroscopy was a useful tool for the rapid identification of hydrothermal alteration minerals in the bulk samples examined in this study. Raman microspectroscopy, in most cases, allowed a better spatial and chemical characterization of hydrothermal alteration at the microscale.

Pyrophyllite was clearly recognized by both Vis-NIR-SWIR and Raman spectroscopies at the Vinjer prospect and the Oval Pit mine (Fig. 3.4), and the Raman spectra of pyrophyllite reported in this study closely resemble Raman spectral features of pyrophyllite reported in the literature (Wang et al., 2015; Gates et al., 2017). However, the adjacent Raman band at 3647 cm^{-1} reported by Gates et al. (2017) and Zhai et al. (2008) is not present in Raman spectra of pyrophyllite obtained in this study (Fig. 3.4b; Table 3.3), which implies that pyrophyllite does not contain significant Fe^{3+} in the octahedral site. There does appear to be minor substitution of Si^{4+} by Al^{3+} in tetrahedral coordination (0.009-0.099 a.p.f.u. tetrahedral Al^{3+}; Table 3.4) and this is consistent with pyrophyllite analyses by Rosenberg and Cliff (1980), who suggested that charge balance is obtained in this case by the formation of extra hydroxyl units. Overall, a distinctive Vis-NIR-SWIR and Raman spectrum, as well as its consistent composition, makes pyrophyllite an easily recognizable key hydrothermal alteration mineral in high-sulfidation epithermal systems using either spectroscopic technique.

The distinction of different members of the white mica group ("sericite" minerals) was of particular interest in this study. At Hope Brook, paragonite was recognized by SWIR spectroscopy, using the characteristic Al-OH band at 2192-2201 nm (Fig. 3.5a; Table 3.2). However, further investigation by SEM and EPMA revealed the presence of both muscovite and paragonite (Table 3.4), with clearly zoned mica crystals containing Na-rich cores and K-rich rims (Fig. 3.3e). In these samples, Raman spectroscopy could not discern between muscovite and paragonite (Fig. 3.5b; Table 3.3), showing only minor position shifts in this compositional range (<3-4 cm^{-1}; Table 3.3), with no systematic peak shift linked to changes in K/Na composition. This is consistent with the observations of Wang et al. (2015) and suggests that variable ratios of K^+ to Na^+ in the interlayer position of white mica have a negligible effect on the $(Si_2O_5)^{2-}$ vibration. Conversely, the incorporation of a bivalent cation, such as Ca^{2+}, in the interlayer position of white mica is controlled by a change in Si/Al ratio of the tetrahedral layer in order to achieve charge balance, and would result in distinct Raman spectral features (Wang et al., 2015). In contrast to Raman spectroscopy, the response of the ~2000 nm band in the SWIR spectra allows for the distinction of the main white mica phase at Hope Brook. Short-wave infrared spectroscopy therefore remains nominally superior for discrimination between muscovite and paragonite (Fig. 3.5a), although it will not elucidate fine scale core-rim zoning as observed at Hope Brook and would probably only detect the most abundant white mica phase in a given sample.

At Heritage white mica largely shows very similar Raman spectral features to those at Hope Brook (Fig. 3.5b; Table 3.3). The single notable spectral difference between white mica from these two occurrences resides in the shift of the 1010-1065 cm^{-1} Raman band detected at Hope Brook to 1082-1113 cm^{-1} observed at Heritage (Fig. 3.5b; Table 3.3). In comparison to white mica (muscovite-paragonite) from Hope Brook, white mica at Heritage contains significantly higher contents of tetrahedral Si^{4+}, coupled with lower amounts of $^{IV}Al^{3+}$ (Table 3.4), indicating a higher degree of Tschermak substitution and a composition closer to phengite (Fig. 3.5c). This clearly shows that muscovite/paragonite mica compositions can be successfully discerned from more phengitic-celadonitic ones by Raman spectroscopy, based on the band shift described above. The sensitivity of the ~2000 nm band in the SWIR spectra also allows for a fast distinction between muscovite, paragonite, and phengite, but as stated above, reflectance spectroscopy would only be able to detect the volumetrically dominant white mica phase in a given sample if multiple compositions of white mica and/or zoned white mica crystals are present.

Chlorite samples from the Hope Brook high-sulfidation epithermal deposit and the Heritage low-sulfidation epithermal prospect display coinciding Raman spectral features (Fig. 3.6; Tables 3.2 and 3.3). According to Raman spectra acquired by Wang et al. (2015), Mg-chlorite shows Raman bands at 203 cm^{-1}, 357 cm^{-1}, 552 cm^{-1}, and 683 cm^{-1}, with a peak position downshift of the 683 cm^{-1} peak towards 671 cm^{-1} for Fe-Mg ripidolite. For Heritage and Hope Brook samples, this Si-O-Si related Raman band was found at 658-675 cm^{-1}, and at 670 cm^{-1}, respectively (Figs. 3.6b and 3.8a; Table 3.3), suggesting that these examples of hydrothermal chlorite contain substantial Fe^{2+} in their structure, as confirmed by EPMA results (Table 3.4; Fig. 3.6c). The lower wavelengths of the Si-O-Si Raman band recorded at Heritage (658-675 cm^{-1}) in comparison with Hope Brook (670 cm^{-1}; Figs. 3.6b and 3.8a) is also consistent with the slightly higher Fe^{2+} content observed in the Heritage chlorite (Table 3.4). The position of the Si-O-Si Raman band is obviously sensitive to chlorite composition and can be used for semi-quantitative estimation of the Fe^{2+} content in chlorite (Fig. 3.8c). Magnesium-rich clinochlore with <0.5 a.p.f.u. Fe^{2+} has its major phyllosilicate Raman peak at 682-683 cm^{-1} (Fig. 3.8c). With the increase of Fe^{2+} in the octahedral layer, Fe-Mg chlorite of intermediate composition from this study (ripidolite from Hope Brook and brunsvigite from Heritage) shows a shift of the main phyllosilicate Raman band towards lower wavelengths (670-675 cm^{-1}; Fig. 3.8c). Fe-rich chamosite with >2.5 a.p.f.u. Fe^{2+} displays its major Raman band at 665 cm^{-1} (Fig. 3.8c). Future coupled Raman and electron probe microanalyses of chlorite of variable composition and from diverse geological environments would help establish a better calibration of the relationship shown in Figure 3.8c. With regards to Vis-NIR-SWIR spectra, chlorite from both the Hope Brook and Heritage epithermal occurrences show a Fe-OH absorption band at 2240-2262 nm and a Mg-OH absorption band at 2339-2352 nm (Fig. 3.6a; Table 3.4), indicative of intermediate Fe-Mg chlorite compositions. Iron-rich chlorite can be therefore easily discerned from Mg-rich chlorite by real time reflectance spectroscopy. Raman microspectroscopy, however, has the potential to be used as a tool for the semi-quantitative estimation of Fe^{2+} content in chlorite, providing more detailed geochemical information beneficial to decision-making during mineral exploration campaigns.

Raman spectra of hydrothermal alunite and natroalunite from the Hickey's Pond high-sulfidation epithermal system obtained in this study are consistent with the peak positions reported for alunite group minerals by Maubec et al. (2012). However, an important number of Raman spectra of alunite from Hickey's Pond show shifted Raman band positions intermediate between those of alunite and natroalunite endmembers (Fig. 3.8b), and attributed to the alunite-natroalunite zoning of individual crystals observed by SEM. This interpretation is also consistent with EPMA analyses (Figs. 3.7c and 3.8b; Table 3.4). In contrast, Vis-NIR-SWIR spectra of samples from the Hickey's Pond prospect only detected the presence of natroalunite (Fig. 3.7a; Table 3.4). This is another example of the limitation of reflectance spectroscopy in the characterization of various phase compositions within the same sample and, in particular, the effective averaging of important microscale features such as chemical mineral zonation.

Some of the Raman and Vis-NIR-SWIR spectra of the studied minerals show peculiar artifacts after the background removal process. In Vis-NIR-SWIR spectra, those artifacts emerge as wide concave absorption features between ~600 and ~1600 nm (Figs. 3.4a, 3.5a, and 3.6a). These artifacts might be attributed to the presence and interference of Fe-rich phases. In the case of Raman spectra, artifacts are observed in the lower wavelength region of some spectra (<300 cm^{-1}), where the background follows a wide convex medium-to-high intensity band (Figs, 3.4b, 3.5b, and 3.6b). Such spectral features are attributed to fluorescence effects due to the fine-grained nature of the minerals analyzed and the presence of neighboring Fe-rich phases. The described spectral artifacts are expected in natural geological samples and do not interfere nor modify the position and intensity of the spectral bands most useful for mineral identification and geochemical characterization.

The data presented in this contribution demonstrate that Raman microspectroscopy, in combination with Vis-NIR-SWIR spectroscopy, can accurately characterize key hydrothermal alteration minerals in epithermal systems and can provide complementary high-resolution information at the microscale. A flow chart summarizing the key spectral features for these mineral for both techniques is presented in Figure 3.9. This figure is designed to serve as a spectral reference for geological samples displaying hydrothermal alteration during Vis-NIR-SWIR and Raman spectroscopic studies in mineral exploration or economic geology research settings. As evidenced by the results reported here, there is a clear advantage in adopting the use of Raman microspectroscopy as a complementary technique to Vis-NIR-SWIR, as it will elucidate the micro-spectral characteristics of the main hydrothermal alteration phases present in a sample. When combined with preliminary petrography, Raman microspectroscopy can provide further detailed chemical mineral characterization correlated to specific textures or metal delivery event(s).

3.7.2. Geological significance and implications for mineral exploration

Mineralogical and geochemical characterization of phyllosilicates is crucial in hydrothermal ore deposits research and exploration, since they provide insight into the hydrothermal environment, ore-forming processes, and the timing of ore deposition within a multi-stage system (White and Hedenquist, 1995; Arbiol et al., 2021).

Field-portable short-wave infrared spectroscopy is currently widely deployed in the mineral exploration industry to map hydrothermal alteration assemblages at the regional-to-deposit scale in a broad range of mineral deposits, including porphyry deposits (e.g., Graham et al., 2018), epithermal deposits (e.g., Kerr et al., 2011; Ferrier et al., 2019), iron oxide copper-gold (IOCG) deposits (e.g., Tappert et al., 2013), skarn deposits (e.g., Zhang et al., 2020), and volcanic-hosted massive sulfide deposits (e.g., Jones et al., 2005; Thompson et al., 2009; Buschette and Piercey, 2016; Huang et al., 2018; Gaillard et al., 2018). However, there are some important limitations to this technique: i) the identification of a mineral phase depends on its ability to produce a measurable reflectance signal, ii) sparse hydrothermal alteration can sometimes remain undetected or unquantified, iii) minerals producing stronger reflectance signals, and the presence of multiple minerals with strong reflectance, can mask weaker signals from more diagnostic alteration phases,

iv) many specific absorption bands (e.g., OH band at ~1400 nm, Al-OH band at ~2200 nm) are common to a wide range of phyllosilicates, and v) macroscale spectroscopy cannot discriminate minerals formed by successive hydrothermal events that affected an individual sample.

The mineralogical, spectral, and geochemical data of key hydrothermal alteration phases from epithermal deposits and prospects reported here have application to the initial recognition of epithermal style ore-forming environments, characterization of ore zonation and exploration vectoring, and improving insight into changes in physicochemical conditions during the evolution of hydrothermal systems.

As a component of fine-grained alteration, pyrophyllite can easily be confused with other phyllosilicates in hand specimen or thin section, including talc and the white mica group. Beneficially, it is easily recognized with both Vis-NIR-SWIR spectroscopy and Raman spectroscopy (Fig. 3.9). Although it can occur in other environments (e.g., high grade metapelites), in terranes prospective for epithermal mineralization pyrophyllite is a characteristic mineral of high-sulfidation style hydrothermal alteration. It is indicative of extensive leaching of host rocks by highly acidic hydrothermal fluids and is formed in the initial stages of hydrothermal alteration, generally in zones surrounding the massive silica (vuggy silica) core of typical high-sulfidation epithermal systems (Arribas, 1995; Hedenquist et al., 2000).

In the case of white mica, the presence of paragonitic cores and muscovitic rims at Hope Brook has been interpreted by Arbiol et al. (2021) as the result of the compositional evolution of hydrothermal fluids in this high-sulfidation epithermal system. In contrast, white mica from the Heritage prospect is phengitic in composition and formed under conditions of near-neutral pH, which in the low-sulfidation epithermal environment is achieved by the successful and complete buffering of initially acidic fluids by the host rocks (Gaillard et al., 2018; Arbiol et al., 2021).

Based on chemical composition, chlorite at Hope Brook is classified as ripidolite, whereas chlorite at Heritage is brunsvigite (Fig. 3.6c). Chlorite geothermometry by Arbiol et al. (2021), based on the semi-quantitative geothermometer of Inoue et al. (2018), returned estimated temperatures of formation of hydrothermal chlorite between 201 °C and 297 °C at Hope Brook and between 108 °C and 192 °C at Heritage. This is consistent with the higher temperature range generally perceived for high-sulfidation (proximal to intrusion, magmatic fluids predominate) vs low-sulfidation (more distal from intrusion, circulated meteoric waters dominant) epithermal systems (Hedenquist et al., 2000). According to Arbiol et al. (2021), the higher content of Al in chlorite from Hope Brook is interpreted to be due to a higher degree of Tschermak substitution $((\mathrm{Mg,Fe}^{2+})^{\mathrm{VI}}+\mathrm{Si}^{\mathrm{IV}} \leftrightarrow \mathrm{Al}^{\mathrm{IV}}+(\mathrm{Al,Fe}^{3+})^{\mathrm{VI}})$, which is controlled by temperature, pressure, and fluid and host rock composition (Vidal et al., 2001). Based on textural and chemical observations, as well as on geothermometry, chlorite at Hope Brook is interpreted to have formed during later stages of hydrothermal activity, forming an outer envelope to the vuggy silica core and Au mineralized zone of the epithermal system (Arbiol et al., 2021). In contrast, chlorite at Heritage is widespread in all alteration zones, has elevated contents of Mn (Table 3.4), and is interpreted to have formed during the main stages of hydrothermal activity at Heritage due to pervasive phyllic/chloritic alteration (Arbiol et al., 2021).

Raman spectroscopy not only confirmed the presence of alunite at Hickey's Pond, but also revealed two different compositional populations (Fig. 3.7b), in conjunction with SEM-EDS and EPMA data. In a mineral exploration and/or research setting, Raman microspectroscopy thus emerges as a reliable tool for the identification and discrimination of alunite and natroalunite (Fig. 3.9), as illustrated by this example. In this high-sulfidation epithermal prospect, alunite/natroalunite crystals are interpreted to be hypogene, formed during the main stages of widespread hydrothermal alteration by oxidizing and acidic fluids (Arribas, 1995). The progression from alunite to natroalunite in high-sulfidation epithermal systems, as observed in Hickey's Pond, has been interpreted by various authors to record an increase in fluid temperatures (Stofregen et al., 2000; Deyell and Dipple, 2005). The link between the progression towards Na-rich alunite and gold deposition at Hickey's Pond requires additional, more detailed, examination. However, meter scale alunite-natroalunite zoning might provide a vector towards core zones of precious metal mineralization (Hedenquist et al., 2000; Sillitoe, 2010).

The findings of this study apply most directly to economic geology research and the mineral exploration industry, where the application of Raman microspectroscopy, coupled with Vis-NIR-SWIR spectroscopy, could provide a faster, more precise, and more cost-efficient method, in comparison to more costly and time-consuming electron probe investigations (SEM, EPMA), for the identification and chemical characterization of hydrothermal alteration minerals at the microscale. By measuring key Vis-NIR-SWIR and Raman spectral features (Fig. 3.9), chemical variations for some alteration minerals of interest at both the deposit-scale and the individual grain-scale can be discerned and mapped in real and near-real time, respectively, thus promoting the definition of exploration vectors toward economic mineralization in the epithermal environment and other hydrothermal systems (e.g., porphyry copper, volcanogenic massive sulfides, orogenic gold, etc.). The characterization of key hydrothermal alteration minerals associated with mineralization can provide critical information on ore genesis, physicochemical characteristics of mineralizing hydrothermal fluids, and ore precipitation mechanisms. Additionally, this approach has widespread potential applications in mineralogy, petrology, and planetary exploration. The identification of hydrothermal minerals on Mars or other planetary bodies via Raman spectroscopy could provide evidence for high-temperature hydrothermal activity during future Solar System exploration missions.

3.8. Conclusions

The results presented in this paper demonstrate that Raman microspectroscopy, coupled with Vis-NIR-SWIR spectroscopy, can readily identify and distinguish many important hydrothermal alteration minerals in situ at the microscopic scale, using fairly simple and non-destructive sample preparation. High-quality Raman spectra of alunite (alunite-natroalunite series), pyrophyllite, white mica (phengite and muscovite/paragonite), and Fe-Mg chlorite (ripidolite and brunsvigite) have been obtained from drill core and surface samples using standard instrumentation.

Detailed compositional information can be extracted from the Raman spectra for some phyllosilicates, particularly chlorite, white mica with substantial Tschermak substitution (phengite/celadonite), and members of the alunite-natroalunite solid solution. This additional spectroscopic information could be applied to map solid solution compositional variations of minerals at the deposit-scale, with potential as a vector to ore mineralization during mineral exploration campaigns.

Notably, the reliable identification of specific white mica minerals present in the sample by Vis-NIR-SWIR and Raman spectroscopy can address the commonly widespread and ambiguous classification of “sericite”, a term used widely to refer to fine-grained white mica in ore deposit exploration and research. The sensitivity of the Raman band between 1000 cm^{-1} and 1150 cm^{-1} to changes in Si^{+4} and Al^{+3} in tetrahedral coordination suggests that compositional variations due to Tschermak substitution can be effectively detected by Raman microspectroscopy. Consequently, purely muscovitic/paragonitic mica compositions can be successfully distinguished from more phengitic/celadonitic compositions at the microscale by studying the wavelength of this diagnostic Raman band.

In addition to white mica, the position of the main chlorite Si-O-Si Raman band shifts from 683 cm^{-1} for Mg-rich chlorite to 665 cm^{-1} for Fe-rich chlorite. It therefore appears practical to estimate Fe^{2+} content of hydrothermal chlorite at the microscale using Raman spectroscopy. Further study, incorporating a larger set of samples with diverse Mg-Fe contents would be helpful in elucidating and calibrating this relationship.

These Raman spectral characteristics are potentially useful during mineral exploration campaigns and ore deposits research, where they could be applied in a complementary fashion to initial real time Vis-NIR-SWIR acquisition. The information obtained through the application of Raman spectroscopy at the microscale would be particularly valuable immediately after initial exploration efforts, when suitable outcrop or drill core samples have been collected. Based on the present study of examples from epithermal deposits, Raman microspectroscopy has been shown to be a promising, cost-effective, and near-real time method to obtain mineralogical and geochemical information of key hydrothermal phases at the microscale, with potential application to other ore deposits of hydrothermal origin.

3.9. Acknowledgements

The authors would like to thank Dr. Stephen Piercey and Dr. Erika Merschrod for providing access to the Vis-NIR-SWIR Spectrometer and Raman Spectrometers, respectively. In addition, the authors would like to acknowledge the assistance from Liam Whelan, Lucas Stewart and Silvana Rodrigues Pereira during Raman analysis. Analytical work was funded by an NSERC Discovery Grant to GDL (RGPIN/005037-2017), and fieldwork was possible thanks to a Student Research Grant (SRG) awarded by the Newmont Mining Corporation Fund via the Society of Economic Geologists (SEG) Foundation in 2017.

3.10. References

Arbiol, C., Layne, G.D., Zanoni, G., Šegvić, B., 2021. Characteristics and genesis of phyllosilicate hydrothermal assemblages from Neoproterozoic epithermal Au-Ag mineralization of the Avalon Zone of Newfoundland, Canada. Applied Clay Science 202, 105962. https://doi.org/10.1016/j.clay.2020.105960

Arribas, A., 1995. Characteristics of high-sulfidation epithermal deposits, and their relation to magmatic fluid. Mineralogical Association of Canada Short Course 23, 419-454.

Autefage, F. and Couderc, J.J., 1980. Étude du Mécanisme de la Migration du Sodium et du Potassium au Cours de leur Analyse a la Microsonde Électronique. Bulletin de Minéralogie 130, 623-629.

Bailey, S.W., 1980a. Structures of layer silicates. In: Crystal structures of clay minerals and their x-ray identification (Brindley, G.W. and Brown, G., eds.). Monograph 5, Mineralogical Society, London, 1-124. https://doi.org/10.1180/mono-5.1

Bailey, S.W., 1980b. Summary of recommendations of AIPEA nomenclature committee on clay minerals. American Mineralogist 65, 1-7.

Bergaya, F. and Lagaly, G., 2013. Handbook of Clay Science. Elsevier, 1752 pp.

Berger, B.R. and Bethke, P.M., 1985. Geology and geochemistry of epithermal systems. Reviews in Economic Geology 2, 297 pp. https://doi.org/10.5382/Rev.02

Bishop, J.L. and Murad, E., 2004. Characterization of minerals and biogeochemical markers on Mars: A Raman and IR spectroscopic study of montmorillonite. Journal of Raman Spectroscopy 35, 480-486. https://doi.org/10.1002/jrs.1173

Bishop, J.L. and Murad, E., 2005. The visible and infrared spectral properties of jarosite and alunite. American Mineralogist 90(7), 1100-1107. https://doi.org/10.2138/am.2005.1700

Bishop, J.L., Lane, M.D., Dvar, M.D., Brown, J., 2008a. Reflectance and emission spectroscopy study of four groups of phyllosilicates: smectites, kaolinite-serpentines, chlorites, and micas. Clay Minerals 43, 35-54. https://doi.org/10.1180/claymin.2008.043.1.03

Bishop, J.L., Dobrea, E.Z.N., McKeown, N.K., Parente, M., Ehlmann, B.L., Michalski, J.R., Milliken, R.E., Poulet, F., Swayze, G.A., Mustard, J.F., 2008b. Phyllosilicate diversity and past aqueous activity revealed at Mawrth Vallis, Mars. Science, 321(5890), 830-833. https://doi.org/10.1126/science.1159699

Breitinger, D.K., Krieglstein, R., Bogner, A., Schwab, R.G., Pimpl, Th.H., Mohr, J., Schukow, H., 1997. Vibrational spectra of synthetic minerals of the alunite and crandallite type. Journal of Molecular Structure 408-409, 287-290. https://doi.org/10.1016/S0022-2860(96)09627-5

Buzgar, N., Buzatu, A., Sanislav, I.V., 2009. The Raman study of certain sulfates. Analele Stiintifice ale Universitatii Al. I. Cuza 55, 5-23.

Carrillo-Rosúa, J., Morales-Ruano, S., Esteban-Arispe, I., Fenoll Hach-Alí, P., 2009. Significance of phyllosilicate mineralogy and mineral chemistry in an epithermal environment. Insights from the Palai-Islica Au-Cu deposit (Almería, SE Spain). Clays and Clay Minerals 57-1, 1-24. https://doi.org/10.1346/CCMN.2009.0570101

Clark, R.N., King, T.V., Klejwa, M., Swayze, G.A., Vergo, N., 1990. High spectral resolution reflectance spectroscopy of minerals. Journal of Geophysical Research 95(B8), 12653-12680. https://doi.org/10.1029/JB095iB08p12653

Cooke, D.R. and Simmons, SF., 2000. Characteristics and genesis of epithermal gold deposits. Society of Economic Geologists, Reviews in Economic Geology 13(2), 221-244. https://doi.org/10.5382/Rev.13.06

Cuadros, J., Michalski, J.R., Dekov, V., Bishop, J.L., 2016. Octahedral chemistry of 2:1 clay minerals and hydroxyl band position in the near-infrared: Application to Mars. American Mineralogist 101(3), 554-563. https://doi.org/10.2138/am-2016-5366

Deer, W.A., Howie, R.A., Zussman, J., 1992. An introduction to the rock-forming minerals. Longman, London. https://doi.org/10.1180/DHZ

Deyell, C.L. and Dipple, G.M., 2005. Equilibrium mineral-fluid calculations and their application to the solid solution between alunite and natroalunite in the El Indio-Pascua belt of Chile and Argentina. Chemical Geology 215(1-4), 219-234. https://doi.org/10.1016/j.chemgeo.2004.06.039

Dubé, B., Dunning, G., Lauzière, K., 1995. Geology of the Hope Brook Mine, Newfoundland, Canada: A preserved Late Proterozoic high-sulfidation epithermal gold deposit and its implications for exploration. Economic Geology 93, 405-436. https://doi.org/10.2113/gsecongeo.93.4.405

Duke, E.F., 1994. Near infrared spectra of muscovite, Tschermak substitution, and metamorphic reaction progress: Implications for remote sensing. Geology 22(7), 621-624. https://doi.org/10.1130/0091-7613(1994)022<0621:NISOMT>2.3.CO;2

Etoh, J., Izawa, E., Watanabe, K., Taguchi, S., Sekine, R., 2002. Bladed Quartz and its Relationship to Gold Mineralization in the Hishikari Low-Sulfidation Epithermal Gold Deposit, Japan. Economic Geology 97(8), 1841-1851. https://doi.org/10.2113/gsecongeo.97.8.1841

Farmer, V.C., 1974. The Infrared Spectra of Minerals. Mineralogical Society Monograph 4, Mineralogical Society of Great Britain and Ireland, 527 pp. https://doi.org/10.1180/mono-4

Farmer, V.C., 1998. Differing effects of particle size and shape in the infrared and Raman spectra of kaolinite. Clay Minerals 33(4), 601-604. https://doi.org/10.1180/claymin.1998.033.4.07

Ferrier, G., Ganas, A., Pope, R., Miles, A.J., 2019. Prospectivity Mapping for epithermal deposits of Western Milos using a fuzzy multi criteria evaluation approach parameterized by airborne hyperspectral remote sensing data. Geosciences 9(3), 116. https://doi.org/10.3390/geosciences9030116

Foster, M.D., 1962. Interpretation of the composition and a classification of the chlorites. U.S. Geological Survey Professional Paper 414, 1-33.

Frimmel, H.E., 2008. Earth's continental crustal gold endowment. Earth and Planetary Science Letters 267(1), 45-55. https://doi.org/10.1016/j.epsl.2007.11.022

Frost, R.L., 1995. Fourier transform Raman spectroscopy of kaolinite, dickite, and halloysite. Clays and Clay Minerals 43(2), 191-195. https://doi.org/10.1016/0584-8539(93)80088-R

Frost, R.L., 1997. The structure of the kaolinite minerals - a FT-Raman study. Clay Minerals 32(1), 65-77. https://doi.org/10.1180/claymin.1997.032.1.08

Frost, R.L. and Kloprogge, J.T., 2000. Raman spectroscopy of nontronites. Applied Spectroscopy 54(3), 402-405. https://doi.org/10.1366/0003702001949483

Frost, R.L. and Rintoul, L., 1996. Lattice vibrations of montmorillonite: an FT Raman and X-ray diffraction study. Applied Clay Science 11(2-4), 171-183. https://doi.org/10.1016/S0169-1317(96)00017-8

Frost, R.L. and Shurvell, H.F., 1997. Raman microprobe spectroscopy of halloysite. Clays and Clay Minerals 45(1), 68-72. https://doi.org/10.1346/CCMN.1997.0450107

Frost, R.L. and Van Der Gaast, S.J., 1997. Kaolinite hydroxyls - a Raman microscopy study. Clay Minerals 32(3), 471-484. https://doi.org/10.1180/claymin.1997.032.3.09

Frost, R.L., Wills, R.A., Weier, M.L., Martens, W., Kloprogge, J.T., 2006. A Raman spectroscopic study of alunites. Journal of Molecular Structure 785, 123-132. https://doi.org/10.1016/j.molstruc.2005.10.003

Frost, R.L., Bahfenne, S., Čejka, J., Sejkora, J., Plášil, J., Palmer, S.J., 2010. Raman and infrared study of phyllosilicates containing heavy metals (Sb, Bi): bismutoferrite and chapmanite. Journal of Raman Spectroscopy 41(7), 814-819. https://doi.org/10.1002/jrs.2512

Gaillard, N., Williams-Jones, A.E., Clark, J.R., Lypaczewski, P., Salvi, S., Perrouty, S., Piette-Lauzière, N., Guilmette, C., Linnen, R.L., 2018. Mica composition as a vector to gold mineralization: Deciphering hydrothermal and metamorphic effects in the Malartic district, Quebec. Ore Geology Reviews 95, 789-820. https://doi.org/10.1016/j.oregeorev.2018.02.009

Gates, W., Kloprogge, J.T., Madejova, J., Bergaya, F., 2017. Infrared and Raman spectroscopies of clay minerals. Elsevier, 620 pp.

Gillet, Ph., Barrat, J.A., Deloule, E. Wadhwa, M., Jambon, A., Sautter, V., Devouard, B., Neuville, D., Benzerara, K., Lesourd, M., 2002. Aqueous alteration in the Northwest Africa 817 (NWA 817) Martian meteorite. Earth and Planetary Science Letters 203(1), 431-444. https://doi.org/10.1016/S0012-821X(02)00835-X

Graham, G.E., Kokaly, F., Kelley, K.D., Hoefen, T.M., Johnson, M.R., Hubbard, B.E., 2018. Application of imaging spectroscopy for mineral exploration in Alaska: A study over Porphyry Cu Deposits in the Eastern Alaska Range. Economic Geology 113(2), 489-510. https://doi.org/10.5382/econgeo.2018.4559

Hedenquist, J.W., 1987. Mineralization associated with volcanic-related hydrothermal systems in the Circum-Pacific basin. Transactions of the Fourth Circum-Pacific Conference on Energy and Mineral Resources Conference, Singapore, American Association of Petroleum Geologists, 513-524.

Hedenquist, J.W., Izawa, E., Arribas, A., White, N.C., 1996. Epithermal gold deposits: styles, characteristics, and exploration. Resource Geology Special Publication Number 1, 18 pp.

Hedenquist, J.W., Arribas, A., and Gonzalez-Urien, E., 2000. Exploration for epithermal gold deposits. Economic Geology Reviews 13, 245-277. https://doi.org/10.5382/Rev.13.07

Herrmann, W., Blake, M., Doyle, M., Huston, D., Kamprad, J., Merry, N., Pontual, S., 2001. Short wavelength infrared (SWIR) spectral analysis of hydrothermal alteration zones associated with base metal sulfide deposits at Rosebery and Western Tharsis, Tasmania, and Highway-Reward, Queensland. Economic Geology 96(5), 939-955. https://doi.org/10.2113/gsecongeo.96.5.939

Hochleitner, R., Tarcea, N., Simon, G., Kiefer, W., Popp, J., 2004. Micro-Raman spectroscopy: a valuable tool for the investigation of extraterrestrial material. Journal of Raman Spectroscopy 35(6), 515-518. https://doi.org/10.1002/jrs.1190

Inoue, A., Meunier, A., Beaufort, D., 2004. Illite-smectite mixed-layer minerals in felsic volcaniclastic rocks from drill cores, Kakkonda, Japan. Clays and Clay Minerals 52, 66-84. https://doi.org/10.1346/CCMN.2004.0520108

Inoue, A., Inoué, S., Utada, M., 2018. Application of chlorite thermometry to estimation of formation temperature and redox conditions. Clay Minerals 53(2), 143-158. https://doi.org/10.1180/clm.2018.10

Kerr, A., Rafuse, H., Sparkes, G., Hinchey, J., Sandeman, H., 2011. Visible/infrared spectroscopy (VIRS) as a research tool in economic geology: Background and pilot studies from Newfoundland and Labrador. In Current Research, Newfoundland and Labrador Department of Natural Resources, Geological Survey, Report 11-1, 145-166.

Kloprogge, J.T. and Frost, R.L., 1999. An infrared emission spectroscopic study of synthetic and natural pyrophyllite. Neues Jahrbuch fur Mineralogie, Monatshefte 2, 62-74.

Košařová, V., Hradil, D., Němec, I., Bezdička, P., Kanickýa, V., 2013. Microanalysis of clay-based pigments in painted artworks by the means of Raman spectroscopy. Journal of Raman Spectroscopy 44(11), 1570-1577. https://doi.org/10.1002/jrs.4381

Lantenois, S., Beny, J.M., Muller, F., Champallier, R., 2007. Integration of Fe in natural and synthetic Al-pyrophyllites: an infrared spectroscopic study. Clay Minerals 42(1), 129-141. https://doi.org/10.1180/claymin.2007.042.1.09

Lerouge, C., Beny, C., Fléhoc, C., Guerrot, C., Hikov, A., Kunov, A., Yanev, Y., 2007. Constraints of stable isotopes, Raman spectrometry on the formation of the advanced argillic alteration of the Breznik epithermal Au occurrence in Bulgaria - impact of weathering. Proceedings of the ninth Biennial SGA Meeting, Dublin 2007, 885-888.

Li, H., Zhang, L., Christy, A.G., 2011. The correlation between Raman spectra and the mineral composition of muscovite and phengite. In: Ultrahigh-Pressure Metamorphism (Eds: Dobrzhinetskaya, L.F., Faryad, S.W., Wallis, S., Cuthbert, S.), Elsevier Publishing, 187-212. https://doi.org/10.1016/B978-0-12-385144-4.00006-0

Loh, E., 1973. Optical vibrations in sheet silicates. Journal of Physics C: Solid State Physics 6(6), 1091-1104. https://doi.org/10.1088/0022-3719/6/6/022

Maubec, N., Lahfid, A., Lerouge, C., Wille, G., Michel, K., 2012. Characterization of alunite supergroup minerals by Raman spectroscopy. Spectrochimica Acta Part A: Molecular and Biomolecular Spectroscopy 96, 925-939. https://doi.org/10.1016/j.saa.2012.07.094

Meunier, A., 2005. Clays. Springer, 472 pp. https://doi.org/10.1007/b138672

Millot, G., 1970. Geology of Clays. Springer, 430 pp. https://doi.org/10.1007/978-3-662-41609-9

Neal, L.C., Wilkinson, J.J., Mason, P.J., Chang, Z., 2018. Spectral characteristics of propylitic alteration minerals as a vectoring tool for porphyry copper deposits. Journal of Geochemical Exploration 184(A), 179-198. http://dx.doi.org/10.1016/j.gexplo.2017.10.019

O’Brien, S.J., O’Brien, B.H., Dunning, G.R., and Tucker, R.D., 1996. Late Neoproterozoic Avalonian and related peri-Gondwanan rocks of the Newfoundland Appalachians. In Nance, R. D., and Thompson, M. D., eds.: Avalonian and Related Peri-Gondwanan Terranes of the Circum-North Atlantic: Boulder, Colorado. Geological Society of America Special Paper 304, 9-28. https://doi.org/10.1130/0-8137-2304-3.9

O’Brien, S.J., Dubé, B., O’Driscoll, C.F., and Mills, J., 1998. Geological setting of gold mineralization and related hydrothermal alteration in Late Neoproterozoic (Post -640 Ma) Avalonian rocs of Newfoundland, with a review of the coeval gold deposits elsewhere in the Appalachian Avalonian Belt. In Current Research. Newfoundland Department of Mines and Energy, Geological Survey, Report 98-1, 93-124.

O’Brien, S.J., Dubé, B., and O’Driscoll, C.F., 1999. High-sulphidation, epithermal-style hydrothermal systems in Late Neoproterozoic Avalonian rocks on the Burin Peninsula, Newfoundland: Implications for gold exploration. In Current Research. Newfoundland Department of Mines and Energy, Geological Survey, Report 99-1, 275-296.

Omori, K., 1968. Infrared diffraction and the far infrared spectra of anhydrous sulfates. Mineralogical Journal 5(5), 334-354. https://doi.org/10.2465/minerj1953.5.334

Pouchou, J.L. and Pichoir, F., 1984. A new model for quantitative analyses. I. Application to the analysis of homogeneous samples. La Recherche Aérospatiale, 3, 13-38.

Pouchou, J.L. and Pichoir, F., 1985. ‘‘PAP’’ correction procedure for improved quantitative microanalysis. Pp. 104-106 In: Microbeam Analysis (J.T. Armstrong, editor). San Francisco Press, San Francisco, California, USA.

Prieto, A.C., Dubessy, J., Cathelineau, M., 1991. Structure-composition relationships in trioctahedral chlorites: A vibrational spectroscopy study. Clays and Clay Minerals 39(5), 531-539. https://doi.org/10.1346/CCMN.1991.0390508

Rosenberg, P.E. and Cliff, G., 1980. The formation of pyrophyllite solid solutions. American Mineralogist 65, 1214-1219.

Rudolph, W.W. and Mason, R., 2001. Study of aqueous $Al_2(SO_4)_3$ solution under hydrothermal conditions: Sulfate ion pairing, hydrolysis, and formation of hydronium alunite. Journal of Solution Chemistry 30, 527-548. https://doi.org/10.1023/A:1010334818580

Saikia, B.J., Parthasarathy, G., Borah, R.R., Borthakur, R., 2016. Raman and FTIR spectroscopic evaluation of clay minerals and estimation of metal contaminations in natural deposition of surface sediments from Brahmaputra River. International Journal of Geosciences 7, 873-883. http://dx.doi.org/10.4236/ijg.2016.77064

Sillitoe, R.H., 2010. Porphyry Copper Systems. Economic Geology 105(1), 3-41. https://doi.org/10.2113/gsecongeo.105.1.3

Simmons, S.F., White, N.C., and John, D.A., 2005. Geological characteristics of epithermal precious and base metal deposits. Economic Geology 100th Anniversary Volume, 485-522. https://doi.org/10.5382/AV100.16

Simpson, M.P. and Mauk, J.L., 2011. Hydrothermal alteration and veins at the epithermal Au-Ag deposits and prospects of the Waitekauri area, Hauraki Goldfield, New Zealand. Economic Geology 106(6), 945-973. https://doi.org/10.2113/econgeo.106.6.945

Sparkes, G.W. and Dunning, G.R., 2014. Late Neoproterozoic epithermal alteration and mineralization in the western Avalon zone: A summary of mineralogical investigations and new U/Pb geochronological results. In Current Research, Newfoundland and Labrador Department of Natural Resources, Geological Survey, Report 14-1, 99-128.

Stoffregen, R.E., Alpers, C.N., Jambor, J.L., 2000. Alunite-jarosite crystallography, thermodynamics, and geochronology. Reviews in Mineralogy and Geochemistry 40(1), 453-479. https://doi.org/10.2138/rmg.2000.40.9

Tappert, M.C., Rivard, B., Giles, D., Tappert, R., Mauger, A., 2013. The mineral chemistry, near-infrared, and mid-infrared reflectance spectroscopy of phengite from the Olympic Dam IOCG deposit, South Australia. Ore Geology Reviews 53, 26-38. https://doi.org/10.1016/j.oregeorev.2012.12.006

Thompson, A.J.B., Hauff, P.L., Robitaille, A.J., 1999. Alteration mapping in exploration: Application of Short-Wave Infrared (SWIR) Spectroscopy. Society of Economic Geologists Newsletter 39, 15-27.

Thompson, A., Scott, K., Huntington, J., Yang, K., 2009. Mapping mineralogy with reflectance spectroscopy: examples from volcanogenic massive sulfide deposits. In: Remote Sensing and Spectral Geology (Eds: R. Bedell, A. P. Crósta, E. Grunsky). Reviews in Economic Geology 16, 1-16. https://doi.org/10.5382/Rev.16.04

Tillick, D.A., Peacor, D.R., Mauk, J.L., 2001. Genesis of dioctahedral phyllosilicates during hydrothermal alteration of volcanic rocks: I. The Golden Cross epithermal ore deposit, New Zealand. Clays and Clay Minerals 49-2, 126-140. https://doi.org/10.1346/CCMN.2001.0490203

Tlili, A., Smith, D.C., Beny, J.M., Boyer, H., 1989. A Raman microprobe study of natural micas. Mineralogical Magazine 53(370), 165-179. https://doi.org/10.1180/minmag.1989.053.370.04

Toumi, M. and Tlili, A., 2008. Rietveld refinement and vibrational spectroscopic study of alunite from el Gnater, central Tunisia. Russian Journal of Inorganic Chemistry 53, 1845-1853. https://doi.org/10.1134/S0036023608120048

Velde, B., 1992. Introduction to Clay Minerals. Springer, 198 pp. https://doi.org/10.1007/978-94-011-2368-6

Velde, B., 1995. Origin and Mineralogy of Clays. Springer, 335 pp. https://doi.org/10.1007/978-3-662-12648-6

Vidal, O., Parra, T., Trotet, F., 2001. A thermodynamic model for Fe-Mg aluminous chlorite using data from phase equilibrium experiments and natural pelitic assemblages in the 100° to 600°c, 1 to 25 kb range. American Journal of Science 301(6), 557-592. https://doi.org/10.2475/ajs.301.6.557

Wang, A., Kuebler, K., Jolliff, B., Haskin, L.A., 2004. Mineralogy of a Martial meteorite as determined by Raman spectroscopy. Journal of Raman Spectroscopy 35(6), 504-514. https://doi.org/10.1002/jrs.1175

Wang, A., Freeman, J.J., Jolliff, B.L., Chou, I.M., 2006. Sulfates on Mars: A systematic Raman spectroscopic study of hydration states of magnesium sulfates. Geochimica et Cosmochimica Acta 70(24), 6118-6135. https://doi.org/10.1016/j.gca.2006.05.022

Wang, A., Freeman, J.J., Jolliff, B.L., 2015. Understanding the Raman spectral features of phyllosilicates. Journal of Raman Spectroscopy 46, 829-845. https://doi.org/10.1002/jrs.4680

Wang, L., Zhang, M., Redfern, S.A.T., Zhang, Z., 2002. Dehydroxylation and transformations of the 2:1 phyllosilicate pyrophyllite at elevated temperatures: an infrared spectroscopic study. Clays and Clay Minerals 50(2), 272-283. https://doi.org/10.1346/000986002760832874

Wang, R., Cudahy, T., Laukamp, C., Walshe, J.L., Bath, A., Mei, Y., Young, C., Roache, T.J., Jenkins, A., Roberts, M., Barker, A., Laird, J., 2017. White mica as a hyperspectral tool in exploration for the Sunrise Dam and Kanowna Belle Gold deposits, Western Australia. Economic Geology 112(5), 1153-1176. https://doi.org/10.5382/econgeo.2017.4505

Wardle, R. and Brindley, G.W., 1972. The crystal structures of pyrophyllite, 1Tc, and of its dehydroxylate. American Mineralogist 57, 732-750.

White, W.B., 1974. Order-Disorder Effects. In: The Infrared Spectra of Minerals (Ed., V.C Farmer). Mineralogical Society Monograph, London, 87-110. https://doi.org/10.1180/mono-4.6

White, N.C. and Hedenquist, J.W., 1995. Epithermal gold deposits: styles, characteristics, and exploration. SEG Newsletter 23, 9-13.

Whitney, D.L. and Evans, B.W., 2010. Abbreviations for names of rock-forming minerals. American Mineralogist, 95, 185-187. https://doi.org/10.2138/am.2010.3371

Williams, H., 1979. Appalachian Orogen in Canada. Canadian Journal of Earth Sciences 16(3), 792-807. https://doi.org/10.1139/e79-070

Yan, Y., Tillick, D.A., Peacor, D.R., Simmons, S.F., 2001. Genesis of dioctahedral phyllosilicates during hydrothermal alteration of volcanic rocks: II. The Broadlands-Ohaaki hydrothermal system, New Zealand. Clays and Clay Minerals 49-2, 141-155. https://doi.org/10.1346/CCMN.2001.0490204

Zhai, S., Ito, E., Yoneda, A., 2008. Effects of pre-heated pyrophyllite gaskets on high-pressure generation in the Kawai-type multi-anvil experiments. High Pressure Research 28(3), 265-271. https://doi.org/10.1080/08957950802454050

Zhang, S., Chu, G., Cheng, J, Zhang, Y., Tian, J., Li, J., Sun, S., Wei, K., 2020. Short wavelength infrared (SWIR) spectroscopy of phyllosilicate minerals from the Tonglushan Cu-Au-Fe deposit, Eastern China: New exploration indicators for concealed skarn orebodies. Ore Geology Reviews 122, 103516. https://doi.org/10.1016/j.oregeorev.2020.103516

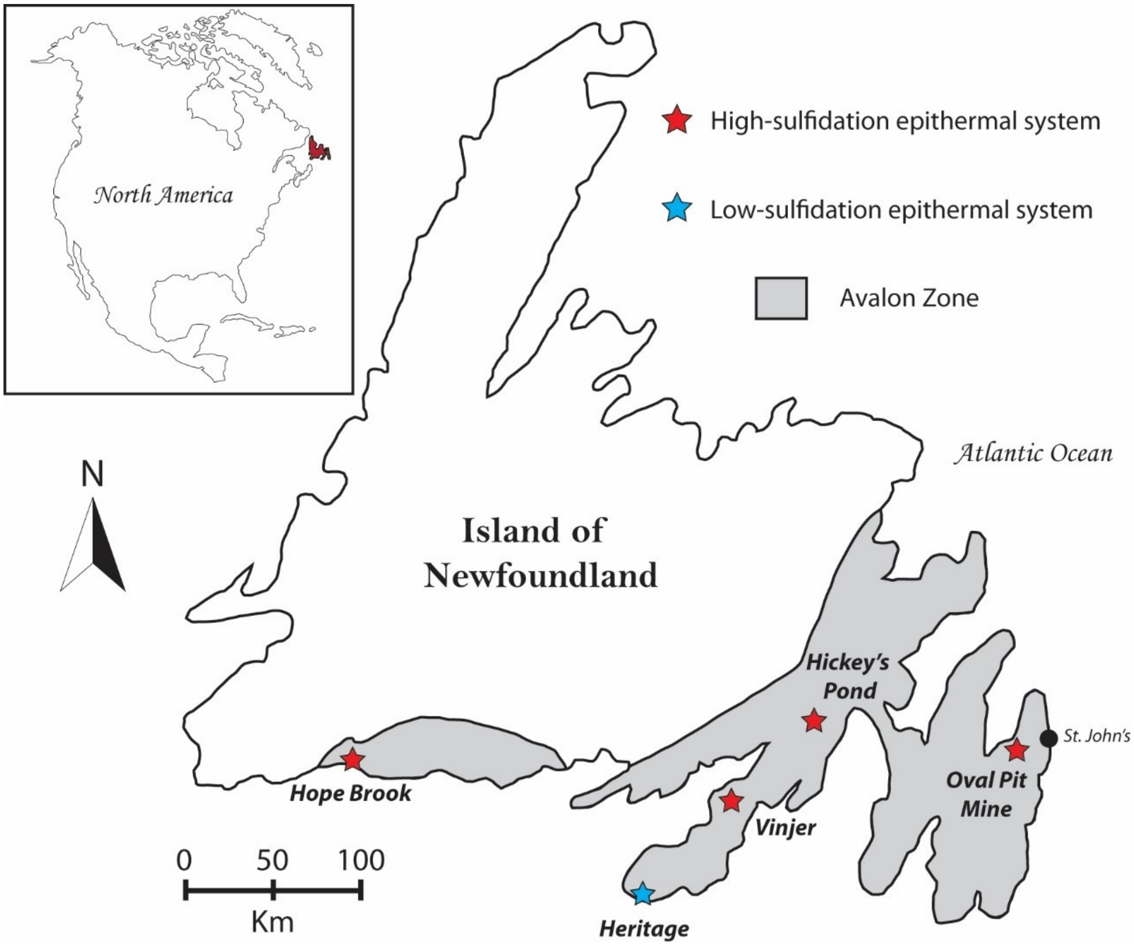

Figure 3.1. Location and geological setting of studied epithermal occurrences in Newfoundland (modified after Dubé et al., 1995).

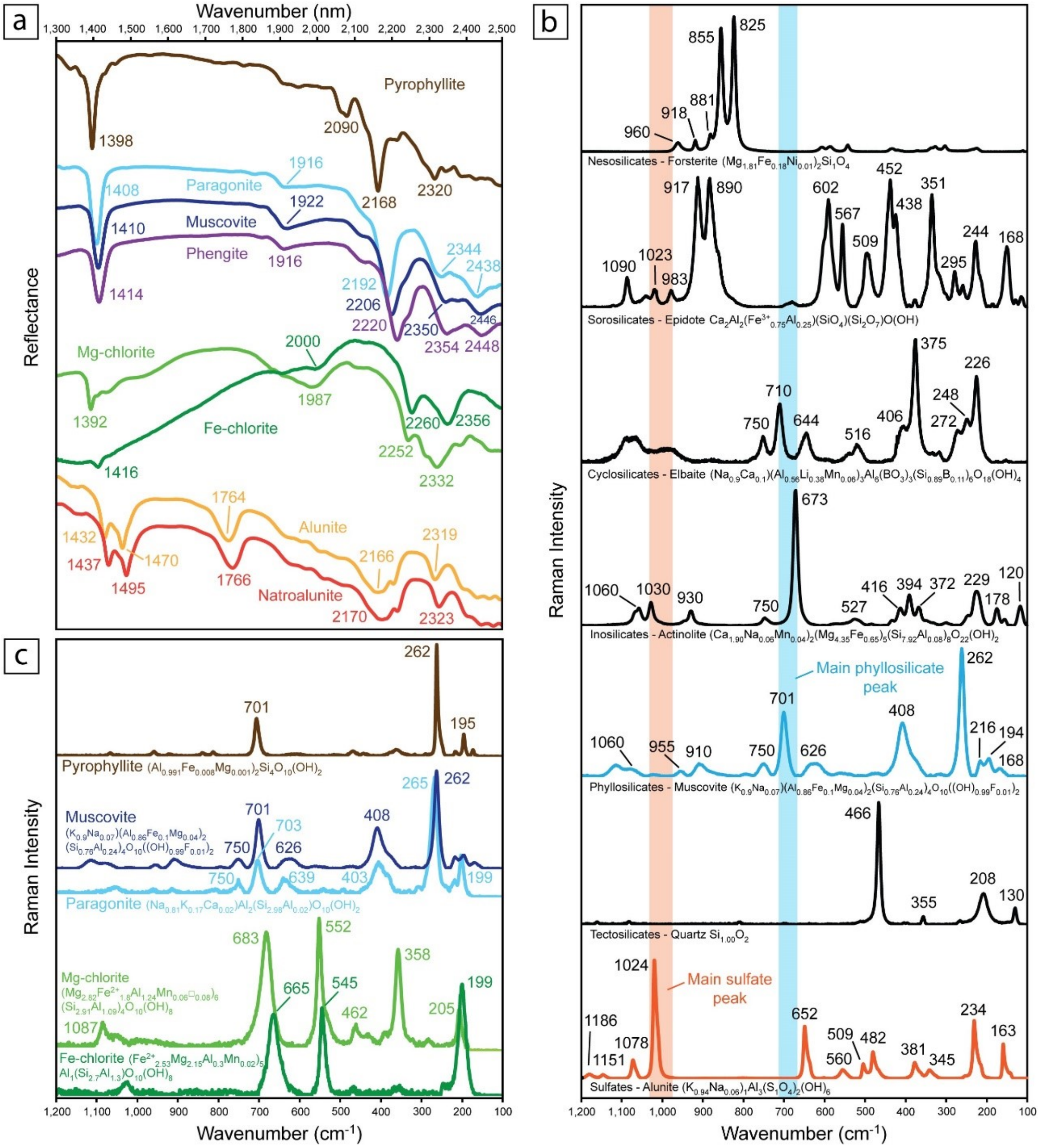

Figure 3.2. Reflectance and Raman spectra of various minerals. (a) Short-Wave Infrared spectra of the main group of minerals studied in this contribution: pyrophyllite, white mica, chlorite, and alunite. SWIR spectra of minerals are from The Spectral Geologist (TSG™) database. (b) Raman spectra of minerals belonging to the different silicate groups and the sulfate group. Raman spectra of minerals are from the RRUFF database: forsterite (nesosilicate) from Sapat, Pakistan (RRUFF ID: R050117); epidote (sorosilicate) from the Calumet mine, Colorado, USA (RRUFF ID: R050131); elbaite (cyclosilicate) from Cruziero mine, Minas Gerais, Brazil (RRUFF ID: R050119); actinolite (inosilicate) from Harford County, Maryland, USA (RRUFF ID: R040063); muscovite (phyllosilicate) from Garnet Hill, Pennsylvania, USA (RRUFF ID: R040124); quartz (tectosilicate) from Piedras Parada, Veracruz, Mexico (RRUFF ID: R060604); alunite (sulfate) from El Indio Gold mine, Chile (RRUFF ID: R060430). (c) Raman spectra of the phyllosilicate minerals considered in this study. Raman spectra of minerals are from the RRUFF database: pyrophyllite from Cottonstone Mountain, North Carolina, USA (RRUFF ID: R050051); muscovite from Garnet Hill, Pennsylvania, USA (RRUFF ID: R040124); paragonite from Switzerland (RRUFF ID: R050447); clinochlore from the Callaghan Creek (RRUFF ID: R061080); chamosite from Slesse Creek (RRUFF ID: R060188).

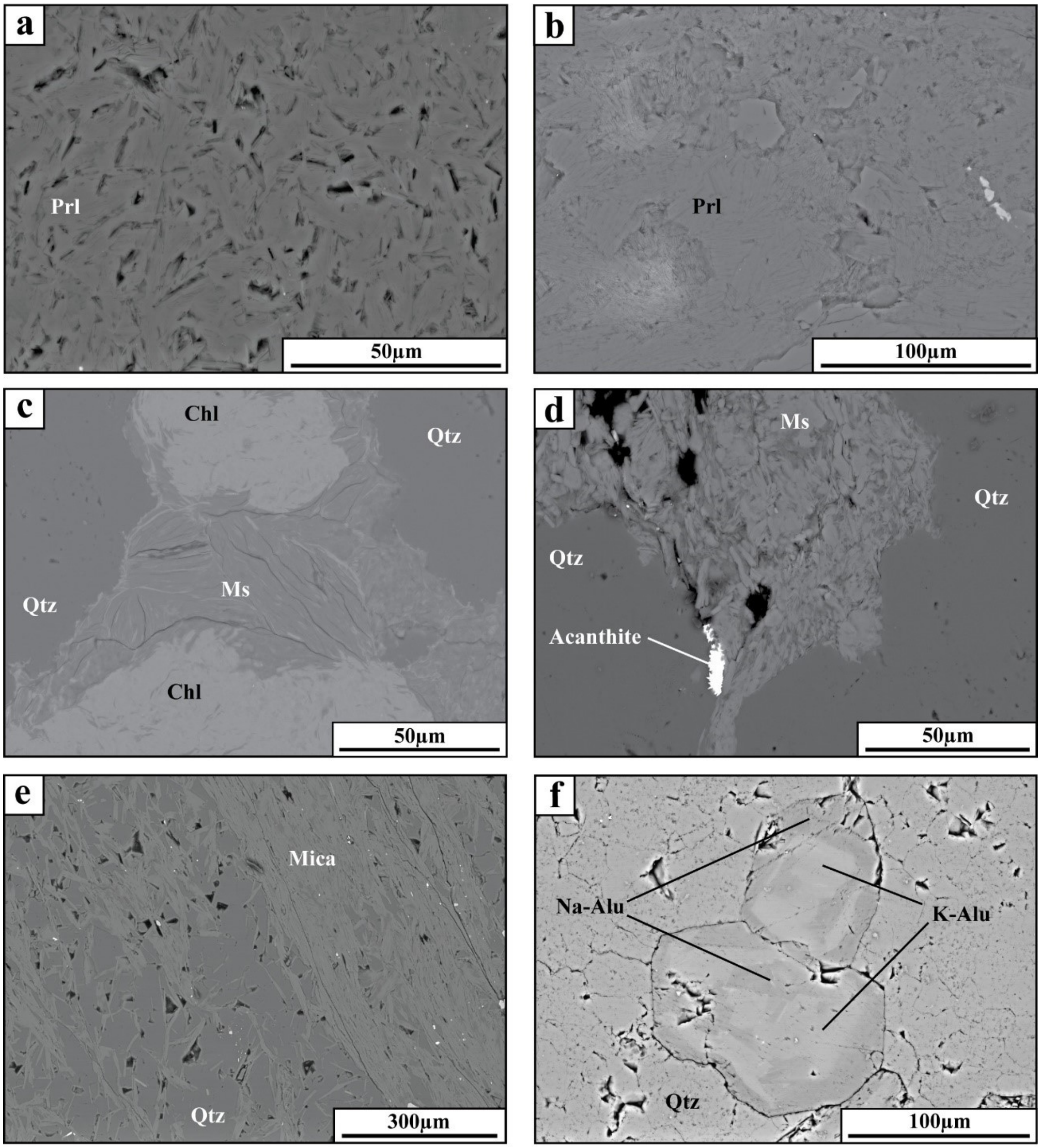

Figure 3.3. Backscattered electron (BSE) photomicrographs of selected hydrothermally altered samples from the studied epithermal occurrences. (a) Oval Pit Mine. Massive pyrophyllite aggregates. (b) Vinjer. Coarse pyrophyllite crystals. (c) Heritage. Overgrowth and intercalation relationship between mica and chlorite in phyllic altered rocks. (d) Heritage. Typical pocket of muscovite alteration in a quartz-rich hydrothermal vein. Sulfide mineralization in the form of acanthite (Ag_2S) in close spatial relationship with muscovite. (e) Hope Brook. Zoned white mica crystals with cores of paragonite and rims of muscovite. (f) Hickey's Pond. Zoned alunite crystals with K-rich cores (alunite) and Na-rich rims (natroalunite) in pervasively silicified host rocks. Abbreviations: Qtz = quartz; Chl = chlorite; Ms = muscovite; Pg = paragonite; Alu = alunite; Cal = calcite; Py = pyrite; Gn = galena; Kln = kaolinite; Prl = pyrophyllite.

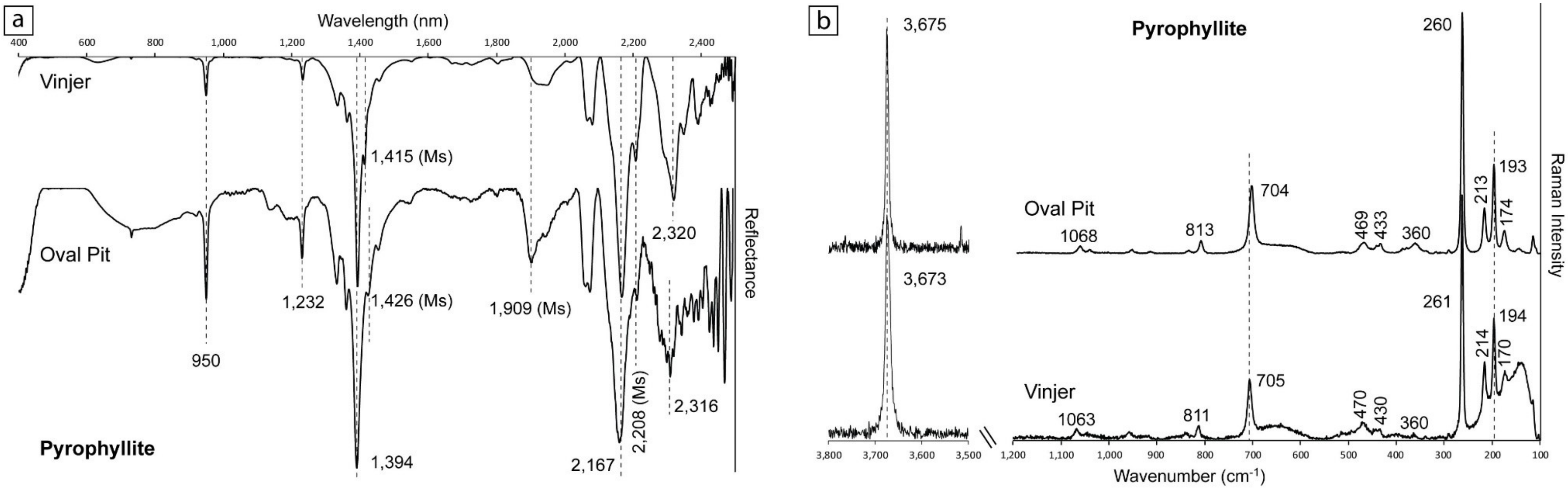

Figure 3.4. Short-Wave Infrared (SWIR) and Raman spectra of pyrophyllite samples. (a) SWIR reflectance spectra of pyrophyllite from the Vinjer high-sulfidation epithermal occurrence (Sample VP-1) and the Oval Pit pyrophyllite mine (Sample MANUELS). Dashed lines indicate characteristic peak positions of pyrophyllite. (b) Raman spectra of pyrophyllite from the Vinjer (Sample VP-1) and the Oval Pit (Sample MANUELS) high-sulfidation epithermal occurrences in the H_2O/OH spectral range (3,500-3,800 cm^{-1}) and the spectral range of the fundamental vibrations of silicates (100-1,200 cm^{-1}). Dashed lines indicate characteristic peak positions of pyrophyllite.

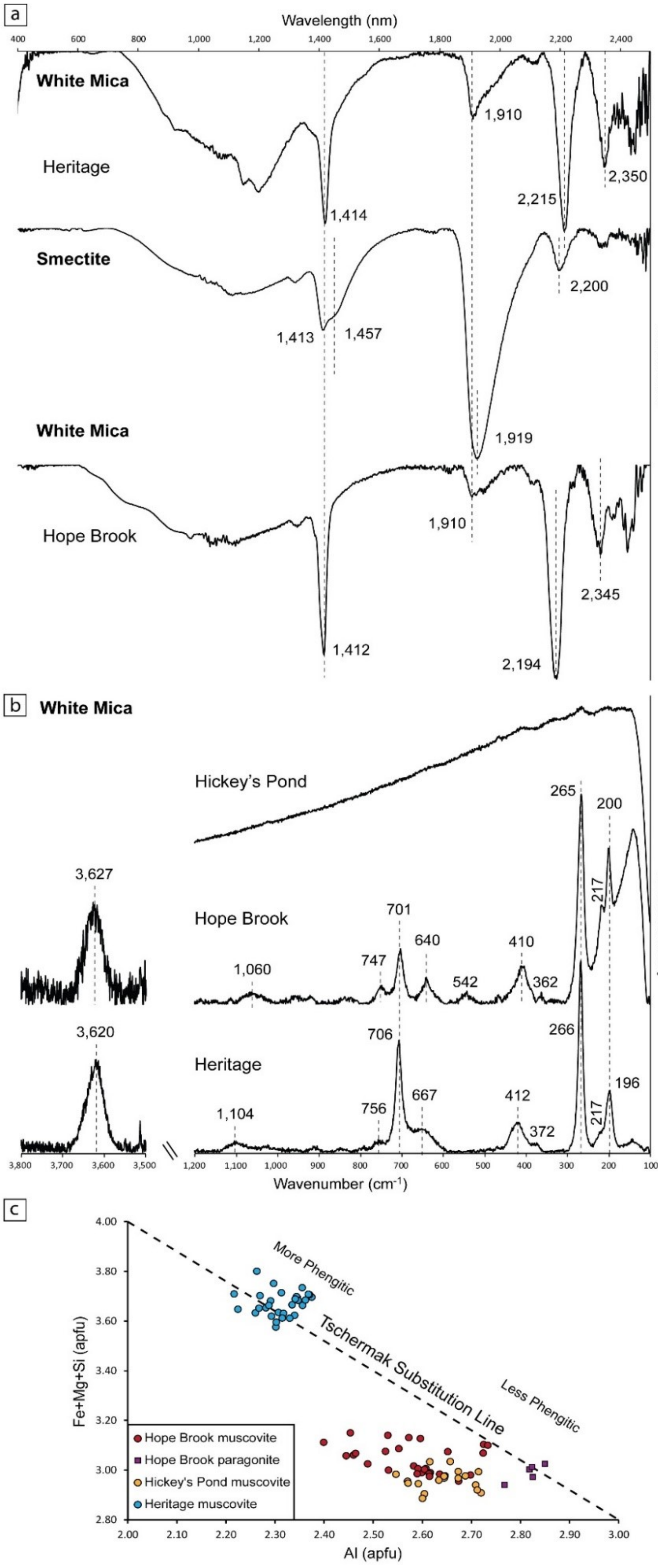

Figure 3.5. Short-Wave Infrared (SWIR) and Raman spectra of white mica samples. (a) SWIR reflectance spectra of phengite (Sample HE48-27) and smectite (Sample HE-24-1R) from the Heritage low-sulfidation epithermal prospect and paragonite (Sample HB-4) from the Hope Brook high-sulfidation epithermal mine. Dashed lines indicate characteristic peak positions of white mica. (b) Raman spectra of muscovite/paragonite from Hope Brook (Sample HB-6) and Heritage (Sample HE36-107) in the H_2O/OH spectral range (3,500-3,800 cm^{-1}) and the spectral range of the fundamental vibrations of silicates (100-1,200 cm^{-1}). Dashed lines indicate characteristic peak positions of white mica. Raman spectra of white mica from Hickey's Pond were not quantifiable due to high fluorescence consequent to the presence of hematite. (c) Al vs. Fe+Mg+Si (a.p.f.u.) binary diagram expressing the various degrees of Tschermak substitution of the different mica varieties (modified after Arbiol et al., 2021).

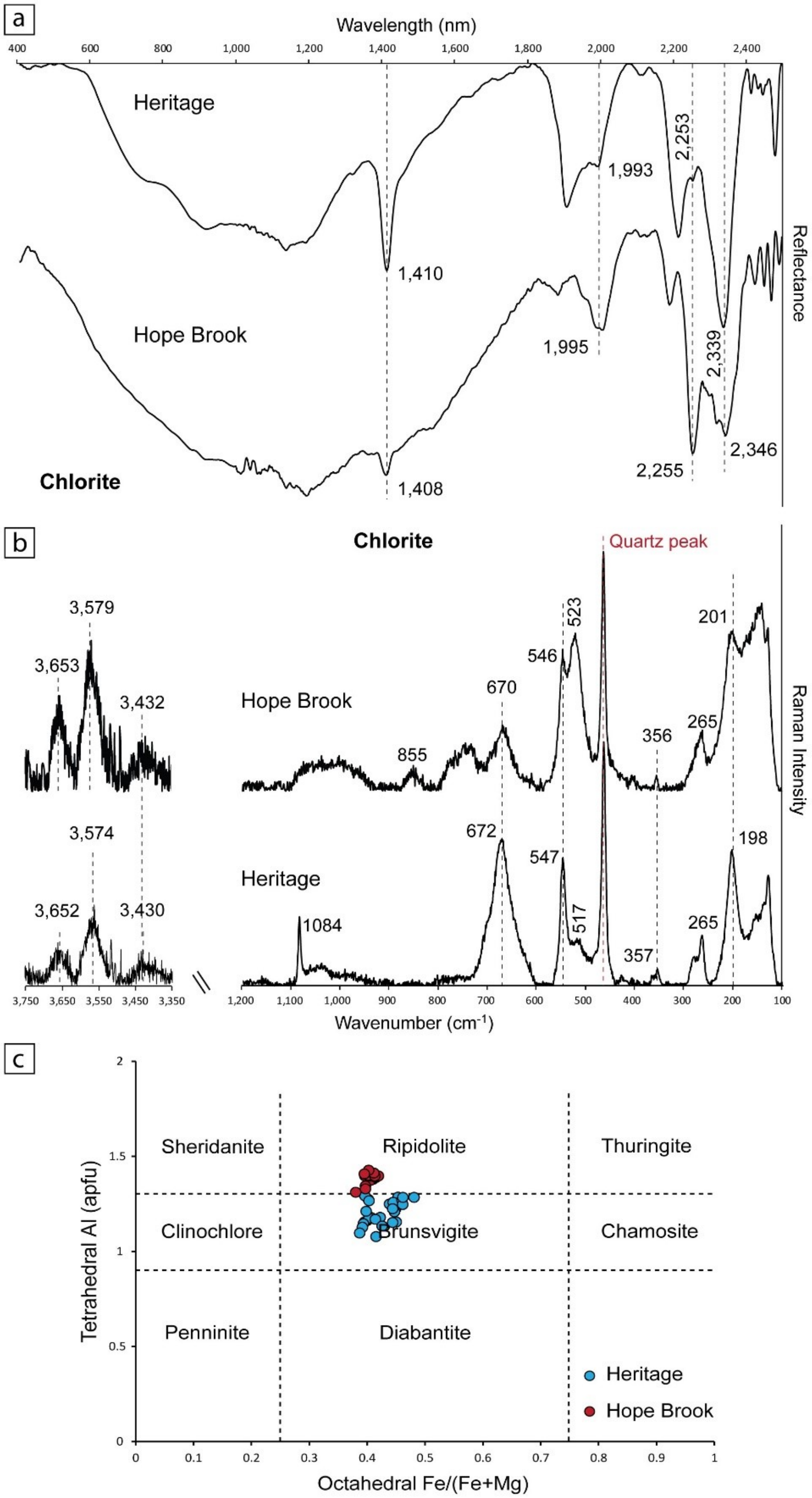

Figure 3.6. Short-Wave Infrared (SWIR) and Raman spectra of chlorite samples. (a) SWIR reflectance spectra of chlorite from the Heritage low-sulfidation epithermal prospect (Sample HE-05-03) and the Hope Brook high-sulfidation epithermal deposit (Sample HB-14). Dashed lines indicate characteristic peak positions of chlorite. (b) Raman spectra of chlorite from Hope Brook (Sample HB-14) and Heritage (Sample HE36-107) in the H_2O/OH spectral range (3,350-3,750 cm^{-1}) and the spectral range of the fundamental vibrations of silicates (100-1,200 cm^{-1}). Dashed lines indicate characteristic peak positions of chlorite. (c) Octahedral Fe/(Fe+Mg) vs. tetrahedral Al binary diagram with the different varieties of Fe-Mg chlorite (modified after Arbiol et al., 2021; chlorite classification after Foster, 1962; clinochlore-chamosite boundary after Bailey, 1980b).

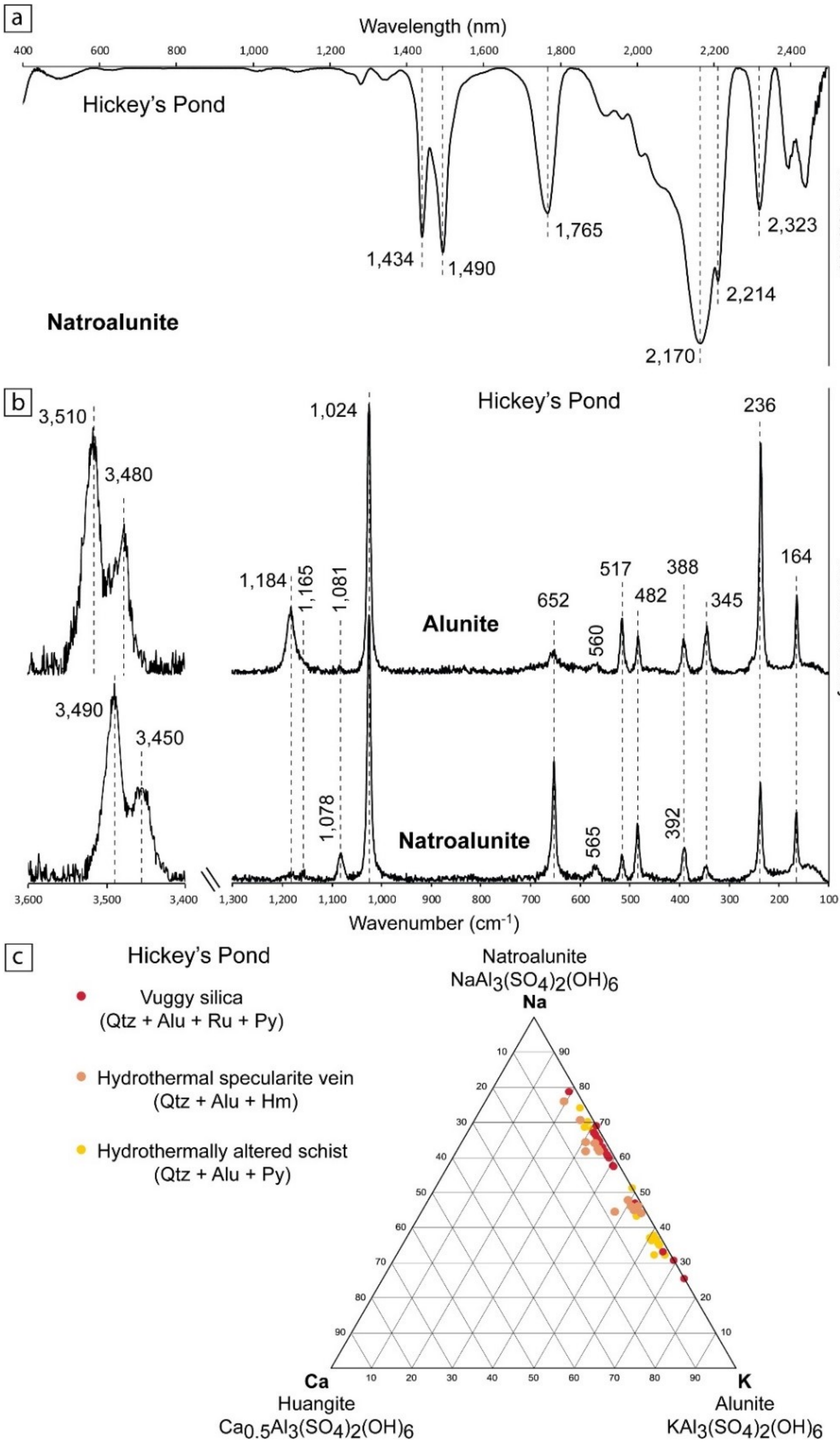

Figure 3.7. Short-Wave Infrared (SWIR) and Raman spectra of alunite group samples. (a) SWIR reflectance spectra of natroalunite from the Hickey's Pond high-sulfidation epithermal system (Sample HP-4B). Dashed lines indicate characteristic peak positions of natroalunite. (b) Raman spectra of alunite (Sample HP-4B) and natroalunite (Sample HP-6) from Hickey's Pond in the H_2O/OH spectral range (3,400-3,600 cm^{-1}) and the spectral range of the fundamental vibrations of silicates (100-1,300 cm^{-1}). Dashed lines indicate characteristic peak positions of alunite and natroalunite. (c) Na-K-Ca triangular plot discerning the type of alunite occurring at the Hickey's Pond high-sulfidation prospect.

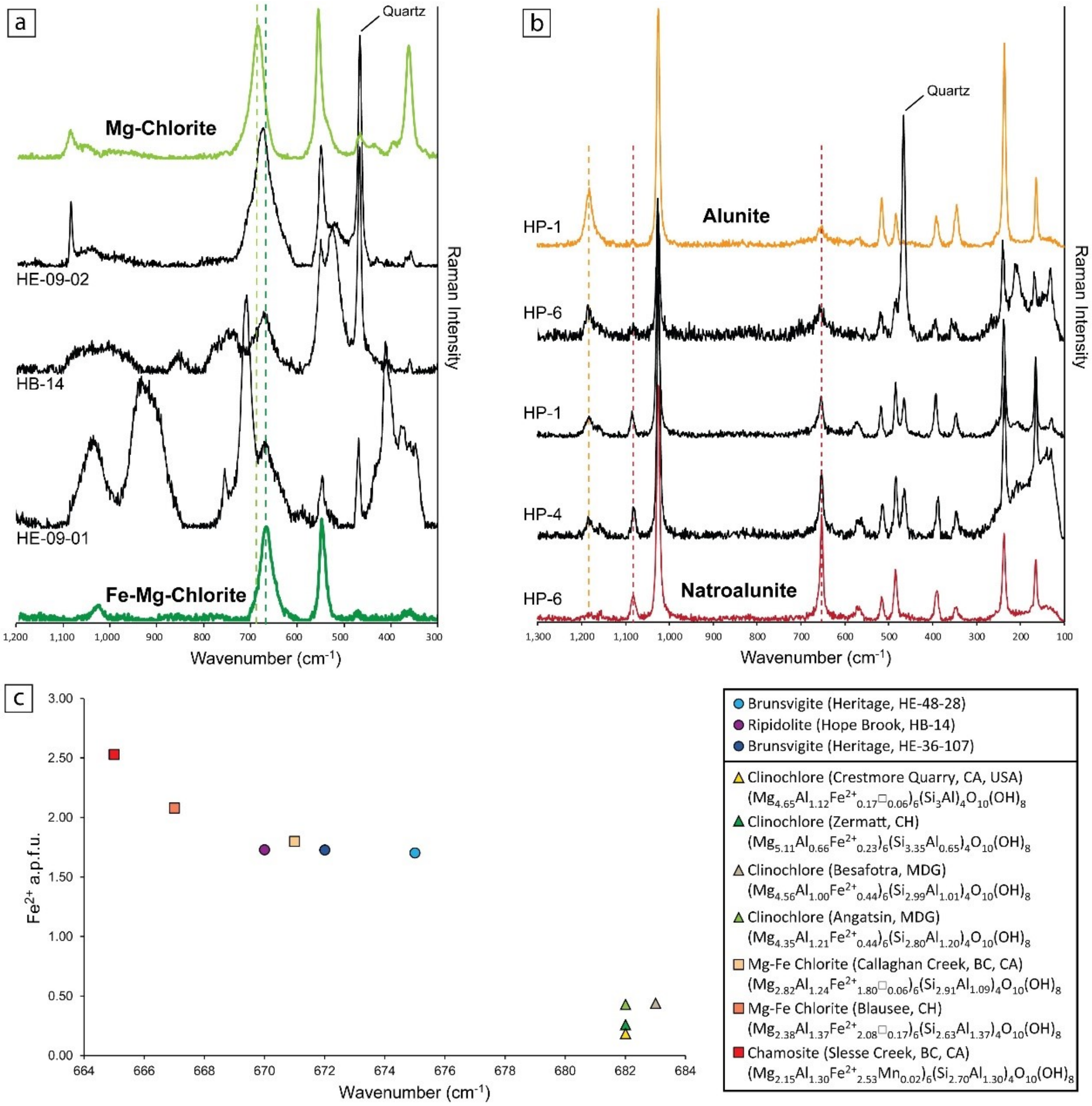

Figure 3.8. (a) Raman spectra of chlorite from various samples from the Hope Brook and Heritage epithermal occurrences. Raman spectra of Mg-chlorite (light green line trace) and Mg-Fe-chlorite (dark green line trace) are from the RRUFF database. (b) Raman spectra of alunite from various samples from the Hickey's Pond high-sulfidation epithermal prospect showing the variability in spectral features between alunite and natroalunite end-member spectra. (c) Binary plot of the Raman shift (cm-1) of the main chlorite Si-O-Si Raman band against Fe^{2+} content (in a.p.f.u.) of chlorite from Hope Brook and Heritage epithermal systems (this study). Data for clinochlore from the Crestmore Quarry (RRUFF ID: R060725), clinochlore from the Callaghan Creek (RRUFF ID: R061080), and chamosite from Slesse Creek (RRUFF ID: R060188) are taken from the RRUFF database. Data for clinochlore from Zermatt, Besafotra, Angatsin, and Mg-Fe chlorite from Blausee are from Prieto et al., 1991.

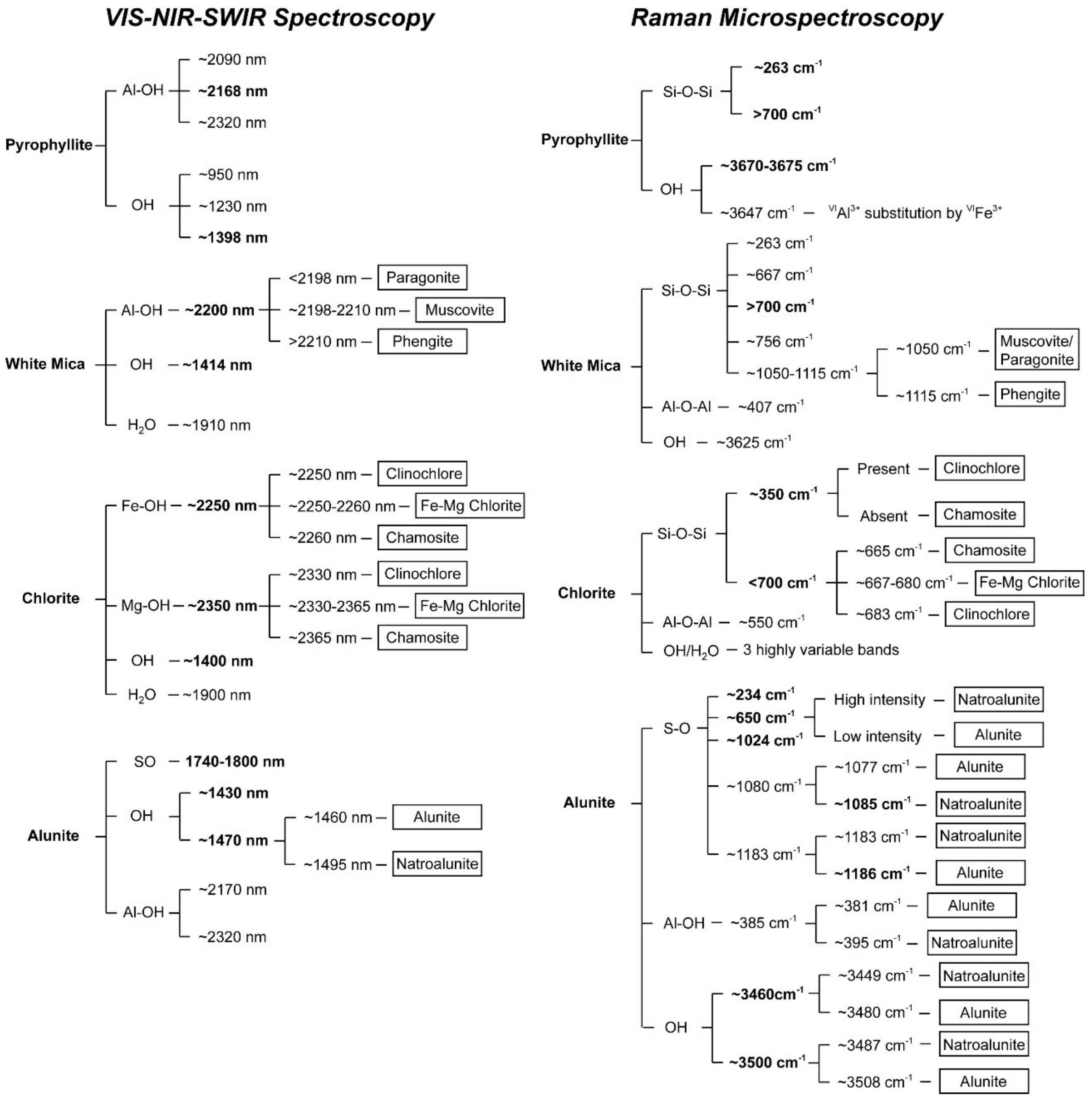

Figure 3.9. Mineral identification chart for pyrophyllite, white mica, chlorite, and alunite based on their main Vis-NIR-SWIR and Raman spectral features. High-intensity spectral features and/or those that provide chemical information and distinction of chemical varieties are marked in bold.

Table 3.1: List of samples analyzed from epithermal deposits/prospects in Newfoundland. Deposit type, short description, mineralogy, and investigated alteration phases by the various analytical methods applied are reported for each sample. *Abbreviations:* Qtz = quartz; Cal = calcite; Kfs = K-feldspar; Pl = plagioclase; Alu= alunite; Hem = hematite; Py = pyrite; Mca = mica-group mineral; Chl = chlorite; Kln = kaolinite group mineral; Prl = pyrophyllite; Sme = smectite; Sp = sphalerite; Rt = rutile. Mineral abbreviations after Whitney and Evans (2010).

Sample	Deposit / Prospect	Description	Mineralogy	SWIR Spectroscopy	Raman	EPMA
High-sulfidation epithermal systems						
HB-1	Hope Brook	Quartz-sericite-chlorite schist	Qtz, mca, pl, chl	Mca	Mca	-
HB-4	Hope Brook	Quartz-sericite schist	Qtz, mca, chl, rt	Mca	Mca	Mca
HB-5	Hope Brook	Quartz-sericite schist	Qtz, mca, py	Mca	Mca	-
HB-6	Hope Brook	Quartz-sericite schist	Qtz, mca, chl, py	Mca	Mca	-
HB-7	Hope Brook	Silicified breccia	Qtz, mca, py, kln	Mca	Mca	-
HB-8	Hope Brook	Vuggy silica zone	Qtz, py, mca, rt	Mca	Mca	-
HB-10	Hope Brook	Vuggy silica zone	Qtz, mca, py, kln	Mca	Mca	-
HB-11	Hope Brook	Massive silica zone	Qtz, mca, rt	Mca	-	-
HB-12	Hope Brook	Silicified breccia	Qtz, py, mca, rt	Mca	-	-
HB-13	Hope Brook	Quartz-sericite-chlorite schist	Qtz, mca, py, rt	Mca	Mca	-
HB-14	Hope Brook	Quartz-sericite-chlorite schist	Chl, qtz, mca, rt	Chl+Mca	Chl	Chl+Mca
HP-1	Hickey's Pond	Quartz-alunite schist	Qtz, alu, mca	Alu	Alu	-
HP-2	Hickey's Pond	Quartz-hematite-alunite schist	Qtz, mca, hem	-	-	Mca
HP-3	Hickey's Pond	Vuggy silica zone	Qtz, py, mca, alu	Alu	-	Alu
HP-4B	Hickey's Pond	Quartz-hematite vein	Qtz, alu, mca, hem	Alu	Alu	Alu
HP-5	Hickey's Pond	Quartz-alunite-pyrite schist	Qtz, alu, mca	Alu	Alu	-
HP-6	Hickey's Pond	Quartz-alunite-hematite vein	Qtz, alu, mca, rt	Alu	Alu	Alu
HP-7	Hickey's Pond	Hematite-rich breccia	Qtz, alu, mca, rt	Alu	Alu	-
VP-1	Vinjer	Quartz-pyrophyllite schist	Qtz, prl, rt	Prl+Mca	Prl	Prl
Manuels	Oval Pit Mine	Massive pyrophyllite	Prl, mca, qtz	Prl	Prl	Prl
Low-sulfidation epithermal systems						
HE36-107	Heritage	Chlorite-oxide-silica breccia	Qtz, cal, mca, chl	Mca+Chl	Mca+Chl	Mca+Chl
HE47-23	Heritage	Silicified hydrothermal vein/breccia	Qtz, mca, py, kfs	Mca+Chl	-	-
HE47-26	Heritage	Silicified hydrothermal vein	Qtz, cal, chl, mca	Mca	Mca	Mca+Chl
HE48-27	Heritage	Silicified hydrothermal vein	Qtz, mca, cal, py	Mca	Mca	Mca+Chl
HE48-28	Heritage	Silicified hydrothermal vein/breccia	Qtz, mca, chl, py	Mca+Chl	Mca+Chl	Mca+Chl
HE-05-03	Heritage	Quartz-carbonate vein/breccia	Qtz, cal, kfs, mca, chl	Mca+Chl	Mca	-
HE-08-01	Heritage	Quartz-chlorite vein/breccia	Qtz, mca, chl	Mca+Chl	Mca+Chl	-
HE-08-02	Heritage	Quartz-carbonate-chlorite vein	Qtz, mca, chl	Chl+Sme	Mca+Chl	-
HE-08-03	Heritage	Quartz-chlorite vein/breccia	Qtz, mca, kfs, py, chl	Mca+Chl	Mca	-
HE-09-01	Heritage	Silicified hydrothermal breccia	Qtz, mca, chl, py	Mca+Chl+Sme	Mca+Chl	-
HE-09-02	Heritage	Quartz-chlorite vein/breccia	Qtz, cal, mca, chl	Chl+Sme	Mca+Chl	-
HE-22-1R	Heritage	Quartz-chlorite-sulfide vein	Qtz, mca, chl, cal, sp	Chl+Sme	Mca+Chl	-

HE-23-1R	Heritage	Quartz-sericite-altered andesite	Qtz, kfs, mca, chl, py	Mca+Chl	Mca+Chl	-
HE-23-3R	Heritage	Quartz-adularia breccia	Qtz, mca, kfs, py, chl	Mca+Chl+Sme	Mca	-
HE-24-1R	Heritage	Quartz-chlorite vein/breccia	Qtz, mca, kfs, py, chl	Mca+Chl+Sme	Mca	-

Table 3.2: Visible - near infrared - short-wave infrared (Vis-NIR-SWIR) absorption band positions of detected hydrothermal alteration minerals in analyzed samples.

Deposit / Prospect	**Mineral**	***Range of diagnostic Vis-NIR-SWIR absorption features (nm)***					
		OH	**H_2O**	**SO_4^{-2}**	**Al-OH**	**Chlorite Fe-OH**	**Chlorite Mg-OH**
Hope Brook	Muscovite	1410	1917		2204		
	Paragonite	1409-1412	1908-1941		2192-2201		
	Fe-Mg Chlorite	1408	1995			2255	2346
Hickey’s Pond	Natroalunite	1434-1435	1490-1491	1763-1766	2165-2170 2212-2214 2319-2323		
Vinjer	Pyrophyllite	950 1394			2167		
	Muscovite	1414			2207		
Oval Pit	Pyrophyllite	950 1394			2167		
Heritage	Phengite	1410-1414	1906-1915		2212-2218		
	Smectite	1412-1414	1440-1460 1919-1929		2200-2227		
	Fe-Mg Chlorite	1410-1414	1987-2002			2240-2262	2339-2352

Table 3.3: Raman microspectroscopy band positions of detected hydrothermal alteration minerals in analyzed samples.

Deposit / Prospect	**Mineral**	***Range of diagnostic Raman peak positions (cm^{-1})***							
		Raman spectral features of phyllosilicates				***Raman spectral features of alunite-group minerals***			
		Main Si-O-Si phyllosilicate peak	**Secondary Si-O-Si bands**	**T-O-T lattice modes**	**Si-O mode**	**Main S-O sulfate peak**	**Secondary S-O bands**	**Al-O modes**	**OH/H$_2$O modes**
Hope Brook	Muscovite Group	701-703	638-657 744-751	197-201 264-266 408-411	1010-1065				3627
	Fe-Mg Chlorite	670		201 356 546					3432 3579 3653
Hickey's Pond	Alunite					1024-1025	651-656 1081-1084 1181-1186	388-390	3476-3480 3510-3516
	Natroalunite					1024-1025	652 1078-1086 1182-1185	390-394	3450-3453 3490
Vinjer	Pyrophyllite	705		194 261 362					3673
Oval Pit	Pyrophyllite	704		193 260 360					3675
Heritage	Phengite	702-706	640-667 749-759	191-202 259-266 412-429	1082-1113				3620-3632
	Fe-Mg Chlorite	658-675		198-214 357-373 541-550					3420-3430 3559-3574 3652-3670

Table 3.4. Selected electron microprobe analyses (in wt%) of pyrophyllite, white mica, chlorite, and alunite from the studied epithermal systems, and respective structural formulas. Abbreviations: Prl (pyrophyllite), Alu (alunite), OP (Oval Pit Mine), VJ (Vinjer high-sulfidation system), HP (Hickey's Pond).

Deposit	OP	OP	OP	OP	OP	VJ	VJ	VJ	VJ	VJ	HP	HP	HP	HP	HP	HP	HP	HP	HP	HP
Sample	MANUELS	MANUELS	MANUELS	MANUELS	MANUELS	VP-2	VP-2	VP-2	VP-2	VP-2	HP-4B	HP-4B	HP-4B	HP-4B	HP-6	HP-6	HP-6	HP-3	HP-3	HP-3
Mineral	Prl	Prl	Prl	Prl	Prl	Prl	Prl	Prl	Prl	Prl	Alu	Alu	Alu	Alu	Alu	Alu	Alu	Alu	Alu	Alu
No. anal.	4	5	7	9	15	3	13	9	19	24	4	5	11	12	2	3	11	14	15	17
SiO_2	67.51	66.73	67.23	66.71	67.30	66.79	65.82	68.18	67.06	67.33	0.43	0.02	0.06	-	0.10	0.06	-	0.04	1.19	0.09
TiO_2	0.01	0.03	0.02	0.02	-	0.02	-	-	-	0.01	-	-	0.01	-	-	-	-	-	0.01	0.01
Al_2O_3	29.82	29.47	29.40	29.08	29.75	29.62	28.75	30.28	29.23	29.41	48.34	47.53	48.73	46.79	47.18	47.09	45.49	46.50	44.43	46.58
Ce_2O_3	-	-	0.04	0.03	-	-	-	-	-	-	0.03	0.16	0.06	0.03	0.01	-	0.06	0.09	0.07	0.04
Fe_2O_3	0.16	0.13	0.21	0.19	0.17	0.31	0.30	0.23	0.28	0.26	0.05	0.11	0.01	0.11	0.03	0.11	0.13	0.05	0.07	0.01
MnO	-	0.01	0.01	-	0.02	0.01	-	-	0.01	-	-	-	-	-	-	0.01	-	-	-	-
MgO	0.01	0.01	0.01	-	-	0.02	0.02	0.00	-	0.01	-	-	-	0.02	0.01	-	-	-	-	-
P_2O_5	0.01	0.00	0.02	0.01	-	0.01	0.01	0.01	-	-	0.46	0.91	0.27	1.29	0.49	0.80	0.78	0.56	0.47	0.61
BaO	-	-	-	-	-	-	-	0.01	-	0.01	0.23	0.43	0.15	0.52	0.20	0.30	0.37	0.26	0.43	0.38
SO_3	-	0.00	-	-	-	-	0.02	0.02	-	-	41.41	39.30	41.57	39.30	41.39	40.17	40.25	41.34	40.07	42.36
SrO	-	-	-	-	-	-	-	-	-	-	0.15	0.25	0.11	0.39	0.21	0.20	0.23	0.35	0.14	0.23
CaO	0.01	0.02	0.02	0.02	0.01	0.03	0.01	0.05	0.01	0.01	0.17	0.24	0.07	0.49	0.19	0.26	0.27	0.15	0.05	0.18
Na_2O	0.10	0.07	0.04	0.05	0.05	0.06	-	0.04	-	0.01	3.70	2.58	3.06	2.01	3.92	2.92	2.92	3.33	1.98	3.50
K_2O	0.03	0.01	0.04	0.02	0.02	0.02	0.02	0.01	0.02	0.02	2.78	4.85	4.37	6.03	2.98	4.60	4.62	3.61	6.74	3.36
Cl	0.02	0.01	-	-	0.03	0.01	0.01	0.02	0.01	0.01	0.03	-	0.02	-	-	0.00	-	-	0.01	0.01
F	-	0.03	0.02	0.06	0.02	0.07	0.02	0.07	0.02	0.02	0.06	0.06	-	-	-	0.06	-	0.04	0.37	-
Total	97.63	96.46	97.02	96.11	97.29	96.86	94.90	98.84	96.59	96.97	97.76	96.31	98.43	96.88	96.66	96.53	95.07	96.25	95.83	97.31
Si	3.928	3.891	3.930	3.886	3.892	3.849	3.911	3.828	3.930	3.918	0.025	0.001	0.003	-	0.006	0.004	-	0.002	0.065	0.005
Ti	0.000	0.001	0.001	0.001	-	0.001	-	-	-	0.000	-	-	0.000	-	-	-	-	-	0.000	0.000
Al_{Total}	2.045	2.025	2.025	1.996	2.028	2.011	2.013	2.003	2.019	2.017	3.260	3.346	3.371	3.355	3.324	3.290	3.291	3.262	2.854	3.249
^{IV}Al	0.072	0.109	0.070	0.114	0.108	0.151	0.089	0.172	0.070	0.082	-	-	-	-	-	-	-	-	-	-
^{VI}Al	1.973	1.916	1.955	1.882	1.920	1.860	1.924	1.831	1.949	1.934	-	-	-	-	-	-	-	-	-	-
Ce	-	-	0.001	0.001	-	-	-	-	-	-	0.001	0.004	0.001	0.001	0.000	-	0.001	0.002	0.001	0.001
Fe^{3+}	0.007	0.006	0.009	0.008	0.007	0.013	0.013	0.010	0.012	0.011	0.002	0.005	0.000	0.004	0.001	0.004	0.005	0.002	0.003	0.000
Mn	-	0.000	0.001	-	0.001	0.000	-	-	0.000	-	-	-	-	-	-	0.001	-	-	-	-
Mg	0.001	0.001	0.001	-	-	0.002	0.002	0.000	-	0.001	-	-	-	0.001	0.001	-	-	-	-	-
P	0.000	0.000	0.001	0.000	-	0.000	0.001	0.001	-	-	0.023	0.046	0.014	0.066	0.025	0.040	0.041	0.028	0.021	0.030
Ba	-	-	-	-	-	-	-	0.000	-	0.000	0.005	0.010	0.003	0.012	0.005	0.007	0.009	0.006	0.009	0.009
S	-	0.000	-	-	-	-	0.001	0.001	-	-	1.778	1.761	1.831	1.794	1.857	1.787	1.854	1.847	1.639	1.881
Sr	-	-	-	-	-	-	-	-	-	-	0.005	0.009	0.004	0.014	0.007	0.007	0.008	0.012	0.004	0.008
Ca	0.001	0.001	0.001	0.001	0.001	0.002	0.000	0.003	0.000	0.001	0.011	0.016	0.004	0.032	0.012	0.016	0.018	0.010	0.003	0.012
Na	0.011	0.008	0.004	0.006	0.006	0.006	-	0.004	-	0.002	0.411	0.299	0.348	0.237	0.454	0.335	0.348	0.385	0.210	0.402
K	0.002	0.001	0.003	0.001	0.001	0.001	0.002	0.001	0.001	0.002	0.203	0.369	0.327	0.468	0.227	0.348	0.362	0.274	0.469	0.254
Cl	0.057	0.011	-	-	0.093	0.024	0.024	0.073	0.030	0.034	0.003	-	0.002	-	-	0.000	-	-	0.001	0.001
F	-	0.084	0.065	0.172	0.065	0.232	0.065	0.242	0.061	0.085	0.012	0.011	-	-	-	0.011	-	0.007	0.065	-
$\sum_{Tetrahedral}$	4.000	4.000	4.000	4.000	4.000	4.000	4.000	4.000	4.000	4.000										
$\sum_{Octahedral}$	1.995	1.933	1.976	1.899	1.935	1.882	1.942	1.850	1.962	1.951										
Oct. Vac.	0.005	0.067	0.024	0.101	0.065	0.118	0.058	0.150	0.038	0.049										

Calculated H_2O contents are reported in Appendix 3.

Table 3.4 (cont.). Selected electron microprobe analyses (in wt%) of pyrophyllite, white mica, chlorite, and alunite from the studied epithermal systems and respective structural formulas.

Deposit	HB	HB	HB	HP	HP	HE	HE	HE	HE	HE	HB	HB	HB	HE	HE	HE	HE	HE	HE	HE
Sample	HB-4	HB-4	HB-4	HP-2	HP-2	HE48-27	HE48-27	HE36-107	HE36-107	HE47-26	HB-4	HB-4	HB-4	HE48-28	HE48-28	HE48-27	HE48-27	HE36-107	HE47-26	HE47-26
Mineral	Mca	Mca	Mca	Mca	Mca	Mca	Mca	Mca	Mca	Mca	Chl	Chl	Chl	Chl	Chl	Chl	Chl	Chl	Chl	Chl
No. anal.	2	9	14	2	12	3	4	6	7	7	3	10	16	2	4	3	8	1	3	9
SiO_2	46.67	49.31	49.13	47.29	46.78	53.93	54.68	54.01	53.52	54.00	25.19	25.10	26.32	28.20	27.61	26.20	26.66	26.88	31.21	30.49
TiO_2	0.08	0.07	0.03	0.06	0.01	-	-	0.04	0.06	0.03	0.31	0.31	0.22	0.01	-	0.03	-	-	-	-
Al_2O_3	36.48	34.39	39.72	36.86	37.91	31.16	31.00	31.25	30.87	31.62	24.15	22.61	22.53	21.35	21.33	21.30	21.68	21.54	18.15	17.64
Cr_2O_3	-	-	-	0.01	-	-	0.02	-	0.01	0.02	0.08	0.04	0.07	-	-	-	0.01	-	-	-
V_2O_3	0.00	0.01	0.05	0.01	0.03	0.07	0.05	0.04	0.05	0.05	0.07	0.04	0.07	0.07	0.07	0.02	0.03	0.03	0.07	0.05
FeO	1.60	1.65	0.49	1.54	1.07	1.03	1.13	2.13	2.20	1.03	20.21	19.40	19.02	19.50	20.65	21.05	22.48	21.03	20.90	18.43
MnO	-	-	0.01	-	0.01	0.06	0.09	0.22	0.28	0.08	0.02	0.07	0.06	3.49	2.83	3.00	3.16	4.39	0.73	0.78
MgO	0.29	0.90	0.09	0.12	0.07	2.70	2.67	2.13	2.10	2.21	16.10	16.52	17.40	16.39	15.82	14.72	14.72	14.78	18.09	17.63
CaO	0.01	-	0.08	0.05	0.05	0.04	0.05	0.18	0.20	0.09	0.02	0.04	0.03	0.03	0.03	0.04	0.03	0.04	0.29	0.59
Na_2O	1.95	1.50	7.12	0.94	1.38	0.11	0.15	0.05	0.10	0.01	0.11	0.07	0.18	0.03	0.04	0.03	0.01	-	0.01	0.03
K_2O	8.97	9.43	1.72	9.84	9.83	8.98	8.88	8.88	9.21	5.60	0.02	0.04	0.08	0.30	0.15	0.15	0.10	0.02	0.02	0.21
Cl	0.01	-	0.01	0.01	0.01	0.01	-	0.02	0.02	0.01	0.01	0.01	0.03	0.02	0.01	0.02	0.01	0.01	0.02	0.02
F	0.10	0.20	0.03	0.29	0.30	0.04	0.30	-	-	0.15	-	-	-	-	-	-	-	-	-	-
Total	96.09	97.36	98.46	96.89	97.31	98.09	98.90	98.91	98.56	94.82	86.18	84.20	85.95	89.18	88.34	86.47	88.74	88.49	89.35	85.74
Si	2.957	2.985	2.991	2.879	2.848	3.350	3.396	3.355	3.324	3.354	2.609	2.655	2.688	2.837	2.821	2.741	2.753	2.775	3.098	3.132
Ti	0.004	0.003	0.001	0.003	0.001	-	-	0.002	0.003	0.001	0.005	0.003	0.005	0.000	-	0.002	-	-	-	-
Al_{Total}	2.724	2.454	2.850	2.645	2.720	2.281	2.270	2.288	2.260	2.315	2.947	2.819	2.712	2.531	2.569	2.626	2.639	2.620	2.123	2.136
^{IV}Al	1.043	1.015	1.009	1.121	1.152	0.650	0.604	0.645	0.676	0.646	1.391	1.345	1.312	1.163	1.179	1.259	1.247	1.225	0.902	0.868
^{VI}Al	1.681	1.439	1.841	1.524	1.568	1.631	1.666	1.643	1.585	1.669	1.555	1.475	1.400	1.368	1.389	1.366	1.392	1.395	1.221	1.268
Cr	-	-	-	0.001	-	-	0.001	-	0.001	0.001	0.007	0.003	0.005	-	-	-	0.001	-	-	-
V	0.000	0.001	0.003	0.001	0.002	0.004	0.003	0.002	0.003	0.003	0.001	0.007	0.005	0.006	0.007	0.002	0.003	0.002	0.006	0.004
Fe^{2+}	0.085	0.083	0.025	0.078	0.055	0.053	0.059	0.111	0.114	0.053	1.750	1.716	1.624	1.640	1.764	1.842	1.942	1.816	1.735	1.584
Mn	-	-	0.000	-	0.000	0.003	0.005	0.012	0.015	0.004	0.027	0.028	0.019	0.297	0.245	0.266	0.276	0.384	0.062	0.068
Mg	0.027	0.082	0.009	0.011	0.006	0.250	0.248	0.197	0.194	0.204	2.486	2.606	2.649	2.458	2.410	2.296	2.265	2.274	2.678	2.700
Ca	0.001	-	0.005	0.003	0.003	0.003	0.003	0.012	0.013	0.006	0.002	0.005	0.003	0.003	0.003	0.005	0.004	0.004	0.031	0.065
Na	0.239	0.176	0.840	0.110	0.162	0.013	0.018	0.006	0.012	0.002	0.022	0.014	0.036	0.006	0.007	0.006	0.003	-	0.003	0.005
K	0.725	0.728	0.134	0.764	0.764	0.711	0.704	0.704	0.730	0.444	0.003	0.005	0.011	0.038	0.020	0.020	0.013	0.003	0.003	0.028
Cl	0.001	-	0.001	0.001	0.001	0.001	-	0.002	0.002	0.001	0.002	0.002	0.006	0.003	0.002	0.004	0.001	0.001	0.003	0.003
F	0.019	0.038	0.009	0.054	0.056	0.005	0.058	-	-	0.029	-	-	-	-	-	-	-	-	-	-
$\sum_{Tetrahedral}$	4.000	4.000	4.000	4.000	4.000	4.000	4.000	4.000	4.000	4.000	4.000	4.000	4.000	4.000	4.000	4.000	4.000	4.000	4.000	4.000
$\sum_{Octahedral}$	1.798	1.608	1.876	1.617	1.631	1.941	1.982	1.967	1.914	1.936	5.859	5.860	5.760	5.816	5.845	5.804	5.898	5.879	5.738	5.721
Oct. Vac.	0.202	0.392	0.124	0.383	0.369	0.059	0.018	0.033	0.086	0.064	0.141	0.140	0.240	0.184	0.155	0.196	0.102	0.121	0.262	0.279
Interlayer	0.965	0.904	0.979	0.878	0.929	0.727	0.725	0.721	0.755	0.452										
Inter. Vac.	0.035	0.096	0.021	0.122	0.071	0.273	0.275	0.279	0.245	0.548										

Calculated H_2O contents are reported in Appendix 3.

Chapter 4: Geochemical signature of hydrothermal rutile associated with orogenic gold mineralization and its potential as an exploration indicator in the Baie Verte region of Newfoundland, Canada

4.1. Abstract

Hydrothermal rutile from representative orogenic gold occurrences in the Baie Verte region of Newfoundland (Animal Pond prospect, Stog'er Tight deposit, and Argyle deposit) was characterized by optical petrography, scanning electron microscopy (SEM), electron probe microanalysis (EPMA), and secondary ion mass spectrometry (SIMS) in order to: (1) elucidate the evolution of Fe-Ti phases, in particular the formation of rutile, with increasing hydrothermal alteration intensity, and the resulting textures; (2) define the minor and trace element geochemical signature(s) of rutile (or other TiO_2 polymorphs); and (3) explore the potential of rutile geochemistry as a vector for orogenic gold deposits in the Baie Verte region. In these examples, hydrothermal rutile is the result of the progressive alteration of Fe-rich phases in the wall rock, including magnetite, Ti-magnetite, ilmenite, and/or titanite. There is an evolution from more Fe-rich phases towards more Ti-rich phases, ultimately rutile (TiO_2), with the increase of hydrothermal alteration intensity and proximity to vein mineralization. In this study, hydrothermal rutile contained as much as 5717 ppm Zr, 9215 ppm Nb, 392 ppm Sn, 582 ppm Sb, 232 ppm Ta, and 4804 ppm W. The mineral originally described as rutile from the essentially barren Animal Pond prospect contains distinctly higher Fe and Mn, and may in fact be brookite, based on its trace element profile. Rutile from the auriferous orogenic vein mineralization in the Stog'er Tight and Argyle deposits contains higher Nb, Sn, Sb, and Ta. Principal component analysis (PCA) clearly discriminates rutile (and/or brookite) from barren versus mineralized gabbro host rocks, with Sb-Sn, Ta-Nb, and W trace element clusters characteristic of vein-proximal rutile from Stog'er Tight and Argyle, and Ca-Mn-Fe-Zr clusters characteristic of rutile/brookite from the barren Animal Pond prospect. There is a progressive compositional transition from Animal Pond (Ca-Mn-Fe-Zr clusters), through intermediate alteration zones at Argyle (Sc-Y-As and Cr clusters), to gold-related proximal rutile at Stog'er Tight and Argyle (Sb-Sn, Ta-Nb, and W clusters). Antimony is a particularly strong discriminator between orogenic gold-related hydrothermal rutile and rutile from unmineralized veins (Au-absent) and host rocks. Gold-related rutile from the Stog'er Tight and Argyle deposits contains Sb > 80 ppm, whereas rutile/brookite from the barren Animal Pond prospect contains <66 ppm Sb. The multi-element geochemical signatures of Au-related rutile documented in this study have potential for future exploration for orogenic gold mineralization in the Baie Verte region, including application to heavy minerals in till and soil samples, with possible extension to other deposits of this type globally.

4.2. Introduction

Orogenic Au deposits hosted in greenschist to amphibolite facies rocks represent a significant source of gold, accounting for about 30% of recent gold production and resources (Frimmel, 2008; Lipson, 2014; Frimmel, 2018), and for >75% of all global extracted gold throughout history (Phillips, 2013). In Canada, 80% of all gold produced to date has been supplied by orogenic Au deposits (Lydon, 2007). This style of gold mineralization shows characteristic hydrothermal alteration due to interaction of hydrothermal fluids with the host wall rocks (Groves et al., 1998; Goldfarb et al., 2005; Phillips and Powell, 2010; Zhu et al., 2011; Pitcairn et al., 2014, 2015; Goldfarb and Groves, 2015; Groves et al., 2019), which produces distinct mineralogical and chemical zonation that can be used as vectors in gold exploration (Bierlein and Crowe, 2000; Goldfarb et al., 2005). Orogenic Au deposits are synchronous with accretion and metamorphism, and resulted from the mobilization of significant volumes of Au-bearing hydrothermal fluids, which precipitated gold at intermediate-to-deep crustal levels (up to 15 km deep; at or above the brittle-ductile transition) in shear and fracture zones (Groves et al., 1998; Goldfarb et al., 2005; Phillips and Powell, 2010; Tomkins 2013; Pitcairn et al., 2014, 2015; Goldfarb and Groves, 2015; Groves et al., 2019). They are usually hosted by deformed and hydrothermally altered rocks with greenschist to amphibolite facies metamorphic assemblages, and alteration assemblages containing carbonates, fine-grained white mica (muscovite), green micas (e.g., fuchsite, roscoelite), chlorite, albite, tourmaline, scheelite, pyrite, hematite, magnetite, and rutile (Goldfarb et al., 2005; Dubé and Gosselin, 2007, Saunders et al., 2014).

In recent decades, the utilization of indicator minerals (ore, accessory, or alteration minerals that are refractory in nature, not prone to physical or chemical weathering, and consequently preserved in soil and surficial sediments) in mineral exploration has been undertaken for many commodities and deposit types (McClenaghan, 2005; 2011; McClenaghan et al., 2013; McClenaghan and Paulen, 2018; Gandhi and Sarkar, 2016; Lougheed et al., 2020). Some general examples of indicator minerals for resource exploration include apatite (e.g., Belousova et al., 2002), rutile (e.g., Agangi et al., 2019; Sciuba and Beaudoin, 2021), zircon (e.g., Pizarro et al., 2020), titanite (e.g., Linnen and Che, 2010), garnet (e.g., Gurney et al., 1993; Gurney and Zweistra, 1995; Griffin and Ryan, 1995), ilmenite (e.g., Griffin and Ryan, 1995), chromite (e.g., Griffin and Ryan, 1995), magnetite (e.g., Pisiak et al., 2017), and ore minerals (e.g., sphalerite and galena; Paulen et al., 2011; Oviatt et al., 2015). Previous literature has demonstrated the particular potential of rutile, the high temperature TiO_2 polymorph, as an indicator mineral to fingerprint orogenic Au deposits (Scott, 2005; Dostal et al., 2009; Scott et al., 2011; Yang et al., 2018; Agangi et al., 2019;

Porter et al., 2020; Sciuba and Beaudoin, 2021), where hydrothermal rutile can contain elevated concentrations of Fe, Cr, Sb, Nb, Ta, W, Sn, and V relative to protolith rutile from the barren country rocks (Scott, 2005; Agangi et al., 2019; Porter et al., 2020; Sciuba and Beaudoin, 2021).

Orogenic gold mineralization has been historically recognized in the cover sequences of the ophiolitic rocks that comprise part of the Baie Verte Peninsula, with the Goldenville deposit representing one of the first orogenic gold producers on the island of Newfoundland (Skulski et al., 2009). Further exploration in the 1970s and 1980s lead to the discovery of numerous orogenic gold occurrences, including the Pine Cove, Stog'er Tight, and Nugget Pond deposits, in host rocks of diverse lithologies (Skulski et al., 2009). Recent regional exploration efforts in the area have included B-horizon soil sampling, soil geochemistry, and trenching (e.g., Copeland et al., 2015; Sparrow et al., 2017).

In this study our central objective was to characterize rutile from representative orogenic Au occurrences in the Baie Verte Peninsula using optical microscopy, scanning electron microscopy incorporating both back-scattered electron imaging (SEM-BSE) and energy dispersive x-ray spectrometry (SEM-EDS), electron probe microanalysis (EPMA) and secondary ion mass spectrometry (SIMS). The goal of this paper is to define the paragenesis, Fe-Ti phase evolution, and major, minor, and trace element geochemical signatures of hydrothermal rutile. Further, we aimed to better understand the genetic relationship between Fe-Ti phases (i.e., magnetite, ilmenite, titanite, rutile) and hydrothermal alteration associated with orogenic Au mineralization. An important ancillary goal was to evaluate the potential of rutile geochemistry as an exploration tool for orogenic Au in Baie Verte, and globally.

4.3. Geological Setting

The Baie Verte Peninsula is located on the north shore of Newfoundland (Fig. 4.1), and straddles the boundary between the Laurentian continental margin rocks of the western Humber Zone and the ophiolitic and related rocks of the eastern Notre Dame subzone in the Dunnage Zone (Williams, 1979, Williams and St. Julien, 1982; Hibbard, 1983; Evans, 2004; van Staal et al., 2007; Skulski et al., 2009). This complex tectonic boundary, known as the Baie Verte Line (Fig. 4.1), consists of poly-phase shear zones and faults that separate oceanic and mantle-derived rocks of the Dunnage Zone from those of the Laurentian continental margin (Williams, 1979; Williams and St. Julien, 1982; Castonguay et al., 2014). The Humber Zone, in the Baie Verte Peninsula region, comprises migmatitic gneisses of the East Pond Metamorphic Suite, representing the Grenvillian basement, and the overlying Mesoproterozoic - Early Paleozoic Fleur de Lys Supergroup rocks, composed of metamorphosed and polydeformed clastic sedimentary rocks, whose protoliths were derived from the eastern continental margin of Laurentia (Williams, 1979; Hibbard, 1983). The Notre Dame subzone (Dunnage Zone), in the Baie Verte Peninsula region, comprises several supra-subduction zone ophiolitic complexes belonging to the Baie Verte Oceanic Tract (BVOT) and their volcano-sedimentary cover sequences, including: (1) the Betts Cove Complex; (2) the Pacquet Complex; (3) the Point Rousse Complex; and (4) the Advocate Complex (Hibbard, 1983; Skulski et al., 2009). The rocks of the Notre Dame subzone were accreted onto the Laurentian margin during the second phase of the Taconic orogeny in the Lower to Middle Ordovician (van Staal et al., 2007; 2012). The BVOT rocks are intruded by several Late Ordovician - Early Silurian granitoid plutons and overlain by Silurian volcanic rocks (Skulski et al., 2009).

A minimum of four deformation events have affected the Baie Verte Peninsula (Castonguay et al., 2009): i) D_1 is only preserved as schistosity in the Fleur de Lys Supergroup and it is related to the obduction of the BVOT during the Ordovician Taconic orogeny (465-460 Ma); ii) D_2 consists of a set of north-dipping faults and shear zones that resulted in the burial of the ophiolitic complexes and simultaneous exhumation of the Fleur de Lys Supergroup during the Silurian Salinic orogeny (432-422 Ma); iii) D_3 consists of folding related to the Devonian (405-385 Ma) dextral transtension to transpression (Anderson et al., 2001); and iv) D_4 consists of N-NE trending anticlines and synclines that affect earlier fabrics and are not uniformly developed throughout the peninsula, and are related to a transpressional to transtensional regime during the Acadian Orogeny (Anderson et al., 2001).

The Baie Verte Peninsula hosts multiple orogenic gold occurrences in the cover sequences of the ophiolitic rocks of the BVOT, particularly in those belonging to the Point Rousse Complex (Evans, 2004; Skulski et al., 2009). Gold mineralization is spatially associated with (and hosted in the hanging wall of) the Scrape Thrust (Fig. 4.1) – a second-order structure of the Baie Verte Line related to the D_2 events (Williams, 1979; Williams and St. Julien, 1982; Ramezani, 1992; Ramezani et al., 2000; Evans, 2004; Skulski et al., 2009; 2010; Castonguay et al., 2014). This complex structure has an extended tectonic and thermal history, with widespread evidence of hydrothermal fluid flow and related orogenic mineralization (Williams, 1979; Williams and St. Julien, 1982; Dubé, 1990; Dubé et al., 1991; 1992; Kirkwood and Dubé, 1992; Ramezani, 1992; Ramezani et al., 2000; Castonguay et al., 2014; Menzel et al., 2018). The host rock tectonostratigraphy of orogenic gold occurrences in the Baie Verte Peninsula has been studied by Skulski et al. (2009; 2010) and Evans (2004). However, the details on hydrothermal alteration, lithogeochemistry, and spatial distribution of alteration phases have only more recently been studied in a comprehensive manner (Ybarra, 2019: Pawlukiewicz, 2019).

The rocks of the Betts Cove Complex and overlying Snooks Arm Group cover sequence are the best preserved and exposed of all the ophiolitic rocks of the BVOT. Consequently, the stratigraphy of the Betts Cove Complex and Snooks Arm Group are taken as a reference template that has been extended to the rest of BVOT rocks (Bédard et al., 2000; Skulski et al., 2010; Figure 4.1). The Point Rousse Complex contains a basal mantle-derived ophiolitic sequence (Betts Cove ophiolite equivalent) consisting of mantle harzburgite, ultramafic cumulates of boninitic composition, and pyroxenite, which are overlain by a layered gabbro unit (Skulski et al., 2009; 2010). A thin layer of massive gabbro precedes the sheeted dyke gabbro complex, which is in turn overlain by a thin unit of boninites with occasional pillow lava formation (Skulski et al., 2010). The top of the ophiolitic sequence is characterized by Ti-boninites and island arc tholeiitic pillow basalts and pillow breccias that are mineralogically and chemically analogous to those of the Mt. Misery formation of the Betts Cove ophiolite (Skulski et al., 2010). The volcaniclastic cover sequence of the Point Rousse Complex is comprised of a basal jasper-magnetite iron formation unit known as the Goldenville horizon, which hosts the Nugget Pond and Goldenville orogenic Au deposits, and an upper unit of siltstones and tuffaceous wackes interbedded with mafic tuffs and Fe-Ti-rich gabbros and basalts belonging to the Scrape Point Formation (Ramezani, 1992; Ramezani et al., 2000; Skulski et al., 2010). Calc-alkaline basalt, mafic tuffs, and mafic epiclastic wackes and conglomerates from the Bobby Cove Formation overlie the Scrape Point Formation rocks (Skulski et al., 2010). Higher in the stratigraphy, the younger Venam's Bight Formation consists of high-Ti basalts of tholeiitic affinity, with interbedded volcanic breccias (Skulski et al., 2010). The top of the cover sequence of the Point Rousse Complex is characterized by mafic epiclastic and volcaniclastic rocks topped by tholeiitic pillow basalts that are correlative with the Round Harbour Formation of the Betts Cove Complex (Bédard et al., 2000; Skulski et al., 2010).

The Point Rousse Complex is disrupted by the Scrape Thrust, which formed during the D_2 event and divides and separates the Point Rousse volcaniclastic cover sequence from the underlying serpentinized ultramafic ophiolitic rocks, forming several fault-bounded thrust sheets (Hibbard, 1983; Dubé et al., 1993; Fig. 4.1). In addition, the Scrape Thrust juxtaposed the cover sequence rocks from the Point Rousse Complex (i.e., Snooks Arm Group) with the Pacquet Harbour Group rocks (Skulski et al., 2009; Fig. 1). This structure, and its second and third order thrusts and shear zones, is spatially associated with the orogenic gold occurrences at the Animal Pond prospect, the Stog'er Tight deposit, and the Argyle deposit (Ramezani, 1992; Ramezani et al., 2000; Evans, 2004; Skulski et al., 2009; 2010; Castonguay et al., 2014).

Orogenic gold occurrences in the Baie Verte Peninsula share some common attributes when it comes to hydrothermal alteration and mineralization style. Notably, in all occurrences, including Animal Pond, Stog'er Tight, Argyle, and Pine Cove, two main hydrothermal events have been recognized (Ramezani, 1992; Ramezani et al., 2000; Pawlukiewicz, 2019; Ybarra, 2019): an early barren epidote-albite-chlorite-calcite alteration event and a late quartz-pyrite-rutile-Au (albite-chlorite-sericite-ankerite) alteration event. Gold mineralization commonly occurs as native Au inclusions in pyrite or within fractures in pyrite grains. However, in detail, hydrothermal alteration assemblages and mineralization styles do show some variation between the studied occurrences, and these are described in detail below. Regionally, and distal to the gold occurrences examined in this study (where host rocks have been altered by focused hydrothermal systems), background greenschist metamorphism is characterized by the presence of metamorphic actinolite and epidote (Ramezani, 1992; Ramezani et al., 2000; Evans, 2004; Skulski et al., 2009; 2010).

4.3.1. The Animal Pond prospect

The Animal Pond prospect is located approximately 2 km northeast of the Pine Cove mine (Fig. 4.1) and consists of a 42 m wide zone of altered gabbro containing quartz stockwork veining with anomalous Au content (up to 61.54 g/t Au in a grab sample; Anaconda Mining Inc. Press Release, October 14th, 2004). Hydrothermal alteration is predominated by an early barren chlorite-epidote-albite assemblage, with minor amounts of pyrite, sericite, and carbonate (Anaconda Mining Inc. Drilling Program, 2005). The second quartz-pyrite-rutile-native gold event is limited in extent to sparse stockwork-like mineralization, with native Au occurring as inclusions in pyrite (Anaconda Mining Inc. Drilling Program, 2005). However, pervasively altered gabbro surrounding this stockwork still preserves the chlorite-epidote-albite assemblage from the first hydrothermal event, with minor second event overprint in the form of ankerite and pyrite (Anaconda Mining Inc. Drilling Program, 2005). Distal gabbro displays hydrothermal alteration consisting of chlorite and epidote (Anaconda Mining Inc. Drilling Program, 2005). Given the restricted extent of the gold mineralization this prospect is currently deemed non-economic and is considered as essentially barren in the context of the current study.

4.3.2. The Stog'er Tight deposit

The Stog'er Tight deposit (116,000 t @ 3.33 g/t Au indicated resources; 344,000 t @ 3.34 g/t Au inferred resources; Pitman et al., 2020) was mined between 2016 and 2019 by Anaconda Mining. The stratabound deposit is hosted in a 11-70 m thick, high Fe-Ti meta-gabbro sill that was emplaced in the Snooks Arm Group (Fig. 4.1) and lies in the hanging wall of the Scrape Thrust and related shear zones (Ramezani, 1992; Ramezani et al., 2000). Mineralization is hosted within coarse-grained gabbro that contains abundant alteration and coarse pyrite grains (Ramezani, 1992; Ramezani et al., 2000).

The two main hydrothermal alteration events are also recognized at Stog'er Tight: an early widespread chlorite-calcite-albite assemblage, followed by a much more focused, volumetrically restricted red albite-rutile-pyrite-native gold assemblage. Hydrothermal alteration varies with proximity to mineralization and exhibits a zonation pattern from (distal to proximal) of: (1) chlorite-calcite; (2) sericite-ankerite (only developed in the hanging wall); (3) chlorite-magnetite (only developed in the footwall); and (4) red albite-pyrite-native gold (Ramezani, 1992; Ramezani et al., 2000). These alteration zones typically extend less than a few meters outward from the mineralization zones. Mixtures of Fe-Ti phases, also referred to as leucoxene, occur throughout all alteration zones (Ramezani, 1992). In the distal chlorite-calcite alteration zone, leucoxene is dominated by titanite incipiently altered to rutile. In the hanging wall, the chlorite-calcite zone grades to a sericite-ankerite zone, in which leucoxene is characterized by acicular rutile aggregates with locally preserved massive titanite cores (Ramezani, 1992). In the footwall of the Scrape Thrust at Stog'er Tight, the chlorite-calcite grades to a chlorite-magnetite assemblage containing leucoxene aggregates overgrown by euhedral hydrothermal Ti-free magnetite. Finally, in the mineralized core of the deposit, the red albite-pyrite-native gold zone occurs as discontinuous lens-shaped areas in close association with the sericite-ankerite zone (Ramezani, 1992). The red albite-pyrite-native gold zone contains rutile as the dominant Fe-Ti phase, and rutile is in close textural association with Au-bearing pyrite. Gold is exclusively found within the wall rock vein selvages in the red albite-pyrite-native gold zone, occurring as inclusions of native Au in pyrite or in fractures in pyrite (Ramezani, 1992; Ramezani et al., 2000). Gold deposition is interpreted to have occurred by sulfidation of Fe-rich wall rocks, leading to the precipitation of both pyrite and gold through the destabilization of gold-bisulfide complexes (Ramezani, 1992; Ramezani et al., 2000). Uranium-Pb dating of hydrothermal zircon from Stog'er Tight veins yielded an age of 420 ± 5 Ma for the mineralization event (Ramezani, 1992; Ramezani et al., 2000), in agreement with Re-Os dating of a hydrothermal pyrite sample at 420 ± 7 Ma (Kerr and Selby, 2012).

4.3.3. The Argyle deposit

The Argyle gold deposit (550,000 t @ 3.00 g/t Au indicated resources; 65,000 t @ 3.85 g/t Au inferred resources; Pitman et al., 2020) began production in 2020 under operation by Anaconda

Mining. It is located 1 km west of the town of Ming's Bight (Fig. 4.1), hosted in a 50-70 m thick tholeiitic gabbro sill that intruded the Scrape Point Formation volcaniclastic cover sequence rocks of the Snooks Arm Group (Pawlukiewicz, 2019). As in the case of Stog'er Tight, host rocks at Argyle were affected by the Scrape Thrust fault, and the mineralized gabbro sill is located in the hanging wall of the fault (Pawlukiewicz, 2019). Gold mineralization occurs predominantly as native Au inclusions in black tarnished sooty pyrite (1-40 mm) and along pyrite crystal boundaries in the gabbro wall rock, in close proximity (<1 m) to quartz-ankerite hydrothermal veins (Pawlukiewicz, 2019). The highest gold contents are reported from samples that display native Au inclusions in pyrite associated with late black chlorite veinlets (Pawlukiewicz, 2019).

As in the case of Animal Pond and Stog'er Tight, there are two successive episodes of hydrothermal alteration recognized at Argyle (Pawlukiewicz, 2019). During the first episode, early barren epidote-albite alteration of the gabbro was overprinted by a second episode characterized by an assemblage of Al-rich muscovite, quartz, ankerite, albite, Fe-rich chlorite, rutile, pyrite, and native gold (Pawlukiewicz, 2019). The second, gold-related, hydrothermal episode resulted in zoning spatially dispersed with respect to proximity to mineralized veins; a distal chlorite-calcite-rutile ± epidote-albite zone (30-70 m), an intermediate chlorite-epidote-albite-calcite ± ankerite-rutile-hematite-sericite-pyrite zone (5-30 m), and a proximal (2-25 m) Al-rich muscovite-quartz-ankerite ± albite-Fe-rich chlorite-rutile-pyrite-native gold zone (Pawlukiewicz, 2019). The transitions between the zones are commonly gradational over 1-3 m and reflect an increase in grain size of the host gabbro towards the core of the sill (Pawlukiewicz, 2019). Fe-Ti oxides (igneous ilmenite/ilmenomagnetite) are partially replaced by tan-yellow "wisp-shaped" rutile grain aggregates (macrotexture observed in drill core samples; Pawlukiewicz, 2019) in distal and intermediate alteration zones, while the primary Fe-Ti oxides are almost completely replaced by tan-brown "wisp-shaped" rutile grains in the proximal alteration zone (Pawlukiewicz, 2019). Late regional lower greenschist metamorphism in the form of chlorite-actinolite-calcite-epidote weakly overprints the hydrothermally altered rocks at Argyle.

4.4. Materials and Methods

Drill core samples of gabbroic host rocks with visually abundant rutile were collected from the Animal Pond prospect, the Stog’er Tight deposit, and the Argyle deposit.

Petrographic polished thin sections were studied using both transmitted and reflected light microscopy to determine the hydrothermal alteration mineralogy, assemblages, textures, and paragenesis. Scanning electron microscopy (SEM) was employed to refine petrographic observations and mineral identification at the microscale, with a particular emphasis on discerning the mineralogy and evolution of Fe-Ti phases. This was accomplished using both the back scattered electron imaging (BSE) and energy dispersive X-ray spectrometry (EDS) capabilities of the FEI MLA 650FEG instrument in the CREAIT MAF Facility (Memorial University). The matching offcuts from the polished thin sections used for petrography and SEM were mounted in 25.4 mm diameter Al rings and prepared as polished pucks for subsequent EPMA and SIMS work.

Electron probe microanalysis (EPMA) was performed with a JEOL JXA 8230 Superprobe (JEOL Ltd., Akishima, Japan) equipped with a wavelength dispersive x-ray spectrometer at the CREAIT TERRA Hibernia Electron Beam Facility (Memorial University). Operating parameters included an accelerating voltage of 15 kV, a 20 nA beam current, and a fully focused 1 μm diameter electron beam. The following elements were analyzed: Ti, V, Cr, Mn, Fe, As, Al, Si, Sb, Sn, Ca, P, Zr, Nb, Ta, and W. Counting times of 20s on peak and 10s on background on both sides of the peak were used for Ti and Fe. Increased counting times of 30s on peak and 15s on background were used for the rest of elemental suite. Limits of detection (LOD) were calculated as the minimum concentration required to produce count rates three times higher than the square root of the measured background (i.e., 3σ; 99% degree of confidence at the lower detection limit). Raw data were corrected for matrix effects using the PAP algorithm as implemented by the JEOL instrument software (Pouchou and Pichoir, 1984, 1985). Natural oxides (corundum, spinel, hematite, and rutile) and silicates (albite, orthoclase, anorthite, and wollastonite) were used for calibration. Analyses with high Si content in rutile (>1 wt.% SiO_2) were interpreted as indicative of the presence of significant silicate micro-inclusions and intergrowths (see Section 4.5.1 below) and were therefore excluded from the dataset. Silicon solubilities of >1% have been observed in natural rutile, but only in rutile formed at extremely high temperatures and pressures (10 GPa, 1800°C; Ren et al., 2009). The calculation of rutile formulae in Table 4.2 was based on 2 oxygen atoms per formula unit and all Fe was assumed to be Fe(III). The latter assumption is discussed in more detail below.

Secondary ion mass spectrometry (SIMS) using a Cameca IMS 4f instrument with improved primary lensing and detection systems (CREAIT MAF Facility, Bruneau, Memorial University) was utilized to determine the trace element composition of hydrothermal rutile. The same polished rock mounts used for EPMA characterization were re-polished, cleaned, and sputter coated with a 30-50 nm layer of gold to minimize charging of the sample during analysis. A primary beam of O^- ions, accelerated through a nominal potential of 10 kV and providing a current of 10-15 nA, was electrostatically focused into a 15-20 µm diameter spot on the sample. A combination of the 150 µm image field setting of the transfer lens optics and a physical field aperture (FA) of 750 µm limited the effective field of view of the sample to a 68 µm diameter. A 250 µm contrast aperture (CA) was used, with the entrance slit narrowed to impinge on the CA image slightly, increasing the effective MRP ($M/\Delta M$) to >350. Each analysis comprised 12 cycles of counting on peaks that included $^{27}Al^+$(1s), $^{30}Si^+$(1s), $^{31}P^+$(4s), $^{42}Ca^+$(4s), $^{45}Sc^+$(4s), $^{47}Ti^+$(2s), $^{51}V^+$(4s), $^{52}Cr^+$(4s),

^{55}Mn^{+}(4s), ^{56}Fe^{+}(2s), ^{75}As^{+}(8s), ^{89}Y^{+}(4s), ^{90}Zr^{+}(4s), ^{93}Nb^{+}(4s), ^{120}Sn^{+}(4s), ^{121}Sb^{+}(8s), ^{181}Ta^{+}(4s), ^{184}W^{+}(4s), plus counting on a background position (26.67 Da (4s)) to monitor detection noise. A magnet wait time of 0.5-2 s was also applied between each magnetic peak switch. Total acquisition time for each trial spot was thus ~18 min, not including a pre-sputtering period of 2 min with a slightly rastered beam to eliminate surface contamination before analysis. Each individual cycle was monitored to detect any obvious inhomogeneities (in particular, negative excursions in ^{47}Ti^{+} intensity) resulting from the primary beam sputtering micro-inclusions with advancing depth in the sample, and such outlier cycles were rejected during initial reduction of the raw data. With regards to Si, substitution of Ti^{4+} by Si^{4+} into rutile is limited and found to be up to 5.4 wt.% SiO_2 at 2000ºC and 23GPa P-T conditions (Ren et al., 2009). These conditions are unreasonable in the crustal hydrothermal environment orogenic Au mineralizations form. Therefore, any Si content above the 1 wt.% threshold was interpreted as an inclusion in rutile and systematically removed from the dataset. Two distinct standards were used during SIMS acquisition. Rutile 123 is a transverse slice of a large (~15 mm diameter) single crystal of natural rutile provided by Pablo Valverde-Vaquero (Instituto Geológico de España (IGME)). Accepted concentrations of V (1380 ppm), Cr (1153 ppm), Fe (6392 ppm), and Nb (1219 ppm) used in our study were originally determined by EPMA using the same approach described in Valverde-Vaquero et al. (2016). All other elements were referenced to NIST 612 glass using the “preferred mean” values from Table 9 of Pearce et al. (1997). For the purpose of normalizing measured ratios to Ti concentration in the treatment of SIMS analyses the value accepted for Ti in NIST 612 was 44.0 ±2.3 ppm (Jochum et al., 2011), and for rutile the calculated [Ti] in stoichiometric pure rutile (599349 ppm). Secondary ions were energy filtered by applying a voltage offset to the nominal +4500 V sample accelerating voltage. This was -125 V for masses of <45 Da, and -105 V for masses of ≥44 Da. This was combined with an energy window of ±30 eV to suppress isobaric interferences, by preferentially selecting higher-energy secondary ions, while maintaining efficient ion transmission. Secondary ions were counted with an ETP 133H electron multiplier operated in pulse-counting mode with an overall counting system dead time of 14 ns. Maximum count rates on Ti were maintained at 900K - 1.1M counts per second (cps). The background signal ("dark noise") of the electron multiplier was typically lower than 1 count per minute. Calculated optimum detection limits (DL) were assessed for a synthetic background signal of 1 count per minute, plus two times the estimated standard deviation (2σ; essentially 1 count per minute) to calculate DL for 12 cycles of analysis. Typical DLs calculated based on analyses of Rutile 123 were 1 ppb (Sc), 2 ppb (Al, P, Y), 3 ppb (Cr, V, Mn), 4 ppb (Nb), 5 ppb (Fe), 6 ppb (Zr), 20 ppb (Ta), 90 ppb (Sn), 95 ppb (Si), 115 ppb (W), 205 ppb (As, W), 265 ppb (Ca) and 395 ppb (Sb). As discussed below, the superior DLs for these elements were of considerable advantage in this study, as the concentrations of Sb, Cr, W, Sn, Ta, W, P, and As were routinely below the DL of EPMA for our samples. The relative analytical error (2σ) was estimated for each spot analysis using the internal precision (standard deviation of the mean) of each 12-cycle analysis, and this is the error stated in the tabled SIMS data.

Principal component analysis (PCA) was performed for both EPMA and SIMS data in order to identify statistical trends and compositionally distinct rutile populations. PCA requires non-zero values for all variables used in an analysis. Consequently, any EPMA values below the detection limit for a given element were replaced with a value equal to 65% of the calculated detection limit, following the guidelines of Palarea-Albaladejo et al. (2013). This is an established statistical approach that allows samples to retain the characteristic of "low" elemental abundances for the purpose of this form of analysis. For comparison, PCA analyses of EPMA data were also performed using only those analysis with all elemental values above the detection limit (and these are also presented in the results below). For EPMA, elements with more than 50 % of determinations below the detection limit were removed completely from the set considered for PCA, with the exception of Mn as it has been documented as an effective discriminator element for rutile associated with Au mineralization (e.g., Agangi et al., 2019; Sciuba and Beaudoin, 2021). In addition to these data filters, a centered-log-ratio (CLR) transformation was applied to the raw EPMA and SIMS data. This is an established method, necessary to mitigate closure problems, false correlations, and data skewness. The procedures of Pawlowsky-Glahn and Egozcue (2006), as defined by Aitchison (1986), were followed. Titanium is the only major element in stoichiometric rutile and was therefore not used as a component for PCA in order to avoid deceptive statistical influence due to its overwhelming dominance in concentration over the rest of the elemental suite analyzed.

For the purpose of initial sample selection, characterization and instrumental analyses, all samples were assumed to contain the rutile polymorph of $TiO_{2.}$ This assumption had no quantitative effect on the analyses by EPMA or SIMS. Our analysis of the trace element data acquired in this study shows evidence that some of the Animal Pond samples may actually contain the brookite polymorph of TiO_2 and this is discussed in detail below.

4.5. Results

4.5.1. Petrography and evolution of Fe-Ti phases

Host rocks at Animal Pond, Stog’er Tight, and Argyle consist mainly of gabbro with occasional intercalations of mafic tuff, locally crosscut by mafic dykes. The general mineralogy and textures of the host rocks are very similar between the deposits and rutile is present in all three deposits. The distribution, mineral associations, and hydrothermal evolution of Fe-Ti phases, however, show considerably variation between deposits, as does the overall intensity of hydrothermal alteration and its relative proximity to mineralization. There are discrete distal, intermediate, and proximal alteration zones, which are defined by the relative abundance of hydrothermal alteration phases, and the presence of key alteration assemblages, Fe-Ti phases, hydrothermal veins, and Au mineralization. A summary of all these key features for the three orogenic gold occurrences examined in this study, both compiled from Anaconda Mining Inc. Drilling Program (2005), Ramezani (1992), Ramezani et al. (2000), and Pawlukiewicz (2019) and refined by the observations included in this chapter, is presented in Table 4.1.

4.5.1.1. Animal Pond

The Animal Pond Au prospect is hosted in medium to coarse-grained plagioclase-rich gabbro. The hydrothermal assemblage in medium-grained gabbro distal (>42 m) to mineralization displays weak-to-intermediate alteration consisting of chlorite, epidote, quartz, carbonate, amphibole, apatite, sericite, magnetite, pyrite, and minor chalcopyrite (Table 4.1). The coarse plagioclase crystals are weakly altered to fine-grained white mica (sericite). Original mafic minerals (biotite, pyroxene) are completely replaced by chlorite and epidote, with the local presence of primary orthomagmatic magnetite. Minor carbonate veins, as well as chlorite-epidote veins crosscut the gabbro. In intermediate and proximal zones (0-42 m), where some anomalous Au contents are recorded (0.44-61.54 g/t Au; Anaconda Mining Inc. Press Release, October 14th, 2004), the intensity of alteration affecting gabbroic host rocks increases. This includes strong sericite alteration of plagioclase crystals, widespread albite-epidote alteration, and an increase in quartz, carbonate, and chlorite veining, with the local development of stockwork zones. Pyrite (containing inclusions of native Au) and minor chalcopyrite are the main sulfides occurring in this zone. Titanite-rutile mixtures (leucoxene) comprise the main Fe-Ti phases present (Table 4.1). Fracturing and shearing in the gabbro are common features related to this alteration, as is the presence of foliation or schistosity.

Overall, the increased intensity of hydrothermal alteration towards the proximal zone is reflected in the progressive alteration of Fe-Ti phases, mainly magnetite and/or Ti-magnetite, to a mineral assemblage dominated by rutile, with variable amounts of titanite and remnant ilmenite (Fig. 4.2a-f). In distal zones, 0.5-1 mm igneous magnetite or Ti-magnetite shows orthomagmatic exsolution to ilmenite resulting in a lamellar texture (Fig. 4.2a,b). Titanite develops along the contact between magnetite and ilmenite lamellae, in a texture suggesting it is the result of the hydrothermal alteration of ilmenite (Fig. 4.2b). In addition, hydrothermal rutile is found in the center of the ilmenite lamellae, where it occurs as very fine 2-3 μm grains; it is interpreted to have formed by hydrothermal replacement of the ilmenite lamellae (Fig. 4.2b). In the intermediate zone, (Ti-)magnetite is progressively replaced by titanite, which becomes the predominant Fe-Ti phase of the assemblage (Fig. 4.2c,d). Remnant orthomagmatic ilmenite lamellae are locally preserved, and rutile content and grain size increases (Fig. 4.2c,d). Rutile develops in clusters replacing ilmenite and magnetite, and individual grains can reach up to 15-20 μm. Solitary zircon crystals are commonplace, associated with rutile, titanite, and ilmenite (Fig. 4d). In proximal alteration zones, rutile is the main Fe-Ti phase (Fig. 4.2e,f) with individual grains up to 100 μm. Within rutile-dominated composite grains, remnants of ilmenite are visible after replacement by titanite (Fig. 4.2e,f). Calcite and chlorite fill some of the intracrystalline space in these same composite grains (Fig. 4.2e,f).

4.5.1.2. Stog’er Tight

The Stog’er Tight deposit is hosted in a gabbro sill affected by the two main hydrothermal alteration events: early epidote-albite alteration and late sericite-chlorite-carbonate-quartz-rutile-pyrite-Au (Ramezani, 1992; Ramezani et al., 2000). In distal zones (15-40 m wide alteration halo), the gabbro contains coarse plagioclase crystals, with biotite, pyroxene, and metamorphic actinolite partially replaced by chlorite and epidote (Table 4.1). Weak-to-medium intensity hydrothermal alteration of the gabbro results in the incipient sericite alteration of plagioclase crystals, the occurrence of albite, and the complete alteration of mafic minerals to chlorite and epidote, with the addition of ankerite (Table 4.1). Disseminated white mica can be abundant, and chlorite veins crosscut the gabbro. Hydrothermal pyrite is the main sulfide in the gabbro, and sometimes contains inclusions of chalcopyrite. Leucoxene assemblages with magnetite-ilmenite-titanite are commonplace in this zone (Table 4.1). Inside this intermediate sericite alteration zone, discontinuous proximal alteration zones (up to 68 g/t Au; Huard, 1990) of up to 40 cm in thickness develop, with the emergence of a sericite-chlorite-albite-carbonate-hematite-pyrite alteration (Table 4.1) and the complete obliteration of plagioclase crystals, which are replaced by white mica and carbonate. Mafic minerals are also completely replaced by chlorite. In addition, carbonate, chlorite, and quartz-calcite veins are abundant crosscutting the gabbro. Leucoxene is mostly replaced by hydrothermal rutile, and orthomagmatic apatite occurs in relatively substantial amounts (~5 %). Disseminated crystals of pyrite, containing inclusions of native Au, are the only sulfide − occurring close to the contact with the wall rocks, as well as within the vein selvages.

The mineral assemblage evolution of Fe-Ti oxides with increasing proximity to auriferous veins at Stog’er Tight is characterized by the progressive replacement of magnetite by rutile (Fig. 4.2g,l). In distal and intermediate zones, magnetite crystals of up to 250 µm are altered to hematite along the rims (Fig. 4.2h), and rutile crystals of up to 25 µm occur disseminated inside magnetite (Fig. 4.2g,h), suggesting the incipient replacement of magnetite by rutile. Rutile also develops pseudomorphically within the vestigial outline of magnetite grains, commonly forming clusters and covering areas of up to 600 µm across in association with magnetite-hematite crystals (Fig. 4.2g,h). Zircon grains occur together with rutile, occasionally displaying baddeleyite cores, suggesting the hydrothermal alteration of baddeleyite to zircon. Original orthomagmatic pyroxene crystals are hydrothermally altered to rutile, chlorite, and calcite and are surrounded by an assemblage consisting of hydrothermal white mica, chlorite, and quartz.

In intermediate and proximal zones, rutile is the main Fe-Ti phase with only minor relict magnetite (Fig. 4.2i-l). Individual rutile crystals of up to 25 μm are clustered in areas that pseudomorph former magnetite grains (Fig. 4.2i-l). Hydrothermal zircon crystals of up to 20 μm occur with rutile. Calcite, chlorite, muscovite, and quartz commonly fill the space between rutile grains (Fig. 4.2i-l).

4.5.1.3. Argyle

As in the case of Animal Pond and Stog'er Tight, the Argyle deposit is hosted in a tabular gabbro sill that increases in both grain size and alteration intensity towards the center of the body. The gabbro shows a similar general alteration pattern to that reported at Stog'er Tight, featuring early epidote-albite, and late sericite-chlorite-carbonate-quartz-rutile-pyrite-native gold hydrothermal events. Distal alteration (30-70 m) of fine-grained gabbro near the sill-host rock contact contains chlorite, calcite, epidote, and albite (Table 4.1). Plagioclase crystals are preserved but show incipient sericite alteration. Disseminated carbonate is abundant. Epidote and chlorite are the product of alteration of protolith mafic minerals. Quartz-carbonate-(±white mica) veins crosscut the gabbro locally. Intermediate zone alteration (5-30 m) of medium-grained gabbro contains more intense sericite and albite alteration of plagioclase, and total replacement of mafic minerals by chlorite, with the later precipitation of calcite (Table 4.1). Chlorite stringers and quartz-white mica veins crosscut the gabbro. Disseminated pyrite crystals contain chalcopyrite inclusions. In addition to the features reported for the intermediate alteration, the proximal alteration zone (2-25 m) affects coarse-grained gabbro at the center of the sill, with pervasive alteration of plagioclase to white mica and carbonate, as well as greater amounts of carbonate, chlorite, and white mica

(Table 4.1) from the replacement of the gabbro matrix and the total obliteration of mafic minerals. Carbonate-chlorite veins locally form fracture-related stockworks that crosscut the gabbro. In these proximal areas of very intense alteration, pyrite is the main sulfide in the gabbro, and hosts gold mineralization in the form of inclusions of native Au.

Distal to mineralization, Fe-Ti phases at Argyle are characterized by (Ti)-magnetite, while rutile is characteristic of the proximal assemblages (Fig. 4.2m-r). In the distal zone, magnetite (or Ti-magnetite) is partially replaced by rutile (Fig. 4.2m,n), often preserving a lamellar texture, where individual 2-5 μm rutile crystals occur along the rims of magnetite and surrounded chlorite-muscovite alteration (Fig. 4.2n). In the intermediate zone, magnetite is completely replaced by lamellae or bands of titanite and rutile in a pseudomorphic lamellar texture (Fig. 4.2o,p). Rutile occurs in the central parts of the lamellae and is surrounded by titanite (Fig. 4.2p). Individual rutile crystals range from <5 μm to 15 μm in size. The space between titanite-rutile lamellae is characterized by abundant disseminated titanite and chlorite (Fig. 4.2p). Rutile is the only Fe-Ti oxide phase present in the proximal zone associated with Au mineralization (Fig. 4.2q,r), and here it displays two textures. The first texture features large prismatic rutile crystals up to >100 μm that are clustered in areas that partially retain the shape of former magnetite grains that were fully altered and replaced by rutile. Quartz, chlorite, and carbonate are commonly found surrounding these large rutile crystals (Fig. 4.2q). The second texture is lamellar, with finely oriented bands made of rutile grains up to 50 μm long. These define a boxwork texture that follows parting (or exsolution) planes of former magnetite crystals (Fig. 4.2r). These latter rutile grains are small (<50 μm) and elongated, and occur proximal to muscovite, quartz, and chlorite (Fig. 4.2r). Hydrothermal zircon crystals are abundant and observed to be overgrowing and/or replacing baddeleyite.

4.5.2. Rutile geochemistry

Representative in situ EPMA analyses of rutile from the three Baie Verte occurrences are shown in Table 4.2, and in situ trace element analyses of rutile by SIMS are shown in Table 4.3. A complete set of SIMS data, including internal precisions of each data point, is included as Appendix 6. Individual analyses with elevated contents of Ca, Al, and Si (25,000 ppm, 15,000 ppm or 45,000 ppm, respectively) were interpreted as mixed analyses, essentially contamination from subsidiary inclusions of carbonate, titanite, and/or quartz, and therefore were excluded from further interpretation. In the initial EPMA dataset, Mn, As, P, Ta, W, Sn, Sb, and Cr were below detection for 59 %, 67 %, 81 %, 85 %, 85 %, 97 %, and 98 % of individual analyses, respectively. The size and the texture of hydrothermal rutile from Animal Pond, Stog'er Tight, and Argyle sometimes limited the acquisition of accurate (unmixed) trace element analyses by SIMS. Due to the incipient and fine-grained (routinely <20 μm) nature of rutile in the distal alteration zones, EPMA analyses of distal alteration rutile from Animal Pond were not acquired, nor were SIMS analyses of distal alteration rutile from any of the three occurrences. However, proximal alteration rutile in these latter zones occurs on a scale of 15 m or more distance from the immediate selvage of auriferous veins, thus allowing assessment of its geochemical signature over a substantial distance from prospective mineralization.

As assessed with EPMA, none of the rutile populations studied displayed significant compositional zonation in Fe, V, and Nb across individual grains.

Rutile from Animal Pond has an average composition of 95.07-100.77 wt.% TiO_2 (0.949-0.993 *apfu* Ti), 0.35-6.09 wt.% Fe_2O_3 (0.003-0.056 *apfu* Fe^{3+}), and <1 wt.% oxide in total for the other elements analyzed by EPMA (Table 4.2). Two distinct compositional varieties of rutile can be distinguished at Animal Pond, and these correlate with alteration zone. Intermediate alteration zone rutile displays lower Fe coupled with higher Ti, V, and Nb (Table 4.2). Conversely, proximal rutile displays higher Fe coupled with lower Ti and V (Table 4.2). In both cases, lower Ti content is strongly correlated with higher Fe + Nb (Fig. 4.3a), which are the predominant cations substituting for Ti in these samples. Trace element SIMS analyses showed that rutile from Animal Pond has relatively lower concentration ranges of Cr (1-31 ppm), Sn (5-47 ppm), and Sb (34-66 ppm), relative to Stog'er Tight and Argyle samples (Fig. 4.3b; Table 4.3). Tungsten is generally below 50 ppm, although a few analyses contained up to 952 ppm. Niobium shows a wide range of concentrations, from 185 ppm to 873 ppm.

Rutile from Stog'er Tight has an average composition of 97.02-101.58 wt.% TiO_2 (0.959-0.994 *apfu* Ti), 0.35-1.18 wt.% Fe_2O_3 (0.003-0.011 *apfu* Fe^{3+}), and <1 wt.% oxide in total for the other elements analyzed by EPMA (Table 4.2). Distal alteration rutile is characterized by 0.52-1.12 wt.% Fe_2O_3 (0.005-0.012 *apfu* Fe^{3+}), 99.04-101.58 wt.% TiO_2 (0.986-0.992 *apfu* Ti), and up to 0.477 wt.% Nb_2O_5 (0.003 *apfu* Nb) (Table 4.2). Intermediate alteration rutile contains relatively lower contents of Fe (<0.85 wt.% Fe_2O_3) and Nb (<0.32 wt.% Nb_2O_5) (Table 4.2). In the proximal zone, rutile is the only Fe-Ti phase present and has a characteristic composition defined by Fe (<0.78 wt.% Fe_2O_3) and Nb (<0.25 wt.% Nb_2O_5), coupled with EPMA detectable amounts of W (up to 0.07 wt.% WO_3) (Table 4.2). SIMS analyses returned W contents of up to 4804 ppm, coupled with relatively higher concentration ranges of Sb (101-582 ppm), Sn (26-392 ppm), and Nb (743-2067 ppm) (Fig. 4.3b; Table 4.3).

Rutile from the Argyle deposit has an average composition of 97.45-101.43 wt.% TiO_2 (0.977-0.995 *apfu* Ti) and 0.24-2.43 wt.% Fe_2O_3 (0.002-0.029 *apfu* Fe^{3+}), and <1 wt.% oxide in total for the other elements analyzed by EPMA (Table 4.2). Rutile from the proximal alteration zone shows higher contents of Fe and V, as opposed to higher contents of Nb in rutile from the distal alteration zone (Table 4.2). Intermediate alteration zone rutile contain higher contents of

SIMS-analyzed trace elements Ca, Sc, V, Cr, Mn, and Y, and lower Nb, Sn, and Ta relative to proximal zone rutile (Fig. 4.3b).

Overall comparisons of the three occurrences demonstrates that rutile from Argyle and Stog’er Tight has wider ranges and higher maximum contents of Nb (Fig. 4.3b,c), Sb (Fig. 4.3b,d), Sn (Fig. 4.3b), and Ta (Fig. 4.3b) relative to Animal Pond, whereas Animal Pond has higher Mn and Fe (Fig. 4.3b, d).

4.5.2.1. Statistical analysis

Principal component analysis (PCA) was applied to the major and trace element dataset acquired by EPMA and SIMS to examine the potential for further defining rutile populations. Results of the various PCA runs applied to the EPMA and SIMS datasets are presented in Figure 4.4 and Figure 4.5, respectively, as a two-dimensional projection of the two main principal components (PC2 vs. PC1). The correlation matrices and scree plots for each of the EPMA and SIMS PCA runs are reported in Appendix 7.

For EPMA data, a total of 285 spot analyses were considered for PCA. Some of the elements listed in Table 1 (namely Sb, Cr, W, Sn, Ta, W, P, and As) returned more than 50% of values below the detection limit and were not considered for PCA. Manganese also presented more than 50% of the values below the detection limit (59%), but it was included during PCA due to its potential relevance as a discriminator element for auriferous mineralization (e.g., Clark and Williams-Jones, 2004; Scott and Radford, 2007; Dostal et al., 2009; Scott et al., 2011; Yang et al., 2018; Agangi et al., 2019; Porter et al., 2020). In sum, a total of 8 elements (Fe, V, Mn, Al, Ca, Nb, Si, and Zr) were retained for PCA of EPMA data.

Figure 4.4a and b show two PCAs calculated from the EPMA dataset, both treated with the analyses below detection assigned a value of 65% of the DL. In Figure 4.4a (PCA for Fe, V, Mn, Al, Ca, Nb, Si, and Zr), the two main principal components (PC1, PC2) account for a total of 43.1% of element variability (24.2% and 18.9%, respectively). Rutile from the Animal Pond proximal zone forms a population closely associated with the Ca-Mn and Fe clusters (Fig. 4.4a). The other data show considerable overlap. However, there is a propensity of rutile composition to trend from positive PC1 and positive PC2 space (Zr cluster) towards negative PC1 and negative PC2 space (Si-Al and V clusters) with the progression from distal to intermediate to proximal zones for both the Argyle and Stog'er Tight samples (Fig. 4.4a).

Figure 4.4b shows a second PCA analysis, without Mn included. This improves the PC1 and PC2 scores slightly (27.2% and 21.7%, respectively) and they now account for a total of 48.9% of element variability. There are three main clusters of elements: Ca-Fe-Zr, Si-Al and V-Nb. Rutile from the Animal Pond proximal zone is closely related to the Ca and the Fe clusters. Rutile from the Argyle distal zone also shows a strong relationship to the Fe-Zr cluster. As for the first PCA analysis, the other data show considerable overlap. However, there is a propensity of rutile composition to trend from positive PC1 and positive PC2 space towards negative PC1 and negative PC2 space with the progression from distal to intermediate to proximal zones for both the Argyle and Stog'er Tight samples (Fig. 4.4b). As for the first PCA analysis, the Al-Si vectors bracket this progression at the proximal zone end.

For comparison, Figure 4.4c and d show PCAs equivalent to 4.4a and b, respectively – but only including those spot analyses with all the elements presenting values above the detection limit. In Figure 4.4c, the two main principal components (PC1, PC2) account for a total of 49.2% of element variability (25.6% and 23.6%, respectively). Rutile from the Animal Pond proximal zone forms a population closely associated with the Fe-Ca clusters (Fig. 4.4c). The other data show considerable overlap. However, the retained samples from the proximal zones at Stog'er Tight and Argyle show an association with the Mn-Nb-V and Al clusters (Fig. 4.4c).

Figure 4.4d shows a PCA analysis with the same data used for the PCA in Figure 4.4c but without Mn included. This improves the PC1 slightly (28.8%: PC2 is 23.4%) and PC1 and PC2 now account for a total of 52.2% of element variability. The element loadings are widely dispersed throughout the PCA space, not showing any clustering (Fig. 4.4d). Rutile from the Animal Pond proximal zone is closely related to the Ca and the Fe clusters. Rutile from the Argyle distal zone also shows a strong relationship to the Zr cluster. As for the first two PCA analysis (Fig. 4.4a and b), the other data show considerable overlap. However, there is a propensity of rutile composition to trend from positive PC1 and positive PC2 space towards negative PC1 and axial PC2 space with the progression from distal to intermediate to proximal zones for both the Argyle and Stog'er Tight samples (Fig. 4.4d). As for the first PCA runs, the Al vector brackets this progression at the proximal zone end.

Two different PCAs were performed on the SIMS dataset: i) Considering the whole SIMS 17 element dataset (Fig. 4.5a), and ii) eliminating Ca, Si, Al and P (the elements most heavily prone to bias from micro-inclusions of other minerals; Fig. 4.5b).

The first PCA included a total of 61 spot analyses and 17 variables (Al, Si, P, Ca, Sc, V, Cr, Mn, Fe, As, Y, Zr, Nb, Sn, Sb, Ta, and W). Principal components 1 and 2 account for a total of 52.8% of element variability (30.7% and 22.1%, respectively), and there is a clear cluster of elements with a combined negative PC1 loading and positive PC2 loading (Ca, Fe, Mn, and Zr; Fig. 4.5a). Eight of the other elements analyzed form a wide fan that spreads through the negative PC2 loading space (Sc, Y, As, Cr, Si, P, V, and W; Fig. 4.5a). There are also two distinct element clusters with combined positive PC1 and PC2 loadings: one defined by Al, Ta, and Nb, and a second defined by Sb and Sn (Fig. 4.5a). The elements Ta and Nb have loadings of the same direction and length in the Al-Ta-Nb elemental cluster, as do Sb and Sn in the Sb-Sn cluster, suggesting they are respectively correlated and account for the same amount of variance in the data (Fig. 4.5a; Appendix 7). Rutile from Animal Pond (proximal zone) is clearly related to the negative PC1-positive PC2 cluster formed by Ca, Fe, Mn, and Zr and forms a distinct population (Fig. 4.5a). Rutile from Stog'er Tight (proximal zone) is described by the Al-Ta-Nb and Sb-Sn clusters. Rutile from intermediate and proximal alteration zones from Argyle were both analyzed by SIMS and subsequently distinguished for PCA. Rutile from the intermediate alteration zone at Argyle is broadly described by the Sc-Y-As-Cr-Si elemental cluster. Rutile from the proximal alteration zone at Argyle largely overlaps rutile from the proximal alteration zone at Stog'er Tight, and is also described by the Al-Ta-Nb and Sb-Sn clusters, with some dispersion towards the Sc-Y-As-Cr-Si cluster.

The second PCA consisted of 61 spot analyses and 13 variables (Sc, V, Cr, Mn, Fe, As, Y, Zr, Nb, Sn, Sb, Ta, and W). PC1 and PC2 account for a total of 63.2% of element variability (36.7% and 26.5%, respectively). Four elemental clusters are distinguished (Fig. 4.5b): 1) A combined positive PC1 loading and negative PC2 loading cluster of Fe, Zr, and Mn; 2) A combined negative PC1 loading and negative PC2 loading cluster defined by Nb and Ta; 3) A combined negative PC1 loading and positive-neutral PC2 loading cluster represented by Sn and Sb; 4) A wide fan with positive PC2 loading defined by Cr, As, Sc, Y, V, and W.

As for the first PCA analysis, above, the element vectors for clusters 2 (Ta-Nb) and 3 (Sb-Sn) show the same direction and length, accounting for the same variance in the data. Rutile from Animal Pond is closely correlated to the Fe-Zr-Mn cluster. Rutile from the intermediate alteration zone at Argyle is associated with the Cr-As-Sc-Y(-V-W) elemental cluster. Rutile from the proximal alteration zone at both Argyle and Stog'er Tight shows strongest correlation with the Ta-Nb and Sn-Sb elemental clusters. Overall, this analysis resulted in discrete grouping of Animal Pond Proximal vs. Argyle Intermediate vs. Argyle Proximal and Stog'er Tight Proximal samples.

4.6. Discussion

4.6.1. Hydrothermal evolution of Fe-Ti phases and its relation to gold mineralization

Orogen-related accretion and associated metamorphism can result in the formation of orogenic Au deposits due to the interaction of hydrothermal fluids with the host rocks along regional scale fault systems (Groves et al., 1998; Ridley and Diamond, 2000; Goldfarb et al., 2005; Zhu et al., 2011; Phillips and Powell, 2010; Pitcairn et al., 2014, 2015; Goldfarb and Groves, 2015; Groves et al., 2019). The evolution of Fe-Ti phases in the Baie Verte orogenic gold occurrences follows a progression of hydrothermal alteration driven by the same fluids associated with gold mineralization. The generalized evolution from distal to proximal zones in the studied occurrences consists of orthomagmatic (Ti)-magnetite/ilmenite to hydrothermal titanite to, ultimately, rutile. This evolution records a chemical progression from Fe-rich phases to Ti-rich phases with increasing hydrothermal alteration and proximity to mineralization, and can be modelled using the following reactions (modified from Ybarra, 2019):

(1) $4CaMgAl_{0.5}Si_{1.5}O_6\ _{(augite)} + Fe_3O_4\ _{(magnetite)} + FeTiO_3\ _{(ilmenite)} + 3CO_2 + 4H_2O = Mg_{2.5}Fe_{2.5}Al_2Si_3O_{10}(OH)_8\ _{(chlorite)} + CaTiSiO_5\ _{(titanite)} + 3CaCO_3\ _{(calcite)} + 2SiO_2\ _{(quartz)} + 1.5Fe^{2+} + 1.5Mg^{2+} + 2.5O_2\ _{(g)}$

(2) $CaTiSiO_5\ _{(titanite)} + CO_2 = TiO_2\ _{(rutile)} + CaCO_3\ _{(calcite)} + SiO_2\ _{(quartz)}$

(3) $FeTiO_3\ _{(ilmenite)} + 2H_2S = FeS_2\ _{(pyrite)} + TiO_2\ _{(rutile)} + H_2O + 2H^+$

(4) $2Fe^{2+}\ _{1+x}(Fe^{3+}\ _{1-x},Ti^{4+}\ _x)_2O_4\ _{(Ti\text{-}magnetite)} + 3S_2\ _{(g)} = Fe_3O_4\ _{(magnetite)} + 3FeS_2\ _{(pyrite)} + 4x*TiO_2\ _{(rutile)} + (2-4x)*O_2\ _{(g)}$;(where $x<0.5$)

At Animal Pond, the initial step in the progression from Fe-rich phases (magnetite, Ti-magnetite) towards Ti-rich phases (titanite, rutile) resembles the hydrothermal alteration of the host rock exemplified in reaction (1). Here, the addition of CO_2 and H_2O to the rock triggered the alteration of mafic minerals and Fe-oxides to form chlorite, calcite, quartz, and titanite as hydrothermal alteration products. Further increase in hydrothermal alteration intensity resulted in the formation of incipient rutile via the alteration of titanite and ilmenite (reactions (2) and (3), respectively). Reaction (3) is an example of the role of wallrock sulfidation in rutile formation, in this case the conversion of ilmenite to rutile. Similar reactions are evidenced by the precipitation of pyrite in association with leucoxene in the gabbro wallrock in close proximity to orogenic quartz veins (Anaconda Mining Inc. Drilling Program, 2005).

At Stog’er Tight, Ti-magnetite was more directly altered to rutile, possibly following a reaction such as reaction (4), again implying a direct role of wallrock sulfidation, as observed by Ramezani (1992). It is suggested that post-mineralization redox events were responsible for the observed partial oxidation of magnetite to hematite in some samples (i.e., martitization; Mücke and Cabral, 2005).

At Argyle, distal zone alteration is characterized by the partial alteration of magnetite to rutile and the presence of minor pyrite, which can be modeled by reaction (4), again predicated on the conversion of Ti-magnetite to magnetite. In intermediate zone alteration, magnetite is partially altered to titanite and rutile, again implying reactions such as (1) and (2). In proximal zone alteration, rutile is the only phase observed, suggesting all precursor magnetite and/or titanite has been completely altered to rutile.

Analogous chemical reactions to those used here to model hydrothermal alteration can also take place during regional metamorphism (Angiboust and Harlov, 2017). However, since our sample material was exclusively derived from focussed hydrothermal vein networks in the occurrences studied, we interpret them as recording hydrothermal processes.

The precipitation of gold in orogenic gold systems is triggered by the destabilization of $Au(HS)_2^-$ complexes that carry the gold in near neutral pH CO_2-rich fluids (Mikucki, 1998; Stefánsson and Seward, 2004; Williams-Jones et al., 2009). There are multiple precipitation mechanisms for gold in orogenic systems, including changes in pressure (phase separation as a result of pressure drop), temperature (adiabatic and conductive cooling), fluid mixing, or a combination of those factors (Phillips and Powell, 1993; Robert et al., 1995; Mikucki, 1998; Zhu et al., 2011). In conjunction with such mechanisms, the chemistry and reactivity of host rocks can play a major role in the destabilization of $Au(HS)_2^-$ complexes and the precipitation of orogenic gold as a result of fluid-rock interaction (Phillips and Groves, 1983; Groves and Phillips, 1987; Mikucki, 1998). One of the most relevant host rock reactivity mechanisms leading to the precipitation of gold involves the reaction of $Au(HS)_2^-$ complexes with Fe-rich host rocks (wallrock sulfidation; Phillips and Groves, 1983; Mikucki, 1998), and has been reported by numerous workers (Dubé et al., 1989; Phillips, 1986; Zoheir et al., 2008).

Wallrock sulfidation has also been documented as a primary mechanism for gold mineralization in the Baie Verte region (Ramezani, 1992; Ramezani et al., 2000; Ybarra, 2019; Pawlukiewicz, 2019). In the Pine Cove deposit, Ybarra (2019) suggested that gold precipitation was triggered by the sulfidation of high-Fe-Ti mafic rocks (gabbros and basalts) belonging to the Venam’s Bight Formation. Similarly, Pawlukiewicz (2019) concluded that wallrock sulfidation was the main precipitation mechanism for gold mineralization at the Argyle deposit, which is hosted in Fe-Ti-rich gabbro, and Ramezani (1992) documented the same relationships at Stog’er Tight. These authors also provided ample textural evidence of gold-pyrite-Fe-(Ti)-phase relationships to demonstrate that sulfidation of Fe-Ti phases was a key process in the orogenic Au deposits in the Baie Verte region.

Ilmenite and Ti-magnetite are both abundant in the gabbroic rocks that host the three Baie Verte examples studied here. In fact, the formation of rutile as a byproduct of the hydrothermal alteration of ilmenite, Ti-magnetite, and/or titanite may have, in many cases, been a direct consequence of Au precipitation from fluids. The interaction of reduced, near neutral fluids carrying gold (i.e., as gold bisulfide complexes) with Fe-rich lithologies resulted in a change of redox state (oxidation) and pH of the fluid, destabilizing the $Au(HS)_2^-$ leading to the precipitation of gold together with the formation of rutile and pyrite (modified after Ramezani, 1992 and Ramezani et al., 2000):

(5) $FeTiO_{3\ (ilmenite)} + Au(HS)_2^-{}_{(aq)} = FeS_{2\ (pyrite)} + Au_{\ (s)} + TiO_{2\ (rutile)} + H_2O_{(l)}$

This interpretation is consistent with the petrographic observations and the Fe-Ti phase evolution reported here, supporting wallrock sulfidation as the main precipitation mechanism for gold and for the concomitant formation of hydrothermal rutile, and in agreement with previous studies on orogenic gold deposits in the Baie Verte region that invoked wallrock sulfidation as the primary mechanism for Au deposition (Ramezani, 1992; Ramezani et al., 2000; Ybarra, 2019; Pawlukiewicz, 2019).

Based on the Fe-Ti phase evolution and the presence/absence of significant Au mineralization, the most notable difference between the essentially barren Animal Pond prospect and the Stog'er Tight and Argyle deposits occurs in the highly altered rocks proximal to auriferous veins. In these proximal zone wallrocks, rutile is the predominant Fe-Ti phase occurring at Stog'er Tight and Argyle, whereas significant quantities of titanite, magnetite, and ilmenite remain present at Animal Pond. This suggests that the overall intensity of the second hydrothermal episode, characterized by quartz-albite-ankerite-chlorite-rutile-pyrite-native gold, was in fact much lower at Animal Pond, and consequently the alteration of magnetite, ilmenite, and titanite to rutile was incomplete. This is in agreement with the observation that the first episode of hydrothermal activity, recorded by chlorite-epidote-albite-carbonate assemblages, is still largely preserved at Animal Pond and only locally overprinted by assemblages from the auriferous second episode. The lower intensity and limited development of Au-related hydrothermal alteration, and the lack of significant Au mineralization at Animal Pond may be associated with a lower fluid/rock ratio during hydrothermal gold delivery event(s) due to the relatively greater distance between Animal Pond and the Scrape Thrust in comparison with the distance between Stog'er Tight and Argyle and Scrape Thrust-related structures (Fig. 4.1; Animal Pond > 1 km from Scrape Thrust; Stog'er Tight ~ 900 m from the Scrape Thrust-related structure; Argyle ~ 300 m from the Scrape Thrust-related structure. Approximate lateral distances are used as a proxy for 3D proximity between the orogenic gold occurrences and the Scrape Thrust-related structures). This resulted in only a partial hydrothermal replacement of original igneous magnetite and ilmenite and more limited formation of rutile at Animal Pond. In contrast, higher fluid/rock ratios during the formation of Stog'er Tight and Argyle, which formed closer to the Scrape Thrust, resulted in the almost complete alteration of original igneous Fe-Ti phases and extensive rutile formation, linked to more extensive Au deposition.

4.6.2. Geochemical signature of hydrothermal rutile and its association with orogenic gold mineralization

Rutile shows similar ranges in concentrations of Al, Si, P, and Ca in all three studied examples of orogenic gold occurrences, and empirically these elements do not provide useful variables for discriminating populations of rutile. Mobile trace elements such as Sc, V, Cr, Mn, Fe, As, Y, Zr, Nb, Sn, Sb, Ta, and W have been found to be characteristic of rutile from multiple orogenic gold deposits (e.g., Clark and Williams-Jones, 2004; Scott and Radford, 2007; Dostal et al., 2009; Scott et al., 2011; Yang et al., 2018; Agangi et al., 2019; Porter et al., 2020). In this study, principal component analysis of potential discriminator trace elements in rutile by SIMS (Fig. 4.5b) suggests that Ta, Nb, Sn, Sb, and W are strongly correlated with auriferous mineralization at Stog'er Tight and Argyle (Fig. 4.5b; elements with negative PC1 loadings). Conversely, rutile from the essentially barren Animal Pond prospect, as well as intermediate zone rutile from the Argyle deposit do not show this affinity (Fig. 4.5b).

In hydrothermal gold deposits in general, As is commonly positively associated with Au in pyrite from diverse environments of formation, including orogenic Au systems (Colvine et al., 1988; Reich et al., 2005; Deditius et al., 2008; 2014; Morishita et al., 2018). Despite this empirical association, and further to the PCA results reported in this study and the relatively low As contents recorded (<100 ppm, Fig. 4.3b), As in rutile does not appear to be a good discriminator for orogenic gold mineralization in the Baie Verte region. In the Baie Verte occurrences, native gold occurs either as inclusions in pyrite, coating pyrite grain margins, as free gold in microfractures in pyrite grains or as intergrowths with ankerite, chlorite, albite, quartz, and/or zircon (Ramezani, 1992; Ramezani et al., 2000; Ybarra, 2019; Pawlukiewicz, 2019). Even though arsenopyrite occurs as rare micro-inclusions inside pyrite, As does not seem to have been incorporated into the pyrite structure together with gold (Ramezani, 1992; Ramezani et al., 2000; Ybarra, 2019; Pawlukiewicz, 2019), and therefore a cogenetic association cannot be established.

The substitution of various trace elements, and in particular high field strength elements (HFSE) such as Zr, Nb, and Ta, into the structure of rutile is common to multiple geological environments (Foley et al., 2000; Zack et al., 2002; Klemme et al., 2005). In fact, Nb and Ta have estimated partition coefficients ranging from 2 to > 100, indicating a strong compatibility of those elements with rutile with respect to melt/fluid in orthomagmatic systems (Klemme et al., 2005). The affinity of these two elements for hydrothermal rutile can also be observed in Figure 4.5a and b, where they form a clearly distinct elemental cluster with virtually identical direction and length loadings (Appendix 7). This affinity is not unexpected, given the fact that both elements have the same ionic radii and oxidation state (5+), and therefore may be introduced in the same way into the rutile structure and by the same mass transportation processes. High field strength elements have been described as immobile in most geological settings (e.g., Corfu and Davis, 1991), but multiple studies have shown that HFSE can be mobile under certain conditions during magmatic, metamorphic, and hydrothermal processes (e.g., Nesbitt et al., 1999; Jiang, 2000; Jiang et al., 2005). Figure 4.6a compares the Nb and Ta contents of rutile from various orogenic Au deposits, as well as from various barren magmatic and metamorphic rocks. Rutile from most environments generally accommodates Nb and Ta contents of 100-10000 ppm and 1-1000 ppm, respectively (Fig. 4.6a). Magmatic rutile hosted in carbonatitic rocks shows Nb/Ta ratios that diverge from the crustal Nb/Ta array (Fig. 4.6a). Rutile from orogenic gold deposits and occurrences from the Baie Verte region display Nb/Ta ratios similar to other orogenic gold deposits, but also similar to many barren metamorphic and magmatic rocks (Fig. 4.6a), and lie close to the crustal Nb/Ta abundance line (Fig. 4.6a). This observation suggests that similar Nb/Ta ratios in rutile are maintained in diverse geological environments and formation processes that involve either fluids or melts, due to the uniformly strong compatibility of Nb and Ta within the rutile crystal structure (Foley et al., 2000; Zack et al., 2002; Klemme et al., 2005). Therefore, though these two elements may be sourced from orogenic-related hydrothermal fluids, their abundance and ratio alone do not generate a unique geochemical signature of hydrothermal rutile linked to orogenic gold events.

In principle, simple binary plots of non-tetravalent elements in rutile, in terms of atomic cation percent, may yield some indication of their valence state (e.g., Adlakha et al 2020) based on slopes produced by coupled substitution in the nominal Ti^{4+} site. Some simple binary plots are presented in Figure 4.7. to test for indication of coupled substitution Fe or Fe+V for Nb. However, there is no strong correlation that would indicate such a substitution. In the case of our samples these relationships are almost certainly complicated by the presence of a large number of non-tetravalent cations at the > 500 ppm level: Ca ($^{2+}$), Mn ($^{2+,\,3+}$), Fe ($^{2+,3+}$), Al $^{(3+)}$, V ($^{3+,4+}$), Sb($^{3+,5+}$), Nb($^{5+}$), Ta($^{5+}$), W($^{6+}$). Full elucidation of valence state behavior may require direct analysis by Mossbauer Spectroscopy or other means.

Texturally, intermediate and proximal rutile from Animal Pond shows numerous inclusions of ilmenite, titanite, and calcite (Fig. 4.2e,f). Depth profiling during SIMS analysis, however, showed relatively homogeneous Fe and Mn contents throughout the rutile crystals. The higher concentrations of Fe and Mn in rutile from the essentially barren Animal Pond in comparison to that from Stog’er Tight and Argyle (Fig. 4.3c) are empirically associated with a lack of extensive Au-related hydrothermal alteration of Fe-Ti phases to rutile. This may be a consequence of high Fe and Mn in rutile linked to formation during the first sequence of epidote-albite alteration at Animal Pond, which was not effectively removed by overprinting by the second sequence of quartz-albite-ankerite-Fe-chlorite-rutile-pyrite-native gold alteration, as it was at Argyle and Stog’er Tight.

The W and Sn contents of rutile have been applied to discriminate between rutile from barren and mineralized rocks for a wide range of metamorphosed metallic ore deposits, utilizing the Ti - 100*(Fe + Cr + V) - 1000*W ternary diagram (Clark and Williams-Jones, 2004). However, recent studies have shown that rutile from unmineralized magmatic and metamorphic rocks can accommodate W and Sn in similar concentrations to that associated with metallic ore deposits (Agangi et al., 2019). Further, high contents of W in hydrothermal rutile might be indicative of leaching of regionally specific W-rich metamorphic fluid sources or country rocks, as in the case of W-bearing rutile from the Jiaodong gold province in China (Yang et al., 2018). Therefore, W concentration in rutile may not be a geochemical feature that can be unequivocally linked to hydrothermal Au mineralization. Figure 4.6b shows the Ti - 100*(Fe + Cr + V) - 1000*W plot for rutile analyses from the studied orogenic gold occurrences. As observed in this figure, most of the rutile from the mineralized Stog'er Tight and Argyle orogenic gold deposits falls within the field of mineralized rutile established by Clark and Williams-Jones (2004), while rutile from the unmineralized Animal Pond prospect plots outside of that field. Some of the rutile samples from the mineralized Stog'er Tight and Argyle deposits show low concentrations of W (Table 4.3) and plot outside of the "Mineralized" rutile field of Clark and Williams-Jones (2004) (Fig. 4.6b), supporting the equivocal association of W with hydrothermal Au mineralization in the Baie Verte region. Importantly, Plavsa et al. (2018) used the same Ti - 100*(Fe + Cr + V) - 1000*W plot in order to effectively differentiate between the titania polymorphs rutile, anatase, and brookite. In that study, samples of known rutile, anatase, and brookite from mineralized and barren ore systems were analyzed in order to elucidate systematic compositional variations between these three titania polymorphs. Plavsa et al. (2018) reported that concentrations of key ore discriminator elements such as Fe, Cr, V, W, Sn, and Sb are systematically lower in anatase and brookite. The titania polymorph fields established by Plavsa et al. (2018) are also shown in Figure 4.6b. The majority of rutile analyses from the mineralized Stog'er Tight and Argyle deposits plot inside or close to the rutile polymorph field (Fig. 4.6b), while rutile analyses from the barren Animal Pond prospect plot inside or close to the brookite polymorph field (Fig. 4.6b). Agangi et al. (2019) studied rutile polymorph samples from a wide range of orogenic gold occurrences and found that some of those rutile samples plotted in the brookite field of the Ti - 100*(Fe + Cr + V) - 1000*W, suggesting that the discrimination of titania polymorphs might not be able to accurately be use for that purpose. Nevertheless, Figure 4.6b strongly implies the presence of brookite in the Animal Pond samples. This is a potentially useful discovery. Trace element analyses of titania polymorphs (whether rutile or brookite), especially by SIMS, still provides a strong discrimination between barren and fertile occurrences (i.e., Fig. 4.4). However, the characterization of a non-rutile polymorph as characteristic of barren occurrences provides an extra dimension that could be used in the assessment of both hard rock and till samples. In the case of till surveys, samples that plot in or near the brookite (or anatase) fields on the Ti – 100*(Fe + Cr + V) – 1000*W plot following initial microanalysis by EPMA or SIMS could then be selectively assessed for polymorph type using EBSD (Electron Backscatter Diffraction) or Raman spectroscopy. Future research should incorporate explicit identification of titania polymorphs in orogenic gold occurrences from the Baie Verte region.

Antimony has been shown to be enriched in rutile from various gold deposits (Agangi et al., 2019). In fact, Sb has been reported to be stoichiometrically incorporated in the rutile structure (Verberne et al., 2017), possibly through the aforementioned $2Ti^{4+} = M^{3+} + M^{5+}$ coupled substitution, where Sb^{5+} can substitute for Nb^{5+} (Smith and Perseil, 1997). This coupled substitution is believed to be controlled by temperature (Smith and Perseil, 1997; Agangi et al., 2019), with higher Sb^{5+} contents in rutile suggesting higher temperature of formation. In addition, our SIMS PCA results reveal a strong connection between Sb and Sn, which form an elemental cluster with virtually the same direction and length loadings (Figs. 4.5a,b). This observation suggests the high mobility of both Sb and Sn in hydrothermal solutions, with their incorporation into the structure of rutile being associated to the same processes.

The Sb content of rutile from orogenic gold deposits in the Baie Verte region and elsewhere, as well as from unmineralized metamorphic and magmatic rocks, is compared in Figure 4.6c. Antimony contents in rutile from the Animal Pond, Stog’er Tight, and Argyle occurrences are comparable to those reported for orogenic gold deposits in Western Australia, South Africa, and Ghana (Fig. 4.6c). However, higher amounts of Sb are observed in rutile from mineralized samples from the Stog’er Tight and Argyle orogenic gold deposits, in contrast with lower Sb contents in rutile from the essentially barren Animal Pond prospect (Fig. 4.6c). Rutile of metamorphic origin from various global locations consistently shows Sb contents of <10 ppm, coupled with generally <1000 ppm W (Fig. 4.6c). In a similar fashion, rutile of magmatic origin generally also contains less than 10 ppm Sb, although with generally higher average W contents than metamorphic rutile (Fig. 4.6c). Rutile with Sb contents of >10 ppm is mostly related to orogenic gold mineralization (Fig. 4.6c). In rutile from the studied orogenic gold occurrences of the Baie Verte region, Sb contents range between 34 ppm and 582 ppm (Figs. 4.3b and 4.6c). However, rutile from the economically mineralized Stog'er Tight and Argyle deposits generally shows Sb values above 80-100 ppm, whereas rutile from the barren Animal Pond prospect shows Sb contents below 66 ppm (Figs. 4.3b and 4.6c). Even though these observed differences in Sb concentrations in rutile are quite narrow considering the existing database, these results are in broad agreement with those reported by Agangi et al. (2019) and support the significance of Sb as a strong discriminator for rutile related to orogenic gold mineralization globally. In particular, they are specifically useful in the Baie Verte region to discern Sb-rich hydrothermal rutile related to Au mineralization from Sb-poor rutile formed during Au-poor hydrothermal events. Based on our study, Sb is even more effective when used as part of a multi-element discrimination incorporating the elements shown in Figure 4.5.

In summary, hydrothermal rutile (and/or brookite) associated with Au mineralization at Baie Verte shows the following geochemical characteristics: (i) statistically correlated by PCA with Ta, Nb, Sn, and Sb; (ii) parallels the natural abundance of Nb/Ta, comparable with other orogenic gold occurrences and barren metamorphic and magmatic rocks; (iii) low Fe and Mn content; and (iv) high contents of Sb (> 80-100 ppm).

4.6.3. Rutile geochemistry as a potential exploration tool for orogenic Au in the Baie Verte region of Newfoundland

The results reported here have potential application to mineral exploration efforts in the Baie Verte region. To test this potential, soil/till deposits covering relevant geophysical or structural anomalies in the Baie Verte region could be sampled, and detrital rutile grains then concentrated by conventional heavy mineral separation techniques (e.g., magnetic, heavy liquid, or other density methods). This approach requires subsequent analysis of large numbers of detrital mineral grains. Consequently, rutile separates could initially be analyzed by EPMA for readily detectable elements including those in Fig. 4.4a (Ca, Al, Si, Fe, Mn, V, Zr, Nb). Ideally, an enhanced EPMA setup to provide optimal detection limits for Sb using WDS could be added in order to also identify Sb-rich rutile (>80-100 ppm Sb). The subset of samples with similar EPMA-analyzed characteristics to the proximal samples in this study could be subjected to verification analysis using SIMS. Areas with high concentration of rutile with proximal characteristics could then be targeted for further exploration (e.g., trenching or diamond drilling).

In the case of rock samples, from drill core or outcrop, basic petrography could be used discern the level of textural "maturity" of Fe-Ti phases as a means to estimate the potential for gold mineralization. As observed in this study, hydrothermally-altered gabbroic rocks closely related to Au mineralization (proximal alteration zones) contain relatively inclusion-free rutile as the only Fe-Ti oxide phase present in the sample. The presence of other Fe-Ti phases, such as magnetite, hematite, ilmenite, or titanite, may be indicative of intermediate to distal settings devoid of significant Au mineralization. This petrographic exploration tool could be enhanced by the use of automated instrumentation, such as the mineral liberation analyzer (SEM-MLA), where the assemblage of Fe-Ti phases could be enumerated for multiple samples. Samples deemed hydrothermally "mature" (containing predominantly rutile without substantial inclusions of other

Fe-Ti phases), could subsequently be analyzed by in situ microanalytical techniques, such as EPMA or SIMS, to document major and trace element contents for the purpose of confirming potential association with Au mineralization.

Based on the implication that brookite may be characteristic of barren occurrences, a component of selective characterization of TiO_2 polymorph type is recommended as a part of any soil/till or hard rock survey.

4.7. Conclusions

The hydrothermal evolution of Fe-Ti phases in orogenic gold occurrences in the Baie Verte region resulted in the formation of hydrothermal rutile, and variations in its chemical composition show potential as an exploration vector in the area. Hydrothermal rutile was the result of progressive alteration of orthomagmatic Fe-rich phases, particularly magnetite, Ti-magnetite, and/or ilmenite. The hydrothermal alteration of such Fe-rich phases evolved towards more Ti-rich phases (titanite, rutile) with increasing alteration intensity and proximity to orogenic veins. Wallrock sulfidation is suggested as the primary mechanism responsible for the destabilization of $Au(HS)_2^-$ complexes carried by hydrothermal fluids and the consequent precipitation of Au, but also resulted in the concomitant formation of abundant hydrothermal rutile. In hydrothermally-altered rocks proximal to auriferous veining at Stog'er Tight and Argyle, rutile is the only Fe-Ti phase observed, whereas remnant titanite, magnetite, and ilmenite are present in proximal alteration at Animal Pond, suggesting lower fluid/rock ratios and a less intense Au-related hydrothermal alteration episode at Animal Pond. . Further, the measured trace element contents for Animal Pond samples strongly imply that the TiO_2 polymorph there may be brookite rather than rutile. Empirically, the samples from Animal Pond shows significantly higher Fe and Mn contents, whereas rutile from the Stog’er Tight and Argyle deposits shows distinct enrichments in Nb, Sb, Sn, and Ta. Explicit characterization of the Animal Pond samples for polymorph species is an important subject for additional research, as it provides a potentially useful additional criterion for comparing fertile and barren occurrences.

Principal component analysis of the multi-element data from EPMA and SIMS microanalysis revealed shifts of trace element clusters between deposits and with proximity to mineralization. With specific reference to SIMS-based analysis (Fig. 4.5a,b), three well-separated populations are recognized: i) rutile/brookite from proximal zone alteration at Animal Pond is, as for the EPMA-based analyses, associated with a Ca(-Mn)-Fe-Zr cluster, ii) rutile from intermediate zone alteration at Argyle is associated with a broad Cr-As-Sc-Y(-V-W-P) cluster, and iii) rutile from proximal zone alteration at both Stog’er Tight and Argyle is most strongly associated with Sb-Sn and Ta-Nb clusters. The latter observation is compatible with the observations by Agangi et al. (2019) and others (as summarized in Fig 4.6), which suggests that Sb is a useful discriminator between rutile associated with orogenic gold occurrences and rutile formed in non-auriferous metamorphic and igneous rocks. For orogenic gold occurrences in the Baie Verte region, rutile from proximal alteration zones of the Au-mineralized Stog’er Tight and Argyle deposits contains Sb concentrations > 80-100 ppm, while rutile from the barren Animal Pond prospect contains Sb concentrations < 66 ppm. The recognition of the characteristically Fe-Mn-poor and Sb-enriched composition, and distinct multi-element trace element signature, of rutile associated with the broad (10s of m) alteration haloes surrounding auriferous veins has significant potential application to the exploration for orogenic gold deposits in the Baie Verte region and elsewhere.

4.8. Acknowledgements

This research was supported by funding from Anaconda Mining Ltd., the GeoExplore program of the Newfoundland and Labrador Department of Industry, Energy, and Technology, and an NSERC Collaborative Research and Development Grant to SJP. Additional funding was provided by an NSERC Discovery Grant (RGPIN/005037-2017) to GDL. The authors acknowledge the support in the field by Carly Mueller, as well as drill core access and sampling permission from Anaconda Mining Inc. We thank David Copeland and Paul McNeill of Anaconda Mining for their assistance and support throughout this project. Gratitude goes to Dylan Goudie (MAF) and Wanda Aylward (Terra) for providing excellent microbeam conditions in the Memorial University CREAIT Facilities. Glenn Piercey of Memorial University CREAIT MAF is thanked for his care and patience in facilitating the SIMS analyses, as well as Pablo Valverde-Vaquero for providing the Rutile 123 reference material.

4.9. References

Adlakha, E.E., Hattori, K., Kerr, M.J., Boucher, B.M., 2020. The origin of Ti-oxide minerals below and within the eastern Athabasca Basin, Canada. American Mineralogist 105(12), 1875-1888. https://doi.org/10.2138/am-2020-7235

Agangi, A., Reddy, S.M., Plavsa, D., Fougerouse, D., Clark, C., Roberts, M., Johnson, T.E., 2019. Antimony in rutile as a pathfinder for orogenic gold deposits. Ore Geology Reviews 106, 1-11. https://doi.org/10.1016/j.oregeorev.2019.01.018

Aitchison, J., 1982. The statistical analysis of compositional data. Journal of the Royal Statistical Society: Series B (Methodological) 44(2), 139-160. https://doi.org/10.1111/j.2517-6161.1982.tb01195.x

Anderson, S.D., Jamieson, R.A., Reynolds, P.H., Dunning, G.R., 2001. Devonian extension in northwestern Newfoundland: ^{40}Ar/^{39}Ar and U-Pb data from the Ming's Bight area, Baie Verte Peninsula. The Journal of Geology 109(2), 191-211. https://doi.org/10.1086/319237

Angiboust, S., Harlov, D., 2017. Ilmenite breakdown and rutile-titanite stability in metagranitoids: natural observations and experimental results. American Mineralogist 102(8), 1696-1708. https://doi.org/10.2138/am-2017-6064

Barth, M. G., McDonough, W. F., Rudnick, R. L., 2000. Tracking the budget of Nb and Ta in the continental crust. Chemical Geology 165(3-4), 197-213. https://doi.org/10.1016/S0009-2541(99)00173-4

Bédard, J. H., Lauziere, K., Tremblay, A., Sangster, A. L., Douma, S., Dec, T., 2000. Betts Cove ophiolite and its cover rocks. Geological Survey of Canada Bulletin 550, 76 pp.

Belousova, E.A., Griffin, W.L., O'Reilly, S.Y., Fisher, N.I., 2002. Apatite as an indicator mineral for mineral exploration: trace-element compositions and their relationship to host rock type. Journal of Geochemical Exploration 76(1), 45-69. https://doi.org/10.1016/S0375-6742(02)00204-2

Bierlein, F.P. and Crowe, D.E., 2000. Phanerozoic Orogenic Lode Gold Deposits. In Gold in 2000 (S.G. Hagemann and P.E. Brown, eds.). Reviews in Economic Geology 13, 103-140. https://doi.org/10.5382/Rev.13.03

Castonguay, S., Skulski, T., van Staal., C., Currie, M., 2009. New insights on the structural geology of the Pacquet Harbour Group and Point Rousse Complex, Baie Verte Peninsula, Newfoundland. Current research, Newfoundland and Labrador Department of Natural Resources, Geological Survey Report 09-1, 147-158.

Castonguay, S., van Staal, C.R., Joyce, N., Skulski, T., Hibbard, J.P., 2014. Taconic metamorphism preserved in the Baie Verte Peninsula, Newfoundland Appalachians: Geochronological evidence for ophiolite obduction and subduction and exhumation of the leading edge of the Laurentian (Humber) margin during closure of the Taconic Seaway. Geoscience Canada 41(4), 459-482. https://doi.org/10.12789/geocanj.2014.41.055

Clark, J.R. and Williams-Jones, A.E., 2004. Rutile as a potential indicator mineral for metamorphosed metallic ore deposits. Rapport Final de DIVEX, Sous-projet SC2: Montreal, 17 p.

Colvine, A.C., Fyon, J.A., Heather, K.B., Marmont, S., Smith, P.M., Troop, D.G., 1988. Archean lode gold deposits in Ontario. Ontario Geological Survey, Miscellaneous Paper 139, 136 p.

Copeland, D.A., Pitman, C., Evans, D.T.W., McNeill, P., Slepcev, G., 2015. Mineral resource and mineral reserve update on the Pine Cove Mine and mineral resource estimate on the Stog'er Tight deposit, Point Rousse Project Baie Verte. NI-43-101 Technical Report: Anaconda Mining Inc., Newfoundland and Labrador, Canada, 249 p.

Corfu, F. and Davis, D.W., 1991. Comment on "Archaean hydrothermal zircon in the Abitibi greenstone belt: constraints on the timing of gold mineralization" by J.C. Claoue-Long, R.W. King, and R. Kerrich. Earth and Planetary Sciences Letters 104(2-4), 545-552. https://doi.org/10.1016/0012-821X(91)90229-B

Deditius, A.P., Utsunomiya, S., Renock, D., Ewing, R.C., Ramana, C.V., Becker, U., Kesler, S.E., 2008. A proposed new type of arsenian pyrite: composition, nanostructure and geological significance. Geochimica et Cosmochimica Acta 72(12), 2919-2933. https://doi.org/10.1016/J.GCA.2008.03.014

Deditius, A.P., Reich, M., Kesler, S.E., Utsunomiya, S., Chryssoulis, S.L., Walshe, J., Ewing, R.C., 2014. The coupled geochemistry of Au and As in pyrite from hydrothermal ore deposits. Geochimica et Cosmochimica Acta 140, 644-670. https://doi.org/10.1016/j.gca.2014.05.045

Dostal, J., Kontak, D.J., Chatterjee, A.K., 2009. Trace element geochemistry of scheelite and rutile from metaturbidite-hosted quartz vein gold deposits, Meguma Terrane, Nova Scotia, Canada: genetic implications. Mineralogy and Petrology 97(95), 95-109. https://doi.org/10.1007/s00710-009-0067-0

Dubé, B., 1990. A preliminary report on contrasting structural styles of gold-only deposits in western Newfoundland. Current Research, Geological Survey of Canada, Paper 90-1B, 77-90.

Dubé, B., Poulsen, H.K., Guha, J., 1989. The effects of layer anisotropy on auriferous shear zones: The Norbeau Mine, Quebec. Economic Geology 84(4), 871-878. https://doi.org/10.2113/gsecongeo.84.4.871

Dubé, B., Lauziére, K., and Gaboury, D., 1991. Structural control on the mesothermal vein-type, Rendell-Jackman gold deposit, Springdale Peninsula, Newfoundland. Newfoundland Geological Survey, Department of Mines and Energy, 81.

Dubé, B., Lauziére, K., and Gaboury, D., 1992. Preliminary report on the structural control of the Rendell-Jackman gold deposit, Springdale Peninsula, Newfoundland. Current Research, Geological Survey of Canada, Paper 92-1D, 1-10.

Dubé, B., Lauziére, K., Poulsen, H.K., 1993. The Deer Cove deposit: An example of "thrust'-related breccia-vein type gold mineralization in the Baie Verte Peninsula, Newfoundland. Geological Survey, Newfoundland and Labrador Department of Natural Resources, Current Research, Report 93-ID, 1-10.

Dubé, B. and Gosselin, P., 2007. Greenstone-hosted quartz-carbonate vein deposits. In Mineral Deposits of Canada: A Synthesis of Major Deposit-Types, District Metallogeny, the Evolution of Geological Provinces, and Exploration Methods (W.D. Goodfellow, ed.). Geological Association of Canada, Mineral Deposits Division, Special Publication No. 5, 49-73.

Evans, D.T.W., 2004. Epigenetic gold occurrences, Baie Verte Peninsula, (NTS 12H/09, 16 and 12I/01) Newfoundland. Government of Newfoundland and Labrador, Department of Natural Resources, Geological Survey, Mineral Resource Report No. 11, 157 p.

Foley, S.F., Barth, M.G., Jenner, G.A., 2000. Rutile/melt partition coefficients for trace elements and an assessment of the influence of rutile on the trace element characteristics of subduction zone magmas. Geochimica et Cosmochimica Acta 64(5), 933-938. https://doi.org/10.1016/S0016-7037(99)00355-5

Frimmel, H.E., 2008. Earth's continental crustal gold endowment. Earth and Planetary Science Letters 267(1-2), 45-55. https://doi.org/10.1016/j.epsl.2007.11.022

Frimmel, H.E., 2018. Episodic concentration of gold to ore grade through Earth's history. Earth-Science Reviews 180, 148-158. https://doi.org/10.1016/j.earscirev.2018.03.011

Gandhi, S.M. and Sarkar, B.C., 2016. Geochemical Exploration. In Essentials of Mineral Exploration and Evaluation (S.M. Gandhi and B.C. Sarkar, eds.). Elsevier, 125-158. https://doi.org/10.1016/B978-0-12-805329-4.00013-2

Goldfarb, R.J. and Groves, D.I., 2015. Orogenic gold: Common or evolving fluid and metal sources through time. Lithos 233, 2-26. https://doi.org/10.1016/j.lithos.2015.07.011

Goldfarb, R.J., Baker, T., Dubé, B., Groves, D.I., Hart, C.J.R., Gosselin, P., 2005. Distribution, Character, and Genesis of Gold Deposits in Metamorphic Terranes. Economic Geology 100th Anniversary Volume, 407-450. https://doi.org/10.5382/AV100.14

Griffin, W.L. and Ryan, C.G., 1995. Trace elements in indicator minerals: area selection and target evaluation in diamond exploration. Journal of Geochemical Exploration 53(1-3), 311-337. https://doi.org/10.1016/0375-6742(94)00015-4

Groves, D.I., Phillips, G.N., 1987. The genesis and tectonic controls on Archaean gold deposits of the Western Australian Shield: A metamorphic-replacement model. Ore Geology Reviews 2(4), 287-322. https://doi.org/10.1016/0169-1368(87)90009-6

Groves, D.I., Goldfarb, R.J., Gebre-Mariam, M., Hagemann, S.G., Robert, F., 1998. Orogenic gold deposits—a proposed classification in the context of their crustal distribution and relationship to other gold deposit types. Ore Geology Reviews 13(1-5), 7-27. https://doi.org/10.1016/S0169-1368(97)00012-7

Groves, D.I., Santosh, M., Deng, J., Wang, Q., Yang, L., Zhang, L., 2019. A holistic model for the origin of orogenic gold deposits and its implications for exploration. Mineralium Deposita 55, 275-292. https://doi.org/10.1007/s00126-019-00877-5

Gurney, J.J., Helmstaedt, H., Moore, R.O., 1993. A review of the use and application of mantle mineral geochemistry in diamond exploration. Pure and Applied Chemistry 65(12), 2423-2442. https://doi.org/10.1351/pac199365122423

Gurney, J.J. and Zweistra, P., 1995. The interpretation of the major element compositions of mantle minerals in diamond exploration. Journal of Geochemical Exploration 53(1-3), 293-309. https://doi.org/10.1016/0375-6742(94)00021-3

Hibbard, J., 1983. Geology of the Baie Verte Peninsula, Newfoundland. Government of Newfoundland and Labrador, Department of Mines and Energy, Mineral Development Division, v. 2, 280 p.

Huard, A., 1990. The Noranda/Impala Stog'er Tight deposit. International Association on the Genesis of Ore Deposits, 8th Symposium, Field Trip Guide, 173-177.

Jiang, S.Y., 2000. Controls on the mobility of high field strength elements (HFSE), U, and Th in an ancient submarine hydrothermal system of the Proterozoic Sullivan Pb-Zn-Ag deposit, British Columbia, Canada. Geochemical Journal 34(5), 341-348. https://doi.org/10.2343/geochemj.34.341

Jiang, S.Y., Wang, R.C., Xu, X.S., Zhao, K.D., 2005. Mobility of high field strength elements (HFSE) in magmatic-, metamorphic-, and submarine-hydrothermal systems. Physics and Chemistry of the Earth 30(17-18), 1020-1029. https://doi.org/10.1016/j.pce.2004.11.004

Jochum K.P., Weis U., Stoll B., Kuzmin D., Yang Q., Raczek I., Jacob D.E., Stracke , A., Birbaum, K., Frick, D.A., Günther, D., Enzweiler J., 2011. Determination of reference values for NIST SRM 610-617 glasses following ISO guidelines. Geostandards and Geoanalytical Research, 35(4) , 397-429. https://doi.org/10.1111/j.1751-908X.2011.00120.x

Kerr, A. and Selby, D., 2012. The timing of epigenetic gold mineralization on the Baie Verte Peninsula, Newfoundland, Canada: new evidence from Re-Os pyrite geochronology. Mineralium Deposita 47, 325-337. https://doi.org/10.1007/s00126-011-0375-2

Kirkwood, D. and Dubé, B., 1992. Structural control of sill-hosted gold mineralization: the Stog'er Tight Gold Deposit. Current Research, Geological Survey of Canada, Report 92-1D, 211-221.

Klemme, S., Prowatke, S., Hametner, K., Günther, D., 2005. Partitioning of trace elements between rutile and silicate melts: Implications for subduction zones. Geochimica et Cosmochimica Acta 69(9), 2361-2371. https://doi.org/10.1016/j.gca.2004.11.015

Linnen, R. and Che, X., 2010. Evaluation of titanite as an indicator mineral for tungsten-skarn mineralization. In Yukon exploration and Geology 2009 (K.E. MacFarlane, L.H. Weston, L.R. Blackburn, eds.). Yukon Geological Survey, 223-228.

Lipson, R., 2014. The promise and perils of porphyry deposits in the future gold production. SEG Newsletter 98, 1-21. https://doi.org/10.5382/SEGnews.2014-98.fea

Lougheed, H.D., McClenaghan, M.B., Layton-Matthews, D., Leybourne, M., 2020. Exploration potential of fine-fraction heavy mineral concentrates from till using automated mineralogy: a case study from the Izok Lake Cu-Zn-Pb-Ag VMS deposit, Nunavut, Canada. Minerals 10(4), 310. https://doi.org/10.3390/min10040310

Luvizotto, G.L. and Zack, T., 2009. Nb and Zr behavior in rutile during high-grade metamorphism and retrogression: An example from the Ivrea-Verbano Zone. Chemical Geology 261(3-4), 303-317. https://doi.org/10.1016/j.chemgeo.2008.07.023

Lydon, J.W., 2007. An overview of the economic and geological contexts of Canada's major mineral deposit types. In Mineral Deposits of Canada: A synthesis of major deposit-types, district metallogeny, the evolution of geological provinces, and exploration methods (W.D. Goodfellow, ed.). Geological Association of Canada, Mineral Deposits Division, Special Publication No. 5, 3-48.

McClenaghan, M.B., 2005. Indicator mineral methods in mineral exploration. Geochemistry: Exploration, Environment, Analysis 5(3), 233-245. https://doi.org/10.1144/1467-7873/03-066

McClenaghan, M.B., 2011. Overview of common processing methods for recovery of indicator minerals from sediment and bedrock in mineral exploration. Geochemistry: Exploration, Environment, Analysis 11, 265-278. https://doi.org/10.1144/1467-7873/10-IM-025

McClenaghan, M.B. and Paulen, R.C., 2018. Application of till mineralogy and geochemistry to mineral exploration. In Past Glacial Environments (J. Menzies and J.J.M. van der Meer, eds.). Elsevier, 2nd Edition, 689-751. https://doi.org/10.1016/B978-0-08-100524-8.00022-1

McClenaghan, M.B., Plouffe, A., McMartin, I., Campbell, J.E., Spirito, W.A., Paulen, R.C., Garrett, R.G., Hall, G.E.M., 2013. Till sampling and geochemical analytical protocols used by the Geological Survey of Canada. Geochemistry: Exploration, Environment, Analysis 13, 285-301. https://doi.org/10.1144/geochem2011-083

Menzel, M. D., Garrido, C. J., López Sánchez-Vizcaíno, V., Marchesi, C., Hidas, K., Escayola, M. P., Delgado Huertas, A., 2018. Carbonation of mantle peridotite by CO2-rich fluids: the formation of listvenites in the Advocate ophiolite complex (Newfoundland, Canada). Lithos 323, 238-261. https://doi.org/10.1016/j.lithos.2018.06.001

Mikucki, E.J., 1998. Hydrothermal transport and depositional processes in Archean lode-gold systems: A review. Ore Geology Reviews 13(1-5), 307-321. https://doi.org/10.1016/S0169-1368(97)00025-5

Morishita, Y., Shimada, N., Shimada, K., 2018. Invisible gold in arsenian pyrite from the high-grade Hishikari gold deposit, Japan: significance of variation and distribution of Au/As ratios in pyrite. Ore Geology Reviews 95, 79-93. https://doi.org/10.1016/J.OREGEOREV.2018.02.029

Mücke, A. and Cabral, A.R., 2005. Redox and nonredox reactions of magnetite and hematite in rocks. Chemie der Erde 65(3), 271-278. https://doi.org/10.1016/j.chemer.2005.01.002

Murad, E., Cashion, J.D., Noble, C.J., Pilbrow, J.R., 1995. The chemical state of Fe in rutile from an albitite in Norway. Mineralogical Magazine 59(3), 557-560. https://doi.org/10.1180/minmag.1995.059.396.17

Nesbitt, R.W., Pascual, E., Fanning, C.M., Toscano, M., Saez, R., Almodovar, G.R., 1999. U-Pb dating of stockwork zircons from the eastern Iberian Pyrite belt. Journal of the Geological Society 156(1), 7-10. https://doi.org/10.1144/gsjgs.156.1.0007

Oviatt, N.M., Gleeson, S.A., Paulen, R.C., McClenaghan, M.B., Paradis, S., 2015. Characterization and dispersal of indicator minerals associated with the Pine Point Mississippi Valley-type (MVT) district, Northwest Territories, Canada. Canadian Journal of Earth Sciences 52(9), 776-794. https://doi.org/10.1139/cjes-2014-0108

Palarea-Albaladejo, J., and Martín-Fernández, J.A., 2013. Values below detection limit in compositional chemical data. Analytica Chimica Acta 764, 32-43. https://doi.org/10.1016/j.aca.2012.12.029

Paulen, R.C., Paradis, S., Plouffe, A., Smith, I.R., 2011. Pb and S isotopic composition of indicator minerals in glacial sediments from NW Alberta, Canada: implications for Zn-Pb base metal exploration. Geochemistry: Exploration, Environment, Analysis 11(4), 309-320. https://doi.org/10.1144/1467-7873/10-IM-032

Pawlowsky-Glahn, V. and Egozcue, J.J., 2006. Compositional data and their analysis: an introduction. In Compositional Data Analysis in the Geosciences: From Theory to Practice (A. Buccianti, G. Mateu-Figueras, V. Pawlowsky-Glahn, eds.) Geological Society, London, Special Publication 264(1), 1-10.https://doi.org/10.1144/GSL.SP.2006.264.01.01

Pawlukiewicz, M., 2019. Hydrothermal reconstruction and lithogeochemistry of the Argyle orogenic gold deposit, Baie Verte, Newfoundland. Unpublished Master Thesis, Memorial University of Newfoundland, 426 pp.

Pearce, N.J.G, Perkins, W.T., Westgate, J.A., Gorton, M.P., Jackson, S.E, Neal, C.R., Chenery, S.P., 1997. A compilation of new and published major and trace element data for NIST SRM 610 and NIST SRM 612 glass reference materials. Geostandards Newsletter 21(1), 115-144. https://doi.org/10.1111/j.1751-908X.1997.tb00538.x

Phillips, G.N., 1986. Geology and Alteration in the Golden Mile, Kalgoorlie. Economic Geology 81(4), 779-808. https://doi.org/10.2113/gsecongeo.81.4.779

Phillips, G.N., 2013. Australian and global setting for gold in 2013. In Proceedings world gold 2013, Brisbane, Australia, 26-29 September 2013, The Australasian Institute of Mining and Metallurgy, 15-21.

Phillips, G.N. and Groves, D.I., 1983. The nature of Archaean gold bearing fluids as deduced from gold deposits from Western Australia. Journal of the Geological Society of Australia 30(1-2), 25-39. https://doi.org/10.1080/00167618308729234

Phillips, G.N. and Powell, R., 1993. Link between Gold Provinces. Economic Geology 88(5), 1084-1098. https://doi.org/10.2113/gsecongeo.88.5.1084

Phillips, G.N. and Powell, R., 2010. Formation of gold deposits: a metamorphic devolatilization model. Journal of Metamorphic Geology 28(6), 689-718. https://doi.org/10.1111/j.1525-1314.2010.00887.x

Pisiak, L.K., Canil, D., Lacourse, T., Plouffe, A., Ferbey, T., 2017. Magnetite as an indicator mineral in the exploration of porphyry deposits: A case study in till near the Mount Polley Cu-Au Deposit, British Columbia, Canada. Economic Geology 112(4), 919-940. https://doi.org/10.2113/econgeo.112.4.919

Pitcairn, I.K., Craw, D., Teagle, D.A.H., 2014. The gold conveyor belt: Large-scale gold mobility in an active orogen. Ore Geology Reviews 62, 129-142. https://doi.org/10.1016/j.oregeorev.2014.03.006

Pitcairn, I.K., Craw, D., Teagle, D.A.H., 2015. Metabasalts as sources of metals in orogenic gold deposits. Mineralium Deposita 50, 373-390. https://doi.org/10.1007/s00126-014-0547-y

Pitman, C., Cullen, M., Harrington, M., Copeland, D., McNeill, P., Bullock, K., Budgell, C., Cramm, J., 2020. NI 43-101 Technical report, mineral resource and mineral reserve update on the Point Rousse project, Baie Verte, Newfoundland and Labrador, Canada. Anaconda Mining Technical Report NI43-101, 300 pp.

Pizarro, H., Campos, E., Bouzari, F., Rousse, S., Bissig, T., Gregoire, M., Riquelme, R., 2020. Porphyry indicator zircons (PIZs): Application to exploration of porphyry copper deposits. Ore Geology Reviews 126, 103771. https://doi.org/10.1016/j.oregeorev.2020.103771

Plavsa, D., Reddy, S.M., Agangi, A., Clark, C., Kylander-Clark, A., Tiddy, C.J., 2018. Microstructural, trace element and geochronological characterization of TiO2 polymorphs and implications for mineral exploration. Chemical Geology 476, 130-149. https://doi.org/10.1016/j.chemgeo.2017.11.011

Porter, J.K., McNaughton, N.J., Evans, N.J., McDonald, B.J., 2020. Rutile as a pathfinder for metals exploration. Ore Geology Reviews 120, 103406. https://doi.org/10.1016/j.oregeorev.2020.103406

Pouchou, J.L. and Pichoir, F., 1984. A new model for quantitative analyses. I. Application to the analysis of homogeneous samples. La Recherche Aérospatiale, 3, 13-38.

Pouchou, J.L. and Pichoir, F., 1985. ‘‘PAP’’ correction procedure for improved quantitative microanalysis. Pp. 104-106 in: Microbeam Analysis (J.T. Armstrong, editor). San Francisco Press, San Francisco, California, USA.

Ramezani, J., 1992. The geology, geochemistry and U-Pb geochronology of the Stog’er Tight Gold Prospect, Baie Verte Peninsula, Newfoundland. Unpublished Master Thesis. Department of Earth Sciences, Memorial University of Newfoundland, 312 pp.

Ramezani, J., Dunning, G.R., Wilson, M.R., 2000. Geologic setting, geochemistry of alteration, and U-Pb age of hydrothermal zircon from the Silurian Stog’er Tight gold prospect, Newfoundland Appalachians, Canada. Exploration Mining Geology 9(3-4), 171-188. https://doi.org/10.2113/0090171

Reich, M., Kesler, S.E., Utsunomiya, S., Palenik, C.S., Chryssoulis, S.L., Ewing, R.C., 2005. Solubility of gold in arsenian pyrite. Geochimica et Cosmochimica Acta 69(11), 2781-2796. https://doi.org/10.1016/j.gca.2005.01.011

Ren, Y., Fei, Y., Yang. J., 2009. SiO_2 solubility in rutile at high temperature and high pressure. Journal of Earth Sciences 20, 274-283. https://doi.org/10.1007/s12583-009-0025-0

Ridley, J.R. and Diamond, L.W., 2000. Fluid chemistry of orogenic lode deposits and implications for genetic models. Economic Geology Reviews 13, 141-162. https://doi.org/10.5382/Rev.13.04

Robert, F., Boullier, A.M., Firdaous, K., 1995. Gold-quartz veins in metamorphic terranes and their bearing on the role of fluids in faulting. Journal of Geophysical Research 100(B7), 12861-12879. https://doi.org/10.1029/95JB00190

Saunders, J.A., Hofstra, A.H., Goldfarb, R.J., Reed, M.H., 2014. Geochemistry of hydrothermal gold deposits. In Treatise on Geochemistry (H.D. Holland and K.K. Turekian, eds.), Elsevier, 383-424.

Sciuba, M. and Beaudoin, G., 2021. Texture and trace element composition of rutile in orogenic gold deposits. Economic Geology 116(8), 1865-1892. https://doi.org/10.5382/econgeo.4857

Scott, K.M., 2005. Rutile geochemistry as a guide to porphyry Cu-Au mineralization, Northparkes, New South Wales, Australia. Geochemistry: Exploration, Environment, Analysis 5(3), 247-253. https://doi.org/10.1144/1467-7873/03-055

Scott, K.M. and Radford, N.W., 2007. Rutile compositions at the Big Bell Au deposit as a guide for exploration. Geochemistry: Exploration, Environment, Analysis 7(4), 353-361. https://doi.org/10.1144/1467-7873/07-135

Scott, K.M, Radford, N.W., Hough, R.M., Reddy, S.M., 2011. Rutile compositions in the Kalgoorlie Goldfields and their implications for exploration. Australian Journal of Earth Sciences 58(7), 803-812. https://doi.org/10.1080/08120099.2011.600334

Skublov, S.G., Zack, T., Berezin, A.V., Mel'nik, A.E., Rizvanova, N.G., 2013. In situ LA-ICP-MS investigation of the geochemistry and U-Pb age of rutile from the rocks of the Belomorian Mobile Belt. Geochemistry International 51(2), 164-171. https://doi.org/10.1134/S0016702912120051

Skulski, T., Castonguay, S., van Staal, C. R., Rogers, N., McNicoll, V., Kerr, A., Escayola, M., 2009. Baie Verte Peninsula: an evolving geological story. Geological Association of Canada, Newfoundland and Labrador Section, Annual Field Trip Guide, St. John's, Newfoundland, v. 60, 1-60.

Skulski, T., Castonguay, S., McNicoll, V., van Staal, C., Kidd, W., Rogers, N., Morris, W., Ugalde, H., Slavinski, H., Spicer, W., 2010. Tectonostratigraphy of the Baie Verte oceanic tract and its ophiolite cover sequence on the Baie Verte Peninsula. Geological Survey, Newfoundland and Labrador Department of Natural Resources, Current Research, Report 10-1, 315-337.

Smith, D.C. and Perseil, E.A., 1997. Sb-rich rutile in the manganese concentrations St. Marcel-Praborna, Aosta Valley, Italy: petrology and crystal-chemistry. Mineralogical Magazine 61(5), 655-669. https://doi.org/10.1180/minmag.1997.061.408.04

Sparrow, B., Barrett, S., Copeland, D.A., Walsh, M., 2017. Argyle Prospect Mineral Licenses 012433M (11th year) and 020060M (5th year) Point Rousse Project, Baie Verte Peninsula, NL NTS sheet 12H/16. Assessment Report: Anaconda Mining Inc., Newfoundland and Labrador, Canada, 481 p.

Stefánsson, A. and Seward, T.M., 2004. Gold(I) complexing in aqueous sulphide solutions to 500°C at 500 bar. Geochimica et Cosmochimica Acta 68(20), 4121-4143. https://doi.org/10.1016/j.gca.2004.04.006

Tomkins, A.G., 2013. On the source of orogenic gold. Geology 41(12), 1255-1256. https://doi.org/10.1130/focus122013.1

Urban, A.J., Hoskins, B.F., Grey, I.E., (1992): Characterization of V-Sb-W-bearing rutile from the Hemlo gold deposit, Ontario. The Canadian Mineralogist 30, 319-326.

Valverde-Vaquero, P., González, M., Beranoaguirre, A., Ibarguchi, J., 2016. Rutile chemistry and thermometry in eo-Variscan eclogites/granulites from the Cabo Ortegal and the Malpica-Tui complexes Química y termometría de rutilo en eclogitas/granulitas eo-Variscas de los complejos de Cabo Ortegal y Malpica-Tui. IX Congreso Geológico de España, September 2016, Geotemas 16(2) ISSN 1576-5172.

van Staal, C.R., Whalen, J.B., McNicoll, V.J., Pehrsson, S., Lissenberg, C.J., Zagorevski, A., van Breemen, O., Jenner, G.A., 2007. The Notre Dame arc and the Taconic orogeny in Newfoundland. In 4-D Framework of Continental Crust (R.D. Hatcher, M.P., Carlson, J.H. McBride, J.R., Martínez Catalán, eds.). Geological Society of America Memoir 200, 511-552. https://doi.org/10.1130/2007.1200(26)

van Staal, C.R., Barr, S.,M., Percival, J., 2012. Lithospheric architecture and tectonic evolution of the Canadian Appalachians and associated Atlantic Margin. In Tectonic styles in Canada: the LITHOPROBE perspective (J.A. Percival, F.A. Cook, and R.M. Clowes, eds.). Geological Association of Canada, Special Paper 49, 41-95.

Verberne, R., Reddy, S.M., Saxey, D.W., Rickard, W.D.A., Fougerouse, D., Plavsa, D., Agangi, A., 2017. Trace element nanoclusters in natural rutile (TiO_2) and their geological significance. In: 5th Australian Atom Prove Workshop, Magnetic Island, Australia.

Williams, H., 1979. Appalachian orogen in Canada. Canadian Journal of Earth Sciences 16(3), 792-807. https://doi.org/10.1139/e79-070

Williams, H. and St. Julien, P., 1982. The Baie Verte Brompton Line: Early Paleozoic continent ocean interface in the Canadian Appalachians. In Major Structural zones and faults of the northern Appalachians (P. St. Julien and J. Beland, eds.). Geological Association of Canada, Special Paper 24, 177-208.

Williams-Jones, A.E., Bowell, R.J., Migdisov, A.A., 2009. Gold in solution. Elements 5(5), 281-287. https://doi.org/10.2113/gselements.5.5.281

Yang, B., Xiang, Y., Gu, X., 2018. Tungsten-bearing rutile from the Jiaodong gold province, Shandong, China and its implication for gold mineralization. European Journal of Mineralogy 30(5), 975-980. https://doi.org/10.1127/ejm/2018/0030-2757

Ybarra, S., 2019. Hydrothermal alteration and lithogeochemistry of the Pine Cove orogenic gold deposit, Baie Verte Peninsula, Newfoundland, Canada. Unpublished Master Thesis, Memorial University of Newfoundland, 172 pp.

Zack, T., Kronz, A., Foley, S.F., Rivers, T., 2002. Trace element abundances in rutiles from eclogites and associated garnet mica schists. Chemical Geology 184(1-2), 97-122. https://doi.org/10.1016/S0009-2541(01)00357-6

Zhu, Y., An, F., Tan, J., 2011. Geochemistry of hydrothermal gold deposits: A review. Geoscience Frontiers 2(3), 367-374. https://doi.org/10.1016/j.gsf.2011.05.006

Zoheir, B., Akawy, A., Hassan, I., 2008. Role of fluid mixing and wallrock sulfidation in gold mineralization at the Semna mine area, central Eastern Desert of Egypt: Evidence from hydrothermal alteration, fluid inclusions and stable isotope data. Ore Geology Reviews 34(4), 580-596. https://doi.org/10.1016/j.oregeorev.2008.09.007

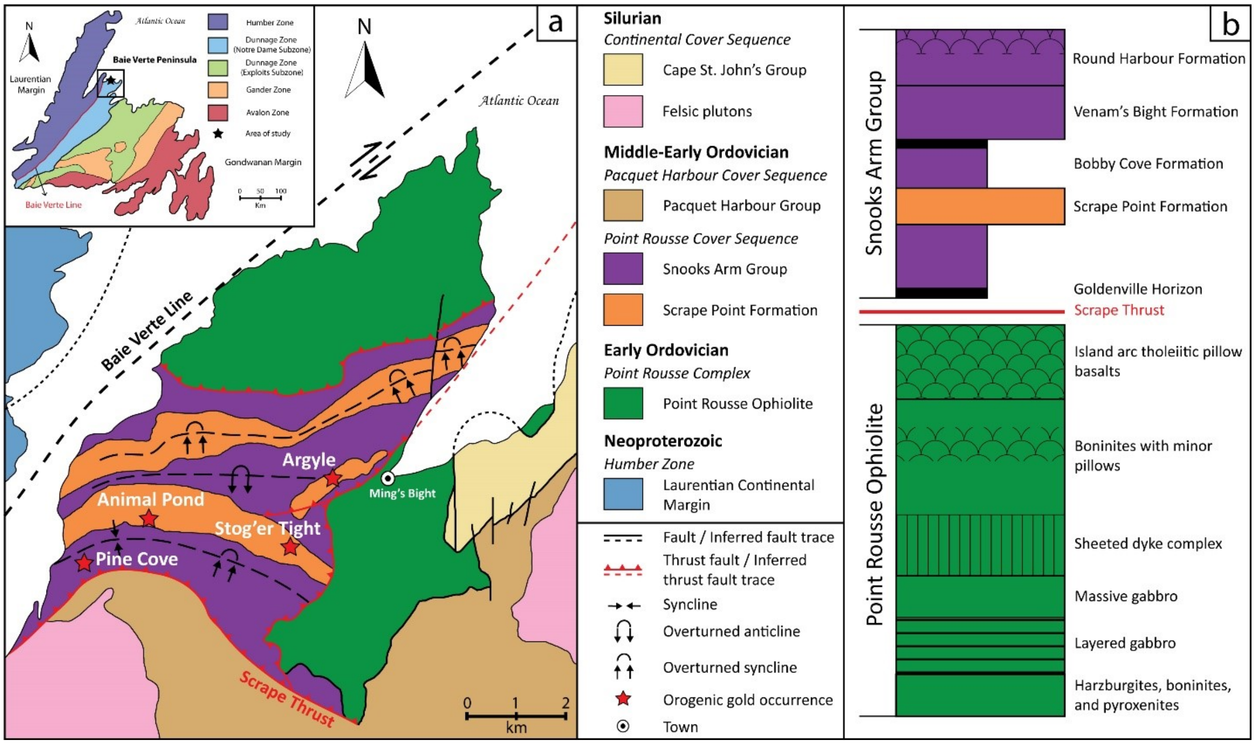

Figure 4.1.: Geological setting and stratigraphy of the studied orogenic gold occurrences. (a) Simplified geological map of the Point Rousse orogenic gold district on the Baie Verte Peninsula, northern Newfoundland, Canada. Modified from Skulski et al. (2010) and Pawlukiewicz (2019). (b) Stratigraphy of the Point Rousse Complex (modified after Skulski et al., 2009).

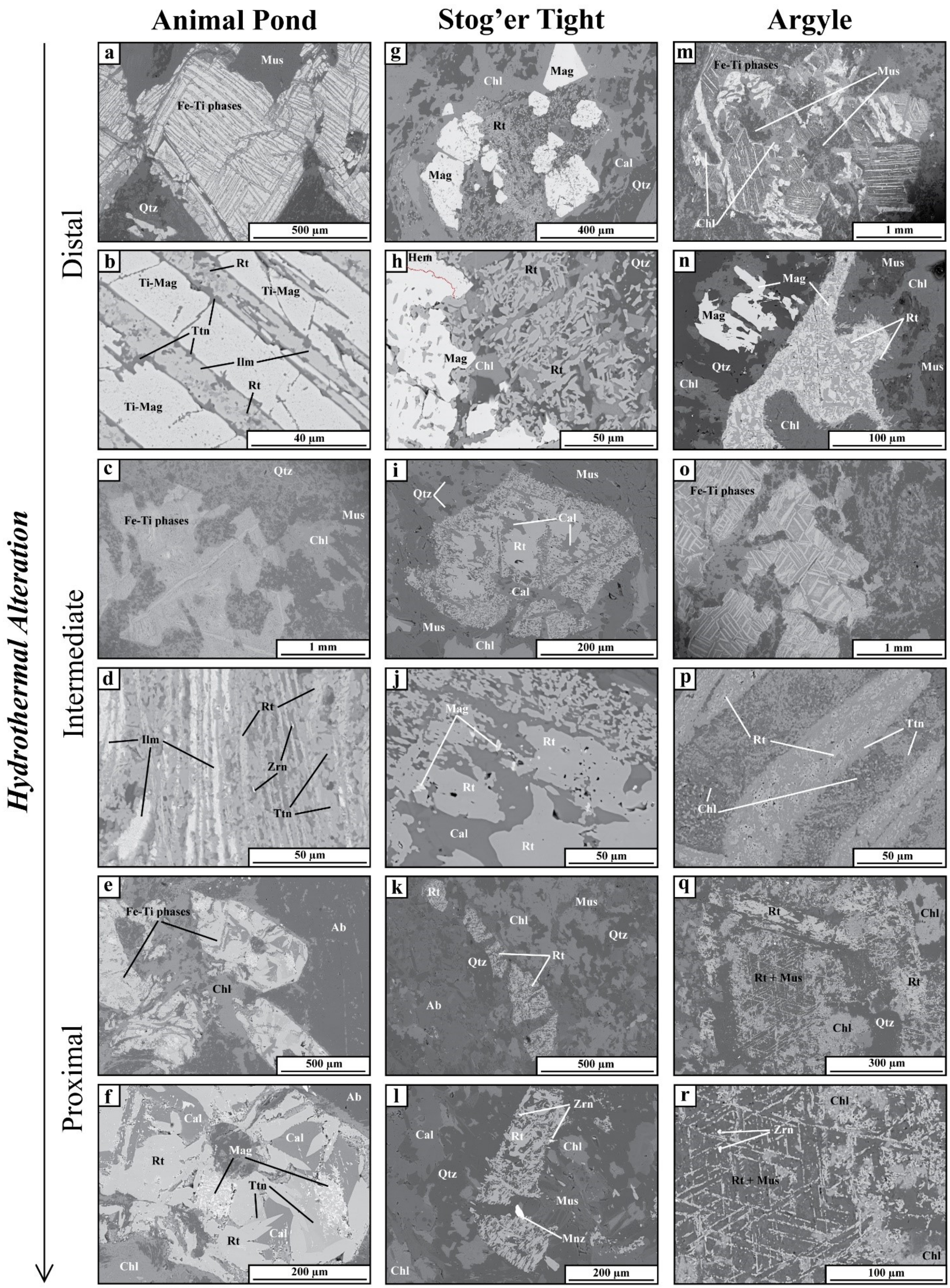

Animal Pond
Stog'er Tight
Argyle
Hydrothermal Alteration
Distal
Intermediate
Proximal
a
Mus
Fe-Ti phases
Qtz
500 µm
b
Rt
Ti-Mag
Ti-Mag
Ttn
Ilm
Rt
Ti-Mag
40 µm
c
Qtz
Fe-Ti phases
Mus
Chl
1 mm
d
Rt
Ilm
Zrn
Ttn
50 µm
e
Fe-Ti phases
Ab
Chl
500 µm
f
Ab
Cal
Cal
Mag
Rt
Ttn
Cal
Rt
Chl
200 µm
g
Mag
Chl
Rt
Mag
Cal
Qtz
400 µm
h
Hem
Rt
Qtz
Mag
Chl
Rt
50 µm
i
Mus
Qtz
Cal
Rt
Cal
Mus
Chl
200 µm
j
Mag
Rt
Rt
Cal
Rt
50 µm
k
Rt
Mus
Chl
Qtz
Rt
Qtz
Ab
500 µm
l
Zrn
Cal
Rt
Chl
Qtz
Mus
Mnz
Chl
200 µm
m
Fe-Ti phases
Mus
Chl
1 mm
n
Mus
Mag
Chl
Mag
Rt
Qtz
Mus
Chl
Chl
100 µm
o
Fe-Ti phases
1 mm
p
Rt
Ttn
Chl
50 µm
q
Rt
Chl
Rt + Mus
Rt
Chl
Qtz
300 µm
r
Chl
Zrn
Rt + Mus
Chl
100 µm

Figure 4.2.: Backscattered electron (BSE) photomicrographs of Fe-Ti phases from progressive alteration zones in the studied orogenic gold occurrences. ***Animal Pond prospect***: (a) Sample AP-704: Distal Fe-Ti phases consist of magmatic Ti-magnetite (darker phase)-ilmenite (lighter phase) exsolutions with quartz and muscovite; (b) Sample AP-704: Zoom of (a). Magmatic Ti-magnetite-ilmenite exsolution is defined by alternating lamellae of Ti-magnetite and ilmenite following magnetite parting planes. Hydrothermal alteration of these phases resulted in the formation of titanite along the contact between Ti-magnetite and ilmenite lamellae, as well as the formation of incipient rutile in the center of ilmenite lamellae; (c) Sample AP-714: Fe-Ti phases in intermediate alteration zone consisting of fine-grained lamellae of ilmenite, titanite, and rutile. Quartz, muscovite, and chlorite surround the mass of Fe-Ti phases; (d) Sample AP-714: Zoom of (c). Remnant magmatic ilmenite lamellae after hydrothermal alteration of ilmenite to titanite and rutile. Muscovite and quartz occur filling the space between the Ti-rich phases. Zircon grains are observed; (e) Sample AP-722: Fe-Ti phases in proximal alteration zone mainly consist of rutile, with minor ilmenite and titanite. Rutile grains are surrounded by albite and chlorite; (f) Sample AP-722: Zoom of (e). Rutile is the main oxide and has intergrown inclusions of calcite. Remnants of Ti-magnetite and titanite are observed. **Stog'er Tight deposit:** (g) Sample BN-739: Distal magnetite and rutile with calcite and quartz in chloritized host rock; (h) Sample BN-739: Zoom of (g). Magnetite grains showing incipient alteration to rutile, and hematite rimming. Fine grained prismatic rutile with chlorite-quartz-calcite, interpreted as a replacement of magmatic pyroxene; (i) Sample BN-748: Intermediate alteration zone characterized by rutile crystals intergrown with calcite in a phyllosilicate-rich (muscovite + chlorite) rock. Rutile crystals are pseudomorphic after magmatic magnetite and are more coarse-grained and contiguous in the center of the replaced magnetite, becoming fine-grained along the rims; (j) Sample BN-748: Zoom of (i). Coarser rutile crystals in the center of the magnetite pseudomorph with small inclusions of remnant magnetite; (k) Sample BN-730: Rutile in proximal alteration zone surrounded by quartz, albite, muscovite, and chlorite; (l) Sample BN-730: Zoom of (k). Rutile is the only significant Fe-Ti phase present in this sample. Rutile crystals are intergrowth with quartz. Monazite and zircon grains are also observed, usually spatially associated with rutile. **Argyle deposit:** (m) Sample AE-659: Fe-Ti phases in distal alteration setting. Relicts of the original magmatic magnetite-ilmenite exsolution texture can be observed; (n) Sample AE-659: Two generations of magnetite. Larger mass of magnetite is partially replaced by rutile. A generation of coarser euhedral magnetite is not replaced. The Fe-Ti phases are surrounded by quartz, chlorite, and muscovite; (o) Sample AE-676: Fe-Ti phases in intermediate alteration zone showing macroscopic texture of magmatic magnetite-ilmenite exsolution; (p) Sample AE-676: Zoom of (o). Exsolution lamellae of ilmenite and magnetite are hydrothermally altered to mixtures of rutile-titanite and titanite-chlorite, respectively. Rutile is the result of the progressive hydrothermal alteration of titanite in the central areas of the titanite-rutile lamellae; (q) Sample AE-660: Rutile crystals in proximal alteration zone. Fine-grained rutile is arranged following the parting planes of the precursor magmatic magnetite crystals (skeletal texture). Quartz, chlorite, and muscovite are the main silicates associated with rutile; (r) Sample AE-660: Zoom of (q). Fine-grained skeletal rutile is arranged following the octahedral parting planes of the precursor magmatic magnetite crystals, with the interstitial space filled by muscovite and chlorite. Zircon grains are also observed, usually spatially associated with rutile and muscovite.

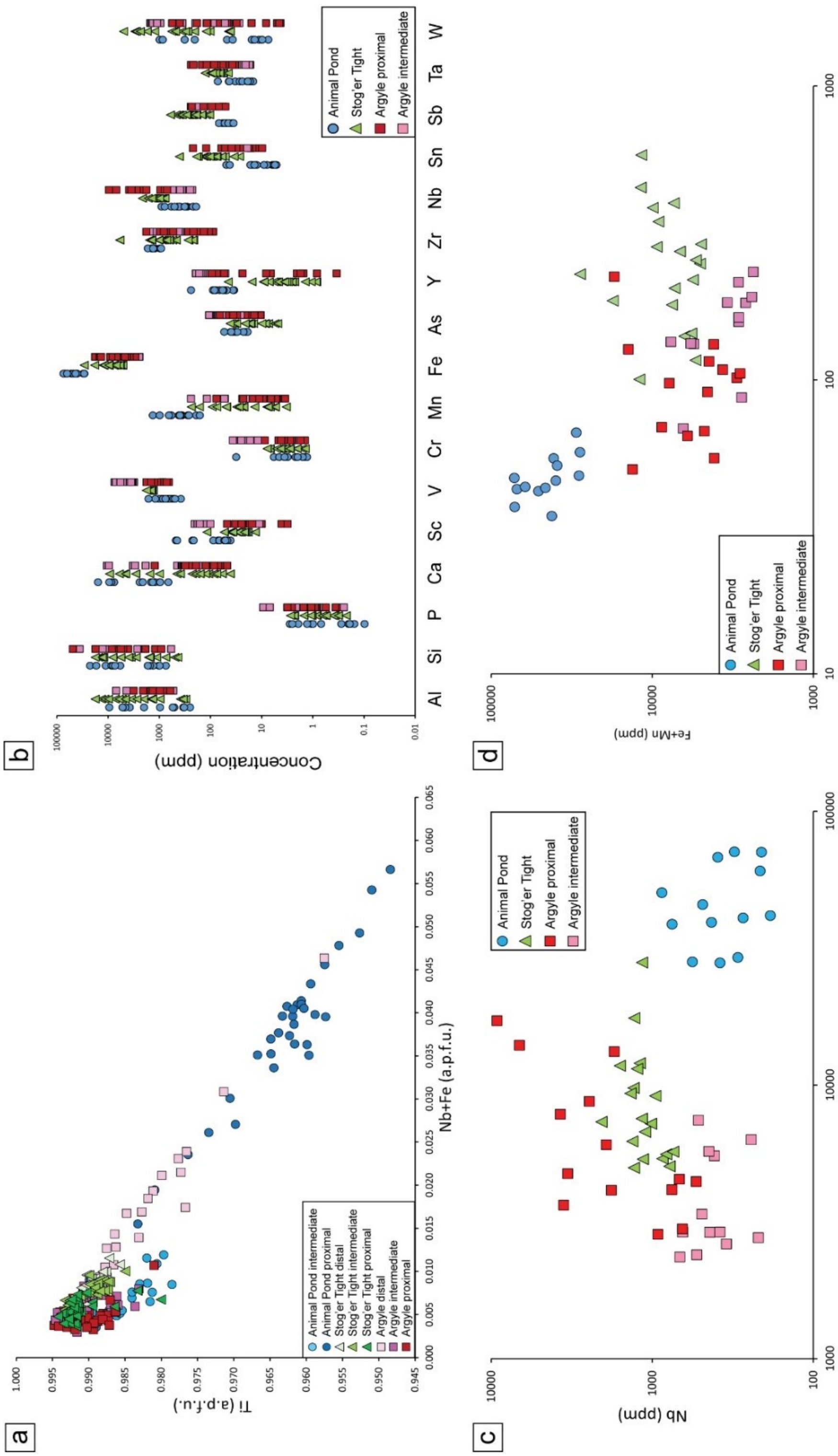

Figure 4.3.: Chemical discrimination plots for rutile from the three analyzed orogenic gold occurrences. (a) titanium vs. niobium + iron contents in rutile by EPMA; (b) Individual trace element concentrations in rutile by SIMS, coded by occurrence; (c) niobium vs. iron contents in rutile by SIMS; and (d) iron + manganese vs. antimony contents in rutile by SIMS.

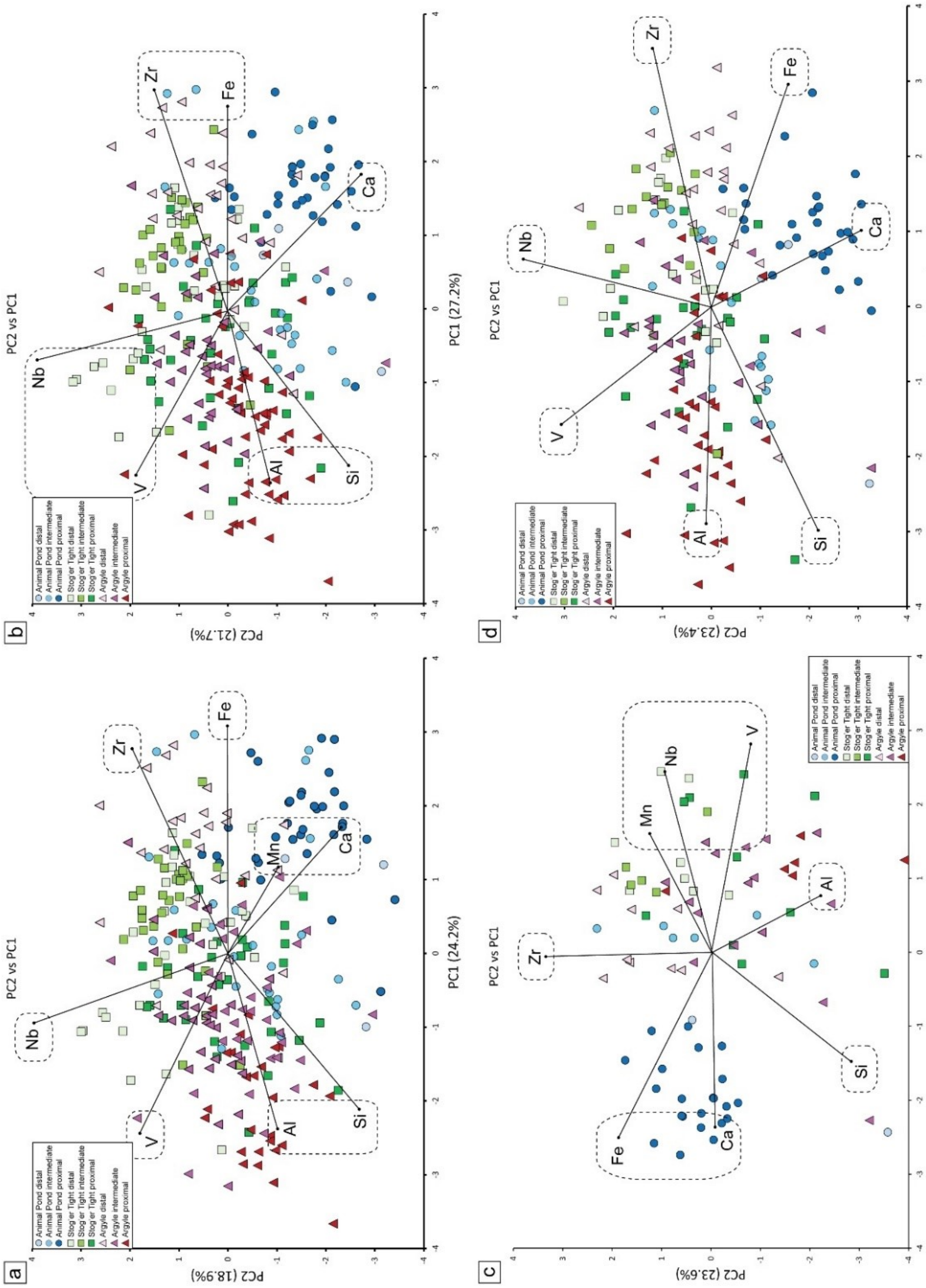

Figure 4.4.: Principal component analysis (PCA) of in situ electron probe rutile geochemical analyses from the studied orogenic gold occurrences. (a) Principal component analysis of EPMA data based on 8 variables (Fe, V, Mn, Al, Ca, Nb, Si, and Zr). Analyses with below detection values were assigned 65% of the detection limit. (b) Principal component analysis of EPMA data based on 7 variables (Fe, V, Al, Ca, Nb, Si, and Zr). Analyses with below detection values were assigned 65% of the detection limit. (c) Principal component analysis of EPMA data above detection limit only based on 8 variables (Fe, V, Mn, Al, Ca, Nb, Si, and Zr). (d) Principal component analysis of EPMA data above detection limit only based on 7 variables (Fe, V, Al, Ca, Nb, Si, and Zr). Loadings of elements showing similar direction and length are grouped in clusters (dashed boxes).

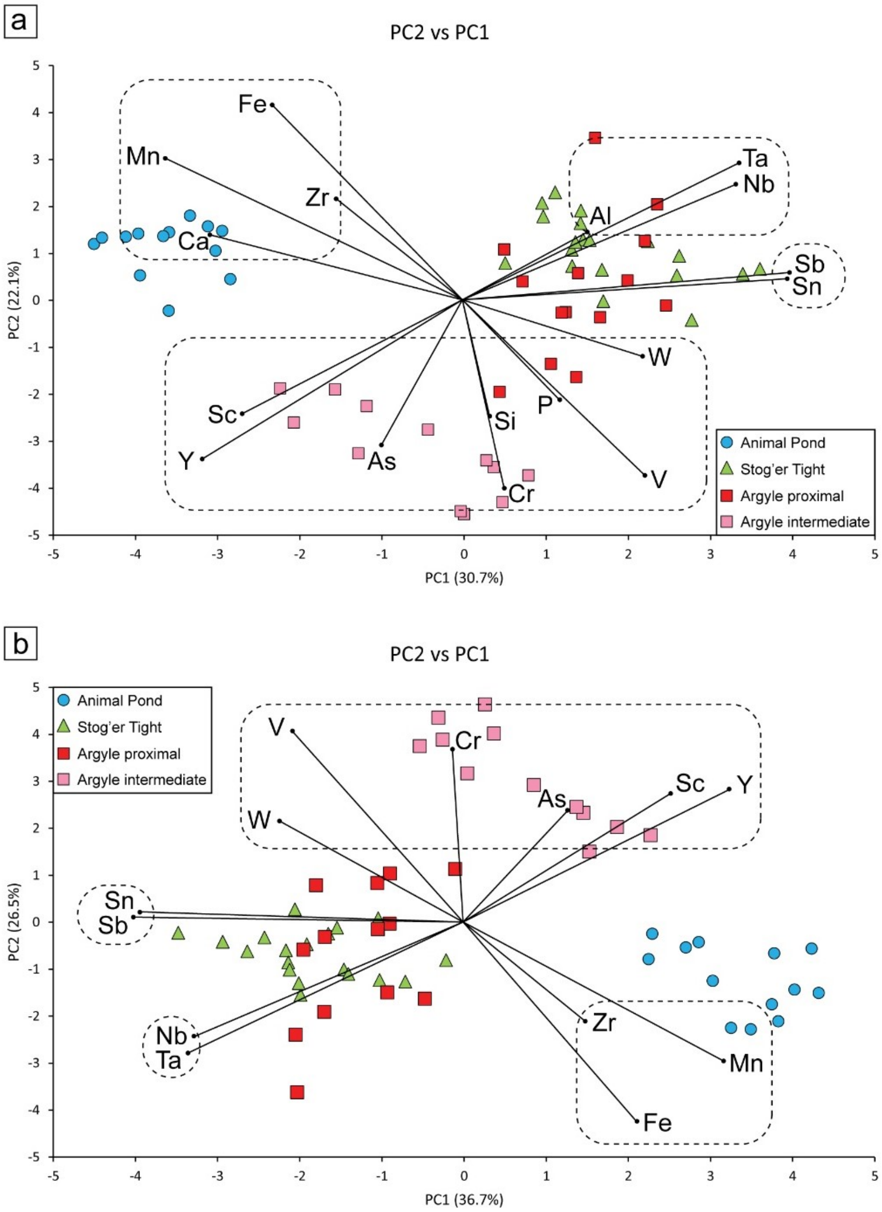

Figure 4.5.: Principal component analysis (PCA) of in situ SIMS rutile geochemical analyses from the studied orogenic gold occurrences. (a) Principal component analysis of SIMS data based on 17 variables (Al, Si, P, Ca, Sc, V, Cr, Mn, Fe, As, Y, Zr, Nb, Sn, Sb, Ta, and W). Loadings of elements showing similar direction and length are grouped in clusters (dashed boxes); and (b) Principal component analysis of SIMS data based on 13 variables (Sc, V, Cr, Mn, Fe, As, Y, Zr, Nb, Sn, Sb, Ta, and W). Loadings of elements showing similar direction and length are grouped in clusters (dashed boxes).

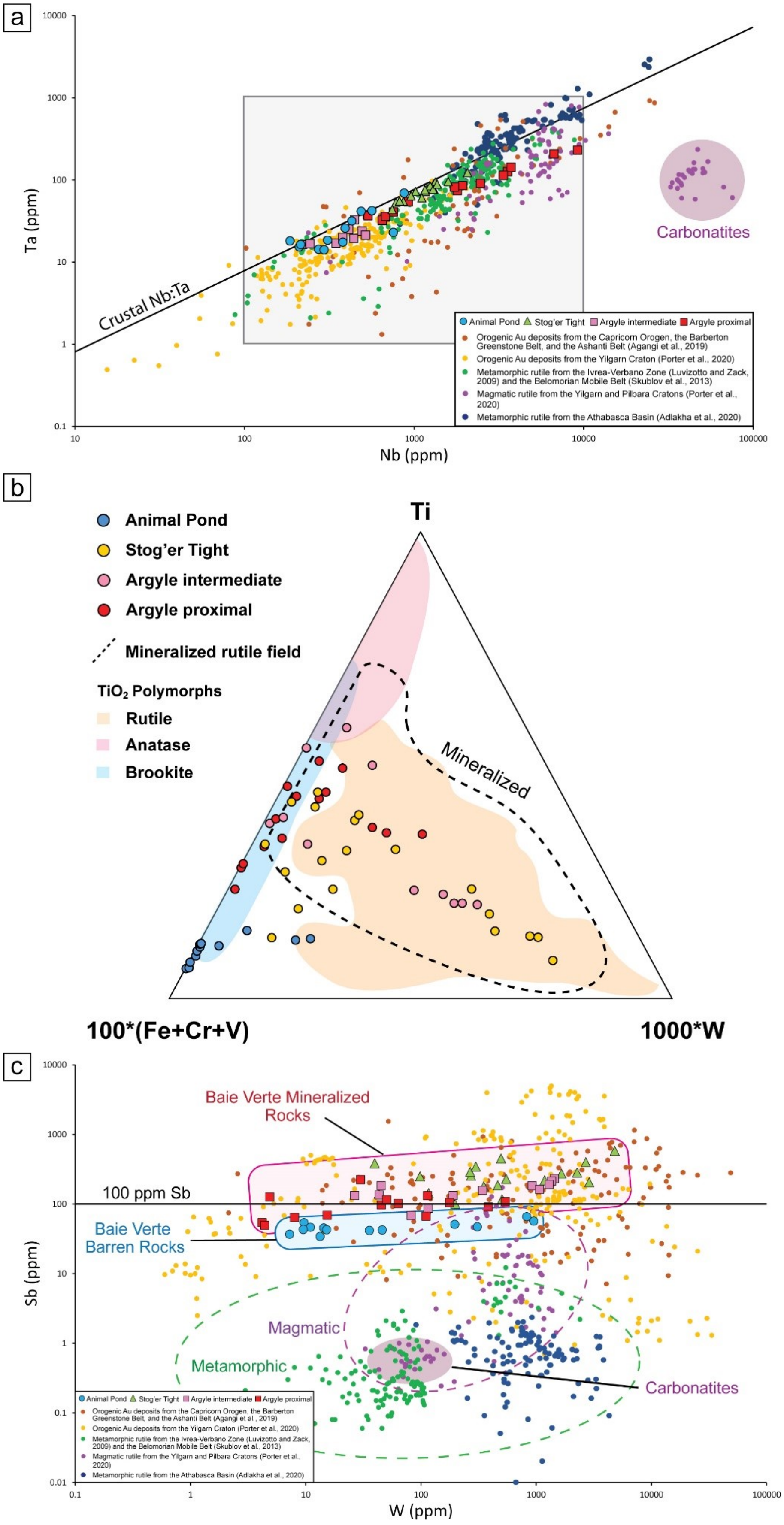
a
Ta (ppm)
Nb (ppm)
Crustal Nb:Ta
Carbonatites
Animal Pond
Stog'er Tight
Argyle intermediate
Argyle proximal
Orogenic Au deposits from the Capricorn Orogen, the Barberton Greenstone Belt, and the Ashanti Belt (Agangi et al., 2019)
Orogenic Au deposits from the Yilgarn Craton (Porter et al., 2020)
Metamorphic rutile from the Ivrea-Verbano Zone (Luvizotto and Zack, 2009) and the Belomorian Mobile Belt (Skublov et al., 2013)
Magmatic rutile from the Yilgarn and Pilbara Cratons (Porter et al., 2020)
Metamorphic rutile from the Athabasca Basin (Adlakha et al., 2020)
b
Ti
Animal Pond
Stog'er Tight
Argyle intermediate
Argyle proximal
Mineralized rutile field
TiO$_2$ Polymorphs
Rutile
Anatase
Brookite
Mineralized
100*(Fe+Cr+V)
1000*W
c
Sb (ppm)
W (ppm)
Baie Verte Mineralized Rocks
100 ppm Sb
Baie Verte Barren Rocks
Magmatic
Metamorphic
Carbonatites
Animal Pond
Stog'er Tight
Argyle intermediate
Argyle proximal
Orogenic Au deposits from the Capricorn Orogen, the Barberton Greenstone Belt, and the Ashanti Belt (Agangi et al., 2019)
Orogenic Au deposits from the Yilgarn Craton (Porter et al., 2020)
Metamorphic rutile from the Ivrea-Verbano Zone (Luvizotto and Zack, 2009) and the Belomorian Mobile Belt (Skublov et al., 2013)
Magmatic rutile from the Yilgarn and Pilbara Cratons (Porter et al., 2020)
Metamorphic rutile from the Athabasca Basin (Adlakha et al., 2020)

Figure 4.6.: Chemical analysis of rutile (SIMS) from the studied orogenic gold occurrences in the Baie Verte region compared to those for other mineralized and unmineralized rocks. (a) Tantalum vs. Niobium contents in rutile. Grey shaded box encompasses most frequent ranges of Nb and Ta contents in rutile from barren magmatic and metamorphic rocks, as well as from orogenic Au occurrences and deposits. Violet shaded circle area shows the distinct Nb and Ta chemical signature of rutile from carbonatitic rocks. The Crustal Nb:Ta line was calculated using the upper continental crust calculations of Barth et al. (2000), who estimated an upper crust average of 11.5±2.6 ppm Nb and 0.92±0.12 ppm Ta; (b) Ti-100*(Fe+Cr+V)-1000*W in rutile based on plot from Clark and Williams-Jones (2004). Mineralized rutile field from Clark and Williams-Jones (2004). Titania polymorph fields from Plavsa et al. (2018); (c) Antimony vs. tungsten in rutile. High contents of Sb in rutile are associated with Au mineralization globally. In the Baie Verte region, contents of Sb higher than 80 ppm are characteristic of hydrothermal rutile associated with orogenic gold occurrences. Hydrothermal rutile from orogenic gold occurrences from Agangi et al. (2019) include: i) Fortnum, Killara, and Nathans deposits (Capricorn Orogen, Western Australia); ii) Sheba and Fairview mines (Barberton Greenstone Belt, Southern Africa); and iii) Obuasi deposit (Ashanti Belt, West African Craton). Hydrothermal rutile from orogenic gold occurrences from Porter et al. (2020) include Harbour Lights, Boorara, Golden Pike, Golden Kilometre, Victory-Defiance, Lake View, Royal Standard, and Hercules (Yilgarn Craton, Western Australia). Metamorphic rutile from various barren metamorphic rocks were compiled from the Ivrea-Verbano Zone (Southern Alps; Luvizotto and Zack, 2009), the Belomorian Mobile Belt (Eastern Finland - Western Russia; Skublov et al., 2013), and the Athabasca Basin (Canada; Adlakha et al., 2020). Magmatic rutile from barren carbonatite, rhyolite, monzogranite, tonalite, and volcaniclastic rocks from the Pilbara Craton, the Yilgarn Craton, and Paleo-Mesoproterozoic orogens and basins from Western Australia (Porter et al., 2020).

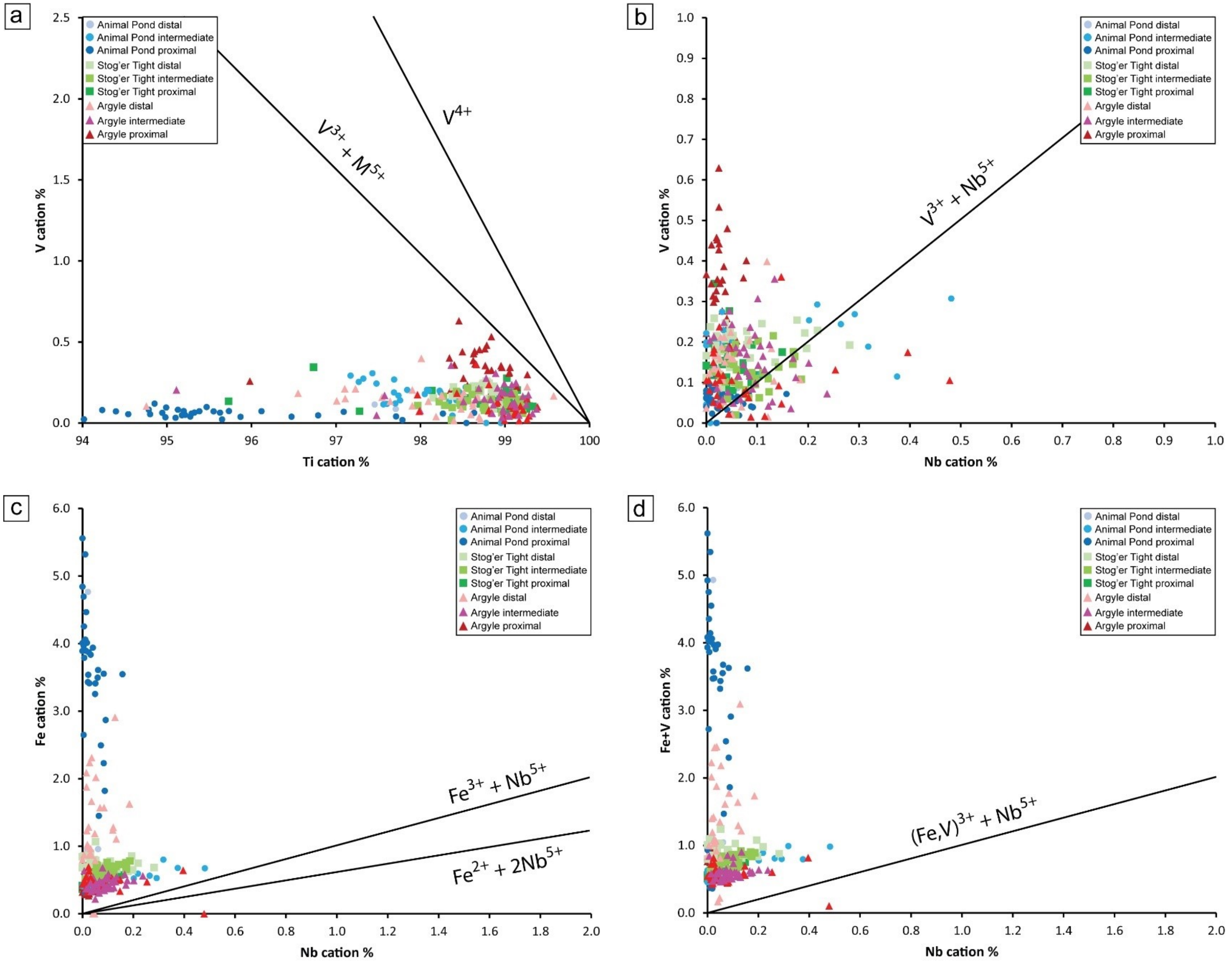

Figure 4.7.: Biplots of element abundances in rutile using EPMA data recalculated as atomic cation percent. (a) V and Ti; (b) V and Nb; (c) Fe and Nb; (d) Fe+V and Nb. Trendlines rooted at zero are shown representing different substitution mechanisms.

Table 4.1. Summary of mineral alteration assemblages, including Fe-Ti phases, of the main hydrothermal alteration events with regards to proximity to Au mineralization in the three studied orogenic gold occurrences. The term “Au” refers to “native gold”. Phases in bold in the “Main Alteration Phases” row from each deposit indicate those phases that are common to all three orogenic gold occurrences in a given alteration zone with regards to proximity to gold mineralization. Phases in bold in the “Fe-Ti Phases” row indicate the predominant Fe-Ti Phase in a given alteration zone for each orogenic gold occurrence. Color bars in the rows referring to the main two hydrothermal alteration events indicate the extent of each event with respect to proximity to gold mineralization. Mineralogical data from Animal Pond was sourced from Anaconda Mining Inc. Drilling Program (2005), with input and refinement from the observations reported in his study, in particular with regards to Fe-Ti phases. Mineralogical data from Stog’er Tight was sourced from Ramezani (1992) and Ramezani et al. (2000), with input and refinement from the observations reported in his study, in particular with regards to Fe-Ti phases. Mineralogical data from Argyle was sourced from Pawlukiewicz (2019), with input and refinement from the observations reported in his study, in particular with regards to Fe-Ti phases.

<table>
<tr><th></th><th></th><th colspan="6">Proximity to Gold Mineralization Zone(s)</th></tr>
<tr><th></th><th></th><th colspan="2">Distal</th><th colspan="2">Intermediate</th><th colspan="2">Proximal</th></tr>
<tr><td rowspan="4">Animal Pond</td><td>Early epidote-chlorite-calcite-albite</td><td colspan="6">🟦</td></tr>
<tr><td>Late quartz-albite-pyrite-Au</td><td colspan="3"></td><td colspan="3">🟦</td></tr>
<tr><td>Main Alteration Phases</td><td colspan="2">Chlorite-epidote-quartz-calcite-sericite-pyrite-chalcopyrite</td><td colspan="2">Sericite-albite-epidote-quartz-calcite-chlorite-pyrite-chalcopyrite</td><td colspan="2">Sericite-albite-epidote-quartz-ankerite-chlorite-pyrite-chalcopyrite-Au</td></tr>
<tr><td>Fe-Ti Phases</td><td colspan="2">(Ti-)magnetite, ilmenite, titanite, incipient rutile</td><td colspan="2">Titanite, (Ti-)magnetite, ilmenite, rutile</td><td colspan="2">Rutile, remnant ilmenite</td></tr>
<tr><td rowspan="4">Stog'er Tight</td><td>Barren epidote-chlorite-calcite-albite</td><td colspan="6">🟩</td></tr>
<tr><td>Late quartz-albite-pyrite-Au</td><td colspan="4"></td><td colspan="2">🟩</td></tr>
<tr><td>Main Alteration Phases</td><td colspan="2">Chlorite-calcite-epidote</td><td>Hanging wall alteration: sericite-ankerite-chlorite-epidote-pyrite-chalcopyrite</td><td>Footwall alteration: chlorite-magnetite</td><td colspan="2">Quartz-sericite-chlorite-calcite-ankerite-albite-pyrite-Au</td></tr>
<tr><td>Fe-Ti Phases</td><td colspan="2">Magnetite, rutile, hematite</td><td colspan="2">Rutile, remnant magnetite</td><td colspan="2">Rutile, remnant magnetite</td></tr>
<tr><td rowspan="4">Argyle</td><td>Barren epidote-chlorite-calcite-albite</td><td colspan="6">🟧</td></tr>
<tr><td>Late quartz-albite-pyrite-Au</td><td></td><td colspan="5">🟧</td></tr>
<tr><td>Main Alteration Phases</td><td colspan="2">Chlorite-calcite-epidote-albite-sericite-quartz</td><td colspan="2">Chlorite-epidote-albite-calcite-ankerite-sericite-pyrite-chalcopyrite</td><td colspan="2">Muscovite-quartz-ankerite-chlorite-pyrite-Au</td></tr>
<tr><td>Fe-Ti Phases</td><td colspan="2">(Ti-)magnetite, rutile</td><td colspan="2">Titanite, rutile</td><td colspan="2">Rutile</td></tr>
</table>

Table 4.2. Selected electron microprobe analyses (in wt.%) of rutile from the studied orogenic gold occurrences and respective structural formulas.

Deposit	AP	AP	AP	AP	AP	AP	AP	AP	AP	AP	AP	AP	AP	AP	AP
Sample	714	714	714	714	714	714	714	722	722	722	722	722	722	722	722
No. anal.	1	4	7	11	16	21	28	2	9	13	17	19	24	29	35
TiO_2	98.35	99.29	99.24	99.32	100.03	100.14	98.98	95.93	96.36	96.96	97.31	97.61	98.91	96.62	97.90
SiO_2	0.06	0.06	0.04	0.02	0.02	0.04	0.03	0.10	0.20	0.09	0.23	0.15	0.10	0.16	0.26
Fe_2O_3	0.87	0.62	0.58	0.46	0.53	0.45	0.41	4.35	4.38	3.88	3.97	3.13	2.45	3.88	2.91
Cr_2O_3	b.d.	b.d.	b.d.	b.d.	b.d.	b.d.	b.d.	b.d.	b.d.	b.d.	b.d.	b.d.	b.d.	b.d.	b.d.
V_2O_3	0.18	0.23	0.26	0.14	b.d.	0.20	0.22	0.07	0.05	0.07	0.06	0.04	0.07	0.03	0.07
MnO	0.01	b.d.	b.d.	0.01	b.d.	b.d.	0.01	b.d.	0.04	b.d.	b.d.	0.01	b.d.	0.02	0.03
Al_2O_3	0.01	0.01	0.01	0.01	0.01	0.01	0.02	0.02	0.03	0.03	0.02	0.02	0.02	0.03	0.03
CaO	0.56	0.91	0.77	0.51	0.34	0.98	0.44	0.21	0.16	0.18	0.38	0.08	0.21	0.77	0.46
P_2O_5	b.d.	0.01	b.d.	b.d.	b.d.	b.d.	b.d.	b.d.	b.d.	b.d.	b.d.	b.d.	0.01	0.01	b.d.
ZrO_2	0.14	0.12	0.13	0.11	0.05	0.12	0.03	0.09	0.18	0.14	0.10	0.20	0.10	0.07	0.06
As_2O_5	b.d.	b.d.	b.d.	b.d.	b.d.	b.d.	b.d.	b.d.	0.02	0.05	b.d.	0.02	0.01	b.d.	0.02
Nb_2O_5	0.53	0.45	0.49	0.07	0.01	0.08	0.06	b.d.	0.03	0.14	0.10	0.15	0.14	0.04	0.01
WO_3	b.d.	b.d.	b.d.	b.d.	b.d.	b.d.	0.04	b.d.	0.01	b.d.	b.d.	b.d.	b.d.	b.d.	b.d.
Ta_2O_5	b.d.	b.d.	b.d.	b.d.	b.d.	b.d.	b.d.	b.d.	b.d.	b.d.	b.d.	0.02	b.d.	b.d.	b.d.
SnO_2	b.d.	b.d.	b.d.	b.d.	b.d.	b.d.	b.d.	0.01	0.01	b.d.	b.d.	b.d.	b.d.	b.d.	b.d.
Sb_2O_5	b.d.	b.d.	b.d.	b.d.	b.d.	b.d.	b.d.	b.d.	b.d.	b.d.	b.d.	b.d.	b.d.	b.d.	b.d.
Total	99.74	100.39	100.36	99.89	100.39	100.60	99.60	100.03	100.76	100.78	101.20	100.99	101.37	100.14	100.75
a.p.f.u.															
Ti	0.982	0.982	0.983	0.990	0.993	0.986	0.991	0.963	0.961	0.965	0.963	0.971	0.976	0.962	0.970
Si	0.001	0.001	0.001	<0.001	<0.001	0.001	<0.001	0.001	0.003	0.001	0.003	0.002	0.001	0.002	0.003
Fe^{3+}	0.008	0.006	0.005	0.004	0.005	0.004	0.004	0.040	0.041	0.036	0.036	0.029	0.022	0.036	0.027
Cr	-	-	-	-	-	-	-	-	-	-	-	-	-	-	-
V	0.002	0.002	0.003	0.001	-	0.002	0.002	0.001	<0.001	0.001	0.001	<0.001	0.001	<0.001	0.001
Mn	<0.001	-	-	<0.001	-	-	<0.001	-	0.001	-	-	<0.001	-	<0.001	0.001
Al	<0.001	<0.001	<0.001	<0.001	<0.001	<0.001	<0.001	<0.001	<0.001	<0.001	<0.001	<0.001	<0.001	<0.001	<0.001
Ca	0.008	0.013	0.011	0.007	0.005	0.014	0.006	0.003	0.002	0.003	0.005	0.001	0.003	0.011	0.006
P	-	<0.001	-	-	-	-	-	-	-	-	-	-	<0.001	<0.001	-
Zr	0.001	0.001	0.001	0.001	<0.001	0.001	<0.001	0.001	0.001	0.001	0.001	0.001	0.001	<0.001	<0.001
As	-	-	-	-	-	-	-	-	<0.001	<0.001	-	<0.001	<0.001	-	<0.001
Nb	0.003	0.003	0.003	<0.001	<0.001	<0.001	<0.001	-	<0.001	0.001	0.001	0.001	0.001	<0.001	<0.001
W	-	-	-	-	-	-	<0.001	-	<0.001	-	-	-	-	-	-
Ta	-	-	-	-	-	-	-	-	-	-	-	<0.001	-	-	-
Sn	-	-	-	-	-	-	-	<0.001	<0.001	-	-	-	-	-	-
Sb	-	-	-	-	-	-	-	-	-	-	-	-	-	-	-
Total	1.005	1.007	1.006	1.005	1.003	1.008	1.004	1.010	1.010	1.008	1.010	1.006	1.006	1.013	1.009

Rutile formulae calculated on the basis of 2 oxygen atoms and all iron was considered as Fe^{3+}. Abbreviations: AP = Animal Pond prospect; BN = Stog'er Tight deposit; AE = Argyle deposit.

Table 4.2. Continued.

Deposit Sample No. anal.	BN 730 6	BN 730 10	BN 730 17	BN 730 24	BN 730 32	BN 739 2	BN 739 6	BN 739 12	BN 739 26	BN 739 31	BN 748 4	BN 748 9	BN 748 16	BN 748 25	BN 748 30
TiO_2	99.33	100.28	99.65	99.29	99.38	100.90	100.58	100.12	99.98	99.04	99.58	99.84	99.67	99.08	99.95
SiO_2	0.12	b.d.	0.22	0.06	0.04	0.04	0.03	0.04	0.03	0.03	0.15	b.d.	b.d.	b.d.	0.01
Fe_2O_3	0.35	0.48	0.58	0.58	0.68	0.69	0.68	0.72	0.60	0.62	0.69	0.70	0.72	0.58	0.71
Cr_2O_3	b.d.	b.d.	b.d.	b.d.	0.01	b.d.	b.d.	b.d.	b.d.	b.d.	b.d.	b.d.	b.d.	b.d.	b.d.
V_2O_3	0.17	0.14	0.19	0.08	0.12	0.19	0.15	0.14	0.20	0.11	0.10	0.19	0.17	0.09	0.12
MnO	0.01	b.d.	0.02	b.d.	0.01	0.02	0.01	b.d.	b.d.	0.03	b.d.	b.d.	0.01	b.d.	b.d.
Al_2O_3	0.06	0.02	0.00	0.02	0.02	0.01	0.02	0.01	0.02	0.02	0.12	0.02	0.01	0.02	0.01
CaO	0.13	0.13	0.54	0.13	0.00	0.01	0.01	0.03	0.32	0.11	0.17	0.44	0.22	0.05	0.37
P_2O_5	b.d.	b.d.	b.d.	b.d.	b.d.	0.01	0.01	b.d.	0.01	b.d.	0.01	b.d.	0.01	b.d.	b.d.
ZrO_2	0.07	0.02	0.04	0.06	0.01	0.08	0.06	0.17	0.03	0.06	0.03	0.04	0.03	0.03	0.17
As_2O_5	0.01	b.d.	b.d.	0.01	b.d.	b.d.	0.03	0.01	b.d.	b.d.	b.d.	b.d.	0.02	0.07	b.d.
Nb_2O_5	0.03	0.05	0.05	0.04	0.12	0.14	0.14	0.23	0.06	0.04	0.20	0.10	0.29	0.06	0.15
WO_3	0.01	b.d.	0.01	b.d.	b.d.	b.d.	b.d.	b.d.	b.d.	b.d.	b.d.	b.d.	b.d.	b.d.	b.d.
Ta_2O_5	b.d.	0.02	b.d.	b.d.	0.02	b.d.	b.d.	0.02	b.d.	b.d.	b.d.	b.d.	0.03	b.d.	b.d.
SnO_2	b.d.	b.d.	b.d.	b.d.	b.d.	b.d.	b.d.	b.d.	b.d.	b.d.	b.d.	b.d.	b.d.	b.d.	b.d.
Sb_2O_5	b.d.	b.d.	b.d.	b.d.	0.01	b.d.	b.d.	b.d.	b.d.	b.d.	b.d.	b.d.	b.d.	b.d.	b.d.
Total	100.03	100.85	100.50	99.90	100.33	101.92	101.58	101.27	100.70	99.83	100.46	100.62	100.71	99.73	100.77
a.p.f.u.															
Ti	0.992	0.994	0.987	0.992	0.992	0.991	0.991	0.990	0.990	0.992	0.988	0.989	0.989	0.993	0.989
Si	0.002	-	0.003	0.001	0.001	0.001	<0.001	<0.001	<0.001	<0.001	0.002	-	-	-	<0.001
Fe^{3+}	0.003	0.004	0.005	0.005	0.006	0.006	0.006	0.007	0.006	0.006	0.006	0.006	0.007	0.005	0.007
Cr	-	-	-	-	<0.001	-	-	-	-	-	-	-	-	-	-
V	0.002	0.001	0.002	0.001	0.001	0.002	0.002	0.002	0.002	0.001	0.001	0.002	0.002	0.001	0.001
Mn	<0.001	-	<0.001	-	<0.001	<0.001	<0.001	-	-	<0.001	-	-	<0.001	-	-
Al	0.001	<0.001	<0.001	<0.001	<0.001	<0.001	<0.001	<0.001	<0.001	<0.001	0.002	<0.001	<0.001	<0.001	<0.001
Ca	0.002	0.002	0.008	0.002	<0.001	<0.001	<0.001	<0.001	0.004	0.002	0.002	0.006	0.003	0.001	0.005
P	-	-	-	-	-	<0.001	<0.001	-	<0.001	-	<0.001	-	<0.001	-	-
Zr	<0.001	<0.001	<0.001	<0.001	<0.001	<0.001	<0.001	0.001	<0.001	<0.001	<0.001	<0.001	<0.001	<0.001	0.001
As	<0.001	-	-	<0.001	-	-	<0.001	<0.001	-	-	-	-	<0.001	<0.001	-
Nb	<0.001	<0.001	<0.001	<0.001	0.001	0.001	0.001	0.001	<0.001	<0.001	0.001	0.001	0.002	<0.001	0.001
W	<0.001	-	<0.001	-	-	-	-	-	-	-	-	-	-	-	-
Ta	-	<0.001	-	-	<0.001	-	-	<0.001	-	-	-	-	<0.001	-	-
Sn	-	-	-	-	-	-	-	-	-	-	-	-	-	-	-
Sb	-	-	-	-	<0.001	-	-	-	-	-	-	-	-	-	-
Total	1.002	1.002	1.005	1.002	1.002	1.002	1.001	1.002	1.004	1.002	1.003	1.005	1.003	1.001	1.004

Rutile formulae calculated on the basis of 2 oxygen atoms and all iron was considered as Fe^{3+}. Abbreviations: AP = Animal Pond prospect; BN = Stog'er Tight deposit; AE = Argyle deposit.

Table 4.2. Continued.

Deposit	AE	AE	AE	AE	AE	AE	AE	AE	AE	AE	AE	AE	AE	AE	AE
Sample	660	660	660	660	659	659	659	679	679	679	679	684	684	684	684
No. anal.	5	9	14	25	8	17	27	4	11	21	27	4	14	20	32
TiO_2	98.50	99.57	98.82	99.70	99.02	98.80	98.98	99.40	100.20	99.51	99.21	99.85	100.17	100.01	97.69
SiO_2	0.16	0.14	0.17	0.29	0.12	0.07	0.05	0.23	0.07	0.02	0.17	0.17	0.15	0.10	0.17
Fe_2O_3	0.48	0.37	0.40	0.41	0.95	1.35	0.87	0.36	0.76	0.38	0.40	0.41	0.42	0.52	0.63
Cr_2O_3	b.d.	b.d.	b.d.	b.d.	b.d.	b.d.	b.d.	b.d.	b.d.	b.d.	b.d.	b.d.	b.d.	b.d.	b.d.
V_2O_3	0.38	0.45	0.42	0.22	0.18	0.38	0.04	0.34	0.12	0.11	0.06	0.20	0.18	0.05	0.13
MnO	0.01	0.01	0.02	0.03	0.02	b.d.	b.d.	b.d.	b.d.	0.01	b.d.	b.d.	b.d.	b.d.	0.01
Al_2O_3	0.05	0.05	0.04	0.08	0.02	0.01	0.03	0.08	0.04	0.02	0.05	0.03	b.d.	0.03	0.06
CaO	0.22	0.05	0.09	0.15	0.05	0.03	0.11	0.02	0.03	0.20	0.05	0.29	0.06	0.05	0.05
P_2O_5	b.d.	b.d.	b.d.	b.d.	b.d.	0.00	b.d.	0.02	b.d.	b.d.	0.01	0.01	b.d.	0.01	b.d.
ZrO_2	0.08	b.d.	0.04	0.09	0.18	0.04	0.28	0.03	0.08	b.d.	b.d.	0.04	0.08	0.04	0.13
As_2O_5	b.d.	b.d.	0.06	b.d.	b.d.	b.d.	0.03	b.d.	0.02	b.d.	0.05	b.d.	b.d.	b.d.	0.01
Nb_2O_5	0.13	0.07	0.04	0.07	0.05	0.20	b.d.	0.25	0.04	0.10	0.04	0.03	0.21	0.22	0.17
WO_3	0.18	b.d.	0.05	b.d.	0.02	0.08	b.d.	b.d.	b.d.	b.d.	b.d.	b.d.	0.03	b.d.	b.d.
Ta_2O_5	b.d.	b.d.	b.d.	b.d.	b.d.	b.d.	b.d.	b.d.	b.d.	b.d.	b.d.	b.d.	b.d.	0.03	b.d.
SnO_2	b.d.	b.d.	b.d.	b.d.	b.d.	0.03	b.d.	b.d.	b.d.	b.d.	0.01	b.d.	b.d.	b.d.	0.01
Sb_2O_5	b.d.	b.d.	b.d.	b.d.	b.d.	b.d.	b.d.	b.d.	b.d.	b.d.	b.d.	b.d.	b.d.	b.d.	b.d.
Total	99.66	100.37	99.95	100.65	100.38	100.79	100.08	100.61	101.04	99.93	99.87	100.52	101.09	100.80	98.83
a.p.f.u.															
Ti	0.987	0.990	0.989	0.988	0.988	0.983	0.989	0.988	0.991	0.993	0.992	0.990	0.991	0.992	0.988
Si	0.002	0.002	0.002	0.004	0.002	0.001	0.001	0.003	0.001	0.000	0.002	0.002	0.002	0.001	0.002
Fe^{3+}	0.004	0.003	0.004	0.004	0.009	0.012	0.008	0.003	0.007	0.004	0.004	0.004	0.004	0.005	0.006
Cr	-	-	-	-	-	-	-	-	-	-	-	-	-	-	-
V	0.004	0.005	0.004	0.002	0.002	0.004	<0.001	0.004	0.001	0.001	0.001	0.002	0.002	0.001	0.001
Mn	<0.001	<0.001	<0.001	<0.001	<0.001	-	-	-	-	<0.001	-	-	-	-	<0.001
Al	0.001	0.001	0.001	0.001	<0.001	<0.001	<0.001	0.001	0.001	<0.001	0.001	<0.001	-	<0.001	0.001
Ca	0.003	0.001	0.001	0.002	0.001	<0.001	0.002	<0.001	<0.001	0.003	0.001	0.004	0.001	0.001	0.001
P	-	-	-	-	-	<0.001	-	<0.001	-	-	<0.001	<0.001	-	<0.001	-
Zr	0.001	-	<0.001	0.001	0.001	<0.001	0.002	<0.001	0.001	-	-	<0.001	<0.001	<0.001	0.001
As	-	-	<0.001	-	-	-	<0.001	-	<0.001	-	<0.001	-	-	-	<0.001
Nb	0.001	<0.001	<0.001	<0.001	<0.001	0.001	-	0.001	<0.001	0.001	<0.001	<0.001	0.001	0.001	0.001
W	0.001	-	<0.001	-	<0.001	<0.001	-	-	-	-	-	-	<0.001	-	-
Ta	-	-	-	-	-	-	-	-	-	-	-	-	-	<0.001	-
Sn	-	-	-	-	-	<0.001	-	-	-	-	<0.001	-	-	-	<0.001
Sb	-	-	-	-	-	-	-	-	-	-	-	-	-	-	-
Total	1.003	1.002	1.002	1.003	1.003	1.003	1.002	1.002	1.002	1.002	1.001	1.003	1.001	1.001	1.002

Rutile formulae calculated on the basis of 2 oxygen atoms and all iron was considered as Fe^{3+}. Abbreviations: AP = Animal Pond prospect; BN = Stog'er Tight deposit; AE = Argyle deposit.

Table 4.3. Secondary ion mass spectrometry (SIMS) analyses of hydrothermal rutile (in ppm) from the Animal Pond orogenic gold prospect.

Deposit	Sample #	Analysis #	Ti $_{\text{est}}$	Al	Si	P	Ca	Sc	V	Cr	Mn	Fe	As	Y	Zr	Nb	Sn	Sb	Ta	W
Animal Pond	AP-722	5	504998	9131	10750	3	952	40	650	31	559	70956	38	50	917	210	6	37	15	7
Animal Pond	AP-722	7	552656	316	986	0	2106	69	545	2	184	40805	20	50	1248	273	12	54	14	10
Animal Pond	AP-722	8	565148	242	720	0	1405	219	868	2	156	27955	18	34	1162	380	15	57	18	952
Animal Pond	AP-722	9	557345	328	952	0	7329	206	963	1	344	29266	22	35	1339	294	16	66	14	827
Animal Pond	AP-722	11	547047	3635	5585	1	1168	47	366	1	362	39347	31	64	1167	429	6	46	32	14
Animal Pond	AP-722	18	562756	492	1272	0	2334	457	1157	1	268	28230	22	46	1303	564	48	47	43	308
Animal Pond	AP-722	19	492952	4646	21656	1	8363	85	819	3	1290	67989	33	54	938	392	13	43	26	46
Animal Pond	AP-722	6	522547	4450	16358	2	2031	65	598	2	401	50504	39	81	1244	873	8	42	70	36
Animal Pond	AP-722	5	532083	937	8268	2	9117	46	588	2	375	45699	31	232	1377	487	5	43	42	15
Animal Pond	AP-722	9	497241	5015	7742	1	15106	65	513	6	625	71209	52	76	1305	309	9	46	19	11
Animal Pond	AP-722	10	545973	1917	7043	1	644	432	1572	2	255	38707	36	86	1616	754	41	51	23	196
Animal Pond	AP-722	8	532583	317	1467	0	1295	52	476	4	949	60563	29	56	1269	214	6	43	16	10
Animal Pond	AP-722	1	552231	528	1610	0	927	50	730	3	383	41623	38	81	889	185	5	34	18	13

The Ti content reported in the table was calculated based on the Ti content in stochiometric rutile (599349 ppm Ti) minus de content of each of the analyzed elements present as cations in the structure of rutile.

Table 4.3. Secondary ion mass spectrometry (SIMS) analyses of hydrothermal rutile (in ppm) from the Stog'er Tight orogenic gold deposit.

Deposit	Sample #	Analysis #	Ti$_{est}$	Al	Si	P	Ca	Sc	V	Cr	Mn	Fe	As	Y	Zr	Nb	Sn	Sb	Ta	W
Stog'er Tight	BN-748	F1-1	562819	13003	14745	2	83	24	1424	4	7	5383	14	3	206	864	92	117	55	505
Stog'er Tight	BN-748	F1-2	588252	1322	1558	1	105	18	1359	3	5	5052	9	1	456	781	26	249	54	98
Stog'er Tight	BN-748	F1-3	588454	933	1084	0	40	13	1401	3	3	5364	7	1	254	1143	50	256	72	272
Stog'er Tight	BN-748	F1-4	575911	3386	3440	1	57	29	1346	3	22	12017	10	5	1492	1194	59	101	79	199
Stog'er Tight	BN-748	F1-5	588961	294	483	0	220	21	1357	2	5	4981	7	6	1006	1301	58	290	89	267
Stog'er Tight	BN-748	F1-8	586164	372	422	0	2781	21	1325	2	90	6227	5	2	257	1331	72	141	94	43
Stog'er Tight	BN-748	F2-1	577560	1933	1562	0	4645	30	1485	3	47	7222	17	1	530	1020	129	205	73	2887
Stog'er Tight	BN-748	F2-2	577540	5138	5393	1	1475	39	1269	2	23	5585	33	4	451	821	117	219	56	1185
Stog'er Tight	BN-748	2	559133	11213	13264	2	120	25	1680	7	13	7341	16	7	844	2067	392	400	123	2701
Stog'er Tight	BN-748	5	584068	1385	1456	1	187	27	1434	4	8	7543	16	9	1360	1164	85	180	73	351
Stog'er Tight	BN-748	6	559576	11171	11803	1	85	25	1491	3	30	11771	37	2	608	1588	115	452	96	496
Stog'er Tight	BN-748	8	579033	332	718	0	5803	19	1410	3	159	9760	8	3	215	1307	75	385	77	40
Stog'er Tight	BN-748	10	555109	7028	7666	1	9030	21	1622	3	230	11460	30	3	265	1243	167	582	85	4804
Stog'er Tight	BN-748	14	586511	1296	1505	0	963	38	1448	1	22	5710	5	1	769	743	34	144	44	117
Stog'er Tight	BN-748	11	532111	17229	17215	2	154	28	1372	4	73	28032	40	5	971	1158	100	229	76	549
Stog'er Tight	BN-748	7	559916	9426	12473	2	73	114	1555	7	7	6742	18	15	5717	1111	179	274	61	1660
Stog'er Tight	BN-748	8	567227	5871	7824	3	439	52	1354	5	27	9126	16	44	5621	959	74	346	64	299
Stog'er Tight	BN-748	9	568886	4449	3825	1	375	21	1407	4	48	17568	20	3	620	1294	100	186	77	465
Stog'er Tight	BN-748	2	573586	2628	2731	1	4360	36	1725	8	48	9326	10	9	695	1366	180	284	89	2269

The Ti content reported in the table was calculated based on the Ti content in stochiometric rutile (599349 ppm Ti) minus de content of each of the analyzed elements present as cations in the structure of rutile.

Table 4.3. Secondary ion mass spectrometry (SIMS) analyses of hydrothermal rutile (in ppm) from the Argyle orogenic gold deposit.

Deposit	Sample #	Analysis #	Ti_{est}	Al	Si	P	Ca	Sc	V	Cr	Mn	Fe	As	Y	Zr	Nb	Sn	Sb	Ta	W
Argyle	AE-660	F1-4	574791	722	15551	2	148	112	3544	13	7	2898	41	65	465	440	30	158	20	342
Argyle	AE-660	F1-5	582774	1755	2505	1	205	128	4311	15	8	5518	60	124	1166	411	22	133	25	190
Argyle	AE-660	F1-7	569447	1308	14709	2	3143	100	3017	9	51	5727	57	114	1006	446	22	133	33	27
Argyle	AE-660	F1-2	579466	843	6525	1	356	153	7169	27	8	2629	85	188	396	347	37	183	17	920
Argyle	AE-660	F1-12	571937	1513	14239	2	418	174	5675	16	6	2354	60	139	375	675	57	233	36	1442
Argyle	AE-660	F3-1	542907	903	43595	9	2856	117	3215	24	52	3375	68	174	1272	492	37	183	24	45
Argyle	AE-660	F3-5	580225	4233	4842	2	1787	111	3320	12	20	2770	32	50	1487	220	19	87	16	116
Argyle	AE-660	F3---5	561018	6712	10905	3	9266	97	3449	18	114	6318	32	74	915	243	16	68	17	82
Argyle	AE-660	F4-1	583380	761	2590	1	430	198	6077	14	10	2904	94	147	429	648	57	215	32	1363
Argyle	AE-660	F4-2	573819	830	12379	1	354	173	6792	16	8	2399	100	186	198	530	42	192	38	1293
Argyle	AE-660	F4-3	552603	703	34695	2	340	156	5572	12	6	2905	103	160	427	380	34	163	20	1068
Argyle	AE-679	F1-3b	588584	556	5087	1	116	17	636	1	5	2981	16	8	465	650	29	102	33	63
Argyle	AE-679	F1-6b	584963	658	7425	1	216	32	1174	3	5	2849	42	81	521	923	118	105	55	177
Argyle	AE-679	F2-1	584297	1412	6554	1	61	10	838	2	3	4128	10	2	86	1798	16	54	74	4
Argyle	AE-679	F2-4	564673	1207	3895	1	46	22	796	3	6	17205	13	6	1734	9215	41	225	232	30
Argyle	AE-679	F2-6	587201	660	1153	0	237	23	1665	5	9	3644	32	67	265	3553	60	108	127	540
Argyle	AE-679	F2-7	575925	3055	8107	1	69	4	633	2	14	8718	14	2	155	2460	15	69	91	15
Argyle	AE-679	3	573140	850	1801	1	1188	4	628	2	74	13988	20	0	609	6680	22	127	209	5
Argyle	AE-679	7	579197	657	5508	1	322	16	783	2	23	7824	31	23	934	3724	17	98	143	45
Argyle	AE-679	8	587194	1997	883	0	83	11	879	3	5	6050	38	1	104	1932	11	65	86	8
Argyle	AE-679	11	591559	514	567	0	311	11	747	2	8	4438	25	8	406	534	19	116	37	50
Argyle	AE-679	7	576912	1292	4923	1	120	3	771	4	22	13266	30	2	130	1727	10	50	82	4
Argyle	AE-679	8	570908	768	16922	3	228	24	1726	8	9	4749	42	53	209	3358	50	67	114	111
Argyle	AE-679	9	586630	591	5434	1	185	15	697	2	6	4145	35	8	520	756	38	132	41	114
Argyle	AE-679	11	542822	938	46951	3	301	46	1395	4	11	4533	64	92	786	679	213	91	36	385

The Ti content reported in the table was calculated based on the Ti content in stochiometric rutile (599349 ppm Ti) minus de content of each of the analyzed elements present as cations in the structure of rutile.

Chapter 5: Summary of conclusions and directions for future research

5.1. Conclusions and key findings

This thesis focused on the characterization of hydrothermal alteration phases linked to precious metal mineralization in both epithermal and orogenic environments, combining a wide range of analytical techniques to elucidate: (1) the origin, mineralogy, and geochemistry of hydrothermal phyllosilicates in Neoproterozoic epithermal deposits in the Avalon Zone terrane of Newfoundland; (2) the main macro- and micro-spectroscopic features of key hydrothermal alteration minerals from these examples of epithermal deposits and their application to mineral exploration; (3) the evolution of Fe-Ti phases, such as rutile, with increasing intensity of alteration in orogenic gold deposits of Silurian age from the Baie Verte region of Newfoundland, and; (4) the potential of rutile geochemistry as a tool for exploration for orogenic gold deposits in this studied region, and globally.

Key research findings include:

i. The studied high-sulfidation epithermal examples (Hope Brook deposit and Hickey's Pond prospect) are characterized by a hydrothermal phyllosilicate assemblage consisting of Fe-bearing muscovite, paragonite, Al-clinochlore, pyrophyllite, kaolinite, and minor mixed-layer phases. At Hope Brook, Fe-bearing muscovite replaces original paragonite, and is defined by $2M_1$ polytypism and limited Tschermak substitution. The Al-clinochlore has a ripidolitic composition at Hope Brook, is defined by *IIb* polytypism, and shows limited Tschermak substitution. Geothermometric calculations indicate crystallization temperatures between 200 °C and 300 °C. This mineralogy and its spatial distribution are consistent with the progressive cooling and neutralization of initially hot and acidic magmatic-hydrothermal fluids, with these high-sulfidation deposits displaying the following proximal-to-distal zonation: (a) massive silicic zone(s) (i.e., vuggy silica) with negligible phyllosilicate content, (b) advanced argillic alteration (pyrophyllite, kaolinite group minerals - and minor paragonite being replaced by Fe-bearing muscovite), (c) argillic alteration (Fe-bearing muscovite, kaolinite group minerals), and (d) sericitic and propylitic alterations (Fe-bearing muscovite and Al-clinochlore).

ii. The Heritage low-sulfidation epithermal prospect is characterized by a hydrothermal phyllosilicate assemblage of Fe-Mg-muscovite, Al-clinochlore, clinochlore, and minor mixed-layer clay minerals. The Fe-Mg-bearing muscovite is defined by the prevalence of $2M_2$ polytypism and extensive Tschermak substitution (with phengitic composition). The Al-clinochlore has a brunsvigite composition, shows high contents of Mn (up to 4.39 wt.% MnO), *IIb* polytypism, and limited Tschermak substitution. Geothermometric calculations imply crystallization temperatures between 100 °C and 200 °C. Conversely, clinochlore is of brunsvigite-diabantite composition, displaying *Ib* polytypism, and higher degrees of Tschermak substitution. Geothermometric calculations imply relatively lower crystallization temperatures, between 90 °C and 130 °C. This phyllosilicate chemistry is consistent with formation by neutral and reducing hydrothermal fluids. The Fe-Mg muscovite and Al-clinochlore are widespread throughout the broad zone of silicification that contains epithermal veins and breccias − showing no regular/concentric zonation patterns. In this example, alteration zoning is better defined by non-phyllosilicates, with a mineralized core rich in chalcedony and adularia, while quartz becomes more dominant in the distal part of the system.

iii. Raman microspectroscopy can identify and distinguish many important hydrothermal alteration minerals of epithermal origin at the microscopic scale, including alunite group minerals (alunite and natroalunite endmembers), pyrophyllite, white mica (muscovite/paragonite and phengite), and Fe-Mg chlorite (clinochlore and chamosite end-members). For white mica, the sensitivity of the Raman band between 1000 cm^{-1} and 1150 cm^{-1} to changes in Si and Al in tetrahedral coordination suggests that compositional variations due to Tschermak substitution can be effectively detected by Raman microspectroscopy. Consequently, pure muscovitic/paragonitic mica compositions can be successfully distinguished from more phengitic/celadonitic compositions. For chlorite, the position of the main chlorite Si-O-Si band shifts from >680 cm^{-1} for Mg-rich chlorite to <670 cm^{-1} for Fe-rich chlorite. It is therefore possible to estimate the Fe^{2+} content in chlorite by determining the position of this main chlorite Raman band. Raman microspectroscopy has been shown to be a promising, cost-effective, and near-real time method to obtain mineralogical and geochemical information of key hydrothermal phases at the microscale, with potential application during mineral exploration campaigns, where it could be applied for a wide array of hydrothermal ore deposits alongside reflectance spectroscopy.

iv. The hydrothermal evolution of Fe-Ti phases in orogenic gold occurrences in the Baie Verte region (Animal Pond, Stog’er Tight, and Argyle occurrences) ultimately results in the formation of hydrothermal rutile from the progressive alteration of magmatic magnetite, Ti-magnetite, and ilmenite. The generalized evolution from distal to proximal zones in the studied examples consists of (Ti)-magnetite - ilmenite - titanite - rutile, which reflects a chemical progression from Fe-rich phases to Ti-rich phases with increasing hydrothermal alteration and proximity to mineralization. This reflects the relatively mobile character of Fe and immobile character of Ti in the hydrothermal fluids.

v. Hydrothermal rutile from the studied orogenic gold occurrences is characterized by trace element contents of up to 5717 ppm Zr, 9215 ppm Nb, 392 ppm Sn, 582 ppm Sb, 232 ppm Ta, and 4804 ppm W. Rutile/brookite from the essentially barren Animal Pond prospect contains distinctly higher concentrations of Fe and Mn, while rutile from the auriferous orogenic vein systems of the Stog'er Tight and Argyle deposits contains higher concentrations of Nb, Sb, Sn, and Ta. Based on principal component analysis (PCA), Sb-Sn, Nb-Ta, and W clusters coincide with rutile from mineralized orogenic gold systems, as opposed to Ca-Mn-Fe-Zr clusters being characteristics of rutile/brookite from the barren Animal Pond prospect. There appears to be a progressive compositional transition from Animal Pond (Ca-Mn-Fe-Zr clusters), through intermediate alteration zones at Argyle (Sc-Y-As and Cr clusters), to Au-related proximal rutile at Stog'er Tight and Argyle (Sb-Sn, Ta-Nb, and W clusters). Antimony in particular was found to provide strong discrimination between hydrothermal rutile related to orogenic gold mineralization and rutile from unmineralized magmatic and metamorphic rocks. Rutile from the mineralized Stog'er Tight and Argyle deposits generally shows Sb values above 80-100 ppm, while rutile from the barren Animal Pond prospect shows Sb contents below 66 ppm. This characteristic Fe-Mn-poor and Sb-enriched composition of rutile associated with auriferous veins has potential application to gold exploration in the Baie Verte region and elsewhere.

5.2. Relevance of the thesis

This study contributes to the characterization and understanding of hydrothermal alteration processes in two economically relevant types of hydrothermal gold deposit, by integrating innovative combinations of state-of-the-art analytical techniques. Relevant analytical improvements include the advancement of Raman spectroscopy for the study of hydrous alteration minerals in ore deposits in general, and the use of secondary ion mass spectrometry to quantify key trace elements in rutile for use as pathfinders in gold exploration.

The results reported here potentially have a direct positive impact on the mineral exploration industry, as they define mineralogical and geochemical alteration signatures in rutile for the exploration for new orogenic gold occurrences specifically in the Baie Verte region of Newfoundland. The distinct mineralogical and geochemical evolution of Fe-Ti phases reported in this thesis could also be applied to other orogenic terranes, where wallrock sulfidation and extensive rutile formation are the main precipitation mechanism for gold. Furthermore, this study was also intended to increase awareness of the prospectivity for epithermal Au-Ag systems in Proterozoic terranes (in Newfoundland and elsewhere), which are significantly underexplored given their traditional perception as having poor preservation potential.

5.3. Directions for future work

This study has provided new insights into the mineralogy, geochemistry, and characteristic spectral features of hydrothermal alteration minerals linked to epithermal precious metals, based on deposits of Neoproterozoic age in the Avalon Zone terrane. In addition, it has provided novel information on the mineralogy and geochemistry of rutile from various orogenic gold deposits in Newfoundland, with a direct application for regional gold exploration.

Nonetheless, some questions remain unanswered and there is great potential for further research that follows the themes of this dissertation. The main directions for future work are presented below:

i. For the studied epithermal occurrences, the trace element analysis of hydrothermal phyllosilicates could provide relevant new information on epithermal processes, such as origin of fluids, hydrothermal fluid composition, and precipitation mechanism of precious metals. Rare earth element (REE) signatures, in particular, could reveal critical data on the REE content of hydrothermal fluids, their origin, and the influence of precursor mineral chemistry during hydrothermal alteration and mineralization. This same approach could be applied to other hydrothermal deposit types.

ii. The general Raman spectral features of phyllosilicates have been recently reported by Wang et al. (2015) and Gates et al. (2017). The Raman band assignments reported by these authors were the groundwork on which the Raman band assignments of hydrothermal phyllosilicates from epithermal deposits presented in this thesis are based. However, in order for this technique to become more common in the study of hydrothermal phyllosilicates, it is necessary to create a more comprehensive Raman spectra database, where multiple chemistries of compositionally variable phyllosilicate species, from various hydrothermal ore deposits, are reported. This would encourage more economic geologists to consider Raman in their analytical routines to characterize the composition of hydrothermal alteration phases.

iii. Rapid field identification and chemical characterization of hydrothermal alteration mineralogy is critical for exploration and ore mapping. This is the reason field portable spectroscopic techniques are becoming more popular during mineral exploration campaigns. The recent emergence of field portable Raman spectroscopes is very promising, given that a wide range of hydrothermal alteration minerals can be identified, including quartz, feldspars, garnets, pyroxenes, amphiboles, phyllosilicates, sulfates, and other hydrous and anhydrous phases. Reflectance spectroscopy, and in particular VIS-NIR-SWIR spectroscopy, is limited by being able to only identify hydrous phases. A more comprehensive comparison of the performance of field portable technologies for identification of hydrothermal alteration phases is therefore needed in order to assess the most appropriate instrument for specific mineral groups and mineral deposit types.

iv. Raman spectroscopy is an excellent tool to study the chemical differences of hydrothermal alteration phases at the microscale. Hydrothermal alteration is a very complex process and multiple hydrothermal alteration events are commonplace in hydrothermal ore deposits. Therefore, the development of nano-spectroscopic techniques, such as Tip-Enhanced Raman Spectroscopy (TERS), could prove highly valuable on discerning critical compositional information of alteration minerals spatially, temporally, and genetically associated with Au-Ag mineralization in the epithermal environment and elsewhere.

v. Rutile related to orogenic gold mineralization in the Baie Verte region has a distinctive trace element composition, including anomalous Sb contents, compared to rutile from non-auriferous environments. To test the potential of this geochemical signature of rutile for its application to exploration of orogenic gold deposits in this region, a field campaign to sample till and soil material in the area should be conducted. Rutile should be separated and consecutively analyzed by SEM, EPMA, and SIMS, in order to detect field areas with high concentrations of rutile with the same geochemical signature as the one reported in this thesis from orogenic gold occurrences (in particular, low Fe and Mn contents, high Sb content).

vi. The careful characterization of titania polymorphs by electron backscatter diffraction analysis (EBSD) or Raman microspectroscopy should be integrated into future studies, as this might provide an additional criterion for discrimination between mineralized and barren orogenic gold occurrences in the Baie Verte region and elsewhere.

vii. As a complement to rutile geochemistry, the chemistry of other Fe-Ti phases modified during orogenic gold mineralization, particularly titanite, should be investigated. For these phases, there is additional potential to trace back the incorporation of certain trace elements during specific hydrothermal events, further supporting exploration for orogenic gold deposits.

viii. The work reported here on orogenic gold deposits reaffirmed that there are significant knowledge gaps with respect to the source and behaviour of specific fluid-mobile trace elements that are important indicators for this style of gold mineralization; in particular, Sb, Sn, Nb, Ta, and W. An exhaustive examination into the probably distal origin of these mobile trace elements was beyond the scope of this study, but it remains a complex and important topic in the field of ore deposit geochemistry.

5.4. References

Gates, W., Kloprogge, J.T., Madejova, J., Bergaya, F. (2017): Infrared and Raman spectroscopies of clay minerals. Elsevier, 620 pp.

Wang, A., Freeman, J.J., Jolliff, B.L. (2015): Understanding the Raman spectral features of phyllosilicates. Journal of Raman Spectroscopy 46, 829-845. https://doi.org/10.1002/jrs.4680

Bibliography and References

Abd Elmola, A., Charpentier, D., Buatier, M., Lanari, P., Monié, P., 2017. Textural-chemical changes and deformation conditions registered by phyllosilicates in a fault zone (Pic de Port Vieux thrust, Pyrenees). Applied Clay Science 144, 88-103. https://doi.org/10.1016/j.clay.2017.05.008

Adlakha, E.E., Hattori, K., Kerr, M.J., Boucher, B.M., 2020. The origin of Ti-oxide minerals below and within the eastern Athabasca Basin, Canada. American Mineralogist 105(12), 1875-1888. https://doi.org/10.2138/am-2020-7235

Agangi, A., Reddy, S.M., Plavsa, D., Fougerouse, D., Clark, C., Roberts, M., Johnson, T.E., 2019. Antimony in rutile as a pathfinder for orogenic gold deposits. Ore Geology Reviews 106, 1-11. https://doi.org/10.1016/j.oregeorev.2019.01.018

Aitchison, J., 1982. The statistical analysis of compositional data. Journal of the Royal Statistical Society: Series B (Methodological) 44(2), 139-160. https://doi.org/10.1111/j.2517-6161.1982.tb01195.x

Anaconda Mining Inc. https://www.anacondamining.com (Accessed: 18 October 2019).

Anaconda Mining Inc. Technical Report NI 43-101: Mineral resource and mineral reserve update on the Point Rousse project Baie Verte, Newfoundland and Labrador, Canada. Prepared by: Cullen, M. Pitman, C., Coperland, D., McNeill, P., Slepcev, G. February 22, 2018.

Anderson, S.D., Jamieson, R.A., Reynolds, P.H., Dunning, G.R., 2001. Devonian extension in northwestern Newfoundland: ^{40}Ar/^{39}Ar and U-Pb data from the Ming's Bight area, Baie Verte Peninsula. The Journal of Geology 109(2), 191-211. https://doi.org/10.1086/319237

Angiboust, S., Harlov, D., 2017. Ilmenite breakdown and rutile-titanite stability in metagranitoids: natural observations and experimental results. American Mineralogist 102(8), 1696-1708. https://doi.org/10.2138/am-2017-6064

Arbiol, C., Layne, G.D., Zanoni, G., Šegvić, B., 2021. Characteristics and genesis of phyllosilicate hydrothermal assemblages from Neoproterozoic epithermal Au-Ag mineralization of the Avalon Zone of Newfoundland, Canada. Applied Clay Science 202, 105962. https://doi.org/10.1016/j.clay.2020.105960

Árkai, P., Livi, K.J.T., Horváth, P., 2008. Dioctahedral mixed K-Na-micas and paragonite in diagenetic to low-temperature metamorphic terranes: bulk rock chemical, thermodynamic and textural constraints. Central European Geology 51/4, 283-314. https://doi.org/10.1556/ceugeol.51.2008.4.1

Arribas, A., 1995. Characteristics of high-sulfidation epithermal deposits, and their relation to magmatic fluid. Mineralogical Association of Canada Short Course 23, 419-454.

Autefage, F. and Couderc, J.J., 1980. Étude du Mécanisme de la Migration du Sodium et du Potassium au Cours de leur Analyse a la Microsonde Électronique. Bulletin de Minéralogie 130, 623-629.

Bailey, S.W., 1980a. Structures of layer silicates. In: Brindley, G.W., Brown, G., editors. Crystal structures of clay minerals and their X-ray identification, Monograph 5. London Mineralogical Society, 1-123. https://doi.org/10.1180/mono-5.1

Bailey, S.W., 1980b. Summary of recommendations of AIPEA nomenclature committee on clay minerals. American Mineralogist 65, 1-7.

Barth, M. G., McDonough, W. F., Rudnick, R. L., 2000. Tracking the budget of Nb and Ta in the continental crust. Chemical Geology 165(3-4), 197-213. https://doi.org/10.1016/S0009-2541(99)00173-4

Barton, P.B., Bethke, P.M., Roedder, E, 1977. Environment of ore deposition in the Creede mining district, San Juan Mountains, Colorado; Part III, Progress toward interpretation of the chemistry of the ore-forming fluid for the OH Vein. Economic Geology 72, 1-24. https://doi.org/10.2113/gsecongeo.72.1.1

Bath, A.B., Walshe, J.L., Cloutier, J., Verrall, M., Cleverley, J.S., Pownceby, M.I., Macrae, C.M., Wilson, N.C., Tunjic, J., Nortje, G.S., and Robinson, P., 2013. Biotite and apatite as tools for tracking pathways of oxidized fluids in the Archean East Repulse gold deposit, Australia. Economic Geology 108, 667-690. https://doi.org/10.2113/econgeo.108.4.667

Beaufort, D., Rigault, C., Billon, S., Billault, V., Inoue, A., Inoue, S., Patrier, P., 2015. Chlorite and chloritization processes through mixed-layer mineral series in low-temperature geological systems - a review. Clay Minerals 50, 497-523. https://doi.org/10.1180/claymin.2015.050.4.06

Bédard, J. H., Lauziere, K., Tremblay, A., Sangster, A. L., Douma, S., Dec, T., 2000. Betts Cove ophiolite and its cover rocks. Geological Survey of Canada Bulletin 550, 76 pp.

Belousova, E.A., Griffin, W.L., O'Reilly, S.Y., Fisher, N.I., 2002. Apatite as an indicator mineral for mineral exploration: trace-element compositions and their relationship to host rock type. Journal of Geochemical Exploration 76(1), 45-69. https://doi.org/10.1016/S0375-6742(02)00204-2

Bergaya, F. and Lagaly, G., 2013. Handbook of Clay Science. Elsevier, 1752 pp.

Berger, B.R. and Bethke, P.M., 1985. Geology and geochemistry of epithermal systems. Reviews in Economic Geology 2, 297 pp. https://doi.org/10.5382/Rev.02

Berger, B.R. and Henley, R.W., 1989. Advances in the understanding of epithermal gold-silver deposits, with special reference to the western United States. Economic Geology Monograph 6, 405-423. https://doi.org/10.5382/Mono.06.32

Bierlein, F.P. and Crowe, D.E., 2000. Phanerozoic Orogenic Lode Gold Deposits. In Gold in 2000 (S.G. Hagemann and P.E. Brown, eds.). Reviews in Economic Geology 13, 103-140. https://doi.org/10.5382/Rev.13.03

Bishop, J.L. and Murad, E., 2004. Characterization of minerals and biogeochemical markers on Mars: A Raman and IR spectroscopic study of montmorillonite. Journal of Raman Spectroscopy 35, 480-486. https://doi.org/10.1002/jrs.1173

Bishop, J.L. and Murad, E., 2005. The visible and infrared spectral properties of jarosite and alunite. American Mineralogist 90(7), 1100-1107. https://doi.org/10.2138/am.2005.1700

Bishop, J.L., Lane, M.D., Dvar, M.D., Brown, J., 2008a. Reflectance and emission spectroscopy study of four groups of phyllosilicates: smectites, kaolinite-serpentines, chlorites, and micas. Clay Minerals 43, 35-54. https://doi.org/10.1180/claymin.2008.043.1.03

Bishop, J.L., Dobrea, E.Z.N., McKeown, N.K., Parente, M., Ehlmann, B.L., Michalski, J.R., Milliken, R.E., Poulet, F., Swayze, G.A., Mustard, J.F., 2008b. Phyllosilicate diversity and past aqueous activity revealed at Mawrth Vallis, Mars. Science, 321(5890), 830-833. https://doi.org/10.1126/science.1159699

Bonham, H.F., 1986. Models for volcanic-hosted epithermal precious metal deposits: A review: Volcanism, hydrothermal systems and related mineralization, 5th International Volcanological Congress, University of Auckland, Auckland, New Zealand, Proceedings, 13-17.

Bourdelle, F., 2021. Low-temperature chlorite geothermometry and related recent analytical advances: a review. Minerals 11(2), 130. https://doi.org/10.3390/min11020130

Bourdelle, F., Parra, T., Chopin, C., Beyssac, O., 2013. A new chlorite geothermometer for diagenetic to low-grade metamorphic conditions. Contributions to Mineralogy and Petrology 165, 723-735. https://doi.org/10.1007/s00410-012-0832-7

Breitinger, D.K., Krieglstein, R., Bogner, A., Schwab, R.G., Pimpl, Th.H., Mohr, J., Schukow, H., 1997. Vibrational spectra of synthetic minerals of the alunite and crandallite type. Journal of Molecular Structure 408-409, 287-290. https://doi.org/10.1016/S0022-2860(96)09627-5

Brigatti, M.F., Malferrari, D., Poppi, M., Poppi, L., 2005. The *$2M_1$* dioctahedral mica polytype: a crystal chemical study. Clays and Clay Minerals 53, 190-197. https://doi.org/10.1346/CCMN.2005.0530209

Brindley, G.W. and Wardle, R., 1970. Monoclinic and triclinic forms of pyrophyllite and pyrophyllite anhydride. The American Mineralogist 55, 1259-1272.

Bucher, K., 2005. Facies and Zones. In: Metamorphic Rocks. Encyclopedia of Geology, 402-409. https://doi.org/10.1016/B0-12-369396-9/00319-1

Buzgar, N., Buzatu, A., Sanislav, I.V., 2009. The Raman study of certain sulfates. Analele Stiintifice ale Universitatii Al. I. Cuza 55, 5-23.

Carrillo-Rosúa, J., Morales-Ruano, S., Esteban-Arispe, I., Fenoll Hach-Alí, P., 2009. Significance of phyllosilicate mineralogy and mineral chemistry in an epithermal environment. Insights from the Palai-Islica Au-Cu deposit (Almería, SE Spain). Clays and Clay Minerals 57(1), 1-24. https://doi.org/10.1346/CCMN.2009.0570101

Castonguay, S., Skulski, T., van Staal., C., Currie, M., 2009. New insights on the structural geology of the Pacquet Harbour Group and Point Rousse Complex, Baie Verte Peninsula, Newfoundland. Current research, Newfoundland and Labrador Department of Natural Resources, Geological Survey Report 09-1, 147-158.

Castonguay, S., van Staal, C.R., Joyce, N., Skulski, T., and Hibbard, J.P., 2014. Taconic metamorphism preserved in the Baie Verte Peninsula, Newfoundland Appalachians: Geochronological evidence for ophiolite obduction and subduction and exhumation of the leading edge of the Laurentian (Humber) margin during closure of the Taconic Seaway. Geoscience Canada 41 (4), 459-482. https://doi.org/10.12789/geocanj.2014.41.055

Cathelineau, M., 1988. Cation site occupancy in chlorites and illites as a function of temperature. Clay Minerals 23, 471-485. https://doi.org/10.1180/claymin.1988.023.4.13

Cathelineau, M. and Nieva, D., 1985. A chlorite solid solution geothermometer: The Los Azufres (Mexico) geothermal system. Contributions to Mineralogy and Petrology 91, 235-244. https://doi.org/10.1007/BF00413350

Çelik, M., Karakaya, N., Temel, A., 1999. Clay minerals in hydrothermally altered volcanic rocks, Eastern Pontides, Turkey. Clays and Clay Minerals 47, 708-717. https://doi.org/10.1346/CCMN.1999.0470604

Clark, J.R. and Williams-Jones, A.E., 2004. Rutile as a potential indicator mineral for metamorphosed metallic ore deposits. Rapport Final de DIVEX, Sous-projet SC2: Montreal, 17 p.

Clark, R.N., King, T.V., Klejwa, M., Swayze, G.A., Vergo, N., 1990. High spectral resolution reflectance spectroscopy of minerals. Journal of Geophysical Research 95(B8), 12653-12680. https://doi.org/10.1029/JB095iB08p12653

Clarke, M., 2013. Host lithologies, breccia development, alteration and gold mineralization at the Big Easy Prospect. St. John's, NL: Memorial University of Newfoundland and Labrador.

Colvine, A.C., Fyon, J.A., Heather, K.B., Marmont, S., Smith, P.M., Troop, D.G., 1988. Archean lode gold deposits in Ontario. Ontario Geological Survey, Miscellaneous Paper 139, 136 p.

Cooke, D.R. and Simmons, SF., 2000. Characteristics and genesis of epithermal gold deposits. Society of Economic Geologists, Reviews in Economic Geology 13, 221-244. https://doi.org/10.5382/Rev.13.06

Copeland, D.A., Pitman, C., Evans, D.T.W., McNeill, P., Slepcev, G., 2015. Mineral resource and mineral reserve update on the Pine Cove Mine and mineral resource estimate on the Stog'er Tight deposit, Point Rousse Project Baie Verte. NI-43-101 Technical Report: Anaconda Mining Inc., Newfoundland and Labrador, Canada, 249 p.

Corfu, F. and Davis, D.W., 1991. Comment on "Archaean hydrothermal zircon in the Abitibi greenstone belt: constraints on the timing of gold mineralization" by J.C. Claoue-Long, R.W. King, and R. Kerrich. Earth and Planetary Sciences Letters 104(2-4), 545-552. https://doi.org/10.1016/0012-821X(91)90229-B

Cuadros, J., Michalski, J.R., Dekov, V., Bishop, J.L., 2016. Octahedral chemistry of 2:1 clay minerals and hydroxyl band position in the near-infrared: Application to Mars. American Mineralogist 101(3), 554-563. https://doi.org/10.2138/am-2016-5366

Curtis, C.D.; Hughes, C.R.; Whiteman, J.A.; Whittle, C.K., 1985. Compositional variations within some sedimentary chlorites and some comments on their origin. Mineralogical Magazine 49, 375-386.

Dec, T., O'Brien, S.J., and Knight, I., 1992. Late Precambrian volcaniclastic deposits of the Avalonian Eastport Basin (Newfoundland Appalachians): Petrofacies, detrital clinopyroxene geochemistry and paleotectonic implications. Precambrian Research 59, 243-262. https://doi.org/10.1016/0301-9268(92)90059-W

De Caritat, P., Hutcheon, I., Walshe, J.L., 1993. Chlorite geothermometry: a review. Clays and Clay Minerals 41, 219-239. https://doi.org/10.1346/CCMN.1993.0410210

Deditius, A.P., Utsunomiya, S., Renock, D., Ewing, R.C., Ramana, C.V., Becker, U., Kesler, S.E., 2008. A proposed new type of arsenian pyrite: composition, nanostructure and geological significance. Geochimica et Cosmochimica Acta 72(12), 2919-2933. https://doi.org/10.1016/J.GCA.2008.03.014

Deditius, A.P., Reich, M., Kesler, S.E., Utsunomiya, S., Chryssoulis, S.L., Walshe, J., Ewing, R.C., 2014. The coupled geochemistry of Au and As in pyrite from hydrothermal ore deposits. Geochimica et Cosmochimica Acta 140, 644-670. https://doi.org/10.1016/j.gca.2014.05.045

Deer, W.A., Howie, R.A., Zussman, J., 1966. An introduction to the rock forming minerals. Longman Scientific and Technical, Essex (1966), 498 pp. https://doi.org/10.1180/DHZ

Deyell, C.L. and Dipple, G.M., 2005. Equilibrium mineral-fluid calculations and their application to the solid solution between alunite and natroalunite in the El Indio-Pascua belt of Chile and Argentina. Chemical Geology 215(1-4), 219-234. https://doi.org/10.1016/j.chemgeo.2004.06.039

Dimmell, P., 2012. Report of 2012 Exploration (Prospecting, Stream Sediment Geochemistry, Airborne Geophysics, Diamond Drilling, Compilation,) on the Big Easy (BE) Property. St. John's, NL: Department of Natural Resources.

Drits, V.A. and Sakharov, B.A., 1976. X-ray Structural Analysis of Mixed-layer Minerals. Nauka, Moscow, Russian Federation.

Dostal, J., Kontak, D.J., Chatterjee, A.K., 2009. Trace element geochemistry of scheelite and rutile from metaturbidite-hosted quartz vein gold deposits, Meguma Terrane, Nova Scotia, Canada: genetic implications. Mineralogy and Petrology 97(95), 95-109. https://doi.org/10.1007/s00710-009-0067-0

Dubé, B., 1990. A preliminary report on contrasting structural styles of gold-only deposits in western Newfoundland. Current Research, Geological Survey of Canada, Paper 90-1B, 77-90.

Dubé, B., Poulsen, H.K., Guha, J., 1989. The effects of layer anisotropy on auriferous shear zones: The Norbeau Mine, Quebec. Economic Geology 84(4), 871-878. https://doi.org/10.2113/gsecongeo.84.4.871

Dubé, B., Lauziére, K., and Gaboury, D., 1991. Structural control on the mesothermal vein-type, Rendell-Jackman gold deposit, Springdale Peninsula, Newfoundland. Newfoundland Geological Survey, Department of Mines and Energy, 81.

Dubé, B., Lauziére, K., and Gaboury, D., 1992. Preliminary report on the structural control of the Rendell-Jackman gold deposit, Springdale Peninsula, Newfoundland. Current Research, Geological Survey of Canada, Paper 92-1D, 1-10.

Dubé, B., Lauziére, K., Poulsen, H.K., 1993. The Deer Cove deposit: An example of "thrust'-related breccia-vein type gold mineralization in the Baie Verte Peninsula, Newfoundland. Geological Survey, Newfoundland and Labrador Department of Natural Resources, Current Research, Report 93-ID, 1-10.

Dubé, B., Dunning, G., Lauzière, K., 1995. Geology of the Hope Brook Mine, Newfoundland, Canada: A preserved Late Proterozoic high-sulfidation epithermal gold deposit and its implications for exploration. Economic Geology 93, 405-436. https://doi.org/10.2113/gsecongeo.93.4.405

Dubé, B. and Gosselin, P., 2007. Greenstone-hosted quartz-carbonate vein deposits. In Goodfellow, W.D., ed.: Mineral Deposits of Canada: A Synthesis of Major Deposit-Types, District Metallogeny, the Evolution of Geological Provinces, and Exploration Methods. Geological Association of Canada, Mineral Deposits Division, Special Publication 5, 49-73.

Duke, E.F., 1994. Near infrared spectra of muscovite, Tschermak substitution, and metamorphic reaction progress: Implications for remote sensing. Geology 22(7), 621-624. https://doi.org/10.1130/0091-7613(1994)022<0621:NISOMT>2.3.CO;2

Dunning, G. and O'Brien, S.J., 1989. Late Proterozoic-Early Paleozoic crust in the Hermitage flexure, Newfoundland Appalachians: U-Pb ages and tectonic significance. Geology 17, 548-551. https://doi.org/10.1130/0091-7613(1989)017<0548:LPEPCI>2.3.CO;2

Einaudi, M.T., Hedenquist, J.W., and Inan, E.E., 2003. Sulfidation state of fluids in active and extinct hydrothermal systems: Transitions from porphyry to epithermal environments. Society of Economic Geologists Special Publication 10, 285-313. https://doi.org/10.5382/SP.10.15

Etoh, J., Izawa, E., Watanabe, K., Taguchi, S., Sekine, R., 2002. Bladed quartz and its relationship to gold mineralization in the Hishikari low-sulfidation epithermal gold deposit, Japan. Economic Geology 97, 1841-1851. https://doi.org/10.2113/gsecongeo.97.8.1841

Evans, D.T.W., 2004. Epigenetic gold occurrences, Baie Verte Peninsula (NTS 12H/09, 16 and 12I/01), Newfoundland. Government of Newfoundland and Labrador, Department of Natural Resources, Geological Survey. Mineral Resources Report 11, 157 pp.

Farmer, V.C., 1974. The Infrared Spectra of Minerals. Mineralogical Society Monograph 4, Mineralogical Society of Great Britain and Ireland, 527 pp. https://doi.org/10.1180/mono-4

Farmer, V.C., 1998. Differing effects of particle size and shape in the infrared and Raman spectra of kaolinite. Clay Minerals 33(4), 601-604. https://doi.org/10.1180/claymin.1998.033.4.07

Ferguson, S.A., 2017. Late Neoproterozoic epithermal-style Au mineralization of the Burin Peninsula, Newfoundland: U-Pb geochronology and deposit characteristics. Unpublished Master Thesis. Department of Earth Sciences, Memorial University of Newfoundland, 393 pp.

Ferrier, G., Ganas, A., Pope, R., Miles, A.J., 2019. Prospectivity Mapping for epithermal deposits of Western Milos using a fuzzy multi criteria evaluation approach parameterized by airborne hyperspectral remote sensing data. Geosciences 9(3), 116. https://doi.org/10.3390/geosciences9030116

Foley, S.F., Barth, M.G., Jenner, G.A., 2000. Rutile/melt partition coefficients for trace elements and an assessment of the influence of rutile on the trace element characteristics of subduction zone magmas. Geochimica et Cosmochimica Acta 64(5), 933-938. https://doi.org/10.1016/S0016-7037(99)00355-5

Foster, M.D., 1962. Interpretation of the composition and a classification of the chlorites. U.S. Geological Survey Professional Paper 414, 1-33.

Foster, M. D., 1969. Studies of celadonite and glauconite. U.S. Geological Survey Professional Paper 614-F, Shorter Contributions to General Geology, 117 pp.

Frimmel, H.E., 2008. Earth's continental crustal gold endowment. Earth and Planetary Science Letters 267(1), 45-55. https://doi.org/10.1016/j.epsl.2007.11.022

Frimmel, H.E., 2018. Episodic concentration of gold to ore grade through Earth's history. Earth-Science Reviews 180, 148-158. https://doi.org/10.1016/j.earscirev.2018.03.011

Frost, R.L., 1995. Fourier transform Raman spectroscopy of kaolinite, dickite, and halloysite. Clays and Clay Minerals 43(2), 191-195. https://doi.org/10.1016/0584-8539(93)80088-R

Frost, R.L., 1997. The structure of the kaolinite minerals - a FT-Raman study. Clay Minerals 32(1), 65-77. https://doi.org/10.1180/claymin.1997.032.1.08

Frost, R.L. and Kloprogge, J.T., 2000. Raman spectroscopy of nontronites. Applied Spectroscopy 54(3), 402-405. https://doi.org/10.1366/0003702001949483

Frost, R.L. and Rintoul, L., 1996. Lattice vibrations of montmorillonite: an FT Raman and X-ray diffraction study. Applied Clay Science 11(2-4), 171-183. https://doi.org/10.1016/S0169-1317(96)00017-8

Frost, R.L. and Shurvell, H.F., 1997. Raman microprobe spectroscopy of halloysite. Clays and Clay Minerals 45(1), 68-72. https://doi.org/10.1346/CCMN.1997.0450107

Frost, R.L. and Van Der Gaast, S.J., 1997. Kaolinite hydroxyls - a Raman microscopy study. Clay Minerals 32(3), 471-484. https://doi.org/10.1180/claymin.1997.032.3.09

Frost, R.L., Wills, R.A., Weier, M.L., Martens, W., Kloprogge, J.T., 2006. A Raman spectroscopic study of alunites. Journal of Molecular Structure 785, 123-132. https://doi.org/10.1016/j.molstruc.2005.10.003

Frost, R.L., Bahfenne, S., Čejka, J., Sejkora, J., Plášil, J., Palmer, S.J., 2010. Raman and infrared study of phyllosilicates containing heavy metals (Sb, Bi): bismutoferrite and chapmanite. Journal of Raman Spectroscopy 41(7), 814-819. https://doi.org/10.1002/jrs.2512

Gaillard, N., Williams-Jones, A.E., Clark, J.R., Lypaczewski, P., Salvi, S., Perrouty, S., Piette-Laurière, N., Guilmette, C., Linnen, R.L., 2018. Mica composition as a vector to gold mineralization: Deciphering hydrothermal and metamorphic effects in the Malartic district, Quebec. Ore Geology Reviews 95, 789-820. https://doi.org/10.1016/j.oregeorev.2018.02.009

Gandhi, S.M. and Sarkar, B.C., 2016. Geochemical Exploration. In Essentials of Mineral Exploration and Evaluation (S.M. Gandhi and B.C. Sarkar, eds.). Elsevier, 125-158. https://doi.org/10.1016/B978-0-12-805329-4.00013-2

Gates, W., Kloprogge, J.T., Madejova, J., Bergaya, F., 2017. Infrared and Raman spectroscopies of clay minerals. Elsevier, 620 pp.

Gillet, Ph., Barrat, J.A., Deloule, E. Wadhwa, M., Jambon, A., Sautter, V., Devouard, B., Neuville, D., Benzerara, K., Lesourd, M., 2002. Aqueous alteration in the Northwest Africa 817 (NWA 817) Martian meteorite. Earth and Planetary Science Letters 203(1), 431-444. https://doi.org/10.1016/S0012-821X(02)00835-X

Goldfarb, R.J., Baker, T., Dubé, B., Groves, D.I., Hart, C.J.R., & Gosselin, P., 2005. Distribution, Character, and Genesis of Gold Deposits in Metamorphic Terranes. Economic Geology 100th Anniversary Volume, 407-450. https://doi.org/10.5382/AV100.14

Goldfarb, R.J. and Groves, D.I., 2015. Orogenic Gold: Common or evolving fluid and metal sources through time. Lithos 233, 2-16. https://doi.org/10.1016/j.lithos.2015.07.011

Graham, G.E., Kokaly, F., Kelley, K.D., Hoefen, T.M., Johnson, M.R., Hubbard, B.E., 2018. Application of imaging spectroscopy for mineral exploration in Alaska: A study over Porphyry Cu Deposits in the Eastern Alaska Range. Economic Geology 113(2), 489-510. https://doi.org/10.5382/econgeo.2018.4559

Grathoff, G.H. and Moore, D.M., 1996. Illite polytype quantification using wildfire© calculated x-ray diffraction patterns. Clays and Clay Minerals 44, 835-842. https://doi.org/10.1346/CCMN.1996.0440615

Griffin, W.L. and Ryan, C.G., 1995. Trace elements in indicator minerals: area selection and target evaluation in diamond exploration. Journal of Geochemical Exploration 53(1-3), 311-337. https://doi.org/10.1016/0375-6742(94)00015-4

Groves, D.I., Phillips, G.N., 1987. The genesis and tectonic controls on Archaean gold deposits of the Western Australian Shield: A metamorphic-replacement model. Ore Geology Reviews 2(4), 287-322. https://doi.org/10.1016/0169-1368(87)90009-6

Groves, D.I., Phillips, G.N., Ho, S.E., Houstoun, S.M., and Standing, C.A., 1987. Craton-scale distribution of Archean greenstone gold deposits – predictive capacity of the metamorphic model. Economic Geology 82(8), 2045-2058. https://doi.org/10.2113/gsecongeo.82.8.2045

Groves, D.I., Goldfarb, R.J., Gebre-Mariam, M., Hagemann, S.G., and Robert, F., 1998. Orogenic gold deposits: a proposed classification in the context of their crustal distribution and relationship to other gold deposit types. Ore Geology Reviews 13(1-5), 7-27. https://doi.org/10.1016/S0169-1368(97)00012-7

Groves, D.I., Santosh, M., Deng, J., Wang, Q., Yang, L., and Zhang, L., 2019. A holistic model for the origin of orogenic gold deposits and its implications for exploration. Mineralium Deposita 55, 275-292. https://doi.org/10.1007/s00126-019-00877-5

Gurney, J.J., Helmstaedt, H., Moore, R.O., 1993. A review of the use and application of mantle mineral geochemistry in diamond exploration. Pure and Applied Chemistry 65(12), 2423-2442. https://doi.org/10.1351/pac199365122423

Gurney, J.J. and Zweistra, P., 1995. The interpretation of the major element compositions of mantle minerals in diamond exploration. Journal of Geochemical Exploration 53(1-3), 293-309. https://doi.org/10.1016/0375-6742(94)00021-3

Hallberg, A., 1994. The Enåsen gold deposit, central Sweden. Mineralium Deposita 29, 150-162. https://doi.org/10.1007/BF00191512

Hatcher, R.D., 2010. The Appalachian orogen: A brief summary. In Tollo, R.P., Bartholomew, M.J., Hibbard, J.P., and Karabinos, P.M., eds.: From Rodinia to Pangea: The Lithotectonic Record of the Appalachian Region. Geological Society of America Memoir 206, 1-19. https://doi.org/10.1130/2010.1206(01)

Hayes, J. B., 1970. Polytypism of chlorite in sedimentary rocks. Clays & Clay Minerals 18, 285-306.

Heald, P., Hayba, D.O., and Foley, N.K., 1987. Comparative anatomy of volcanic-hosted epithermal deposits: Acid-sulfate and adularia-sericite types. Economic Geology 82(1), 1-26. https://doi.org/10.2113/gsecongeo.82.1.1

Hedenquist, J.W., 1987. Mineralization associated with volcanic-related hydrothermal systems in the Circum-Pacific basin. Transactions of the Fourth Circum-Pacific Conference on Energy and Mineral Resources Conference, Singapore, American Association of Petroleum Geologists, 513-524.

Hedenquist, J.W., 2015. Recent developments in understanding of and exploration for epithermal deposits in volcanic arcs. PACRIM 2015 Congress Abstract, 1-6.

Hedenquist, J.W., Izawa, E., Arribas, A., White, N.C., 1996. Epithermal gold deposits: styles, characteristics, and exploration. Resource Geology Special Publication Number 1, 18 pp.

Hedenquist, J.W., Arribas, A., and Gonzalez-Urien, E., 2000. Exploration for epithermal gold deposits. Economic Geology Reviews 13, 245-277. https://doi.org/10.5382/Rev.13.07

Heinrich, C.A., 2005. The physical and chemical evolution of low- to medium-salinity magmatic fluids at the porphyry to epithermal transition: a thermodynamic study. Mineralium Deposita 39, 864-889. https://doi.org/10.1007/s00126-004-0461-9

Heinrich, C.A., Driesner, T., Stefánsson, A., and Seward, T.M., 2004. Magmatic vapor contraction and the transport of gold from the porphyry environment to epithermal ore deposits. Geology 32(9), 761-764. https://doi.org/10.1130/G20629.1

Herrmann, W., Blake, M., Doyle, M., Huston, D., Kamprad, J., Merry, N., Pontual, S., 2001. Short wavelength infrared (SWIR) spectral analysis of hydrothermal alteration zones associated with base metal sulfide deposits at Rosebery and Western Tharsis, Tasmania, and Highway-Reward, Queensland. Economic Geology 96(5), 939-955. https://doi.org/10.2113/gsecongeo.96.5.939

Hibbard, J., 1983. Geology of the Baie Verte Peninsula, Newfoundland. Mineral Development Division Department of Mines and Energy, Government of Newfoundland and Labrador, Memoir 2, 279 pp.

Hibbard, J.P., van Staal, C.R., and Miller, B.V., 2007. Links among Carolinia, Avalonia, and Ganderia in the Appalachian peri-Gondwanan realm. In Sears, J.W., Harms, T.A., and Evenchick, C.A., eds.: Whence the Mountains? Inquiries into the Evolution of Orogenic

Systems. Geological Society of America Special Paper 433, 291-311. https://doi.org/10.1130/2007.2433(14)

Hikov, A., 2014. Paragonite and paragonitic altered rocks from the Asarel porphyry copper deposit, central Srednogorie. Comptes rendus de l'Académie bulgare des sciences: sciences mathématiques et naturelles 67(8), 1119-1128.

Ho Ahn, J., Peacor, D.R., Essene, E.J., 1985. Coexisting paragonite-phengite in blueschist eclogite: a TEM study. American Mineralogist 70, 1193-1204.

Hochleitner, R., Tarcea, N., Simon, G., Kiefer, W., Popp, J., 2004. Micro-Raman spectroscopy: a valuable tool for the investigation of extraterrestrial material. Journal of Raman Spectroscopy 35(6), 515-518. https://doi.org/10.1002/jrs.1190

Hoffer, E., 1978. On the "late" formation of paragonite and its breakdown in pelitic rocks of the southern Damara orogen (Namibia). Contributions to Mineralogy and Petrology 67, 209-219. https://doi.org/10.1007/BF01046577

Hu, Y., Ray, J.R., Jun, Y.-S., 2011. Biotite-Brine Interactions under Acidic Hydrothermal Conditions: Fibrous Illite, Goethite, and Kaolinite Formation and Biotite Surface Cracking. Environmental Science and Technology 45, 6175-6180. https://doi.org/10.1021/es200489y

Huard, A., 1989. Epithermal alteration and gold mineralization in Late Precambrian volcanic rocks on the northern Burin Peninsula, southeastern Newfoundland, Canada. Unpublished M.Sc. thesis, Memorial University of Newfoundland, St. John's, Newfoundland, 273 pp.

Huard, A., 1990. The Noranda/Impala Stog'er Tight deposit. International Association on the Genesis of Ore Deposits, 8th Symposium, Field Trip Guide, 173-177.

Huard, A. and O'Driscoll, C., 1986. Epithermal gold mineralization in late Precambrian volcanic rocks on the Burin Peninsula. Current Research, Newfoundland Department of Mines and Energy, Mineral Development Division, Report 86-1, 65-78.

Inoue, A., 1995. Formation of Clay Minerals in Hydrothermal Environments. In: Velde, B. (Ed.), Origin and Mineralogy of Clays: Clays and the Environment. Springer, Berlin, Heidelberg, 268-329. https://doi.org/10.1007/978-3-662-12648-6_7

Inoue, A., Meunier, A., Beaufort, D., 2004. Illite-smectite mixed-layer minerals in felsic volcaniclastic rocks from drill cores, Kakkonda, Japan. Clays and Clay Minerals 52, 66-84. https://doi.org/10.1346/CCMN.2004.0520108

Inoue, A., Kurokawa, K., Hatta, T., 2009. Application of chlorite geothermometry to hydrothermal alteration in Toyoha Geothermal System, southwestern Hokkaido, Japan. Resource Geology 60, 52-70. https://doi.org/10.1111/j.1751-3928.2010.00114.x

Inoue, A., Inoué, S., Utada, M., 2018. Application of chlorite thermometry to estimation of formation temperature and redox conditions. Clay Minerals 53, 143-158. https://doi.org/10.1180/clm.2018.10

Jiang, W. and Peacor, D.R., 1993. Formation and modification of metastable intermediate sodium potassium mica paragonite, and muscovite in hydrothermally altered metabasites from northern Wales. American Mineralogist 78, 782-793.

Jiang, S.Y., 2000. Controls on the mobility of high field strength elements (HFSE), U, and Th in an ancient submarine hydrothermal system of the Proterozoic Sullivan Pb-Zn-Ag deposit, British Columbia, Canada. Geochemical Journal 34(5), 341-348. https://doi.org/10.2343/geochemj.34.341

Jiang, S.Y., Wang, R.C., Xu, X.S., Zhao, K.D., 2005. Mobility of high field strength elements (HFSE) in magmatic-, metamorphic-, and submarine-hydrothermal systems. Physics and Chemistry of the Earth 30(17-18), 1020-1029. https://doi.org/10.1016/j.pce.2004.11.004

Jochum K.P., Weis U., Stoll B., Kuzmin D., Yang Q., Raczek I., Jacob D.E., Stracke , A., Birbaum, K., Frick, D.A., Günther, D., Enzweiler J., 2011. Determination of reference values for NIST

SRM 610-617 glasses following ISO guidelines. Geostandards and Geoanalytical Research, 35(4) , 397-429. https://doi.org/10.1111/j.1751-908X.2011.00120.x

John, D.A., Hofstra, A.H., Fleck, R.J., Brummer, J.E., Saderholm, E.C., 2003. Geologic setting and genesis of the Mule Canyon low-sulfidation epithermal gold-silver deposit, North-Central Nevada. Economic Geology 98, 425-463. http://dx.doi.org/10.2113/gsecongeo.98.2.425

Kerr, A., Rafuse, H., Sparkes, G., Hinchey, J., Sandeman, H., 2011. Visible/infrared spectroscopy (VIRS) as a research tool in economic geology: Background and pilot studies from Newfoundland and Labrador. In Current Research, Newfoundland and Labrador Department of Natural Resources, Geological Survey, Report 11-1, 145-166.

Kerr, A. and Selby, A., 2012. The timing of epigenetic gold mineralization on the Baie Verte Peninsula, Newfoundland, Canada: new evidence from Re-Os pyrite geochronology. Mineralium Deposita 47, 325-337. https://doi.org/10.1007/s00126-011-0375-2

Kerrich, R. and Fyfe, W.S., 1981. The gold–carbonate association: source of CO_2, and CO_2 fixation reactions in Archaean lode deposits. Chemical Geology 33(1-4), 265-294. https://doi.org/10.1016/0009-2541(81)90104-2

Kirkwood, D. and Dubé, B., 1992. Structural control of sill-hosted gold mineralization: the Stog'er Tight Gold Deposit. Current Research, Geological Survey of Canada, Report 92-1D, 211-221.

Klemme, S., Prowatke, S., Hametner, K., Günther, D., 2005. Partitioning of trace elements between rutile and silicate melts: Implications for subduction zones. Geochimica et Cosmochimica Acta 69(9), 2361-2371. https://doi.org/10.1016/j.gca.2004.11.015

Kloprogge, J.T. and Frost, R.L., 1999. An infrared emission spectroscopic study of synthetic and natural pyrophyllite. Neues Jahrbuch fur Mineralogie, Monatshefte 2, 62-74.

Kogure, T., Jige, M., Kameda, J., Yamagishi, A., Miyawaki, R., Kitagawa, R., 2006. Stacking structures in pyrophyllite revealed by high-resolution transmission electron microscopy (HRTEM). American Mineralogist 91, 1293-1299. https://doi.org/10.2138/am.2006.1997

Košařová, V., Hradil, D., Němec, I., Bezdička, P., Kanickýa, V., 2013. Microanalysis of clay-based pigments in painted artworks by the means of Raman spectroscopy. Journal of Raman Spectroscopy 44(11), 1570-1577. https://doi.org/10.1002/jrs.4381

Kranidiotis, P. and MacLean, W.H., 1987. Systematics of chlorite at the Phelps Dodge massive sulfide deposit, Matagami, Quebec. Economic Geology 82, 1898-1911. https://doi.org/10.2113/gsecongeo.82.7.1898

Kusukabe, M., Komoda, Y., Takano, B., Abiko, T., 2000. Sulfur isotopic effects in the disproportionation reaction of sulfur dioxide in hydrothermal fluids: implications of the $\delta^{34}S$ variations of dissolved bisulfate and elemental sulfur from active crater lakes. Journal of Volcanology and Geothermal Research 97(1-4), 287-307. https://doi.org/10.1016/S0377-0273(99)00161-4

Lanari, P., Wagner, T., Vidal, O., 2014. A thermodynamic model for di-trioctahedral chlorite from experimental and natural data in the system $MgO-FeO-Al_2O_3-SiO_2-H_2O$: applications to P-T sections and geothermometry. Contributions to Mineralogy and Petrology 167, 968. https://doi.org/10.1007/s00410-014-0968-8

Lantenois, S., Beny, J.M., Muller, F., Champallier, R., 2007. Integration of Fe in natural and synthetic Al-pyrophyllites: an infrared spectroscopic study. Clay Minerals 42(1), 129-141. https://doi.org/10.1180/claymin.2007.042.1.09

Lerouge, C., Beny, C., Fléhoc, C., Guerrot, C., Hikov, A., Kunov, A., Yanev, Y., 2007. Constraints of stable isotopes, Raman spectrometry on the formation of the advanced argillic alteration of the Breznik epithermal Au occurrence in Bulgaria - impact of weathering. Proceedings of the ninth Biennial SGA Meeting, Dublin 2007, 885-888.

Li, H., Zhang, L., Christy, A.G., 2011. The correlation between Raman spectra and the mineral composition of muscovite and phengite. In: Ultrahigh-Pressure Metamorphism (Eds: Dobrzhinetskaya, L.F., Faryad, S.W., Wallis, S., Cuthbert, S.), Elsevier Publishing, 187-212. https://doi.org/10.1016/B978-0-12-385144-4.00006-0

Lindgren, W., 1933. Mineral Deposits. New York, McGraw-Hill, 4th ed., 930 pp.

Linnen, R. and Che, X., 2010. Evaluation of titanite as an indicator mineral for tungsten-skarn mineralization. In Yukon exploration and Geology 2009 (K.E. MacFarlane, L.H. Weston, L.R. Blackburn, eds.). Yukon Geological Survey, 223-228.

Lipson, R., 2014. The promise and perils of porphyry deposits in the future gold production. SEG Newsletter 98, 1-21.

Loh, E., 1973. Optical vibrations in sheet silicates. Journal of Physics C: Solid State Physics 6(6), 1091-1104. https://doi.org/10.1088/0022-3719/6/6/022

Lougheed, H.D., McClenaghan, M.B., Layton-Matthews, D., Leybourne, M., 2020. Exploration potential of fine-fraction heavy mineral concentrates from till using automated mineralogy: a case study from the Izok Lake Cu-Zn-Pb-Ag VMS deposit, Nunavut, Canada. Minerals 10(4), 310. https://doi.org/10.3390/min10040310

Luvizotto, G.L. and Zack, T., 2009. Nb and Zr behavior in rutile during high-grade metamorphism and retrogression: An example from the Ivrea-Verbano Zone. Chemical Geology 261(3-4), 303-317. https://doi.org/10.1016/j.chemgeo.2008.07.023

Lydon, J.W., 2007. An overview of the economic and geological contexts of Canada's major mineral deposit types. In Mineral Deposits of Canada: A synthesis of major deposit-types, district metallogeny, the evolution of geological provinces, and exploration methods (W.D.

Goodfellow, ed.). Geological Association of Canada, Mineral Deposits Division, Special Publication No. 5, 3-48.

Martin-Garcia, J.M., Delgado, G., Sanchez-Maranon, M., Parraga, J.F., Delgado, R., 1997. Nature of dioctahedral micas in Spanish red soils. Clay Minerals 32, 107-121.

Maubec, N., Lahfid, A., Lerouge, C., Wille, G., Michel, K., 2012. Characterization of alunite supergroup minerals by Raman spectroscopy. Spectrochimica Acta Part A: Molecular and Biomolecular Spectroscopy 96, 925-939. https://doi.org/10.1016/j.saa.2012.07.094

Maydagán, L., Franchini, M., Impiccini, A., Lentz, D., Patrier, P., Beaufort, D., 2018. Chlorite, white mica and clay minerals as proximity indicators to ore in the shallow porphyry environment of Quebrada de la Mina deposit, Argentina. Ore Geology Reviews 92, 297-317. https://doi.org/10.1016/j.oregeorev.2017.11.028

McClenaghan, M.B., 2005. Indicator mineral methods in mineral exploration. Geochemistry: Exploration, Environment, Analysis 5(3), 233-245. https://doi.org/10.1144/1467-7873/03-066

McClenaghan, M.B., 2011. Overview of common processing methods for recovery of indicator minerals from sediment and bedrock in mineral exploration. Geochemistry: Exploration, Environment, Analysis 11, 265-278. https://doi.org/10.1144/1467-7873/10-IM-025

McClenaghan, M.B. and Paulen, R.C., 2018. Application of till mineralogy and geochemistry to mineral exploration. In Past Glacial Environments (J. Menzies and J.J.M. van der Meer, eds.). Elsevier, 2nd Edition, 689-751. https://doi.org/10.1016/B978-0-08-100524-8.00022-1

McClenaghan, M.B., Plouffe, A., McMartin, I., Campbell, J.E., Spirito, W.A., Paulen, R.C., Garrett, R.G., Hall, G.E.M., 2013. Till sampling and geochemical analytical protocols used by the Geological Survey of Canada. Geochemistry: Exploration, Environment, Analysis 13, 285-301. https://doi.org/10.1144/geochem2011-083

McDermott, J.M., Ono, S., Tivey, M.K., Seewald, J.S., Shanks III, W.C., Solow, A.R., 2015. Identification of sulfur sources and isotopic equilibria in submarine hot-springs using multiple sulfur isotopes. Geochimica et Cosmochimica Acta 160, 169-187. https://doi.org/10.1016/j.gca.2015.02.016

McKenzie, C.B., 1986. Geology and mineralization of the Chetwynd deposit, southwestern Newfoundland, Canada. In Macdonald, A.J., Gold '86: Willowdale, Ontario, Konsult International, 137-148.

Menzel, M. D., Garrido, C. J., López Sánchez-Vizcaíno, V., Marchesi, C., Hidas, K., Escayola, M. P., Delgado Huertas, A., 2018. Carbonation of mantle peridotite by CO2-rich fluids: the formation of listvenites in the Advocate ophiolite complex (Newfoundland, Canada). Lithos 323, 238-261. https://doi.org/10.1016/j.lithos.2018.06.001

Merriman, R.J., 2005. Clay minerals and sedimentary basin history. European Journal of Mineralogy 17, 7-20. https://doi.org/10.1127/0935-1221/2005/0017-0007

Meunier, A., 2005. Clays. Springer, 472 pp. https://doi.org/10.1007/b138672

Mikucki, E.J., 1998. Hydrothermal transport and depositional processes in Archean lode-gold systems: A review. Ore Geology Reviews 13(1-5), 307-321. https://doi.org/10.1016/S0169-1368(97)00025-5

Millot, G., 1970. Geology of Clays. Springer, 430 pp. https://doi.org/10.1007/978-3-662-41609-9

Miyashiro, A., 1994. Metamorphic petrology, UCL Press, London, 404 pp.

Moore, D.M. and Reynolds, R.C., 1997. X-Ray Diffraction and the Identification and Analysis of Clay Minerals, 2nd ed. Oxford University Press.

Morishita, Y., Shimada, N., Shimada, K., 2018. Invisible gold in arsenian pyrite from the high-grade Hishikari gold deposit, Japan: significance of variation and distribution of Au/As ratios in pyrite. Ore Geology Reviews 95, 79-93. https://doi.org/10.1016/J.OREGEOREV.2018.02.029

Mücke, A. and Cabral, A.R., 2005. Redox and nonredox reactions of magnetite and hematite in rocks. Chemie der Erde 65(3), 271-278. https://doi.org/10.1016/j.chemer.2005.01.002

Mueller, A.G., 1992. Petrogenesis of amphibole–biotite–calcite–plagioclase alteration and laminated gold–silver quartz veins in four Archean shear zones of the Norseman district, Western Australia. Canadian Journal of Earth Sciences 29(3), 388-417. https://doi.org/10.1139/e92-036

Murad, E., Cashion, J.D., Noble, C.J., Pilbrow, J.R., 1995. The chemical state of Fe in rutile from an albitite in Norway. Mineralogical Magazine 59(3), 557-560. https://doi.org/10.1180/minmag.1995.059.396.17

Murphy, J.B., Keppie, J.D., Nance, R.D., and Dostal, J., 2010. Comparative evolution of the Iapetus and Rheic oceans: A North America perspective. Gondwana Research 17, 482-499. https://doi.org/10.1016/j.gr.2009.08.009

Neal, L.C., Wilkinson, J.J., Mason, P.J., Chang, Z., 2018. Spectral characteristics of propylitic alteration minerals as a vectoring tool for porphyry copper deposits. Journal of Geochemical Exploration 184(A), 179-198. http://dx.doi.org/10.1016/j.gexplo.2017.10.019

Nesbitt, R.W., Pascual, E., Fanning, C.M., Toscano, M., Saez, R., Almodovar, G.R., 1999. U-Pb dating of stockwork zircons from the eastern Iberian Pyrite belt. Journal of the Geological Society 156(1), 7-10. https://doi.org/10.1144/gsjgs.156.1.0007

O'Brien, S.J., Wardle, R.J., and King, A.F., 1983. The Avalon Zone: A Pan-African terrane in the Appalachian Orogen of Canada. Geological Journal 18(3), 195-222. https://doi.org/10.1002/gj.3350180302

O'Brien, B.H., O'Brien, S.J., and Dunning, G.R., 1991. Silurian cover, Late Precambrian-Early Ordovician basement, and the chronology of Silurian orogenesis in the Hermitage flexure (Newfoundland Appalachians). American Journal of Science 291, 760-799.

O'Brien, S.J., Tucker, R.D., and O'Driscoll, C.F., 1994. Neoproterozoic basement-cover relationships and the tectono-magmatic record of the Avalon Zone on the Hermitage Peninsula and environs, Newfoundland: New perspectives in the Appalachian-Caledonian Orogen. Geological Association of Canada Nuna Conference, Program and Abstracts, 21-22.

O'Brien, S.J., O'Brien, B.H., Dunning, G.R., and Tucker, R.D., 1996. Late Neoproterozoic Avalonian and related peri-Gondwanan rocks of the Newfoundland Appalachians. In Nance, R. D., and Thompson, M. D., eds.: Avalonian and Related Peri-Gondwanan Terranes of the Circum-North Atlantic: Boulder, Colorado. Geological Society of America Special Paper 304, 9-28. https://doi.org/10.1130/0-8137-2304-3.9

O'Brien, S.J., King, A.F., and O'Driscoll, C.F., 1997. Late Neoproterozoic geology of the central Avalon Peninsula, Newfoundland, with an overview of mineralization and hydrothermal alteration. Current Research, Newfoundland Department of Mines and Energy, Geological Survey, Report 97-1, 257-282.

O'Brien, S.J., Dubé, B., O'Driscoll, C.F., and Mills, J., 1998. Geological setting of gold mineralization and related hydrothermal alteration in Late Neoproterozoic (Post -640 Ma) Avalonian rocs of Newfoundland, with a review of the coeval gold deposits elsewhere in the Appalachian Avalonian Belt. In Current Research. Newfoundland Department of Mines and Energy, Geological Survey, Report 98-1, 93-124.

O'Brien, S.J., Dubé, B., and O'Driscoll, C.F., 1999. High-sulphidation, epithermal-style hydrothermal systems in Late Neoproterozoic Avalonian rocks on the Burin Peninsula, Newfoundland: Implications for gold exploration. In Current Research. Newfoundland Department of Mines and Energy, Geological Survey, Report 99-1, 275-296.

Omori, K., 1968. Infrared diffraction and the far infrared spectra of anhydrous sulfates. Mineralogical Journal 5(5), 334-354. https://doi.org/10.2465/minerj1953.5.334

Oviatt, N.M., Gleeson, S.A., Paulen, R.C., McClenaghan, M.B., Paradis, S., 2015. Characterization and dispersal of indicator minerals associated with the Pine Point Mississippi Valley-type (MVT) district, Northwest Territories, Canada. Canadian Journal of Earth Sciences 52(9), 776-794. https://doi.org/10.1139/cjes-2014-0108

Palarea-Albaladejo, J., and Martín-Fernández, J.A., 2013. Values below detection limit in compositional chemical data. Analytica Chimica Acta 764, 32-43. https://doi.org/10.1016/j.aca.2012.12.029

Parry, W.T., Ballantyne, J.M., and Jacobs, D.C., 1984. Geochemistry of hydrothermal sericite from Roosevelt Hot Springs and the Tintic and Santa Rita porphyry copper systems. Economic Geology 79, 72-86. https://doi.org/10.2113/gsecongeo.79.1.72

Paulen, R.C., Paradis, S., Plouffe, A., Smith, I.R., 2011. Pb and S isotopic composition of indicator minerals in glacial sediments from NW Alberta, Canada: implications for Zn-Pb base metal exploration. Geochemistry: Exploration, Environment, Analysis 11(4), 309-320. https://doi.org/10.1144/1467-7873/10-IM-032

Pawlowsky-Glahn, V. and Egozcue, J.J., 2006. Compositional data and their analysis: an introduction. In Compositional Data Analysis in the Geosciences: From Theory to Practice (A. Buccianti, G. Mateu-Figueras, V. Pawlowsky-Glahn, eds.) Geological Society, London, Special Publication 264(1), 1-10.https://doi.org/10.1144/GSL.SP.2006.264.01.01

Pawlukiewicz, M., 2020. Hydrothermal reconstruction and lithogeochemistry of the Argyle Orogenic Gold Deposit, Baie Verte, Newfoundland. Unpublished Master Thesis. Department of Earth Sciences, Memorial University of Newfoundland, 426 pp.

Pearce, N.J.G, Perkins, W.T., Westgate, J.A., Gorton, M.P., Jackson, S.E, Neal, C.R., Chenery, S.P., 1997. A compilation of new and published major and trace element data for NIST SRM 610 and NIST SRM 612 glass reference materials. Geostandards Newsletter 21(1), 115-144. https://doi.org/10.1111/j.1751-908X.1997.tb00538.x

Phillips, G.N., 1986. Geology and Alteration in the Golden Mile, Kalgoorlie. Economic Geology 81(4), 779-808. https://doi.org/10.2113/gsecongeo.81.4.779

Phillips, G.N., 2013. Australian and global setting for gold in 2013. In Proceedings world gold 2013, Brisbane, Australia, 26-29 September 2013, The Australasian Institute of Mining and Metallurgy, 15-21.

Phillips, G.N. and Groves, D.I., 1983. The nature of Archaean gold bearing fluids as deduced from gold deposits from Western Australia. Journal of the Geological Society of Australia 30(1-2), 25-39. https://doi.org/10.1080/00167618308729234

Phillips, G.N. and Powell, R., 1993. Link between Gold Provinces. Economic Geology 88(5), 1084-1098. https://doi.org/10.2113/gsecongeo.88.5.1084

Phillips, G.N. & Powell, R., 2010. Formation of gold deposits: a metamorphic devolatilization model. Journal of Metamorphic Geology 28(6), 689–718. https://doi.org/10.1111/j.1525-1314.2010.00887.x

Pires, G.L.C., Renac, C., Bongiolo, E.M., Neumann, R., 2020. Gossan mineralogy, textures, and gold enrichment over the Au (As, Bi, Ag) deposit in the Buracão Area (Brasília Fold Belt, Brazil): Implications for gold prospecting in weathering profiles. Journal of Geochemical Exploration 218, 106615. https://doi.org/10.1016/j.gexplo.2020.106615

Pisiak, L.K., Canil, D., Lacourse, T., Plouffe, A., Ferbey, T., 2017. Magnetite as an indicator mineral in the exploration of porphyry deposits: A case study in till near the Mount Polley Cu-Au Deposit, British Columbia, Canada. Economic Geology 112(4), 919-940. https://doi.org/10.2113/econgeo.112.4.919

Pitcairn, I.K., Craw, D., & Teagle, D.A.H., 2014. The gold conveyor belt: Large-scale gold mobility in an active orogen. Ore Geology Reviews 62, 129–142. https://doi.org/10.1016/j.oregeorev.2014.03.006

Pitcairn, I.K., Craw, D., & Teagle, D.A.H., 2015. Metabasalts as sources of metals in orogenic gold deposits. Mineralium Deposita 50, 373–390. https://doi.org/10.1007/s00126-014-0547-y

Pitman, C., Cullen, M., Harrington, M., Copeland, D., McNeill, P., Bullock, K., Budgell, C., Cramm, J., 2020. NI 43-101 Technical report, mineral resource and mineral reserve update on the Point Rousse project, Baie Verte, Newfoundland and Labrador, Canada. Anaconda Mining Technical Report NI43-101, 300 pp.

Pizarro, H., Campos, E., Bouzari, F., Rousse, S., Bissig, T., Gregoire, M., Riquelme, R., 2020. Porphyry indicator zircons (PIZs): Application to exploration of porphyry copper deposits. Ore Geology Reviews 126, 103771. https://doi.org/10.1016/j.oregeorev.2020.103771

Plavsa, D., Reddy, S.M., Agangi, A., Clark, C., Kylander-Clark, A., Tiddy, C.J., 2018. Microstructural, trace element and geochronological characterization of TiO2 polymorphs and implications for mineral exploration. Chemical Geology 476, 130-149. https://doi.org/10.1016/j.chemgeo.2017.11.011

Porter, J.K., McNaughton, N.J., Evans, N.J., McDonald, B.J., 2020. Rutile as a pathfinder for metals exploration. Ore Geology Reviews 120, 103406. https://doi.org/10.1016/j.oregeorev.2020.103406

Pouchou, J.L. and Pichoir, F., 1984. A new model for quantitative analyses. I. Application to the analysis of homogeneous samples. La Recherche Aérospatiale, 3, 13-38.

Pouchou, J.L. and Pichoir, F., 1985. ''PAP'' correction procedure for improved quantitative microanalysis. Pp. 104-106 in: Microbeam Analysis (J.T. Armstrong, editor). San Francisco Press, San Francisco, California, USA.

Prieto, A.C., Dubessy, J., Cathelineau, M., 1991. Structure-composition relationships in trioctahedral chlorites: A vibrational spectroscopy study. Clays and Clay Minerals 39(5), 531-539. https://doi.org/10.1346/CCMN.1991.0390508

Rafiei, M., Kennedy, M., 2019. Weathering in a world without terrestrial life recorded in the Mesoproterozoic Velkerri Formation. Nature Communications 10, 3448. https://doi.org/10.1038/s41467-019-11421-4

Ramezani, J., 1992. The geology, geochemistry and U-Pb geochronology of the Stog'er Tight Gold Prospect, Baie Verte Peninsula, Newfoundland. Unpublished Master Thesis. Department of Earth Sciences, Memorial University of Newfoundland, 312 pp.

Ramezani, J., Dunning, G.R., and Wilson, M.R., 2000. Geologic setting, geochemistry of alteration, and U-Pb age of hydrothermal zircon from the Silurian Stog'er Tight gold prospect, Newfoundland Appalachians, Canada. Exploration Mining Geology 9(3-4), 171-188. https://doi.org/10.2113/0090171

Reich, M., Kesler, S.E., Utsunomiya, S., Palenik, C.S., Chryssoulis, S.L., Ewing, R.C., 2005. Solubility of gold in arsenian pyrite. Geochimica et Cosmochimica Acta 69(11), 2781-2796. https://doi.org/10.1016/j.gca.2005.01.011

Ren, Y., Fei, Y., Yang. J., 2009. SiO_2 solubility in rutile at high temperature and high pressure. Journal of Earth Sciences 20, 274-283. https://doi.org/10.1007/s12583-009-0025-0

Reynolds, R.C. and Hower, J., 1970. The Nature of Interlayering in Mixed-Layer Illite-Montmorillonites. Clays and Clay Minerals 18, 25-36. https://doi.org/10.1346/CCMN.1970.0180104

Richards, J.P., 2011. Magmatic to hydrothermal metal fluxes in convergent and collided margins. Ore Geology Reviews 40(1), 1-26. https://doi.org/10.1016/j.oregeorev.2011.05.006

Ridley, J.R. and Diamond, L.W., 2000. Fluid chemistry of orogenic lode deposits and implications for genetic models. Economic Geology Reviews 13, 141-162. https://doi.org/10.5382/Rev.13.04

Rivai, T.A., Yonezu, K., Afrizal, S., Sanematsu, K., Kusumanto, D., Imai, A., Watanabe, K., 2019. A low-sulfidation epithermal mineralization in the River Reef Zone, the Poboya prospect, Central Sulawesi, Indonesia: vein textures, ore mineralogy, and fluid inclusions. Resource geology 69, 385-401. https://doi.org/10.1111/rge.12206

Robb, L., 2005. Introduction to ore-forming processes. Blackwell Publishing, 373 pp.

Robert, F., Boullier, A.M., Firdaous, K., 1995. Gold-quartz veins in metamorphic terranes and their bearing on the role of fluids in faulting. Journal of Geophysical Research 100(B7), 12861-12879. https://doi.org/10.1029/95JB00190

Rosenberg, P.E. and Cliff, G., 1980. The formation of pyrophyllite solid solutions. American Mineralogist 65, 1214-1219.

Rudolph, W.W. and Mason, R., 2001. Study of aqueous $Al_2(SO_4)_3$ solution under hydrothermal conditions: Sulfate ion pairing, hydrolysis, and formation of hydronium alunite. Journal of Solution Chemistry 30, 527-548. https://doi.org/10.1023/A:1010334818580

Saccocia, P.J. and Gillis, K.M., 1995. Hydrothermal upflow zones in the oceanic crust. Earth and Planetary Science Letters 136, 1-16. https://doi.org/10.1016/0012-821X(95)00155-5

Saikia, B.J., Parthasarathy, G., Borah, R.R., Borthakur, R., 2016. Raman and FTIR spectroscopic evaluation of clay minerals and estimation of metal contaminations in natural deposition of surface sediments from Brahmaputra River. International Journal of Geosciences 7, 873-883. http://dx.doi.org/10.4236/ijg.2016.77064

Sánchez España, J., Velasco, F., and Yusta, I., 2000. Hydrothermal alteration of felsic volcanic rocks associated with massive sulphide deposition in the northern Iberian Pyrite Belt (SW Spain). Applied Geochemistry 15, 1265-1290. https://doi.org/10.1016/S0883-2927(99)00119-5

Saunders, J.A., Hofstra, A.H., Goldfarb, R.J., Reed, M.H., 2014. Geochemistry of hydrothermal gold deposits. In Treatise on Geochemistry (H.D. Holland and K.K. Turekian, eds.), Elsevier, 383-424.

Schmidt, D., Schmidt, S.T, Mullis, J., Ferreiro Mählmann, R., Frey, M., 1997. Very low metamorphism of the Taveyanne formation of western Switzerland. Contributions to Mineralogy and Petrology 129, 385-403. https://doi.org/10.1007/s004100050344

Sciuba, M. and Beaudoin, G., 2021. Texture and trace element composition of rutile in orogenic gold deposits. Economic Geology 116(8), 1865-1892. https://doi.org/10.5382/econgeo.4857

Scott, K.M., 2005. Rutile geochemistry as a guide to porphyry Cu-Au mineralization, Northparkes, New South Wales, Australia. Geochemistry: Exploration, Environment, Analysis 5(3), 247-253. https://doi.org/10.1144/1467-7873/03-055

Scott, K.M. and Radford, N.W., 2007. Rutile compositions at the Big Bell Au deposit as a guide for exploration. Geochemistry: Exploration, Environment, Analysis 7(4), 353-361. https://doi.org/10.1144/1467-7873/07-135

Scott, K.M, Radford, N.W., Hough, R.M., Reddy, S.M., 2011. Rutile compositions in the Kalgoorlie Goldfields and their implications for exploration. Australian Journal of Earth Sciences 58(7), 803-812. https://doi.org/10.1080/08120099.2011.600334

Seedorff, E., Dilles, J.H., Proffett, J.M., Einaudi, M.T., Zurcher, L., Stavast, W.J.A., Johnson, D.A., Barton, M.D., 2005. Porphyry deposits: characteristics and origin of hypogene features. Economic Geology 100th Anniversary volume, 251-298. https://doi.org/10.5382/AV100.10

Šegvić, B., Benvenuti, A., Moscariello, A., 2016. Illite-Smectite-Rich Clay Parageneses from Quaternary Tunnel Valley Sediments of the Dutch Southern North Sea – Mineral Origin and Paleoenvironment Implications. Clays and Clay Minerals 64(5), 608-627. https://doi.org/10.1346/000986016820500438

Šegvić, B., Lugović, B., Slovenec, D., Meyer, H.P., 2016. Mineralogy, petrology and geochemistry of amphibolites from the Kalnik Mt. (Sava Unit, North Croatia): Implications for the evolution of north-westernmost part of the Dinaric-Vardar branch of Mesozoic Tethys. Ofioliti 41, 35-58. https://doi.org/10.4454/ofioliti.v41i1.441

Sillitoe, R.H., 1977. Metallic mineralization affiliated to subaerial volcanism: A review. In: Volcanic processes in ore-genesis: London, Institution of Mining and Metallurgy and Geological Society, 99–116. https://doi.org/10.1144/GSL.SP.1977.007.01.13

Sillitoe, R.H., 1993. Epithermal models: Genetic types, geometrical controls and shallow features. Geological Association of Canada Special Paper 40, 403-417.

Sillitoe, R.H., 2010. Porphyry copper systems. Economic Geology 105(1), 3-41. https://doi.org/10.2113/gsecongeo.105.1.3

Simmons, S.F. and Browne, P.R.L., 2000. Hydrothermal minerals and precious metals in the Broadlands-Ohaaki geothermal system: Implications for understanding low-sulfidation epithermal environments. Economic Geology 95, 971-999. https://doi.org/10.2113/gsecongeo.95.5.971

Simmons, S.F. and Christenson, B.W., 1994. Origins of calcite in a boiling geothermal system. American Journal of Science 294, 361-400. https://doi.org/10.2475/ajs.294.3.361

Simmons, S.F., White, N.C., and John, D.A., 2005. Geological characteristics of epithermal precious and base metal deposits. Economic Geology 100th Anniversary Volume, 485-522. https://doi.org/10.5382/AV100.16

Simpson, M.P. and Mauk, J.L., 2011. Hydrothermal alteration and veins at the epithermal Au-Ag deposits and prospects of the Waitekauri area, Hauraki Goldfield, New Zealand. Economic Geology 106, 945-973. https://doi.org/10.2113/econgeo.106.6.945

Skublov, S.G., Zack, T., Berezin, A.V., Mel'nik, A.E., Rizvanova, N.G., 2013. In situ LA-ICP-MS investigation of the geochemistry and U-Pb age of rutile from the rocks of the Belomorian Mobile Belt. Geochemistry International 51(2), 164-171. https://doi.org/10.1134/S0016702912120051

Skulski, T., Castonguay, S., van Staal, C., Rogers, N., McNicoll, V., Kerr, A., and Escayola, M., 2009. Baie Verte Peninsula: An evolving geological story. Geological Association of Canada, Newfoundland and Labrador Section, Annual Fall Field Trip Guide, 76 pp.

Skulski, T., Castonguay, S., McNicoll, V., van Staal, C., Kidd, W., Rogers, N., Morris, W., Ugalde, H., Slavinski, H., Spicer, W., and Moussallam, Y., 2010. Tectonostratigraphy of the Baie Verte oceanic tract and its ophiolite cover sequence on the Baie Verte Peninsula. Current Research, Newfoundland and Labrador, Department of Natural Resources, Geological Survey, Report 10-1, 315-337.

Smith, D.C. and Perseil, E.A., 1997. Sb-rich rutile in the manganese concentrations St. Marcel-Praborna, Aosta Valley, Italy: petrology and crystal-chemistry. Mineralogical Magazine 61(5), 655-669. https://doi.org/10.1180/minmag.1997.061.408.04

Sparkes, G.W., 2012. New developments concerning epithermal alteration and related mineralization along the western margin of the Avalon zone, Newfoundland. In Current Research. Newfoundland and Labrador Department of Natural Resources, Geological Survey, Report 12-1, 103-120.

Sparkes, G.W., O'Brien, S.J., Dunning, G.R., Dubé., 2005. U-Pb geochronological constraints on the timing of magmatism, epithermal alteration and low-sulphidation gold mineralization, eastern Avalon Zone, Newfoundland. In: Current Research. Newfoundland and Labrador Department of Natural Resources, Geological Survey, Report 05-1, 115-130.

Sparkes, G.W. and Dunning, G.R., 2014. Late Neoproterozoic epithermal alteration and mineralization in the western Avalon zone: A summary of mineralogical investigations and new U/Pb geochronological results. In Current Research. Newfoundland and Labrador Department of Natural Resources, Geological Survey, Report 14-1, 99-128.

Sparkes, G.W., Ferguson, S.A., Layne, G.D., Dunning, G.R., O’Brien, S.J., and Langille, A., 2016. The nature and timing of Neoproterozoic high-sulfidation gold mineralization from the Newfoundland Avalon zone: Insights from new U-Pb ages, ore petrography, and spectral data from the Hickey’s Pond prospect. In Current Research. Newfoundland and Labrador Department of Natural Resources, Geological Survey, Report 16-1, 91-116.

Sparrow, B., Barrett, S., Copeland, D.A., Walsh, M., 2017. Argyle Prospect Mineral Licenses 012433M (11th year) and 020060M (5th year) Point Rousse Project, Baie Verte Peninsula, NL NTS sheet 12H/16. Assessment Report: Anaconda Mining Inc., Newfoundland and Labrador, Canada, 481 p.

Środoń, J., 2006. Identification and quantitative analysis of clay minerals, in: Handbook of Clay Science. Elsevier Ltd., Amsterdam, 765-787. https://doi.org/10.1016/B978-0-08-098259-5.00004-4

Stefánsson, A. and Seward, T.M., 2004. Gold(I) complexing in aqueous sulphide solutions to 500°C at 500 bar. Geochimica et Cosmochimica Acta 68(20), 4121-4143. https://doi.org/10.1016/j.gca.2004.04.006

Stoffregen, R.E., Alpers, C.N., Jambor, J.L., 2000. Alunite-jarosite crystallography, thermodynamics, and geochronology. Reviews in Mineralogy and Geochemistry 40(1), 453-479. https://doi.org/10.2138/rmg.2000.40.9

Sugimori, H., Iwatsuki, T., Murakami, T., 2008. Chlorite and biotite weathering, Fe^{2+}-rich corrensite formation, and Fe behavior under low PO_2 conditions and their implication for Precambrian weathering. American Mineralogist 93, 1080-1089. https://doi.org/10.2138/am.2008.2663

Tappert, M.C., Rivard, B., Giles, D., Tappert, R., Mauger, A., 2013. The mineral chemistry, near-infrared, and mid-infrared reflectance spectroscopy of phengite from the Olympic Dam IOCG deposit, South Australia. Ore Geology Reviews 53, 26-38. https://doi.org/10.1016/j.oregeorev.2012.12.006

Thompson, J.F.H., Lessman, J., Thompson, A.J.B., 1986. The Temora gold-silver deposit: a newly recognized style of high sulfur mineralization in the lower Paleozoic of Australia. Economic Geology 81, 732-738. https://doi.org/10.2113/gsecongeo.81.3.732

Thompson, A.J.B., Hauff, P.L., Robitaille, A.J., 1999. Alteration mapping in exploration: Application of Short-Wave Infrared (SWIR) Spectroscopy. Society of Economic Geologists Newsletter 39, 15-27.

Thompson, A., Scott, K., Huntington, J., Yang, K., 2009. Mapping mineralogy with reflectance spectroscopy: examples from volcanogenic massive sulfide deposits. In: Remote Sensing and Spectral Geology (Eds: R. Bedell, A. P. Crósta, E. Grunsky). Reviews in Economic Geology 16, 1-16. https://doi.org/10.5382/Rev.16.04

Tillick, D.A., Peacor, D.R., Mauk, J.L., 2001. Genesis of dioctahedral phyllosilicates during hydrothermal alteration of volcanic rocks: I. The Golden Cross epithermal ore deposit, New Zealand. Clays and Clay Minerals 49-2, 126-140. https://doi.org/10.1346/CCMN.2001.0490203

Tischendorf, G., Förster, H.J., Gottesmann, B., Rieder, M., 2007. True and brittle micas: composition and solid-solution series. Mineralogical Magazine 71 (3), 285-320. https://doi.org/10.1180/minmag.2007.071.3.285

Tlili, A., Smith, D.C., Beny, J.M., Boyer, H., 1989. A Raman microprobe study of natural micas. Mineralogical Magazine 53(370), 165-179. https://doi.org/10.1180/minmag.1989.053.370.04

Tollo, R.P., Corriveau, L., McLelland, J., and Bartholomew, M.J., 2004. Proterozoic tectonic evolution of the Grenville orogen in North America: An introduction. In Tollo, R.P., Corriveau, L., McLelland, J., and Bartholomew, M.J., eds.: Proterozoic tectonic evolution of the Grenville orogen in North America: Boulder, Colorado. Geological Society of America Memoir 197, 1-18. https://doi.org/10.1130/MEM197

Tomkins, A.G., 2013. On the source of orogenic gold. Geology 41(12), 1255-1256. https://doi.org/10.1130/focus122013.1

Toumi, M. and Tlili, A., 2008. Rietveld refinement and vibrational spectroscopic study of alunite from el Gnater, central Tunisia. Russian Journal of Inorganic Chemistry 53, 1845-1853. https://doi.org/10.1134/S0036023608120048

Urban, A.J., Hoskins, B.F., Grey, I.E., (1992): Characterization of V-Sb-W-bearing rutile from the Hemlo gold deposit, Ontario. The Canadian Mineralogist 30, 319-326.

Uzarowicz, Ł., Skiba, S., Skiba, M., Šegvić, B., 2011. Clay-Mineral Formation in Soils Developed in the Weathering Zone of Pyrite-Bearing Schists: A Case Study from the Abandoned Pyrite Mine in Wieœciszowice, Lower Silesia, SW Poland. Clays and Clay Minerals 59(6), 581–594. https://doi.org/10.1346/CCMN.2011.0590604

Uzarowicz, Ł., Šegvić, B., Michalik, M., Bylina, P., 2012. The effect of hydrochemical conditions and pH of the environment on phyllosilicate transformations in the weathering zone of pyrite-bearing schists in Wieściszowice (SW Poland). Clay Minerals 47, 401-417. http://dx.doi.org/10.1180/claymin.2012.047.4.01

Valverde-Vaquero, P., González, M., Beranoaguirre, A., Ibarguchi, J., 2016. Rutile chemistry and thermometry in eo-Variscan eclogites/granulites from the Cabo Ortegal and the Malpica-Tui complexes Química y termometría de rutilo en eclogitas/granulitas eo-Variscas de los complejos de Cabo Ortegal y Malpica-Tui. IX Congreso Geológico de España, September 2016, Geotemas 16(2) ISSN 1576-5172.

van Staal, C.R. and Barr, S.M., 2012. Lithospheric architecture and tectonic evolution of the Canadian Appalachians and associated Atlantic margin. Chapter 2 in J.A. Percival, F.A. Cook, and R.M. Clowes, eds.: Tectonic Styles in Canada: the LITHOPROBE Perspective. Geological Association of Canada, Special Paper 49, 41-95.

van Staal, C.R., Sullivan, R.W., and Whalen, J.B., 1996. Provenance and tectonic history of the Gander Margin in the Caledonian/Appalachian Orogen: Implications for the origin and assembly of Avalonia. In Nance, R.D., and Thompson, M.D., eds.: Avalonian and related peri-Gondwanan terranes of the Circum-North Atlantic. Geological Society of America Special Papers 304, 347-367. https://doi.org/10.1130/0-8137-2304-3.347

van Staal, C.R., Whalen, J.B., McNicoll, V.J., Pehrsson, S., Lissenberg, C.J., Zagorevski, A., van Breemen, O., and Jenner, G.A., 2007. The Notre Dame arc and the Taconic orogeny in Newfoundland. In Hatcher, R.D., Jr., Carlson, M.P., McBride, J.H., and Martínez Catalán, J.R., eds.: 4-D Framework of Continental Crust. Geological Society of America Memoir 200, 511-552. https://doi.org/10.1130/2007.1200(26)

van Staal, C.R., Barr, S.,M., Percival, J., 2012. Lithospheric architecture and tectonic evolution of the Canadian Appalachians and associated Atlantic Margin. In Tectonic styles in Canada: the LITHOPROBE perspective (J.A. Percival, F.A. Cook, and R.M. Clowes, eds.). Geological Association of Canada, Special Paper 49, 41-95.

Velde, B., 1992. Introduction to Clay Minerals. Springer, 198 pp. https://doi.org/10.1007/978-94-011-2368-6

Velde, B., 1995. Origin and Mineralogy of Clays. Springer, 335 pp. https://doi.org/10.1007/978-3-662-12648-6

Verberne, R., Reddy, S.M., Saxey, D.W., Rickard, W.D.A., Fougerouse, D., Plavsa, D., Agangi, A., 2017. Trace element nanoclusters in natural rutile (TiO_2) and their geological significance. In: 5th Australian Atom Prove Workshop, Magnetic Island, Australia.

Vidal, O., Parra, T., Trotet, F., 2001. A thermodynamic model for Fe-Mg aluminous chlorite using data from phase equilibrium experiments and natural pelitic assemblages in the 100° to 600°c, 1 to 25 kb range. American Journal of Science 301(6), 557-592. https://doi.org/10.2475/ajs.301.6.557

Vidal, O., De Andrade, V., Lewin, E., Muñoz, M., Parra, T., Pascarelli, S., 2006. P-T-deformation-Fe^{3+}/Fe^{2+} mapping at the thin section scale and comparison with XANES mapping: application to a garnet-bearing metapelite from the Sambagawa metamorphic belt (Japan).

Journal of Metamorphic Geology 24, 669-683. https://doi.org/10.1111/j.1525-1314.2006.00661.x

Vidal, O., Lanari, P., Muñoz, M., Bourdelle, F., De Andrade, V., 2016. Deciphering temperature, pressure and oxygen-activity conditions of chlorite formation. Clay Minerals 51, 615-633. https://doi.org/10.1180/claymin.2016.051.4.06

Waldron, J.W.F. and van Staal, C.R., 2001. Taconian orogeny and the accretion of the Dashwoods block: A peri-Laurentian microcontinent in the Iapetus Ocean. Geological Society of America 29(9), 881-814. https://doi.org/10.1130/0091-7613(2001)029<0811:TOATAO>2.0.CO;2

Walker, J.R., 1993. Chlorite polytype geothermometry. Clays and Clay Minerals 41, 260-267. https://doi.org/10.1346/CCMN.1993.0410212

Walshe, J.L., 1986. A six-component chlorite solid solution model and the conditions of chlorite formation in hydrothermal and geothermal systems. Economic Geology 81, 681-703. https://doi.org/10.2113/gsecongeo.81.3.681

Walshe, J.L., Halley, S.W., Hall, G.A., and Kitto, P., 2003. Contrasting fluid systems, chemical gradients and controls on large-tonnage, high-grade Au deposits, Eastern Goldfields Province, Yilgarn Craton, Western Australia. In Mineral Exploration and Sustainable Development, 7th Biennial SGA Meeting, Athens, 827–830.

Wang, A., Kuebler, K., Jolliff, B., Haskin, L.A., 2004. Mineralogy of a Martial meteorite as determined by Raman spectroscopy. Journal of Raman Spectroscopy 35(6), 504-514. https://doi.org/10.1002/jrs.1175

Wang, A., Freeman, J.J., Jolliff, B.L., Chou, I.M., 2006. Sulfates on Mars: A systematic Raman spectroscopic study of hydration states of magnesium sulfates. Geochimica et Cosmochimica Acta 70(24), 6118-6135. https://doi.org/10.1016/j.gca.2006.05.022

Wang, A., Freeman, J.J., Jolliff, B.L., 2015. Understanding the Raman spectral features of phyllosilicates. Journal of Raman Spectroscopy 46, 829-845. https://doi.org/10.1002/jrs.4680

Wang, L., Zhang, M., Redfern, S.A.T., Zhang, Z., 2002. Dehydroxylation and transformations of the 2:1 phyllosilicate pyrophyllite at elevated temperatures: an infrared spectroscopic study. Clays and Clay Minerals 50(2), 272-283. https://doi.org/10.1346/000986002760832874

Wang, R., Cudahy, T., Laukamp, C., Walshe, J.L., Bath, A., Mei, Y., Young, C., Roache, T.J., Jenkins, A., Roberts, M., Barker, A., Laird, J., 2017. White mica as a hyperspectral tool in exploration for the Sunrise Dam and Kanowna Belle Gold deposits, Western Australia. Economic Geology 112(5), 1153-1176. https://doi.org/10.5382/econgeo.2017.4505

Wang, Z., Chen, B., Yan, X., Li, S., 2018. Characteristics of hydrothermal chlorite from the Niujuan Ag-Au-Pb-Zn deposit in the north margin of NCC and implications for exploration tools for ore deposits. Ore Geology Reviews 101, 398-412. https://doi.org/10.1016/j.oregeorev.2018.08.003

Wardle, R. and Brindley, G.W., 1972. The crystal structures of pyrophyllite, 1Tc, and of its dehydroxylate. American Mineralogist 57, 732-750.

White, W.B., 1974. Order-Disorder Effects. In: The Infrared Spectra of Minerals (Ed., V.C Farmer). Mineralogical Society Monograph, London, 87-110. https://doi.org/10.1180/mono-4.6

White, N.C. and Hedenquist, J.W., 1990. Epithermal environments and styles of mineralization: variations and their causes, and guidelines for exploration. Journal of Geochemical Exploration 36, 445-474. https://doi.org/10.1016/0375-6742(90)90063-G

White, N.C. and Hedenquist, J.W., 1995. Epithermal gold deposits: styles, characteristics, and exploration. SEG Newsletter 23, 9-13.

Whitney, D.L. and Evans, B.W., 2010. Abbreviations for names of rock-forming minerals. American Mineralogist, 95, 185-187. https://doi.org/10.2138/am.2010.3371

Wilkinson, J.J., Chang, Z., Cooke, D.R., Baker, M.J., Wilkinson, C.C., Inglis, S., Chen, H., Gemmell, J.B., 2015. The chlorite proximitor: A new tool for detecting porphyry ore deposits. Journal of Geochemical Exploration 152, 10-26. https://doi.org/10.1016/j.gexplo.2015.01.005

Williams, H., 1979. Appalachian Orogen in Canada. Canadian Journal of Earth Sciences 16 (3), 792-807. https://doi.org/10.1139/e79-070

Williams, H. and St. Julien, P., 1982. The Baie Verte Brompton Line: Early Paleozoic continent ocean interface in the Canadian Appalachians. In Major Structural zones and faults of the northern Appalachians (P. St. Julien and J. Beland, eds.). Geological Association of Canada, Special Paper 24, 177-208.

Williams, P.F., Elliott, C.G., and Lafrance, B.D., 1988. Structural geology and mélanges of eastern Notre Dame Bay, Newfoundland. Geological Association of Canada, Annual Meeting, St. John's, Newfoundland, Field Trip Guidebook, Trip B2, 99 pp.

Williams-Jones, A.E. and Heinrich, C.A., 2005. Vapor transport of metals and the formation of magmatic-hydrothermal ore deposits. Economic Geology 100(7), 1287-1312. https://doi.org/10.2113/gsecongeo.100.7.1287

Williams-Jones, A.E., Bowell, R.J., Migdisov, A.A., 2009. Gold in solution. Elements 5(5), 281-287. https://doi.org/10.2113/gselements.5.5.281

Willner, A.P., Gerdes, A., Massonne, H.J., van Staal, C.R., and Zagorevski, A., 2014. Crustal evolution of the northeast Laurentian margin and the peri-Gondwanan microcontinent Ganderia prior to and during closure of the Iapetus Ocean: Detrital zircon U-Pb and Hf isotope evidence from Newfoundland. Geoscience Canada 41(3), 345-364. https://doi.org/10.12789/geocanj.2014.41.046

Wilson, M.J., 2004. Weathering of the primary rock-forming minerals: processes, products, and rates. Clay Minerals 39, 233-266. https://doi.org/10.1180/0009855043930133

Yan, Y., Tillick, D.A., Peacor, D.R., Simmons, S.F., 2001. Genesis of dioctahedral phyllosilicates during hydrothermal alteration of volcanic rocks: II. The Broadlands-Ohaaki hydrothermal system, New Zealand. Clays and Clay Minerals 49-2, 141-155. https://doi.org/10.1346/CCMN.2001.0490204

Yang, B., Xiang, Y., Gu, X., 2018. Tungsten-bearing rutile from the Jiaodong gold province, Shandong, China and its implication for gold mineralization. European Journal of Mineralogy 30(5), 975-980. https://doi.org/10.1127/ejm/2018/0030-2757

Ybarra, S., 2019. Hydrothermal alteration and lithogeochemistry of the Pine Cove orogenic gold deposit, Baie Verte Peninsula, Newfoundland, Canada. Unpublished Master Thesis. Department of Earth Sciences, Memorial University of Newfoundland, 172 pp.

Yoneda, T. and Maeda, H., 2008. The Chemical Composition of Chlorites from Hydrothermal Ore Deposits and its Applicability to Geothermometers. Journal of MMIJ 124, 694-699. https://doi.org/10.2473/journalofmmij.124.694

Zaccarini, F., Garuti, G., Rossi, A., Carrillo Rosúa, F.J., Morales Ruano, S., and Fenoll Hach-Alí, P., 2003. Application of chlorite and fluid-inclusion geothermometry to vein and stratiform Fe-Cu-Zn sulphide deposits of the northern Apennine ophiolites (Emilia Romagna and Liguria, Italy). Atti Ticinensi di Scienze della Terra 9, 109-111.

Zack, T., Kronz, A., Foley, S.F., Rivers, T., 2002. Trace element abundances in rutiles from eclogites and associated garnet mica schists. Chemical Geology 184(1-2), 97-122. https://doi.org/10.1016/S0009-2541(01)00357-6

Zane, A. and Weiss, Z., 1998. A procedure for classifying rock-forming chlorites based on microprobe data. Rendiconti Lincei 9, 51-56. https://doi.org/10.1007/BF02904455

Zanoni, G., Šegvić, B., Moscariello, A., 2016. Clay mineral diagenesis in Cretaceous clastic reservoirs from West African passive margins (the South Gabon Basin) and its impact on regional geology and basin evolution history. Applied Clay Science, 134, 186-209. https://doi.org/10.1016/j.clay.2016.09.032

Zhai, S., Ito, E., Yoneda, A., 2008. Effects of pre-heated pyrophyllite gaskets on high-pressure generation in the Kawai-type multi-anvil experiments. High Pressure Research 28(3), 265-271. https://doi.org/10.1080/08957950802454050

Zhang, S., Chu, G., Cheng, J, Zhang, Y., Tian, J., Li, J., Sun, S., Wei, K., 2020. Short wavelength infrared (SWIR) spectroscopy of phyllosilicate minerals from the Tonglushan Cu-Au-Fe deposit, Eastern China: New exploration indicators for concealed skarn orebodies. Ore Geology Reviews 122, 103516. https://doi.org/10.1016/j.oregeorev.2020.103516

Zhang, S., Xiao, B., Long, X., Chu, G., Cheng, J., Zhang, Y., Tian, J., Xu, G., 2020. Chlorite as an exploration indicator for concealed skarn mineralization: Perspective from the Tonglushan Cu-Au-Fe skarn deposit, Eastern China. Ore Geology Reviews 126, 1-14. https://doi.org/10.1016/j.oregeorev.2020.103778

Zhou, X., Liu, D., Bu, H., Deng, L., Liu, H., Yuan, P., Du, P., Song, H., 2018. XRD-based quantitative analysis of clay minerals using reference intensity ratios, mineral intensity factors, Rietveld, and full pattern summation methods: A critical review. Solid Earth Sciences 3, 16-29. https://doi.org/10.1016/j.sesci.2017.12.002

Zhu, Y., An, F., and Tan, J., 2011. Geochemistry of hydrothermal gold deposits: A review. Geoscience Frontiers 2, 367-374. https://doi.org/10.1016/j.gsf.2011.05.006

Zoheir, B., Akawy, A., Hassan, I., 2008. Role of fluid mixing and wallrock sulfidation in gold mineralization at the Semna mine area, central Eastern Desert of Egypt: Evidence from hydrothermal alteration, fluid inclusions and stable isotope data. Ore Geology Reviews 34(4), 580-596. https://doi.org/10.1016/j.oregeorev.2008.09.007

Appendices

Appendix 1. Copyright agreement information and documents granting the publication of copyrighted figures in Chapter 1 - Introduction of this thesis.

Copyright Agreements - Chapter 1

Through Copyright Clearance Center				
Figure	**Licence Number**	**License Date**	**Content Publisher**	**Publication**
1.1a	5174280846823	22/Oct/21	Elsevier	Ore Geology Reviews
1.1b	5155350879772	24/Sep/21	Elsevier	Earth & Planetary Science Letters
1.2	5080990767863	2/Jun/21	John Wiley & Sons	Wiley Books
1.3	5030991272264	2/Jun/21	Springer Nature	Mineralium Deposita
1.4	508I000286807	2/Jun/21	Elsevier	Gondwana Research

Other				
1.6, 1.7, 1.8	Open Source	10/Jun/21	Govt. of NL	see attached email
1.9		3/Jun/21	CIMM	see attached email

Copyright Permission for Figures 1.6, 1.7, and 1.8.

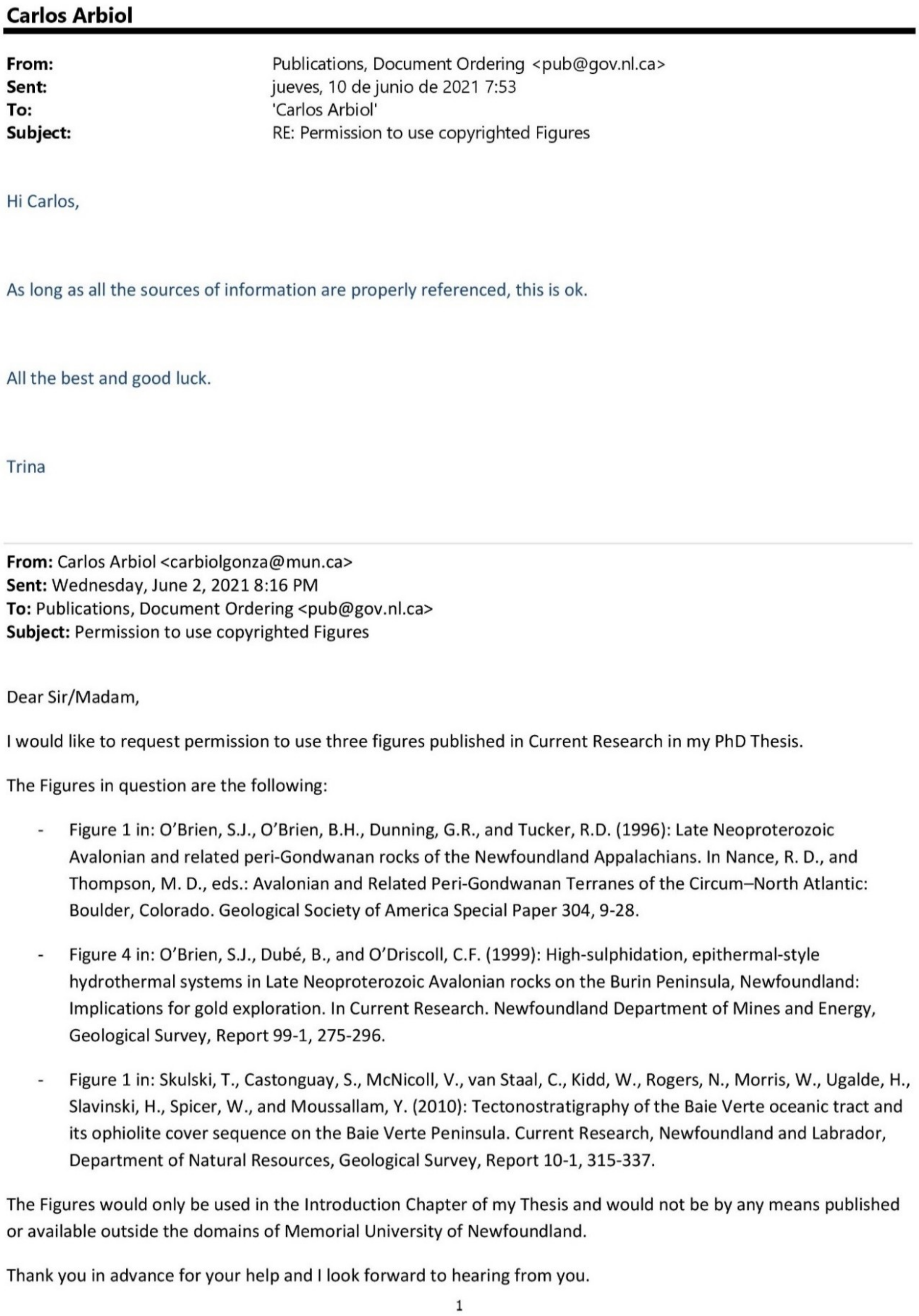

Carlos Arbiol

From: Publications, Document Ordering <pub@gov.nl.ca>
Sent: jueves, 10 de junio de 2021 7:53
To: 'Carlos Arbiol'
Subject: RE: Permission to use copyrighted Figures

Hi Carlos,

As long as all the sources of information are properly referenced, this is ok.

All the best and good luck.

Trina

From: Carlos Arbiol <carbiolgonza@mun.ca>
Sent: Wednesday, June 2, 2021 8:16 PM
To: Publications, Document Ordering <pub@gov.nl.ca>
Subject: Permission to use copyrighted Figures

Dear Sir/Madam,

I would like to request permission to use three figures published in Current Research in my PhD Thesis.

The Figures in question are the following:

- Figure 1 in: O'Brien, S.J., O'Brien, B.H., Dunning, G.R., and Tucker, R.D. (1996): Late Neoproterozoic Avalonian and related peri-Gondwanan rocks of the Newfoundland Appalachians. In Nance, R. D., and Thompson, M. D., eds.: Avalonian and Related Peri-Gondwanan Terranes of the Circum–North Atlantic: Boulder, Colorado. Geological Society of America Special Paper 304, 9-28.
- Figure 4 in: O'Brien, S.J., Dubé, B., and O'Driscoll, C.F. (1999): High-sulphidation, epithermal-style hydrothermal systems in Late Neoproterozoic Avalonian rocks on the Burin Peninsula, Newfoundland: Implications for gold exploration. In Current Research. Newfoundland Department of Mines and Energy, Geological Survey, Report 99-1, 275-296.
- Figure 1 in: Skulski, T., Castonguay, S., McNicoll, V., van Staal, C., Kidd, W., Rogers, N., Morris, W., Ugalde, H., Slavinski, H., Spicer, W., and Moussallam, Y. (2010): Tectonostratigraphy of the Baie Verte oceanic tract and its ophiolite cover sequence on the Baie Verte Peninsula. Current Research, Newfoundland and Labrador, Department of Natural Resources, Geological Survey, Report 10-1, 315-337.

The Figures would only be used in the Introduction Chapter of my Thesis and would not be by any means published or available outside the domains of Memorial University of Newfoundland.

Thank you in advance for your help and I look forward to hearing from you.

Sincerely,

Carlos Arbiol

Carlos Arbiol
Ph.D. Candidate in Economic Geology

Department of Earth Sciences
Memorial University
Office ER-5015A, Alexander Murray Building
St. John's, Newfoundland, A1B 3X5 Canada

Copyright Permission for Fig. 1.9.

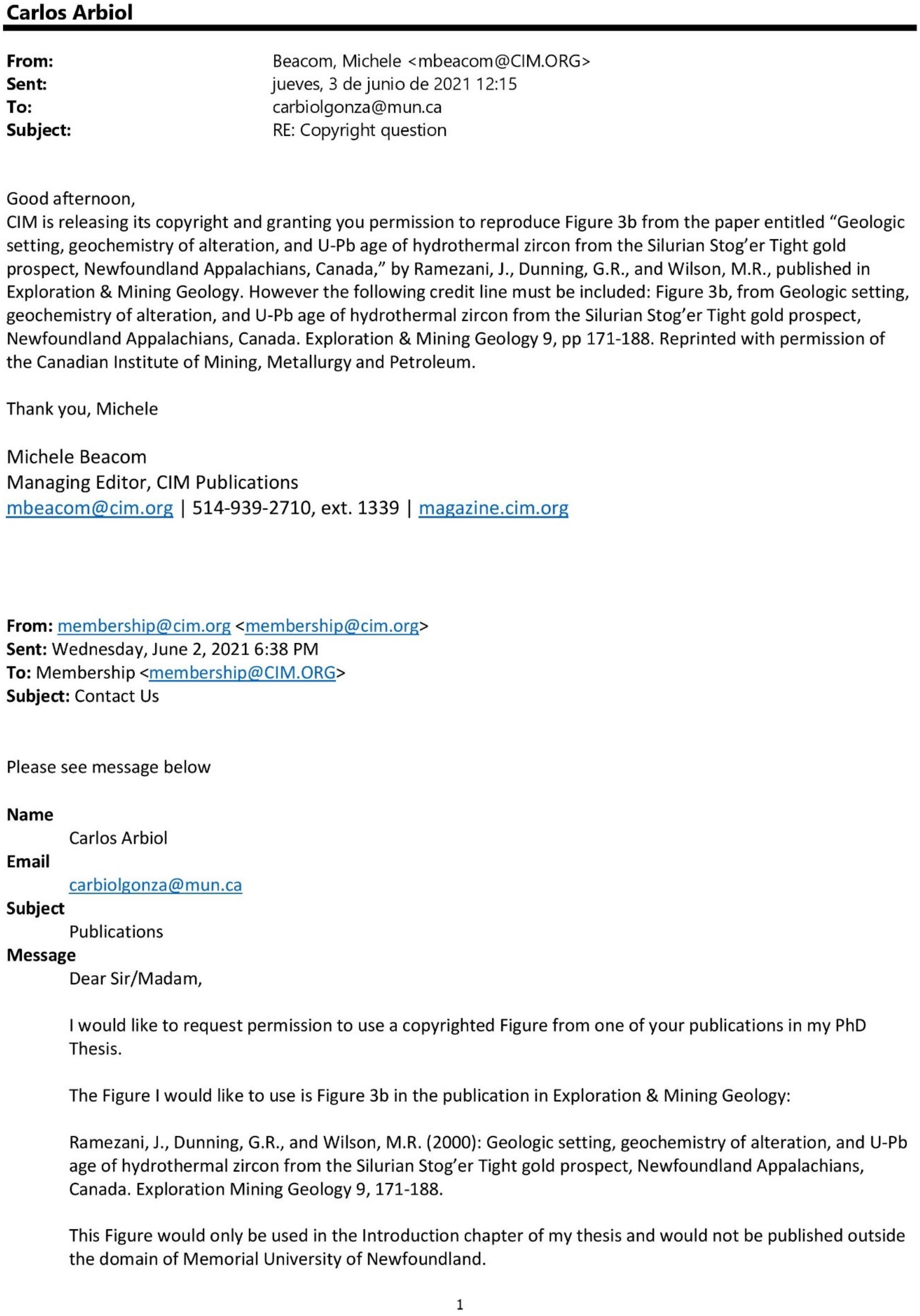

Carlos Arbiol

From: Beacom, Michele <mbeacom@CIM.ORG>
Sent: jueves, 3 de junio de 2021 12:15
To: carbiolgonza@mun.ca
Subject: RE: Copyright question

Good afternoon,
CIM is releasing its copyright and granting you permission to reproduce Figure 3b from the paper entitled "Geologic setting, geochemistry of alteration, and U-Pb age of hydrothermal zircon from the Silurian Stog'er Tight gold prospect, Newfoundland Appalachians, Canada," by Ramezani, J., Dunning, G.R., and Wilson, M.R., published in Exploration & Mining Geology. However the following credit line must be included: Figure 3b, from Geologic setting, geochemistry of alteration, and U-Pb age of hydrothermal zircon from the Silurian Stog'er Tight gold prospect, Newfoundland Appalachians, Canada. Exploration & Mining Geology 9, pp 171-188. Reprinted with permission of the Canadian Institute of Mining, Metallurgy and Petroleum.

Thank you, Michele

Michele Beacom
Managing Editor, CIM Publications
mbeacom@cim.org | 514-939-2710, ext. 1339 | magazine.cim.org

From: membership@cim.org <membership@cim.org>
Sent: Wednesday, June 2, 2021 6:38 PM
To: Membership <membership@CIM.ORG>
Subject: Contact Us

Please see message below

Name
Carlos Arbiol
Email
carbiolgonza@mun.ca
Subject
Publications
Message
Dear Sir/Madam,

I would like to request permission to use a copyrighted Figure from one of your publications in my PhD Thesis.

The Figure I would like to use is Figure 3b in the publication in Exploration & Mining Geology:

Ramezani, J., Dunning, G.R., and Wilson, M.R. (2000): Geologic setting, geochemistry of alteration, and U-Pb age of hydrothermal zircon from the Silurian Stog'er Tight gold prospect, Newfoundland Appalachians, Canada. Exploration Mining Geology 9, 171-188.

This Figure would only be used in the Introduction chapter of my thesis and would not be published outside the domain of Memorial University of Newfoundland.

Thank you in advance and I look forward to hearing from you.

Sincerely,

Carlos Arbiol

Appendix 2. X-Ray Diffraction pattern of whole-rock, clay separates, and glycolated clay separates from studied epithermal occurrences.

Hope Brook - Sample HB-1

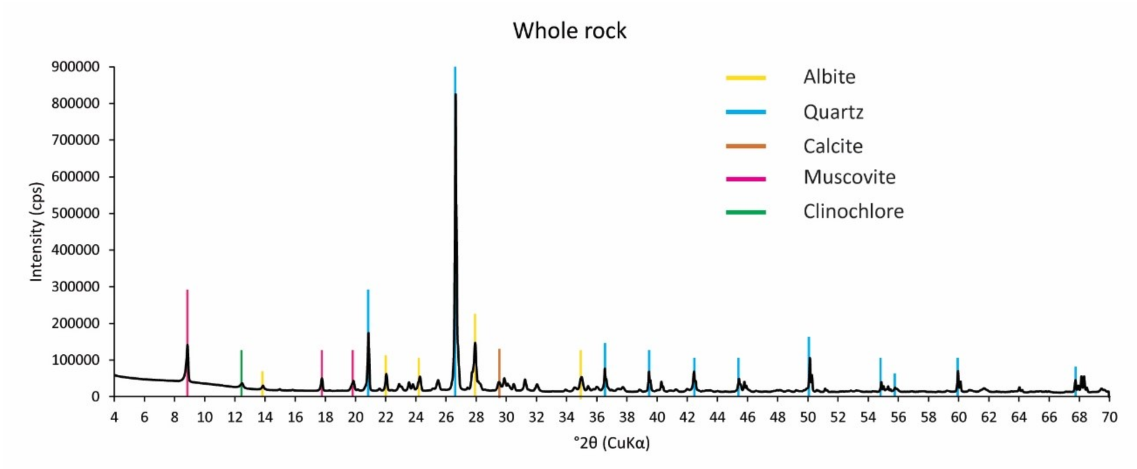

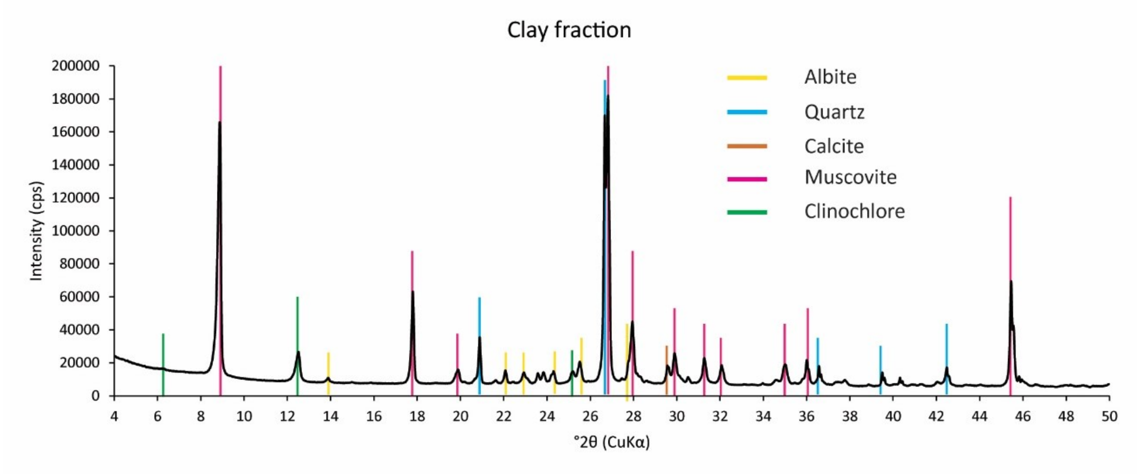

Hope Brook - Sample HB-2

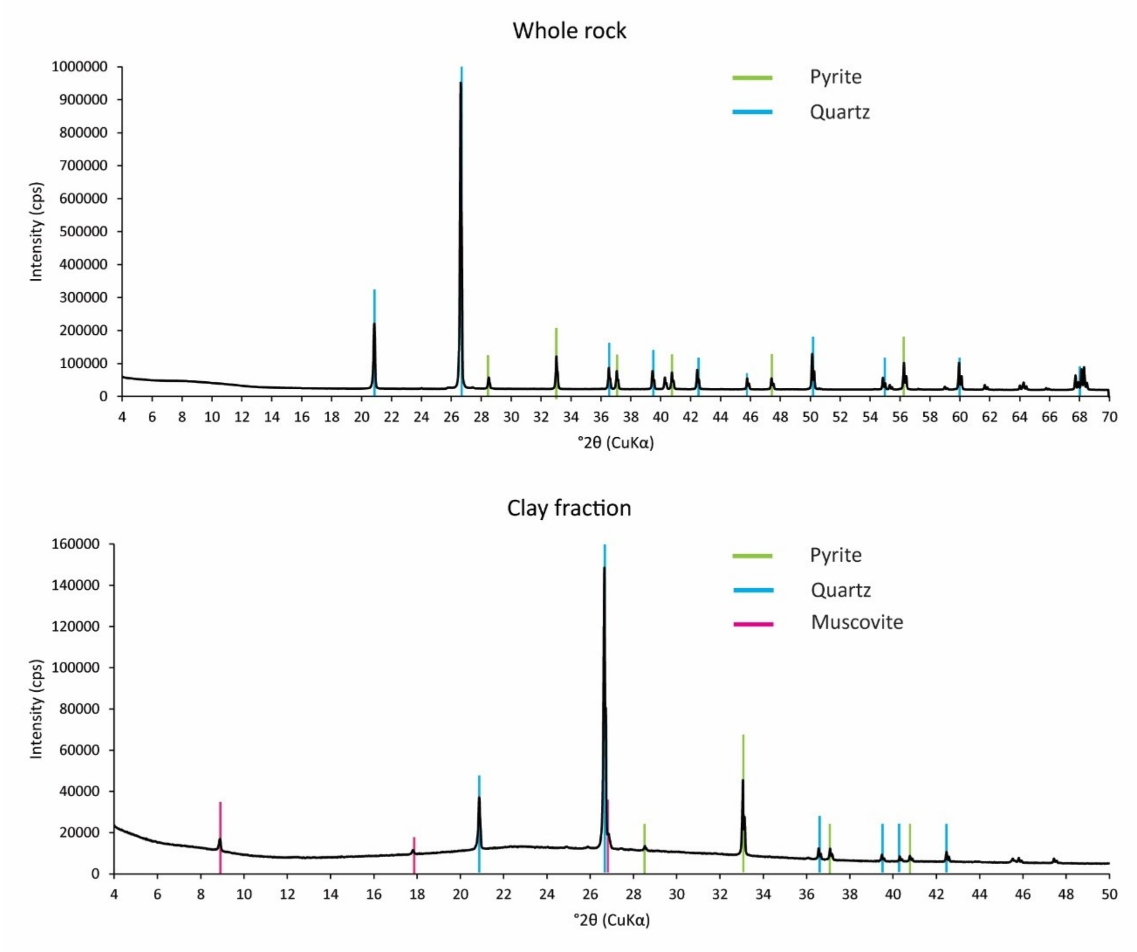

Hope Brook - Sample HB-3

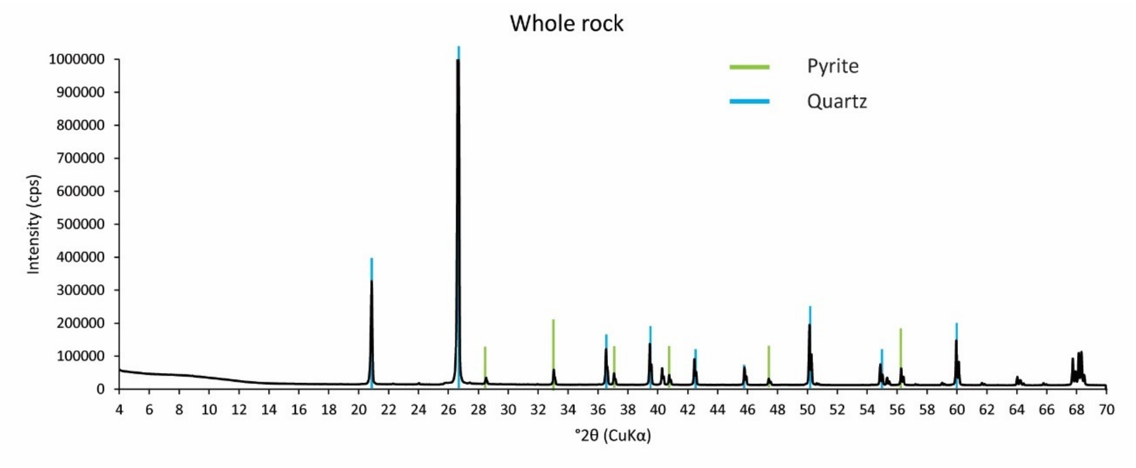

Hope Brook - Sample HB-4

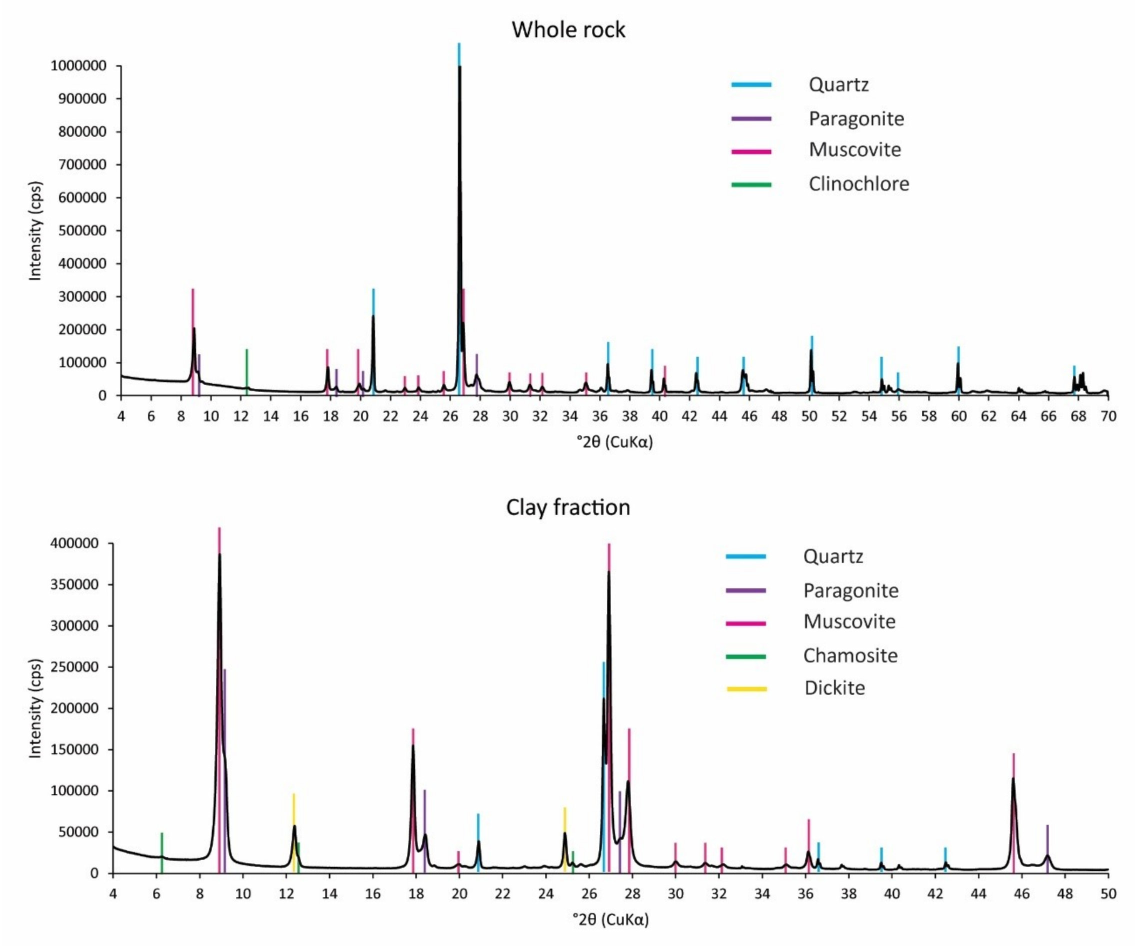

Hope Brook - Sample HB-5

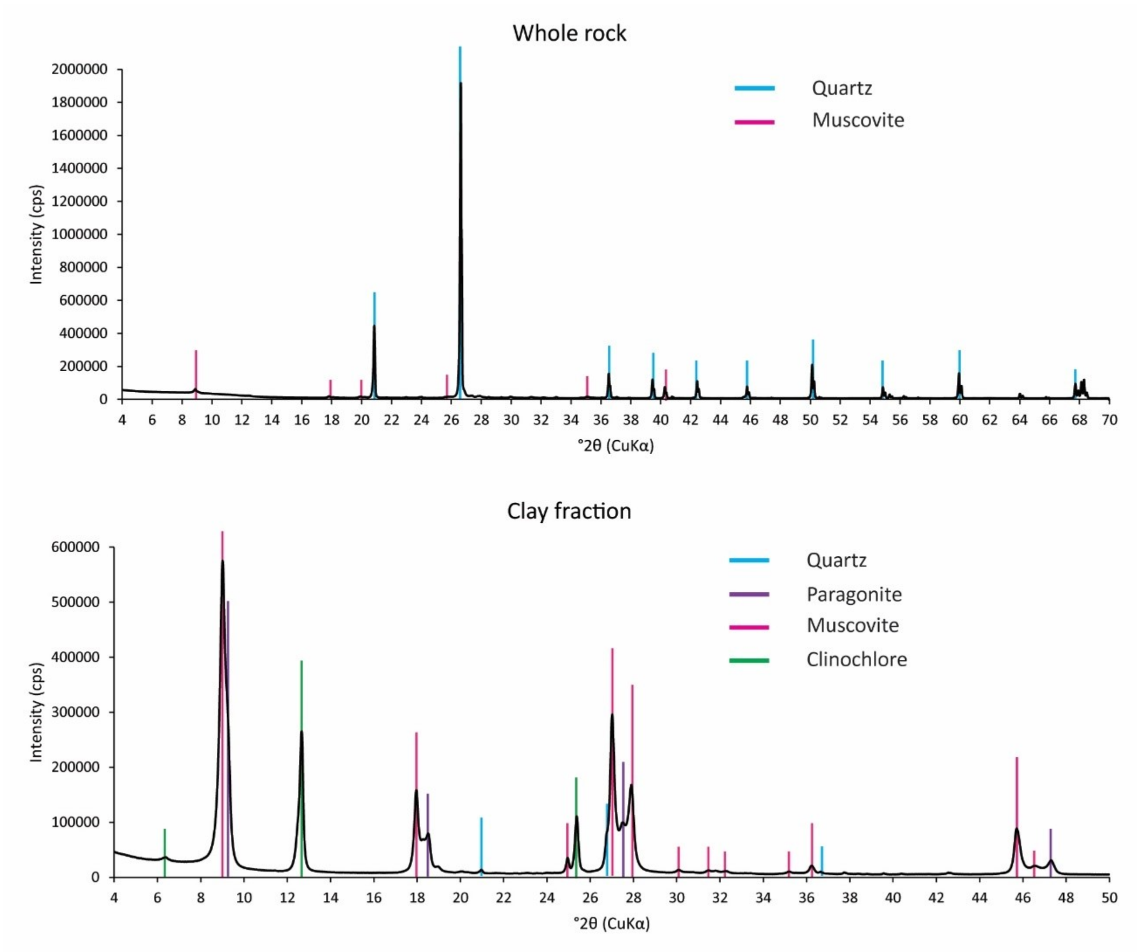

Hope Brook - Sample HB-6

Whole rock

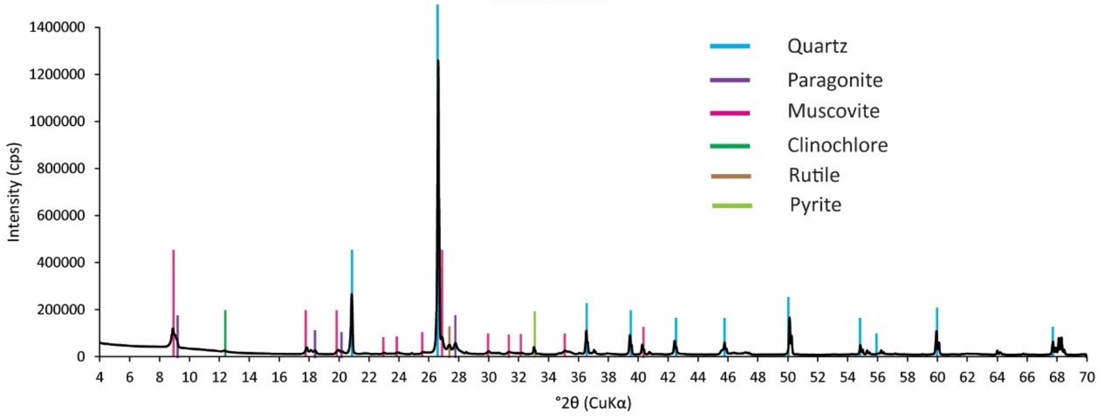

Clay fraction

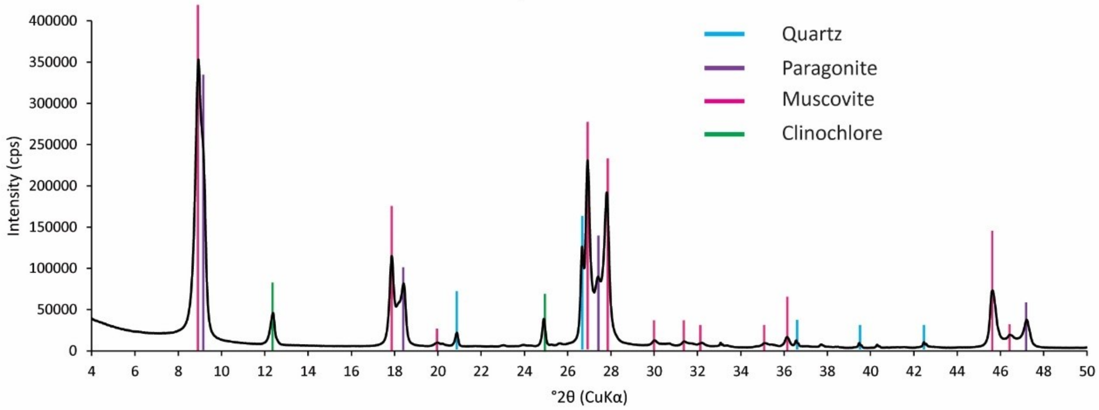

Hope Brook - Sample HB-7

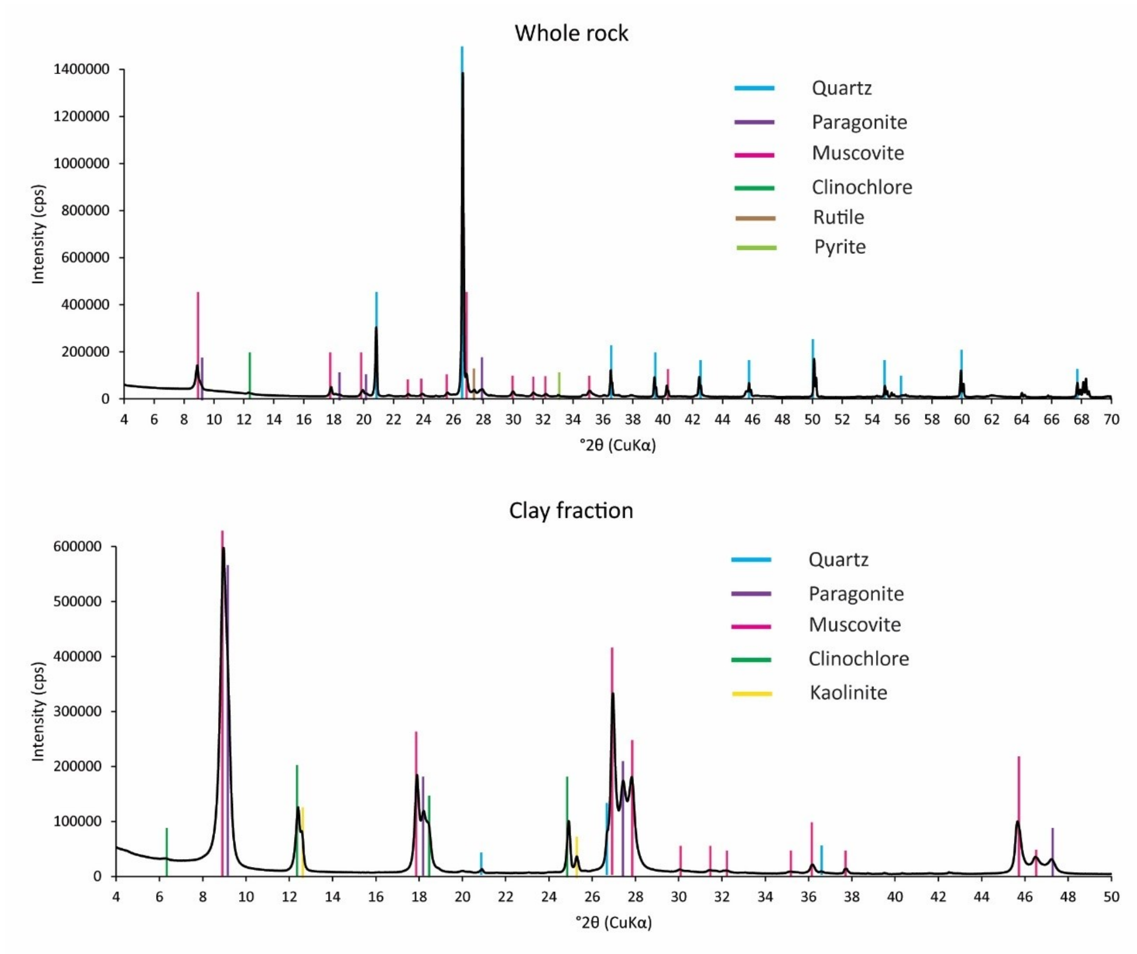

Hope Brook - Sample HB-8

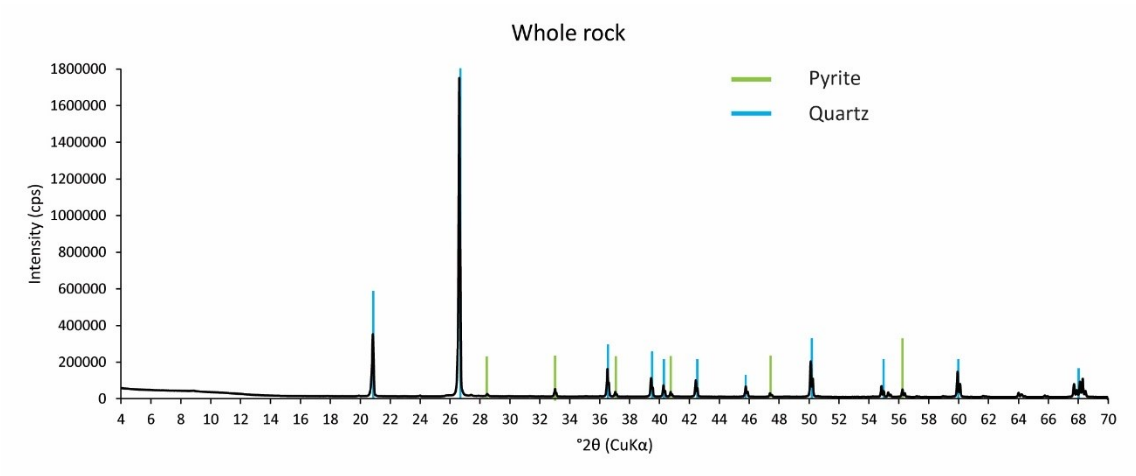

Hope Brook - Sample HB-9

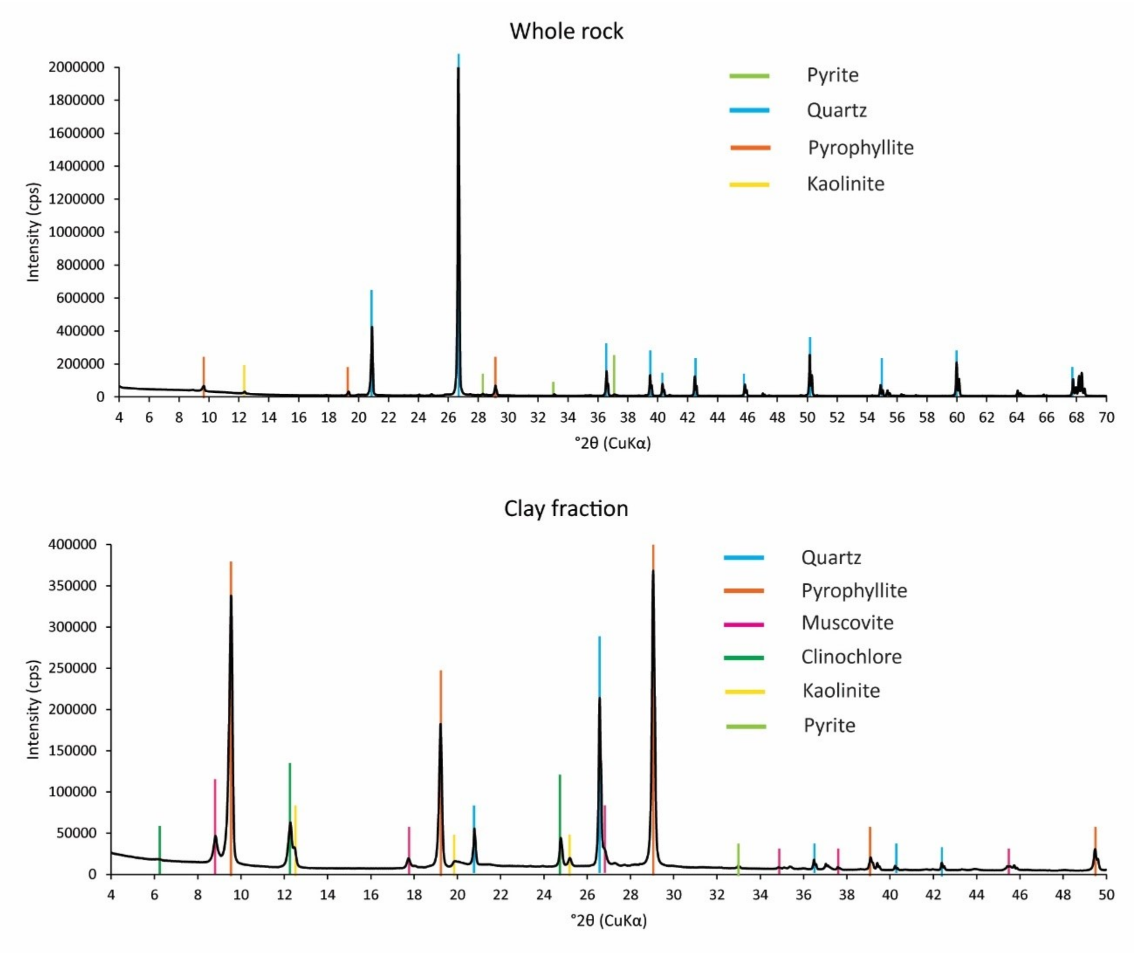

Hope Brook - Sample HB-10

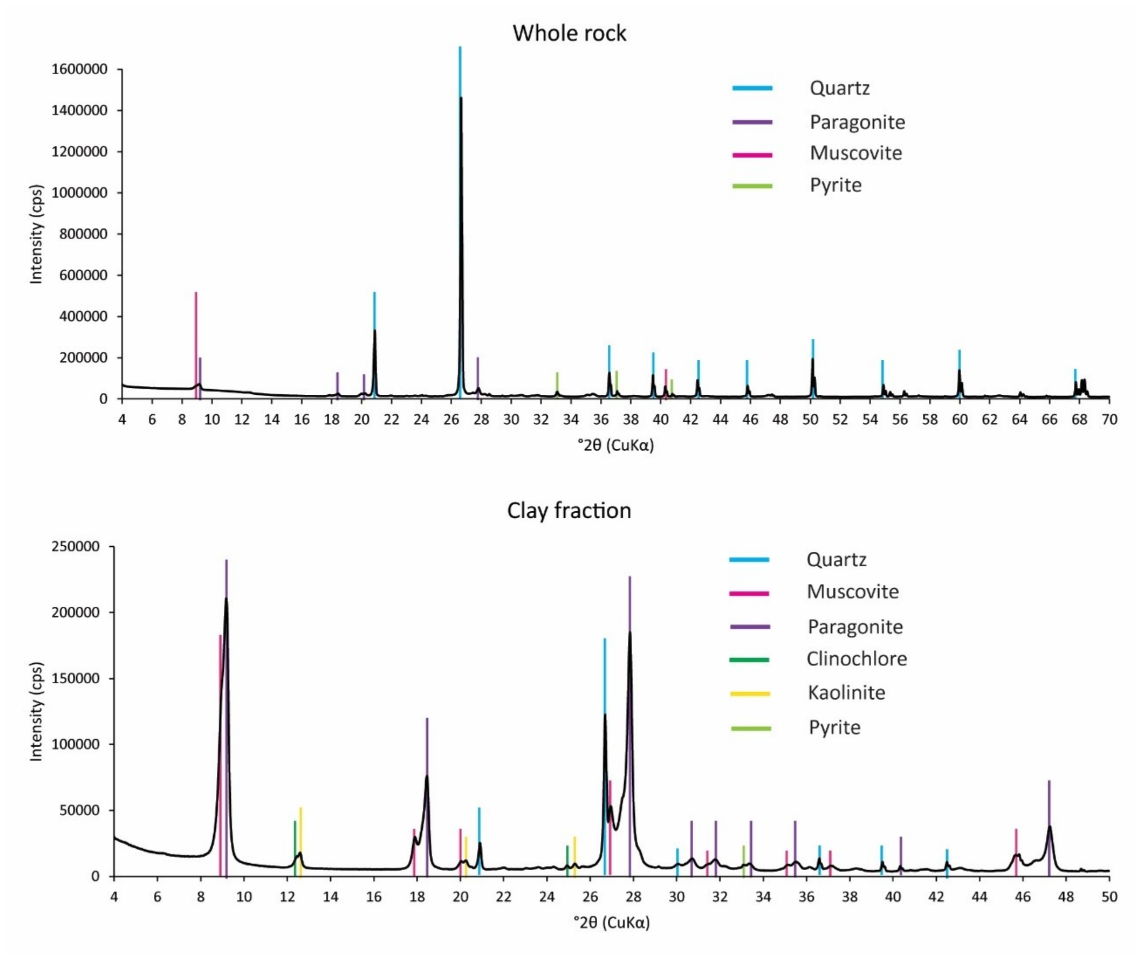

Hope Brook - Sample HB-11

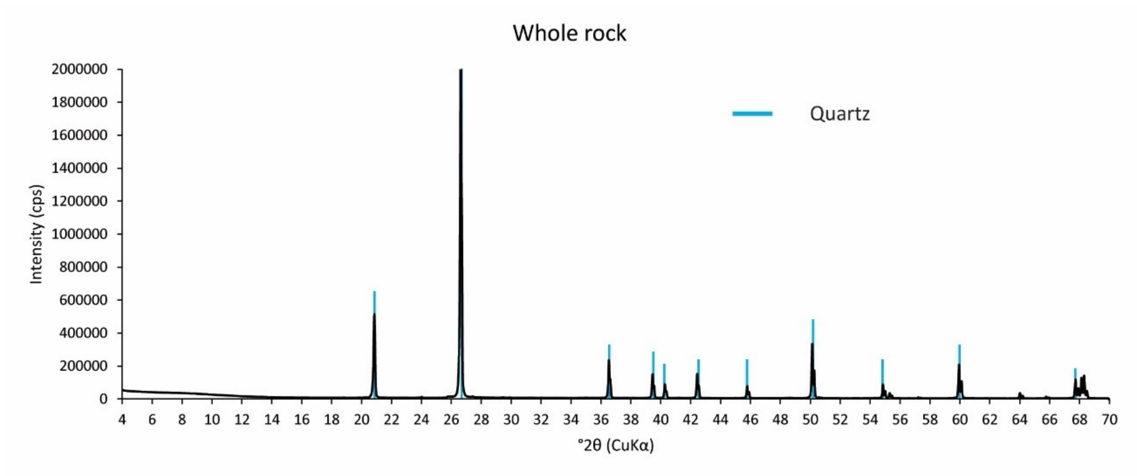

Hope Brook - Sample HB-12

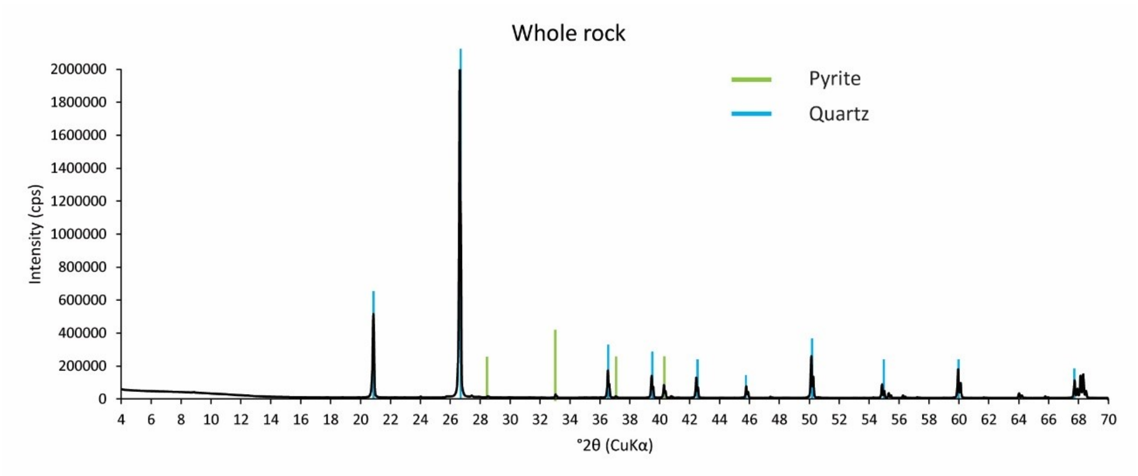

Hope Brook - Sample HB-13

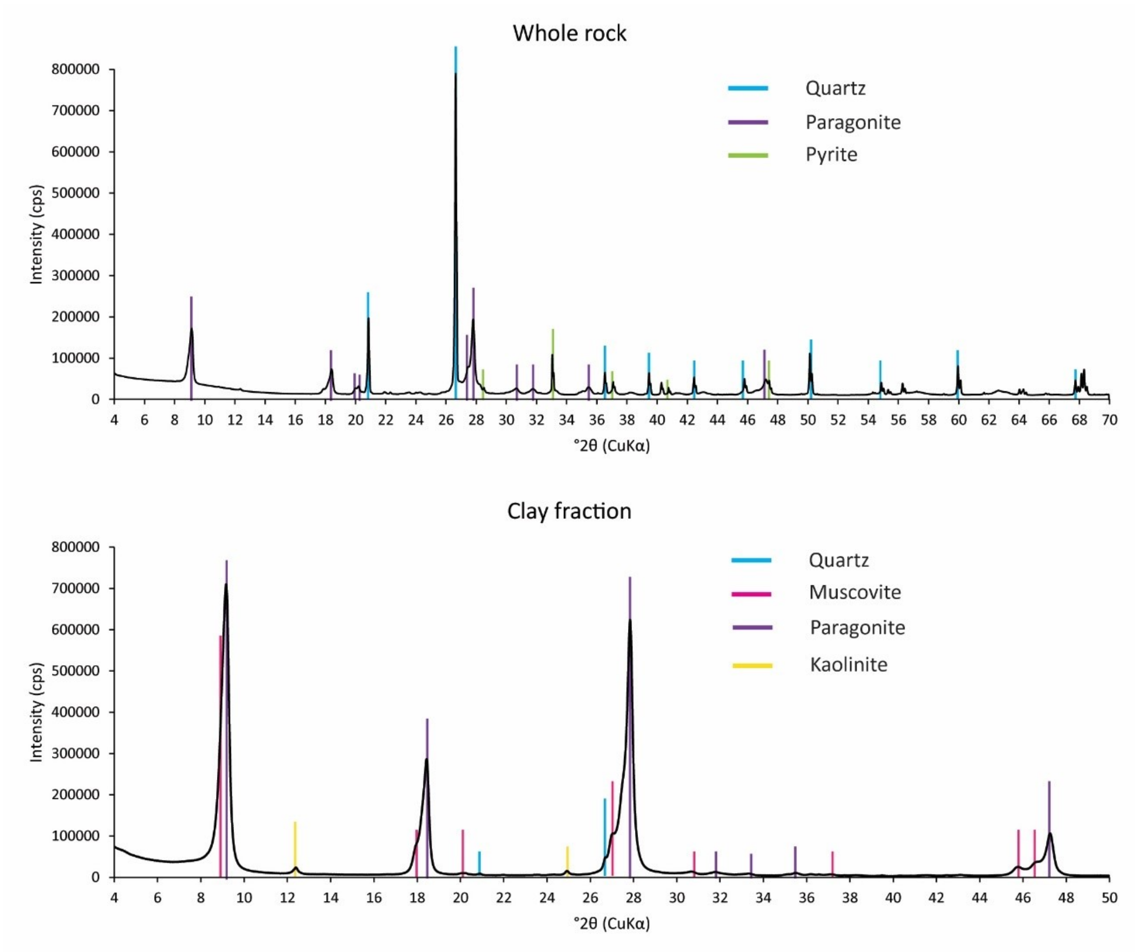

Hope Brook - Sample HB-14

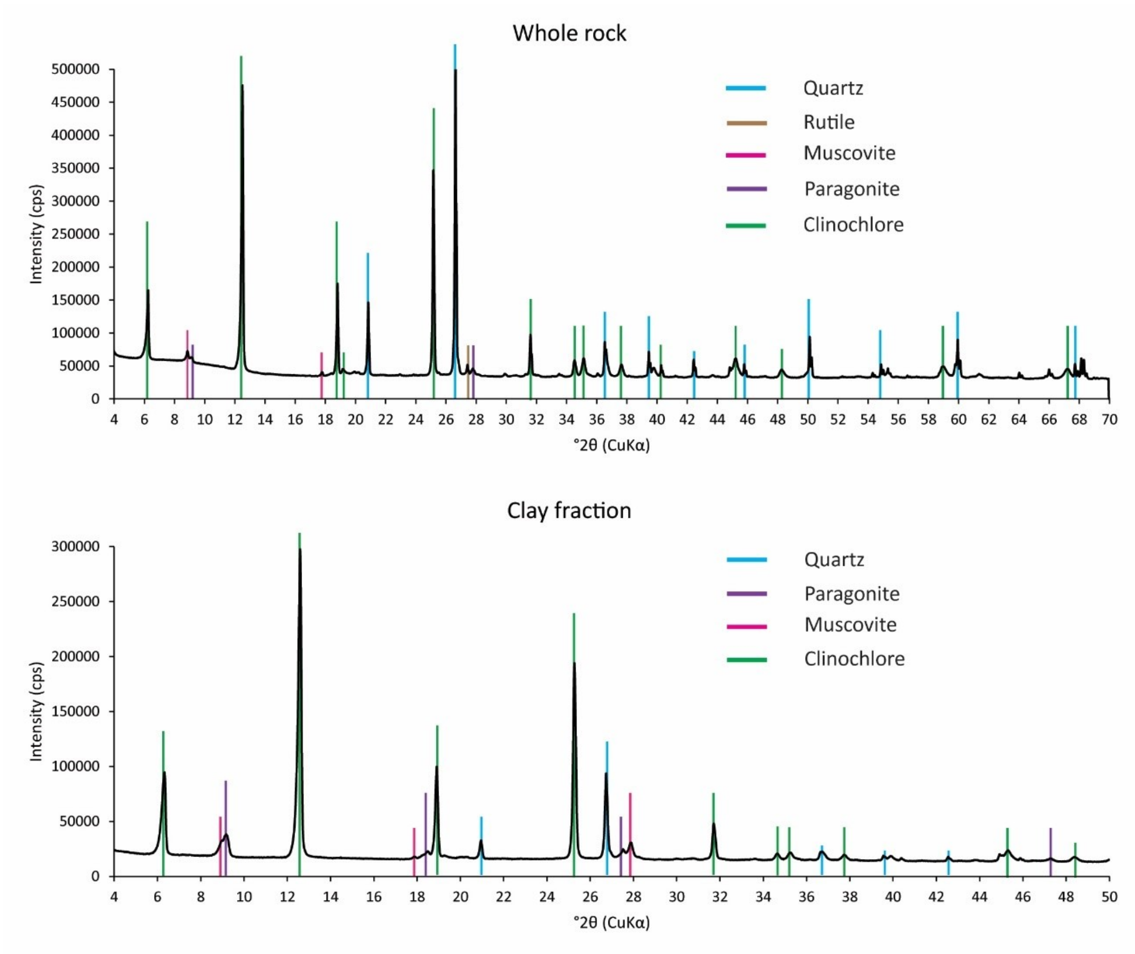

Hickey's Pond - Sample HP-1

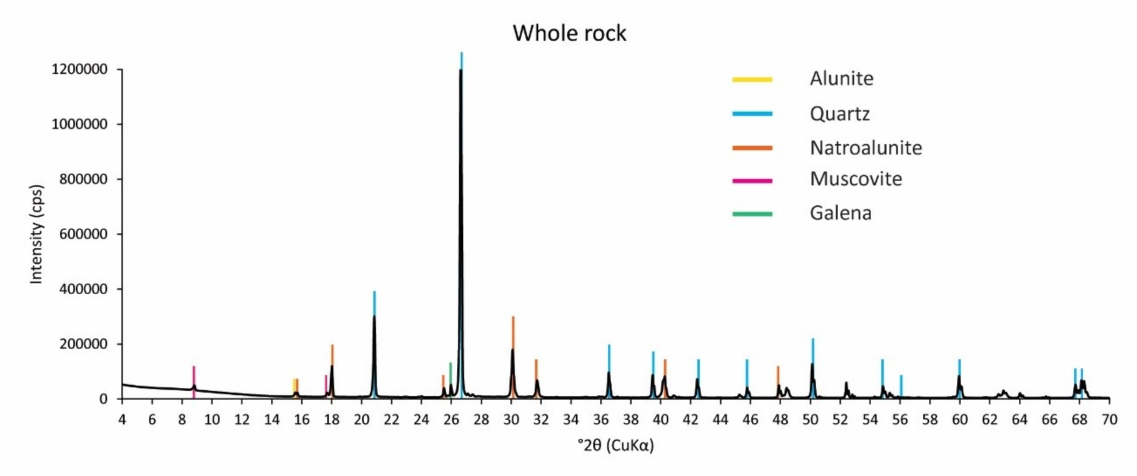

Hickey’s Pond - Sample HP-2

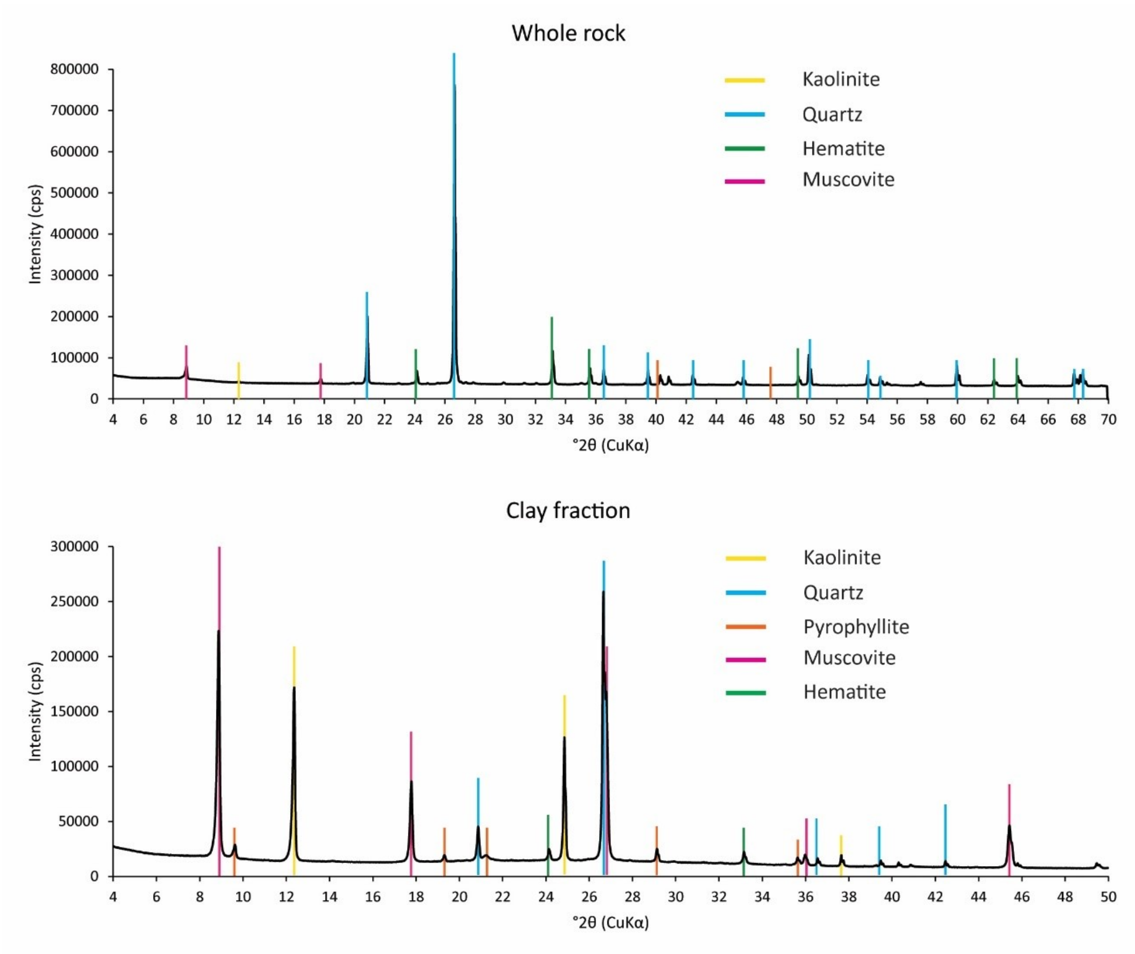

Hickey’s Pond - Sample HP-3

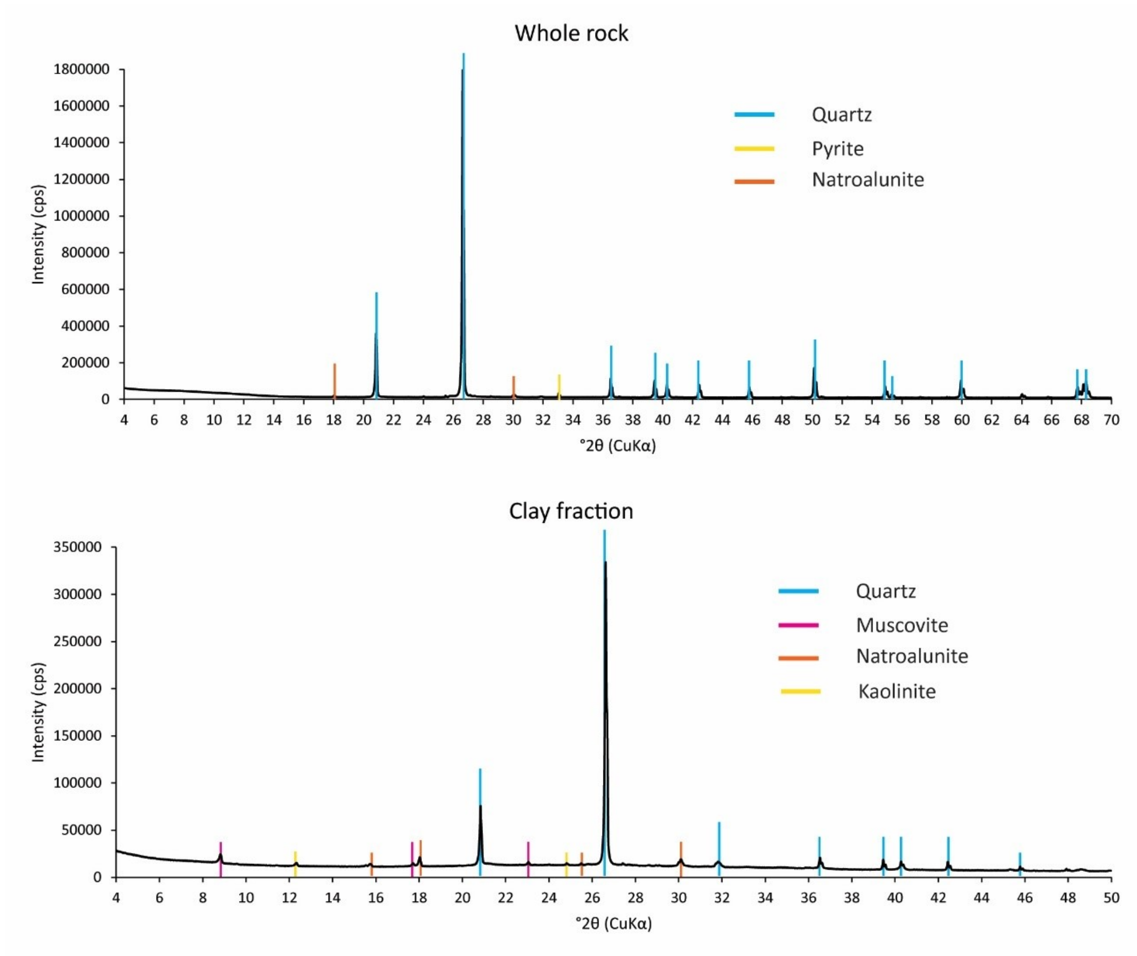

Hickey’s Pond - Sample HP-4a

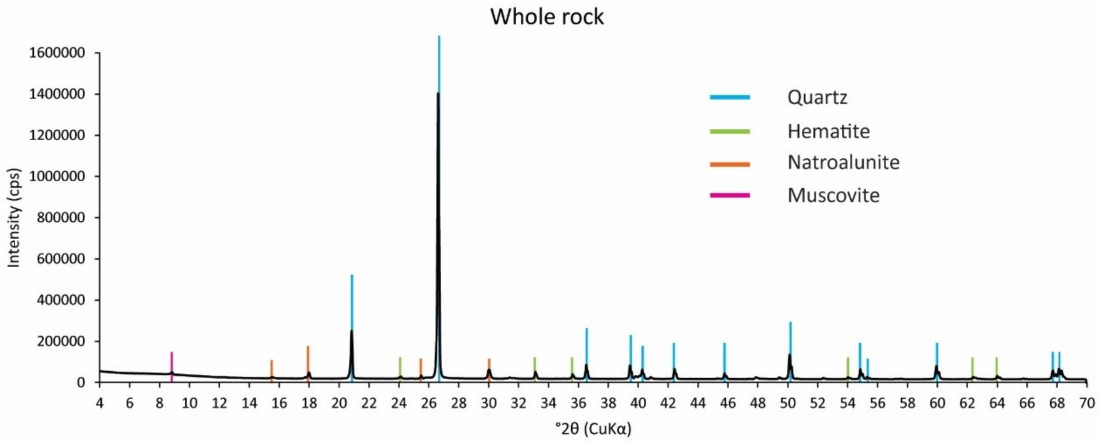

Hickey’s Pond - Sample HP-4b

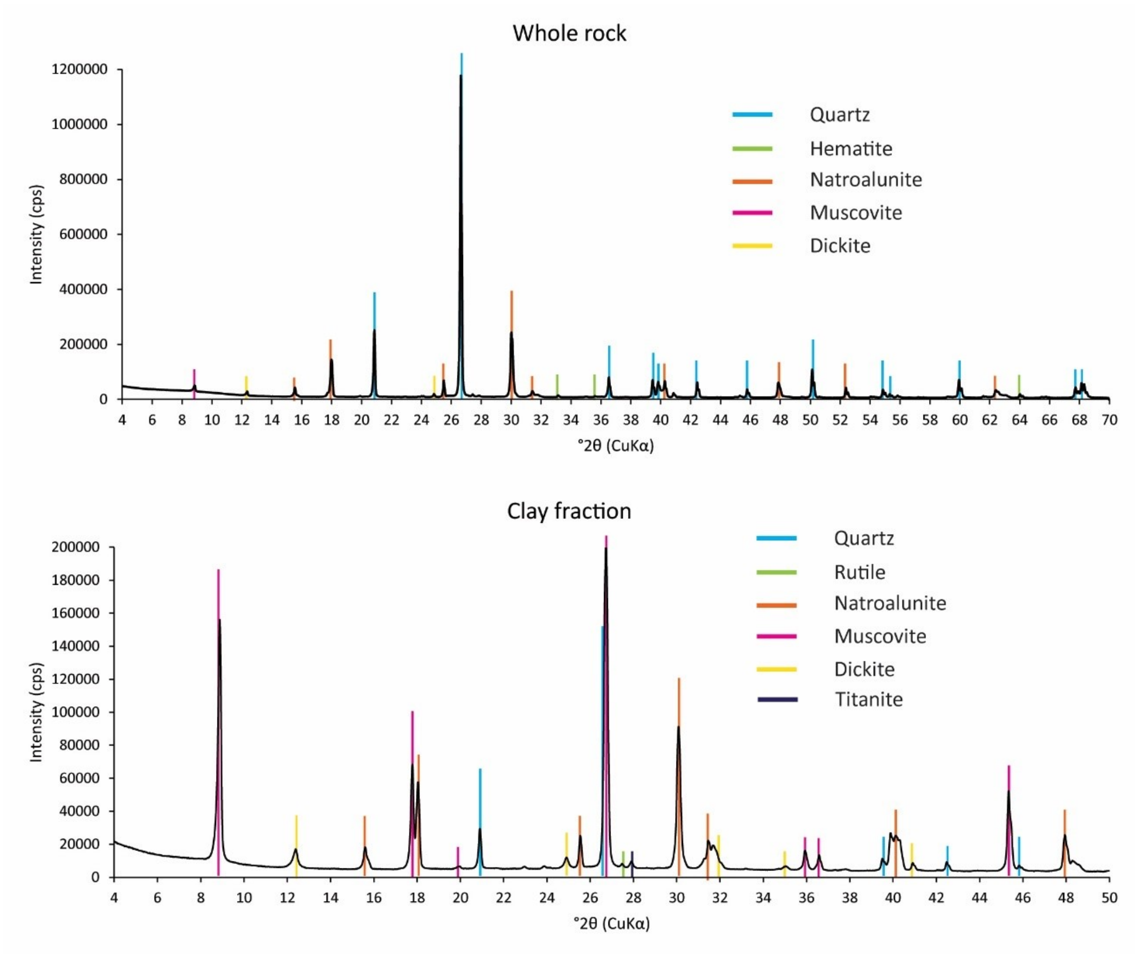

Hickey’s Pond - Sample HP-5

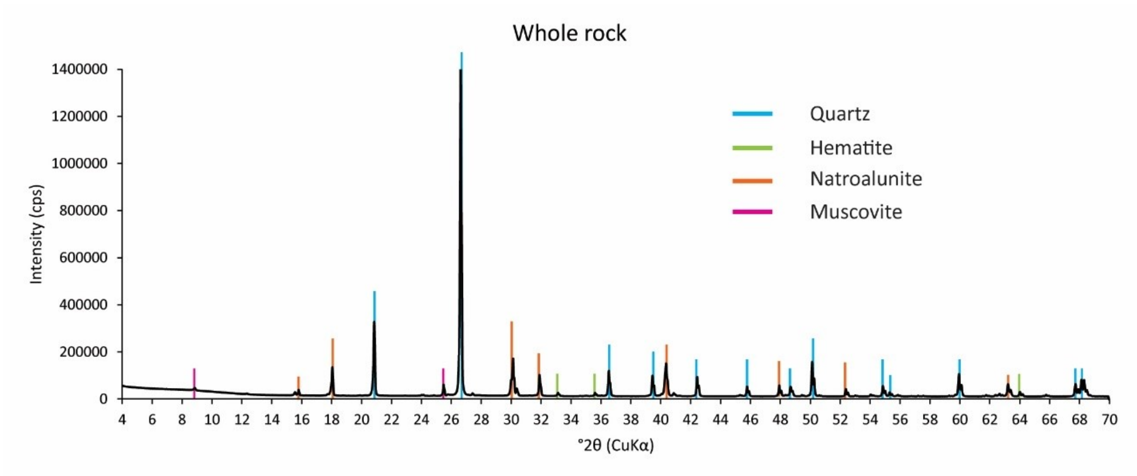

Hickey's Pond - Sample HP-6

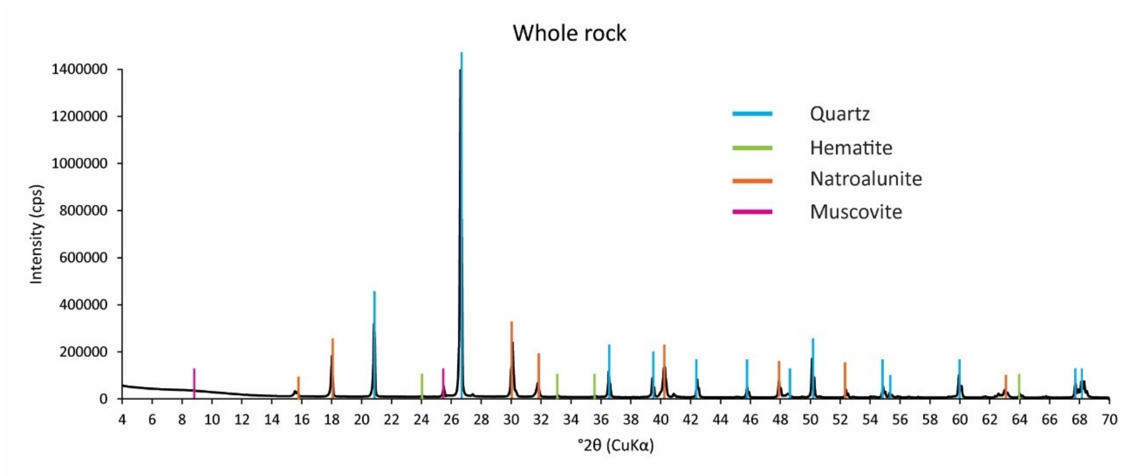

Hickey’s Pond - Sample HP-7

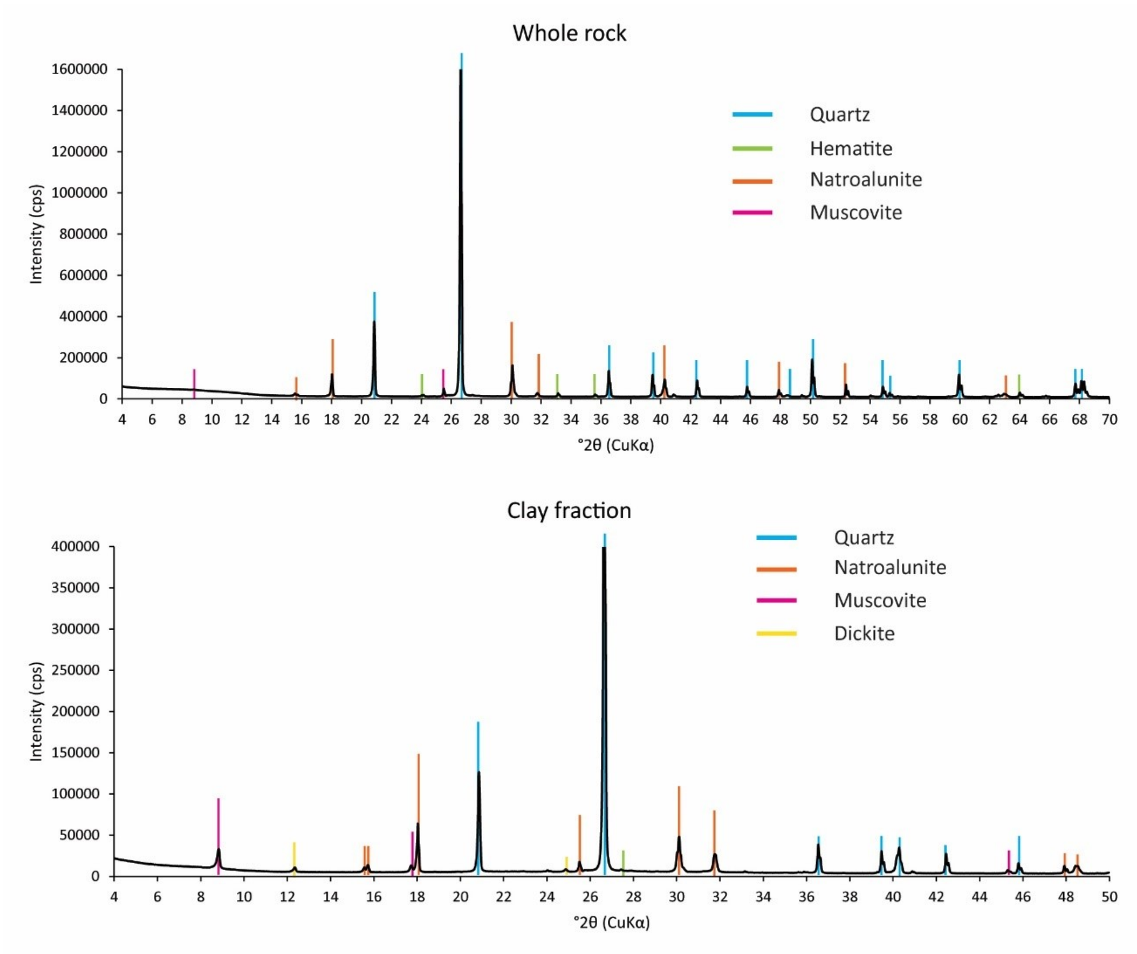

Oval Pit Mine - Sample MANUELS

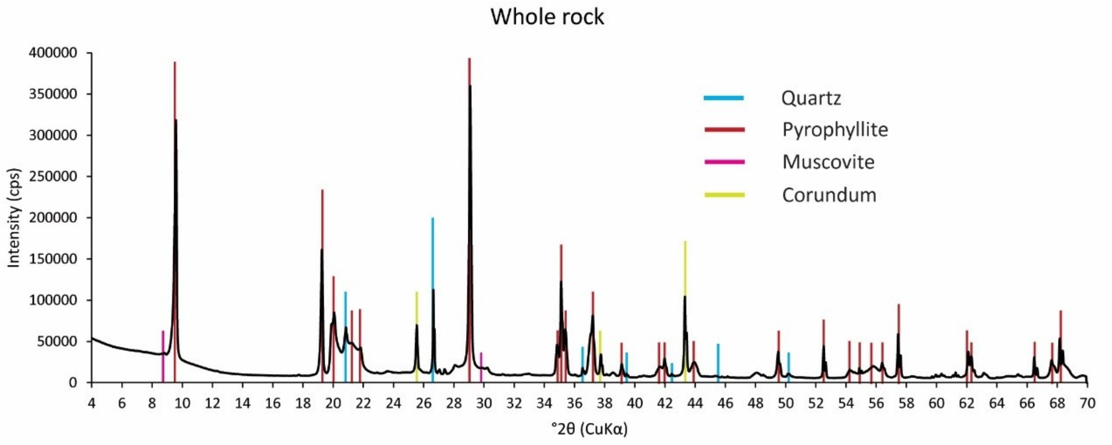

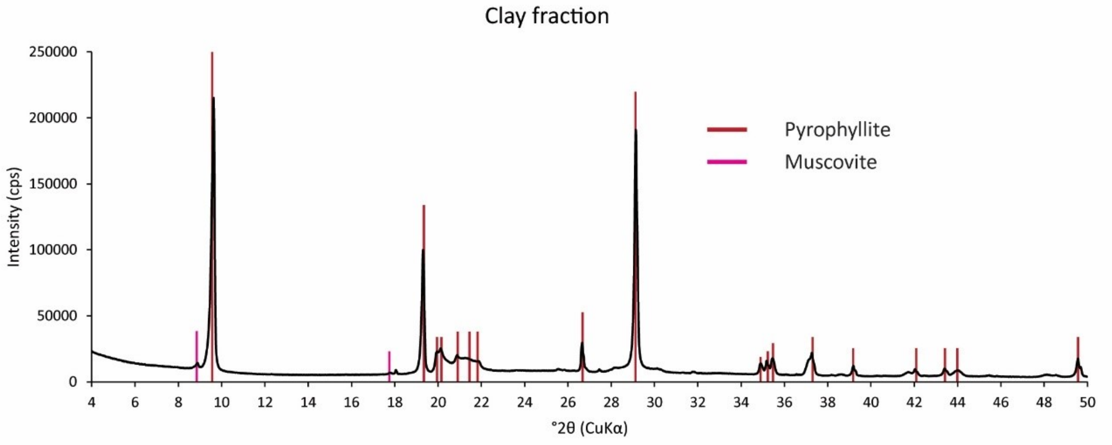

Vinjer - Sample Vinjer

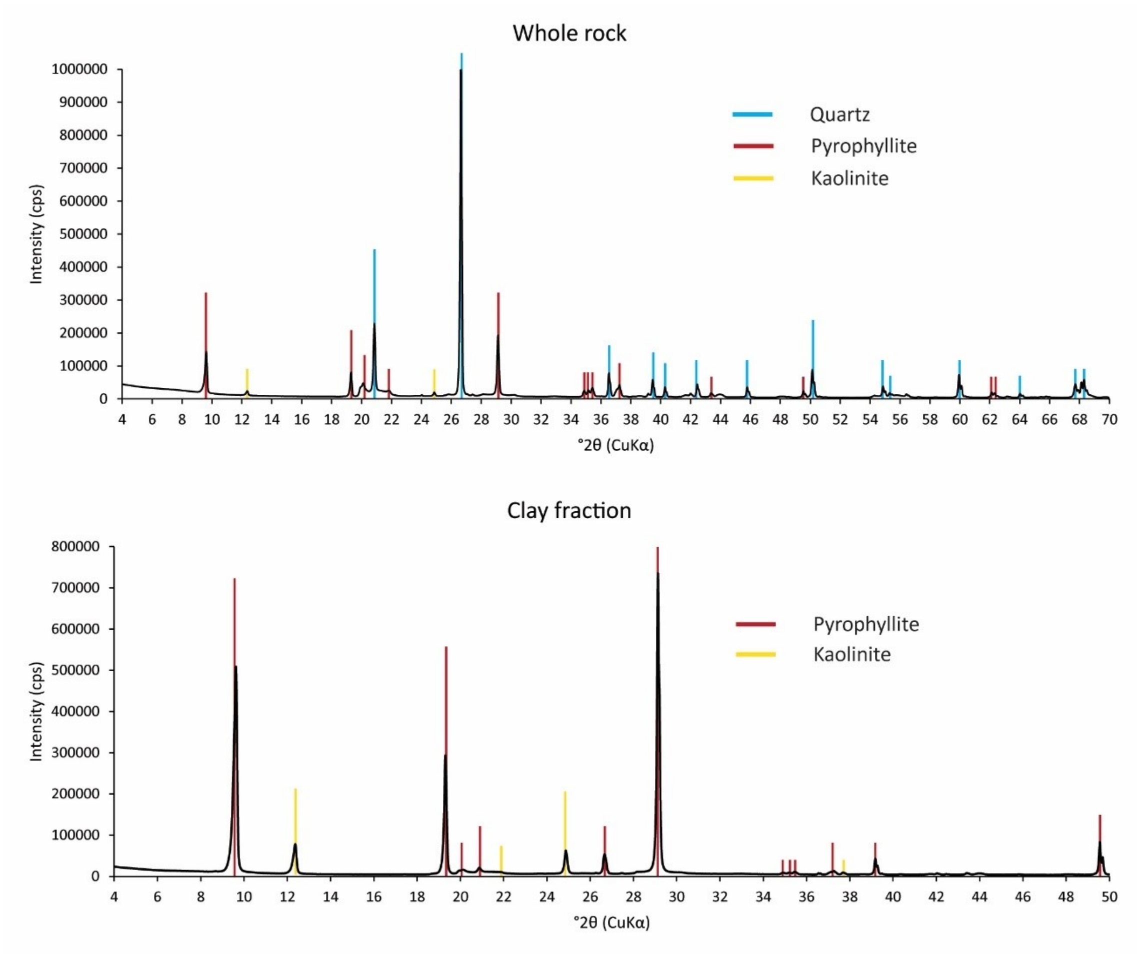

Heritage - Sample HE-02-03

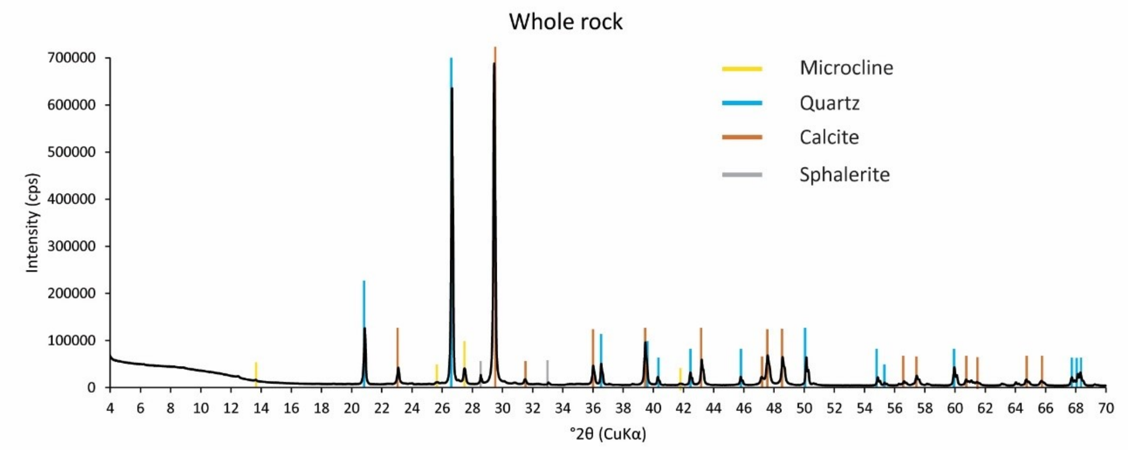

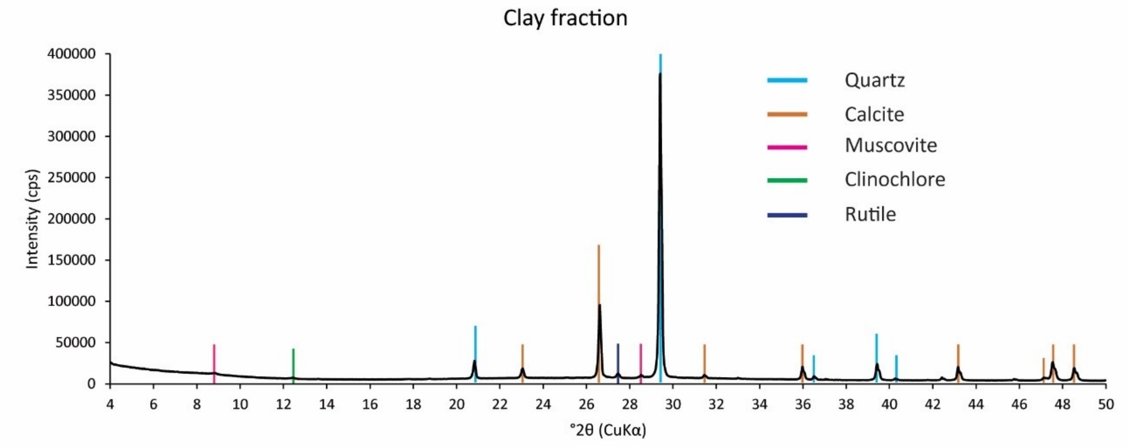

Heritage - Sample HE-02-04

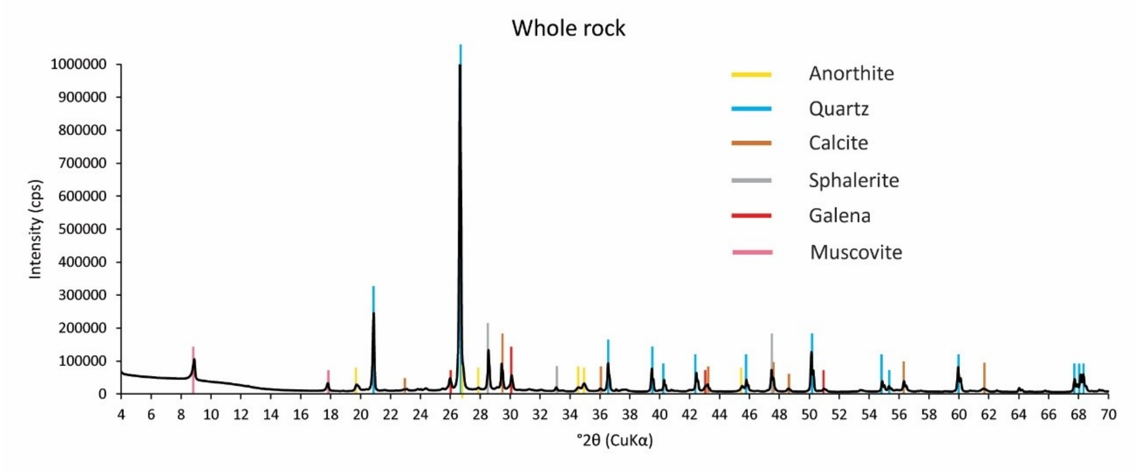

Heritage - Sample HE-03-03

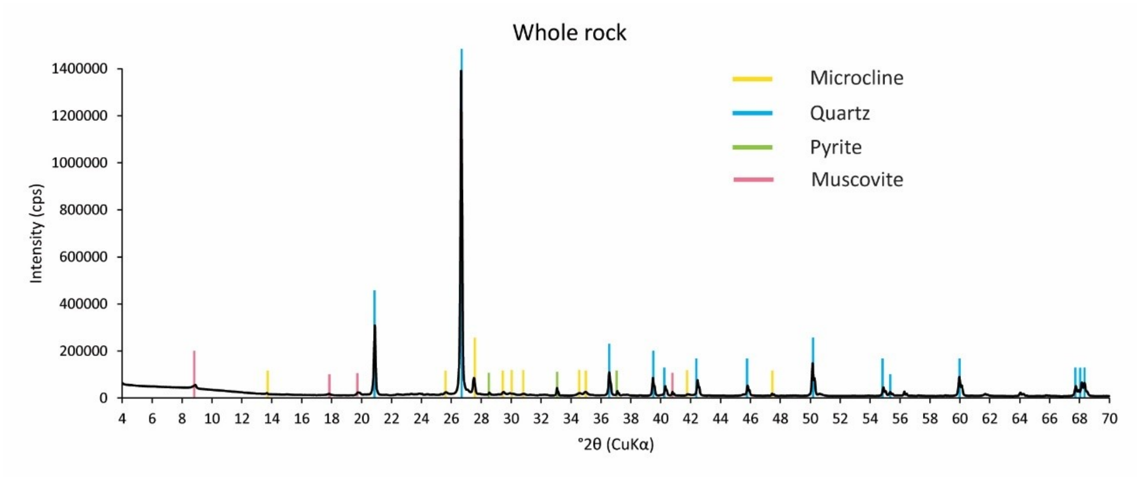

Heritage - Sample HE-05-03

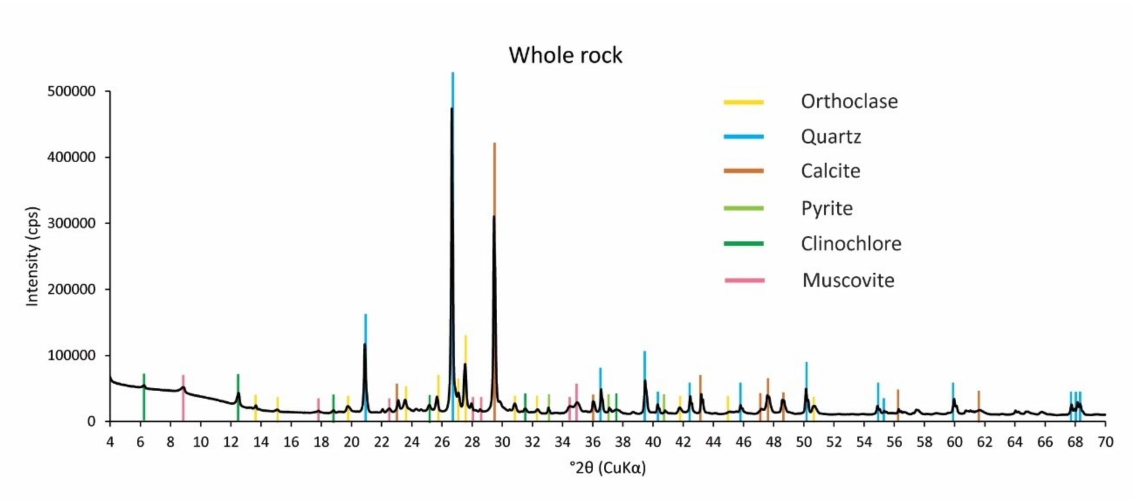

Heritage - Sample HE-05-odd_host_rock

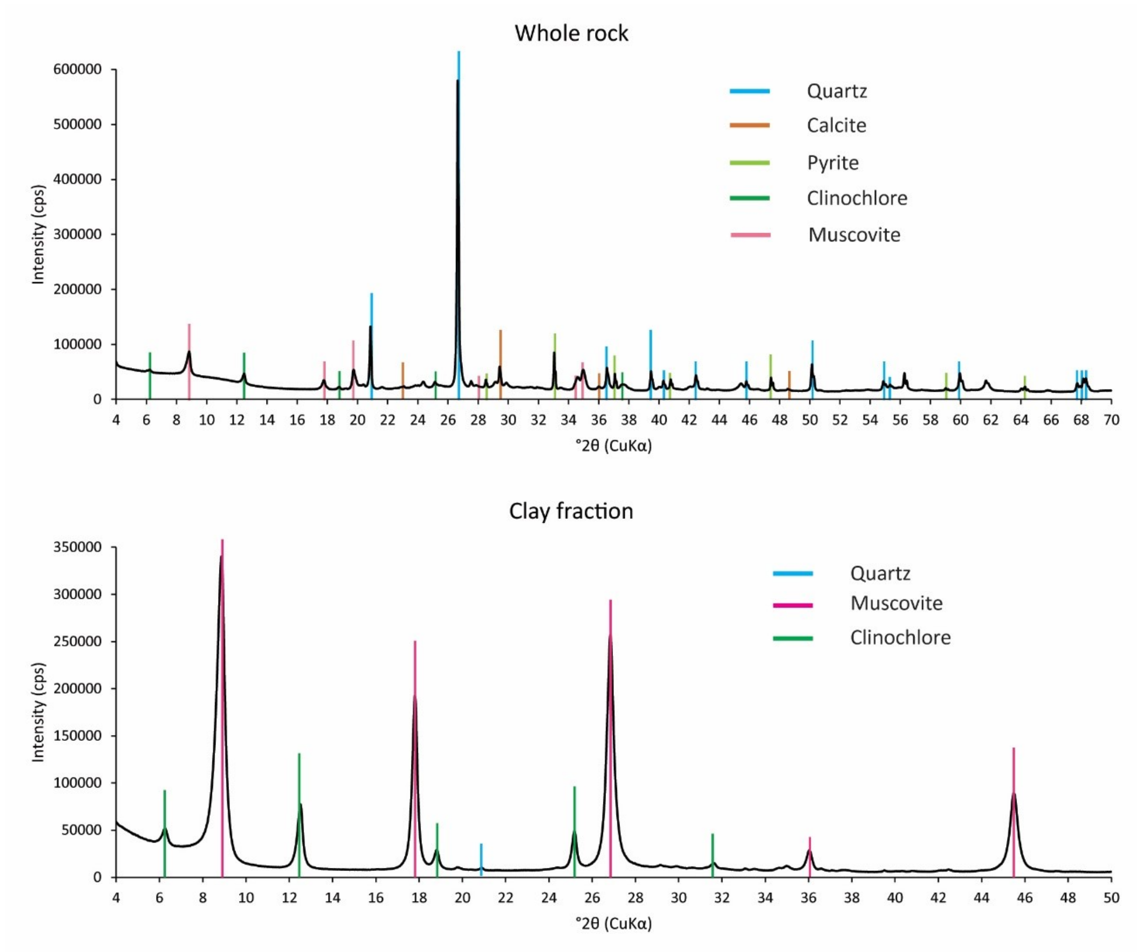

Heritage - Sample HE-05-odd_vein

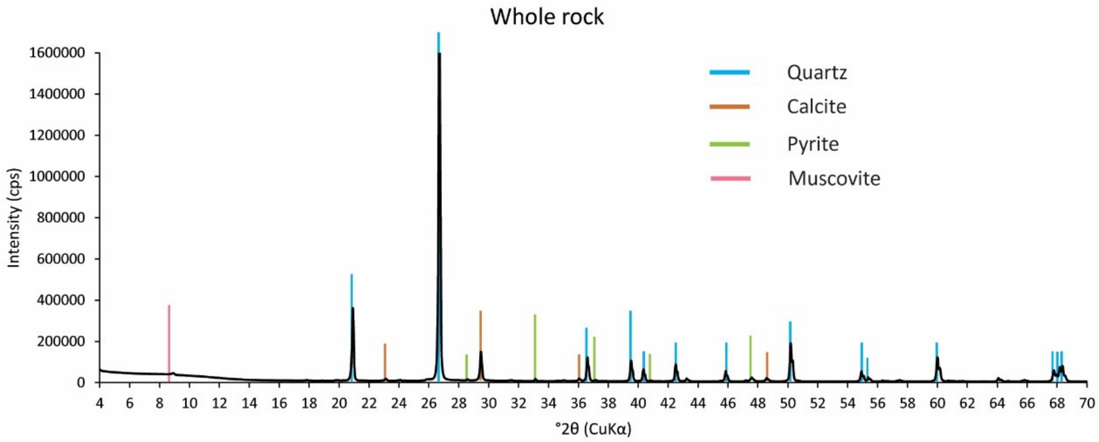
Whole rock

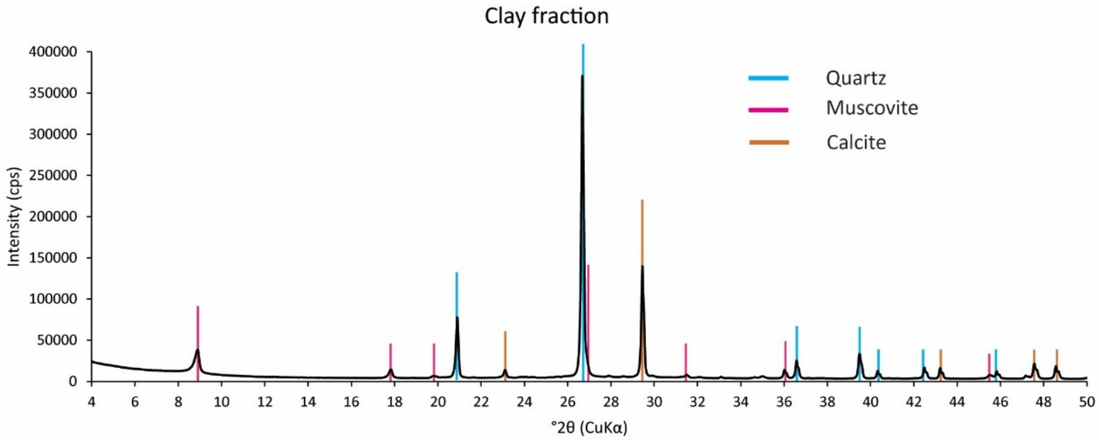
Clay fraction

Heritage - Sample HE-07-03

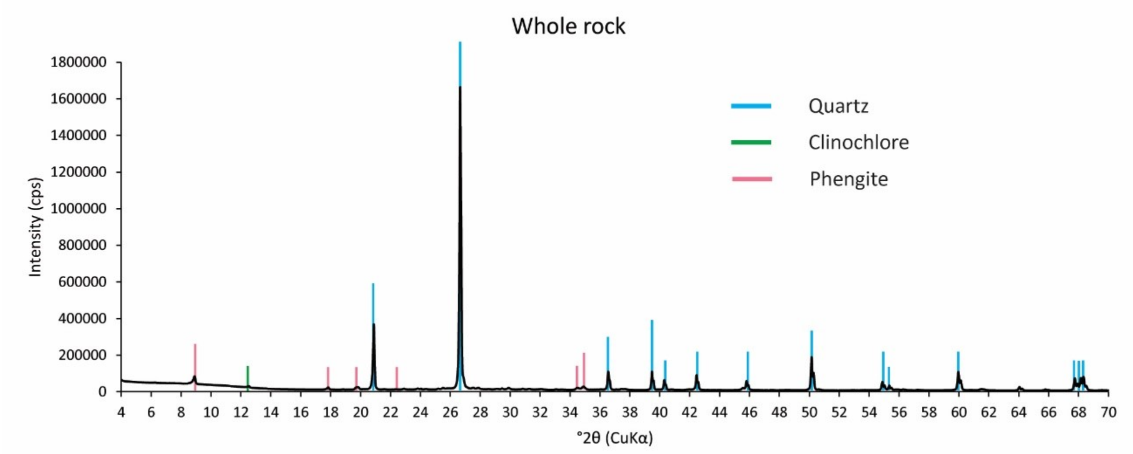

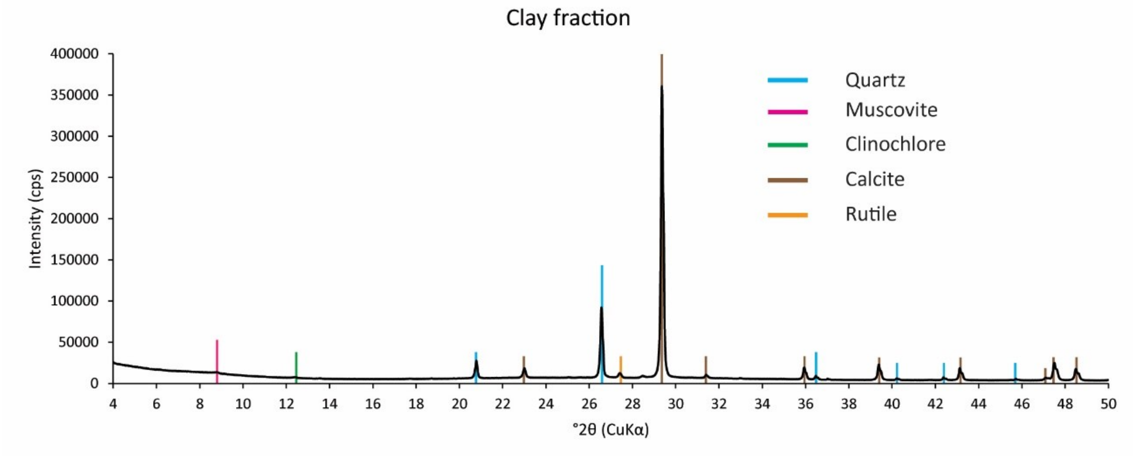

Heritage - Sample HE-08-01

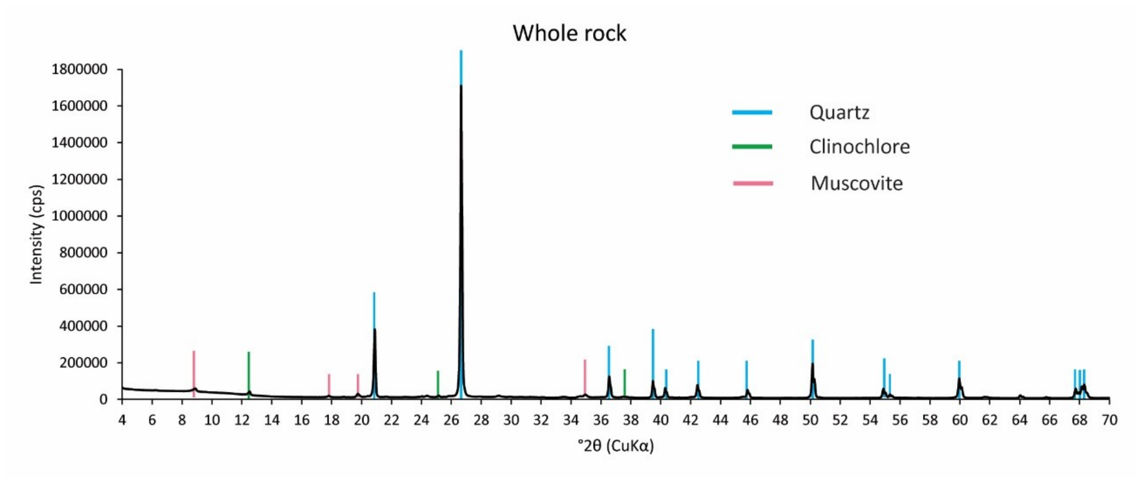

Heritage - Sample HE-08-02

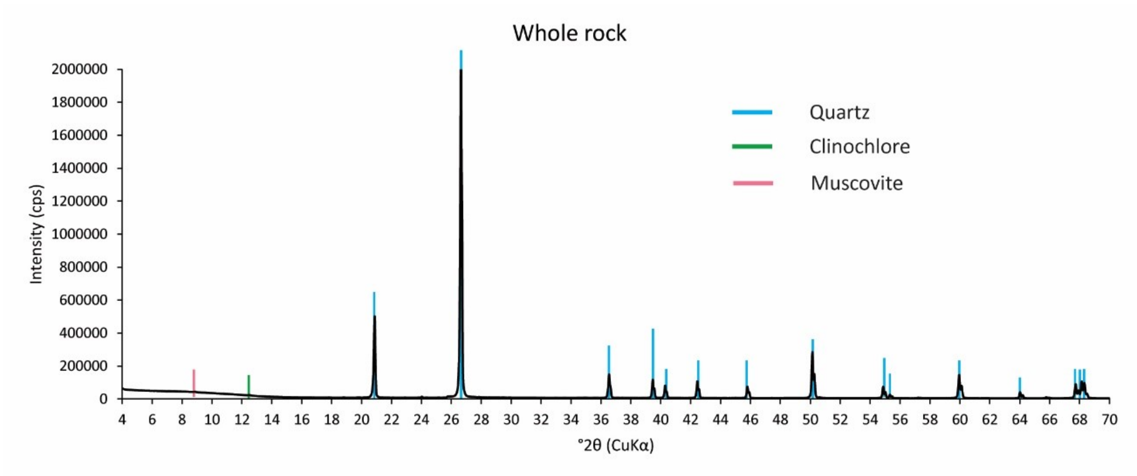

Heritage - Sample HE-08-03

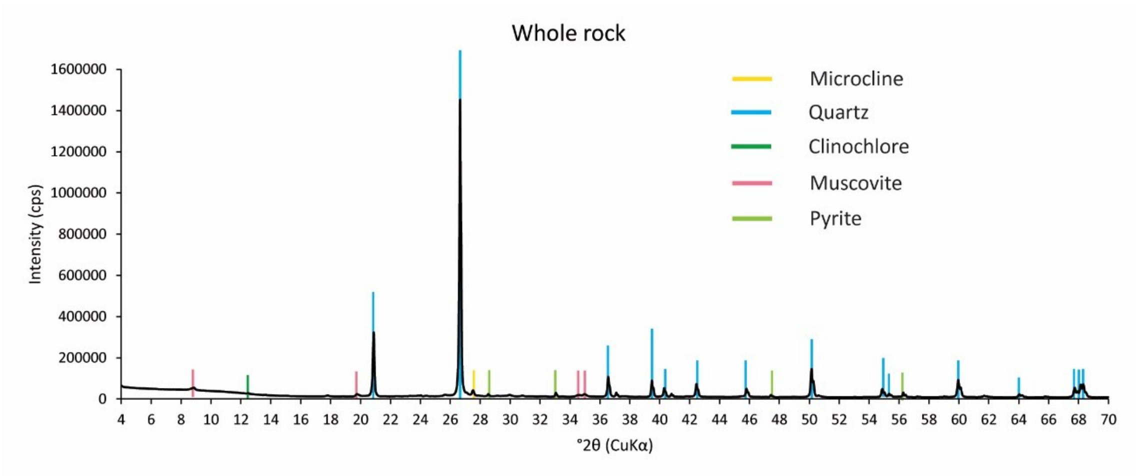

Heritage - Sample HE-09-01

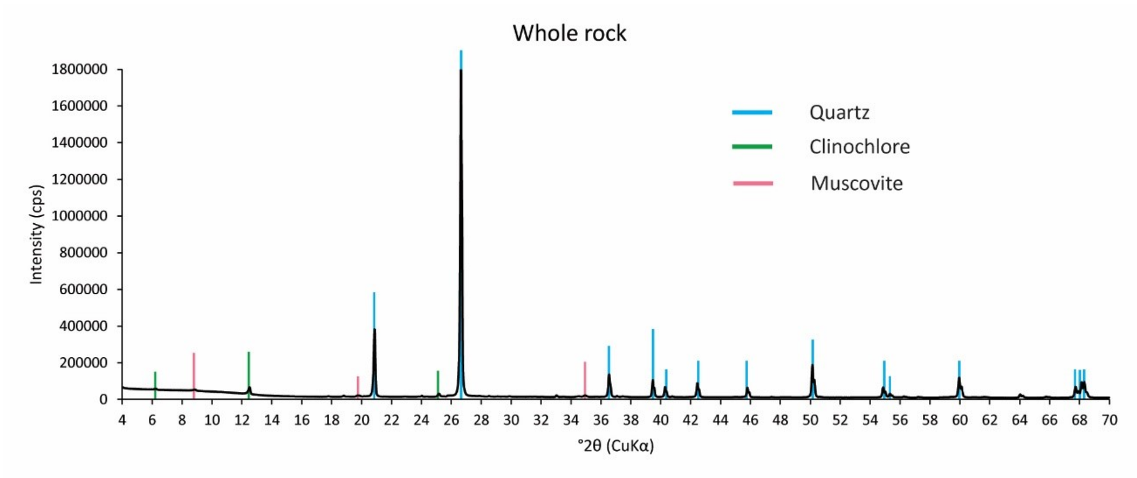

Heritage - Sample HE-09-02

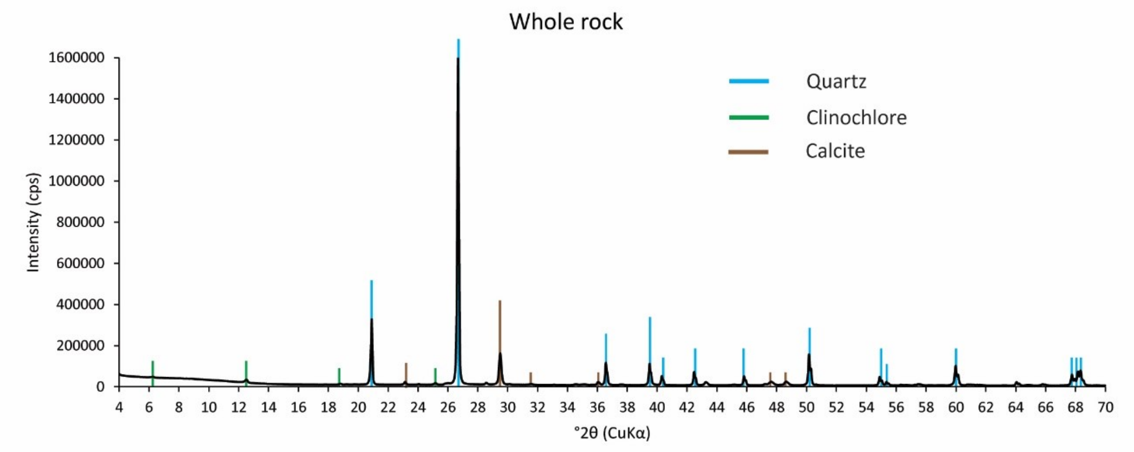
Whole rock

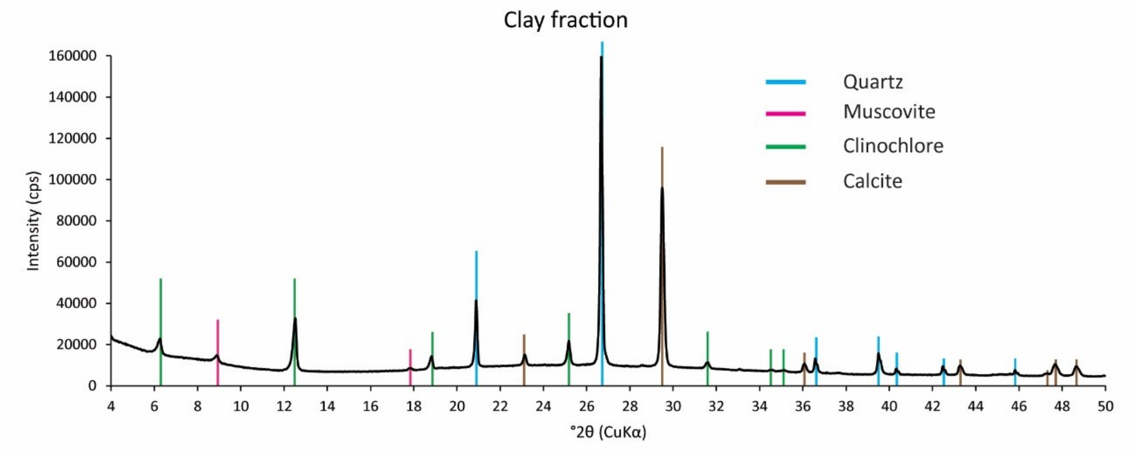
Clay fraction

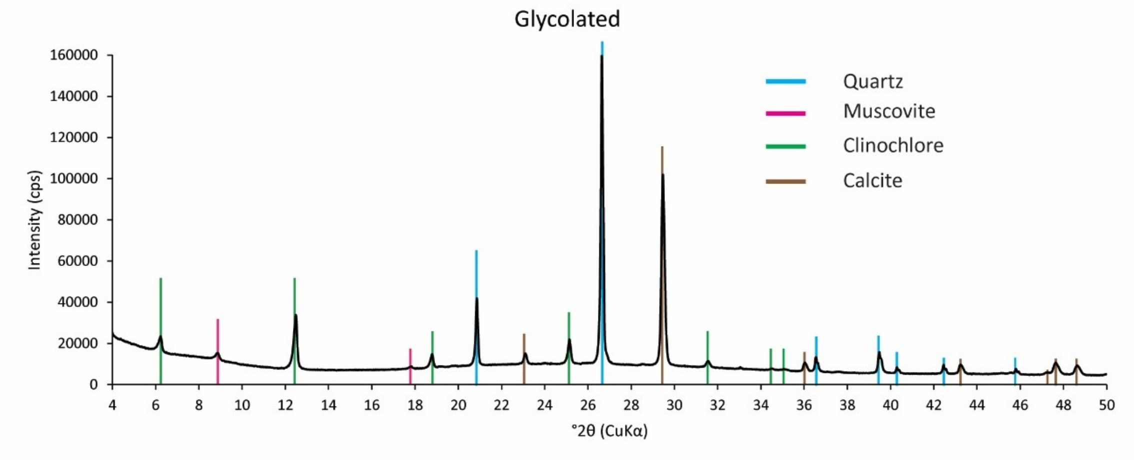
Glycolated

Heritage - Sample HE-22-1R

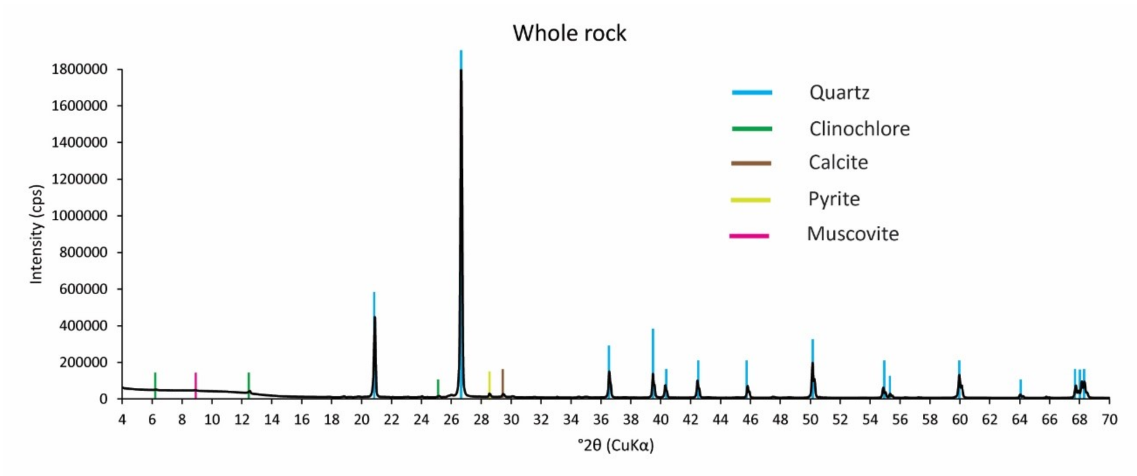

Heritage - Sample HE-23-1R

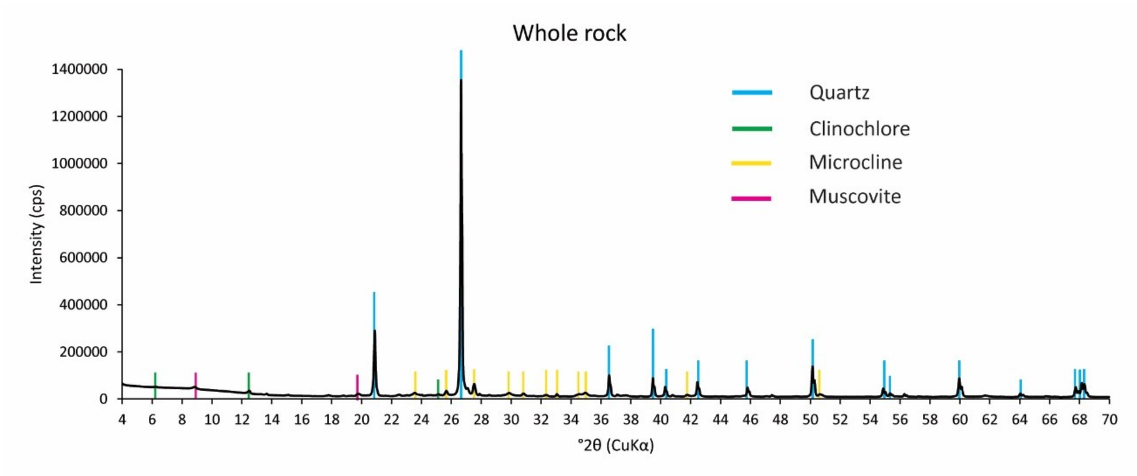

Heritage - Sample HE-23-2R

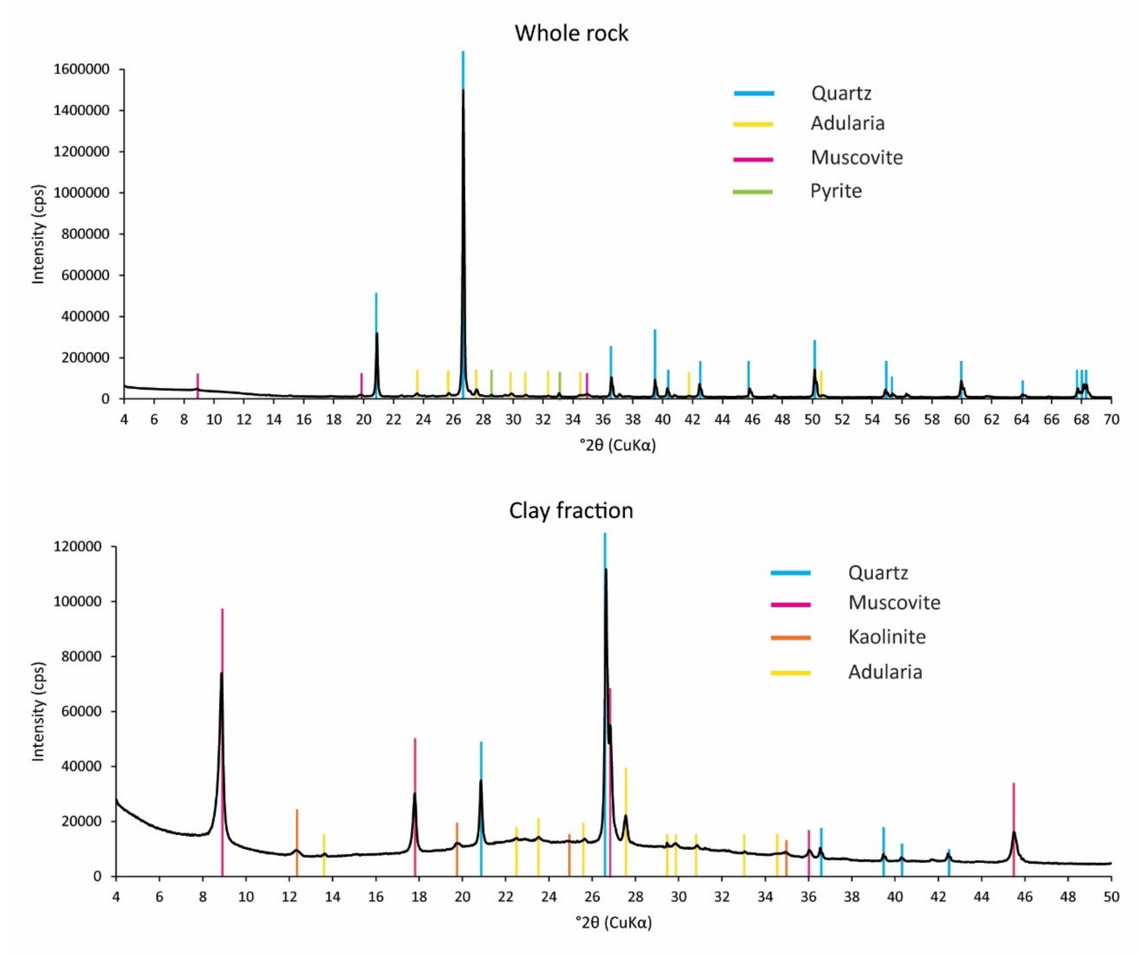

Heritage - Sample HE-23-3R

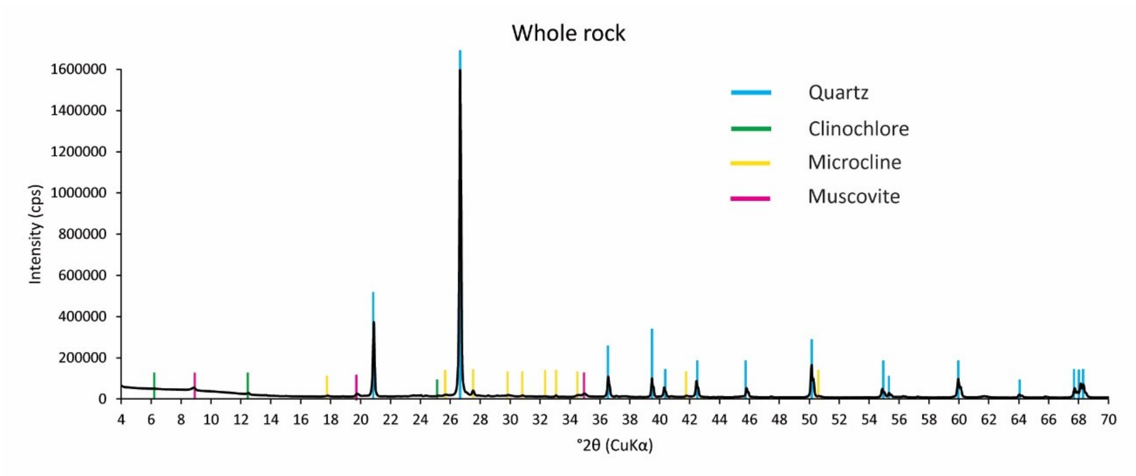

Heritage - Sample HE-24-1R

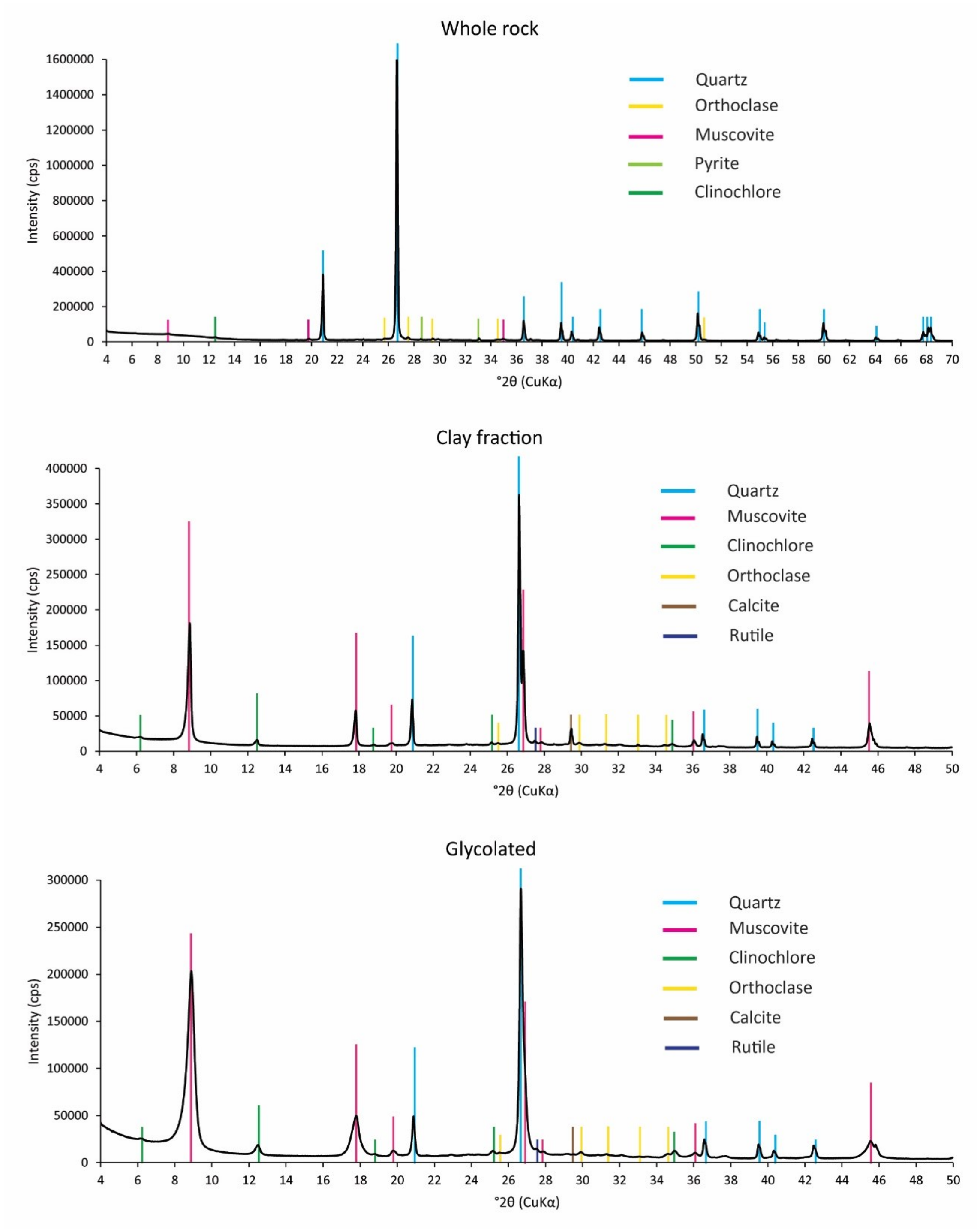

Heritage - Sample HE-32-25

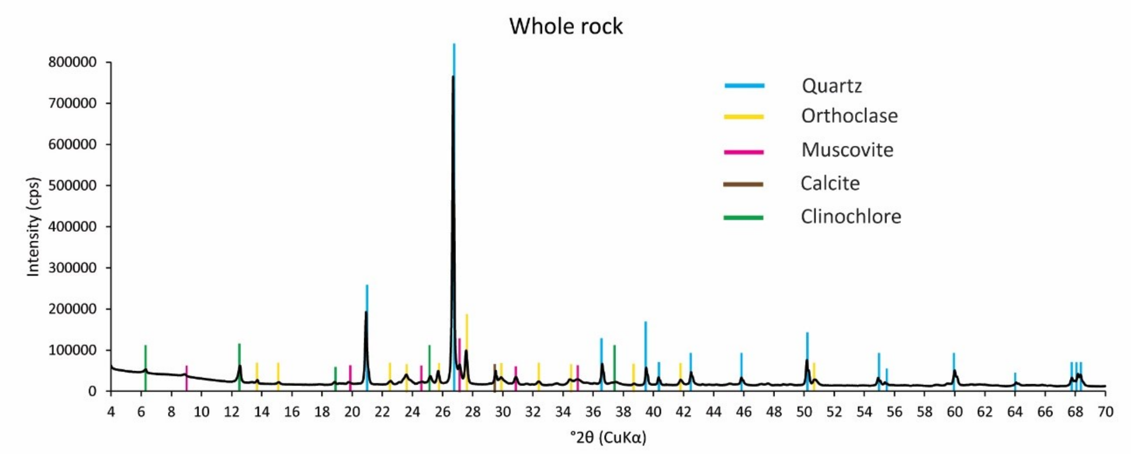

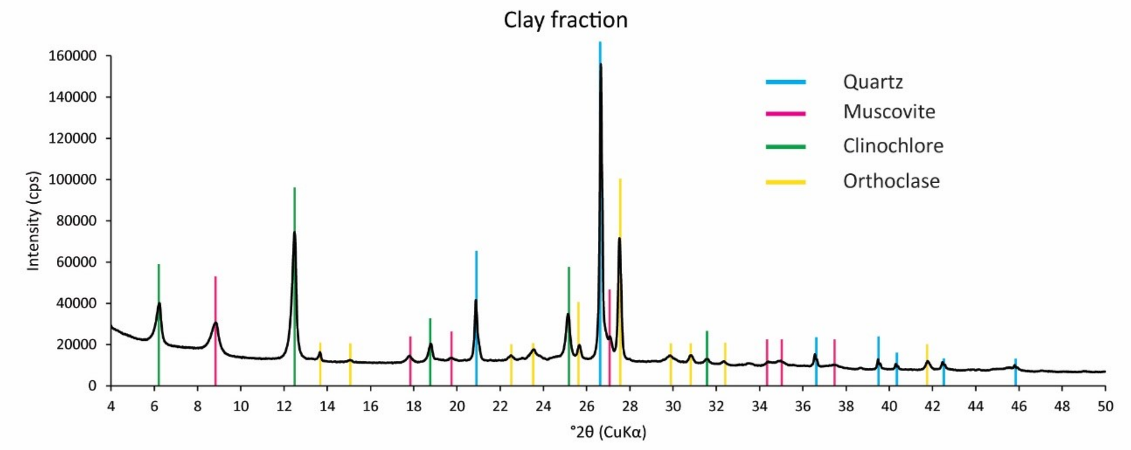

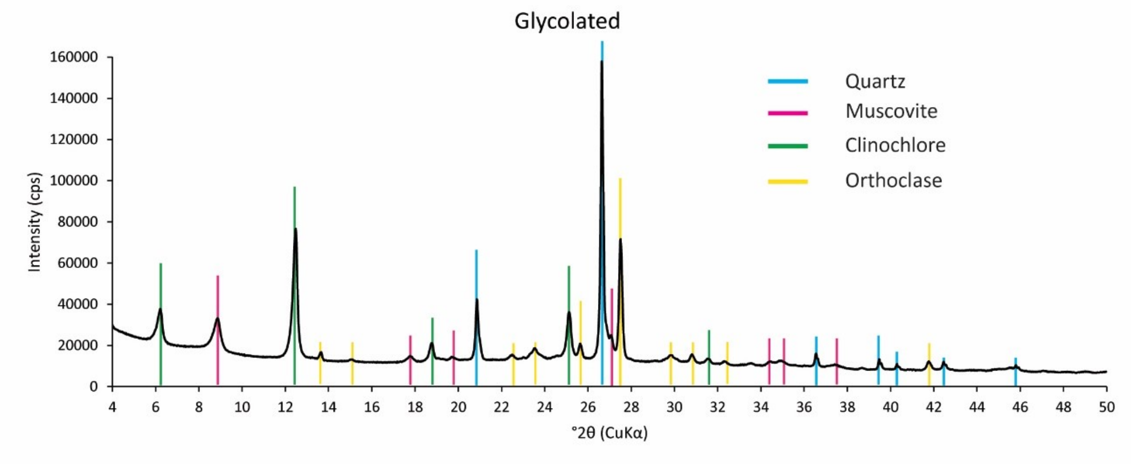

Heritage - Sample HE-33-68

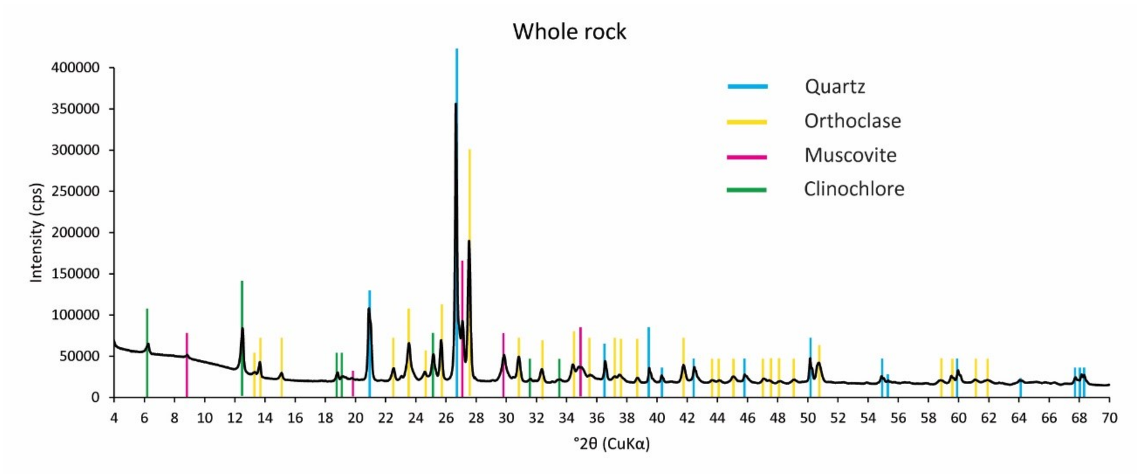

Heritage - Sample HE-35-50

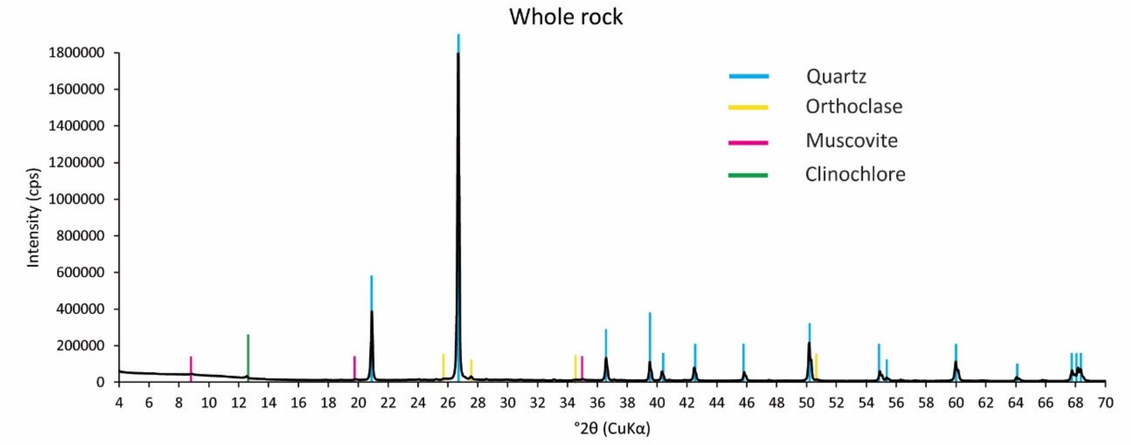

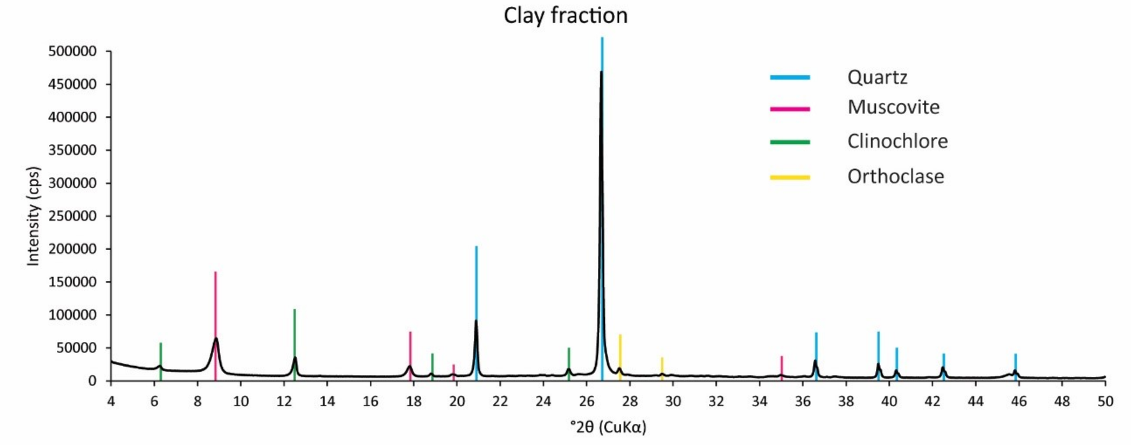

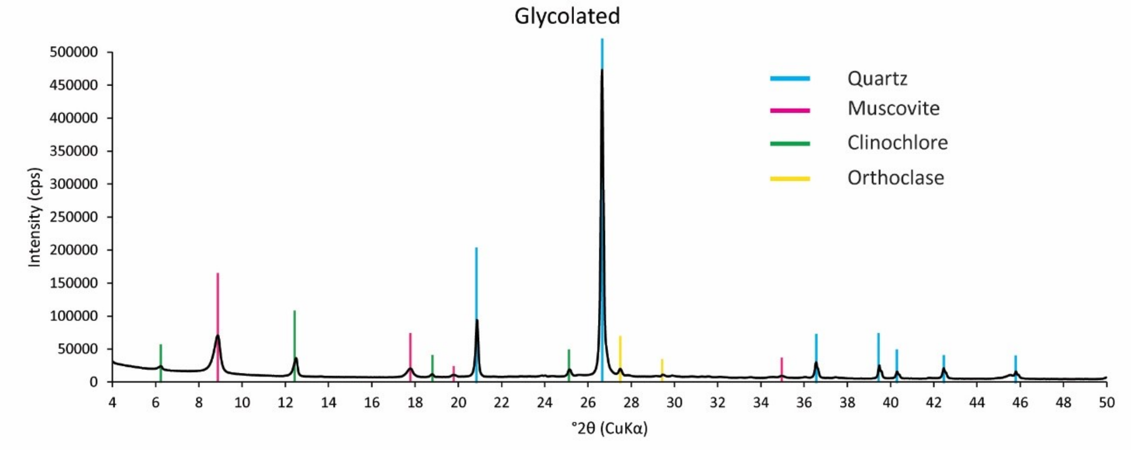

Heritage - Sample HE-36-98

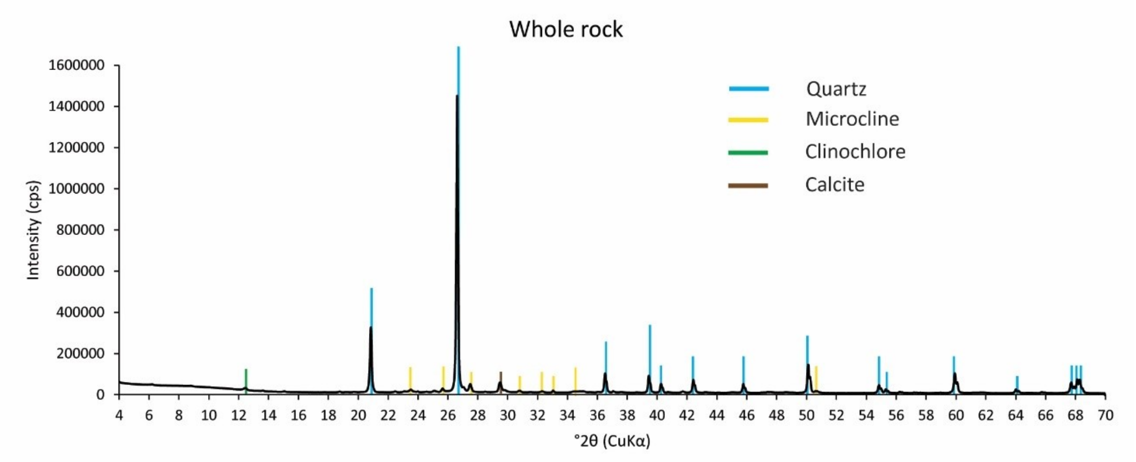

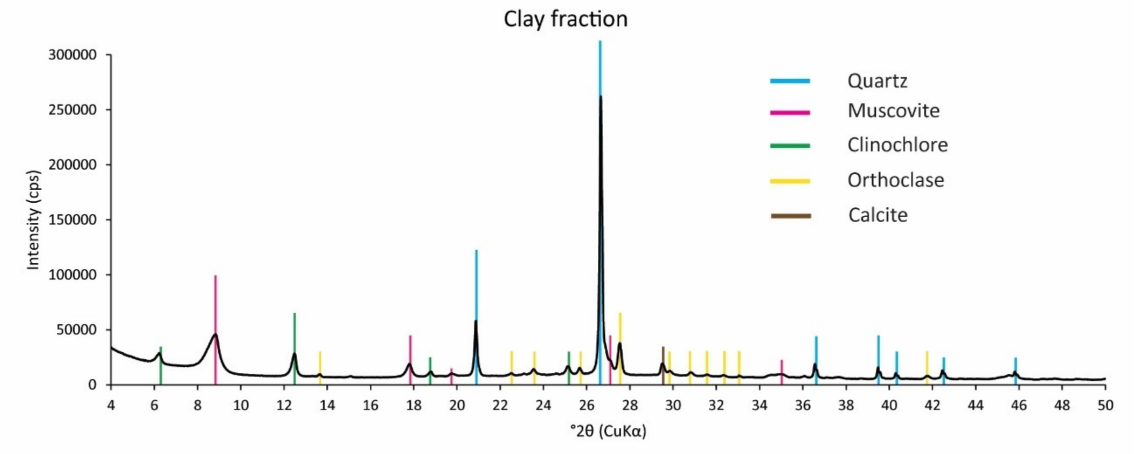

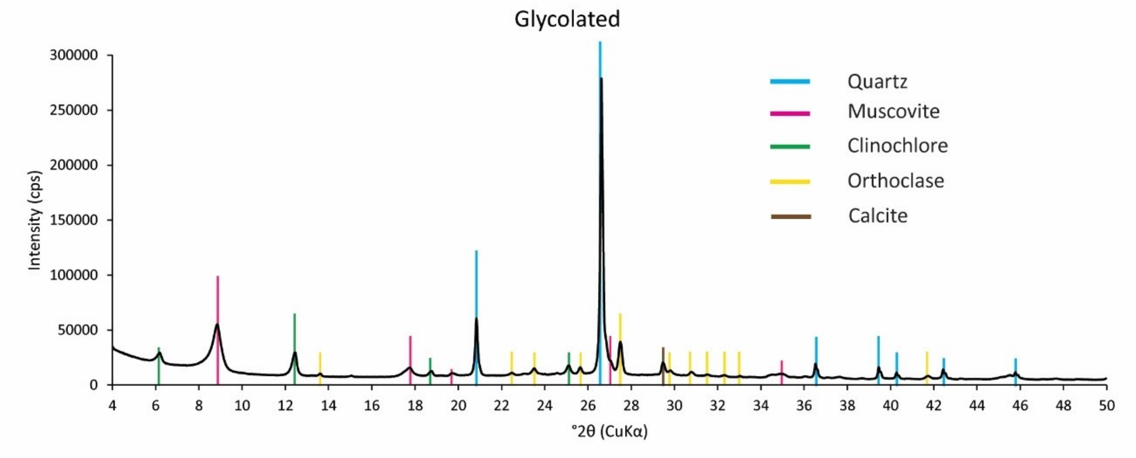

Heritage - Sample HE-36-107

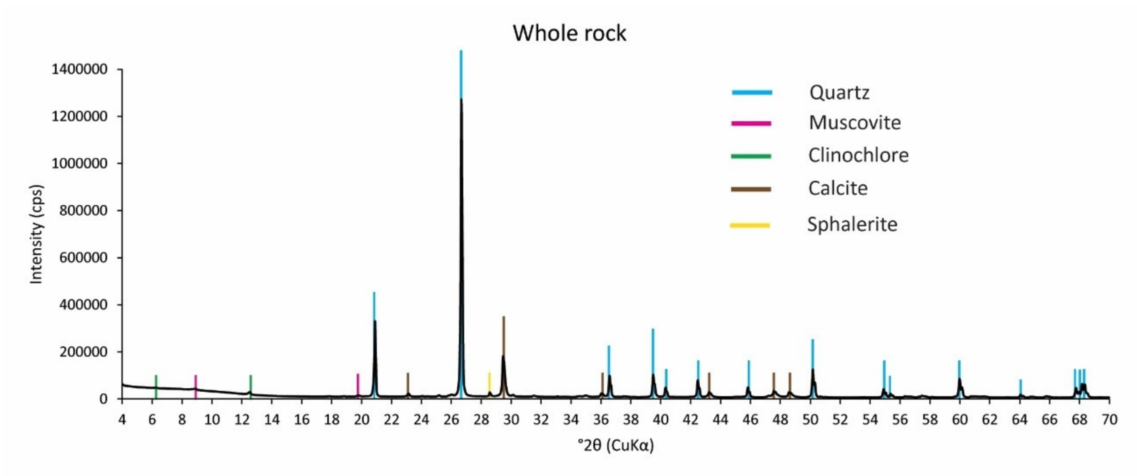

Heritage - Sample HE-47-23

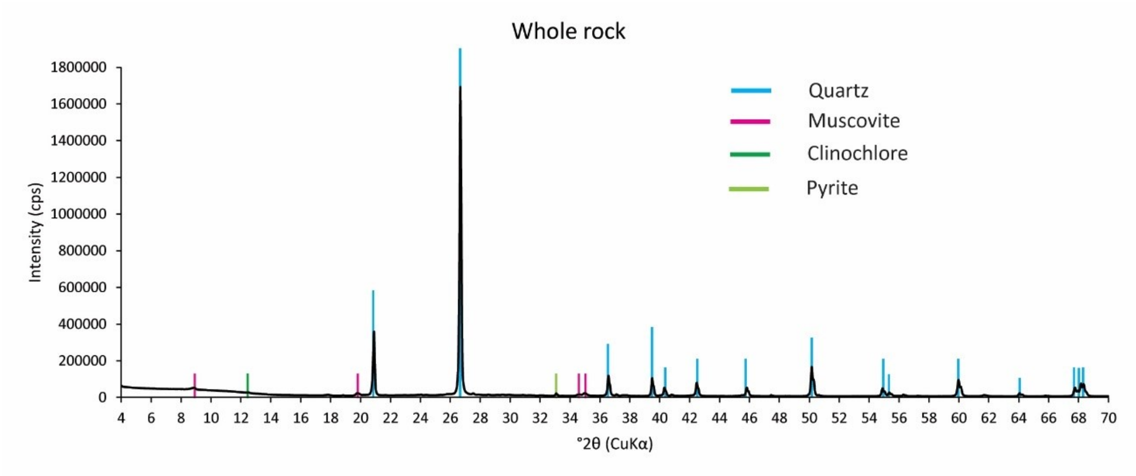

Heritage - Sample HE-47-26

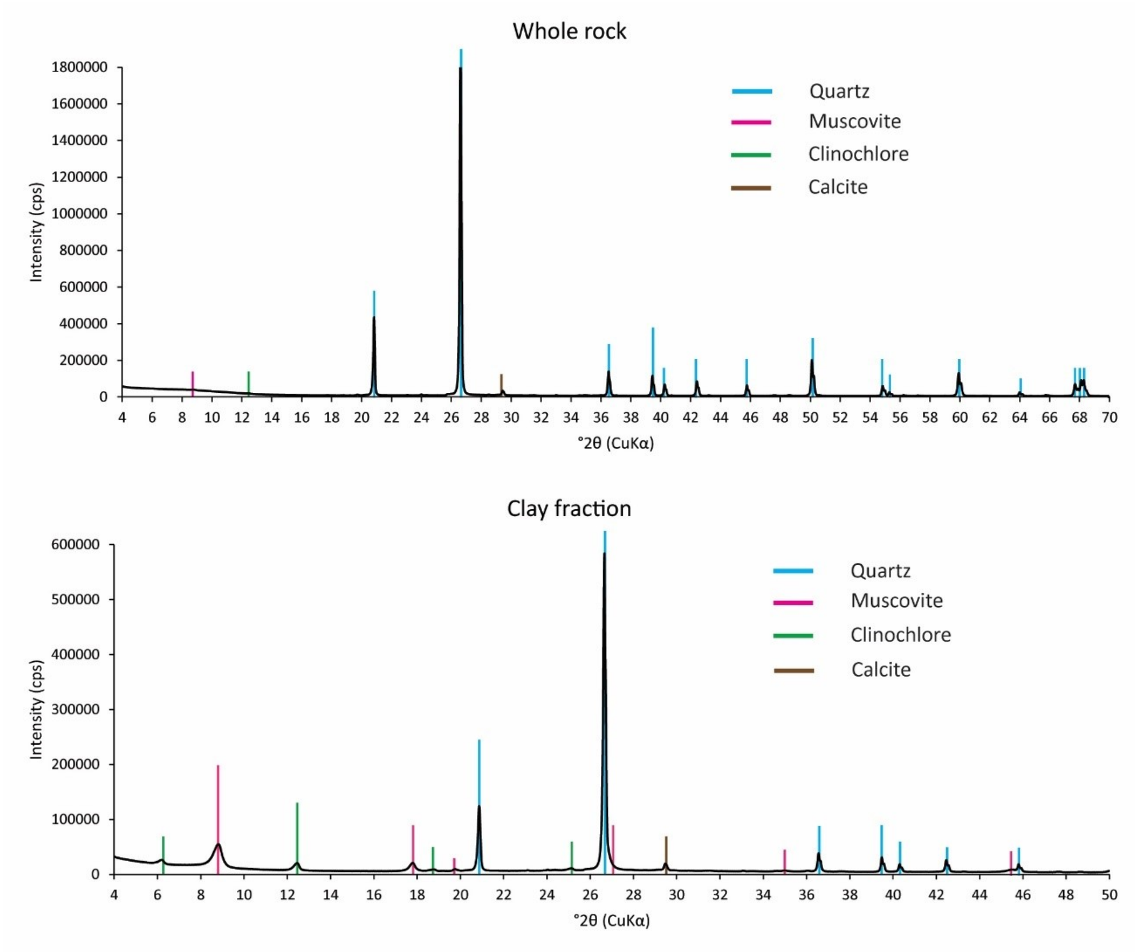

Heritage - Sample HE-48-27

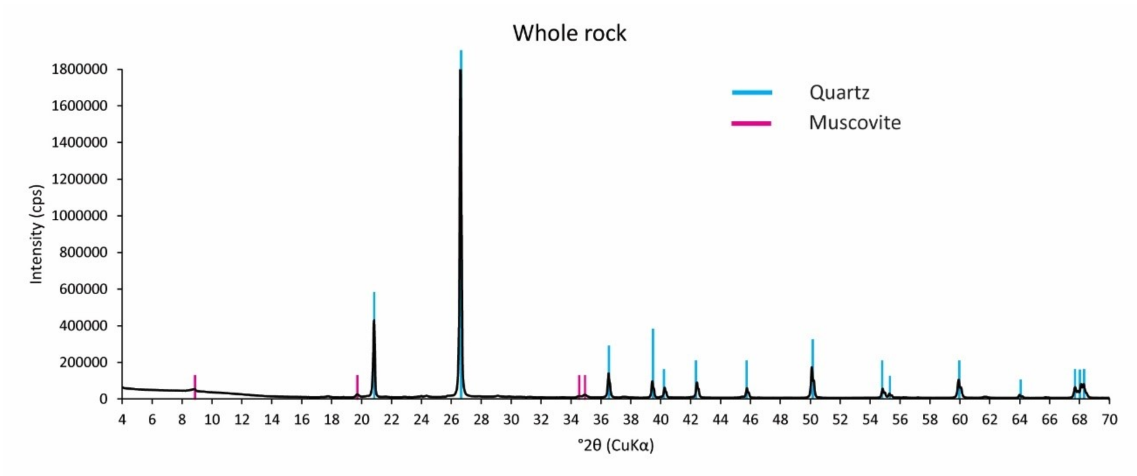

Heritage - Sample HE-48-2

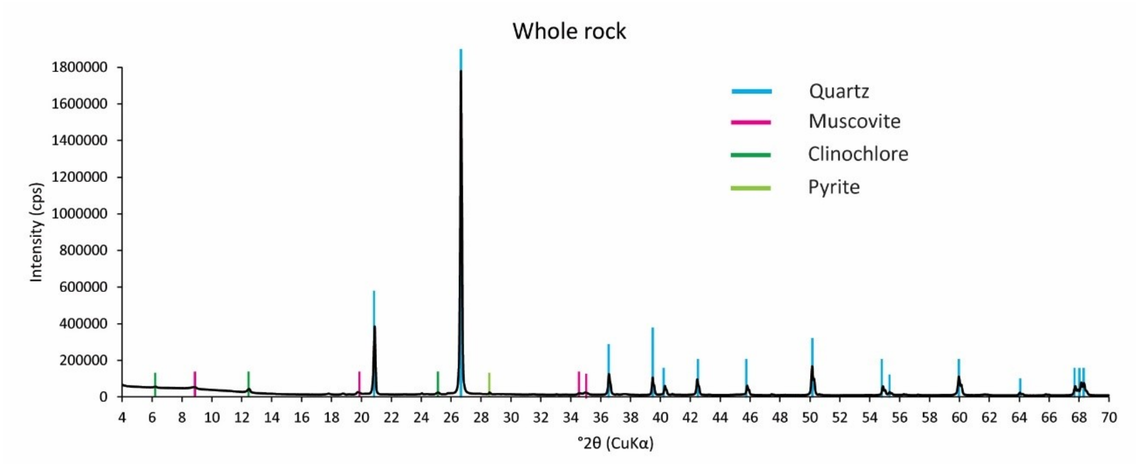

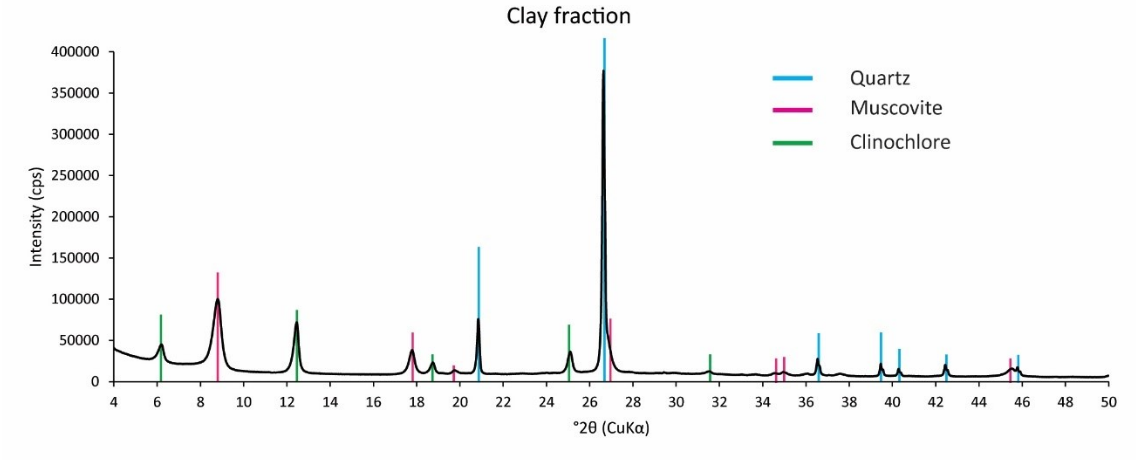

Appendix 3. Electron microprobe analyses

Appendix 3.1. List of electron microprobe minerals/compounds used for geochemical analysis of mica and chlorite.

Element	Standard	X-ray	Mass (%)	Crystal	Peak (sec)	Background (sec)
F	JMH_fluorapatite_319	Ka	3.77	LDE1	10	5
Mn	Rhodonite	Ka	54.14	LIFL	40	20
V	V	Ka	146.82	LIFL	40	20
Ti	rutile	Ka	99.98	LIFL	40	20
Cl	Tugtupite	Ka	7.57	PETL	10	5
K	Orthoclase	Ka	15.25	PETL	20	10
Ca	Diopside	Ka	24.79	PETL	30	15
Na	Albite	Ka	11.59	TAP	10	5
Al	Al	Ka	188.95	TAP	30	15
Si	Diopside	Ka	55.34	TAP	20	10
Mg	Diopside	Ka	17.76	TAP	30	15
Fe	Almandine_Garnet	Ka	23.88	LIFH	40	20
Cr	Chromium_Oxide	Ka	100.01	LIFH	40	20

Appendix 3.1. List of electron microprobe minerals/compounds used for geochemical analysis of pyrophyllite, kaolinite, and alunite.

Element	Standard	X-ray	Mass (%)	Crystal	Peak (sec)	Background (sec)
F	Apatite	Ka	3.74	LDE1	10	5
Cl	Tugtupite	Ka	7.57	PETL	10	5
S	Pyrite	Ka	134.17	PETL	30	15
Sr	Celestite	La	57.04	PETL	30	15
K	Orthoclase	Ka	15.25	PETL	20	10
Ca	Diopside	Ka	24.79	PETL	30	15
P	Apatite	Ka	41.39	PETL	30	15
Ba	Barite	La	64.95	PETL	30	15
Na	Albite	Ka	11.59	TAP	20	10
Al	Al	Ka	188.95	TAP	20	10
Si	Albite	Ka	68.52	TAP	20	10
Mg	Almandine_Garnet	Ka	10.15	TAP	30	15
Fe	Almandine_Garnet	Ka	23.88	LIFH	30	15
Mn	Rhodonite	Ka	42.30	LIFH	30	15
Ce	CeP_5O_{14}	La	31.62	LIFH	30	15
Ti	Rutile	Ka	99.98	LIFH	30	15

Appendix 3.1. List of electron microprobe minerals/compounds used for geochemical analysis of rutile.

Element	Standard	X-ray	Mass (%)	Crystal	Peak (sec)	Background (sec)
W	W	Ma	3.74	TAP	30	15
Ta	Ta	Ma	7.57	TAP	30	15
Nb	Nb	La	134.17	PETL	30	15
Zr	Syn-Zirc	La	57.04	PETL	30	15
P	Apatite	Ka	15.25	PETL	30	15
Ca	Almandine_Garnet	Ka	24.79	PETL	30	15
Sn	Cassiterite	La	41.39	PETL	30	15
Sb	Stibnite	La	64.95	PETL	30	15
Si	Almandine_Garnet	Ka	11.59	TAP	30	15
Al	Cal-STD	Ka	188.95	TAP	30	15
As	Arsenopyrite	La	68.52	TAP	30	15
Fe	Almandine_Garnet	Ka	10.15	LIFH	20	10
Mn	Rhodenite	Ka	23.88	LIFH	30	15
Cr	Chromium_Oxide	Ka	42.30	LIFH	30	15
V	V	Ka	31.62	LIFH	30	15
Ti	Rutile	Ka	99.98	LIFH	20	10

Appendix 3.2. Electron microprobe analyses (in wt.%) of mica from the studied epithermal systems and respective structural formulas.

Deposit	HB	HB	HB	HB	HB	HB	HB	HB	HB	HB	HB	HB	HB	HB	HB	HB
Sample	HB-4	HB-4	HB-4	HB-4	HB-4	HB-4	HB-4	HB-4	HB-4	HB-4	HB-4	HB-4	HB-4	HB-4	HB-4	HB-4
No. anal.	1	2	3	4	5	6	7	8	9	10	11	12	13	14	15	16
SiO_2	47.48	46.67	48.81	47.27	48.54	48.61	47.89	45.72	49.31	46.76	48.22	48.15	48.22	47.97	48.50	48.17
TiO_2	0.09	0.08	0.06	0.07	0.07	0.05	0.08	0.11	0.07	1.78	0.08	0.06	0.08	0.01	0.07	0.09
Al_2O_3	36.64	36.48	33.82	34.37	35.55	34.74	35.81	35.54	34.39	34.52	35.67	35.21	34.60	35.20	34.74	39.11
Cr_2O_3	0.00	BDL	BDL	BDL	0.01	BDL	BDL	BDL	BDL	0.01	0.01	0.01	BDL	BDL	BDL	BDL
V_2O_3	0.01	0.00	BDL	BDL	BDL	BDL	0.02	BDL	0.01	0.02	0.02	0.01	BDL	BDL	BDL	0.02
FeO	1.50	1.60	1.78	2.53	1.88	1.53	1.63	1.62	1.65	1.85	1.96	1.51	1.62	1.76	1.69	0.88
MnO	BDL	BDL	BDL	BDL	BDL	BDL	0.01	BDL	BDL	BDL	BDL	BDL	0.01	0.01	0.01	BDL
MgO	0.31	0.29	0.94	0.61	0.62	0.88	0.52	0.29	0.90	0.61	0.53	0.73	0.79	0.66	0.72	0.13
CaO	0.0	0.0	0.0	BDL	0.0	BDL	0.0	0.0	BDL	0.0	0.0	0.0	0.0	0.0	0.0	0.0
Na_2O	3.00	1.95	1.42	1.63	1.95	1.55	1.92	1.82	1.50	1.67	1.77	2.10	1.66	1.58	1.68	6.60
K_2O	7.66	8.97	8.95	9.29	9.10	9.21	8.70	9.19	9.43	9.03	9.06	8.65	9.17	9.34	9.12	3.83
Cl	0.01	0.01	BDL	BDL	0.00	0.00	0.01	0.01	BDL	0.01	0.01	0.00	0.00	BDL	0.01	0.00
F	0.07	0.10	0.25	0.17	0.20	0.25	0.23	0.07	0.20	0.13	0.13	0.14	0.24	0.25	0.23	0.07
H_2O (calc)	2.34	2.32	2.37	2.32	2.39	2.39	2.39	2.26	2.38	2.33	2.36	2.35	2.37	2.38	2.38	2.42
Total	99.12	98.47	98.40	98.26	100.32	99.22	99.23	96.63	99.84	98.74	99.83	98.95	98.78	99.17	99.17	101.35
Si	2.996	2.957	2.938	2.952	2.926	2.903	2.872	2.984	2.985	2.933	2.978	2.985	2.909	2.878	2.919	2.947
Ti	0.004	0.004	0.003	0.003	0.003	0.002	0.004	0.005	0.003	0.084	0.004	0.003	0.003	0.000	0.003	0.004
Al_{Total}	2.725	2.724	2.399	2.530	2.525	2.445	2.531	2.734	2.454	2.552	2.596	2.573	2.460	2.489	2.464	2.820
^{IV}Al	1.004	1.043	1.062	1.048	1.074	1.097	1.128	1.016	1.015	1.067	1.022	1.015	1.091	1.122	1.081	1.053
^{VI}Al	1.721	1.681	1.337	1.482	1.451	1.348	1.403	1.717	1.439	1.485	1.574	1.558	1.369	1.367	1.383	1.766
Cr	0.000	-	-	-	0.000	-	-	-	-	0.000	0.000	0.000	-	-	-	-
V	0.000	0.000	-	-	-	-	0.001	-	0.001	0.001	0.001	0.001	-	-	-	0.001
Fe^{2+}	0.079	0.085	0.090	0.132	0.095	0.077	0.082	0.088	0.083	0.097	0.101	0.078	0.082	0.088	0.085	0.045
Mn	-	-	-	-	-	-	0.000	-	-	-	-	-	0.000	0.000	0.001	-
Mg	0.029	0.027	0.084	0.056	0.055	0.078	0.047	0.028	0.082	0.057	0.049	0.068	0.071	0.059	0.065	0.012
Σ Oct.	1.833	1.798	1.514	1.673	1.605	1.506	1.537	1.840	1.608	1.725	1.729	1.708	1.525	1.515	1.537	1.828
Ca	0.001	0.001	0.000	-	0.001	-	0.001	0.001	-	0.001	0.001	0.001	0.001	0.000	0.001	0.002
Na	0.367	0.239	0.166	0.197	0.227	0.179	0.223	0.231	0.176	0.204	0.212	0.253	0.194	0.184	0.196	0.783
K	0.616	0.725	0.687	0.740	0.700	0.702	0.666	0.765	0.728	0.723	0.714	0.684	0.706	0.715	0.700	0.299
Σ Int.	0.985	0.965	0.853	0.937	0.928	0.881	0.890	0.996	0.904	0.927	0.926	0.937	0.902	0.899	0.896	1.084
Cl	0.001	0.001	-	-	0.001	0.000	0.001	0.001	-	0.001	0.001	0.000	0.000	-	0.001	0.001
F	0.014	0.019	0.048	0.034	0.038	0.048	0.044	0.015	0.038	0.025	0.026	0.028	0.046	0.048	0.044	0.013
OH	0.985	0.980	0.952	0.966	0.962	0.952	0.955	0.985	0.962	0.974	0.973	0.972	0.954	0.952	0.955	0.986

Mica formulae calculated on basis of 11 oxygen atoms and all iron was considered as Fe^{2+}. Water (H_2O calc) was calculated based on OH+Cl+F= 1 apfu. Abbreviations: HB (Hope Brook high-sulfidation epithermal deposit); HP (Hickey's Pond high-sulfidation epithermal system); HE (Heritage low-sulfidation epithermal prospect); BDL (below detection limit).

Appendix 3.2. Electron microprobe analyses (in wt.%) of mica from the studied epithermal systems and respective structural formulas.

Deposit	HB	HB	HB	HB	HB	HB	HB	HB	HB	HB	HB	HB	HB	HB	HB	HB
Sample	HB-4	HB-4	HB-4	HB-14	HB-14	HB-14	HB-14	HB-14	HB-14	HB-14	HB-14	HB-14	HB-14	HB-14	HB-14	HB-14
No. anal.	17	19	20	1	2	3	4	5	6	7	8	9	10	11	12	13
SiO_2	48.37	48.04	48.58	47.14	47.44	47.39	47.42	47.07	47.09	46.94	48.25	47.56	47.34	47.19	47.05	47.22
TiO_2	0.04	0.06	0.05	0.20	0.05	0.09	0.12	0.21	0.11	0.11	0.08	0.10	0.08	0.09	0.06	0.15
Al_2O_3	39.54	39.00	39.33	36.22	36.33	36.30	35.99	36.46	36.73	37.27	36.96	36.11	37.60	36.43	36.44	36.09
Cr_2O_3	BDL	BDL	BDL	0.09	0.03	0.01	0.09	0.09	0.05	0.00	0.01	0.05	0.07	0.02	0.01	0.11
V_2O_3	0.01	0.03	BDL	0.11	0.12	0.08	0.09	0.14	0.12	0.09	0.07	0.11	0.09	0.07	0.05	0.11
FeO	0.66	0.74	0.79	1.65	1.49	1.71	1.65	1.84	1.73	1.41	1.82	1.40	1.51	1.50	1.55	1.48
MnO	BDL	BDL	BDL	0.01	0.01	0.03	0.01	BDL	BDL	BDL	0.01	0.02	BDL	0.01	0.02	0.02
MgO	0.07	0.12	0.14	0.40	0.48	0.35	0.51	0.34	0.32	0.29	0.50	0.44	0.24	0.40	0.34	0.40
CaO	0.0	0.0	0.0	0.0	0.0	0.2	0.0	0.0	0.0	0.0	0.0	0.0	0.0	0.0	0.0	0.0
Na_2O	7.45	6.94	7.11	1.61	1.53	2.20	1.41	1.39	2.18	1.98	1.36	1.56	2.06	1.36	1.31	1.50
K_2O	2.13	2.88	2.99	9.56	9.54	8.32	9.37	9.80	8.98	9.22	9.28	9.36	9.09	9.31	9.94	9.60
Cl	0.00	0.02	0.01	0.00	0.00	0.01	0.01	BDL	0.00	0.01	0.01	BDL	0.01	0.00	BDL	BDL
F	0.09	0.12	0.06	0.03	0.05	BDL	0.03	BDL	BDL	BDL	0.17	0.12	0.02	0.09	BDL	0.08
H_2O (calc)	2.43	2.43	2.43	2.31	2.32	2.31	2.31	2.30	2.31	2.31	2.40	2.34	2.34	2.32	2.29	2.32
Total	100.82	100.43	101.53	99.33	99.39	99.00	99.03	99.65	99.67	99.64	100.96	99.18	100.46	98.82	99.08	99.07
Si	2.932	2.893	2.958	2.870	2.888	2.885	2.887	2.866	2.867	2.858	2.937	2.896	2.882	2.873	2.865	2.875
Ti	0.002	0.003	0.002	0.009	0.002	0.004	0.006	0.009	0.005	0.005	0.004	0.005	0.003	0.004	0.003	0.007
Al_{Total}	2.825	2.768	2.822	2.599	2.607	2.605	2.583	2.616	2.636	2.674	2.652	2.591	2.698	2.614	2.615	2.590
^{IV}Al	1.068	1.107	1.042	1.130	1.112	1.115	1.113	1.134	1.133	1.142	1.063	1.104	1.118	1.127	1.135	1.125
^{VI}Al	1.757	1.660	1.780	1.469	1.495	1.490	1.469	1.482	1.502	1.532	1.589	1.487	1.580	1.487	1.479	1.465
Cr	-	-	-	0.004	0.001	0.001	0.004	0.004	0.003	0.000	0.000	0.003	0.003	0.001	0.001	0.005
V	0.001	0.002	-	0.006	0.006	0.005	0.005	0.008	0.007	0.005	0.004	0.006	0.005	0.004	0.003	0.006
Fe^{2+}	0.033	0.037	0.040	0.084	0.076	0.087	0.084	0.094	0.088	0.072	0.093	0.071	0.077	0.076	0.079	0.075
Mn	-	-	-	0.001	0.000	0.002	0.001	-	-	-	0.001	0.001	-	0.001	0.001	0.001
Mg	0.006	0.010	0.013	0.036	0.043	0.032	0.046	0.031	0.029	0.027	0.045	0.040	0.022	0.036	0.031	0.036
Σ Oct.	1.800	1.713	1.835	1.609	1.625	1.619	1.615	1.628	1.634	1.640	1.735	1.612	1.691	1.610	1.597	1.595
Ca	0.001	0.003	0.002	0.000	0.000	0.013	0.001	0.001	0.002	0.001	0.003	0.000	0.001	0.001	0.001	0.001
Na	0.876	0.810	0.840	0.190	0.181	0.259	0.167	0.165	0.258	0.233	0.161	0.184	0.244	0.160	0.154	0.177
K	0.165	0.221	0.232	0.743	0.741	0.646	0.728	0.761	0.698	0.716	0.721	0.727	0.706	0.723	0.772	0.746
Σ Int.	1.042	1.034	1.074	0.933	0.922	0.918	0.896	0.926	0.958	0.950	0.884	0.912	0.950	0.885	0.927	0.923
Cl	0.000	0.002	0.001	0.000	0.000	0.002	0.001	-	0.000	0.001	0.001	-	0.001	0.000	-	-
F	0.017	0.022	0.011	0.006	0.010	-	0.005	-	-	-	0.032	0.024	0.004	0.017	-	0.016
OH	0.983	0.976	0.988	0.994	0.990	0.998	0.994	1.000	1.000	0.999	0.967	0.976	0.995	0.982	1.000	0.984

Mica formulae calculated on basis of 11 oxygen atoms and all iron was considered as Fe^{2+}. Water (H_2O calc) was calculated based on OH+Cl+F= 1 apfu. Abbreviations: HB (Hope Brook high-sulfidation epithermal deposit); HP (Hickey's Pond high-sulfidation epithermal system); HE (Heritage low-sulfidation epithermal prospect); BDL (below detection limit).

Appendix 3.2. Electron microprobe analyses (in wt.%) of mica from the studied epithermal systems and respective structural formulas.

Deposit	HB	HB	HP	HP	HP	HP	HP	HP	HP	HP	HP	HP	HP	HP	HP	HP
Sample	HB-14	HB-14	HP-2	HP-2	HP-2	HP-2	HP-2	HP-2	HP-2	HP-2	HP-2	HP-2	HP-2	HP-2	HP-2	HP-2
No. anal.	14	15	1	2	3	4	5	6	7	8	9	10	11	12	13	14
SiO_2	49.13	47.65	48.20	47.29	47.04	47.35	47.69	46.10	45.41	45.96	47.33	47.02	47.31	46.78	47.44	46.91
TiO_2	0.03	0.02	0.04	0.06	0.03	0.05	0.03	0.04	0.04	0.03	0.02	0.05	0.02	0.01	0.03	0.04
Al_2O_3	39.72	40.74	37.03	36.86	36.71	36.88	37.26	36.30	35.49	35.82	37.26	37.75	37.75	37.91	36.85	37.80
Cr_2O_3	BDL	0.01	BDL	0.01	BDL	BDL	0.01	BDL	0.01	0.01	BDL	0.02	BDL	BDL	0.01	0.02
V_2O_3	0.05	0.03	0.05	0.01	0.00	0.02	0.02	0.04	0.03	0.03	0.04	0.01	0.03	0.03	0.04	0.04
FeO	0.49	0.38	1.57	1.54	1.48	1.61	1.56	1.52	3.76	2.67	1.38	1.34	0.92	1.07	1.35	1.17
MnO	0.01	BDL	0.03	BDL	BDL	BDL	BDL	0.01	BDL	BDL	BDL	0.02	0.01	0.01	BDL	BDL
MgO	0.09	0.03	0.23	0.12	0.22	0.14	0.14	0.24	0.30	0.24	0.18	0.10	0.15	0.07	0.21	0.06
CaO	0.08	0.08	0.03	0.05	0.04	0.01	0.07	0.03	0.05	0.04	0.09	0.07	0.05	0.05	0.10	0.05
Na_2O	7.12	8.64	0.89	0.94	0.95	1.19	0.94	0.94	0.88	0.86	0.91	1.07	0.95	1.38	1.20	1.22
K_2O	1.72	0.63	9.94	9.84	9.99	9.98	9.85	10.19	9.95	10.16	9.80	9.86	10.07	9.83	9.86	9.77
Cl	0.01	0.02	BDL	0.01	0.01	0.00	BDL	0.02	0.00	0.01	BDL	0.04	0.01	0.01	0.02	BDL
F	0.03	0.02	0.36	0.29	0.29	0.22	0.45	0.32	0.40	0.37	0.36	0.45	0.34	0.30	0.75	0.32
H_2O (calc)	2.43	2.42	2.45	2.40	2.40	2.38	2.47	2.38	2.38	2.38	2.43	2.49	2.44	2.42	2.57	2.42
Total	100.91	100.66	100.81	99.41	99.17	99.84	100.49	98.12	98.70	98.57	99.80	100.30	100.07	99.86	100.43	99.81
Si	2.991	2.901	2.934	2.879	2.864	2.883	2.903	2.806	2.765	2.798	2.881	2.863	2.880	2.848	2.888	2.856
Ti	0.001	0.001	0.002	0.003	0.002	0.002	0.001	0.002	0.002	0.001	0.001	0.002	0.001	0.001	0.001	0.002
Al_{Total}	2.850	2.923	2.657	2.645	2.634	2.646	2.673	2.604	2.546	2.570	2.673	2.709	2.709	2.720	2.644	2.712
^{IV}Al	1.009	1.099	1.066	1.121	1.136	1.117	1.097	1.194	1.235	1.202	1.119	1.137	1.120	1.152	1.112	1.144
^{VI}Al	1.841	1.824	1.591	1.524	1.498	1.529	1.576	1.411	1.311	1.368	1.555	1.572	1.589	1.568	1.532	1.568
Cr	-	0.000	-	0.001	-	-	0.001	-	0.000	0.000	-	0.001	-	-	0.000	0.001
V	0.003	0.002	0.003	0.001	0.000	0.001	0.001	0.002	0.002	0.001	0.002	0.001	0.002	0.002	0.002	0.002
Fe^{2+}	0.025	0.019	0.080	0.078	0.075	0.082	0.080	0.077	0.191	0.136	0.070	0.068	0.047	0.055	0.069	0.060
Mn	0.000	-	0.001	-	-	-	-	0.001	-	-	-	0.001	0.001	0.000	-	-
Mg	0.009	0.003	0.021	0.011	0.020	0.013	0.012	0.021	0.028	0.022	0.016	0.009	0.014	0.006	0.019	0.005
Σ Oct.	1.878	1.849	1.697	1.617	1.595	1.627	1.671	1.515	1.534	1.529	1.645	1.654	1.653	1.631	1.624	1.638
Ca	0.005	0.005	0.002	0.003	0.003	0.001	0.005	0.002	0.003	0.002	0.006	0.005	0.003	0.003	0.007	0.003
Na	0.840	1.019	0.105	0.110	0.112	0.140	0.110	0.112	0.103	0.102	0.107	0.127	0.112	0.162	0.141	0.144
K	0.134	0.049	0.772	0.764	0.776	0.775	0.765	0.791	0.773	0.789	0.761	0.766	0.782	0.764	0.766	0.759
Σ Int.	0.979	1.073	0.879	0.878	0.890	0.916	0.880	0.905	0.879	0.894	0.874	0.898	0.897	0.929	0.914	0.906
Cl	0.001	0.002	-	0.001	0.001	0.000	-	0.002	0.000	0.001	-	0.004	0.001	0.001	0.002	-
F	0.007	0.004	0.065	0.054	0.055	0.042	0.080	0.059	0.074	0.068	0.066	0.078	0.062	0.056	0.121	0.059
OH	0.992	0.994	0.935	0.946	0.944	0.957	0.920	0.939	0.926	0.931	0.934	0.918	0.936	0.943	0.878	0.941

Mica formulae calculated on basis of 11 oxygen atoms and all iron was considered as Fe^{2+}. Water (H_2O calc) was calculated based on OH+Cl+F= 1 apfu. Abbreviations: HB (Hope Brook high-sulfidation epithermal deposit); HP (Hickey's Pond high-sulfidation epithermal system); HE (Heritage low-sulfidation epithermal prospect); BDL (below detection limit).

Appendix 3.2. Electron microprobe analyses (in wt.%) of mica from the studied epithermal systems and respective structural formulas.

Deposit	HP	HP	HP	HP	HP	HP	HE	HE	HE	HE	HE	HE	HE	HE	HE	HE
Sample	HP-2	HP-2	HP-2	HP-2	HP-2	HP-2	HE-48-28	HE-48-28	HE-48-28	HE-48-28	HE-48-28	HE-48-28	HE-48-27	HE-48-27	HE-48-27	HE-48-27
No. anal.	15	16	17	18	19	20	3	5	7	8	9	10	1	2	3	4
SiO_2	47.41	47.84	45.26	46.51	45.72	45.84	54.58	55.03	55.00	56.01	53.26	53.93	54.08	55.14	54.23	54.79
TiO_2	0.02	0.03	0.04	0.05	0.04	0.03	BDL	BDL	0.02	BDL	BDL	BDL	0.03	0.01	BDL	BDL
Al_2O_3	37.46	37.83	35.83	36.45	36.13	36.24	30.59	30.50	31.19	29.12	29.99	31.16	31.89	32.17	32.19	31.60
Cr_2O_3	0.01	BDL	0.03	BDL	BDL	0.02	0.02	0.03	BDL	BDL	BDL	BDL	BDL	BDL	0.01	BDL
V_2O_3	0.01	0.04	BDL	0.04	0.02	0.02	0.10	0.13	0.13	0.10	0.09	0.07	0.05	0.04	0.07	0.07
FeO	1.53	1.45	3.62	3.71	2.95	1.56	1.43	1.60	1.28	1.88	1.55	1.03	1.11	1.06	1.07	1.07
MnO	0.02	BDL	BDL	0.01	BDL	0.01	0.14	0.14	0.13	0.18	0.17	0.06	0.09	0.09	0.10	0.08
MgO	0.14	0.09	0.10	0.16	0.14	0.19	3.05	3.16	2.79	3.14	3.23	2.70	2.69	2.75	2.58	2.75
CaO	0.07	0.07	0.04	0.09	0.04	0.05	0.02	0.04	0.03	0.04	0.03	0.04	0.05	0.05	0.05	0.07
Na_2O	1.12	1.24	1.00	0.89	0.99	1.06	0.11	0.10	0.11	0.08	0.04	0.11	0.13	0.15	0.10	0.17
K_2O	9.58	9.55	9.92	9.70	9.95	9.88	9.68	9.55	9.13	9.60	8.52	8.98	9.38	9.47	9.40	8.81
Cl	0.01	0.01	0.00	0.00	0.01	0.02	BDL	0.01	0.01	0.00	0.01	0.01	0.01	BDL	BDL	0.00
F	0.39	0.33	0.22	0.32	0.32	0.36	0.06	0.16	0.22	0.04	BDL	0.04	0.22	0.26	0.35	0.28
H_2O (calc)	2.46	2.45	2.32	2.41	2.37	2.38	2.41	2.47	2.49	2.42	2.34	2.39	2.48	2.52	2.52	2.50
Total	100.24	100.93	98.38	100.33	98.67	97.67	102.18	102.92	102.52	102.61	99.24	100.52	102.20	103.71	102.68	102.21
Si	2.886	2.913	2.755	2.832	2.784	2.791	3.356	3.242	3.176	3.442	3.410	3.350	3.359	3.425	3.368	3.404
Ti	0.001	0.002	0.002	0.002	0.002	0.001	-	-	0.001	-	-	-	0.001	0.000	-	-
Al_{Total}	2.688	2.715	2.571	2.615	2.592	2.601	2.217	2.118	2.122	2.110	2.263	2.281	2.335	2.355	2.356	2.313
^{IV}Al	1.114	1.087	1.245	1.168	1.216	1.209	0.644	0.758	0.824	0.558	0.590	0.650	0.641	0.575	0.632	0.596
^{VI}Al	1.574	1.627	1.326	1.447	1.376	1.391	1.573	1.360	1.298	1.552	1.673	1.631	1.694	1.781	1.725	1.717
Cr	0.000	-	0.001	-	-	0.001	0.001	0.001	-	-	-	-	-	-	0.000	-
V	0.001	0.002	-	0.002	0.001	0.001	0.005	0.007	0.006	0.005	0.005	0.004	0.003	0.002	0.004	0.004
Fe^{2+}	0.078	0.074	0.184	0.189	0.150	0.079	0.074	0.079	0.062	0.097	0.083	0.053	0.058	0.055	0.056	0.056
Mn	0.001	-	-	0.000	-	0.001	0.007	0.007	0.006	0.009	0.009	0.003	0.005	0.005	0.005	0.004
Mg	0.013	0.008	0.009	0.014	0.012	0.017	0.280	0.278	0.240	0.288	0.308	0.250	0.249	0.254	0.239	0.255
Σ Oct.	1.669	1.713	1.523	1.655	1.541	1.492	1.940	1.732	1.613	1.951	2.079	1.942	2.010	2.098	2.029	2.036
Ca	0.005	0.004	0.002	0.006	0.003	0.003	0.001	0.003	0.002	0.003	0.002	0.003	0.003	0.003	0.003	0.005
Na	0.132	0.146	0.118	0.105	0.117	0.125	0.013	0.011	0.012	0.009	0.006	0.013	0.016	0.017	0.012	0.020
K	0.744	0.741	0.770	0.753	0.773	0.768	0.759	0.718	0.672	0.753	0.696	0.711	0.743	0.750	0.745	0.698
Σ Int.	0.881	0.892	0.891	0.864	0.893	0.896	0.773	0.732	0.687	0.765	0.704	0.728	0.762	0.771	0.761	0.723
Cl	0.001	0.001	0.001	0.000	0.001	0.002	-	0.001	0.001	0.000	0.001	0.001	0.001	-	-	0.000
F	0.070	0.061	0.044	0.060	0.059	0.067	0.011	0.030	0.040	0.008	-	0.008	0.040	0.047	0.061	0.050
OH	0.929	0.939	0.956	0.939	0.940	0.931	0.989	0.969	0.959	0.992	0.999	0.990	0.959	0.953	0.939	0.949

Mica formulae calculated on basis of 11 oxygen atoms and all iron was considered as Fe^{2+}. Water (H_2O calc) was calculated based on OH+Cl+F= 1 apfu. Abbreviations: HB (Hope Brook high-sulfidation epithermal deposit); HP (Hickey's Pond high-sulfidation epithermal system); HE (Heritage low-sulfidation epithermal prospect); BDL (below detection limit).

Appendix 3.2. Electron microprobe analyses (in wt.%) of mica from the studied epithermal systems and respective structural formulas.

Deposit	HE	HE	HE	HE	HE	HE	HE	HE	HE	HE	HE	HE	HE	HE	HE	HE
Sample	HE-48-27	HE-48-27	HE-48-27	HE-48-27	HE-48-27	HE-48-27	IE-36-107	IE-36-107	IE-36-107	IE-36-107	IE-36-107	IE-36-107	IE-36-107	IE-36-107	HE-47-26	HE-47-26
No. anal.	5	6	7	8	9	10	1	2	3	4	6	7	8	10	1	2
SiO_2	55.45	54.68	51.76	53.03	54.44	54.04	53.61	53.87	55.31	53.36	54.01	53.52	53.89	53.90	55.10	54.00
TiO_2	BDL	BDL	0.01	BDL	0.01	0.01	0.14	0.11	0.10	0.11	0.04	0.06	0.04	0.04	0.01	BDL
Al_2O_3	31.38	31.00	31.99	31.44	31.30	30.39	31.96	31.83	32.44	31.45	31.25	30.87	31.51	30.97	32.04	31.32
Cr_2O_3	0.01	0.02	BDL	BDL	BDL	0.01	0.01	BDL	0.01	0.01	BDL	0.01	BDL	0.01	0.01	0.01
V_2O_3	0.04	0.05	0.06	0.05	0.06	0.03	0.08	0.07	0.06	0.08	0.04	0.05	0.02	0.03	0.10	0.07
FeO	1.10	1.13	0.90	0.99	1.09	0.98	1.91	1.81	1.82	1.95	2.13	2.20	2.02	2.29	0.98	0.98
MnO	0.08	0.09	0.08	0.07	0.11	0.08	0.12	0.10	0.10	0.10	0.22	0.28	0.13	0.20	0.07	0.09
MgO	2.70	2.67	2.21	2.49	2.63	2.60	2.09	1.85	1.80	1.94	2.13	2.10	1.97	2.00	2.39	2.32
CaO	0.04	0.05	0.04	0.04	0.08	0.05	0.13	0.18	0.17	0.17	0.18	0.20	0.17	0.21	0.09	0.09
Na_2O	0.08	0.15	0.12	0.10	0.19	0.13	0.06	0.07	0.06	0.08	0.05	0.10	0.06	0.03	0.07	0.05
K_2O	9.01	8.88	8.81	9.60	8.94	8.50	9.43	8.64	8.47	8.97	8.88	9.21	8.57	8.70	9.03	8.94
Cl	0.01	BDL	0.01	0.01	0.01	0.01	0.01	0.01	0.02	0.01	0.02	0.02	0.01	0.01	BDL	BDL
F	0.29	0.30	0.22	0.16	0.32	0.33	BDL	BDL	BDL	BDL	BDL	BDL	BDL	BDL	0.06	0.02
H_2O (calc)	2.52	2.49	2.40	2.41	2.50	2.47	2.39	2.38	2.44	2.37	2.39	2.37	2.38	2.37	2.44	2.37
Total	102.71	101.51	98.61	100.40	101.67	99.63	101.96	100.91	102.79	100.60	101.35	100.98	100.79	100.77	102.37	100.27
Si	3.444	3.396	3.215	3.294	3.382	3.357	3.330	3.346	3.435	3.315	3.355	3.324	3.348	3.348	3.423	3.355
Ti	-	-	0.001	-	0.000	0.001	0.007	0.005	0.005	0.005	0.002	0.003	0.002	0.002	0.000	-
Al_{Total}	2.297	2.270	2.342	2.302	2.291	2.225	2.340	2.330	2.375	2.303	2.288	2.260	2.307	2.267	2.345	2.293
^{IV}Al	0.556	0.604	0.785	0.706	0.618	0.643	0.670	0.654	0.565	0.685	0.645	0.676	0.652	0.652	0.577	0.645
^{VI}Al	1.742	1.666	1.557	1.596	1.673	1.581	1.670	1.676	1.810	1.617	1.643	1.585	1.655	1.615	1.768	1.647
Cr	0.000	0.001	-	-	-	0.001	0.000	-	0.001	0.000	-	0.001	-	0.000	0.000	0.000
V	0.002	0.003	0.003	0.003	0.003	0.001	0.004	0.004	0.003	0.004	0.002	0.003	0.001	0.002	0.005	0.004
Fe^{2+}	0.057	0.059	0.047	0.051	0.056	0.051	0.099	0.094	0.095	0.101	0.111	0.114	0.105	0.119	0.051	0.051
Mn	0.004	0.005	0.004	0.004	0.006	0.004	0.006	0.005	0.005	0.005	0.012	0.015	0.007	0.011	0.004	0.005
Mg	0.250	0.248	0.205	0.230	0.243	0.240	0.194	0.171	0.167	0.180	0.197	0.194	0.182	0.185	0.221	.215
Σ Oct.	2.056	1.981	1.817	1.885	1.982	1.880	1.981	1.956	2.085	1.914	1.967	1.914	1.952	1.935	2.050	1.922
Ca	0.003	0.003	0.002	0.003	0.005	0.003	0.009	0.012	0.012	0.011	0.012	0.013	0.012	0.014	0.006	0.006
Na	0.009	0.018	0.014	0.012	0.023	0.016	0.007	0.008	0.007	0.010	0.006	0.012	0.007	0.003	0.008	0.006
K	0.714	0.704	0.698	0.761	0.708	0.674	0.747	0.685	0.671	0.710	0.704	0.730	0.679	0.689	0.716	0.709
Σ Int.	0.726	0.725	0.715	0.775	0.736	0.693	0.763	0.705	0.690	0.731	0.721	0.755	0.698	0.707	0.729	0.721
Cl	0.001	-	0.001	0.001	0.001	0.001	0.001	0.001	0.002	0.001	0.002	0.002	0.002	0.001	-	-
F	0.052	0.054	0.042	0.031	0.057	0.059	-	-	-	-	-	-	-	-	0.011	0.004
OH	0.947	0.946	0.957	0.968	0.942	0.940	0.999	0.999	0.998	0.999	0.998	0.998	0.998	0.999	0.989	0.996

Mica formulae calculated on basis of 11 oxygen atoms and all iron was considered as Fe^{2+}. Water (H_2O calc) was calculated based on OH+Cl+F= 1 apfu. Abbreviations: HB (Hope Brook high-sulfidation epithermal deposit); HP (Hickey's Pond high-sulfidation epithermal system); HE (Heritage low-sulfidation epithermal prospect); BDL (below detection limit).

Appendix 3.2. Electron microprobe analyses (in wt.%) of mica from the studied epithermal systems and respective structural formulas.

Deposit	HE	HE	HE	HE	HE	HE	HE
Sample	HE-47-26	HE-47-26	HE-47-26	HE-47-26	HE-47-26	HE-47-26	HE-47-26
No. anal.	3	4	5	6	7	9	10
SiO_2	55.21	54.97	55.19	54.47	55.19	55.03	55.50
TiO_2	BDL	0.01	BDL	0.03	BDL	BDL	BDL
Al_2O_3	32.02	32.06	32.26	31.65	32.38	31.98	32.35
Cr_2O_3	BDL	0.02	BDL	BDL	BDL	0.00	BDL
V_2O_3	0.05	0.11	0.06	0.07	0.05	0.07	0.06
FeO	0.93	1.03	0.99	0.92	1.00	0.99	0.92
MnO	0.08	0.09	0.08	0.08	0.07	0.07	0.08
MgO	2.39	2.33	2.22	2.17	2.44	2.37	2.30
CaO	0.08	0.08	0.10	0.10	0.09	0.09	0.13
Na_2O	0.06	0.04	0.05	0.07	0.03	0.06	0.07
K_2O	9.22	8.66	8.64	8.77	9.07	8.94	8.97
Cl	BDL	0.01	0.01	BDL	0.01	0.01	0.02
F	0.05	0.09	BDL	0.06	BDL	0.11	0.07
I_2O (calc)	2.44	2.45	2.42	2.40	2.43	2.45	2.47
Total	102.53	101.95	102.01	100.77	102.76	102.18	102.92
Si	3.429	3.415	3.428	3.383	3.428	3.418	3.447
Ti	-	0.001	-	0.001	-	-	-
Al_{Total}	2.344	2.347	2.362	2.317	2.371	2.341	2.368
^{IV}Al	0.571	0.585	0.572	0.617	0.572	0.582	0.553
^{VI}Al	1.773	1.762	1.790	1.701	1.799	1.760	1.816
Cr	-	0.001	-	-	-	0.000	-
V	0.003	0.006	0.004	0.004	0.003	0.004	0.004
Fe^{2+}	0.049	0.054	0.051	0.048	0.052	0.052	0.048
Mn	0.004	0.005	0.004	0.004	0.004	0.004	0.004
Mg	0.221	0.216	0.206	0.201	0.226	0.219	0.213
Σ Oct.	2.050	2.044	2.055	1.958	2.083	2.038	2.084
Ca	0.005	0.006	0.007	0.007	0.006	0.006	0.008
Na	0.007	0.005	0.006	0.008	0.004	0.007	0.008
K	0.731	0.686	0.684	0.695	0.718	0.709	0.711
Σ Int.	0.744	0.697	0.696	0.710	0.728	0.721	0.727
Cl	-	0.001	0.001	-	0.001	0.001	0.002
F	0.009	0.017	-	0.011	-	0.020	0.014
OH	0.991	0.982	0.999	0.970	0.999	0.979	0.984

Mica formulae calculated on basis of 11 oxygen atoms and all iron was considered as Fe^{2+}. Water (H_2O calc) was calculated based on OH+Cl+F= 1 apfu. Abbreviations: HB (Hope Brook high-sulfidation epithermal deposit); HP (Hickey's Pond high-sulfidation epithermal system); HE (Heritage low-sulfidation epithermal prospect); BDL (below detection limit

Appendix 3.2. Electron microprobe analyses (in wt.%) of chlorite from the studied epithermal systems and calculated structural formulas.

Deposit	HB	HB	HB	HB	HB	HB	HB	HB	HB	HB	HB	HB	HB	HB	HB
Sample	HB-14	HB-14	HB-14	HB-14	HB-14	HB-14	HB-14	HB-14	HB-14	HB-14	HB-14	HB-14	HB-14	HB-14	HB-14
No. anal.	1	2	3	4	5	6	7	8	9	10	11	12	13	14	15
SiO_2	25.02	25.21	25.19	25.17	25.12	25.05	24.81	24.85	24.78	25.10	24.69	24.85	24.93	25.28	24.74
TiO_2	0.08	0.05	0.07	0.06	0.04	0.05	0.05	0.05	0.06	0.04	0.05	0.04	0.02	0.02	0.05
Al_2O_3	23.67	23.90	24.15	23.78	23.10	23.74	23.44	23.67	23.27	22.61	23.65	23.72	24.12	24.16	23.50
Cr_2O_3	0.08	0.07	0.08	0.06	0.04	0.02	0.03	0.05	0.08	0.04	0.09	0.11	0.05	0.06	0.08
V_2O_3	0.04	0.06	0.02	0.04	0.03	0.07	0.05	0.04	0.03	0.07	0.03	0.03	0.06	0.06	0.07
FeO	19.64	20.07	20.21	20.30	19.98	20.16	19.76	20.29	19.84	19.40	20.20	20.12	20.04	19.91	19.99
MnO	0.38	0.31	0.31	0.32	0.29	0.32	0.36	0.30	0.33	0.31	0.29	0.31	0.25	0.28	0.25
MgO	16.79	16.20	16.10	16.63	16.42	16.61	16.27	16.04	15.76	16.52	15.95	16.67	15.56	16.60	15.93
CaO	0.01	0.03	0.02	0.01	0.01	0.01	0.02	0.00	0.05	0.04	0.01	0.00	0.03	0.01	0.02
Na_2O	0.03	0.08	0.11	0.03	0.03	0.04	0.12	0.02	0.13	0.07	BDL	0.06	0.07	0.04	0.06
K_2O	0.01	0.03	0.02	0.01	0.01	BDL	0.03	BDL	0.07	0.04	0.01	0.01	0.07	0.02	0.03
Cl	0.01	0.01	0.01	0.03	0.02	0.01	0.02	0.01	0.03	0.01	0.01	0.01	0.02	0.02	0.02
F	BDL	BDL	BDL	BDL	BDL	BDL	BDL	BDL	BDL	BDL	BDL	BDL	BDL	BDL	BDL
H_2O (calc)	11.53	11.54	11.58	11.67	11.47	11.54	11.47	11.41	11.40	11.34	11.38	11.52	11.48	11.66	11.40
Total	97.29	97.53	97.86	98.12	96.56	97.61	96.45	96.72	95.84	95.59	96.38	97.44	96.70	98.12	96.14
Si	2.603	2.620	2.609	2.584	2.626	2.603	2.593	2.611	2.605	2.655	2.602	2.587	2.602	2.599	2.603
Al_{Total}	2.902	2.928	2.947	2.877	2.847	2.907	2.888	2.931	2.882	2.819	2.937	2.911	2.967	2.927	2.914
^{IV}Al	1.397	1.380	1.391	1.416	1.374	1.397	1.407	1.389	1.395	1.345	1.398	1.413	1.398	1.401	1.397
^{VI}Al	1.505	1.548	1.555	1.461	1.473	1.510	1.481	1.542	1.487	1.475	1.540	1.498	1.569	1.526	1.516
Ti	0.007	0.004	0.005	0.005	0.003	0.004	0.004	0.004	0.005	0.003	0.004	0.003	0.001	0.002	0.004
Cr	0.007	0.006	0.007	0.005	0.004	0.001	0.002	0.005	0.007	0.003	0.008	0.009	0.004	0.005	0.006
V	0.004	0.005	0.001	0.004	0.003	0.006	0.005	0.003	0.003	0.007	0.003	0.002	0.005	0.005	0.007
Fe^{2+}	1.708	1.744	1.750	1.743	1.747	1.752	1.727	1.783	1.744	1.716	1.781	1.752	1.750	1.712	1.759
Mn	0.034	0.027	0.027	0.028	0.026	0.029	0.032	0.027	0.029	0.028	0.026	0.027	0.022	0.024	0.022
Mg	2.603	2.510	2.486	2.545	2.558	2.573	2.536	2.512	2.469	2.606	2.506	2.587	2.422	2.544	2.498
Σ Oct.$_{(Fe+Mg+AlVI)}$	5.816	5.802	5.792	5.749	5.778	5.835	5.744	5.837	5.700	5.796	5.826	5.837	5.741	5.782	5.774
Ca	0.002	0.003	0.002	0.002	0.001	0.001	0.003	0.000	0.005	0.005	0.001	0.001	0.004	0.002	0.002
Na	0.006	0.016	0.022	0.007	0.006	0.007	0.024	0.004	0.026	0.014	-	0.011	0.014	0.008	0.011
K	0.001	0.003	0.003	0.002	0.002	-	0.004	-	0.010	0.005	0.002	0.002	0.010	0.002	0.004
Cl	0.002	0.001	0.002	0.005	0.004	0.002	0.004	0.001	0.005	0.002	0.001	0.002	0.003	0.003	0.003
F	-	-	-	-	-	-	-	-	-	-	-	-	-	-	-
OH	7.998	7.999	7.998	7.995	7.996	7.998	7.996	7.999	7.995	7.998	7.999	7.998	7.997	7.997	7.997
Geothermometry (°C)															
(1) Empirical	194	194	195	195	191	195	194	195	193	188	196	196	195	194	194
(2) Semi-empirical	281	270	268	253	256	293	249	293	231	258	288	297	247	265	260

Chlorite formulae calculated on basis of 14 oxygen atoms and all iron was considered as Fe^{2+}. Water (H_2O calc) was calculated based on OH+Cl+F= 8 apfu. (1) Empirical geothermometry calculation after Kranidiotis and MacLean (1987). (2) Semi-empirical geothermometry calculation after Inoue et al. (2018). Abbreviations: HB (Hope Brook); HE (Heritage); BDL (below detection limit).

Appendix 3.2. Electron microprobe analyses (in wt.%) of chlorite from the studied epithermal systems and calculated structural formulas.

Deposit	HB	HB	HB	HB	HB	HE	HE	HE	HE	HE	HE	HE	HE	HE	HE
Sample	HB-14	HB-14	HB-14	HB-14	HB-14	HE-48-28	HE-48-28	HE-48-28	HE-48-28	HE-48-28	HE-48-28	HE-48-28	HE-48-28	HE-48-28	HE-48-28
No. anal.	16	17	18	19	20	1	2	3	4	5	6	7	8	9	10
SiO_2	26.32	25.04	25.89	24.53	25.04	26.56	28.20	26.44	27.61	26.09	26.06	27.67	28.19	27.61	27.07
TiO_2	0.07	0.06	0.07	0.04	0.03	0.02	0.01	BDL	BDL	0.01	BDL	0.01	BDL	BDL	BDL
Al_2O_3	22.53	24.22	23.95	23.70	23.89	21.55	21.35	21.42	21.33	21.58	21.32	20.76	20.89	20.60	21.75
Cr_2O_3	0.07	0.08	0.21	0.05	0.08	BDL	BDL	BDL	BDL	BDL	BDL	0.01	BDL	BDL	BDL
V_2O_3	0.06	0.05	0.06	0.05	0.05	0.08	0.07	0.06	0.07	0.04	0.06	0.04	0.03	0.03	0.07
FeO	19.02	20.30	18.79	19.68	19.39	19.68	19.50	21.68	20.65	19.27	19.33	20.24	19.21	19.89	18.97
MnO	0.22	0.28	0.31	0.39	0.32	3.86	3.49	1.51	2.83	3.99	3.72	3.59	3.17	3.53	3.80
MgO	17.40	16.28	16.01	16.38	16.65	16.42	16.39	15.56	15.82	16.49	16.05	16.60	16.47	16.54	16.07
CaO	0.03	0.00	0.09	0.01	0.03	0.03	0.03	0.02	0.03	0.02	0.02	0.04	0.04	0.04	0.02
Na_2O	0.18	0.05	0.25	0.07	0.09	0.07	0.03	0.06	0.04	0.03	0.02	BDL	0.03	0.05	0.04
K_2O	0.08	0.02	0.04	0.03	0.06	0.03	0.30	0.01	0.15	0.03	0.05	0.08	0.25	0.10	0.22
Cl	0.03	0.01	0.02	0.02	0.02	0.01	0.02	0.02	0.01	0.01	0.01	0.01	0.03	0.01	BDL
F	BDL	BDL	BDL	BDL	BDL	BDL	BDL	BDL	BDL	BDL	BDL	BDL	BDL	BDL	BDL
H_2O (calc)	11.73	11.60	11.62	11.44	11.58	11.68	11.92	11.53	11.74	11.56	11.44	11.76	11.87	11.72	11.64
Total	97.75	98.01	97.31	96.39	97.21	99.98	101.30	98.33	100.29	99.10	98.08	100.79	100.18	100.13	99.66
Si	2.688	2.587	2.670	2.572	2.592	2.726	2.837	2.750	2.821	2.707	2.733	2.820	2.845	2.824	2.788
Al_{Total}	2.712	2.950	2.911	2.928	2.915	2.607	2.531	2.625	2.569	2.640	2.635	2.494	2.485	2.484	2.640
^{IV}Al	1.312	1.413	1.330	1.428	1.408	1.274	1.163	1.250	1.179	1.293	1.267	1.180	1.155	1.176	1.212
^{VI}Al	1.400	1.537	1.582	1.500	1.507	1.333	1.368	1.375	1.389	1.347	1.367	1.315	1.330	1.308	1.428
Ti	0.005	0.005	0.006	0.003	0.002	0.001	0.000	-	-	0.001	-	0.001	-	-	-
Cr	0.005	0.007	0.017	0.004	0.006	-	-	-	-	-	-	0.001	-	-	-
V	0.005	0.004	0.006	0.005	0.004	0.007	0.006	0.005	0.007	0.004	0.006	0.003	0.003	0.003	0.006
Fe^{2+}	1.624	1.755	1.621	1.725	1.679	1.689	1.640	1.886	1.764	1.672	1.695	1.725	1.622	1.702	1.634
Mn	0.019	0.025	0.027	0.035	0.028	0.335	0.297	0.133	0.245	0.350	0.330	0.310	0.271	0.306	0.331
Mg	2.649	2.508	2.462	2.561	2.570	2.513	2.458	2.413	2.410	2.550	2.509	2.522	2.478	2.522	2.468
Σ Oct.$_{(Fe+Mg+AlVI)}$	5.674	5.799	5.665	5.786	5.755	5.535	5.466	5.673	5.563	5.569	5.572	5.562	5.430	5.531	5.530
Ca	0.003	0.000	0.010	0.001	0.003	0.003	0.003	0.003	0.003	0.002	0.003	0.004	0.004	0.005	0.003
Na	0.036	0.011	0.051	0.015	0.018	0.013	0.006	0.012	0.007	0.006	0.003	-	0.007	0.011	0.009
K	0.011	0.002	0.005	0.004	0.008	0.004	0.038	0.002	0.020	0.004	0.006	0.011	0.032	0.013	0.029
Cl	0.006	0.002	0.003	0.003	0.004	0.002	0.003	0.003	0.002	0.001	0.001	0.001	0.005	0.002	-
F	-	-	-	-	-	-	-	-	-	-	-	-	-	-	-
OH	7.994	7.998	7.997	7.997	7.996	7.998	7.997	7.997	7.998	7.999	7.999	7.999	7.995	7.998	8.000
Geothermometry (°C)															
(1) Empirical	181	197	186	197	194	181	169	181	173	184	181	172	166	171	176
(2) Semi-empirical	201	277	205	273	254	158	124	192	149	169	166	147	116	139	146

Chlorite formulae calculated on basis of 14 oxygen atoms and all iron was considered as Fe^{2+}. Water (H_2O calc) was calculated based on OH+Cl+F= 8 apfu. (1) Empirical geothermometry calculation after Kranidiotis and MacLean (1987). (2) Semi-empirical geothermometry calculation after Inoue et al. (2018). Abbreviations: HB (Hope Brook); HE (Heritage); BDL (below detection limit).

Appendix 3.2. Electron microprobe analyses (in wt.%) of chlorite from the studied epithermal systems and calculated structural formulas.

Deposit	HE	HE	HE	HE	HE	HE	HE	HE	HE	HE	HE	HE	HE	HE	HE
Sample	HE-48-27	HE-48-27	HE-48-27	HE-48-27	HE-48-27	HE-48-27	HE-48-27	HE-48-27	HE-36-107B	HE-36-107B	HE-36-107B	HE-36-107B	HE-36-107B	HE-36-107B	HE-36-107B
No. anal.	1	2	3	4	7	8	9	10	1	2	3	4	5	6	7
SiO_2	26.42	26.43	26.20	25.99	27.01	26.66	25.75	26.26	26.88	28.31	26.61	28.59	29.93	26.41	26.68
TiO_2	BDL	BDL	0.03	BDL	BDL	BDL	BDL	BDL	BDL	0.02	0.05	0.02	0.01	0.02	0.02
Al_2O_3	21.60	22.87	21.30	20.81	22.05	21.68	21.68	22.27	21.54	21.69	19.72	20.85	22.52	19.72	19.11
Cr_2O_3	BDL	0.01	BDL	BDL	BDL	0.01	BDL	0.01	BDL	0.01	BDL	0.02	BDL	0.01	BDL
V_2O_3	0.02	0.02	0.02	0.01	0.02	0.03	0.03	0.03	0.03	0.05	0.02	0.02	0.02	0.02	0.04
FeO	20.73	21.78	21.05	21.74	20.70	22.48	22.83	22.08	21.03	20.41	20.60	19.73	19.87	20.55	19.55
MnO	3.33	3.25	3.00	2.94	3.06	3.16	3.34	3.24	4.39	3.57	3.79	3.36	3.42	3.63	3.42
MgO	14.28	14.73	14.72	14.31	14.36	14.72	13.81	14.43	14.78	16.20	14.11	17.05	17.31	14.43	14.77
CaO	0.08	0.03	0.04	0.05	0.06	0.03	0.01	0.03	0.04	0.05	0.41	0.06	0.05	0.09	0.07
Na_2O	0.02	BDL	0.03	BDL	0.02	0.01	0.03	0.03	BDL	BDL	0.01	BDL	0.02	BDL	BDL
K_2O	0.22	0.10	0.15	0.03	0.45	0.10	0.01	0.04	0.02	0.01	0.01	0.01	0.09	0.00	0.07
Cl	0.01	BDL	0.02	0.04	0.01	0.01	0.01	0.01	0.01	0.01	0.01	0.02	0.01	0.00	0.03
F	BDL	BDL	BDL	BDL	BDL	BDL	BDL	BDL	BDL	BDL	BDL	BDL	BDL	BDL	BDL
H_2O (calc)	11.41	11.68	11.46	11.41	11.60	11.61	11.37	11.60	11.61	11.99	11.21	12.01	12.50	11.12	11.16
Total	98.12	100.89	98.04	97.34	99.35	100.50	98.89	100.02	100.32	102.32	96.56	101.74	105.76	96.00	94.92
Si	2.777	2.714	2.741	2.729	2.791	2.753	2.715	2.715	2.775	2.830	2.845	2.853	2.872	2.847	2.866
Al_{Total}	2.676	2.768	2.626	2.576	2.686	2.639	2.694	2.715	2.620	2.556	2.485	2.453	2.547	2.506	2.419
^{IV}Al	1.223	1.286	1.259	1.271	1.209	1.247	1.285	1.285	1.225	1.170	1.155	1.147	1.128	1.153	1.134
^{VI}Al	1.452	1.482	1.366	1.305	1.477	1.392	1.409	1.430	1.395	1.387	1.330	1.306	1.419	1.354	1.285
Ti	-	-	0.002	-	-	-	-	-	-	0.001	0.004	0.002	0.001	0.001	0.002
Cr	-	0.001	-	-	-	0.001	-	0.001	-	0.001	-	0.001	-	0.001	-
V	0.002	0.001	0.002	0.001	0.002	0.003	0.003	0.002	0.002	0.004	0.002	0.002	0.002	0.002	0.003
Fe^{2+}	1.822	1.870	1.842	1.909	1.789	1.942	2.013	1.909	1.816	1.707	1.842	1.647	1.595	1.853	1.756
Mn	0.297	0.283	0.266	0.261	0.268	0.276	0.298	0.284	0.384	0.302	0.343	0.284	0.278	0.332	0.311
Mg	2.237	2.254	2.296	2.240	2.212	2.265	2.170	2.224	2.274	2.414	2.249	2.537	2.476	2.319	2.365
Σ Oct.$_{(Fe+Mg+AlVI)}$	5.511	5.607	5.503	5.455	5.478	5.599	5.592	5.563	5.485	5.508	5.421	5.489	5.490	5.526	5.406
Ca	0.009	0.003	0.005	0.006	0.007	0.004	0.001	0.004	0.004	0.006	0.047	0.007	0.005	0.010	0.008
Na	0.004	-	0.006	-	0.005	0.003	0.007	0.007	-	-	0.002	-	0.003	-	-
K	0.030	0.013	0.020	0.004	0.060	0.013	0.002	0.005	0.003	0.002	0.001	0.001	0.012	0.000	0.010
Cl	0.001	-	0.004	0.007	0.002	0.001	0.001	0.002	0.001	0.002	0.002	0.004	0.002	0.001	0.005
F	-	-	-	-	-	-	-	-	-	-	-	-	-	-	-
OH	7.999	8.000	7.996	7.993	7.998	7.999	7.999	7.998	7.999	7.998	7.998	7.996	7.998	7.999	7.995
Geothermometry (°C)															
(1) Empirical	180	188	181	181	178	184	189	187	180	171	172	166	165	173	166
(2) Semi-empirical	147	182	152	145	138	172	179	171	142	135	118	125	123	137	110

Chlorite formulae calculated on basis of 14 oxygen atoms and all iron was considered as Fe^{2+}. Water (H_2O calc) was calculated based on OH+Cl+F= 8 apfu. (1) Empirical geothermometry calculation after Kranidiotis and MacLean (1987). (2) Semi-empirical geothermometry calculation after Inoue et al. (2018). Abbreviations: HB (Hope Brook); HE (Heritage); BDL (below detection limit).

Appendix 3.2. Electron microprobe analyses (in wt.%) of chlorite from the studied epithermal systems and calculated structural formulas.

Deposit	HE	HE	HE	HE	HE	HE	HE	HE	HE	HE	HE
Sample	HE-36-107B	HE-36-107B	HE-47-26	HE-47-26	HE-47-26	HE-47-26	HE-47-26	HE-47-26	HE-47-26	HE-47-26	HE-47-26
No. anal.	8	9	1	3	4	5	6	7	8	9	10
SiO_2	26.79	29.04	31.59	31.21	32.15	32.83	30.75	31.86	30.73	30.49	28.60
TiO_2	BDL	0.02	0.02	BDL	BDL	BDL	BDL	BDL	0.01	BDL	BDL
Al_2O_3	18.75	20.41	18.23	18.15	19.03	18.71	17.92	18.35	18.47	17.64	17.38
Cr_2O_3	0.02	BDL	0.01	BDL	0.01	0.01	BDL	0.01	BDL	BDL	BDL
V_2O_3	0.06	0.03	0.06	0.07	0.07	0.09	0.08	0.06	0.04	0.05	0.06
FeO	18.76	19.33	19.98	20.90	21.09	20.03	20.29	20.38	19.64	18.43	19.03
MnO	3.26	3.26	0.76	0.73	0.78	0.73	0.69	0.72	0.82	0.78	0.96
MgO	14.80	17.17	18.41	18.09	18.91	19.01	17.83	18.78	18.33	17.63	15.43
CaO	0.05	0.06	0.36	0.29	0.29	0.33	0.33	0.32	0.62	0.59	0.54
Na_2O	BDL	BDL	0.07	0.01	0.05	0.07	0.04	0.05	0.08	0.03	0.05
K_2O	0.20	0.01	0.02	0.02	0.01	0.02	0.02	0.02	0.10	0.21	0.44
Cl	0.01	0.02	0.01	0.02	0.02	0.02	0.01	0.01	0.02	0.02	0.02
F	BDL	BDL	BDL	BDL	BDL	BDL	BDL	BDL	BDL	BDL	BDL
H_2O (calc)	10.99	11.99	12.11	12.08	12.49	12.50	11.87	12.25	12.06	11.67	11.13
Total	93.69	101.34	101.62	101.57	104.89	104.35	99.84	102.80	100.94	97.54	93.63
Si	2.921	2.903	3.129	3.098	3.087	3.148	3.107	3.118	3.053	3.132	3.081
Al_{Total}	2.410	2.404	2.127	2.123	2.153	2.115	2.133	2.116	2.162	2.136	2.207
^{IV}Al	1.079	1.097	0.871	0.902	0.913	0.852	0.893	0.882	0.947	0.868	0.919
^{VI}Al	1.331	1.307	1.257	1.221	1.239	1.264	1.240	1.234	1.215	1.268	1.288
Ti	-	0.002	0.002	-	-	-	-	-	0.001	-	-
Cr	0.002	-	0.001	-	0.001	0.001	-	0.000	-	-	-
V	0.006	0.003	0.006	0.006	0.006	0.007	0.007	0.005	0.003	0.004	0.006
Fe^{2+}	1.711	1.616	1.655	1.735	1.694	1.607	1.714	1.668	1.632	1.584	1.715
Mn	0.301	0.276	0.063	0.062	0.063	0.060	0.059	0.060	0.069	0.068	0.087
Mg	2.406	2.559	2.718	2.678	2.706	2.718	2.685	2.739	2.715	2.700	2.478
Σ Oct.$_{(Fe+Mg+AlVI)}$	5.448	5.483	5.629	5.633	5.639	5.588	5.639	5.642	5.563	5.551	5.481
Ca	0.005	0.007	0.038	0.031	0.030	0.034	0.036	0.034	0.066	0.065	0.062
Na	-	-	0.014	0.003	0.009	0.014	0.009	0.009	0.015	0.005	0.010
K	0.027	0.001	0.003	0.003	0.001	0.002	0.002	0.003	0.013	0.028	0.061
Cl	0.003	0.003	0.002	0.003	0.003	0.003	0.002	0.002	0.004	0.003	0.004
F	-	-	-	-	-	-	-	-	-	-	-
OH	7.997	7.997	7.998	7.997	7.997	7.997	7.998	7.998	7.996	7.997	7.996
Geothermometry (°C)											
(1) Empirical	161	160	137	140	141	133	140	138	143	135	142
(2) Semi-empirical	108	116	117	123	126	104	123	122	110	97	91

Chlorite formulae calculated on basis of 14 oxygen atoms and all iron was considered as Fe^{2+}. Water (H_2O calc) was calculated based on OH+Cl+F= 8 apfu. (1) Empirical geothermometry calculation after Kranidiotis and MacLean (1987). (2) Semi-empirical geothermometry calculation after Inoue et al. (2018). Abbreviations: HB (Hope Brook); HE (Heritage); BDL (below detection limit).

Appendix 3.2. Electron microprobe analyses (in wt%) of pyrophyllite from the studied epithermal systems and respective structural formulas.

Deposit	OP	OP	OP	OP	OP	OP	OP	OP	OP	OP	OP	OP	OP	OP	OP	OP	OP	OP
Sample	MP	MP	MP	MP	MP	MP	MP	MP	MP	MP	MP	MP	MP	MP	MP	MP	MP	MP
No. anal.	1	2	3	4	5	6	7	8	9	10	11	12	13	14	15	16	17	18
SiO_2	65.47	66.05	66.37	67.51	66.73	66.57	67.23	66.74	66.71	67.65	66.62	66.70	67.27	66.78	67.30	66.58	66.99	66.60
TiO_2	BDL	0.01	BDL	0.01	0.03	BDL	0.02	0.01	0.02	BDL	0.02	BDL	BDL	BDL	BDL	BDL	BDL	BDL
Al_2O_3	28.85	28.93	29.33	29.82	29.47	29.27	29.40	29.48	29.08	29.81	29.56	29.59	29.79	29.33	29.75	29.09	29.66	29.36
Ce_2O_3	BDL	0.01	BDL	BDL	BDL	0.03	0.04	BDL	0.03	0.05	0.02	BDL	0.05	0.04	BDL	0.01	0.02	BDL
Fe_2O_3	0.15	0.18	0.12	0.16	0.13	0.15	0.21	0.22	0.19	0.20	0.15	0.12	0.17	0.14	0.17	0.17	0.14	0.16
MnO	BDL	BDL	BDL	BDL	0.01	0.01	0.01	BDL	BDL	BDL	BDL	BDL	BDL	BDL	0.02	0.01	BDL	BDL
MgO	BDL	0.01	0.01	0.01	0.01	0.01	0.01	BDL	BDL	0.01	0.00	0.01	0.01	BDL	BDL	0.01	0.00	0.01
P_2O_5	0.03	0.05	BDL	0.01	0.00	BDL	0.02	BDL	0.01	0.01	BDL	0.01	BDL	BDL	BDL	BDL	0.01	0.01
BaO	BDL	BDL	BDL	BDL	BDL	BDL	BDL	0.02	BDL	BDL	BDL	BDL	BDL	BDL	BDL	BDL	0.01	BDL
SO_3	0.01	BDL	0.01	BDL	0.00	BDL	BDL	0.02	BDL	0.01	0.01	0.01	0.00	0.01	BDL	0.00	BDL	BDL
SrO	0.03	BDL	BDL	BDL	BDL	0.02	BDL	0.02	BDL	0.05	BDL	BDL	BDL	BDL	BDL	0.01	BDL	BDL
CaO	0.01	0.01	BDL	0.01	0.02	0.01	0.02	0.00	0.02	0.02	0.00	0.01	0.01	0.01	0.01	0.01	0.01	0.01
Na_2O	0.05	0.08	0.12	0.10	0.07	0.07	0.04	0.07	0.05	0.07	0.08	0.08	0.11	0.08	0.05	0.04	0.07	0.08
K_2O	0.02	0.02	0.03	0.03	0.01	0.02	0.04	0.02	0.02	0.03	0.01	0.03	0.13	0.01	0.02	0.02	0.06	0.03
Cl	0.00	0.01	0.01	0.02	0.01	0.01	BDL	BDL	BDL	0.01	0.01	BDL	0.01	0.02	0.03	0.00	BDL	0.01
F	BDL	BDL	BDL	BDL	0.03	BDL	0.02	BDL	0.06	BDL	0.05	BDL	0.05	0.06	0.02	0.04	0.03	BDL
H_2O (calc)	4.94	4.96	4.99	5.01	4.72	4.97	4.93	5.07	4.60	5.07	4.62	5.07	4.71	4.43	4.77	4.70	4.90	5.00
Total	99.55	100.33	100.97	102.67	101.24	101.15	101.99	101.66	100.79	102.97	101.16	101.65	102.31	100.93	102.14	100.70	101.92	101.26
Si	3.946	3.948	3.941	3.928	3.891	3.941	3.930	3.947	3.886	3.938	3.867	3.944	3.875	3.848	3.892	3.903	3.914	3.941
Ti	-	0.000	-	0.000	0.001	-	0.001	0.001	0.001	-	0.001	-	-	-	-	-	-	-
Al_{Total}	2.049	2.038	2.052	2.045	2.025	2.042	2.025	2.055	1.996	2.045	2.022	2.062	2.022	1.992	2.028	2.010	2.043	2.048
^{IV}Al	0.054	0.052	0.059	0.072	0.109	0.059	0.070	0.052	0.114	0.062	0.132	0.055	0.125	0.151	0.108	0.097	0.086	0.059
^{VI}Al	1.995	1.986	1.993	1.973	1.916	1.983	1.955	2.003	1.882	1.983	1.890	2.007	1.898	1.840	1.920	1.913	1.956	1.988
Ce	-	0.000	-	-	-	0.001	0.001	-	0.001	0.001	0.000	-	0.001	0.001	-	0.000	0.001	-
Fe^{3+}	0.007	0.008	0.005	0.007	0.006	0.007	0.009	0.010	0.008	0.009	0.007	0.005	0.007	0.006	0.007	0.007	0.006	0.007
Mn	-	-	-	-	0.000	0.001	0.001	-	-	-	-	-	-	-	0.001	0.000	-	-
Mg	-	0.001	0.001	0.001	0.001	0.001	0.001	-	-	0.000	0.000	0.001	0.001	-	-	0.001	0.000	0.001
P	0.001	0.003	-	0.000	0.000	-	0.001	-	0.000	0.001	-	0.001	-	-	-	-	0.001	0.000
Ba	-	-	-	-	-	-	-	0.000	-	-	-	-	-	-	-	-	0.000	-
S	0.000	-	0.000	-	0.000	-	-	0.001	-	0.000	0.001	0.001	0.000	0.001	-	0.000	-	-
Sr	0.001	-	-	-	-	0.001	-	0.001	-	0.002	-	-	-	-	-	0.000	-	-
Ca	0.001	0.001	-	0.001	0.001	0.001	0.001	0.000	0.001	0.001	0.000	0.001	0.001	0.001	0.001	0.001	0.001	0.001
Na	0.006	0.010	0.013	0.011	0.008	0.008	0.004	0.008	0.006	0.008	0.009	0.010	0.013	0.009	0.006	0.005	0.008	0.010
K	0.001	0.001	0.002	0.002	0.001	0.001	0.003	0.001	0.001	0.002	0.001	0.002	0.009	0.001	0.001	0.001	0.005	0.002
Cl	0.016	0.020	0.023	0.057	0.042	0.037	-	-	-	0.031	0.045	-	0.035	0.084	0.093	0.014	-	0.028
F	-	-	-	-	0.121	-	0.078	-	0.213	-	0.168	-	0.156	0.214	0.065	0.148	0.089	-
OH	1.984	1.980	1.977	1.943	1.837	1.963	1.922	2.000	1.787	1.969	1.787	2.000	1.810	1.702	1.842	1.838	1.911	1.972

Pyrophyllite formulae calculated on basis of 11 oxygen atoms. All iron was considered as Fe^{3+}. Al was allocated in tetrahedral position up to ΣTetrahedral = 4 a.p.f.u. Excess Al was assigned as ^{VI}Al. Water (H_2O calc) was calculated based on OH+Cl+F= 2 apfu. Abbreviations: OP (Oval Pit Mine); VJ (Vinjer high-sulfidation system); BDL (below detection limit).

Appendix 3.2. Electron microprobe analyses (in wt%) of pyrophyllite from the studied epithermal systems and respective structural formulas.

Deposit	OP	OP	OP	OP	OP	OP	OP	OP	OP	OP	OP	OP	OP	OP	VJ	VJ	VJ	VJ
Sample	MP	MP	MP	MP	MP	MP	MP	MP	MP	MP	MP	MP	MP	MP	VP-2	VP-2	VP-2	VP-2
No. anal.	19	20	21	22	23	24	25	26	27	28	29	30	31	32	1	2	3	4
SiO_2	66.53	66.60	65.63	65.94	65.73	65.78	65.34	64.67	65.08	64.74	65.13	65.56	65.21	64.92	64.78	66.15	66.79	66.68
TiO_2	0.02	0.02	0.02	BDL	0.03	BDL	0.01	0.02	BDL	BDL	0.02	0.02	BDL	0.01	BDL	BDL	0.02	BDL
Al_2O_3	29.56	29.21	28.93	29.17	29.09	29.50	29.21	29.24	29.10	29.11	28.87	28.77	29.03	28.87	28.50	30.45	29.62	29.79
Ce_2O_3	0.02	BDL	BDL	0.02	0.01	0.04	BDL	BDL	BDL	BDL	BDL	0.02	BDL	BDL	0.01	0.02	BDL	BDL
Fe_2O_3	0.14	0.19	0.16	0.12	0.14	0.10	0.16	0.17	0.21	0.14	0.14	0.16	0.18	0.15	0.34	0.27	0.31	0.23
MnO	0.01	0.00	0.01	BDL	0.00	BDL	0.01	0.01	BDL	BDL	0.00	0.01	BDL	BDL	BDL	BDL	0.01	BDL
MgO	BDL	0.01	0.00	BDL	BDL	0.00	0.02	BDL	BDL	BDL	BDL	0.01	BDL	BDL	BDL	0.02	0.02	0.01
P_2O_5	0.02	BDL	BDL	BDL	BDL	0.01	BDL	0.01	0.02	BDL	BDL	0.00	BDL	BDL	BDL	BDL	0.01	0.01
BaO	BDL	BDL	BDL	BDL	BDL	BDL	BDL	BDL	BDL	0.01	BDL	BDL	BDL	BDL	BDL	BDL	BDL	BDL
SO_3	0.00	BDL	BDL	0.01	BDL	BDL	BDL	0.02	BDL	0.01	BDL	0.02	0.01	BDL	0.02	0.01	BDL	BDL
SrO	BDL	0.01	0.02	0.03	0.01	0.01	0.04	BDL	0.01	0.01	0.01	0.01	0.02	BDL	BDL	BDL	BDL	0.02
CaO	0.01	0.03	0.01	0.01	0.02	0.01	0.00	0.01	BDL	0.00	0.01	0.02	0.03	0.01	0.03	0.04	0.03	0.02
Na_2O	0.05	0.04	0.09	0.07	0.06	0.07	0.09	0.07	0.08	0.04	0.14	0.08	0.10	0.07	0.09	0.06	0.06	0.05
K_2O	0.01	0.03	0.00	0.01	0.02	0.01	0.02	0.11	0.07	0.05	0.02	0.02	0.02	0.01	0.04	0.01	0.02	0.02
Cl	BDL	0.01	BDL	BDL	0.00	BDL	0.01	0.00	0.01	BDL	BDL	0.01	0.01	BDL	0.01	0.01	0.01	0.00
F	0.04	0.11	BDL	0.01	0.01	BDL	0.03	0.06	BDL	BDL	BDL	BDL	BDL	0.04	0.07	0.04	0.07	BDL
H_2O (calc)	4.80	4.16	4.98	4.91	4.89	5.01	4.65	4.44	4.89	4.94	4.95	4.93	4.93	4.64	4.34	4.73	4.54	5.05
Total	101.21	100.41	99.86	100.30	100.01	100.54	99.59	98.83	99.48	99.06	99.30	99.63	99.52	98.73	98.23	101.80	101.49	101.89
Si	3.897	3.807	3.950	3.932	3.928	3.933	3.877	3.833	3.921	3.930	3.944	3.946	3.932	3.889	3.847	3.839	3.849	3.929
Ti	0.001	0.001	0.001	-	0.001	-	0.000	0.001	-	-	0.001	0.001	-	0.001	-	-	0.001	-
Al_{Total}	2.041	1.968	2.053	2.050	2.049	2.079	2.043	2.042	2.066	2.083	2.060	2.041	2.063	2.039	1.995	2.083	2.011	2.069
^{IV}Al	0.103	0.193	0.050	0.068	0.072	0.067	0.123	0.166	0.079	0.070	0.056	0.053	0.067	0.111	0.152	0.160	0.151	0.071
^{VI}Al	1.938	1.774	2.003	1.982	1.977	2.012	1.920	1.876	1.987	2.013	2.004	1.988	1.996	1.927	1.843	1.923	1.860	1.998
Ce	0.001	-	-	0.001	0.000	0.001	-	-	-	-	-	0.000	-	-	0.000	0.000	-	-
Fe^{3+}	0.006	0.008	0.007	0.005	0.006	0.005	0.007	0.008	0.010	0.006	0.006	0.007	0.008	0.007	0.015	0.012	0.013	0.010
Mn	0.000	0.000	0.000	-	0.000	-	0.000	0.000	-	-	0.000	0.000	-	-	-	-	0.000	-
Mg	-	0.001	0.000	-	-	0.000	0.002	-	-	-	-	0.001	-	-	-	0.002	0.002	0.001
P	0.001	-	-	-	-	0.000	-	0.000	0.001	-	-	0.000	-	-	-	-	0.000	0.001
Ba	-	-	-	-	-	-	-	-	-	0.000	-	-	-	-	-	-	-	-
S	0.000	-	-	0.000	-	-	-	0.001	-	0.000	-	0.001	0.000	-	0.001	0.000	-	-
Sr	-	0.000	0.001	0.001	0.000	0.000	0.002	-	0.000	0.000	0.000	0.000	0.001	-	-	-	-	0.001
Ca	0.001	0.002	0.001	0.001	0.001	0.000	0.000	0.000	-	0.000	0.000	0.001	0.002	0.001	0.002	0.002	0.002	0.001
Na	0.006	0.004	0.010	0.008	0.007	0.008	0.010	0.008	0.009	0.005	0.017	0.010	0.011	0.009	0.010	0.007	0.006	0.005
K	0.001	0.002	0.000	0.001	0.001	0.000	0.001	0.008	0.005	0.004	0.002	0.001	0.002	0.001	0.003	0.001	0.001	0.002
Cl	-	0.030	-	-	0.010	-	0.036	0.015	0.034	-	-	0.021	0.018	-	0.045	0.038	0.024	0.015
F	0.126	0.386	-	0.046	0.042	-	0.124	0.229	-	-	-	-	-	0.148	0.234	0.132	0.232	-
OH	1.874	1.584	2.000	1.954	1.948	2.000	1.840	1.755	1.966	2.000	2.000	1.979	1.982	1.852	1.721	1.830	1.745	1.985

Pyrophyllite formulae calculated on basis of 11 oxygen atoms. All iron was considered as Fe^{3+}. Al was allocated in tetrahedral position up to ΣTetrahedral = 4 a.p.f.u. Excess Al was assigned as ^{VI}Al. Water (H_2O calc) was calculated based on OH+Cl+F= 2 apfu. Abbreviations: OP (Oval Pit Mine); VJ (Vinjer high-sulfidation system); BDL (below detection limit).

Appendix 3.2. Electron microprobe analyses (in wt%) of pyrophyllite from the studied epithermal systems and respective structural formulas.

Deposit	VJ	VJ	VJ	VJ	VJ	VJ	VJ	VJ	VJ	VJ	VJ	VJ	VJ	VJ	VJ	VJ	VJ	VJ
Sample	VP-2	VP-2	VP-2	VP-2	VP-2	VP-2	VP-2	VP-2	VP-2	VP-2	VP-2	VP-2	VP-2	VP-2	VP-2	VP-2	VP-2	VP-2
No. anal.	5	6	7	8	9	10	11	12	13	14	15	16	17	18	19	20	21	22
SiO_2	67.40	66.90	67.36	66.49	68.18	63.62	67.51	66.36	65.82	65.67	66.15	65.58	56.50	61.74	67.06	65.98	67.15	66.43
TiO_2	BDL	BDL	0.01	0.02	BDL	BDL	BDL	BDL	BDL	BDL	BDL	BDL	BDL	BDL	BDL	0.02	BDL	BDL
Al_2O_3	29.59	29.81	29.70	29.12	30.28	28.93	29.47	29.08	28.75	29.76	28.96	30.24	34.08	31.04	29.23	29.65	29.30	29.17
Ce_2O_3	0.02	BDL	BDL	BDL	BDL	0.04	BDL	0.04	BDL	BDL	0.02	0.02	BDL	BDL	BDL	BDL	BDL	BDL
Fe_2O_3	0.23	0.20	0.22	0.33	0.23	0.21	0.29	0.25	0.30	0.27	0.25	0.24	0.16	0.21	0.28	0.26	0.23	0.22
MnO	BDL	0.01	0.01	0.01	BDL	BDL	BDL	0.01	BDL	BDL	0.02	0.01	0.01	0.02	0.01	0.02	BDL	BDL
MgO	BDL	0.01	0.01	0.01	0.00	0.01	BDL	0.01	0.02	0.02	BDL	BDL	BDL	0.02	BDL	0.01	0.01	BDL
P_2O_5	0.02	BDL	BDL	BDL	0.01	BDL	0.01	0.01	0.01	0.01	BDL	BDL	BDL	BDL	BDL	0.01	BDL	0.01
BaO	BDL	BDL	BDL	BDL	0.01	BDL	BDL	BDL	BDL	BDL	BDL	BDL	BDL	BDL	BDL	BDL	BDL	BDL
SO_3	0.01	0.01	BDL	0.01	0.02	BDL	BDL	0.01	0.02	0.01	0.02	0.02	BDL	0.02	BDL	BDL	BDL	0.01
SrO	BDL	BDL	BDL	0.01	BDL	0.05	0.05	BDL	BDL	0.01	0.03	BDL	BDL	0.04	BDL	BDL	BDL	0.02
CaO	0.00	0.03	0.00	0.02	0.05	0.01	0.01	0.02	0.01	0.00	0.01	0.00	0.01	0.01	0.01	0.00	BDL	0.01
Na_2O	0.05	0.01	0.07	0.02	0.04	0.01	0.03	0.03	BDL	0.01	0.02	0.02	0.01	0.04	BDL	0.02	0.04	0.05
K_2O	0.01	0.01	0.01	0.02	0.01	0.01	0.01	0.03	0.02	0.02	0.02	0.01	BDL	0.05	0.02	BDL	0.01	0.02
Cl	BDL	0.02	0.01	0.00	0.02	0.02	0.02	0.03	0.01	0.01	0.01	BDL	0.01	BDL	0.01	0.00	0.01	BDL
F	BDL	0.08	BDL	BDL	0.07	BDL	BDL	0.06	0.02	BDL	BDL	0.06	BDL	BDL	0.02	BDL	BDL	BDL
H_2O (calc)	5.11	4.40	5.02	5.02	4.50	4.69	4.99	4.43	4.71	4.97	4.97	4.57	4.63	4.87	4.88	5.01	5.03	5.04
Total	102.44	101.48	102.41	101.08	103.44	97.61	102.38	100.35	99.69	100.74	100.47	100.77	95.42	98.06	101.51	100.97	101.77	100.97
Si	3.954	3.823	3.935	3.950	3.828	3.884	3.938	3.853	3.911	3.908	3.950	3.820	3.566	3.799	3.930	3.924	3.954	3.954
Ti	-	-	0.000	0.001	-	-	-	-	-	-	-	-	-	-	-	0.001	-	-
Al_{Total}	2.046	2.007	2.045	2.039	2.003	2.082	2.026	1.990	2.013	2.088	2.038	2.076	2.535	2.251	2.019	2.078	2.034	2.046
^{IV}Al	0.046	0.177	0.065	0.049	0.171	0.116	0.062	0.146	0.088	0.091	0.049	0.179	0.434	0.200	0.070	0.076	0.046	0.045
^{VI}Al	2.000	1.831	1.980	1.990	1.832	1.965	1.964	1.844	1.925	1.997	1.989	1.897	2.101	2.051	1.949	2.002	1.988	2.001
Ce	0.001	-	-	-	-	0.001	-	0.001	-	-	0.000	0.000	-	-	-	-	-	-
Fe^{3+}	0.010	0.009	0.010	0.015	0.010	0.010	0.013	0.011	0.013	0.012	0.011	0.010	0.008	0.010	0.012	0.011	0.010	0.010
Mn	-	0.000	0.000	0.001	-	-	-	0.000	-	-	0.001	0.000	0.001	0.001	0.000	0.001	-	-
Mg	-	0.001	0.001	0.001	0.000	0.001	-	0.001	0.002	0.001	-	-	-	0.002	-	0.001	0.001	-
P	0.001	-	-	-	0.001	-	0.001	0.000	0.001	0.000	-	-	-	-	-	0.000	-	0.001
Ba	-	-	-	-	0.000	-	-	-	-	-	-	-	-	-	-	-	-	-
S	0.000	0.000	-	0.001	0.001	-	-	0.000	0.001	0.001	0.001	0.001	-	0.001	-	-	-	0.000
Sr	-	-	-	0.000	-	0.002	0.002	-	-	0.000	0.001	-	-	0.001	-	-	-	0.001
Ca	0.000	0.002	0.000	0.001	0.003	0.001	0.001	0.001	0.000	0.000	0.000	0.000	0.001	0.001	0.000	0.000	-	0.000
Na	0.006	0.001	0.008	0.002	0.004	0.002	0.004	0.004	-	0.001	0.003	0.002	0.002	0.005	-	0.002	0.005	0.006
K	0.001	0.001	0.001	0.001	0.001	0.001	0.001	0.002	0.002	0.001	0.001	0.001	-	0.004	0.001	-	0.001	0.002
Cl	-	0.067	0.043	0.011	0.073	0.090	0.060	0.088	0.049	0.028	0.019	-	0.052	-	0.030	0.013	0.023	-
F	-	0.258	-	-	0.242	-	-	0.196	0.082	-	-	0.225	-	-	0.061	-	-	-
OH	2.000	1.675	1.957	1.989	1.686	1.910	1.940	1.717	1.869	1.972	1.981	1.775	1.948	2.000	1.908	1.987	1.977	2.000

Pyrophyllite formulae calculated on basis of 11 oxygen atoms. All iron was considered as Fe^{3+}. Al was allocated in tetrahedral position up to ΣTetrahedral = 4 a.p.f.u. Excess Al was assigned as ^{VI}Al. Water (H_2O calc) was calculated based on OH+Cl+F= 2 apfu. Abbreviations: OP (Oval Pit Mine); VJ (Vinjer high-sulfidation system); BDL (below detection limit).

Appendix 3.2. Electron microprobe analyses (in wt%) of pyrophyllite from the studied epithermal systems and respective structural formulas.

Deposit	VJ	VJ	VJ
Sample	VP-2	VP-2	VP-2
No. anal.	23	24	25
SiO_2	66.62	67.33	66.12
TiO_2	0.01	0.01	BDL
Al_2O_3	29.13	29.41	28.73
Ce_2O_3	BDL	BDL	BDL
Fe_2O_3	0.26	0.26	0.30
MnO	0.01	BDL	BDL
MgO	BDL	0.01	BDL
P_2O_5	BDL	BDL	BDL
BaO	BDL	0.01	BDL
SO_3	0.02	BDL	0.01
SrO	0.02	BDL	BDL
CaO	0.01	0.01	0.00
Na_2O	0.04	0.01	0.06
K_2O	0.02	0.02	0.02
Cl	0.01	0.01	0.01
F	BDL	0.02	BDL
H_2O (calc)	4.98	4.85	4.95
Total	101.12	101.95	100.20
Si	3.946	3.918	3.955
Ti	0.000	0.000	-
Al_{Total}	2.034	2.017	2.026
^{IV}Al	0.053	0.082	0.045
^{VI}Al	1.981	1.934	1.981
Ce	-	-	-
Fe^{3+}	0.012	0.011	0.013
Mn	0.000	-	-
Mg	-	0.001	-
P	-	-	-
Ba	-	0.000	-
S	0.001	-	0.000
Sr	0.001	-	-
Ca	0.000	0.001	0.000
Na	0.005	0.002	0.007
K	0.002	0.002	0.002
Cl	0.032	0.034	0.026
F	-	0.085	-
OH	1.968	1.881	1.974

Pyrophyllite formulae calculated on basis of 11 oxygen atoms. All iron was considered as Fe^{3+}. Al was allocated in tetrahedral position up to ΣTetrahedral = 4 a.p.f.u. Excess Al was assigned as ^{VI}Al. Water (H_2O calc) was calculated based on OH+Cl+F= 2 apfu. Abbreviations: OP (Oval Pit Mine); VJ (Vinjer high-sulfidation system); BDL (below detection limit).

Appendix 3.2. Electron microprobe analyses (in wt%) of alunite from the studied epithermal systems and respective structural formulas.

Deposit	HP	HP	HP	HP	HP	HP	HP	HP	HP	HP	HP	HP	HP	HP	HP	HP	HP	HP
Sample	HP-4B	HP-4B	HP-4B	HP-4B	HP-4B	HP-4B	HP-4B	HP-4B	HP-4B	HP-4B	HP-4B	HP-4B	HP-4B	HP-4B	HP-4B	HP-4B	HP-4B	HP-4B
No. anal.	1	2	3	4	5	6	7	8	9	10	11	12	13	14	15	16	17	18
SiO_2	BDL	0.28	BDL	0.43	0.02	0.11	BDL	0.06	0.02	BDL	BDL	BDL	0.04	BDL	0.06	BDL	BDL	0.02
TiO_2	0.01	BDL	0.04	BDL	BDL	BDL	0.01	BDL	BDL	0.01	0.01	BDL	BDL	BDL	0.01	BDL	BDL	BDL
Al_2O_3	45.82	47.92	46.40	48.34	47.53	47.50	47.20	48.19	47.99	47.84	47.18	47.34	47.72	46.44	48.73	48.84	46.79	48.74
Ce_2O_3	0.14	0.03	0.09	0.03	0.16	BDL	0.05	0.01	0.05	0.06	0.06	BDL	0.05	0.07	0.06	BDL	0.03	0.04
Fe_2O_3	0.09	0.10	0.16	0.05	0.11	0.05	0.12	0.05	0.12	0.11	0.15	0.11	0.06	0.17	0.01	0.10	0.11	0.07
MnO	0.01	BDL	BDL	BDL	BDL	BDL	0.02	0.01	BDL	BDL	BDL	0.01	BDL	BDL	BDL	0.02	BDL	BDL
MgO	BDL	BDL	0.02	BDL	BDL	BDL	0.01	BDL	BDL	0.01	BDL	BDL	BDL	0.01	BDL	BDL	0.02	BDL
P_2O_5	0.88	0.41	1.39	0.46	0.91	0.54	0.58	0.39	0.38	0.49	0.36	0.48	0.43	0.57	0.27	0.36	1.29	0.77
BaO	0.36	0.25	1.16	0.23	0.43	0.25	0.42	BDL	0.20	0.27	0.19	0.25	BDL	0.25	0.15	0.12	0.52	0.29
SO_3	39.91	41.14	38.08	41.41	39.30	41.66	41.42	41.90	40.85	39.75	40.57	41.01	42.25	39.44	41.57	42.01	39.30	42.34
SrO	0.29	0.13	0.49	0.15	0.25	0.22	0.25	0.15	0.11	0.13	0.15	0.23	0.09	0.18	0.11	0.15	0.39	0.27
CaO	0.25	0.13	0.29	0.17	0.24	0.17	0.15	0.13	0.12	0.12	0.12	0.13	0.14	0.14	0.07	0.11	0.49	0.28
Na_2O	2.36	3.98	2.23	3.70	2.58	3.99	2.36	3.78	2.04	2.34	2.23	2.19	3.72	2.23	3.06	2.26	2.01	3.93
K_2O	5.76	2.41	5.73	2.78	4.85	2.72	6.02	2.53	6.30	5.76	6.02	6.03	2.73	6.07	4.37	5.97	6.03	2.37
Cl	0.02	0.00	0.00	0.03	BDL	0.00	0.01	BDL	BDL	0.00	0.00	0.02	0.01	BDL	0.02	0.01	BDL	BDL
F	BDL	0.04	BDL	0.06	0.06	BDL	BDL	BDL	0.05	0.10	0.09	0.08	BDL	0.08	BDL	0.02	BDL	BDL
Total	95.84	96.76	96.05	97.76	96.31	97.18	98.59	93.67	98.19	96.92	97.06	97.80	93.37	95.61	98.43	99.88	96.88	99.07
Si	-	0.016	-	0.025	0.001	0.006	-	0.004	0.001	-	-	-	0.002	-	0.003	-	-	0.001
Ti	0.000	-	0.002	-	-	-	0.001	-	-	0.001	0.000	-	-	-	0.000	-	-	-
Al_{Total}	3.292	3.324	3.380	3.260	3.346	3.321	3.297	3.358	3.324	3.308	3.257	3.248	3.317	3.282	3.371	3.335	3.355	3.341
Ce	0.003	0.001	0.002	0.001	0.004	-	0.001	0.000	0.001	0.001	0.001	-	0.001	0.002	0.001	-	0.001	0.001
Fe^{3+}	0.004	0.004	0.007	0.002	0.005	0.002	0.005	0.002	0.005	0.004	0.006	0.004	0.002	0.007	0.000	0.004	0.004	0.003
Mn	0.000	-	-	-	-	-	0.001	0.001	-	-	-	0.000	-	-	-	0.001	-	-
Mg	-	-	0.002	-	-	-	0.001	-	-	0.001	-	-	-	0.001	-	-	0.001	-
P	0.046	0.021	0.073	0.023	0.046	0.027	0.029	0.020	0.019	0.024	0.018	0.024	0.021	0.029	0.014	0.018	0.066	0.038
Ba	0.009	0.006	0.028	0.005	0.010	0.006	0.010	-	0.005	0.006	0.004	0.006	-	0.006	0.003	0.003	0.012	0.007
S	1.826	1.817	1.766	1.778	1.761	1.855	1.843	1.859	1.802	1.750	1.783	1.792	1.870	1.775	1.831	1.826	1.794	1.848
Sr	0.010	0.004	0.017	0.005	0.009	0.007	0.009	0.005	0.004	0.004	0.005	0.008	0.003	0.006	0.004	0.005	0.014	0.009
Ca	0.016	0.008	0.019	0.011	0.016	0.011	0.010	0.008	0.008	0.007	0.008	0.008	0.009	0.009	0.004	0.007	0.032	0.017
Na	0.278	0.454	0.267	0.411	0.299	0.459	0.272	0.433	0.233	0.266	0.253	0.247	0.426	0.259	0.348	0.254	0.237	0.443
K	0.448	0.181	0.452	0.203	0.369	0.206	0.455	0.191	0.472	0.431	0.450	0.448	0.205	0.464	0.327	0.441	0.468	0.176
Cl	0.002	0.000	0.000	0.003	-	0.000	0.001	-	-	0.000	0.000	0.002	0.001	-	0.002	0.001	-	-
F	-	0.007	-	0.012	0.011	-	-	-	0.009	0.018	0.017	0.014	-	0.015	0.000	0.004	-	-

Alunite formulae calculated on basis of 11 oxygen atoms. All iron was considered as Fe^{3+}. Abbreviations: HP (Hickey's Pond high-sulfidation deposit); BDL (below detection limit).

Appendix 3.2. Electron microprobe analyses (in wt%) of alunite from the studied epithermal systems and respective structural formulas.

Deposit	HP	HP	HP	HP	HP	HP	HP	HP	HP	HP	HP	HP	HP	HP	HP	HP	HP	HP
Sample	HP-4B	HP-4B	HP-4B	HP-6	HP-6	HP-6	HP-6	HP-6	HP-6	HP-6	HP-6	HP-6	HP-6	HP-6	HP-6	HP-6	HP-6	HP-6
No. anal.	19	20	21	1	2	3	4	5	6	7	8	9	10	11	12	13	14	15
SiO_2	BDL	0.15	0.28	0.14	0.10	0.06	0.19	0.08	BDL	0.13	BDL	BDL	0.03	BDL	BDL	BDL	BDL	BDL
TiO_2	BDL	BDL	BDL	BDL	BDL	BDL	0.01	BDL	0.01	BDL	BDL	0.01	0.02	0.01	BDL	BDL	BDL	BDL
Al_2O_3	46.79	48.55	45.44	48.40	47.18	47.09	45.60	47.02	46.32	46.60	46.73	47.08	46.43	46.19	47.30	45.49	45.91	47.58
Ce_2O_3	BDL	0.08	0.07	0.07	0.01	BDL	0.07	0.03	0.03	0.06	0.12	0.02	0.19	0.03	BDL	0.06	0.08	0.09
Fe_2O_3	0.13	0.05	0.08	0.07	0.03	0.11	0.17	0.05	0.09	0.09	0.11	0.03	0.14	0.20	0.10	0.13	0.13	0.16
MnO	BDL	0.01	BDL	0.00	BDL	0.01	0.02	0.02	BDL	BDL	BDL	0.03	BDL	BDL	BDL	BDL	BDL	0.00
MgO	BDL	BDL	0.01	BDL	0.01	BDL	BDL	BDL	BDL	BDL	BDL	BDL	BDL	0.02	0.01	BDL	0.01	0.02
P_2O_5	0.65	0.62	0.56	1.44	0.49	0.80	0.85	1.06	0.94	1.08	0.90	0.09	2.61	0.70	1.07	0.78	0.55	0.61
BaO	0.36	0.27	0.25	0.42	0.20	0.30	0.38	0.24	0.33	0.43	0.44	0.12	0.83	0.33	0.53	0.37	0.26	0.23
SO_3	39.48	41.73	39.38	41.41	41.39	40.17	41.47	40.99	39.59	41.48	40.84	41.26	39.07	40.67	41.37	40.25	41.16	40.87
SrO	0.24	0.21	0.21	0.37	0.21	0.20	0.23	0.32	0.33	0.30	0.28	0.08	0.66	0.23	0.37	0.23	0.28	0.22
CaO	0.19	0.21	0.21	0.49	0.19	0.26	0.29	0.34	0.24	0.38	0.29	0.21	0.84	0.22	0.42	0.27	0.21	0.18
Na_2O	2.25	4.28	2.29	3.64	3.92	2.92	2.92	3.72	2.71	3.65	2.92	2.74	2.59	2.83	4.44	2.92	2.86	2.86
K_2O	5.64	2.21	5.98	2.59	2.98	4.60	4.75	3.18	4.74	3.00	4.60	5.13	4.16	4.74	1.78	4.62	4.78	4.71
Cl	0.01	0.01	BDL	BDL	BDL	0.00	BDL	BDL	BDL	BDL	BDL	0.01	BDL	BDL	0.00	BDL	BDL	0.01
F	0.02	BDL	BDL	0.12	BDL	0.06	0.07	0.04	0.02	BDL	0.02	0.08	0.12	0.07	BDL	BDL	0.03	0.09
Total	95.73	98.31	94.69	99.11	96.66	96.53	96.95	97.00	95.27	97.12	97.21	96.82	97.59	96.16	97.32	95.07	96.22	97.57
Si	-	0.009	0.018	0.008	0.006	0.004	0.011	0.005	-	0.008	-	-	0.002	-	-	-	-	-
Ti	-	-	-	-	-	-	0.000	-	0.000	-	-	0.000	0.001	0.000	-	-	-	-
Al_{Total}	3.347	3.351	3.322	3.208	3.324	3.290	3.164	3.265	3.327	3.272	3.292	3.241	3.169	3.229	3.301	3.291	3.244	3.254
Ce	-	0.002	0.002	0.001	0.000	-	0.001	0.001	0.001	0.001	0.003	0.000	0.004	0.001	-	0.001	0.002	0.002
Fe^{3+}	0.005	0.002	0.003	0.003	0.001	0.004	0.007	0.002	0.004	0.004	0.004	0.001	0.005	0.008	0.004	0.005	0.005	0.006
Mn	-	0.000	-	0.000	-	0.001	0.001	0.001	-	-	-	0.001	-	-	-	-	-	0.000
Mg	-	-	0.001	-	0.001	-	-	-	-	-	-	-	-	0.002	0.001	-	0.001	0.002
P	0.034	0.031	0.029	0.069	0.025	0.040	0.042	0.053	0.048	0.054	0.045	0.005	0.128	0.035	0.053	0.041	0.028	0.030
Ba	0.009	0.006	0.006	0.009	0.005	0.007	0.009	0.005	0.008	0.010	0.010	0.003	0.019	0.008	0.012	0.009	0.006	0.005
S	1.798	1.834	1.833	1.748	1.857	1.787	1.832	1.812	1.810	1.855	1.832	1.809	1.698	1.810	1.839	1.854	1.852	1.780
Sr	0.009	0.007	0.007	0.012	0.007	0.007	0.008	0.011	0.012	0.010	0.010	0.003	0.022	0.008	0.013	0.008	0.010	0.008
Ca	0.013	0.013	0.014	0.030	0.012	0.016	0.018	0.021	0.016	0.025	0.018	0.013	0.052	0.014	0.027	0.018	0.013	0.011
Na	0.265	0.485	0.275	0.397	0.454	0.335	0.333	0.425	0.321	0.421	0.338	0.311	0.291	0.326	0.510	0.348	0.333	0.322
K	0.437	0.165	0.474	0.186	0.227	0.348	0.357	0.239	0.369	0.228	0.351	0.382	0.307	0.359	0.134	0.362	0.366	0.348
Cl	0.001	0.001	-	-	-	0.000	-	-	-	-	-	0.001	-	-	0.001	-	-	0.001
F	0.004	-	-	0.021	-	0.011	0.012	0.008	0.004	-	0.003	0.015	0.022	0.013	-	-	0.006	0.016

Alunite formulae calculated on basis of 11 oxygen atoms. All iron was considered as Fe^{3+}. Abbreviations: HP (Hickey's Pond high-sulfidation deposit); BDL (below detection limit).

Appendix 3.2. Electron microprobe analyses (in wt%) of alunite from the studied epithermal systems and respective structural formulas.

Deposit	HP	HP	HP	HP	HP	HP	HP	HP	HP	HP	HP	HP	HP	HP	HP	HP	HP	HP
Sample	HP-6	HP-6	HP-6	HP-6	HP-6	HP-6	HP-6	HP-3A	HP-3A	HP-3A	HP-3A	HP-3A	HP-3A	HP-3A	HP-3A	HP-3A	HP-3A	HP-3A
No. anal.	16	17	18	19	20	21	22	1	2	3	4	5	6	7	8	9	10	11
SiO_2	BDL	BDL	BDL	0.01	BDL	BDL	BDL	0.43	0.11	0.46	0.33	0.35	0.47	0.28	0.30	0.23	0.06	0.06
TiO_2	BDL	0.01	0.01	BDL	BDL	0.02	0.01	BDL	0.01	BDL	0.03	0.04	0.01	0.03	BDL	BDL	BDL	0.02
Al_2O_3	47.43	46.61	46.91	46.03	49.49	48.14	47.31	45.88	48.09	47.71	49.37	48.67	47.78	47.98	47.95	48.04	48.72	48.23
Ce_2O_3	0.04	0.05	0.03	BDL	BDL	BDL	BDL	BDL	0.01	BDL	BDL	0.03	0.01	0.02	0.06	BDL	0.12	0.06
Fe_2O_3	0.07	0.14	0.08	0.11	0.09	0.10	0.13	0.04	0.06	0.03	0.09	0.05	0.05	0.04	0.02	0.03	0.02	0.04
MnO	0.01	0.00	0.05	BDL	BDL	BDL	0.03	BDL	BDL	BDL	BDL	0.01	BDL	BDL	BDL	BDL	BDL	0.00
MgO	BDL	BDL	BDL	BDL	BDL	BDL	BDL	BDL	BDL	BDL	BDL	BDL	0.01	BDL	BDL	BDL	BDL	BDL
P_2O_5	0.73	0.58	0.95	0.62	0.72	1.56	0.48	0.58	0.75	0.48	0.43	0.68	0.51	0.35	0.47	0.68	0.62	0.61
BaO	0.28	0.29	0.31	0.25	0.37	0.50	0.20	0.24	0.21	0.26	0.20	0.29	0.24	0.15	0.26	0.17	0.25	0.17
SO_3	42.48	41.30	41.75	40.44	41.67	39.81	41.70	41.78	42.67	40.89	42.40	41.92	41.21	40.98	40.84	41.47	41.79	40.69
SrO	0.18	0.19	0.24	0.29	0.21	0.59	0.14	0.24	0.37	0.22	0.27	0.42	0.28	0.44	0.24	0.40	0.42	0.25
CaO	0.27	0.17	0.35	0.19	0.24	0.58	0.15	0.14	0.18	0.12	0.15	0.16	0.12	0.10	0.09	0.18	0.14	0.12
Na_2O	3.78	2.89	4.05	2.83	3.56	3.51	2.86	3.39	3.83	3.55	3.57	3.79	3.82	3.54	3.62	3.89	3.68	3.63
K_2O	2.99	4.94	2.29	4.88	2.85	2.78	4.85	3.56	2.75	3.39	3.22	2.66	3.06	1.29	3.43	2.79	3.14	3.63
Cl	0.01	BDL	BDL	BDL	0.01	0.01	BDL	BDL	0.01	BDL	BDL	0.01	0.01	BDL	BDL	BDL	0.01	BDL
F	BDL	0.02	0.03	0.02	BDL	0.10	BDL	0.18	0.03	0.06	0.08	0.09	0.02	BDL	0.01	0.02	0.03	0.03
Total	98.15	97.12	97.02	95.63	99.10	97.57	97.79	96.32	99.06	97.07	100.09	99.13	97.59	95.17	97.21	97.85	98.96	97.50
Si	-	-	-	0.001	-	-	-	0.024	0.006	0.027	0.019	0.020	0.028	0.017	0.018	0.014	0.004	0.003
Ti	-	0.000	0.000	-	-	0.001	0.001	-	0.000	-	0.001	0.002	0.001	0.001	-	-	-	0.001
Al_{Total}	3.278	3.277	3.256	3.292	3.393	3.264	3.317	3.069	3.259	3.294	3.282	3.241	3.313	3.396	3.356	3.323	3.321	3.358
Ce	0.001	0.001	0.001	-	-	-	-	-	0.000	-	-	0.001	0.000	0.000	0.001	-	0.002	0.001
Fe^{3+}	0.003	0.006	0.003	0.004	0.003	0.004	0.005	0.001	0.002	0.001	0.004	0.002	0.002	0.002	0.001	0.001	0.001	0.001
Mn	0.001	0.000	0.002	-	-	-	0.002	-	-	-	-	0.000	-	-	-	-	-	0.000
Mg	-	-	-	-	-	-	-	-	-	-	-	-	0.001	-	-	-	-	-
P	0.036	0.029	0.047	0.032	0.036	0.076	0.024	0.028	0.036	0.024	0.021	0.033	0.025	0.018	0.023	0.034	0.030	0.030
Ba	0.006	0.007	0.007	0.006	0.008	0.011	0.005	0.005	0.005	0.006	0.004	0.006	0.006	0.004	0.006	0.004	0.006	0.004
S	1.870	1.849	1.845	1.842	1.819	1.719	1.862	1.780	1.842	1.798	1.795	1.777	1.820	1.847	1.820	1.826	1.814	1.804
Sr	0.006	0.007	0.008	0.010	0.007	0.020	0.005	0.008	0.012	0.007	0.009	0.014	0.009	0.015	0.008	0.014	0.014	0.009
Ca	0.017	0.011	0.022	0.013	0.015	0.036	0.010	0.008	0.011	0.008	0.009	0.010	0.008	0.007	0.006	0.011	0.009	0.008
Na	0.430	0.334	0.463	0.333	0.402	0.392	0.330	0.373	0.427	0.403	0.391	0.415	0.436	0.412	0.417	0.443	0.412	0.415
K	0.223	0.376	0.172	0.378	0.211	0.204	0.368	0.258	0.202	0.254	0.231	0.192	0.230	0.099	0.260	0.209	0.232	0.273
Cl	0.001	-	-	-	0.001	0.001	-	-	0.000	-	-	0.001	0.001	-	-	-	0.001	-
F	-	0.004	0.005	0.003	-	0.018	-	0.032	0.006	0.011	0.014	0.016	0.003	-	0.003	0.004	0.005	0.005

Alunite formulae calculated on basis of 11 oxygen atoms. All iron was considered as Fe^{3+}. Abbreviations: HP (Hickey's Pond high-sulfidation deposit); BDL (below detection limit).

Appendix 3.2. Electron microprobe analyses (in wt%) of alunite from the studied epithermal systems and respective structural formulas.

Deposit	HP	HP	HP	HP	HP	HP	HP	HP
Sample	HP-3A	HP-3A	HP-3A	HP-3A	HP-3A	HP-3A	HP-3A	HP-3A
No. anal.	12	13	14	15	16	17	18	19
SiO_2	0.11	0.17	0.04	1.19	0.01	0.04	0.01	0.09
TiO_2	0.11	0.01	BDL	0.01	BDL	BDL	1.79	0.01
Al_2O_3	47.08	46.51	46.50	44.43	44.75	47.52	46.53	46.58
Ce_2O_3	0.03	0.05	0.09	0.07	BDL	BDL	BDL	0.04
Fe_2O_3	0.03	0.02	0.05	0.07	0.07	0.09	0.01	0.01
MnO	BDL	0.03	BDL	BDL	BDL	0.01	0.03	BDL
MgO	0.02	BDL	BDL	BDL	BDL	BDL	BDL	BDL
P_2O_5	0.41	1.43	0.56	0.47	0.09	0.48	0.32	0.61
BaO	0.22	0.52	0.26	0.43	BDL	0.20	BDL	0.38
SO_3	40.67	39.56	41.34	40.07	40.00	42.89	41.30	42.36
SrO	0.22	0.50	0.35	0.14	BDL	0.32	0.27	0.23
CaO	0.09	0.14	0.15	0.05	0.00	0.12	0.06	0.18
Na_2O	2.90	2.11	3.33	1.98	1.63	3.69	4.11	3.50
K_2O	4.81	6.30	3.61	6.74	7.18	2.80	2.81	3.36
Cl	BDL	BDL	BDL	0.01	0.02	0.02	BDL	0.01
F	0.09	0.28	0.04	0.37	0.25	BDL	0.03	BDL
Total	96.75	97.52	96.25	95.83	91.28	98.12	97.19	97.31
Si	0.007	0.010	0.002	0.065	0.000	0.003	0.001	0.005
Ti	0.005	0.000	-	0.000	-	-	0.079	0.000
Al_{Total}	3.249	3.040	3.262	2.854	3.020	3.265	3.236	3.249
Ce	0.001	0.001	0.002	0.001	-	-	-	0.001
Fe^{3+}	0.001	0.001	0.002	0.003	0.003	0.004	0.000	0.000
Mn	-	0.001	-	-	-	0.000	0.001	-
Mg	0.002	-	-	-	-	-	-	-
P	0.020	0.067	0.028	0.021	0.005	0.024	0.016	0.030
Ba	0.005	0.011	0.006	0.009	-	0.004	-	0.009
S	1.787	1.647	1.847	1.639	1.719	1.877	1.829	1.881
Sr	0.007	0.016	0.012	0.004	-	0.011	0.009	0.008
Ca	0.006	0.008	0.010	0.003	0.000	0.008	0.004	0.012
Na	0.330	0.227	0.385	0.210	0.180	0.417	0.471	0.402
K	0.359	0.446	0.274	0.469	0.525	0.208	0.212	0.254
Cl	-	-	-	0.001	0.002	0.002	-	0.001
F	0.017	0.049	0.007	0.065	0.046	-	0.005	-

Alunite formulae calculated on basis of 11 oxygen atoms. All iron was considered as Fe^{3+}. Abbreviations: HP (Hickey's Pond high-sulfidation deposit); BDL (below detection limit).

Appendix 3.2. Electron microprobe analyses (in wt%) of rutile and calculated structural formulas.

Deposit	AP	AP	AP	AP	AP	AP	AP	AP	AP	AP	AP	AP	AP	AP
Sample	AP-704	AP-704	AP-704	AP-714	AP-714	AP-714	AP-714	AP-714	AP-714	AP-714	AP-714	AP-714	AP-714	AP-714
Drill hole	AP-05-01	AP-05-01	AP-05-01	AP-05-01	AP-05-01	AP-05-01	AP-05-01	AP-05-01	AP-05-01	AP-05-01	AP-05-01	AP-05-01	AP-05-01	AP-05-01
Depth (m)	14.90-14.97	14.90-14.97	14.90-14.97	42.98-43.07	42.98-43.07	42.98-43.07	42.98-43.07	42.98-43.07	42.98-43.07	42.98-43.07	42.98-43.07	42.98-43.07	42.98-43.07	42.98-43.07
Alteration Zone	Distal	Distal	Distal	Inter	Inter	Inter	Inter	Inter	Inter	Inter	Inter	Inter	Inter	Inter
No. anal.	1	2	3	1	2	4	5	7	8	9	10	11	12	13
TiO_2	100.02	96.01	98.85	98.35	98.18	99.29	98.66	99.24	98.82	98.39	99.22	99.32	100.29	99.17
SiO_2	0.08	1.57	0.11	0.06	0.03	0.06	0.17	0.04	0.32	0.06	0.17	0.02	0.05	0.18
Fe_2O_3	1.06	1.05	0.77	0.87	0.57	0.62	0.74	0.58	0.65	0.73	0.60	0.46	0.52	0.54
Cr_2O_3	BDL	BDL	BDL	BDL	BDL	BDL	BDL	BDL	BDL	BDL	BDL	BDL	BDL	BDL
V_2O_3	0.08	0.15	0.11	0.18	0.24	0.23	0.11	0.26	0.28	0.29	0.12	0.14	BDL	0.18
MnO	BDL	0.01	0.02	0.01	0.01	BDL	BDL	BDL	BDL	BDL	0.01	0.01	0.03	BDL
Al_2O_3	0.02	0.06	0.00	0.01	0.00	0.01	0.01	0.01	0.04	0.02	0.05	0.01	0.01	0.04
CaO	0.73	1.97	1.05	0.56	1.08	0.91	0.65	0.77	0.82	0.67	0.83	0.51	0.33	0.49
P_2O_5	BDL	BDL	BDL	BDL	BDL	0.01	BDL	BDL	BDL	BDL	BDL	BDL	0.01	BDL
ZrO_2	0.05	0.04	0.03	0.14	0.27	0.12	0.16	0.13	0.09	0.08	0.03	0.11	0.16	0.09
As_2O_5	BDL	BDL	BDL	BDL	BDL	BDL	BDL	BDL	0.04	BDL	BDL	BDL	BDL	BDL
Nb_2O_5	0.10	0.03	0.05	0.53	0.34	0.45	0.63	0.49	0.37	0.81	0.18	0.07	0.04	0.03
WO_3	BDL	BDL	BDL	BDL	BDL	BDL	BDL	BDL	BDL	BDL	BDL	BDL	BDL	BDL
Ta_2O_5	0.02	0.01	BDL	BDL	BDL	BDL	0.02	BDL	0.01	BDL	0.03	BDL	BDL	BDL
SnO_2	BDL	BDL	BDL	BDL	BDL	BDL	BDL	BDL	BDL	BDL	BDL	BDL	BDL	BDL
Sb_2O_5	BDL	BDL	BDL	BDL	BDL	BDL	BDL	BDL	BDL	BDL	BDL	BDL	BDL	BDL
Total	100.98	98.13	99.41	99.74	99.14	100.39	100.06	100.36	100.15	100.01	100.03	99.89	100.90	99.93
Ti	0.984	0.955	0.984	0.982	0.981	0.982	0.981	0.983	0.979	0.980	0.984	0.990	0.991	0.987
Si	0.001	0.021	0.001	0.001	0.000	0.001	0.002	0.001	0.004	0.001	0.002	0.000	0.001	0.002
Fe^{3+}	0.010	0.010	0.007	0.008	0.005	0.006	0.007	0.005	0.006	0.007	0.006	0.004	0.005	0.005
Cr	-	-	-	-	-	-	-	-	-	-	-	-	-	-
V	0.001	0.002	0.001	0.002	0.003	0.002	0.001	0.003	0.003	0.003	0.001	0.001	-	0.002
Mn	-	0.000	0.000	0.000	0.000	-	-	-	-	-	0.000	0.000	0.001	-
Al	0.000	0.001	0.000	0.000	0.000	0.000	0.000	0.000	0.001	0.000	0.001	0.000	0.000	0.001
Ca	0.010	0.028	0.015	0.008	0.015	0.013	0.009	0.011	0.012	0.009	0.012	0.007	0.005	0.007
P	-	-	-	-	-	0.000	-	-	-	-	-	-	0.000	-
Zr	0.000	0.000	0.000	0.001	0.002	0.001	0.001	0.001	0.001	0.001	0.000	0.001	0.001	0.001
As	-	-	-	-	-	-	-	-	0.000	-	-	-	-	-
Nb	0.001	0.000	0.000	0.003	0.002	0.003	0.004	0.003	0.002	0.005	0.001	0.000	0.000	0.000
W	-	-	-	-	-	-	-	-	-	-	-	-	-	-
Ta	0.000	0.000	-	-	-	-	0.000	-	0.000	-	0.000	-	-	-
Sn	-	-	-	-	-	-	-	-	-	-	-	-	-	-
Sb	-	-	-	-	-	-	-	-	-	-	-	-	-	-

Rutile formulae calculated on basis of 2 oxygen atoms and all iron was considered as Fe^{3+}. Abbreviations: AP (Animal Pond); BN (Stog'er Tight); AE (Argyle); BDL (below detection limit); Inter (Intermediate alteration zone).

Appendix 3.2. Electron microprobe analyses (in wt%) of rutile and calculated structural formulas.

Deposit	AP	AP	AP	AP	AP	AP	AP	AP	AP	AP	AP	AP	AP	AP
Sample	AP-714	AP-714	AP-714	AP-714	AP-714	AP-714	AP-714	AP-714	AP-714	AP-714	AP-714	AP-714	AP-714	AP-714
Drill hole	AP-05-01	AP-05-01	AP-05-01	AP-05-01	AP-05-01	AP-05-01	AP-05-01	AP-05-01	AP-05-01	AP-05-01	AP-05-01	AP-05-01	AP-05-01	AP-05-01
Depth (m)	42.98-43.07	42.98-43.07	42.98-43.07	42.98-43.07	42.98-43.07	42.98-43.07	42.98-43.07	42.98-43.07	42.98-43.07	42.98-43.07	42.98-43.07	42.98-43.07	42.98-43.07	42.98-43.07
Alteration Zone	Inter	Inter	Inter	Inter	Inter	Inter	Inter	Inter	Inter	Inter	Inter	Inter	Inter	Inter
No. anal.	14	15	16	17	18	19	21	22	23	24	25	26	27	28
TiO_2	100.06	99.61	100.03	99.73	98.70	99.29	100.14	99.73	99.89	99.51	99.78	99.18	98.46	98.98
SiO_2	0.08	0.08	0.02	0.04	0.23	0.10	0.04	0.06	0.04	0.07	0.01	0.04	0.03	0.03
Fe_2O_3	0.45	0.46	0.53	0.53	0.64	0.43	0.45	0.67	0.47	0.52	0.41	0.45	0.45	0.41
Cr_2O_3	BDL	BDL	BDL	BDL	BDL	BDL	BDL	BDL	BDL	BDL	BDL	0.01	BDL	BDL
V_2O_3	0.21	0.18	BDL	0.13	0.26	0.19	0.20	0.11	0.13	0.16	0.13	0.19	0.19	0.22
MnO	0.01	0.01	BDL	BDL	BDL	BDL	BDL	0.02	BDL	0.01	BDL	BDL	BDL	0.01
Al_2O_3	0.01	0.02	0.01	0.03	0.06	0.01	0.01	0.02	0.02	BDL	0.01	0.03	BDL	0.02
CaO	0.47	0.53	0.34	0.59	0.96	0.70	0.98	0.96	1.05	0.99	0.80	0.79	0.36	0.44
P_2O_5	BDL	0.01	BDL	BDL	BDL	BDL	BDL	BDL	BDL	BDL	BDL	0.01	BDL	BDL
ZrO_2	0.01	BDL	0.05	0.03	0.06	0.04	0.12	0.09	0.06	0.11	BDL	0.09	0.10	0.03
As_2O_5	BDL	0.02	BDL	0.01	0.01	BDL	BDL	BDL	0.04	BDL	BDL	BDL	0.05	BDL
Nb_2O_5	BDL	BDL	0.01	0.03	0.05	0.04	0.08	0.20	0.09	0.07	0.03	BDL	0.05	0.06
WO_3	BDL	BDL	BDL	BDL	BDL	BDL	BDL	BDL	BDL	0.02	BDL	BDL	BDL	0.04
Ta_2O_5	BDL	BDL	BDL	BDL	BDL	BDL	BDL	BDL	BDL	BDL	BDL	BDL	BDL	BDL
SnO_2	0.01	BDL	BDL	0.01	0.01	BDL	BDL	BDL	BDL	BDL	BDL	BDL	BDL	BDL
Sb_2O_5	BDL	BDL	BDL	BDL	BDL	BDL	BDL	BDL	BDL	BDL	BDL	BDL	BDL	BDL
Total	100.59	100.04	100.39	100.20	99.56	99.72	100.60	100.48	100.29	100.06	99.93	99.63	99.08	99.60
Ti	0.990	0.990	0.993	0.990	0.982	0.988	0.986	0.984	0.986	0.986	0.990	0.988	0.991	0.991
Si	0.001	0.001	0.000	0.000	0.003	0.001	0.001	0.001	0.001	0.001	0.000	0.001	0.000	0.000
Fe^{3+}	0.004	0.004	0.005	0.005	0.006	0.004	0.004	0.006	0.004	0.005	0.004	0.004	0.004	0.004
Cr	-	-	-	-	-	-	-	-	-	-	-	0.000	-	-
V	0.002	0.002	-	0.001	0.003	0.002	0.002	0.001	0.001	0.002	0.001	0.002	0.002	0.002
Mn	0.000	0.000	-	-	-	-	-	0.000	-	0.000	-	-	-	0.000
Al	0.000	0.000	0.000	0.000	0.001	0.000	0.000	0.000	0.000	-	0.000	0.000	-	0.000
Ca	0.007	0.008	0.005	0.008	0.014	0.010	0.014	0.014	0.015	0.014	0.011	0.011	0.005	0.006
P	-	0.000	-	-	-	-	-	-	-	-	-	0.000	-	-
Zr	0.000	-	0.000	0.000	0.000	0.000	0.001	0.001	0.000	0.001	-	0.001	0.001	0.000
As	-	0.000	-	0.000	0.000	-	-	-	0.000	-	-	-	0.000	-
Nb	-	-	0.000	0.000	0.000	0.000	0.000	0.001	0.001	0.000	0.000	-	0.000	0.000
W	-	-	-	-	-	-	-	-	-	0.000	-	-	-	0.000
Ta	-	-	-	-	-	-	-	-	-	-	-	-	-	-
Sn	0.000	-	-	0.000	0.000	-	-	-	-	-	-	-	-	-
Sb	-	-	-	-	-	-	-	-	-	-	-	-	-	-

Rutile formulae calculated on basis of 2 oxygen atoms and all iron was considered as Fe^{3+}. Abbreviations: AP (Animal Pond); BN (Stog'er Tight); AE (Argyle); BDL (below detection limit); Inter (Intermediate alteration zone).

Appendix 3.2. Electron microprobe analyses (in wt%) of rutile and calculated structural formulas.

Deposit	AP	AP	AP	AP	AP	AP	AP	AP	AP	AP	AP	AP	AP	AP
Sample	AP-714	AP-714	AP-714	AP-722	AP-722	AP-722	AP-722	AP-722	AP-722	AP-722	AP-722	AP-722	AP-722	AP-722
Drill hole	AP-05-01	AP-05-01	AP-05-01	AP-05-01	AP-05-01	AP-05-01	AP-05-01	AP-05-01	AP-05-01	AP-05-01	AP-05-01	AP-05-01	AP-05-01	AP-05-01
Depth (m)	42.98-43.07	42.98-43.07	42.98-43.07	65.67-65.75	65.67-65.75	65.67-65.75	65.67-65.75	65.67-65.75	65.67-65.75	65.67-65.75	65.67-65.75	65.67-65.75	65.67-65.75	65.67-65.75
Alteration Zone	Inter	Inter	Inter	Proximal	Proximal	Proximal	Proximal	Proximal	Proximal	Proximal	Proximal	Proximal	Proximal	Proximal
No. anal.	29	30	31	1	2	3	4	5	6	7	8	9	10	11
TiO_2	100.06	100.36	99.88	96.44	95.93	96.12	100.03	100.77	96.24	95.90	95.07	96.36	96.15	95.34
SiO_2	0.04	0.12	0.14	0.17	0.10	0.18	0.20	0.17	0.15	0.17	0.29	0.20	0.20	0.21
Fe_2O_3	0.45	0.49	0.60	4.25	4.35	4.37	0.40	0.35	4.43	4.31	5.27	4.38	4.64	5.10
Cr_2O_3	BDL	BDL	BDL	BDL	BDL	BDL	BDL	BDL	BDL	BDL	BDL	BDL	BDL	BDL
V_2O_3	0.04	0.17	0.20	0.04	0.07	0.05	BDL	0.06	0.08	0.05	0.08	0.05	0.09	0.05
MnO	BDL	BDL	BDL	BDL	BDL	0.01	0.03	0.04	0.01	0.02	0.01	0.04	0.03	0.01
Al_2O_3	0.01	0.03	0.05	0.03	0.02	0.02	0.02	0.03	0.02	0.04	0.03	0.03	0.03	0.01
CaO	0.73	0.75	0.59	0.31	0.21	0.24	0.51	0.72	0.28	0.21	0.21	0.16	0.17	0.21
P_2O_5	0.01	0.01	BDL	BDL	BDL	BDL	BDL	BDL	BDL	0.01	BDL	BDL	BDL	BDL
ZrO_2	0.11	0.05	0.10	0.08	0.09	0.09	BDL	BDL	0.07	0.06	0.11	0.18	0.06	0.10
As_2O_5	BDL	BDL	BDL	0.04	BDL	0.02	BDL	BDL	0.02	0.02	0.03	0.02	BDL	BDL
Nb_2O_5	BDL	0.04	0.04	BDL	BDL	0.02	0.03	0.02	0.02	0.01	BDL	0.03	0.01	0.01
WO_3	BDL	BDL	0.02	BDL	BDL	BDL	BDL	BDL	0.02	BDL	BDL	0.01	BDL	BDL
Ta_2O_5	BDL	BDL	BDL	0.04	BDL	BDL	BDL	BDL	0.01	BDL	0.02	BDL	BDL	0.03
SnO_2	BDL	0.01	0.01	0.02	0.01	BDL	BDL	BDL	0.01	BDL	BDL	0.01	BDL	BDL
Sb_2O_5	BDL	BDL	BDL	BDL	BDL	BDL	BDL	BDL	BDL	BDL	BDL	BDL	BDL	BDL
Total	100.27	100.93	100.71	100.53	100.03	100.28	100.43	101.12	100.49	99.98	100.21	100.76	100.62	100.15
Ti	0.990	0.987	0.986	0.962	0.963	0.962	0.990	0.989	0.961	0.962	0.953	0.961	0.960	0.956
Si	0.001	0.002	0.002	0.002	0.001	0.002	0.003	0.002	0.002	0.002	0.004	0.003	0.003	0.003
Fe^{3+}	0.004	0.004	0.006	0.039	0.040	0.041	0.004	0.003	0.041	0.040	0.049	0.041	0.043	0.047
Cr	-	-	-	-	-	-	-	-	-	-	-	-	-	-
V	0.000	0.002	0.002	0.000	0.001	0.001	-	0.001	0.001	0.001	0.001	0.000	0.001	0.001
Mn	-	-	-	-	-	0.000	0.001	0.001	0.000	0.000	0.000	0.001	0.001	0.000
Al	0.000	0.001	0.001	0.000	0.000	0.000	0.000	0.000	0.000	0.001	0.001	0.000	0.000	0.000
Ca	0.010	0.011	0.008	0.004	0.003	0.003	0.007	0.010	0.004	0.003	0.003	0.002	0.002	0.003
P	0.000	0.000	-	-	-	-	-	-	-	0.000	-	-	-	-
Zr	0.001	0.000	0.001	0.000	0.001	0.001	-	-	0.000	0.000	0.001	0.001	0.000	0.001
As	-	-	-	0.000	-	0.000	-	-	0.000	0.000	0.000	0.000	-	-
Nb	-	0.000	0.000	-	-	0.000	0.000	0.000	0.000	0.000	-	0.000	0.000	0.000
W	-	-	0.000	-	-	-	-	-	0.000	-	-	0.000	-	-
Ta	-	-	-	0.000	-	-	-	-	0.000	-	0.000	-	-	0.000
Sn	-	0.000	0.000	0.000	0.000	-	-	-	0.000	-	-	0.000	-	-
Sb	-	-	-	-	-	-	-	-	-	-	-	-	-	-

Rutile formulae calculated on basis of 2 oxygen atoms and all iron was considered as Fe^{3+}. Abbreviations: AP (Animal Pond); BN (Stog'er Tight); AE (Argyle); BDL (below detection limit); Inter (Intermediate alteration zone).

Appendix 3.2. Electron microprobe analyses (in wt%) of rutile and calculated structural formulas.

Deposit	AP	AP	AP	AP	AP	AP	AP	AP	AP	AP	AP	AP	AP	AP
Sample	AP-722	AP-722	AP-722	AP-722	AP-722	AP-722	AP-722	AP-722	AP-722	AP-722	AP-722	AP-722	AP-722	AP-722
Drill hole	AP-05-01	AP-05-01	AP-05-01	AP-05-01	AP-05-01	AP-05-01	AP-05-01	AP-05-01	AP-05-01	AP-05-01	AP-05-01	AP-05-01	AP-05-01	AP-05-01
Depth (m)	65.67-65.75	65.67-65.75	65.67-65.75	65.67-65.75	65.67-65.75	65.67-65.75	65.67-65.75	65.67-65.75	65.67-65.75	65.67-65.75	65.67-65.75	65.67-65.75	65.67-65.75	65.67-65.75
Alteration Zone	Proximal	Proximal	Proximal	Proximal	Proximal	Proximal	Proximal	Proximal	Proximal	Proximal	Proximal	Proximal	Proximal	Proximal
No. anal.	12	13	14	15	16	17	18	19	20	21	22	23	24	25
TiO_2	95.08	96.96	95.59	96.80	96.63	97.31	97.15	97.61	97.03	97.75	96.24	96.86	98.91	99.56
SiO_2	0.19	0.09	0.13	0.21	0.09	0.23	0.20	0.15	0.24	0.20	0.23	0.29	0.10	0.06
Fe_2O_3	5.80	3.88	4.19	3.85	3.87	3.97	3.74	3.13	3.56	2.72	4.30	3.75	2.45	1.59
Cr_2O_3	BDL	BDL	BDL	BDL	BDL	BDL	BDL	BDL	BDL	BDL	BDL	BDL	BDL	BDL
V_2O_3	0.02	0.07	0.07	0.05	0.07	0.06	0.02	0.04	0.06	0.05	0.03	0.06	0.07	0.02
MnO	0.02	BDL	BDL	0.01	0.01	BDL	0.01	0.01	BDL	0.01	0.02	0.04	BDL	0.02
Al_2O_3	0.01	0.03	0.00	0.02	0.03	0.02	0.04	0.02	0.04	0.03	0.03	0.05	0.02	0.00
CaO	0.16	0.18	0.97	0.82	0.29	0.38	0.29	0.08	0.34	0.14	0.30	0.50	0.21	0.38
P_2O_5	BDL	BDL	BDL	BDL	0.01	BDL	BDL	BDL	0.01	BDL	BDL	BDL	0.01	BDL
ZrO_2	0.08	0.14	0.20	0.10	0.10	0.10	0.15	0.20	0.23	0.06	0.14	0.48	0.10	0.05
As_2O_5	0.02	0.05	BDL	0.05	BDL	BDL	BDL	0.02	BDL	0.04	BDL	0.02	0.01	BDL
Nb_2O_5	0.02	0.14	0.05	0.10	0.26	0.10	0.09	0.15	0.08	0.12	0.07	0.05	0.14	0.11
WO_3	BDL	BDL	BDL	BDL	BDL	BDL	BDL	BDL	0.01	BDL	BDL	BDL	BDL	BDL
Ta_2O_5	0.04	BDL	BDL	BDL	BDL	BDL	BDL	0.02	BDL	BDL	BDL	BDL	BDL	BDL
SnO_2	0.01	BDL	BDL	BDL	BDL	BDL	BDL	BDL	BDL	BDL	BDL	BDL	BDL	BDL
Sb_2O_5	BDL	BDL	BDL	BDL	BDL	BDL	BDL	BDL	BDL	BDL	BDL	BDL	BDL	BDL
Total	100.61	100.78	99.35	100.47	100.46	101.20	100.77	100.99	100.75	100.57	100.44	100.95	101.37	101.02
Ti	0.951	0.965	0.958	0.960	0.964	0.963	0.965	0.971	0.965	0.974	0.961	0.960	0.976	0.983
Si	0.003	0.001	0.002	0.003	0.001	0.003	0.003	0.002	0.003	0.003	0.003	0.004	0.001	0.001
Fe^{3+}	0.054	0.036	0.039	0.035	0.036	0.036	0.034	0.029	0.033	0.025	0.040	0.035	0.022	0.015
Cr	-	-	-	-	-	-	-	-	-	-	-	-	-	-
V	0.000	0.001	0.001	0.001	0.001	0.001	0.000	0.000	0.001	0.000	0.000	0.001	0.001	0.000
Mn	0.001	-	-	0.000	0.000	-	0.000	0.000	-	0.000	0.000	0.001	-	0.000
Al	0.000	0.000	0.000	0.000	0.001	0.000	0.001	0.000	0.001	0.000	0.000	0.001	0.000	0.000
Ca	0.002	0.003	0.014	0.012	0.004	0.005	0.004	0.001	0.005	0.002	0.004	0.007	0.003	0.005
P	-	-	-	-	0.000	-	-	-	0.000	-	-	-	0.000	-
Zr	0.001	0.001	0.001	0.001	0.001	0.001	0.001	0.001	0.001	0.000	0.001	0.003	0.001	0.000
As	0.000	0.000	-	0.000	-	-	-	0.000	-	0.000	-	0.000	0.000	-
Nb	0.000	0.001	0.000	0.001	0.002	0.001	0.001	0.001	0.001	0.001	0.000	0.000	0.001	0.001
W	-	-	-	-	-	-	-	-	0.000	-	-	-	-	-
Ta	0.000	-	-	-	-	-	-	0.000	-	-	-	-	-	-
Sn	0.000	-	-	-	-	-	-	-	-	-	-	-	-	-
Sb	-	-	-	-	-	-	-	-	-	-	-	-	-	-

Rutile formulae calculated on basis of 2 oxygen atoms and all iron was considered as Fe^{3+}. Abbreviations: AP (Animal Pond); BN (Stog'er Tight); AE (Argyle); BDL (below detection limit); Inter (Intermediate alteration zone).

Appendix 3.2. Electron microprobe analyses (in wt%) of rutile and calculated structural formulas.

Deposit	AP	AP	AP	AP	AP	AP	AP	AP	AP	AP	BN	BN	BN	BN
Sample	AP-722	AP-722	AP-722	AP-722	AP-722	AP-722	AP-722	AP-722	AP-722	AP-722	BN-730	BN-730	BN-730	BN-730
Drill hole	AP-05-01	AP-05-01	AP-05-01	AP-05-01	AP-05-01	AP-05-01	AP-05-01	AP-05-01	AP-05-01	AP-05-01	BN-14-187	BN-14-187	BN-14-187	BN-14-187
Depth (m)	65.67-65.75	65.67-65.75	65.67-65.75	65.67-65.75	65.67-65.75	65.67-65.75	65.67-65.75	65.67-65.75	65.67-65.75	65.67-65.75	14.01-14.16	14.01-14.16	14.01-14.16	14.01-14.16
Alteration Zone	Proximal	Proximal	Proximal	Proximal	Proximal	Proximal	Proximal	Proximal	Proximal	Proximal	Proximal	Proximal	Proximal	Proximal
No. anal.	26	27	28	29	30	31	32	33	34	35	1	2	3	4
TiO_2	98.97	97.61	97.18	96.62	100.44	95.08	95.46	96.25	96.64	97.90	98.66	98.88	98.79	98.57
SiO_2	0.07	0.15	0.13	0.16	0.03	0.12	0.24	0.17	0.22	0.26	0.08	0.10	0.09	0.10
Fe_2O_3	1.99	3.77	4.25	3.88	0.95	6.09	4.22	4.89	4.15	2.91	0.52	0.45	0.43	0.56
Cr_2O_3	BDL	BDL	BDL	BDL	BDL	BDL	BDL	BDL	BDL	BDL	BDL	BDL	BDL	BDL
V_2O_3	0.04	0.04	0.09	0.03	0.06	0.06	0.11	0.08	0.07	0.07	0.13	0.18	0.26	0.19
MnO	BDL	0.01	0.03	0.02	BDL	0.02	0.01	0.01	0.04	0.03	BDL	BDL	0.02	BDL
Al_2O_3	0.02	0.04	0.03	0.03	0.02	0.02	0.04	0.04	0.02	0.03	0.01	0.02	0.01	0.01
CaO	0.09	0.22	0.15	0.77	0.26	0.26	0.42	0.19	0.32	0.46	0.10	0.07	0.02	0.02
P_2O_5	BDL	BDL	BDL	0.01	BDL	BDL	BDL	BDL	BDL	BDL	BDL	BDL	BDL	0.02
ZrO_2	0.14	0.08	0.09	0.07	BDL	0.16	0.13	0.10	0.13	0.06	0.05	0.12	0.11	0.02
As_2O_5	BDL	BDL	BDL	BDL	BDL	0.05	0.04	BDL	BDL	0.02	0.02	BDL	BDL	0.03
Nb_2O_5	0.15	0.04	0.04	0.04	BDL	BDL	0.02	0.03	0.01	0.01	0.12	0.15	0.08	0.06
WO_3	BDL	BDL	BDL	BDL	BDL	BDL	BDL	BDL	BDL	BDL	BDL	BDL	0.01	BDL
Ta_2O_5	0.01	BDL	BDL	BDL	BDL	BDL	0.02	0.03	BDL	BDL	0.04	0.01	BDL	BDL
SnO_2	BDL	BDL	BDL	BDL	BDL	BDL	BDL	0.01	BDL	BDL	BDL	BDL	BDL	BDL
Sb_2O_5	BDL	BDL	BDL	BDL	BDL	BDL	BDL	BDL	BDL	BDL	BDL	BDL	BDL	BDL
Total	101.09	101.11	101.23	100.14	101.21	100.86	99.64	100.98	100.68	100.75	99.49	99.82	99.67	99.53
Ti	0.981	0.967	0.964	0.962	0.990	0.949	0.959	0.958	0.962	0.970	0.992	0.991	0.992	0.992
Si	0.001	0.002	0.002	0.002	0.000	0.002	0.003	0.002	0.003	0.003	0.001	0.001	0.001	0.001
Fe^{3+}	0.018	0.035	0.039	0.036	0.009	0.056	0.039	0.045	0.038	0.027	0.005	0.004	0.004	0.005
Cr	-	-	-	-	-	-	-	-	-	-	-	-	-	-
V	0.000	0.000	0.001	0.000	0.001	0.001	0.001	0.001	0.001	0.001	0.001	0.002	0.003	0.002
Mn	-	0.000	0.001	0.000	-	0.000	0.000	0.000	0.001	0.001	-	-	0.000	-
Al	0.000	0.001	0.000	0.000	0.000	0.000	0.001	0.001	0.000	0.000	0.000	0.000	0.000	0.000
Ca	0.001	0.003	0.002	0.011	0.004	0.004	0.006	0.003	0.005	0.006	0.001	0.001	0.000	0.000
P	-	-	-	0.000	-	-	-	-	-	-	-	-	-	0.000
Zr	0.001	0.000	0.001	0.000	-	0.001	0.001	0.001	0.001	0.000	0.000	0.001	0.001	0.000
As	-	-	-	-	-	0.000	0.000	-	-	0.000	0.000	-	-	0.000
Nb	0.001	0.000	0.000	0.000	-	-	0.000	0.000	0.000	0.000	0.001	0.001	0.000	0.000
W	-	-	-	-	-	-	-	-	-	-	-	-	0.000	-
Ta	0.000	-	-	-	-	-	0.000	0.000	-	-	0.000	0.000	-	-
Sn	-	-	-	-	-	-	-	0.000	-	-	-	-	-	-
Sb	-	-	-	-	-	-	-	-	-	-	-	-	-	-

Rutile formulae calculated on basis of 2 oxygen atoms and all iron was considered as Fe^{3+}. Abbreviations: AP (Animal Pond); BN (Stog'er Tight); AE (Argyle); BDL (below detection limit); Inter (Intermediate alteration zone).

Appendix 3.2. Electron microprobe analyses (in wt%) of rutile and calculated structural formulas.

Deposit	BN	BN	BN	BN	BN	BN	BN	BN	BN	BN	BN	BN	BN	BN
Sample	BN-730	BN-730	BN-730	BN-730	BN-730	BN-730	BN-730	BN-730	BN-730	BN-730	BN-730	BN-730	BN-730	BN-730
Drill hole	BN-14-187	BN-14-187	BN-14-187	BN-14-187	BN-14-187	BN-14-187	BN-14-187	BN-14-187	BN-14-187	BN-14-187	BN-14-187	BN-14-187	BN-14-187	BN-14-187
Depth (m)	14.01-14.16	14.01-14.16	14.01-14.16	14.01-14.16	14.01-14.16	14.01-14.16	14.01-14.16	14.01-14.16	14.01-14.16	14.01-14.16	14.01-14.16	14.01-14.16	14.01-14.16	14.01-14.16
Alteration Zone	Proximal	Proximal	Proximal	Proximal	Proximal	Proximal	Proximal	Proximal	Proximal	Proximal	Proximal	Proximal	Proximal	Proximal
No. anal.	5	6	7	8	9	10	11	12	13	14	15	16	17	18
TiO_2	97.02	99.33	99.08	98.34	99.43	100.28	99.96	100.73	98.74	99.70	100.39	98.51	99.65	98.21
SiO_2	2.66	0.12	0.13	0.12	0.03	BDL	0.03	0.05	0.03	0.04	0.06	0.02	0.22	0.25
Fe_2O_3	0.56	0.35	0.35	0.36	0.69	0.48	0.52	0.64	0.51	0.50	0.50	0.78	0.58	0.59
Cr_2O_3	BDL	BDL	0.01	BDL	BDL	BDL	BDL	BDL	BDL	BDL	BDL	BDL	BDL	BDL
V_2O_3	0.13	0.17	0.15	0.19	0.33	0.14	0.09	0.15	0.18	0.11	0.15	0.07	0.19	0.11
MnO	0.01	0.01	0.04	0.01	BDL	BDL	BDL	0.01	BDL	0.01	BDL	0.03	0.02	0.01
Al_2O_3	0.02	0.06	0.07	0.04	0.00	0.02	0.02	0.03	0.02	0.00	0.03	0.01	0.00	0.01
CaO	0.04	0.13	0.04	0.02	1.61	0.13	0.12	0.37	0.11	0.09	0.17	1.30	0.54	0.17
P_2O_5	0.02	BDL	BDL	BDL	BDL	BDL	BDL	BDL	BDL	BDL	BDL	BDL	BDL	BDL
ZrO_2	0.01	0.07	0.02	BDL	0.02	0.02	0.05	0.07	0.04	0.09	0.08	BDL	0.04	BDL
As_2O_5	BDL	0.01	BDL	BDL	BDL	BDL	BDL	BDL	BDL	0.03	BDL	BDL	BDL	BDL
Nb_2O_5	0.02	0.03	0.07	0.06	0.03	0.05	0.07	0.05	0.03	0.07	0.07	0.05	0.05	0.02
WO_3	BDL	0.01	0.07	0.04	BDL	BDL	0.01	0.01	0.01	BDL	0.02	BDL	0.01	BDL
Ta_2O_5	BDL	BDL	BDL	BDL	BDL	0.02	BDL	BDL	BDL	BDL	BDL	BDL	BDL	BDL
SnO_2	BDL	BDL	BDL	BDL	BDL	BDL	BDL	BDL	BDL	BDL	BDL	BDL	BDL	BDL
Sb_2O_5	BDL	BDL	BDL	BDL	BDL	BDL	BDL	BDL	BDL	BDL	BDL	BDL	BDL	BDL
Total	100.28	100.03	99.80	99.07	100.00	100.85	100.59	101.53	99.43	100.38	101.14	98.94	100.50	98.98
Ti	0.959	0.992	0.992	0.993	0.980	0.994	0.993	0.990	0.993	0.993	0.992	0.983	0.987	0.990
Si	0.035	0.002	0.002	0.002	0.000	-	0.000	0.001	0.000	0.001	0.001	0.000	0.003	0.003
Fe^{3+}	0.005	0.003	0.003	0.003	0.006	0.004	0.005	0.006	0.005	0.005	0.005	0.007	0.005	0.006
Cr	-	-	0.000	-	-	-	-	-	-	-	-	-	-	-
V	0.001	0.002	0.002	0.002	0.003	0.001	0.001	0.002	0.002	0.001	0.002	0.001	0.002	0.001
Mn	0.000	0.000	0.000	0.000	-	-	-	0.000	-	0.000	-	0.000	0.000	0.000
Al	0.000	0.001	0.001	0.001	0.000	0.000	0.000	0.000	0.000	0.000	0.000	0.000	0.000	0.000
Ca	0.000	0.002	0.001	0.000	0.023	0.002	0.002	0.005	0.002	0.001	0.002	0.019	0.008	0.002
P	0.000	-	-	-	-	-	-	-	-	-	-	-	-	-
Zr	0.000	0.000	0.000	-	0.000	0.000	0.000	0.000	0.000	0.001	0.000	-	0.000	-
As	-	0.000	-	-	-	-	-	-	-	0.000	-	-	-	-
Nb	0.000	0.000	0.000	0.000	0.000	0.000	0.000	0.000	0.000	0.000	0.000	0.000	0.000	0.000
W	-	0.000	0.000	0.000	-	-	0.000	0.000	0.000	-	0.000	-	0.000	-
Ta	-	-	-	-	-	0.000	-	-	-	-	-	-	-	-
Sn	-	-	-	-	-	-	-	-	-	-	-	-	-	-
Sb	-	-	-	-	-	-	-	-	-	-	-	-	-	-

Rutile formulae calculated on basis of 2 oxygen atoms and all iron was considered as Fe^{3+}. Abbreviations: AP (Animal Pond); BN (Stog'er Tight); AE (Argyle); BDL (below detection limit); Inter (Intermediate alteration zone).

Appendix 3.2. Electron microprobe analyses (in wt%) of rutile and calculated structural formulas.

Deposit	BN	BN	BN	BN	BN	BN	BN	BN	BN	BN	BN	BN	BN	BN
Sample	BN-730	BN-730	BN-730	BN-730	BN-730	BN-730	BN-730	BN-730	BN-730	BN-730	BN-730	BN-730	BN-730	BN-730
Drill hole	BN-14-187	BN-14-187	BN-14-187	BN-14-187	BN-14-187	BN-14-187	BN-14-187	BN-14-187	BN-14-187	BN-14-187	BN-14-187	BN-14-187	BN-14-187	BN-14-187
Depth (m)	14.01-14.16	14.01-14.16	14.01-14.16	14.01-14.16	14.01-14.16	14.01-14.16	14.01-14.16	14.01-14.16	14.01-14.16	14.01-14.16	14.01-14.16	14.01-14.16	14.01-14.16	14.01-14.16
Alteration Zone	Proximal	Proximal	Proximal	Proximal	Proximal	Proximal	Proximal	Proximal	Proximal	Proximal	Proximal	Proximal	Proximal	Proximal
No. anal.	19	20	21	22	23	24	25	26	27	28	29	30	31	32
TiO_2	98.71	99.16	99.63	99.35	99.42	99.29	99.87	98.45	99.67	99.63	99.32	99.87	98.21	99.38
SiO_2	0.12	0.12	0.04	0.06	0.07	0.06	0.05	0.11	0.06	0.08	0.05	0.04	0.06	0.04
Fe_2O_3	0.46	0.48	0.45	0.48	0.56	0.58	0.48	0.55	0.45	0.40	0.45	0.54	0.67	0.68
Cr_2O_3	BDL	BDL	BDL	BDL	BDL	BDL	BDL	BDL	BDL	BDL	BDL	BDL	BDL	0.01
V_2O_3	0.08	0.19	0.14	0.10	0.09	0.08	0.08	0.09	0.10	0.13	0.13	0.08	0.10	0.12
MnO	BDL	0.01	0.01	BDL	BDL	BDL	0.01	BDL	BDL	BDL	BDL	BDL	BDL	0.01
Al_2O_3	0.01	0.01	0.00	0.01	0.02	0.02	0.02	BDL	0.01	0.02	0.01	0.01	0.03	0.02
CaO	0.23	0.13	0.01	BDL	0.18	0.13	0.03	0.08	0.01	0.07	0.17	0.17	0.04	0.00
P_2O_5	BDL	BDL	BDL	BDL	BDL	BDL	BDL	BDL	BDL	0.01	BDL	0.02	BDL	BDL
ZrO_2	0.01	BDL	0.02	0.04	0.08	0.06	0.03	0.01	BDL	0.06	0.07	0.04	BDL	0.01
As_2O_5	BDL	0.01	0.01	BDL	BDL	0.01	BDL	0.01	BDL	BDL	BDL	0.01	BDL	BDL
Nb_2O_5	0.06	0.02	0.12	0.05	0.04	0.04	0.06	0.15	0.05	BDL	BDL	0.09	0.06	0.12
WO_3	BDL	0.03	BDL	BDL	BDL	BDL	BDL	0.01	BDL	BDL	0.01	0.01	0.05	BDL
Ta_2O_5	BDL	BDL	BDL	0.01	BDL	BDL	BDL	BDL	BDL	BDL	BDL	BDL	BDL	0.02
SnO_2	BDL	BDL	0.01	BDL	BDL	BDL	BDL	BDL	BDL	BDL	BDL	BDL	BDL	BDL
Sb_2O_5	BDL	BDL	BDL	BDL	BDL	BDL	0.02	BDL	0.02	BDL	BDL	BDL	BDL	0.01
Total	99.25	99.85	100.32	99.99	100.10	99.90	100.49	99.33	100.22	100.20	99.87	100.56	99.08	100.33
Ti	0.992	0.992	0.994	0.994	0.992	0.992	0.994	0.992	0.994	0.994	0.993	0.992	0.992	0.992
Si	0.002	0.002	0.001	0.001	0.001	0.001	0.001	0.001	0.001	0.001	0.001	0.001	0.001	0.001
Fe^{3+}	0.004	0.004	0.004	0.004	0.005	0.005	0.004	0.005	0.004	0.004	0.004	0.005	0.006	0.006
Cr	-	-	-	-	-	-	-	-	-	-	-	-	-	0.000
V	0.001	0.002	0.001	0.001	0.001	0.001	0.001	0.001	0.001	0.001	0.001	0.001	0.001	0.001
Mn	-	0.000	0.000	-	-	-	0.000	-	-	-	-	-	-	0.000
Al	0.000	0.000	0.000	0.000	0.000	0.000	0.000	-	0.000	0.000	0.000	0.000	0.000	0.000
Ca	0.003	0.002	0.000	-	0.003	0.002	0.000	0.001	0.000	0.001	0.002	0.002	0.001	0.000
P	-	-	-	-	-	-	-	-	-	0.000	-	0.000	-	-
Zr	0.000	-	0.000	0.000	0.001	0.000	0.000	0.000	-	0.000	0.000	0.000	-	0.000
As	-	0.000	0.000	-	-	0.000	-	0.000	-	-	-	0.000	-	-
Nb	0.000	0.000	0.001	0.000	0.000	0.000	0.000	0.001	0.000	-	-	0.001	0.000	0.001
W	-	0.000	-	-	-	-	-	0.000	-	-	0.000	0.000	0.000	-
Ta	-	-	-	0.000	-	-	-	-	-	-	-	-	-	0.000
Sn	-	-	0.000	-	-	-	-	-	-	-	-	-	-	-
Sb	-	-	-	-	-	-	0.000	-	0.000	-	-	-	-	0.000

Rutile formulae calculated on basis of 2 oxygen atoms and all iron was considered as Fe^{3+}. Abbreviations: AP (Animal Pond); BN (Stog'er Tight); AE (Argyle); BDL (below detection limit); Inter (Intermediate alteration zone).

Appendix 3.2. Electron microprobe analyses (in wt%) of rutile and calculated structural formulas.

Deposit	BN	BN	BN	BN	BN	BN	BN	BN	BN	BN	BN	BN	BN	BN
Sample	BN-730	BN-730	BN-730	BN-739	BN-739	BN-739	BN-739	BN-739	BN-739	BN-739	BN-739	BN-739	BN-739	BN-739
Drill hole	BN-14-187	BN-14-187	BN-14-187	BN-14-187	BN-14-187	BN-14-187	BN-14-187	BN-14-187	BN-14-187	BN-14-187	BN-14-187	BN-14-187	BN-14-187	BN-14-187
Depth (m)	14.01-14.16	14.01-14.16	14.01-14.16	28.35-28.53	28.35-28.53	28.35-28.53	28.35-28.53	28.35-28.53	28.35-28.53	28.35-28.53	28.35-28.53	28.35-28.53	28.35-28.53	28.35-28.53
Alteration Zone	Proximal	Proximal	Proximal	Distal	Distal	Distal	Distal	Distal	Distal	Distal	Distal	Distal	Distal	Distal
No. anal.	33	34	35	1	2	3	4	5	6	7	8	9	10	11
TiO_2	99.42	99.40	99.60	99.98	100.90	100.37	99.42	99.45	100.58	99.09	99.85	100.46	100.70	100.35
SiO_2	0.02	0.05	0.03	0.08	0.04	0.05	0.16	0.04	0.03	0.12	0.03	0.04	0.06	0.04
Fe_2O_3	0.56	0.62	0.59	0.75	0.69	0.78	0.86	0.85	0.68	0.93	0.82	0.75	0.71	0.69
Cr_2O_3	BDL	BDL	BDL	BDL	BDL	BDL	BDL	BDL	BDL	BDL	BDL	BDL	BDL	BDL
V_2O_3	0.12	0.17	0.11	0.19	0.19	0.22	0.20	0.23	0.15	0.21	0.22	0.18	0.18	0.24
MnO	BDL	BDL	BDL	BDL	0.02	BDL	BDL	BDL	0.01	0.01	BDL	BDL	BDL	BDL
Al_2O_3	0.02	0.02	0.01	0.01	0.01	0.01	0.08	0.01	0.02	0.07	0.03	0.02	0.01	0.01
CaO	0.01	0.02	0.01	0.00	0.01	BDL	0.00	BDL	0.01	BDL	BDL	BDL	0.01	0.00
P_2O_5	BDL	BDL	BDL	0.01	0.01	0.01	0.01	BDL	0.01	BDL	BDL	BDL	BDL	BDL
ZrO_2	0.03	0.07	0.04	0.05	0.08	0.04	BDL	0.06	0.06	0.08	0.09	0.07	BDL	0.08
As_2O_5	0.02	0.02	0.01	0.02	BDL	BDL	BDL	BDL	0.03	BDL	BDL	BDL	BDL	BDL
Nb_2O_5	0.14	0.25	0.17	0.14	0.14	0.13	0.09	0.18	0.14	0.32	0.37	0.48	0.33	0.30
WO_3	BDL	BDL	BDL	BDL	BDL	BDL	BDL	BDL	BDL	BDL	0.05	0.03	BDL	BDL
Ta_2O_5	BDL	BDL	BDL	BDL	BDL	BDL	BDL	BDL	BDL	BDL	BDL	0.01	BDL	0.02
SnO_2	BDL	BDL	BDL	BDL	BDL	BDL	0.01	BDL	BDL	BDL	0.01	BDL	BDL	BDL
Sb_2O_5	0.01	BDL	BDL	0.01	BDL	0.01	BDL	0.01	BDL	0.01	BDL	BDL	BDL	0.01
Total	100.29	100.38	100.46	101.07	101.92	101.43	100.63	100.66	101.58	100.60	101.27	101.90	101.69	101.54
Ti	0.993	0.990	0.993	0.990	0.991	0.990	0.988	0.989	0.991	0.986	0.988	0.988	0.990	0.989
Si	0.000	0.001	0.000	0.001	0.001	0.001	0.002	0.001	0.000	0.002	0.000	0.000	0.001	0.001
Fe^{3+}	0.005	0.006	0.005	0.007	0.006	0.007	0.008	0.008	0.006	0.009	0.008	0.007	0.007	0.006
Cr	-	-	-	-	-	-	-	-	-	-	-	-	-	-
V	0.001	0.002	0.001	0.002	0.002	0.002	0.002	0.002	0.002	0.002	0.002	0.002	0.002	0.003
Mn	-	-	-	-	0.000	-	-	-	0.000	0.000	-	-	-	-
Al	0.000	0.000	0.000	0.000	0.000	0.000	0.001	0.000	0.000	0.001	0.000	0.000	0.000	0.000
Ca	0.000	0.000	0.000	0.000	0.000	-	0.000	-	0.000	-	-	-	0.000	0.000
P	-	-	-	0.000	0.000	0.000	0.000	-	0.000	-	-	-	-	-
Zr	0.000	0.000	0.000	0.000	0.000	0.000	-	0.000	0.000	0.001	0.001	0.000	-	0.001
As	0.000	0.000	0.000	0.000	-	-	-	-	0.000	-	-	-	-	-
Nb	0.001	0.001	0.001	0.001	0.001	0.001	0.001	0.001	0.001	0.002	0.002	0.003	0.002	0.002
W	-	-	-	-	-	-	-	-	-	-	0.000	0.000	-	-
Ta	-	-	-	-	-	-	-	-	-	-	-	0.000	-	0.000
Sn	-	-	-	-	-	-	0.000	-	-	-	0.000	-	-	-
Sb	0.000	-	-	0.000	-	0.000	-	0.000	-	0.000	-	-	-	0.000

Rutile formulae calculated on basis of 2 oxygen atoms and all iron was considered as Fe^{3+}. Abbreviations: AP (Animal Pond); BN (Stog'er Tight); AE (Argyle); BDL (below detection limit); Inter (Intermediate alteration zone).

Appendix 3.2. Electron microprobe analyses (in wt%) of rutile and calculated structural formulas.

Deposit	BN	BN	BN	BN	BN	BN	BN	BN	BN	BN	BN	BN	BN	BN
Sample	BN-739	BN-739	BN-739	BN-739	BN-739	BN-739	BN-739	BN-739	BN-739	BN-739	BN-739	BN-739	BN-739	BN-739
Drill hole	BN-14-187	BN-14-187	BN-14-187	BN-14-187	BN-14-187	BN-14-187	BN-14-187	BN-14-187	BN-14-187	BN-14-187	BN-14-187	BN-14-187	BN-14-187	BN-14-187
Depth (m)	28.35-28.53	28.35-28.53	28.35-28.53	28.35-28.53	28.35-28.53	28.35-28.53	28.35-28.53	28.35-28.53	28.35-28.53	28.35-28.53	28.35-28.53	28.35-28.53	28.35-28.53	28.35-28.53
Alteration Zone	Distal	Distal	Distal	Distal	Distal	Distal	Distal	Distal	Distal	Distal	Distal	Distal	Distal	Distal
No. anal.	12	14	15	16	17	18	19	21	22	23	24	25	26	27
TiO_2	100.12	100.59	99.84	100.25	101.58	99.65	100.31	100.71	100.43	100.45	100.77	100.39	99.98	99.17
SiO_2	0.04	BDL	0.01	0.02	0.01	BDL	BDL	BDL	0.01	0.03	0.01	0.01	0.03	0.02
Fe_2O_3	0.72	0.75	0.98	0.77	0.95	0.94	0.82	0.85	0.93	0.88	0.81	1.18	0.60	0.52
Cr_2O_3	BDL	BDL	BDL	BDL	BDL	BDL	BDL	BDL	BDL	BDL	BDL	BDL	BDL	BDL
V_2O_3	0.14	0.11	0.10	0.15	0.23	0.18	0.08	0.24	0.16	0.22	0.20	0.17	0.20	0.13
MnO	BDL	0.01	0.01	BDL	BDL	BDL	0.01	0.01	0.01	0.02	BDL	0.01	BDL	0.03
Al_2O_3	0.01	0.02	0.01	0.01	0.00	0.02	0.02	0.02	0.03	0.02	0.02	0.01	0.02	0.01
CaO	0.03	0.10	0.12	0.64	0.03	0.14	0.11	0.04	0.36	0.11	0.21	0.10	0.32	0.09
P_2O_5	BDL	0.02	BDL	BDL	BDL	BDL	BDL	0.01	0.01	BDL	BDL	BDL	0.01	BDL
ZrO_2	0.17	0.05	BDL	0.05	0.15	0.03	0.11	0.03	0.02	0.07	0.14	0.12	0.03	0.16
As_2O_5	0.01	BDL	BDL	0.01	BDL	0.01	BDL	BDL	0.03	BDL	BDL	BDL	BDL	BDL
Nb_2O_5	0.23	BDL	0.05	0.04	0.01	0.03	0.05	0.06	BDL	0.08	0.06	0.09	0.06	0.08
WO_3	BDL	BDL	BDL	BDL	BDL	BDL	BDL	BDL	BDL	BDL	BDL	0.04	BDL	0.02
Ta_2O_5	0.02	BDL	BDL	BDL	BDL	BDL	BDL	BDL	BDL	BDL	BDL	BDL	BDL	0.01
SnO_2	BDL	BDL	BDL	0.01	BDL	0.01	BDL	BDL	0.01	BDL	BDL	BDL	BDL	0.01
Sb_2O_5	BDL	BDL	BDL	BDL	BDL	BDL	BDL	BDL	BDL	BDL	BDL	BDL	BDL	BDL
Total	101.27	101.31	100.77	100.96	102.71	100.60	101.20	101.72	101.32	101.54	101.74	101.83	100.70	100.02
Ti	0.990	0.992	0.990	0.988	0.990	0.990	0.991	0.991	0.988	0.989	0.989	0.987	0.990	0.992
Si	0.000	-	0.000	0.000	0.000	-	-	-	0.000	0.000	0.000	0.000	0.000	0.000
Fe^{3+}	0.007	0.007	0.009	0.007	0.009	0.009	0.008	0.008	0.008	0.008	0.007	0.011	0.006	0.005
Cr	-	-	-	-	-	-	-	-	-	-	-	-	-	-
V	0.002	0.001	0.001	0.002	0.002	0.002	0.001	0.002	0.002	0.002	0.002	0.002	0.002	0.001
Mn	-	0.000	0.000	-	-	-	0.000	0.000	0.000	0.000	-	0.000	-	0.000
Al	0.000	0.000	0.000	0.000	0.000	0.000	0.000	0.000	0.000	0.000	0.000	0.000	0.000	0.000
Ca	0.000	0.001	0.002	0.009	0.000	0.002	0.002	0.001	0.005	0.001	0.003	0.001	0.004	0.001
P	-	0.000	-	-	-	-	-	0.000	0.000	-	-	-	0.000	-
Zr	0.001	0.000	-	0.000	0.001	0.000	0.001	0.000	0.000	0.000	0.001	0.001	0.000	0.001
As	0.000	-	-	0.000	-	0.000	-	-	0.000	-	-	-	-	-
Nb	0.001	-	0.000	0.000	0.000	0.000	0.000	0.000	-	0.000	0.000	0.001	0.000	0.000
W	-	-	-	-	-	-	-	-	-	-	-	0.000	-	0.000
Ta	0.000	-	-	-	-	-	-	-	-	-	-	-	-	0.000
Sn	-	-	-	0.000	-	0.000	-	-	0.000	-	-	-	-	0.000
Sb	-	-	-	-	-	-	-	-	-	-	-	-	-	-

Rutile formulae calculated on basis of 2 oxygen atoms and all iron was considered as Fe^{3+}. Abbreviations: AP (Animal Pond); BN (Stog'er Tight); AE (Argyle); BDL (below detection limit); Inter (Intermediate alteration zone).

Appendix 3.2. Electron microprobe analyses (in wt%) of rutile and calculated structural formulas.

Deposit	BN	BN	BN	BN	BN	BN	BN	BN	BN	BN	BN	BN	BN	BN
Sample	BN-739	BN-739	BN-739	BN-739	BN-748	BN-748	BN-748	BN-748	BN-748	BN-748	BN-748	BN-748	BN-748	BN-748
Drill hole	BN-14-187	BN-14-187	BN-14-187	BN-14-187	BN-14-187	BN-14-187	BN-14-187	BN-14-187	BN-14-187	BN-14-187	BN-14-187	BN-14-187	BN-14-187	BN-14-187
Depth (m)	28.35-28.53	28.35-28.53	28.35-28.53	28.35-28.53	41.34-41.46	41.34-41.46	41.34-41.46	41.34-41.46	41.34-41.46	41.34-41.46	41.34-41.46	41.34-41.46	41.34-41.46	41.34-41.46
Alteration Zone	Distal	Distal	Distal	Distal	Inter	Inter	Inter	Inter	Inter	Inter	Inter	Inter	Inter	Inter
No. anal.	28	29	30	31	1	2	3	4	5	6	7	8	9	10
TiO_2	99.41	100.47	99.99	99.04	99.39	100.99	100.41	99.58	100.22	100.84	99.28	99.50	99.84	100.47
SiO_2	0.02	0.05	0.03	0.03	BDL	0.01	0.02	0.15	BDL	BDL	0.01	0.02	BDL	BDL
Fe_2O_3	0.52	0.63	0.55	0.62	0.86	0.78	0.80	0.69	0.79	0.74	0.65	0.64	0.70	0.75
Cr_2O_3	BDL	BDL	BDL	BDL	BDL	BDL	BDL	BDL	BDL	BDL	BDL	BDL	BDL	BDL
V_2O_3	0.20	0.25	0.17	0.11	0.10	0.21	0.13	0.10	0.02	0.16	0.07	0.06	0.19	0.13
MnO	BDL	0.02	0.03	0.03	BDL	BDL	BDL	BDL	BDL	BDL	0.01	BDL	BDL	BDL
Al_2O_3	0.02	0.02	0.02	0.02	0.03	0.01	0.03	0.12	0.01	0.01	0.02	0.02	0.02	0.01
CaO	0.22	0.15	0.35	0.11	0.61	0.23	0.23	0.17	0.56	0.48	0.21	0.14	0.44	0.62
P_2O_5	BDL	BDL	BDL	BDL	0.03	BDL	0.01	0.01	BDL	BDL	BDL	BDL	BDL	BDL
ZrO_2	0.09	0.06	0.06	0.06	BDL	0.06	BDL	0.03	0.05	0.02	0.09	0.04	0.04	0.04
As_2O_5	BDL	BDL	BDL	BDL	0.04	BDL	0.03	BDL	BDL	0.03	0.05	0.03	BDL	BDL
Nb_2O_5	0.03	0.03	0.05	0.04	0.31	0.22	0.24	0.20	0.10	0.30	0.21	0.14	0.10	0.10
WO_3	BDL	BDL	BDL	BDL	BDL	BDL	BDL	BDL	BDL	BDL	BDL	BDL	BDL	BDL
Ta_2O_5	BDL	BDL	BDL	BDL	BDL	BDL	BDL	BDL	BDL	BDL	BDL	0.02	BDL	BDL
SnO_2	BDL	0.01	BDL	BDL	BDL	BDL	BDL	BDL	BDL	BDL	BDL	BDL	BDL	BDL
Sb_2O_5	BDL	BDL	BDL	BDL	BDL	BDL	BDL	BDL	BDL	BDL	BDL	BDL	BDL	BDL
Total	100.07	101.36	100.58	99.83	100.47	102.06	101.38	100.46	100.73	101.76	100.07	100.20	100.62	101.12
Ti	0.992	0.991	0.991	0.992	0.985	0.989	0.989	0.988	0.989	0.987	0.990	0.992	0.989	0.988
Si	0.000	0.001	0.000	0.000	-	0.000	0.000	0.002	-	-	0.000	0.000	-	-
Fe^{3+}	0.005	0.006	0.005	0.006	0.008	0.007	0.007	0.006	0.007	0.007	0.006	0.006	0.006	0.007
Cr	-	-	-	-	-	-	-	-	-	-	-	-	-	-
V	0.002	0.003	0.002	0.001	0.001	0.002	0.001	0.001	0.000	0.002	0.001	0.001	0.002	0.001
Mn	-	0.000	0.000	0.000	-	-	-	-	-	-	0.000	-	-	-
Al	0.000	0.000	0.000	0.000	0.000	0.000	0.000	0.002	0.000	0.000	0.000	0.000	0.000	0.000
Ca	0.003	0.002	0.005	0.002	0.009	0.003	0.003	0.002	0.008	0.007	0.003	0.002	0.006	0.009
P	-	-	-	-	0.000	-	0.000	0.000	-	-	-	-	-	-
Zr	0.001	0.000	0.000	0.000	-	0.000	-	0.000	0.000	0.000	0.001	0.000	0.000	0.000
As	-	-	-	-	0.000	-	0.000	-	-	0.000	0.000	0.000	-	-
Nb	0.000	0.000	0.000	0.000	0.002	0.001	0.001	0.001	0.001	0.002	0.001	0.001	0.001	0.001
W	-	-	-	-	-	-	-	-	-	-	-	-	-	-
Ta	-	-	-	-	-	-	-	-	-	-	-	0.000	-	-
Sn	-	0.000	-	-	-	-	-	-	-	-	-	-	-	-
Sb	-	-	-	-	-	-	-	-	-	-	-	-	-	-

Rutile formulae calculated on basis of 2 oxygen atoms and all iron was considered as Fe^{3+}. Abbreviations: AP (Animal Pond); BN (Stog'er Tight); AE (Argyle); BDL (below detection limit); Inter (Intermediate alteration zone).

Appendix 3.2. Electron microprobe analyses (in wt%) of rutile and calculated structural formulas.

Deposit	BN	BN	BN	BN	BN	BN	BN	BN	BN	BN	BN	BN	BN	BN
Sample	BN-748	BN-748	BN-748	BN-748	BN-748	BN-748	BN-748	BN-748	BN-748	BN-748	BN-748	BN-748	BN-748	BN-748
Drill hole	BN-14-187	BN-14-187	BN-14-187	BN-14-187	BN-14-187	BN-14-187	BN-14-187	BN-14-187	BN-14-187	BN-14-187	BN-14-187	BN-14-187	BN-14-187	BN-14-187
Depth (m)	41.34-41.46	41.34-41.46	41.34-41.46	41.34-41.46	41.34-41.46	41.34-41.46	41.34-41.46	41.34-41.46	41.34-41.46	41.34-41.46	41.34-41.46	41.34-41.46	41.34-41.46	41.34-41.46
Alteration Zone	Inter	Inter	Inter	Inter	Inter	Inter	Inter	Inter	Inter	Inter	Inter	Inter	Inter	Inter
No. anal.	11	12	13	14	15	16	17	18	19	20	21	22	23	24
TiO_2	99.83	100.23	100.26	99.83	100.60	99.67	99.71	99.27	100.16	101.15	100.41	99.65	99.55	100.01
SiO_2	0.01	0.02	BDL	0.01	BDL	BDL	0.02	0.03	0.02	0.01	0.01	0.03	0.01	BDL
Fe_2O_3	0.82	0.62	0.78	0.72	0.84	0.72	0.52	0.55	0.67	0.65	0.66	0.63	0.64	0.56
Cr_2O_3	BDL	BDL	BDL	BDL	BDL	BDL	BDL	BDL	BDL	BDL	BDL	BDL	BDL	BDL
V_2O_3	0.14	0.16	0.12	0.19	0.09	0.17	0.17	0.08	0.14	0.06	0.05	0.06	0.11	0.12
MnO	0.03	BDL	BDL	BDL	BDL	0.01	BDL	0.01	BDL	BDL	0.01	0.02	BDL	BDL
Al_2O_3	0.01	0.03	0.03	0.00	0.02	0.01	0.03	0.01	0.02	0.02	0.03	0.01	0.01	0.03
CaO	0.01	0.01	0.13	0.16	0.42	0.22	0.02	0.03	0.01	0.00	0.08	0.07	0.09	0.04
P_2O_5	BDL	0.01	BDL	BDL	BDL	0.01	BDL	BDL	BDL	BDL	0.00	BDL	BDL	BDL
ZrO_2	BDL	BDL	0.09	0.08	0.07	0.03	0.13	0.12	0.16	0.07	0.05	0.13	0.13	0.08
As_2O_5	BDL	BDL	BDL	0.05	BDL	0.02	0.03	BDL	BDL	BDL	0.02	0.04	BDL	0.01
Nb_2O_5	0.29	0.09	0.19	0.17	0.16	0.29	0.06	0.13	0.09	0.07	0.05	0.17	0.05	0.02
WO_3	BDL	BDL	BDL	BDL	BDL	BDL	BDL	BDL	BDL	BDL	BDL	BDL	BDL	BDL
Ta_2O_5	BDL	BDL	BDL	BDL	0.05	0.03	BDL	BDL	BDL	BDL	BDL	BDL	BDL	BDL
SnO_2	BDL	BDL	0.02	0.02	BDL	BDL	BDL	BDL	BDL	BDL	BDL	BDL	BDL	BDL
Sb_2O_5	BDL	BDL	BDL	BDL	BDL	BDL	BDL	BDL	BDL	BDL	BDL	BDL	BDL	BDL
Total	100.92	100.89	101.25	100.92	101.56	100.71	100.49	99.94	100.97	101.75	101.12	100.53	100.33	100.63
Ti	0.990	0.993	0.990	0.989	0.988	0.989	0.992	0.993	0.992	0.993	0.993	0.991	0.992	0.993
Si	0.000	0.000	-	0.000	-	-	0.000	0.000	0.000	0.000	0.000	0.000	0.000	-
Fe^{3+}	0.008	0.006	0.007	0.007	0.008	0.007	0.005	0.005	0.006	0.006	0.006	0.006	0.006	0.005
Cr	-	-	-	-	-	-	-	-	-	-	-	-	-	-
V	0.001	0.002	0.001	0.002	0.001	0.002	0.002	0.001	0.001	0.001	0.000	0.001	0.001	0.001
Mn	0.000	-	-	-	-	0.000	-	0.000	-	-	0.000	0.000	-	-
Al	0.000	0.000	0.000	0.000	0.000	0.000	0.000	0.000	0.000	0.000	0.000	0.000	0.000	0.000
Ca	0.000	0.000	0.002	0.002	0.006	0.003	0.000	0.000	0.000	0.000	0.001	0.001	0.001	0.001
P	-	0.000	-	-	-	0.000	-	-	-	-	0.000	-	-	-
Zr	-	-	0.001	0.001	0.000	0.000	0.001	0.001	0.001	0.000	0.000	0.001	0.001	0.000
As	-	-	-	0.000	-	0.000	0.000	-	-	-	0.000	0.000	-	0.000
Nb	0.002	0.001	0.001	0.001	0.001	0.002	0.000	0.001	0.001	0.000	0.000	0.001	0.000	0.000
W	-	-	-	-	-	-	-	-	-	-	-	-	-	-
Ta	-	-	-	-	0.000	0.000	-	-	-	-	-	-	-	-
Sn	-	-	0.000	0.000	-	-	-	-	-	-	-	-	-	-
Sb	-	-	-	-	-	-	-	-	-	-	-	-	-	-

Rutile formulae calculated on basis of 2 oxygen atoms and all iron was considered as Fe^{3+}. Abbreviations: AP (Animal Pond); BN (Stog'er Tight); AE (Argyle); BDL (below detection limit); Inter (Intermediate alteration zone).

Appendix 3.2. Electron microprobe analyses (in wt%) of rutile and calculated structural formulas.

Deposit	BN	BN	BN	BN	BN	BN	AE	AE	AE	AE	AE	AE	AE	AE
Sample	BN-748	BN-748	BN-748	BN-748	BN-748	BN-748	AE-660	AE-660	AE-660	AE-660	AE-660	AE-660	AE-660	AE-660
Drill hole	BN-14-187	BN-14-187	BN-14-187	BN-14-187	BN-14-187	BN-14-187	AE-16-40	AE-16-40	AE-16-40	AE-16-40	AE-16-40	AE-16-40	AE-16-40	AE-16-40
Depth (m)	41.34-41.46	41.34-41.46	41.34-41.46	41.34-41.46	41.34-41.46	41.34-41.46	31.01-31.14	31.01-31.14	31.01-31.14	31.01-31.14	31.01-31.14	31.01-31.14	31.01-31.14	31.01-31.14
Alteration Zone	Inter	Inter	Inter	Inter	Inter	Inter	Proximal	Proximal	Proximal	Proximal	Proximal	Proximal	Proximal	Proximal
No. anal.	25	26	27	28	29	30	1	2	3	4	5	6	7	8
TiO_2	99.08	99.94	99.02	99.72	100.75	99.95	99.79	99.54	99.67	99.19	98.50	99.07	96.18	99.84
SiO_2	BDL	0.03	0.02	BDL	0.01	0.01	0.14	0.17	0.07	0.12	0.16	0.31	2.28	0.17
Fe_2O_3	0.58	0.50	0.82	0.79	0.71	0.71	0.32	0.29	0.36	0.35	0.48	0.42	0.37	0.38
Cr_2O_3	BDL	BDL	BDL	BDL	BDL	BDL	BDL	BDL	0.01	BDL	BDL	BDL	BDL	BDL
V_2O_3	0.09	0.14	0.10	0.09	0.09	0.12	0.33	0.41	0.33	0.21	0.38	0.41	0.24	0.37
MnO	BDL	0.02	BDL	0.01	BDL	BDL	BDL	BDL	BDL	0.01	0.01	BDL	0.01	BDL
Al_2O_3	0.02	0.03	0.01	0.02	0.01	0.01	0.04	0.06	0.05	0.05	0.05	0.10	0.10	0.05
CaO	0.05	0.04	0.45	0.38	0.25	0.37	0.02	0.22	0.11	0.04	0.22	0.05	0.11	0.21
P_2O_5	BDL	BDL	BDL	BDL	BDL	BDL	BDL	0.01	BDL	BDL	BDL	0.01	BDL	BDL
ZrO_2	0.03	0.04	0.08	0.06	0.09	0.17	BDL	0.02	BDL	BDL	0.08	0.02	BDL	BDL
As_2O_5	0.07	0.03	0.02	BDL	BDL	BDL	BDL	BDL	BDL	BDL	BDL	0.01	BDL	BDL
Nb_2O_5	0.06	0.08	0.16	0.09	0.11	0.15	0.05	0.04	0.05	BDL	0.13	0.02	0.07	0.06
WO_3	BDL	BDL	BDL	BDL	BDL	BDL	BDL	0.02	BDL	0.01	0.18	BDL	BDL	BDL
Ta_2O_5	BDL	BDL	BDL	BDL	BDL	BDL	BDL	BDL	BDL	BDL	BDL	BDL	0.04	BDL
SnO_2	BDL	BDL	BDL	BDL	BDL	BDL	BDL	BDL	BDL	BDL	BDL	BDL	BDL	BDL
Sb_2O_5	BDL	BDL	BDL	BDL	BDL	BDL	BDL	BDL	BDL	BDL	BDL	BDL	BDL	BDL
Total	99.73	100.56	100.00	100.52	101.54	100.77	100.39	100.36	100.28	99.74	99.66	100.09	99.04	100.58
Ti	0.993	0.993	0.987	0.989	0.991	0.989	0.992	0.989	0.992	0.993	0.987	0.987	0.962	0.989
Si	-	0.000	0.000	-	0.000	0.000	0.002	0.002	0.001	0.002	0.002	0.004	0.030	0.002
Fe^{3+}	0.005	0.005	0.008	0.007	0.006	0.007	0.003	0.003	0.003	0.003	0.004	0.004	0.003	0.004
Cr	-	-	-	-	-	-	-	-	0.000	-	-	-	-	-
V	0.001	0.001	0.001	0.001	0.001	0.001	0.003	0.004	0.004	0.002	0.004	0.004	0.003	0.004
Mn	-	0.000	-	0.000	-	-	-	-	-	0.000	0.000	-	0.000	-
Al	0.000	0.000	0.000	0.000	0.000	0.000	0.001	0.001	0.001	0.001	0.001	0.002	0.002	0.001
Ca	0.001	0.001	0.006	0.005	0.004	0.005	0.000	0.003	0.002	0.001	0.003	0.001	0.002	0.003
P	-	-	-	-	-	-	-	0.000	-	-	-	0.000	-	-
Zr	0.000	0.000	0.001	0.000	0.001	0.001	-	0.000	-	-	0.001	0.000	-	-
As	0.000	0.000	0.000	-	-	-	-	-	-	-	-	0.000	-	-
Nb	0.000	0.000	0.001	0.001	0.001	0.001	0.000	0.000	0.000	-	0.001	0.000	0.000	0.000
W	-	-	-	-	-	-	-	0.000	-	0.000	0.001	-	-	-
Ta	-	-	-	-	-	-	-	-	-	-	-	-	0.000	-
Sn	-	-	-	-	-	-	-	-	-	-	-	-	-	-
Sb	-	-	-	-	-	-	-	-	-	-	-	-	-	-

Rutile formulae calculated on basis of 2 oxygen atoms and all iron was considered as Fe^{3+}. Abbreviations: AP (Animal Pond); BN (Stog'er Tight); AE (Argyle); BDL (below detection limit); Inter (Intermediate alteration zone).

Appendix 3.2. Electron microprobe analyses (in wt%) of rutile and calculated structural formulas.

Deposit	AE	AE	AE	AE	AE	AE	AE	AE	AE	AE	AE	AE	AE	AE
Sample	AE-660	AE-660	AE-660	AE-660	AE-660	AE-660	AE-660	AE-660	AE-660	AE-660	AE-660	AE-660	AE-660	AE-660
Drill hole	AE-16-40	AE-16-40	AE-16-40	AE-16-40	AE-16-40	AE-16-40	AE-16-40	AE-16-40	AE-16-40	AE-16-40	AE-16-40	AE-16-40	AE-16-40	AE-16-40
Depth (m)	31.01-31.14	31.01-31.14	31.01-31.14	31.01-31.14	31.01-31.14	31.01-31.14	31.01-31.14	31.01-31.14	31.01-31.14	31.01-31.14	31.01-31.14	31.01-31.14	31.01-31.14	31.01-31.14
Alteration Zone	Proximal	Proximal	Proximal	Proximal	Proximal	Proximal	Proximal	Proximal	Proximal	Proximal	Proximal	Proximal	Proximal	Proximal
No. anal.	9	10	11	12	13	14	15	16	17	19	21	22	23	24
TiO_2	99.57	100.20	99.43	98.74	99.24	98.82	98.87	100.12	100.07	99.83	99.51	99.00	100.27	101.29
SiO_2	0.14	0.10	0.10	0.16	0.05	0.17	0.23	0.18	0.21	0.24	0.17	0.36	BDL	0.02
Fe_2O_3	0.37	0.39	0.31	0.37	0.39	0.40	0.35	0.64	0.47	0.43	0.42	0.47	0.35	0.38
Cr_2O_3	BDL	BDL	BDL	BDL	BDL	BDL	BDL	BDL	BDL	BDL	BDL	BDL	BDL	BDL
V_2O_3	0.45	0.44	0.32	0.33	0.29	0.42	0.31	0.19	0.26	0.35	0.18	0.34	0.28	0.29
MnO	0.01	BDL	0.02	BDL	BDL	0.02	BDL	BDL	BDL	BDL	BDL	0.01	0.03	BDL
Al_2O_3	0.05	0.05	0.05	0.05	0.00	0.04	0.07	0.13	0.07	0.07	0.07	0.10	0.01	0.03
CaO	0.05	0.13	0.10	0.12	0.13	0.09	0.02	0.24	0.26	0.08	0.09	0.07	0.01	0.14
P_2O_5	BDL	0.01	BDL	BDL	BDL	BDL	BDL	BDL	BDL	BDL	BDL	BDL	BDL	BDL
ZrO_2	BDL	BDL	0.04	0.06	BDL	0.04	0.10	0.04	0.03	0.04	0.12	0.01	0.03	0.04
As_2O_5	BDL	BDL	BDL	BDL	BDL	0.06	BDL	BDL	BDL	0.03	BDL	BDL	0.02	BDL
Nb_2O_5	0.07	0.03	0.02	0.04	0.02	0.04	0.06	0.10	0.05	BDL	0.08	0.12	0.02	0.03
WO_3	BDL	BDL	BDL	BDL	0.01	0.05	BDL	BDL	BDL	BDL	BDL	BDL	BDL	BDL
Ta_2O_5	BDL	BDL	BDL	BDL	BDL	BDL	BDL	BDL	BDL	BDL	BDL	BDL	BDL	BDL
SnO_2	BDL	BDL	BDL	0.01	BDL	BDL	BDL	BDL	BDL	BDL	BDL	BDL	BDL	BDL
Sb_2O_5	BDL	BDL	BDL	BDL	BDL	BDL	BDL	BDL	BDL	BDL	BDL	BDL	BDL	BDL
Total	100.37	100.96	100.10	99.57	99.85	99.95	99.74	101.10	100.80	100.73	100.38	100.21	100.86	101.87
Ti	0.990	0.990	0.992	0.990	0.993	0.989	0.990	0.987	0.989	0.989	0.990	0.986	0.994	0.993
Si	0.002	0.001	0.001	0.002	0.001	0.002	0.003	0.002	0.003	0.003	0.002	0.005	-	0.000
Fe^{3+}	0.003	0.004	0.003	0.003	0.004	0.004	0.003	0.006	0.004	0.004	0.004	0.004	0.003	0.003
Cr	-	-	-	-	-	-	-	-	-	-	-	-	-	-
V	0.005	0.005	0.003	0.004	0.003	0.004	0.003	0.002	0.003	0.004	0.002	0.004	0.003	0.003
Mn	0.000	-	0.000	-	-	0.000	-	-	-	-	-	0.000	0.000	-
Al	0.001	0.001	0.001	0.001	0.000	0.001	0.001	0.002	0.001	0.001	0.001	0.002	0.000	0.000
Ca	0.001	0.002	0.001	0.002	0.002	0.001	0.000	0.003	0.004	0.001	0.001	0.001	0.000	0.002
P	-	0.000	-	-	-	-	-	-	-	-	-	-	-	-
Zr	-	-	0.000	0.000	-	0.000	0.001	0.000	0.000	0.000	0.001	0.000	0.000	0.000
As	-	-	-	-	-	0.000	-	-	-	0.000	-	-	0.000	-
Nb	0.000	0.000	0.000	0.000	0.000	0.000	0.000	0.001	0.000	-	0.000	0.001	0.000	0.000
W	-	-	-	-	0.000	0.000	-	-	-	-	-	-	-	-
Ta	-	-	-	-	-	-	-	-	-	-	-	-	-	-
Sn	-	-	-	0.000	-	-	-	-	-	-	-	-	-	-
Sb	-	-	-	-	-	-	-	-	-	-	-	-	-	-

Rutile formulae calculated on basis of 2 oxygen atoms and all iron was considered as Fe^{3+}. Abbreviations: AP (Animal Pond); BN (Stog'er Tight); AE (Argyle); BDL (below detection limit); Inter (Intermediate alteration zone).

Appendix 3.2. Electron microprobe analyses (in wt%) of rutile and calculated structural formulas.

Deposit	AE	AE	AE	AE	AE	AE	AE	AE	AE	AE	AE	AE	AE	AE
Sample	AE-660	AE-660	AE-660	AE-660	AE-660	AE-660	AE-659	AE-659	AE-659	AE-659	AE-659	AE-659	AE-659	AE-659
Drill hole	AE-16-40	AE-16-40	AE-16-40	AE-16-40	AE-16-40	AE-16-40	AE-16-40	AE-16-40	AE-16-40	AE-16-40	AE-16-40	AE-16-40	AE-16-40	AE-16-40
Depth (m)	31.01-31.14	31.01-31.14	31.01-31.14	31.01-31.14	31.01-31.14	31.01-31.14	24.85-25.08	24.85-25.08	24.85-25.08	24.85-25.08	24.85-25.08	24.85-25.08	24.85-25.08	24.85-25.08
Alteration Zone	Proximal	Proximal	Proximal	Proximal	Proximal	Proximal	Distal	Distal	Distal	Distal	Distal	Distal	Distal	Distal
No. anal.	25	26	27	28	29	30	2	3	5	6	8	9	10	11
TiO_2	99.70	100.32	100.03	99.22	100.80	99.32	99.47	98.83	97.84	97.97	99.02	96.88	98.57	98.68
SiO_2	0.29	0.01	0.07	0.21	0.15	0.26	0.01	0.26	0.01	0.01	0.12	0.06	0.07	0.03
Fe_2O_3	0.41	0.49	0.42	0.38	0.33	0.35	1.34	1.83	2.43	2.28	0.95	2.49	0.94	1.11
Cr_2O_3	BDL	BDL	BDL	BDL	BDL	BDL	BDL	BDL	BDL	BDL	BDL	BDL	BDL	BDL
V_2O_3	0.22	0.10	0.31	0.43	0.51	0.60	0.16	0.20	0.20	0.13	0.18	0.14	0.05	0.16
MnO	0.03	0.02	BDL	BDL	BDL	BDL	BDL	0.02	BDL	BDL	0.02	0.02	0.01	BDL
Al_2O_3	0.08	0.02	0.03	0.08	0.03	0.08	0.01	0.13	0.02	0.01	0.02	0.01	0.03	0.02
CaO	0.15	0.34	0.18	0.05	0.02	0.05	0.16	0.25	0.12	0.45	0.05	0.12	0.11	0.26
P_2O_5	BDL	BDL	BDL	BDL	0.01	0.01	BDL	BDL	BDL	BDL	BDL	0.01	BDL	BDL
ZrO_2	0.09	0.07	0.04	BDL	0.04	0.04	0.10	0.11	0.11	0.11	0.18	0.12	0.17	0.16
As_2O_5	BDL	0.04	0.02	BDL	BDL	BDL	BDL	BDL	BDL	BDL	BDL	BDL	0.01	BDL
Nb_2O_5	0.07	0.04	0.03	0.04	0.04	0.04	0.03	0.06	0.05	0.03	0.05	0.06	0.06	0.03
WO_3	BDL	BDL	BDL	BDL	BDL	BDL	BDL	BDL	BDL	BDL	0.02	BDL	BDL	BDL
Ta_2O_5	BDL	0.02	BDL	BDL	BDL	BDL	BDL	BDL	BDL	0.02	BDL	BDL	0.02	BDL
SnO_2	BDL	BDL	BDL	0.01	0.01	BDL	BDL	BDL	BDL	BDL	BDL	0.01	BDL	BDL
Sb_2O_5	BDL	BDL	BDL	BDL	BDL	BDL	BDL	BDL	BDL	BDL	BDL	BDL	BDL	BDL
Total	100.65	100.97	100.80	100.20	101.83	100.48	100.81	101.04	100.21	100.21	100.38	99.47	99.74	99.84
Ti	0.988	0.991	0.991	0.989	0.990	0.987	0.986	0.977	0.978	0.977	0.988	0.977	0.989	0.987
Si	0.004	0.000	0.001	0.003	0.002	0.003	0.000	0.003	0.000	0.000	0.002	0.001	0.001	0.000
Fe^{3+}	0.004	0.004	0.004	0.004	0.003	0.003	0.012	0.017	0.023	0.021	0.009	0.023	0.009	0.010
Cr	-	-	-	-	-	-	-	-	-	-	-	-	-	-
V	0.002	0.001	0.003	0.005	0.005	0.006	0.002	0.002	0.002	0.001	0.002	0.002	0.001	0.002
Mn	0.000	0.000	-	-	-	-	-	0.000	-	-	0.000	0.000	0.000	-
Al	0.001	0.000	0.000	0.001	0.000	0.001	0.000	0.002	0.000	0.000	0.000	0.000	0.001	0.000
Ca	0.002	0.005	0.003	0.001	0.000	0.001	0.002	0.003	0.002	0.006	0.001	0.002	0.002	0.004
P	-	-	-	-	0.000	0.000	-	-	-	-	-	0.000	-	-
Zr	0.001	0.000	0.000	-	0.000	0.000	0.001	0.001	0.001	0.001	0.001	0.001	0.001	0.001
As	-	0.000	0.000	-	-	-	-	-	-	-	-	-	0.000	-
Nb	0.000	0.000	0.000	0.000	0.000	0.000	0.000	0.000	0.000	0.000	0.000	0.000	0.000	0.000
W	-	-	-	-	-	-	-	-	-	-	0.000	-	-	-
Ta	-	0.000	-	-	-	-	-	-	-	0.000	-	-	0.000	-
Sn	-	-	-	0.000	0.000	-	-	-	-	-	-	0.000	-	-
Sb	-	-	-	-	-	-	-	-	-	-	-	-	-	-

Rutile formulae calculated on basis of 2 oxygen atoms and all iron was considered as Fe^{3+}. Abbreviations: AP (Animal Pond); BN (Stog'er Tight); AE (Argyle); BDL (below detection limit); Inter (Intermediate alteration zone).

Appendix 3.2. Electron microprobe analyses (in wt%) of rutile and calculated structural formulas.

Deposit	AE	AE	AE	AE	AE	AE	AE	AE	AE	AE	AE	AE	AE	AE
Sample	AE-659	AE-659	AE-659	AE-659	AE-659	AE-659	AE-659	AE-659	AE-659	AE-659	AE-659	AE-659	AE-659	AE-659
Drill hole	AE-16-40	AE-16-40	AE-16-40	AE-16-40	AE-16-40	AE-16-40	AE-16-40	AE-16-40	AE-16-40	AE-16-40	AE-16-40	AE-16-40	AE-16-40	AE-16-40
Depth (m)	24.85-25.08	24.85-25.08	24.85-25.08	24.85-25.08	24.85-25.08	24.85-25.08	24.85-25.08	24.85-25.08	24.85-25.08	24.85-25.08	24.85-25.08	24.85-25.08	24.85-25.08	24.85-25.08
Alteration Zone	Distal	Distal	Distal	Distal	Distal	Distal	Distal	Distal	Distal	Distal	Distal	Distal	Distal	Distal
No. anal.	12	13	14	15	17	18	19	20	21	22	23	25	26	27
TiO_2	99.19	98.90	97.45	96.11	98.80	99.03	98.94	96.01	99.51	98.54	98.26	99.05	99.62	98.98
SiO_2	0.02	0.02	0.02	BDL	0.07	0.01	0.03	2.70	BDL	0.02	0.02	0.04	0.04	0.05
Fe_2O_3	1.08	2.05	2.18	3.12	1.35	1.29	1.71	1.21	1.40	1.77	1.70	1.05	0.95	0.87
Cr_2O_3	BDL	BDL	BDL	BDL	BDL	BDL	BDL	BDL	BDL	BDL	BDL	BDL	BDL	BDL
V_2O_3	0.08	0.13	0.15	0.17	0.38	0.15	0.04	0.10	0.01	0.10	0.19	0.10	0.12	0.04
MnO	0.01	0.02	0.02	BDL	BDL	0.01	0.02	BDL	0.02	BDL	BDL	BDL	0.02	BDL
Al_2O_3	0.01	0.01	0.01	0.01	0.01	0.00	0.01	0.04	0.02	0.03	0.00	0.02	0.02	0.03
CaO	0.14	0.14	0.06	0.07	0.03	0.04	0.02	0.17	0.04	0.00	0.08	0.06	0.14	0.11
P_2O_5	BDL	BDL	BDL	BDL	0.00	BDL	BDL	0.01	BDL	BDL	BDL	BDL	BDL	BDL
ZrO_2	0.25	0.12	0.11	0.17	0.04	0.05	0.03	0.06	0.10	0.13	0.13	0.15	0.11	0.28
As_2O_5	BDL	BDL	BDL	BDL	BDL	BDL	0.03	BDL	0.01	0.02	BDL	0.01	BDL	0.03
Nb_2O_5	0.04	0.03	0.09	0.21	0.20	0.08	0.12	0.22	0.20	0.31	0.14	0.05	0.01	BDL
WO_3	BDL	BDL	BDL	BDL	0.08	BDL	BDL	BDL	BDL	BDL	BDL	BDL	BDL	BDL
Ta_2O_5	BDL	BDL	BDL	BDL	BDL	BDL	BDL	0.03	BDL	BDL	BDL	BDL	BDL	BDL
SnO_2	BDL	BDL	BDL	BDL	0.03	BDL	BDL	BDL	BDL	0.01	BDL	BDL	BDL	BDL
Sb_2O_5	BDL	BDL	BDL	BDL	BDL	BDL	BDL	BDL	BDL	BDL	BDL	BDL	BDL	BDL
Total	100.34	100.97	99.63	99.35	100.79	100.31	100.65	100.03	101.07	100.60	100.07	100.24	100.67	100.08
Ti	0.988	0.981	0.980	0.972	0.983	0.988	0.985	0.951	0.987	0.982	0.983	0.989	0.989	0.989
Si	0.000	0.000	0.000	-	0.001	0.000	0.000	0.036	-	0.000	0.000	0.000	0.001	0.001
Fe^{3+}	0.010	0.019	0.020	0.029	0.012	0.012	0.016	0.011	0.013	0.016	0.016	0.010	0.009	0.008
Cr	-	-	-	-	-	-	-	-	-	-	-	-	-	-
V	0.001	0.001	0.002	0.002	0.004	0.002	0.000	0.001	0.000	0.001	0.002	0.001	0.001	0.000
Mn	0.000	0.000	0.000	-	-	0.000	0.000	-	0.000	-	-	-	0.000	-
Al	0.000	0.000	0.000	0.000	0.000	0.000	0.000	0.001	0.000	0.000	0.000	0.000	0.000	0.000
Ca	0.002	0.002	0.001	0.001	0.000	0.001	0.000	0.002	0.001	0.000	0.001	0.001	0.002	0.002
P	-	-	-	-	0.000	-	-	0.000	-	-	-	-	-	-
Zr	0.002	0.001	0.001	0.001	0.000	0.000	0.000	0.000	0.001	0.001	0.001	0.001	0.001	0.002
As	-	-	-	-	-	-	0.000	-	0.000	0.000	-	0.000	-	0.000
Nb	0.000	0.000	0.001	0.001	0.001	0.000	0.001	0.001	0.001	0.002	0.001	0.000	0.000	-
W	-	-	-	-	0.000	-	-	-	-	-	-	-	-	-
Ta	-	-	-	-	-	-	-	0.000	-	-	-	-	-	-
Sn	-	-	-	-	0.000	-	-	-	-	0.000	-	-	-	-
Sb	-	-	-	-	-	-	-	-	-	-	-	-	-	-

Rutile formulae calculated on basis of 2 oxygen atoms and all iron was considered as Fe^{3+}. Abbreviations: AP (Animal Pond); BN (Stog'er Tight); AE (Argyle); BDL (below detection limit); Inter (Intermediate alteration zone).

Appendix 3.2. Electron microprobe analyses (in wt%) of rutile and calculated structural formulas.

Deposit	AE	AE	AE	AE	AE	AE	AE	AE	AE	AE	AE	AE	AE	AE
Sample	AE-659	AE-659	AE-659	AE-672	AE-672	AE-672	AE-672	AE-679	AE-679	AE-679	AE-679	AE-679	AE-679	AE-679
Drill hole	AE-16-40	AE-16-40	AE-16-40	AE-16-40	AE-16-40	AE-16-40	AE-16-40	AE-16-46	AE-16-46	AE-16-46	AE-16-46	AE-16-46	AE-16-46	AE-16-46
Depth (m)	24.85-25.08	24.85-25.08	24.85-25.08	72.61-72.83	72.61-72.83	72.61-72.83	72.61-72.83	54.23-54.36	54.23-54.36	54.23-54.36	54.23-54.36	54.23-54.36	54.23-54.36	54.23-54.36
Alteration Zone	Distal	Distal	Distal	Inter	Inter	Inter	Inter	Proximal	Proximal	Proximal	Proximal	Proximal	Proximal	Proximal
No. anal.	28	29	30	1	2	3	4	1	2	3	4	5	6	7
TiO_2	98.73	100.46	98.93	96.91	100.45	98.62	99.21	99.64	99.29	98.69	99.40	97.99	100.38	97.85
SiO_2	0.04	0.06	BDL	1.07	0.04	0.14	0.17	0.09	0.05	0.12	0.23	0.37	0.04	0.37
Fe_2O_3	0.85	0.96	1.40	0.70	0.60	0.74	0.59	0.54	0.55	0.51	0.36	0.69	0.41	0.48
Cr_2O_3	BDL	BDL	BDL	BDL	BDL	BDL	BDL	BDL	BDL	BDL	BDL	BDL	BDL	BDL
V_2O_3	0.02	0.15	0.13	0.19	0.07	0.16	0.05	0.09	0.05	0.12	0.34	0.16	0.14	0.17
MnO	BDL	BDL	BDL	0.01	BDL	BDL	BDL	BDL	BDL	BDL	BDL	BDL	0.01	BDL
Al_2O_3	0.02	0.02	0.01	0.03	0.02	0.03	0.02	0.02	0.03	0.03	0.08	0.14	0.03	0.14
CaO	0.10	0.10	0.15	1.83	0.87	0.86	1.14	0.01	BDL	BDL	0.02	0.06	0.01	0.08
P_2O_5	BDL	BDL	BDL	BDL	BDL	BDL	0.01	BDL	BDL	BDL	0.02	BDL	0.01	BDL
ZrO_2	0.31	0.04	0.36	0.04	0.08	0.04	0.06	BDL	0.29	0.02	0.03	BDL	0.03	0.09
As_2O_5	BDL	BDL	BDL	BDL	BDL	0.03	0.02	BDL	BDL	BDL	BDL	0.03	0.04	BDL
Nb_2O_5	0.08	0.05	0.04	0.01	0.07	0.13	0.04	0.24	0.25	0.42	0.25	0.66	0.02	0.08
WO_3	BDL	BDL	BDL	BDL	BDL	BDL	BDL	BDL	BDL	BDL	BDL	BDL	BDL	0.03
Ta_2O_5	BDL	BDL	BDL	BDL	BDL	BDL	BDL	BDL	0.04	BDL	BDL	0.03	BDL	BDL
SnO_2	BDL	BDL	BDL	BDL	BDL	BDL	BDL	BDL	BDL	BDL	BDL	0.01	0.01	0.01
Sb_2O_5	BDL	BDL	BDL	BDL	BDL	BDL	BDL	BDL	BDL	BDL	BDL	BDL	BDL	BDL
Total	99.90	101.54	100.54	98.35	100.83	99.45	99.68	100.41	100.41	99.72	100.61	99.95	100.97	99.07
Ti	0.989	0.989	0.985	0.965	0.987	0.983	0.984	0.992	0.991	0.990	0.988	0.981	0.994	0.987
Si	0.001	0.001	-	0.014	0.001	0.002	0.002	0.001	0.001	0.002	0.003	0.005	0.001	0.005
Fe^{3+}	0.008	0.009	0.013	0.006	0.005	0.007	0.005	0.005	0.005	0.005	0.003	0.006	0.004	0.005
Cr	-	-	-	-	-	-	-	-	-	-	-	-	-	-
V	0.000	0.002	0.001	0.002	0.001	0.002	0.000	0.001	0.000	0.001	0.004	0.002	0.001	0.002
Mn	-	-	-	0.000	-	-	-	-	-	-	-	-	0.000	-
Al	0.000	0.000	0.000	0.000	0.000	0.000	0.000	0.000	0.000	0.001	0.001	0.002	0.001	0.002
Ca	0.001	0.001	0.002	0.026	0.012	0.012	0.016	0.000	-	-	0.000	0.001	0.000	0.001
P	-	-	-	-	-	-	0.000	-	-	-	0.000	-	0.000	-
Zr	0.002	0.000	0.002	0.000	0.001	0.000	0.000	-	0.002	0.000	0.000	-	0.000	0.001
As	-	-	-	-	-	0.000	0.000	-	-	-	-	0.000	0.000	-
Nb	0.001	0.000	0.000	0.000	0.000	0.001	0.000	0.001	0.001	0.003	0.001	0.004	0.000	0.000
W	-	-	-	-	-	-	-	-	-	-	-	-	-	0.000
Ta	-	-	-	-	-	-	-	-	0.000	-	-	0.000	-	-
Sn	-	-	-	-	-	-	-	-	-	-	-	0.000	0.000	0.000
Sb	-	-	-	-	-	-	-	-	-	-	-	-	-	-

Rutile formulae calculated on basis of 2 oxygen atoms and all iron was considered as Fe^{3+}. Abbreviations: AP (Animal Pond); BN (Stog'er Tight); AE (Argyle); BDL (below detection limit); Inter (Intermediate alteration zone).

Appendix 3.2. Electron microprobe analyses (in wt%) of rutile and calculated structural formulas.

Deposit	AE	AE	AE	AE	AE	AE	AE	AE	AE	AE	AE	AE	AE	AE
Sample	AE-679	AE-679	AE-679	AE-679	AE-679	AE-679	AE-679	AE-679	AE-679	AE-679	AE-679	AE-679	AE-679	AE-679
Drill hole	AE-16-46	AE-16-46	AE-16-46	AE-16-46	AE-16-46	AE-16-46	AE-16-46	AE-16-46	AE-16-46	AE-16-46	AE-16-46	AE-16-46	AE-16-46	AE-16-46
Depth (m)	54.23-54.36	54.23-54.36	54.23-54.36	54.23-54.36	54.23-54.36	54.23-54.36	54.23-54.36	54.23-54.36	54.23-54.36	54.23-54.36	54.23-54.36	54.23-54.36	54.23-54.36	54.23-54.36
Alteration Zone	Proximal	Proximal	Proximal	Proximal	Proximal	Proximal	Proximal	Proximal	Proximal	Proximal	Proximal	Proximal	Proximal	Proximal
No. anal.	8	9	10	11	12	13	14	15	16	17	18	19	20	21
TiO_2	99.83	98.99	99.17	100.20	99.97	99.28	98.25	99.05	100.56	99.44	99.12	99.86	98.57	99.51
SiO_2	0.27	0.07	0.03	0.07	0.09	0.05	0.03	0.07	0.04	0.15	0.12	0.04	0.09	0.02
Fe_2O_3	0.38	0.35	0.59	0.76	0.52	0.53	0.51	0.50	0.49	0.41	0.43	0.48	0.58	0.38
Cr_2O_3	BDL	BDL	BDL	BDL	BDL	BDL	BDL	BDL	BDL	BDL	BDL	BDL	BDL	BDL
V_2O_3	0.22	0.09	0.16	0.12	0.08	0.01	0.04	0.02	0.05	0.10	0.17	0.10	0.02	0.11
MnO	BDL	0.01	BDL	BDL	0.01	0.01	BDL	BDL	0.02	BDL	BDL	BDL	BDL	0.01
Al_2O_3	0.09	0.02	0.03	0.04	0.03	0.05	0.04	0.01	0.01	0.04	0.05	0.03	0.05	0.02
CaO	0.05	0.01	0.16	0.03	0.01	0.02	0.03	0.01	0.20	0.04	0.02	0.15	0.06	0.20
P_2O_5	BDL	BDL	BDL	BDL	BDL	BDL	0.01	BDL	BDL	BDL	BDL	BDL	BDL	BDL
ZrO_2	0.02	0.04	BDL	0.08	0.03	0.08	BDL	0.13	0.03	0.07	0.04	0.04	0.09	BDL
As_2O_5	BDL	BDL	0.03	0.02	0.03	BDL	0.03	BDL	BDL	BDL	0.02	BDL	BDL	BDL
Nb_2O_5	0.04	0.03	0.02	0.04	0.01	0.15	0.04	0.07	0.02	0.08	0.03	BDL	0.19	0.10
WO_3	BDL	BDL	BDL	BDL	BDL	BDL	BDL	BDL	BDL	0.03	0.03	BDL	BDL	BDL
Ta_2O_5	BDL	0.01	BDL	BDL	BDL	BDL	BDL	BDL	BDL	0.02	BDL	BDL	BDL	BDL
SnO_2	0.01	BDL	BDL	BDL	BDL	BDL	BDL	BDL	BDL	BDL	BDL	BDL	BDL	BDL
Sb_2O_5	BDL	BDL	BDL	BDL	BDL	BDL	BDL	BDL	BDL	BDL	BDL	BDL	BDL	BDL
Total	100.76	99.43	99.81	101.04	100.52	99.97	98.73	99.71	100.92	100.23	99.91	100.32	99.38	99.93
Ti	0.990	0.995	0.992	0.991	0.993	0.993	0.994	0.994	0.994	0.992	0.992	0.993	0.991	0.993
Si	0.004	0.001	0.000	0.001	0.001	0.001	0.000	0.001	0.001	0.002	0.002	0.000	0.001	0.000
Fe^{3+}	0.003	0.003	0.006	0.007	0.005	0.005	0.005	0.005	0.004	0.004	0.004	0.004	0.005	0.004
Cr	-	-	-	-	-	-	-	-	-	-	-	-	-	-
V	0.002	0.001	0.002	0.001	0.001	0.000	0.000	0.000	0.001	0.001	0.002	0.001	0.000	0.001
Mn	-	0.000	-	-	0.000	0.000	-	-	0.000	-	-	-	-	0.000
Al	0.001	0.000	0.000	0.001	0.000	0.001	0.001	0.000	0.000	0.001	0.001	0.000	0.001	0.000
Ca	0.001	0.000	0.002	0.000	0.000	0.000	0.000	0.000	0.003	0.000	0.000	0.002	0.001	0.003
P	-	-	-	-	-	-	0.000	-	-	-	-	-	-	-
Zr	0.000	0.000	-	0.001	0.000	0.000	-	0.001	0.000	0.000	0.000	0.000	0.001	-
As	-	-	0.000	0.000	0.000	-	0.000	-	-	-	0.000	-	-	-
Nb	0.000	0.000	0.000	0.000	0.000	0.001	0.000	0.000	0.000	0.000	0.000	-	0.001	0.001
W	-	-	-	-	-	-	-	-	-	0.000	0.000	-	-	-
Ta	-	0.000	-	-	-	-	-	-	-	0.000	-	-	-	-
Sn	0.000	-	-	-	-	-	-	-	-	-	-	-	-	-
Sb	-	-	-	-	-	-	-	-	-	-	-	-	-	-

Rutile formulae calculated on basis of 2 oxygen atoms and all iron was considered as Fe^{3+}. Abbreviations: AP (Animal Pond); BN (Stog'er Tight); AE (Argyle); BDL (below detection limit); Inter (Intermediate alteration zone).

Appendix 3.2. Electron microprobe analyses (in wt%) of rutile and calculated structural formulas.

Deposit	AE	AE	AE	AE	AE	AE	AE	AE	AE	AE	AE	AE	AE	AE
Sample	AE-679	AE-679	AE-679	AE-679	AE-679	AE-679	AE-679	AE-679	AE-684	AE-684	AE-684	AE-684	AE-684	AE-684
Drill hole	AE-16-46	AE-16-46	AE-16-46	AE-16-46	AE-16-46	AE-16-46	AE-16-46	AE-16-46	AE-16-46	AE-16-46	AE-16-46	AE-16-46	AE-16-46	AE-16-46
Depth (m)	54.23-54.36	54.23-54.36	54.23-54.36	54.23-54.36	54.23-54.36	54.23-54.36	54.23-54.36	54.23-54.36	71.34-71.41	71.34-71.41	71.34-71.41	71.34-71.41	71.34-71.41	71.34-71.41
Alteration Zone	Proximal	Proximal	Proximal	Proximal	Proximal	Proximal	Proximal	Proximal	Inter	Inter	Inter	Inter	Inter	Inter
No. anal.	22	23	25	26	27	28	29	30	1	2	3	4	5	6
TiO_2	99.31	100.03	98.83	98.51	99.21	99.27	97.47	99.55	99.74	99.09	99.74	99.85	98.86	101.24
SiO_2	0.08	0.01	0.05	0.23	0.17	0.11	0.07	0.06	0.07	0.13	0.19	0.17	0.10	0.07
Fe_2O_3	0.48	0.43	0.39	0.43	0.40	0.49	0.57	0.69	0.50	0.41	0.24	0.41	0.38	0.37
Cr_2O_3	BDL	BDL	BDL	BDL	BDL	BDL	BDL	BDL	BDL	BDL	BDL	BDL	BDL	BDL
V_2O_3	0.07	0.07	0.08	0.06	0.06	0.10	0.11	0.10	0.14	0.20	0.23	0.20	0.26	0.24
MnO	BDL	0.01	BDL	0.01	BDL	BDL	BDL	BDL	BDL	BDL	BDL	BDL	BDL	0.01
Al_2O_3	0.05	0.02	0.02	0.08	0.05	0.03	0.02	0.03	0.02	0.01	0.04	0.03	0.03	0.03
CaO	0.28	1.01	0.16	0.09	0.05	0.02	0.03	0.03	0.23	0.10	0.11	0.29	0.19	0.06
P_2O_5	0.01	BDL	BDL	BDL	0.01	BDL	BDL	BDL	BDL	BDL	BDL	0.01	BDL	0.00
ZrO_2	BDL	0.02	0.05	0.02	BDL	BDL	0.01	BDL	0.07	0.08	0.03	0.04	0.11	0.01
As_2O_5	0.02	BDL	BDL	BDL	0.05	0.05	0.02	0.02	BDL	0.01	BDL	BDL	0.02	BDL
Nb_2O_5	0.12	0.13	0.13	0.14	0.04	0.01	0.05	0.04	0.12	0.16	0.08	0.03	0.08	0.06
WO_3	BDL	BDL	BDL	BDL	BDL	BDL	BDL	0.01	BDL	BDL	BDL	BDL	BDL	BDL
Ta_2O_5	BDL	0.01	BDL	0.02	BDL	BDL	BDL	BDL	BDL	BDL	BDL	BDL	BDL	0.02
SnO_2	BDL	0.01	BDL	0.03	0.01	BDL	BDL	BDL	BDL	BDL	BDL	BDL	BDL	0.01
Sb_2O_5	BDL	BDL	BDL	BDL	BDL	BDL	BDL	BDL	BDL	BDL	BDL	BDL	BDL	BDL
Total	99.87	100.27	99.31	99.40	99.87	99.93	98.11	100.34	100.46	99.94	100.41	100.52	99.62	101.97
Ti	0.991	0.988	0.993	0.990	0.992	0.993	0.993	0.992	0.991	0.991	0.992	0.990	0.990	0.993
Si	0.001	0.000	0.001	0.003	0.002	0.002	0.001	0.001	0.001	0.002	0.003	0.002	0.001	0.001
Fe^{3+}	0.004	0.004	0.004	0.004	0.004	0.005	0.005	0.006	0.005	0.004	0.002	0.004	0.004	0.003
Cr	-	-	-	-	-	-	-	-	-	-	-	-	-	-
V	0.001	0.001	0.001	0.001	0.001	0.001	0.001	0.001	0.001	0.002	0.002	0.002	0.003	0.002
Mn	-	0.000	-	0.000	-	-	-	-	-	-	-	-	-	0.000
Al	0.001	0.000	0.000	0.001	0.001	0.000	0.000	0.000	0.000	0.000	0.001	0.000	0.001	0.000
Ca	0.004	0.014	0.002	0.001	0.001	0.000	0.000	0.000	0.003	0.001	0.002	0.004	0.003	0.001
P	0.000	-	-	-	0.000	-	-	-	-	-	-	0.000	-	0.000
Zr	-	0.000	0.000	0.000	-	-	0.000	-	0.000	0.001	0.000	0.000	0.001	0.000
As	0.000	-	-	-	0.000	0.000	0.000	0.000	-	0.000	-	-	0.000	-
Nb	0.001	0.001	0.001	0.001	0.000	0.000	0.000	0.000	0.001	0.001	0.001	0.000	0.000	0.000
W	-	-	-	-	-	-	-	0.000	-	-	-	-	-	-
Ta	-	0.000	-	0.000	-	-	-	-	-	-	-	-	-	0.000
Sn	-	0.000	-	0.000	0.000	-	-	-	-	-	-	-	-	0.000
Sb	-	-	-	-	-	-	-	-	-	-	-	-	-	-

Rutile formulae calculated on basis of 2 oxygen atoms and all iron was considered as Fe^{3+}. Abbreviations: AP (Animal Pond); BN (Stog'er Tight); AE (Argyle); BDL (below detection limit); Inter (Intermediate alteration zone).

Appendix 3.2. Electron microprobe analyses (in wt%) of rutile and calculated structural formulas.

Deposit	AE	AE	AE	AE	AE	AE	AE	AE	AE	AE	AE	AE	AE	AE
Sample	AE-684	AE-684	AE-684	AE-684	AE-684	AE-684	AE-684	AE-684	AE-684	AE-684	AE-684	AE-684	AE-684	AE-684
Drill hole	AE-16-46	AE-16-46	AE-16-46	AE-16-46	AE-16-46	AE-16-46	AE-16-46	AE-16-46	AE-16-46	AE-16-46	AE-16-46	AE-16-46	AE-16-46	AE-16-46
Depth (m)	71.34-71.41	71.34-71.41	71.34-71.41	71.34-71.41	71.34-71.41	71.34-71.41	71.34-71.41	71.34-71.41	71.34-71.41	71.34-71.41	71.34-71.41	71.34-71.41	71.34-71.41	71.34-71.41
Alteration Zone	Inter	Inter	Inter	Inter	Inter	Inter	Inter	Inter	Inter	Inter	Inter	Inter	Inter	Inter
No. anal.	7	8	9	10	11	12	13	14	15	16	17	18	19	20
TiO_2	99.54	101.04	100.36	101.32	99.43	100.60	99.57	100.17	99.66	98.80	99.58	98.62	99.94	100.01
SiO_2	0.03	0.06	0.05	0.07	0.07	0.05	0.06	0.15	0.13	0.04	0.09	0.22	0.07	0.10
Fe_2O_3	0.51	0.34	0.54	0.44	0.50	0.41	0.54	0.42	0.60	0.49	0.58	0.53	0.40	0.52
Cr_2O_3	BDL	BDL	BDL	BDL	BDL	BDL	BDL	BDL	BDL	BDL	BDL	BDL	BDL	BDL
V_2O_3	0.12	0.17	0.11	0.18	0.17	0.16	0.14	0.18	0.34	0.05	0.08	0.05	0.11	0.05
MnO	BDL	0.02	BDL	BDL	BDL	BDL	BDL	BDL	BDL	BDL	0.01	0.02	BDL	BDL
Al_2O_3	0.01	0.01	0.01	0.03	0.02	0.01	0.00	BDL	0.04	0.01	0.02	0.03	0.01	0.03
CaO	0.09	0.04	0.16	0.07	0.04	0.02	0.16	0.06	0.13	0.09	0.06	0.11	0.02	0.05
P_2O_5	BDL	BDL	0.01	BDL	0.01	BDL	0.01	BDL	BDL	BDL	BDL	BDL	BDL	0.01
ZrO_2	0.01	BDL	BDL	0.07	0.01	0.03	0.07	0.08	0.25	0.07	0.12	0.04	0.06	0.04
As_2O_5	BDL	BDL	0.03	BDL	0.02	BDL	0.05	BDL	BDL	0.03	BDL	BDL	BDL	BDL
Nb_2O_5	0.13	0.11	0.30	0.07	0.12	0.19	0.34	0.21	0.23	0.09	0.15	0.11	0.11	0.22
WO_3	0.02	BDL	0.02	BDL	BDL	0.01	BDL	0.03	BDL	BDL	BDL	BDL	0.04	BDL
Ta_2O_5	BDL	BDL	0.03	BDL	BDL	BDL	BDL	BDL	BDL	BDL	BDL	BDL	BDL	0.03
SnO_2	BDL	BDL	BDL	0.01	BDL	0.01	BDL	BDL	0.04	BDL	BDL	BDL	BDL	BDL
Sb_2O_5	BDL	BDL	BDL	BDL	BDL	BDL	BDL	BDL	BDL	BDL	BDL	BDL	BDL	BDL
Total	100.22	101.65	101.35	102.01	100.17	101.29	100.63	101.09	101.06	99.42	100.45	99.43	100.60	100.80
Ti	0.993	0.994	0.990	0.993	0.992	0.993	0.989	0.991	0.986	0.993	0.991	0.990	0.994	0.992
Si	0.000	0.001	0.001	0.001	0.001	0.001	0.001	0.002	0.002	0.001	0.001	0.003	0.001	0.001
Fe^{3+}	0.005	0.003	0.005	0.004	0.005	0.004	0.005	0.004	0.006	0.005	0.005	0.005	0.004	0.005
Cr	-	-	-	-	-	-	-	-	-	-	-	-	-	-
V	0.001	0.002	0.001	0.002	0.002	0.002	0.001	0.002	0.004	0.000	0.001	0.001	0.001	0.001
Mn	-	0.000	-	-	-	-	-	-	-	-	0.000	0.000	-	-
Al	0.000	0.000	0.000	0.001	0.000	0.000	0.000	-	0.001	0.000	0.000	0.000	0.000	0.000
Ca	0.001	0.001	0.002	0.001	0.001	0.000	0.002	0.001	0.002	0.001	0.001	0.002	0.000	0.001
P	-	-	0.000	-	0.000	-	0.000	-	-	-	-	-	-	0.000
Zr	0.000	-	-	0.000	0.000	0.000	0.000	0.000	0.002	0.000	0.001	0.000	0.000	0.000
As	-	-	0.000	-	0.000	-	0.000	-	-	0.000	-	-	-	-
Nb	0.001	0.001	0.002	0.000	0.001	0.001	0.002	0.001	0.001	0.001	0.001	0.001	0.001	0.001
W	0.000	-	0.000	-	-	0.000	-	0.000	-	-	-	-	0.000	-
Ta	-	-	0.000	-	-	-	-	-	-	-	-	-	-	0.000
Sn	-	-	-	0.000	-	0.000	-	-	0.000	-	-	-	-	-
Sb	-	-	-	-	-	-	-	-	-	-	-	-	-	-

Rutile formulae calculated on basis of 2 oxygen atoms and all iron was considered as Fe^{3+}. Abbreviations: AP (Animal Pond); BN (Stog'er Tight); AE (Argyle); BDL (below detection limit); Inter (Intermediate alteration zone).

Appendix 3.2. Electron microprobe analyses (in wt%) of rutile and calculated structural formulas.

Deposit	AE	AE	AE	AE	AE	AE	AE	AE	AE	AE	AE	AE	AE	AE
Sample	AE-684	AE-684	AE-684	AE-684	AE-684	AE-684	AE-684	AE-684	AE-684	AE-684	AE-684	AE-684	AE-684	AE-684
Drill hole	AE-16-46	AE-16-46	AE-16-46	AE-16-46	AE-16-46	AE-16-46	AE-16-46	AE-16-46	AE-16-46	AE-16-46	AE-16-46	AE-16-46	AE-16-46	AE-16-46
Depth (m)	71.34-71.41	71.34-71.41	71.34-71.41	71.34-71.41	71.34-71.41	71.34-71.41	71.34-71.41	71.34-71.41	71.34-71.41	71.34-71.41	71.34-71.41	71.34-71.41	71.34-71.41	71.34-71.41
Alteration Zone	Inter	Inter	Inter	Inter	Inter	Inter	Inter	Inter	Inter	Inter	Inter	Inter	Inter	Inter
No. anal.	21	22	23	24	26	27	28	29	30	31	32	33	34	35
TiO_2	99.63	100.21	101.43	100.13	100.49	100.24	99.53	99.61	98.86	100.11	97.69	100.49	99.94	99.32
SiO_2	0.05	0.06	0.05	0.05	0.06	0.05	0.12	0.06	0.07	0.08	0.17	0.03	0.20	0.48
Fe_2O_3	0.55	0.64	0.51	0.42	0.57	0.44	0.38	0.47	0.47	0.45	0.63	0.61	0.43	0.51
Cr_2O_3	BDL	BDL	BDL	BDL	BDL	BDL	BDL	BDL	BDL	BDL	BDL	0.01	BDL	BDL
V_2O_3	0.04	0.03	0.06	0.08	0.29	0.09	0.22	0.15	0.17	0.18	0.13	0.07	0.11	0.13
MnO	0.02	0.01	BDL	BDL	BDL	BDL	0.01	BDL	BDL	BDL	0.01	0.01	BDL	0.01
Al_2O_3	0.02	0.05	0.02	0.00	0.02	0.02	0.02	0.02	0.01	0.00	0.06	0.01	0.01	0.01
CaO	0.06	0.01	0.02	0.01	0.05	0.11	0.02	0.15	0.15	0.04	0.05	0.03	0.03	0.01
P_2O_5	BDL	BDL	BDL	0.01	BDL	BDL	BDL	BDL	BDL	0.01	BDL	0.00	BDL	BDL
ZrO_2	0.10	0.07	0.01	0.06	0.01	0.04	BDL	BDL	BDL	0.04	0.13	BDL	0.01	0.10
As_2O_5	BDL	BDL	BDL	BDL	BDL	BDL	BDL	BDL	0.01	0.02	0.01	0.02	BDL	0.05
Nb_2O_5	0.20	0.28	0.05	0.04	0.17	0.16	0.14	0.29	0.10	0.18	0.17	0.40	0.14	0.19
WO_3	BDL	BDL	BDL	BDL	BDL	BDL	0.01	BDL	BDL	BDL	BDL	BDL	BDL	BDL
Ta_2O_5	BDL	0.02	BDL	BDL	BDL	BDL	BDL	BDL	BDL	BDL	BDL	BDL	0.01	BDL
SnO_2	BDL	BDL	BDL	BDL	BDL	BDL	0.01	0.01	BDL	BDL	0.01	BDL	BDL	BDL
Sb_2O_5	BDL	BDL	BDL	BDL	BDL	BDL	BDL	BDL	BDL	BDL	BDL	BDL	BDL	BDL
Total	100.36	101.28	101.97	100.69	101.44	100.91	100.37	100.40	99.55	100.90	98.83	101.58	100.75	100.60
Ti	0.992	0.991	0.994	0.995	0.991	0.993	0.992	0.991	0.992	0.992	0.988	0.991	0.992	0.986
Si	0.001	0.001	0.001	0.001	0.001	0.001	0.002	0.001	0.001	0.001	0.002	0.000	0.003	0.006
Fe^{3+}	0.005	0.006	0.005	0.004	0.005	0.004	0.003	0.004	0.004	0.004	0.006	0.006	0.004	0.005
Cr	-	-	-	-	-	-	-	-	-	-	-	0.000	-	-
V	0.000	0.000	0.001	0.001	0.003	0.001	0.002	0.002	0.002	0.002	0.001	0.001	0.001	0.001
Mn	0.000	0.000	-	-	-	-	0.000	-	-	-	0.000	0.000	-	0.000
Al	0.000	0.001	0.000	0.000	0.000	0.000	0.000	0.000	0.000	0.000	0.001	0.000	0.000	0.000
Ca	0.001	0.000	0.000	0.000	0.001	0.001	0.000	0.002	0.002	0.001	0.001	0.000	0.000	0.000
P	-	-	-	0.000	-	-	-	-	-	0.000	-	0.000	-	-
Zr	0.001	0.000	0.000	0.000	0.000	0.000	-	-	-	0.000	0.001	-	0.000	0.001
As	-	-	-	-	-	-	-	-	0.000	0.000	0.000	0.000	-	0.000
Nb	0.001	0.002	0.000	0.000	0.001	0.001	0.001	0.002	0.001	0.001	0.001	0.002	0.001	0.001
W	-	-	-	-	-	-	0.000	-	-	-	-	-	-	-
Ta	-	0.000	-	-	-	-	-	-	-	-	-	-	0.000	-
Sn	-	-	-	-	-	-	0.000	0.000	-	-	0.000	-	-	-
Sb	-	-	-	-	-	-	-	-	-	-	-	-	-	-

Rutile formulae calculated on basis of 2 oxygen atoms and all iron was considered as Fe^{3+}. Abbreviations: AP (Animal Pond); BN (Stog'er Tight); AE (Argyle); BDL (below detection limit); Inter (Intermediate alteration zone).

Appendix 4. Visible - near infrared - short-wave infrared (Vis-NIR-SWIR) spectra of studied hydrothermally-altered samples from high- and low-sulfidation epithermal deposits from the Avalon Zone of Newfoundland.

Oval Pit pyrophyllite mine and Vinjer high-sulfidation epithermal prospect

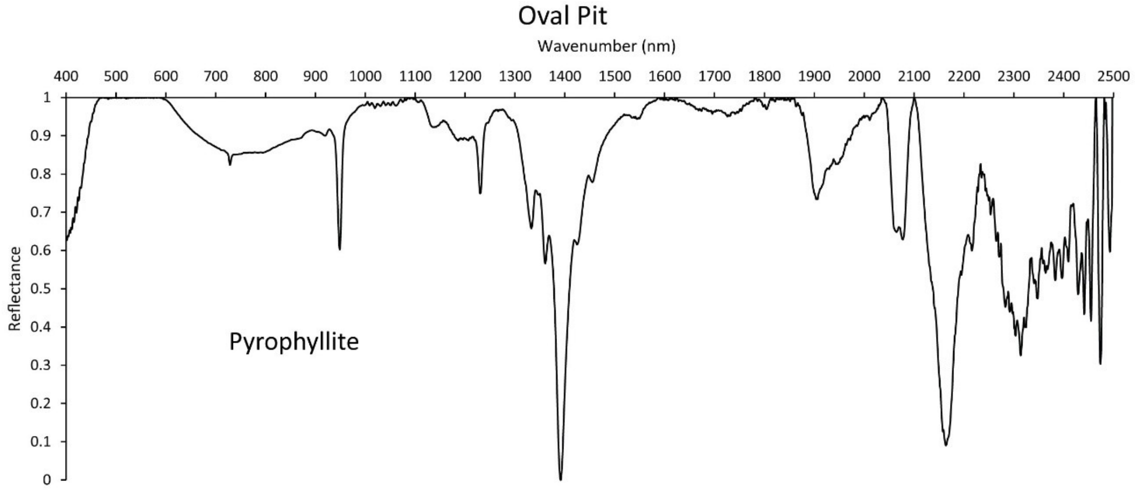

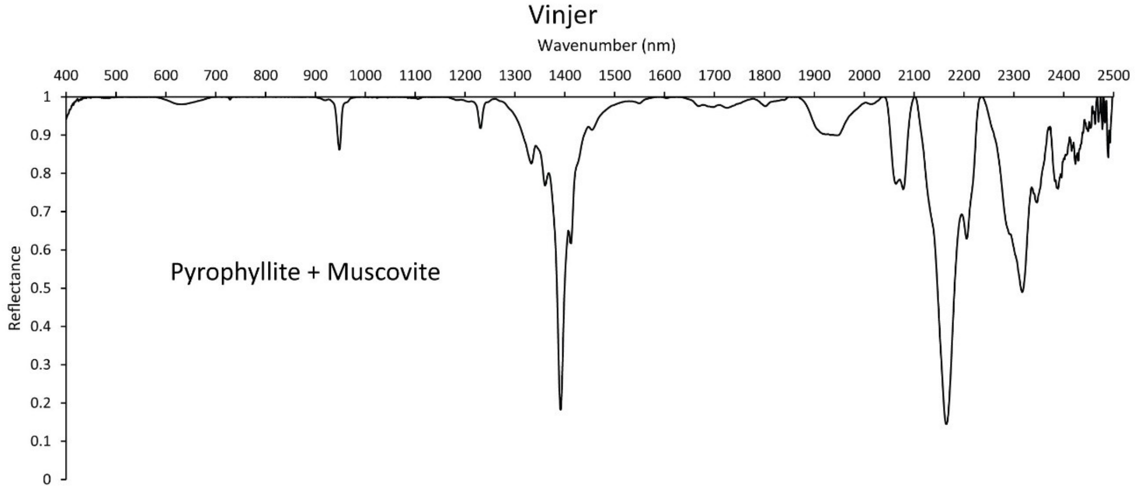

Hickey's Pond high-sulfidation epithermal prospect

HP-1

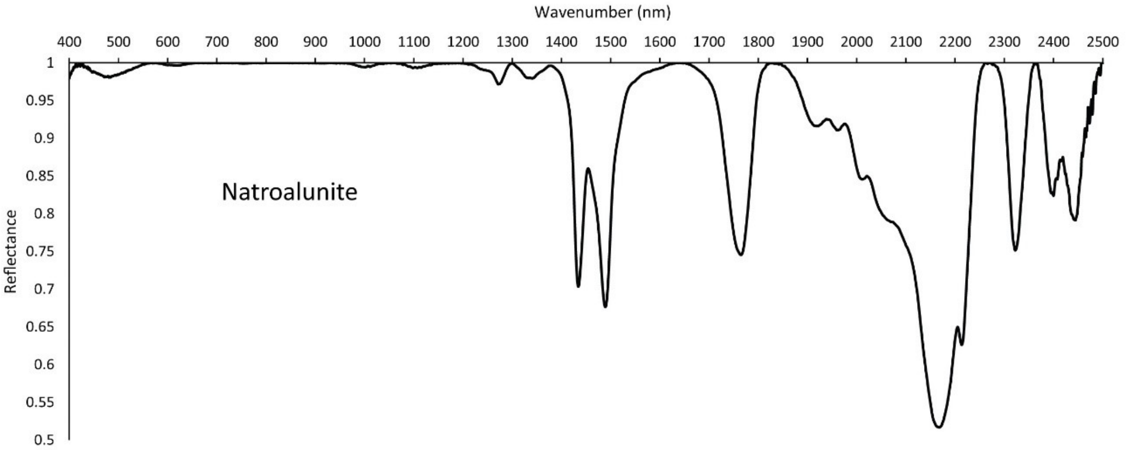

HP-2

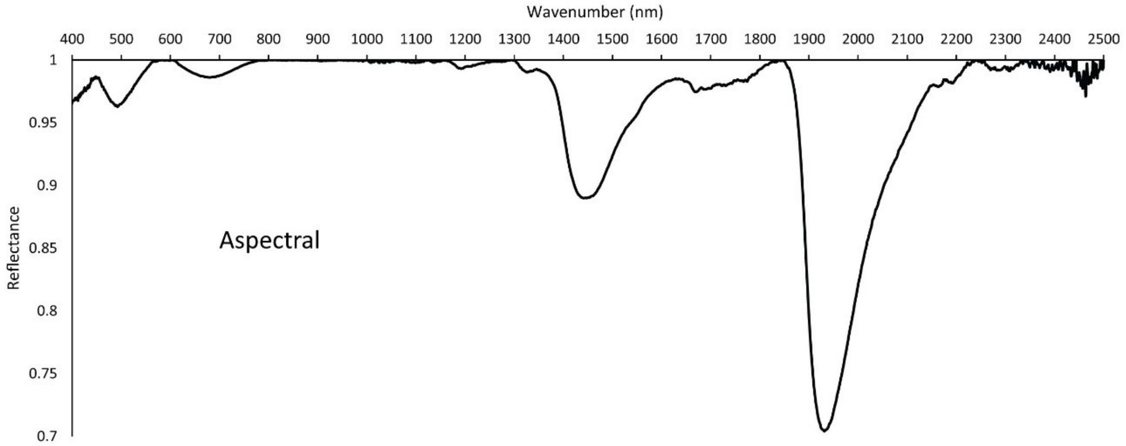

HP-3

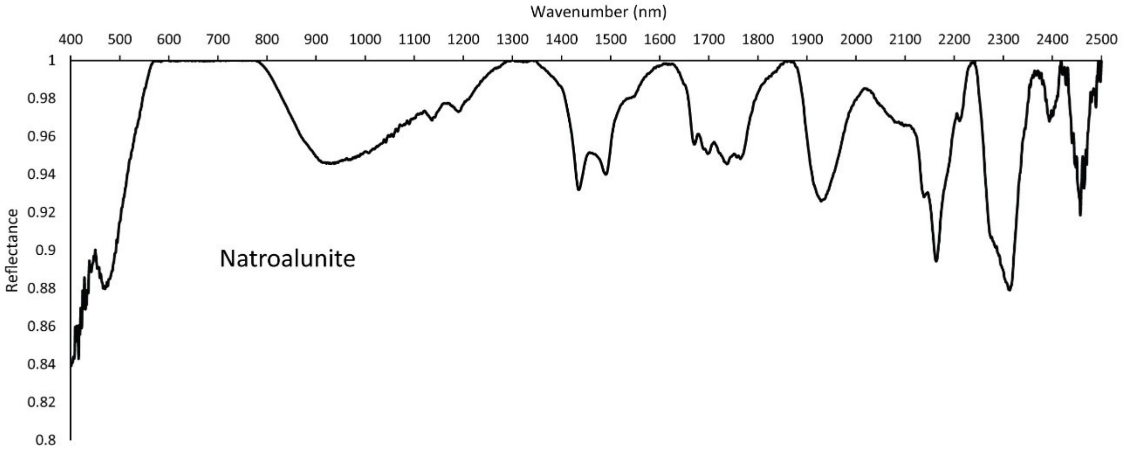

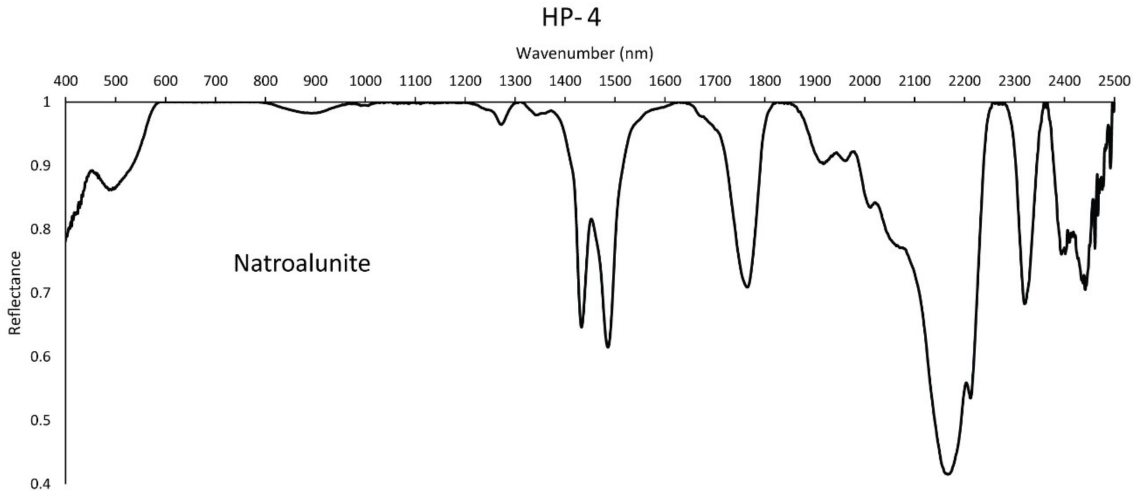
HP- 4
Wavenumber (nm)
400 500 600 700 800 900 1000 1100 1200 1300 1400 1500 1600 1700 1800 1900 2000 2100 2200 2300 2400 2500
Reflectance
1 0.9 0.8 0.7 0.6 0.5 0.4
Natroalunite

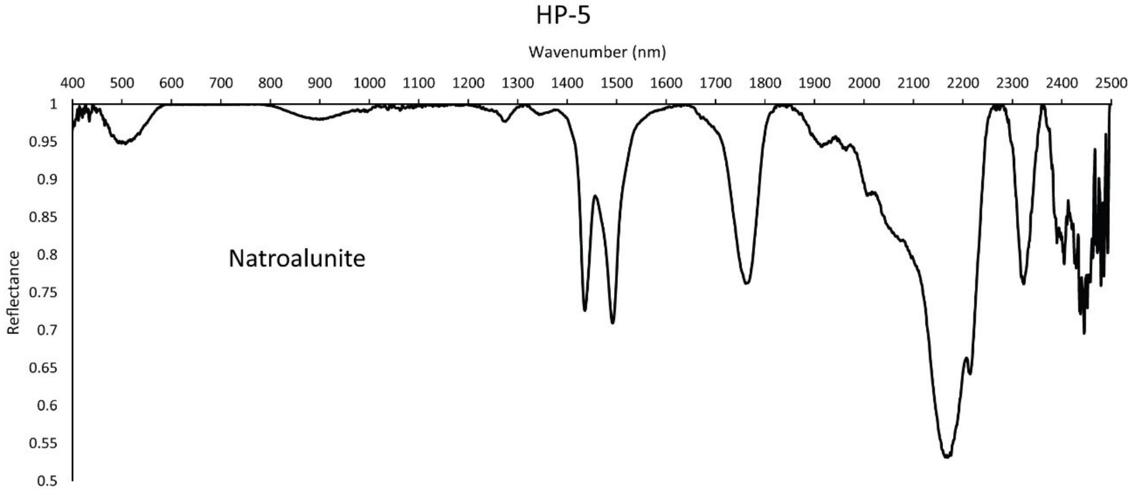
HP-5
Wavenumber (nm)
400 500 600 700 800 900 1000 1100 1200 1300 1400 1500 1600 1700 1800 1900 2000 2100 2200 2300 2400 2500
Reflectance
1 0.95 0.9 0.85 0.8 0.75 0.7 0.65 0.6 0.55 0.5
Natroalunite

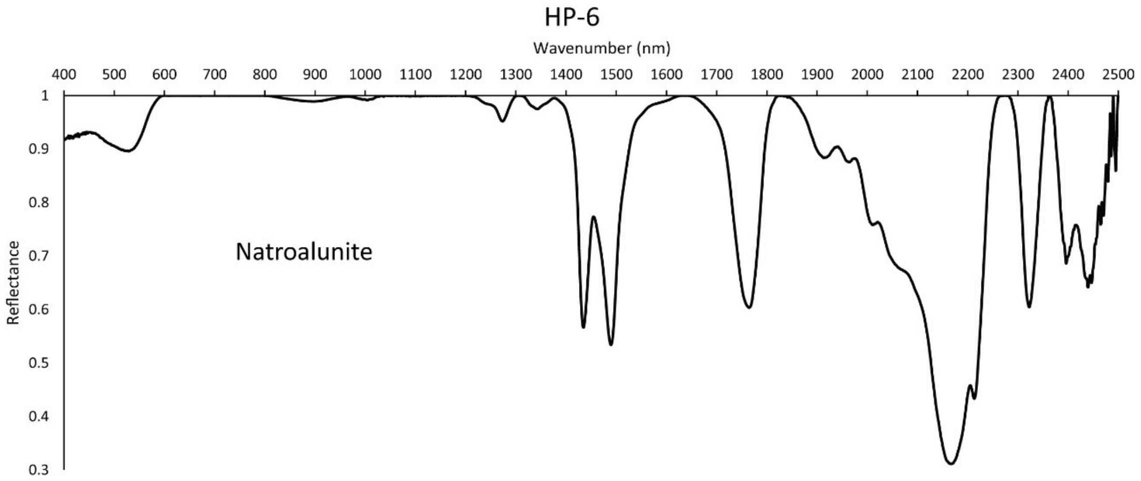
HP-6
Wavenumber (nm)
400 500 600 700 800 900 1000 1100 1200 1300 1400 1500 1600 1700 1800 1900 2000 2100 2200 2300 2400 2500
Reflectance
1 0.9 0.8 0.7 0.6 0.5 0.4 0.3
Natroalunite

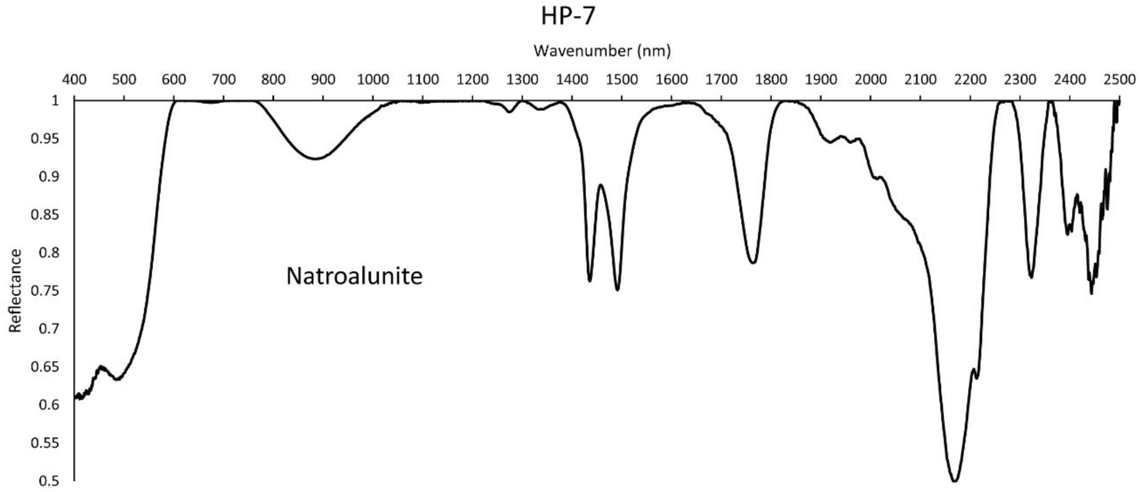
HP-7
Wavenumber (nm)
400
500
600
700
800
900
1000
1100
1200
1300
1400
1500
1600
1700
1800
1900
2000
2100
2200
2300
2400
2500
Reflectance
1
0.95
0.9
0.85
0.8
0.75
0.7
0.65
0.6
0.55
0.5
Natroalunite

Hope Brook high-sulfidation epithermal deposit

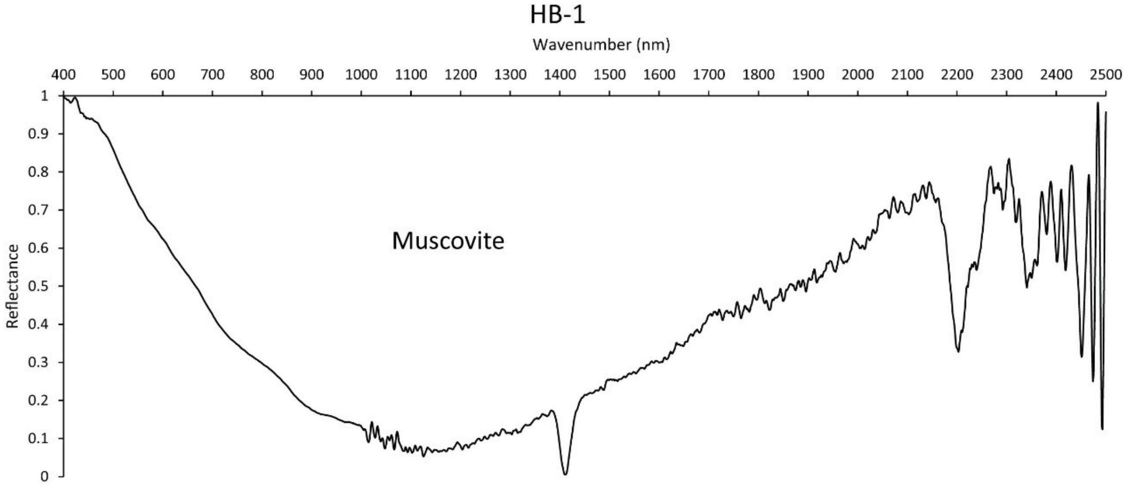

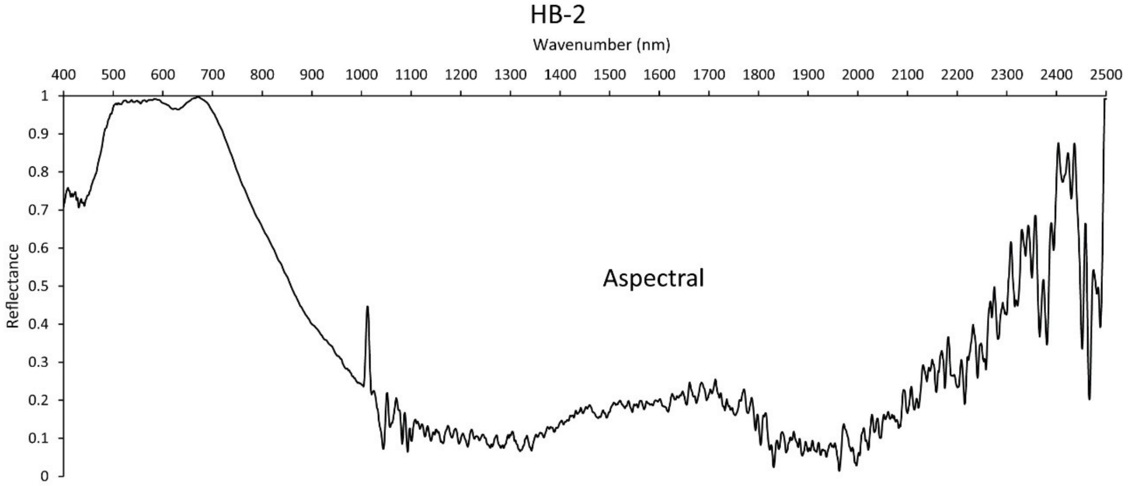

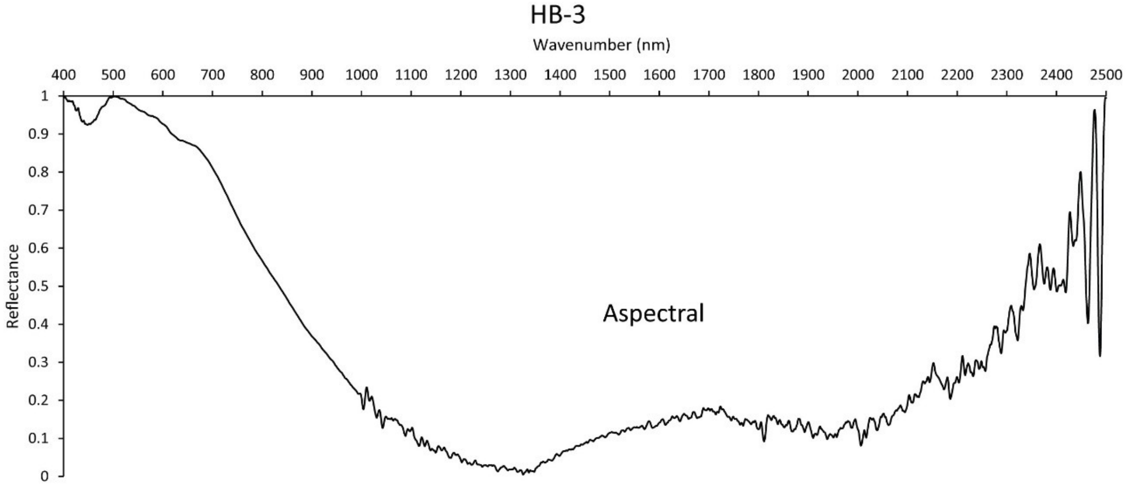

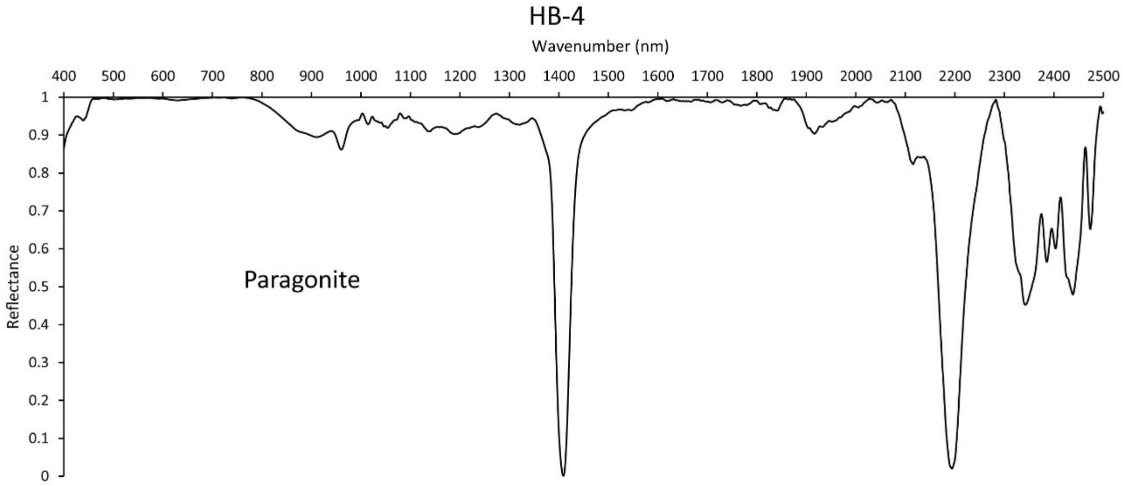
HB-4

Wavenumber (nm)
400 500 600 700 800 900 1000 1100 1200 1300 1400 1500 1600 1700 1800 1900 2000 2100 2200 2300 2400 2500
Reflectance
0 0.1 0.2 0.3 0.4 0.5 0.6 0.7 0.8 0.9 1
Paragonite

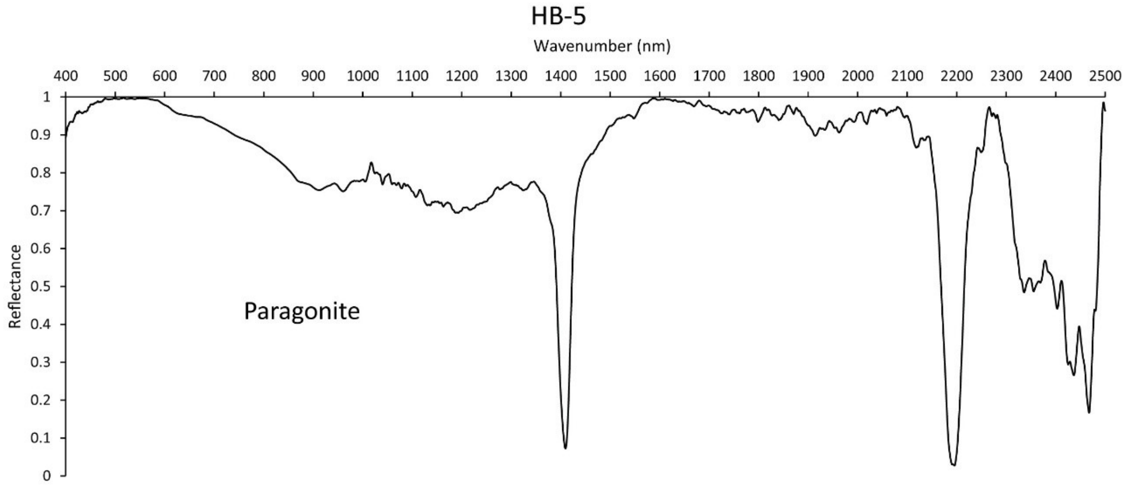
HB-5

Wavenumber (nm)
400 500 600 700 800 900 1000 1100 1200 1300 1400 1500 1600 1700 1800 1900 2000 2100 2200 2300 2400 2500
Reflectance
0 0.1 0.2 0.3 0.4 0.5 0.6 0.7 0.8 0.9 1
Paragonite

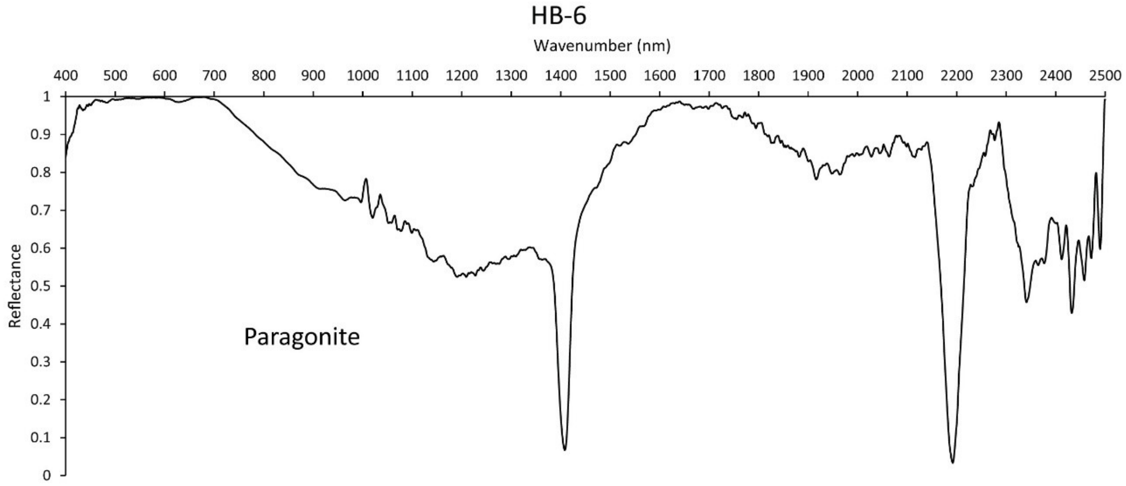
HB-6

Wavenumber (nm)
400 500 600 700 800 900 1000 1100 1200 1300 1400 1500 1600 1700 1800 1900 2000 2100 2200 2300 2400 2500
Reflectance
0 0.1 0.2 0.3 0.4 0.5 0.6 0.7 0.8 0.9 1
Paragonite

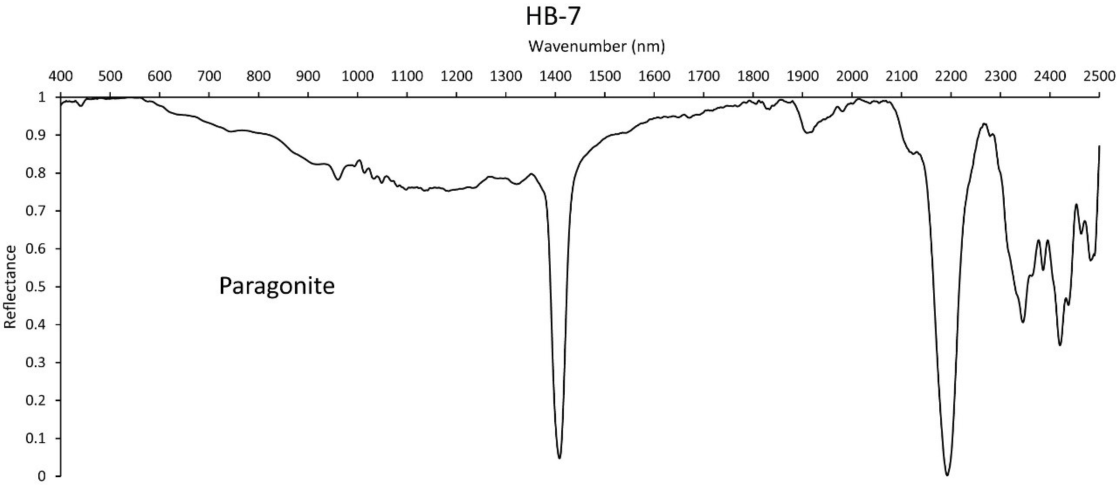
HB-7
Wavenumber (nm)
400
500
600
700
800
900
1000
1100
1200
1300
1400
1500
1600
1700
1800
1900
2000
2100
2200
2300
2400
2500
Reflectance
1
0.9
0.8
0.7
0.6
0.5
0.4
0.3
0.2
0.1
0
Paragonite

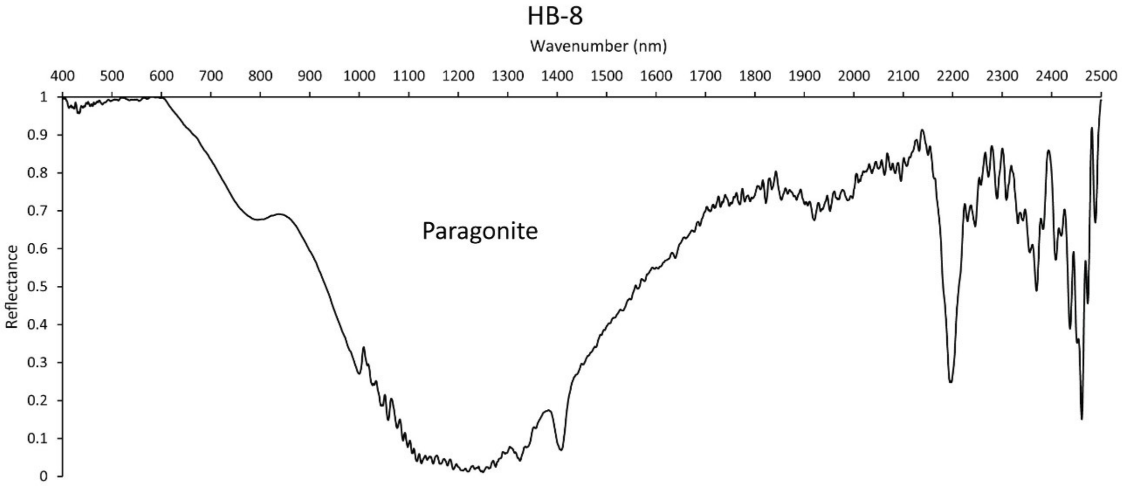
HB-8
Wavenumber (nm)
400
500
600
700
800
900
1000
1100
1200
1300
1400
1500
1600
1700
1800
1900
2000
2100
2200
2300
2400
2500
Reflectance
1
0.9
0.8
0.7
0.6
0.5
0.4
0.3
0.2
0.1
0
Paragonite

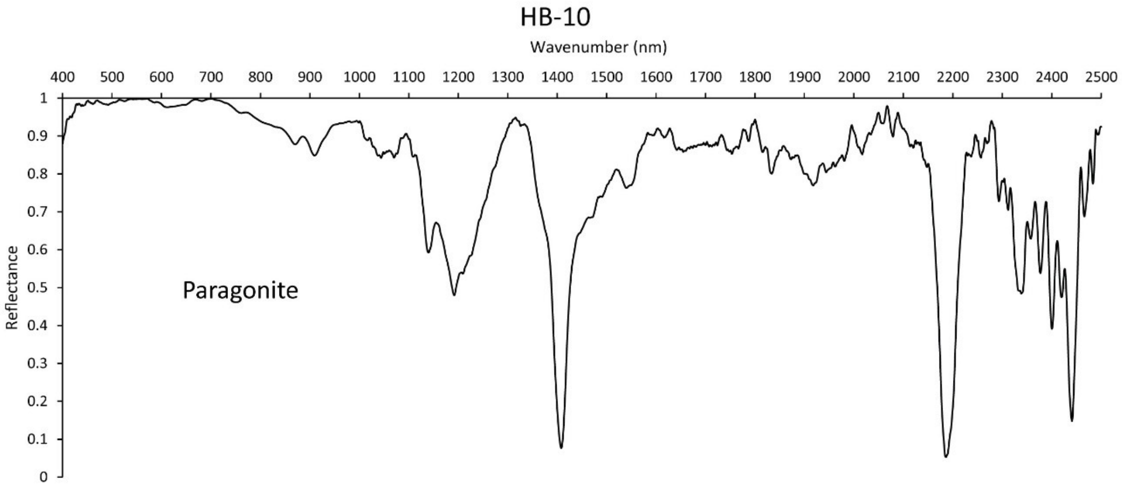
HB-10
Wavenumber (nm)
400
500
600
700
800
900
1000
1100
1200
1300
1400
1500
1600
1700
1800
1900
2000
2100
2200
2300
2400
2500
Reflectance
1
0.9
0.8
0.7
0.6
0.5
0.4
0.3
0.2
0.1
0
Paragonite

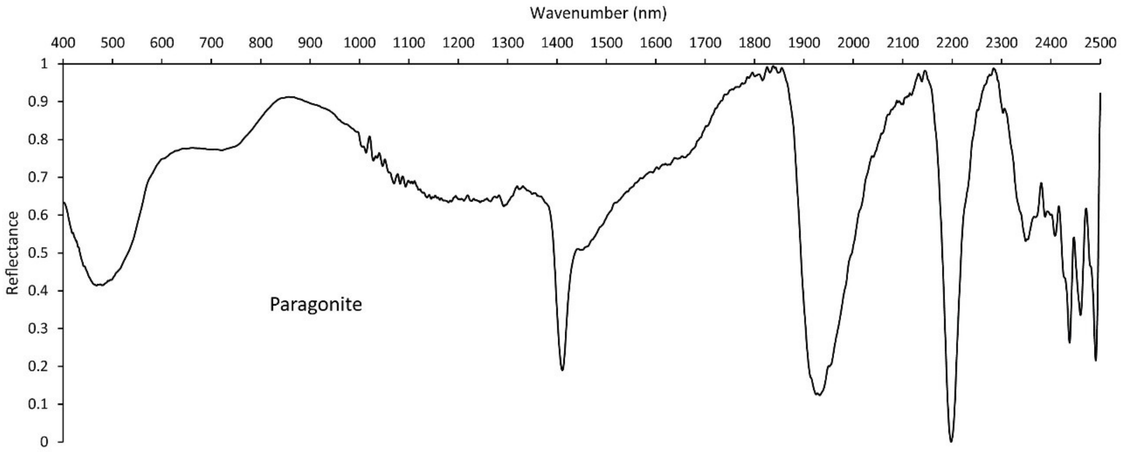
HB-11

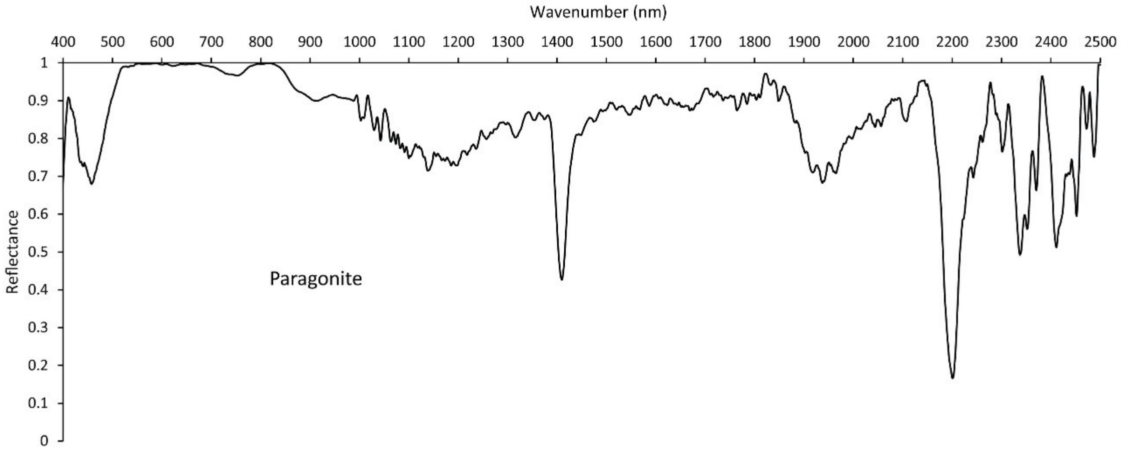
HB-12

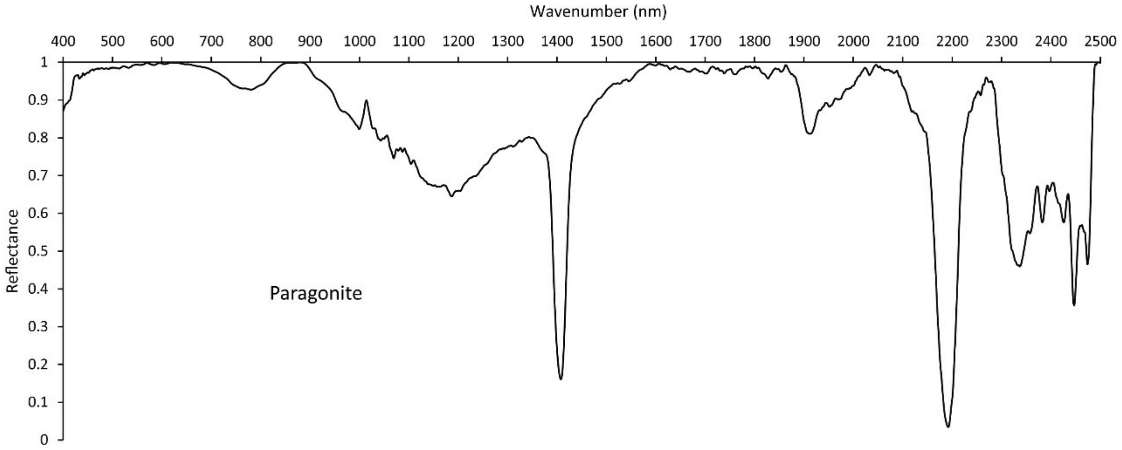
HB-13

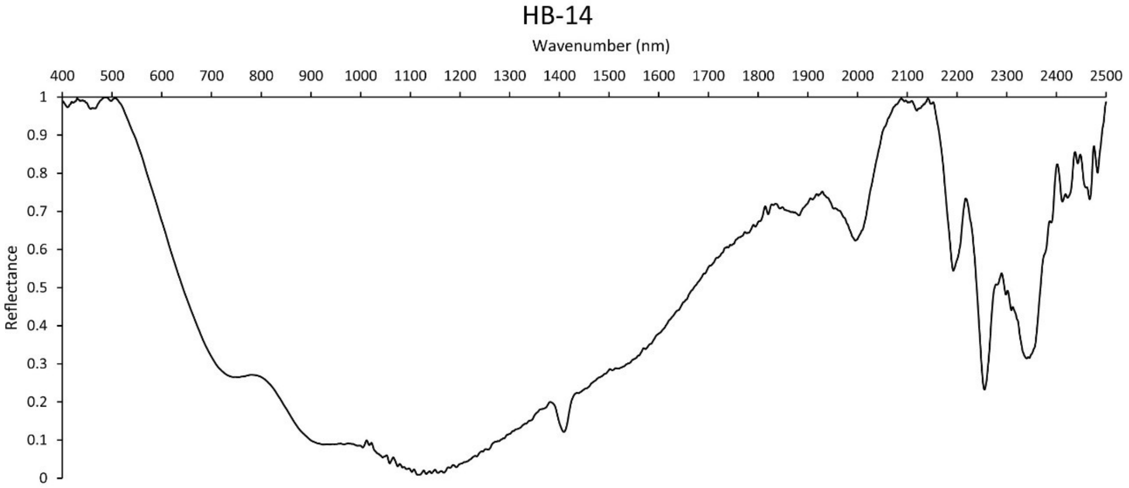
HB-14

Wavenumber (nm)
400
500
600
700
800
900
1000
1100
1200
1300
1400
1500
1600
1700
1800
1900
2000
2100
2200
2300
2400
2500
Reflectance
1
0.9
0.8
0.7
0.6
0.5
0.4
0.3
0.2
0.1
0

Heritage low-sulfidation epithermal prospect

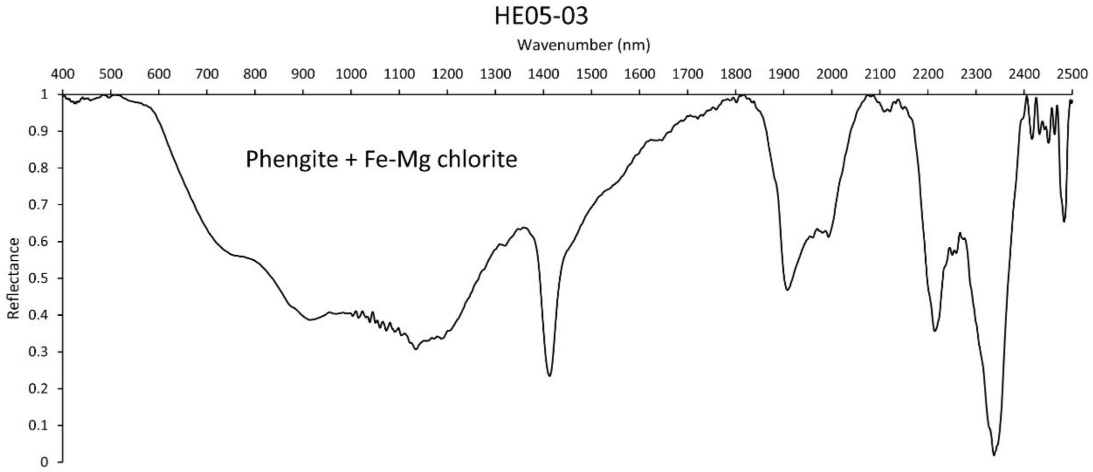

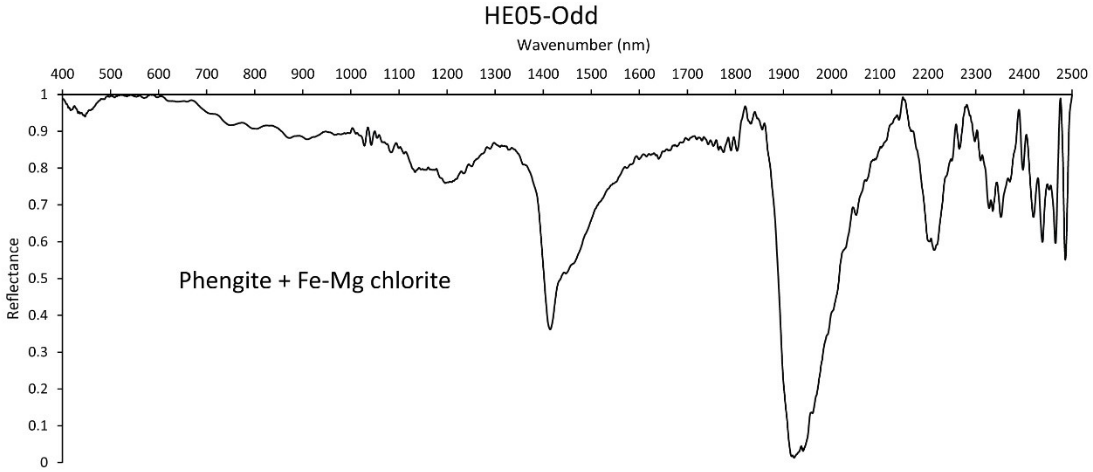

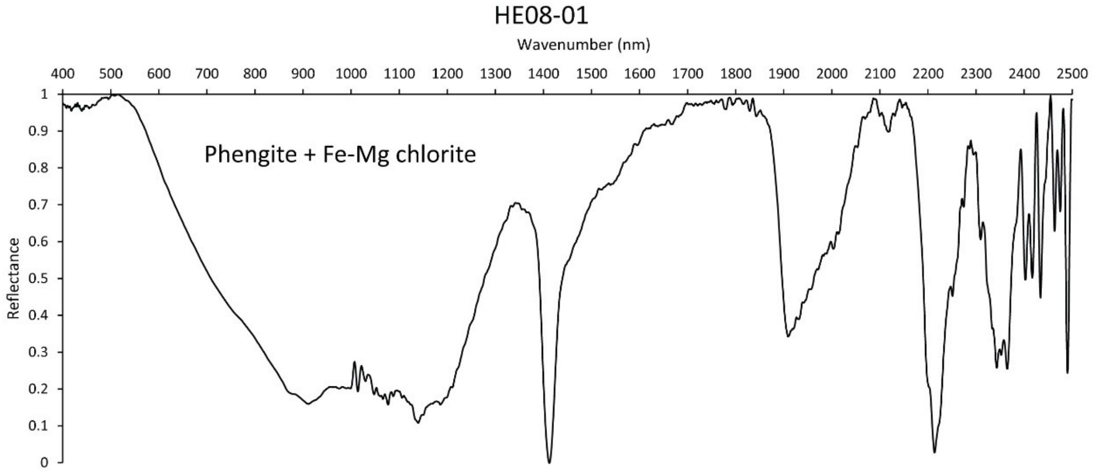

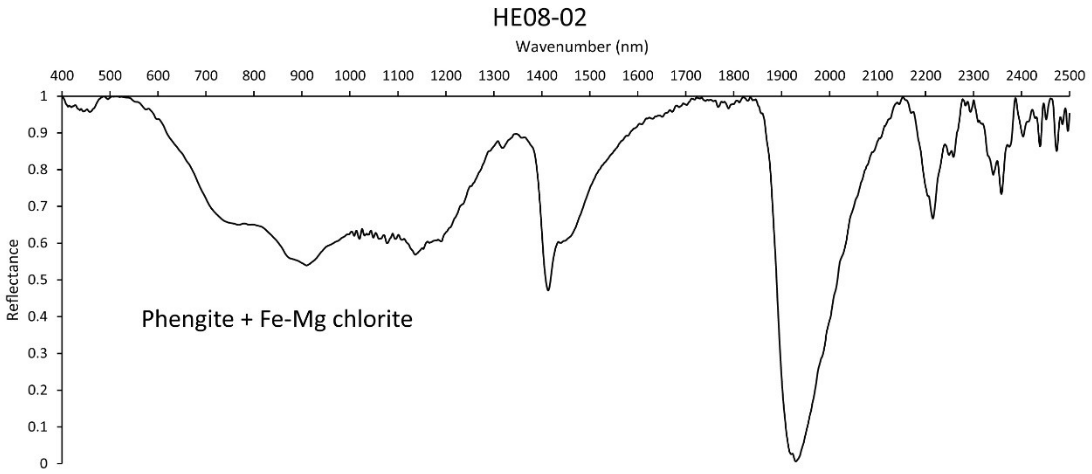
HE08-02
Wavenumber (nm)
400
500
600
700
800
900
1000
1100
1200
1300
1400
1500
1600
1700
1800
1900
2000
2100
2200
2300
2400
2500
Reflectance
1
0.9
0.8
0.7
0.6
0.5
0.4
0.3
0.2
0.1
0
Phengite + Fe-Mg chlorite

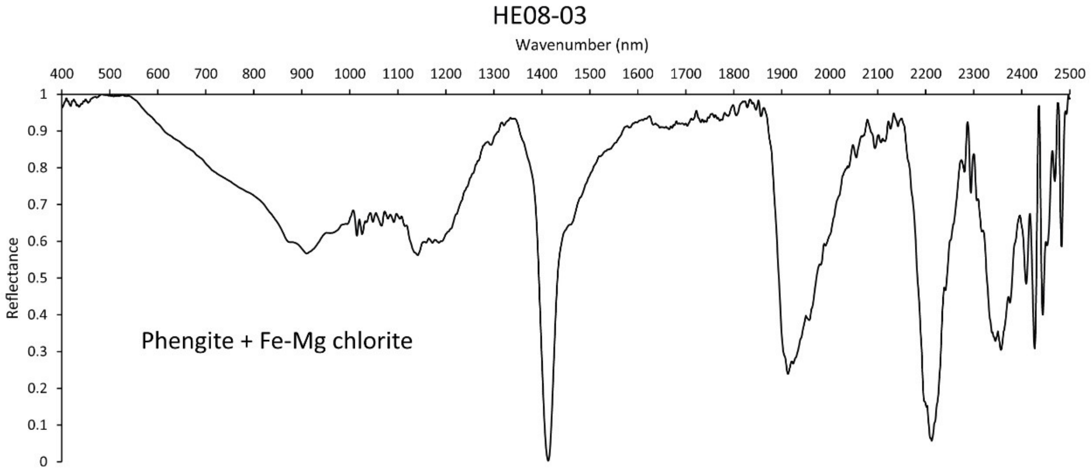
HE08-03
Wavenumber (nm)
400
500
600
700
800
900
1000
1100
1200
1300
1400
1500
1600
1700
1800
1900
2000
2100
2200
2300
2400
2500
Reflectance
1
0.9
0.8
0.7
0.6
0.5
0.4
0.3
0.2
0.1
0
Phengite + Fe-Mg chlorite

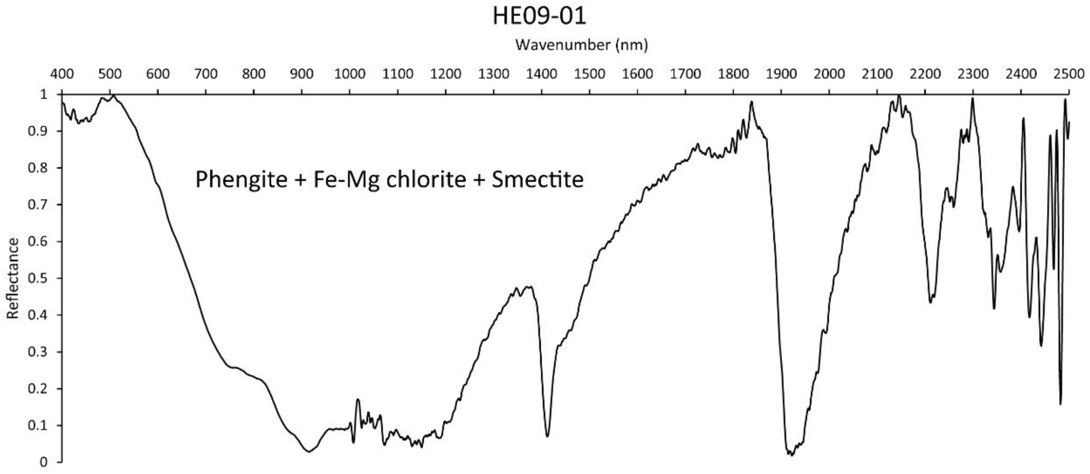
HE09-01
Wavenumber (nm)
400
500
600
700
800
900
1000
1100
1200
1300
1400
1500
1600
1700
1800
1900
2000
2100
2200
2300
2400
2500
Reflectance
1
0.9
0.8
0.7
0.6
0.5
0.4
0.3
0.2
0.1
0
Phengite + Fe-Mg chlorite + Smectite

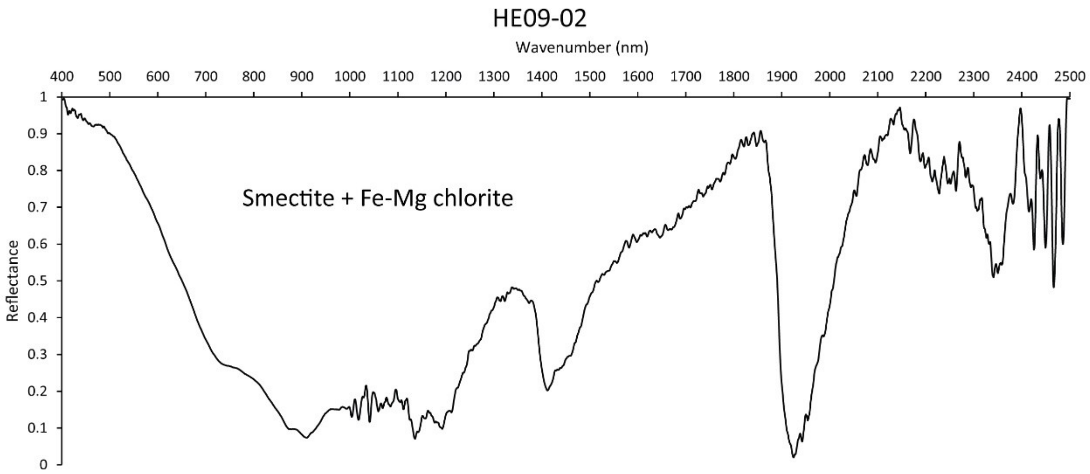
HE09-02
Wavenumber (nm)
400
500
600
700
800
900
1000
1100
1200
1300
1400
1500
1600
1700
1800
1900
2000
2100
2200
2300
2400
2500
Reflectance
1
0.9
0.8
0.7
0.6
0.5
0.4
0.3
0.2
0.1
0
Smectite + Fe-Mg chlorite

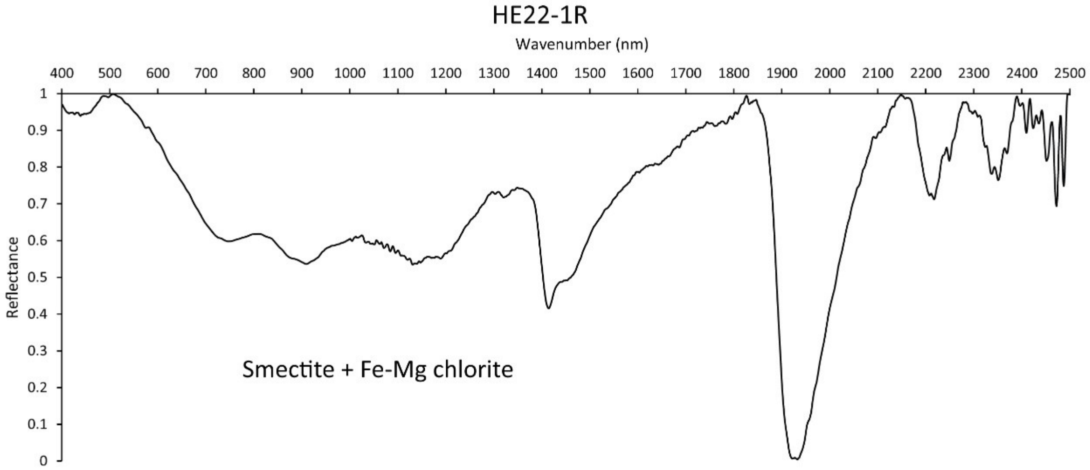
HE22-1R
Wavenumber (nm)
400
500
600
700
800
900
1000
1100
1200
1300
1400
1500
1600
1700
1800
1900
2000
2100
2200
2300
2400
2500
Reflectance
1
0.9
0.8
0.7
0.6
0.5
0.4
0.3
0.2
0.1
0
Smectite + Fe-Mg chlorite

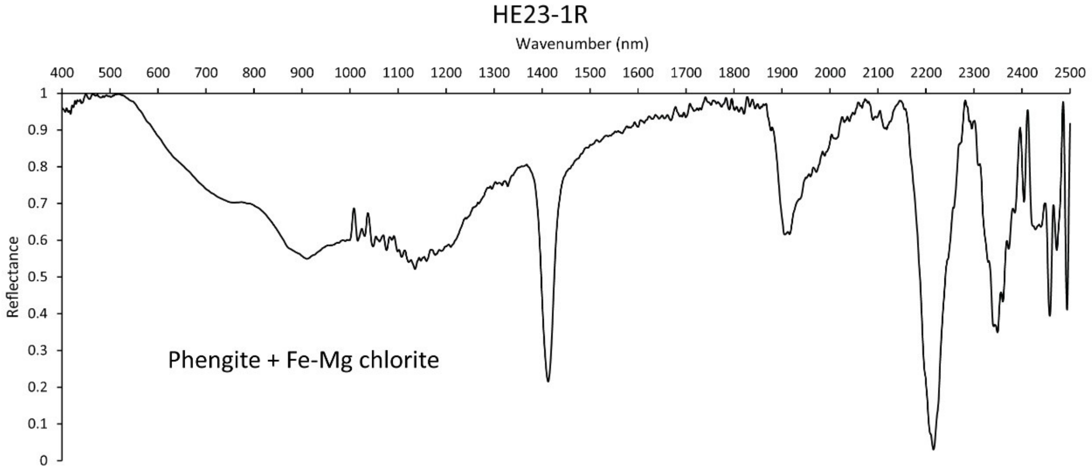
HE23-1R
Wavenumber (nm)
400
500
600
700
800
900
1000
1100
1200
1300
1400
1500
1600
1700
1800
1900
2000
2100
2200
2300
2400
2500
Reflectance
1
0.9
0.8
0.7
0.6
0.5
0.4
0.3
0.2
0.1
0
Phengite + Fe-Mg chlorite

HE23-2R

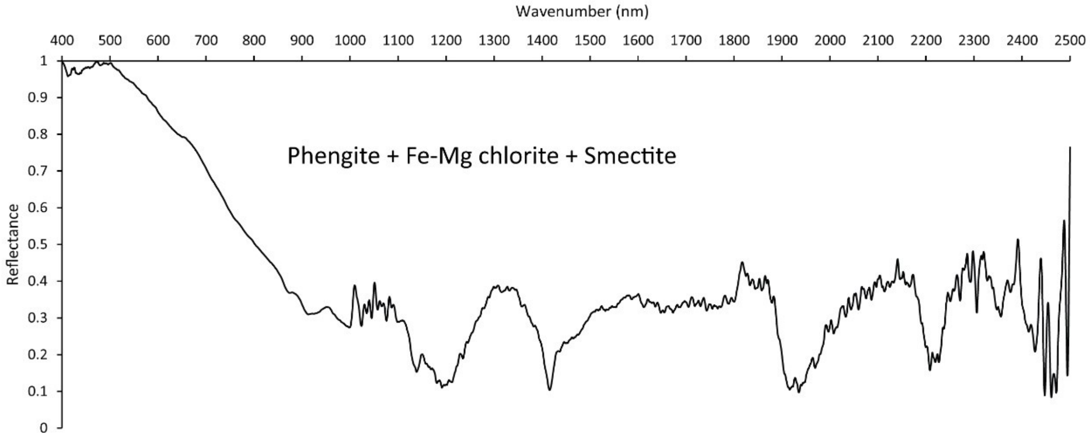

HE23-3R

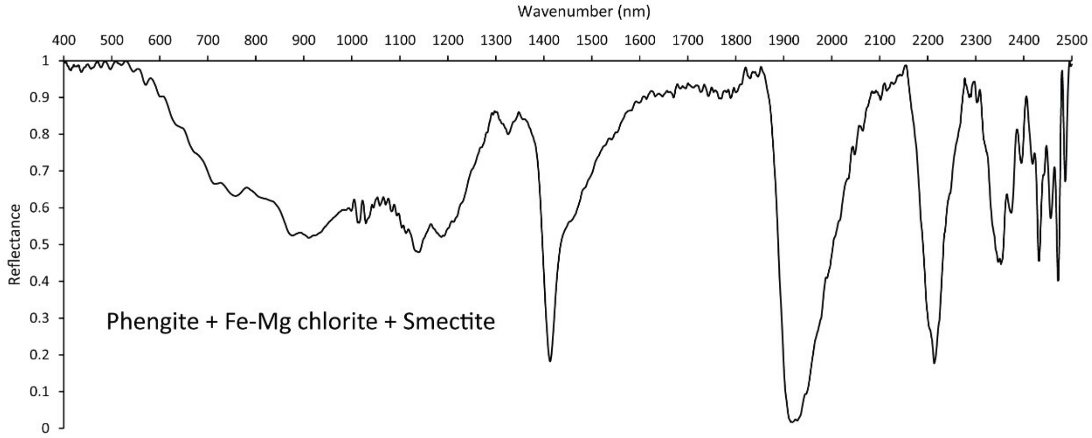

HE24-1R

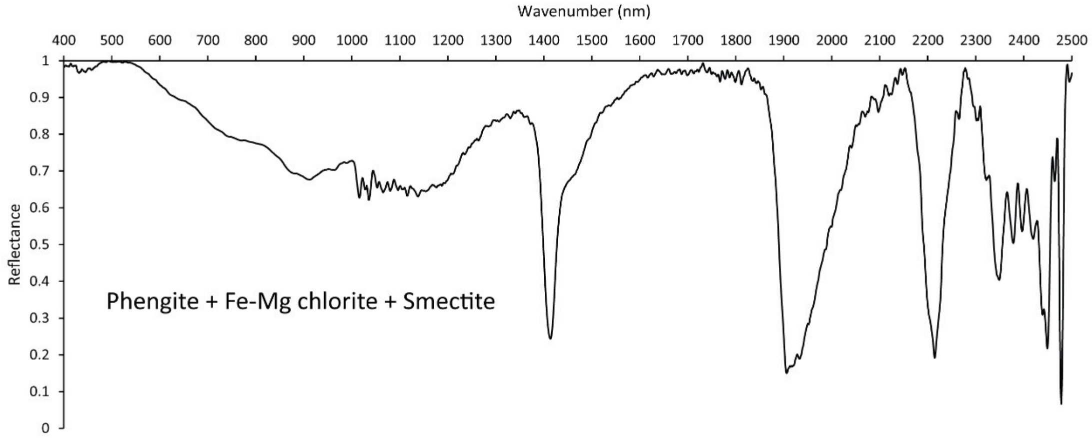

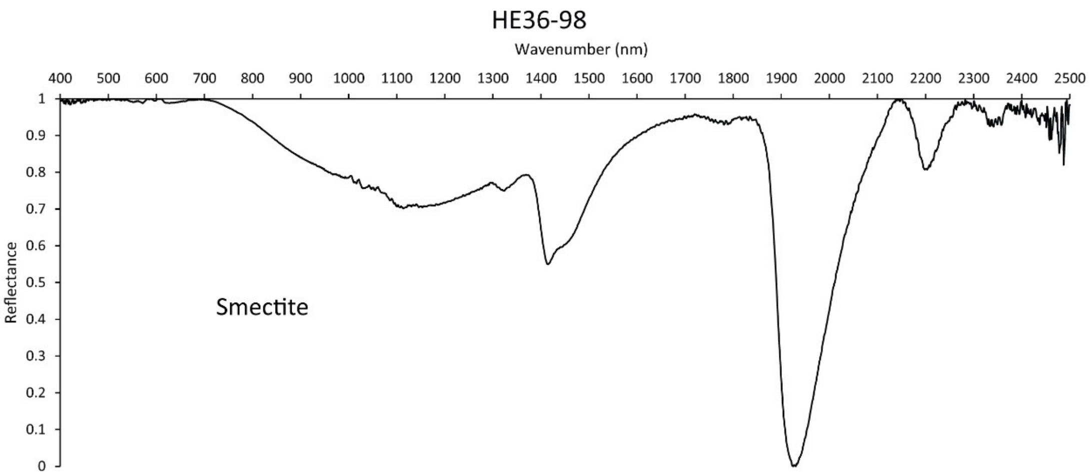
HE36-98
Wavenumber (nm)
400 500 600 700 800 900 1000 1100 1200 1300 1400 1500 1600 1700 1800 1900 2000 2100 2200 2300 2400 2500
Reflectance
1 0.9 0.8 0.7 0.6 0.5 0.4 0.3 0.2 0.1 0
Smectite

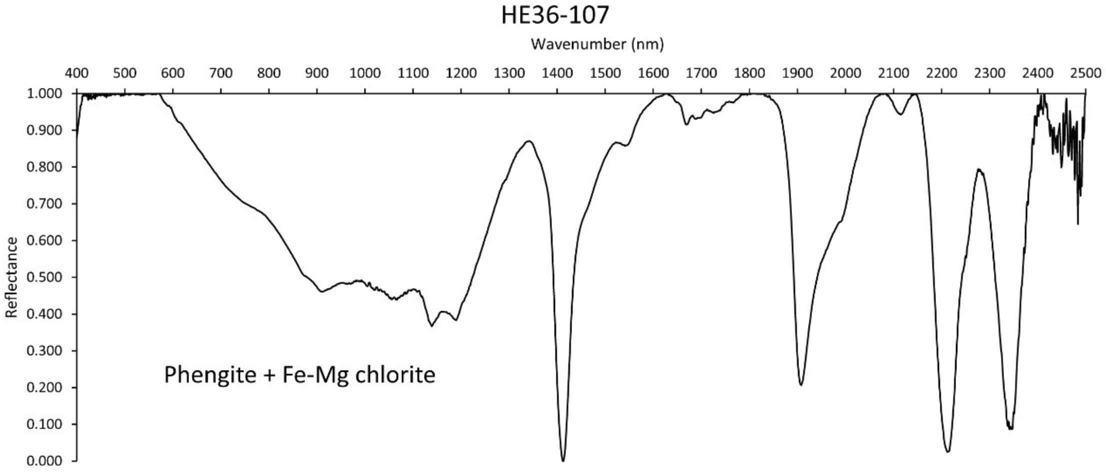
HE36-107
Wavenumber (nm)
400 500 600 700 800 900 1000 1100 1200 1300 1400 1500 1600 1700 1800 1900 2000 2100 2200 2300 2400 2500
Reflectance
1.000 0.900 0.800 0.700 0.600 0.500 0.400 0.300 0.200 0.100 0.000
Phengite + Fe-Mg chlorite

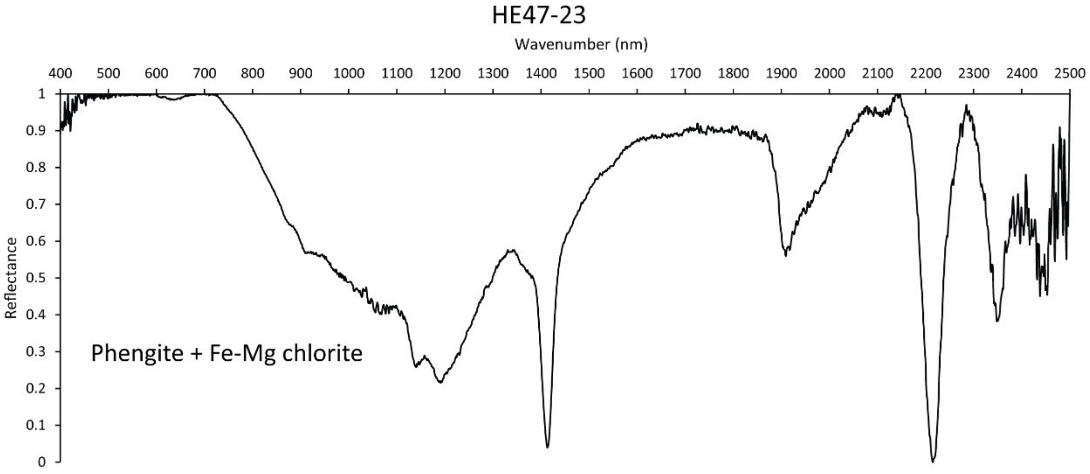
HE47-23
Wavenumber (nm)
400 500 600 700 800 900 1000 1100 1200 1300 1400 1500 1600 1700 1800 1900 2000 2100 2200 2300 2400 2500
Reflectance
1 0.9 0.8 0.7 0.6 0.5 0.4 0.3 0.2 0.1 0
Phengite + Fe-Mg chlorite

HE47-26

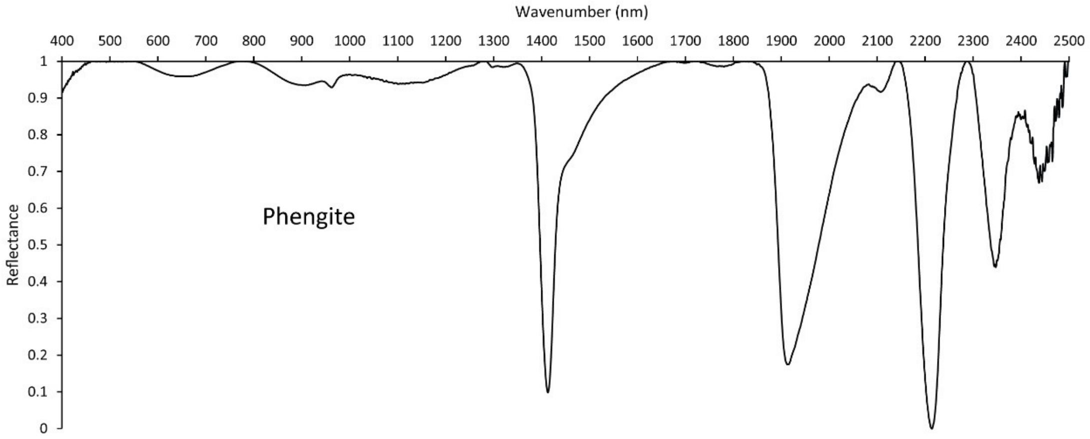

HE47-27

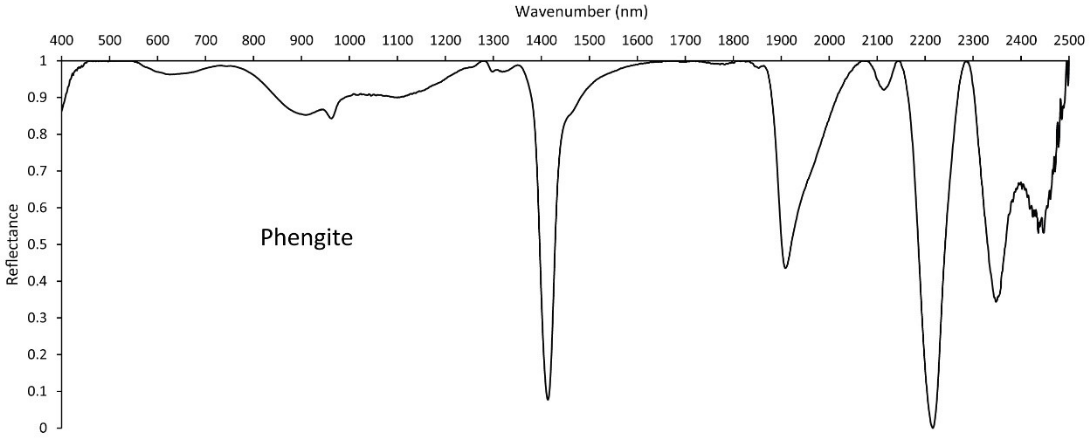

HE48-28

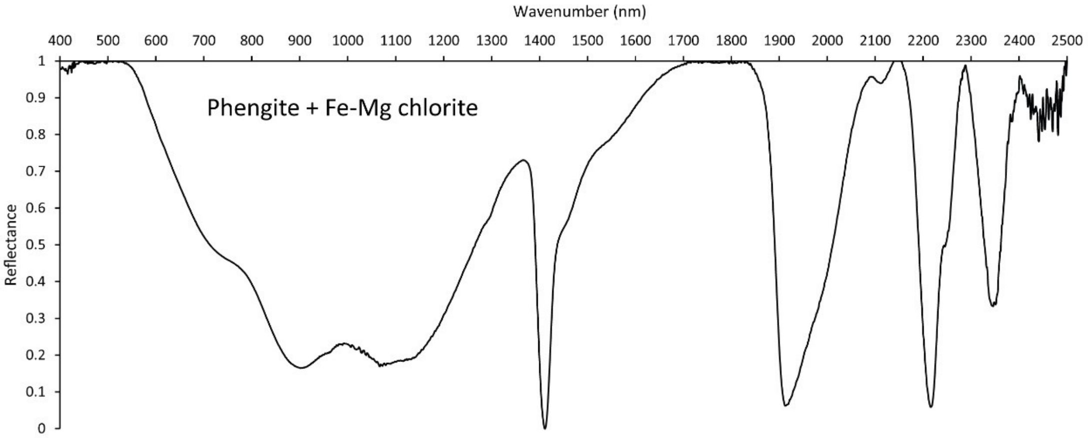

Appendix 5. Raman spectra of studied hydrothermally-altered samples from high- and low-sulfidation epithermal deposits from the Avalon Zone of Newfoundland.

Remarks on the selection of Raman laser wavelength:

The two Raman systems used in this study were equipped with an 830 nm and a 630 nm excitation laser, respectively. The 830 nm system was the primary system used for the present study. The 633nm laser system was used specifically to acquire H_2O and OH group spectra that occur in the 3000-3700 cm^{-1} region.

Excitation lasers in the green-blue range, particularly 532 nm diode lasers, are widely used for the analysis of geological samples. This wavelength is considered broadly beneficial for minimizing fluorescence effects; however, there is no best wavelength prescribed for all cases of mineral analysis (Wang et al., 2015). As described in Chapter 3, the excitation laser wavelengths used in this thesis allowed the acquisition of high-quality Raman spectra comparable with published spectra acquired using other laser wavelengths and instruments. Excitation wavelength should not affect the absolute position of Raman peaks, and in our study, the positions of key Raman bands were found to be in excellent agreement with those available in the published literature.

Remarks on the effect of mineral size and orientation:

Although the literature on the effects of grain size and grain orientation on the Raman spectra of minerals is limited, there is some useful guidance in Sharma et al (2000) based on laboratory measurements of sized mineral particulates:

Based on measurements of sized quartz particulates, Raman lines are expected to broaden somewhat with decreasing grain size, but they remain well-resolved for grain sizes greater than approximately 10 µm. Characteristic band position was constant except for a slight shift (1.1 cm^{-1}) in the finest grained material (<1 – 11µm). There was also an observed decrease in intensity with diminishing grain size, as also documented in several other mineral studies cited therein.

Based on measurements of sized olivine particulates, characteristic band position was constant for grain sizes of 64 – 1000 µm, with a small observed shift (1.0 -1.5 cm^{-1}) for the smallest fraction tested (20-63 µm).

For both minerals, orientation effects on band intensity were most pronounced for grains sizes >100 µm. For finer grain sizes this effect was limited to approximately 10% relative.

Given the spatial resolution (laser spot diameter) of approximately 20 µm, and the manual mode in which sampled grains were selected for our study, the effects document above by Sharma et al (2000) have a negligible effect on the inter-comparability of our data with most published spectra, and allow the resolution of composition vs. band position effects at a 1.0 – 2.0 cm^{-1} level.

Sharma, S.K., Chio, C.H., Deb, P., Lucey, P.G., Domergue-Schmidt, N., Horton, K.A., 2000. Effect of grain size and grain orientation on the Raman spectra of minerals. Lunar and Planetary Science XXXI

Wang, A., Freeman, J.J., Jolliff, B.L., 2015. Understanding the Raman spectral features of phyllosilicates. Journal of Raman Spectroscopy 46, 829-845. https://doi.org/10.1002/jrs.4680

Oval Pit pyrophyllite mine and Vinjer high-sulfidation epithermal prospect

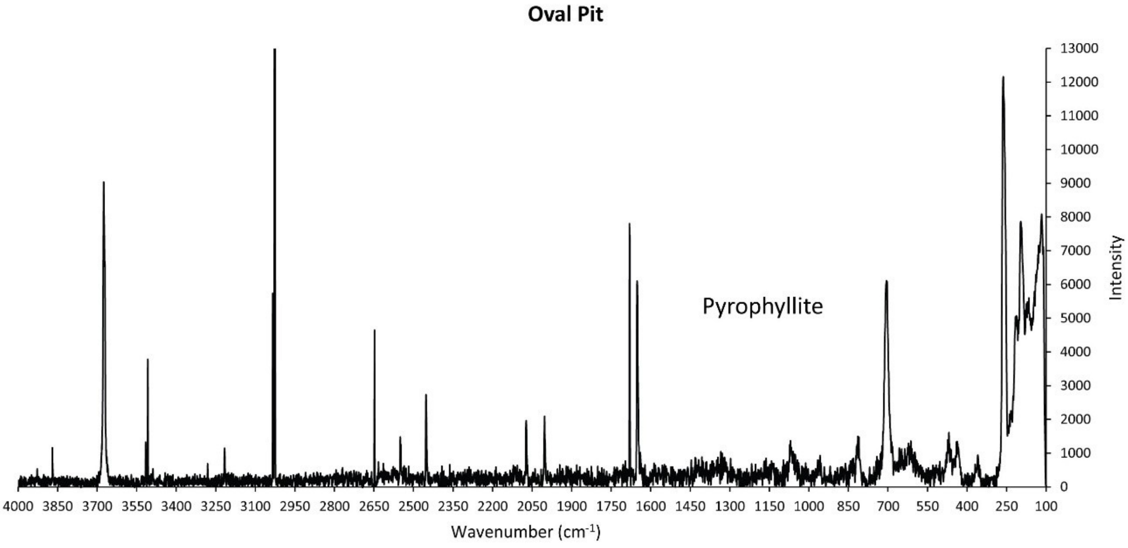

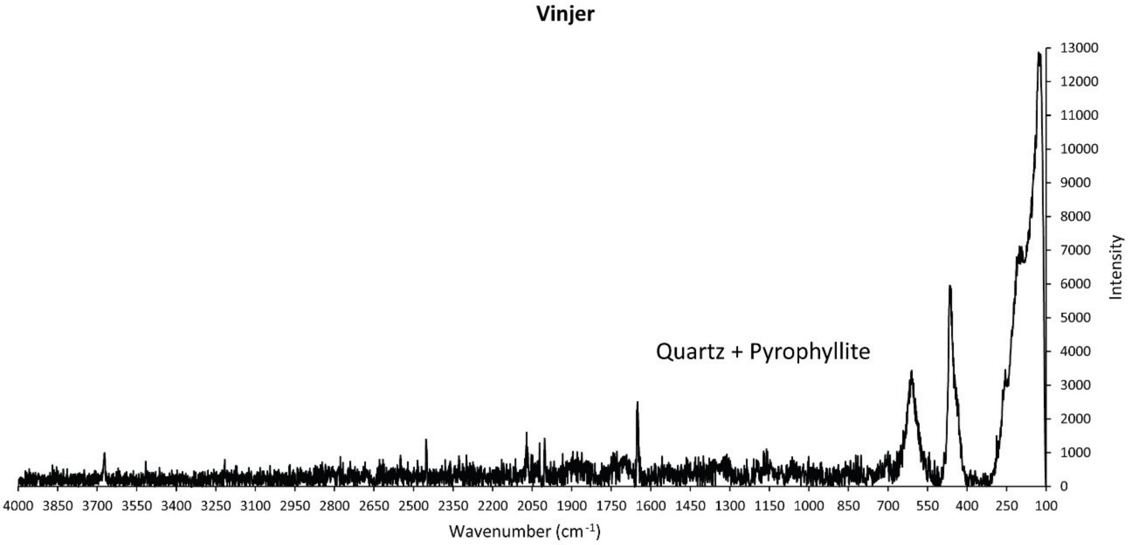

Hickey’s Pond high-sulfidation epithermal prospect

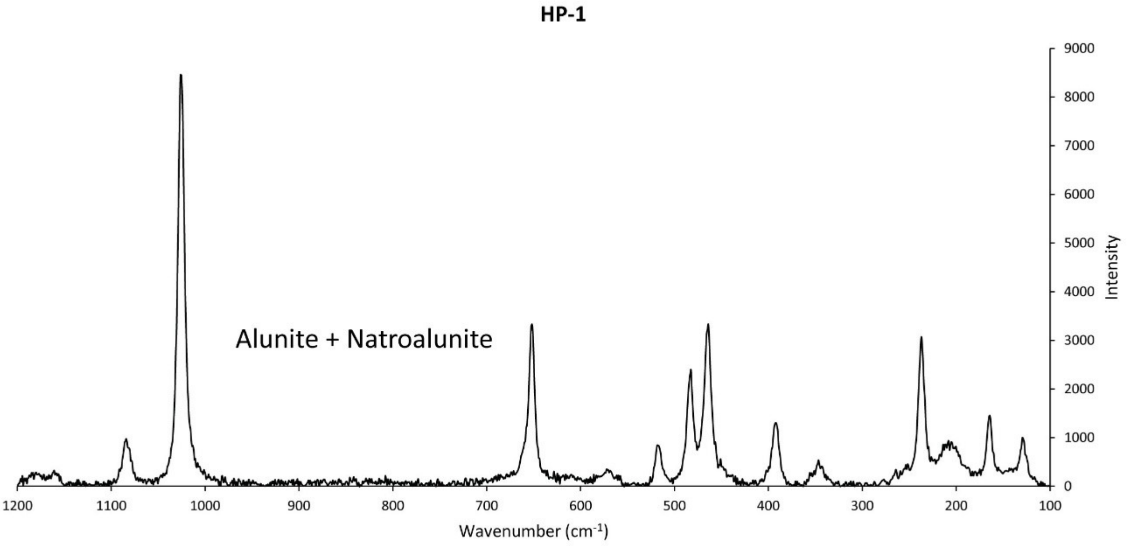

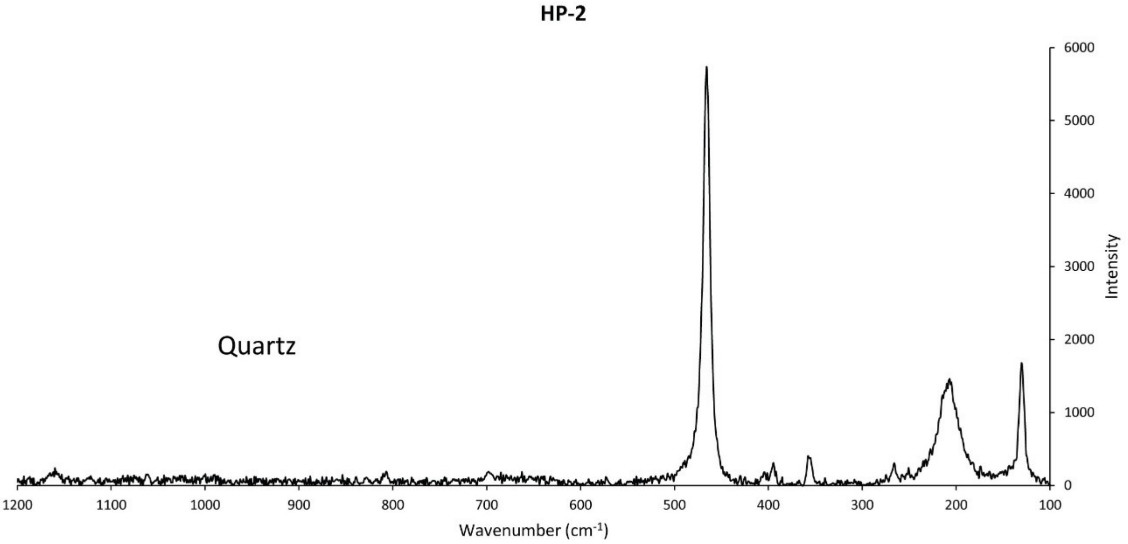

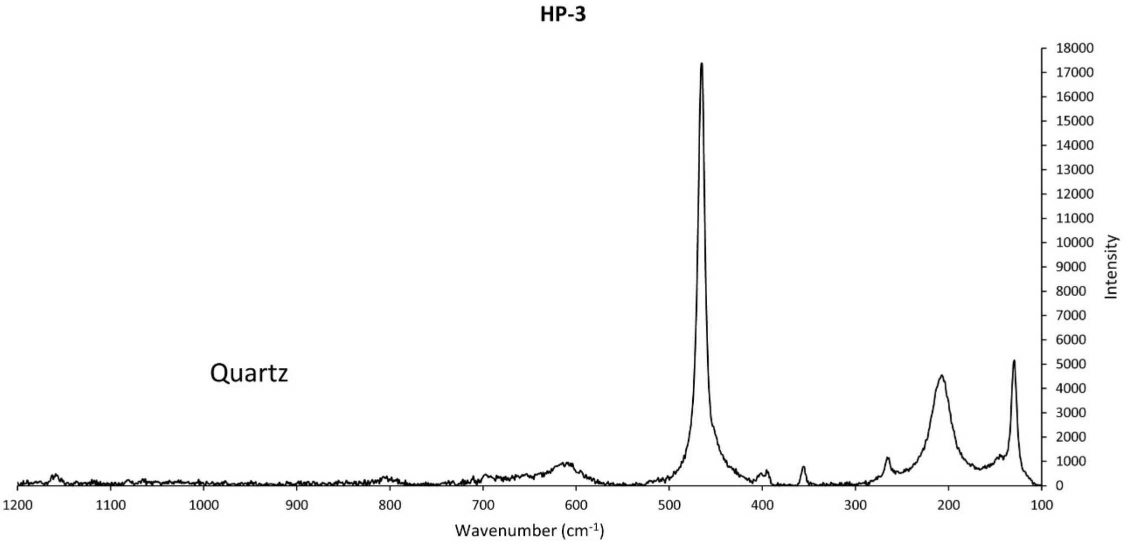

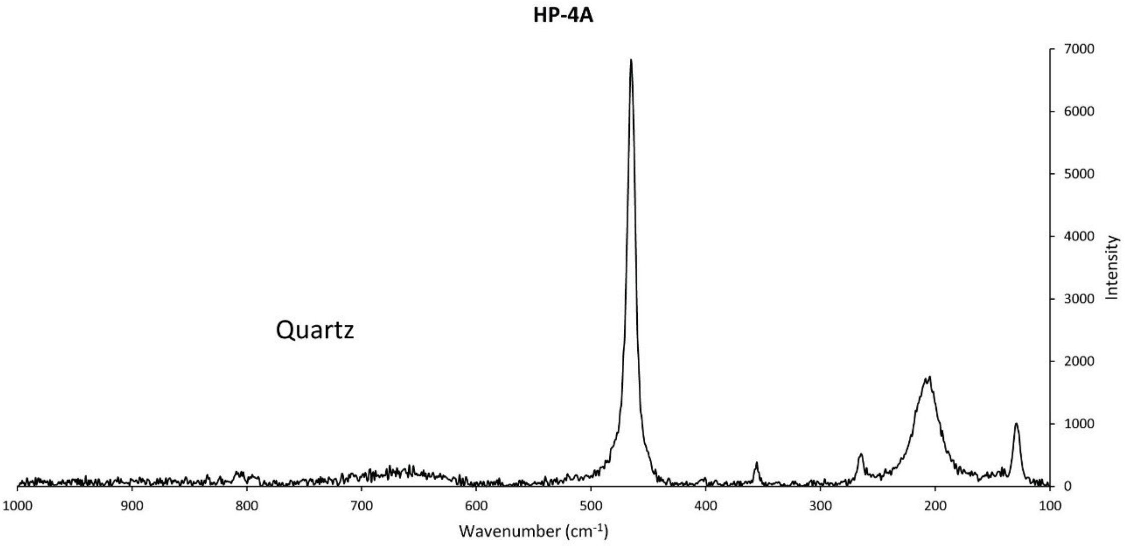

HP-4A

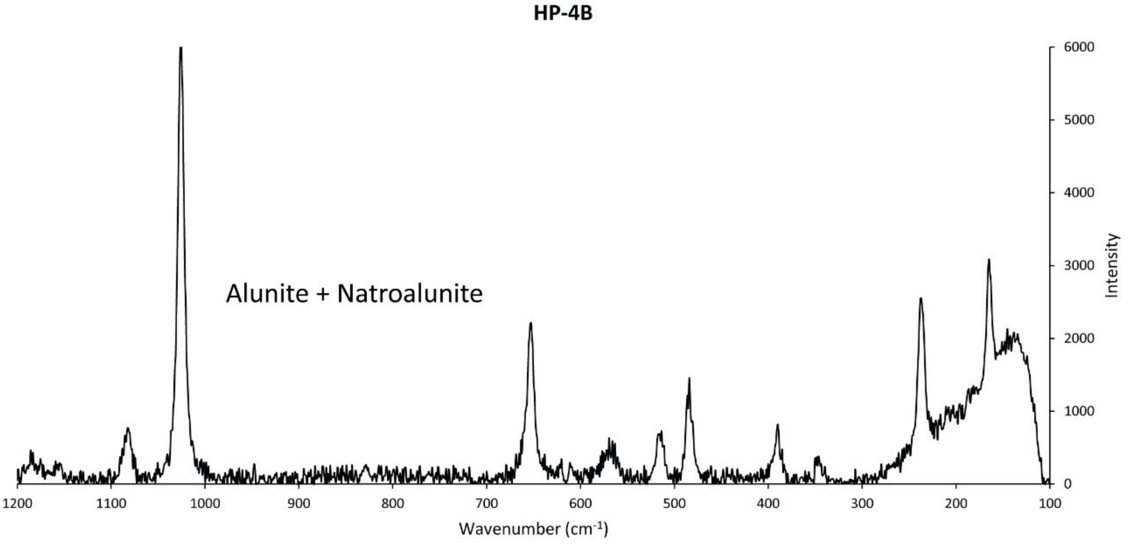

HP-4B

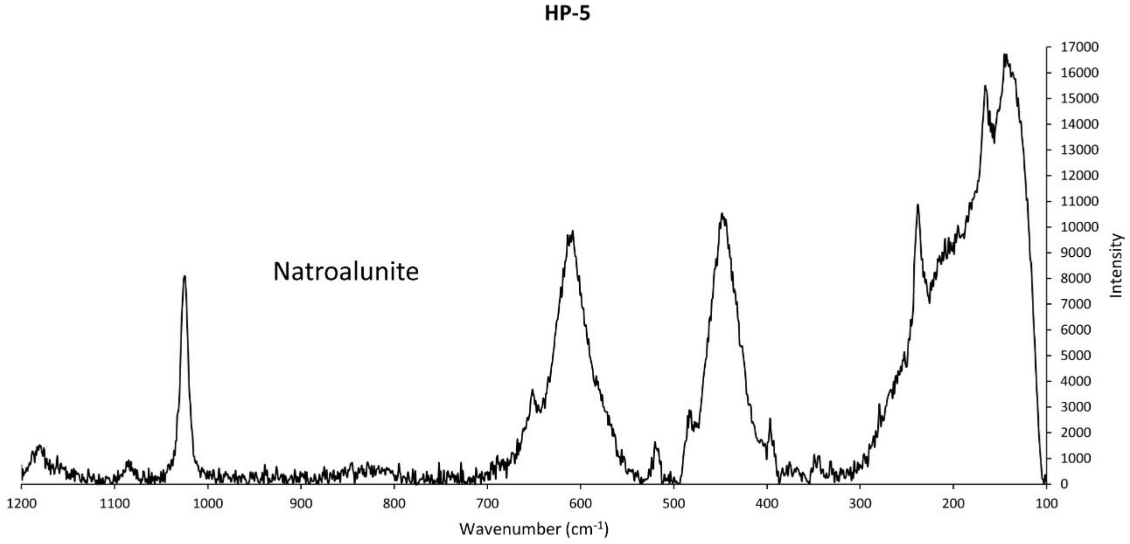

HP-5

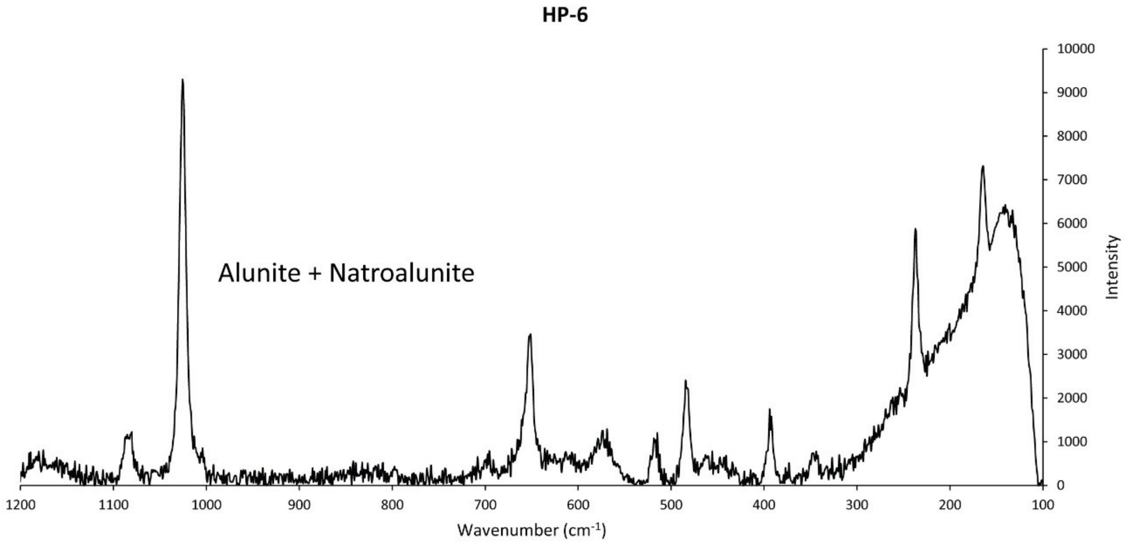
HP-6
Alunite + Natroalunite
Intensity
10000
9000
8000
7000
6000
5000
4000
3000
2000
1000
0
1200
1100
1000
900
800
700
600
500
400
300
200
100
Wavenumber (cm-1)

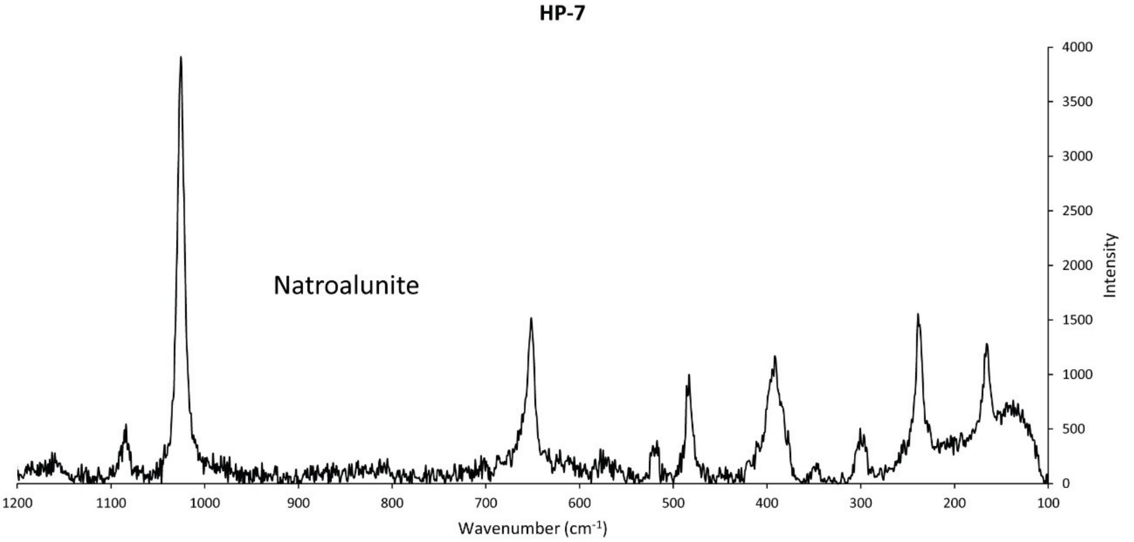
HP-7
Natroalunite
Intensity
4000
3500
3000
2500
2000
1500
1000
500
0
1200
1100
1000
900
800
700
600
500
400
300
200
100
Wavenumber (cm-1)

Hope Brook high-sulfidation epithermal deposit

HB-1

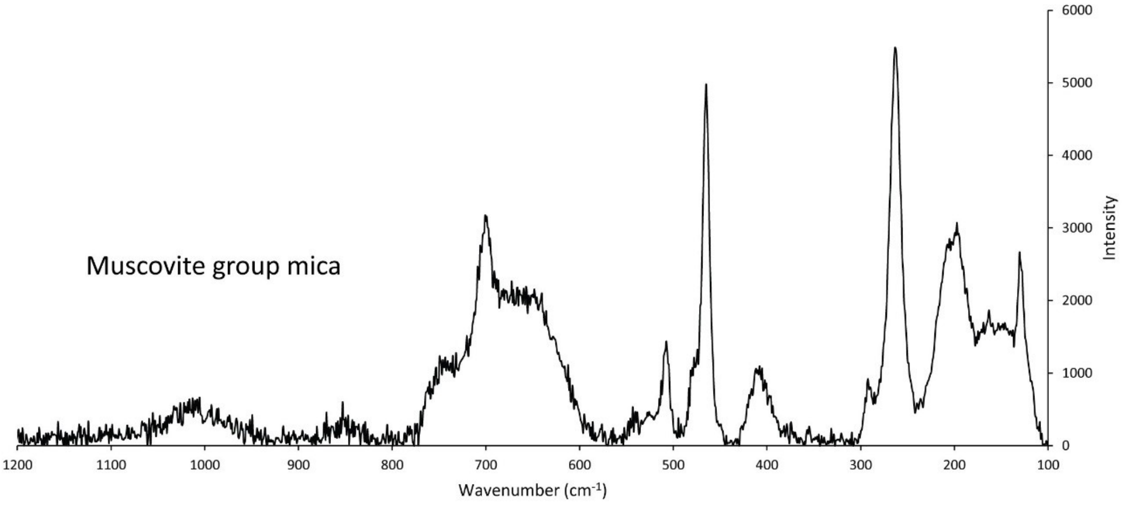

HB-4

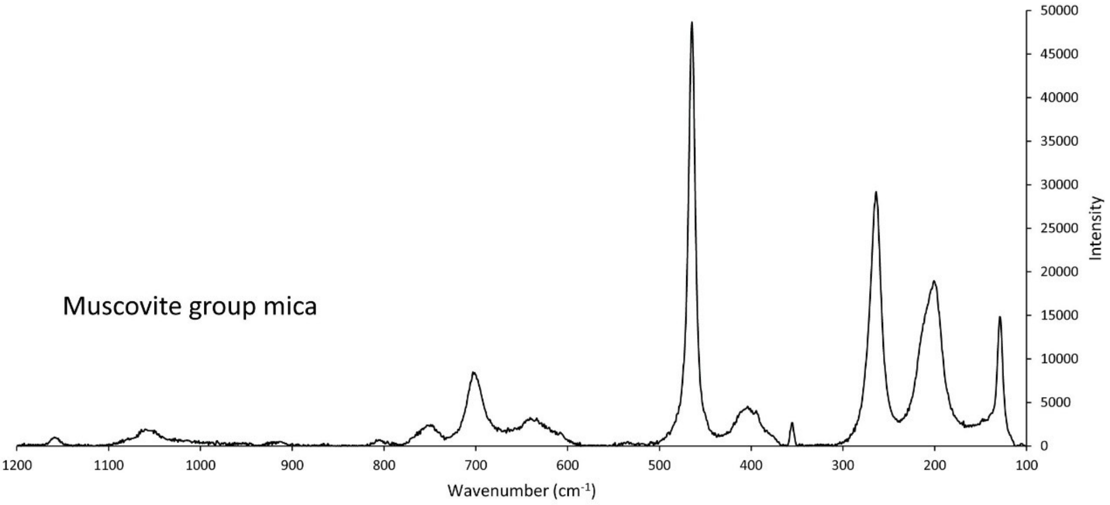

HB-5

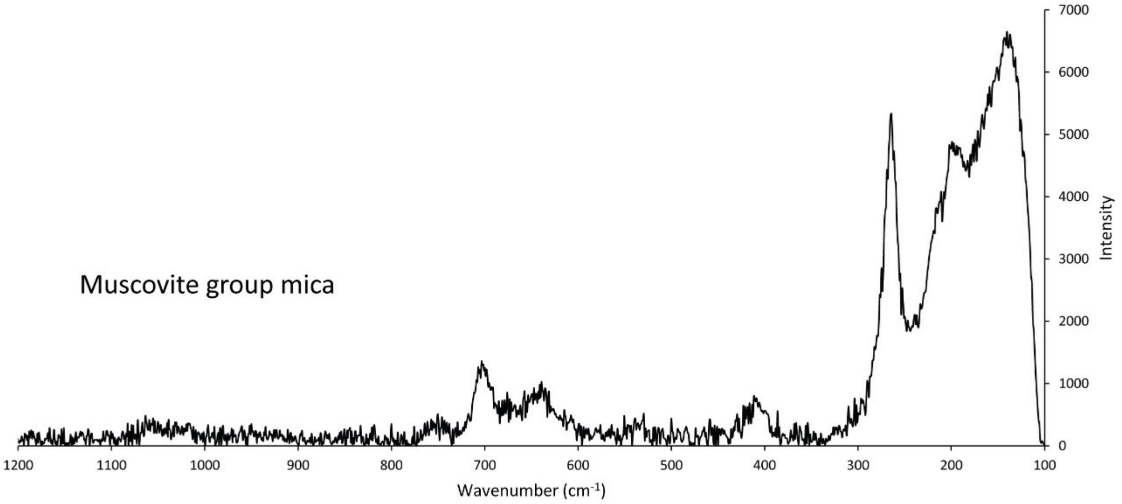

HB-6

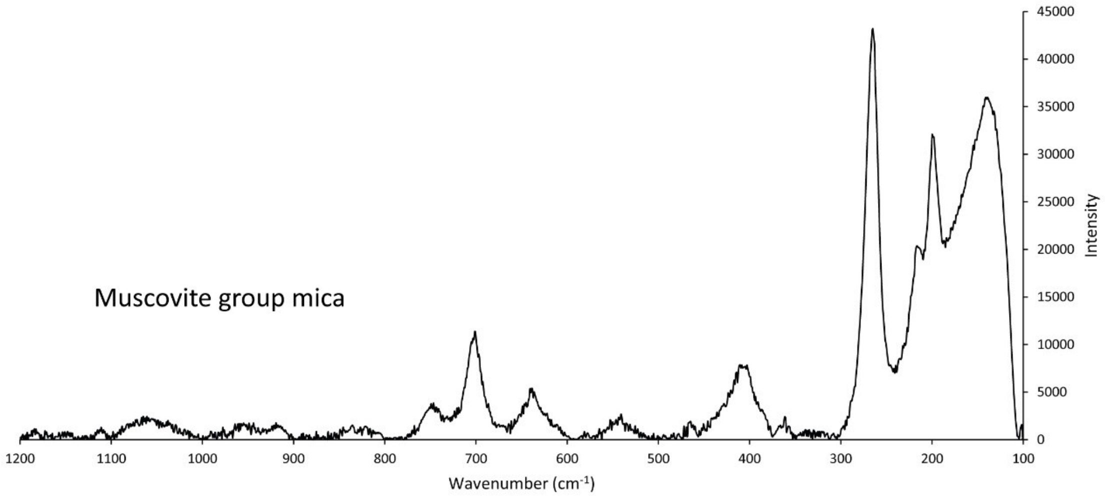

Muscovite group mica

HB-7

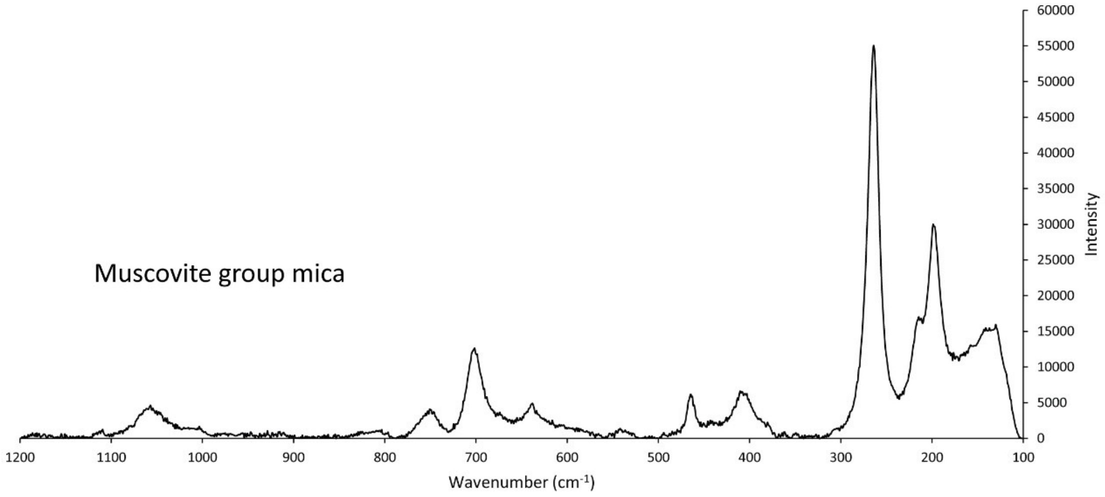

Muscovite group mica

HB-8

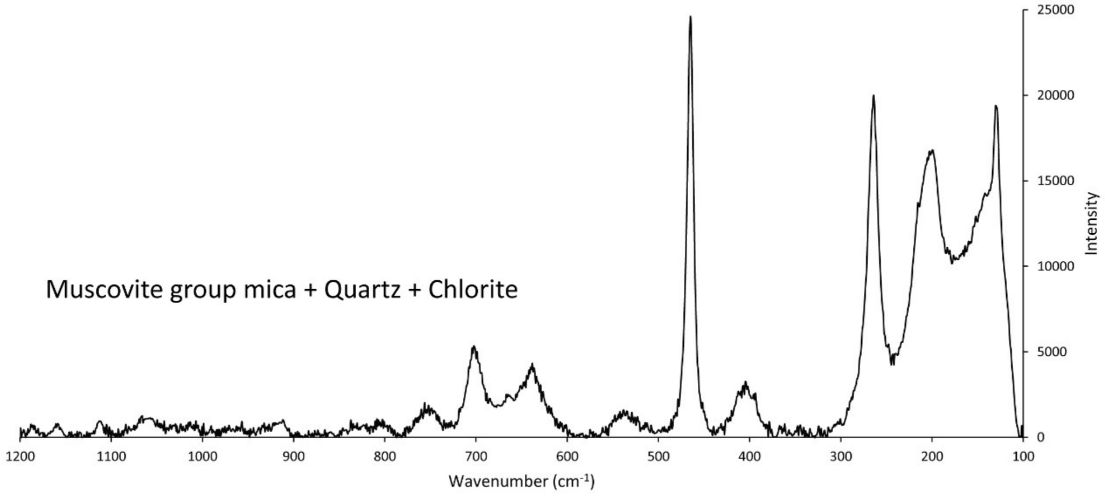

Muscovite group mica + Quartz + Chlorite

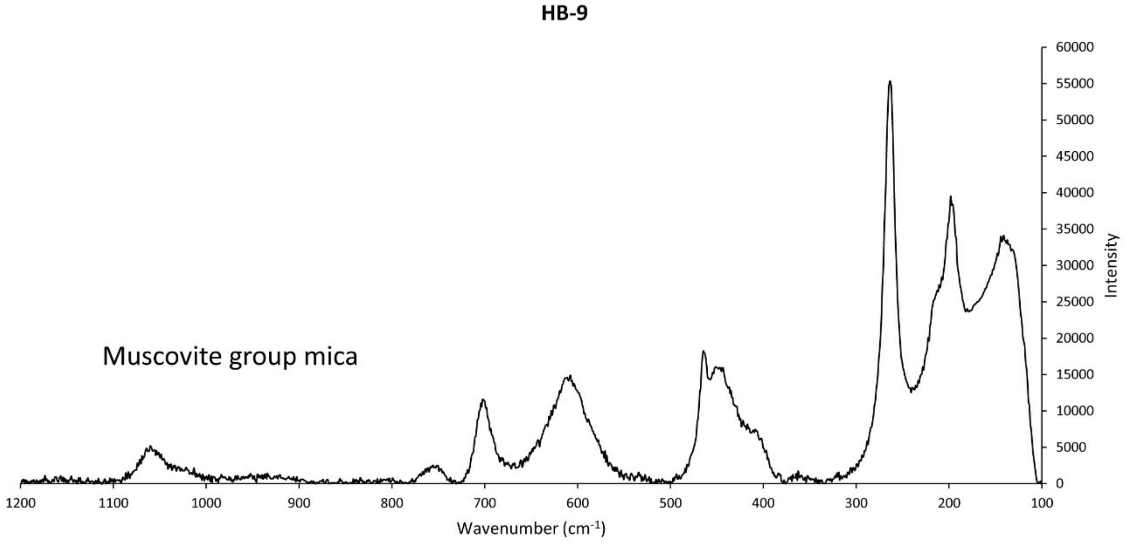
HB-9
Muscovite group mica
Intensity
60000
55000
50000
45000
40000
35000
30000
25000
20000
15000
10000
5000
0
1200
1100
1000
900
800
700
600
500
400
300
200
100
Wavenumber (cm-1)

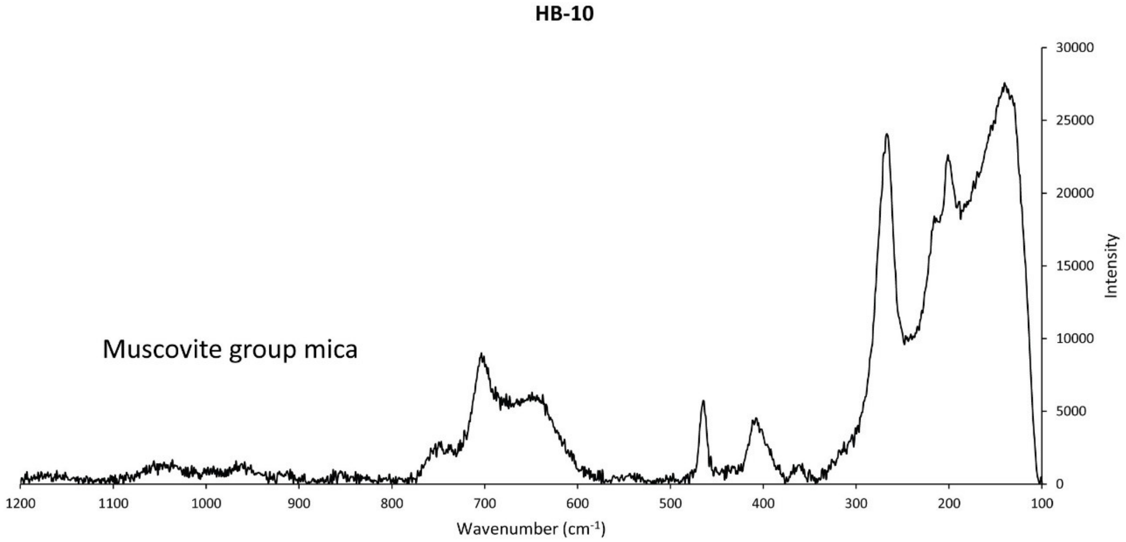
HB-10
Muscovite group mica
Intensity
30000
25000
20000
15000
10000
5000
0
1200
1100
1000
900
800
700
600
500
400
300
200
100
Wavenumber (cm-1)

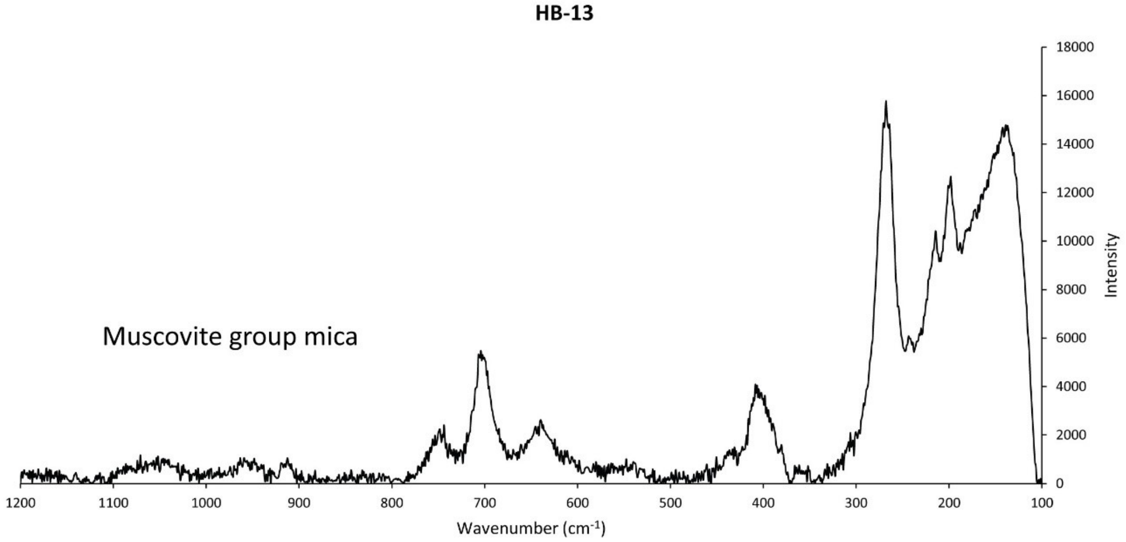
HB-13
Muscovite group mica
Intensity
18000
16000
14000
12000
10000
8000
6000
4000
2000
0
1200
1100
1000
900
800
700
600
500
400
300
200
100
Wavenumber (cm-1)

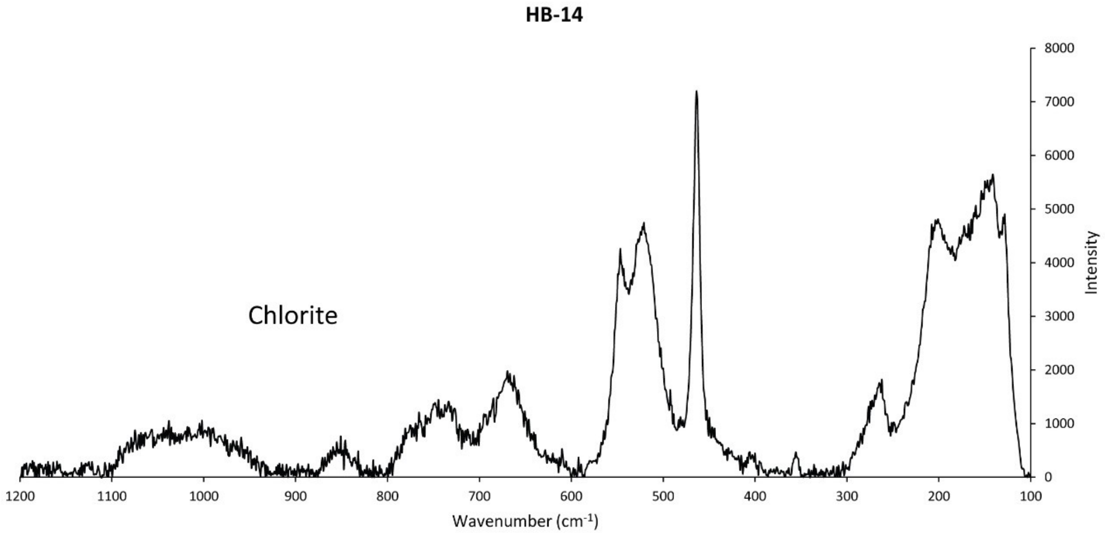
HB-14
Chlorite
Intensity
8000
7000
6000
5000
4000
3000
2000
1000
0
1200
1100
1000
900
800
700
600
500
400
300
200
100
Wavenumber (cm-1)

Heritage low-sulfidation epithermal prospect

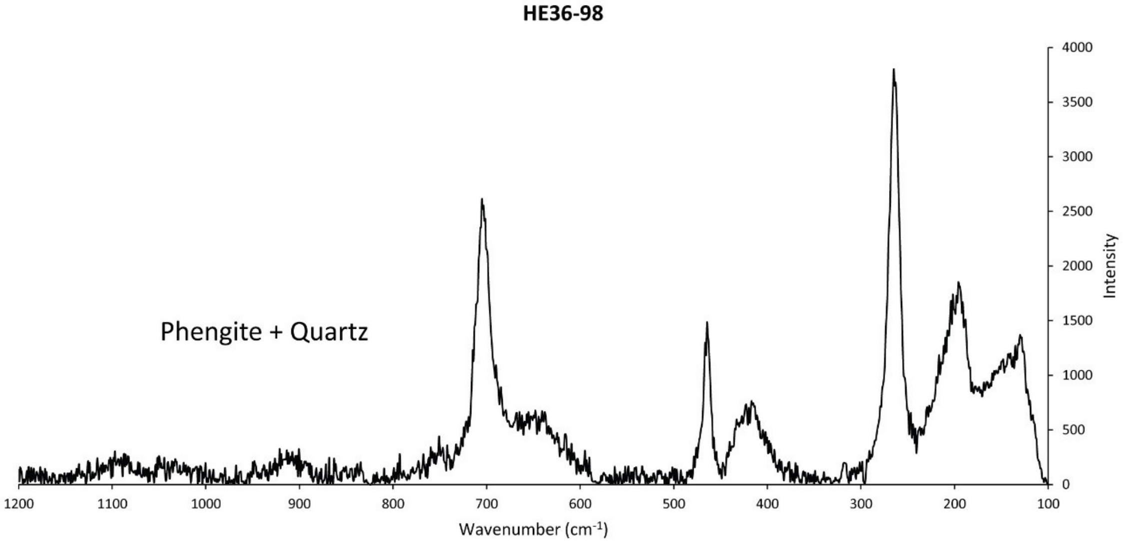

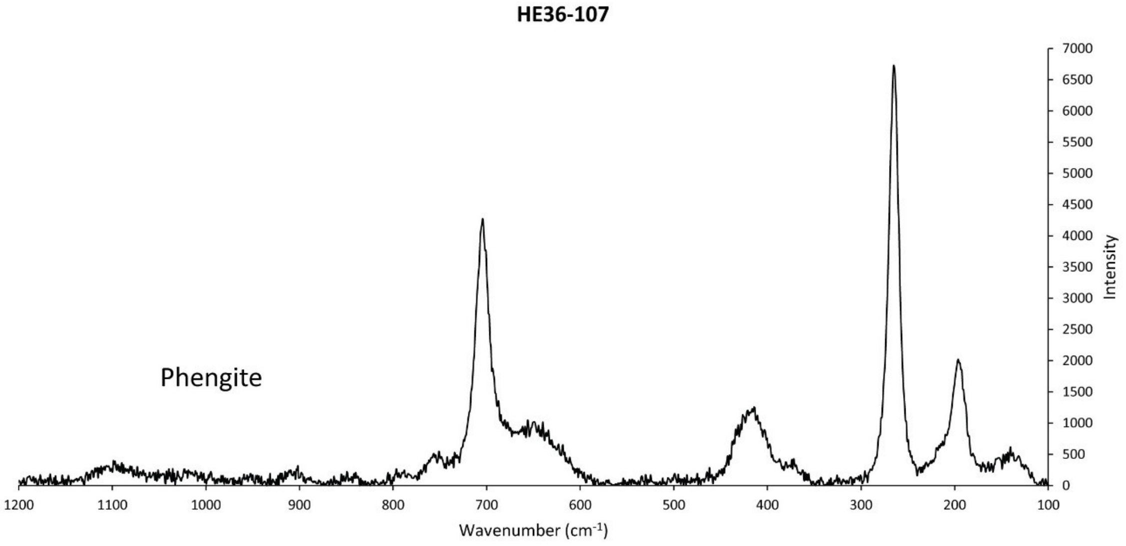

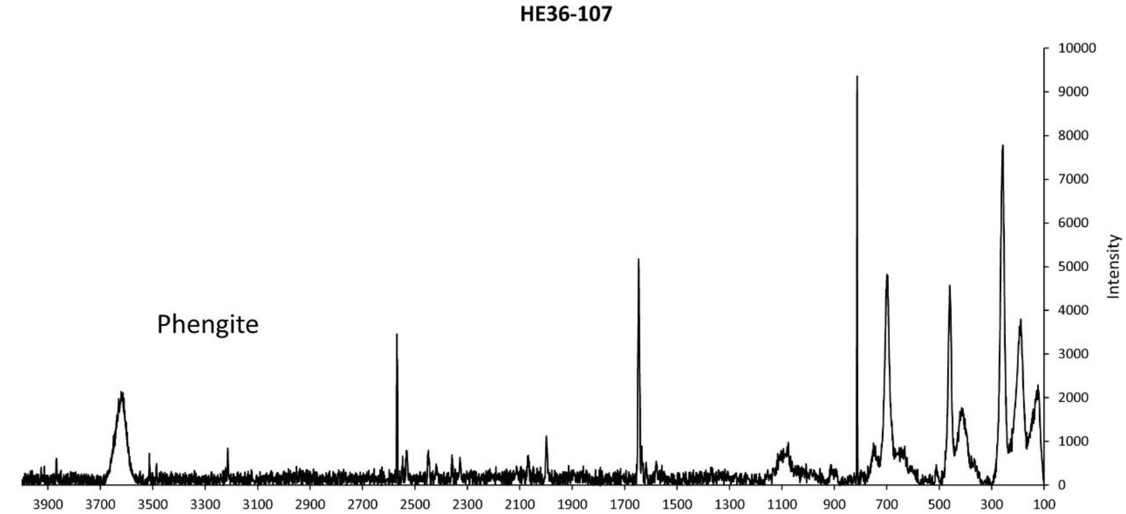

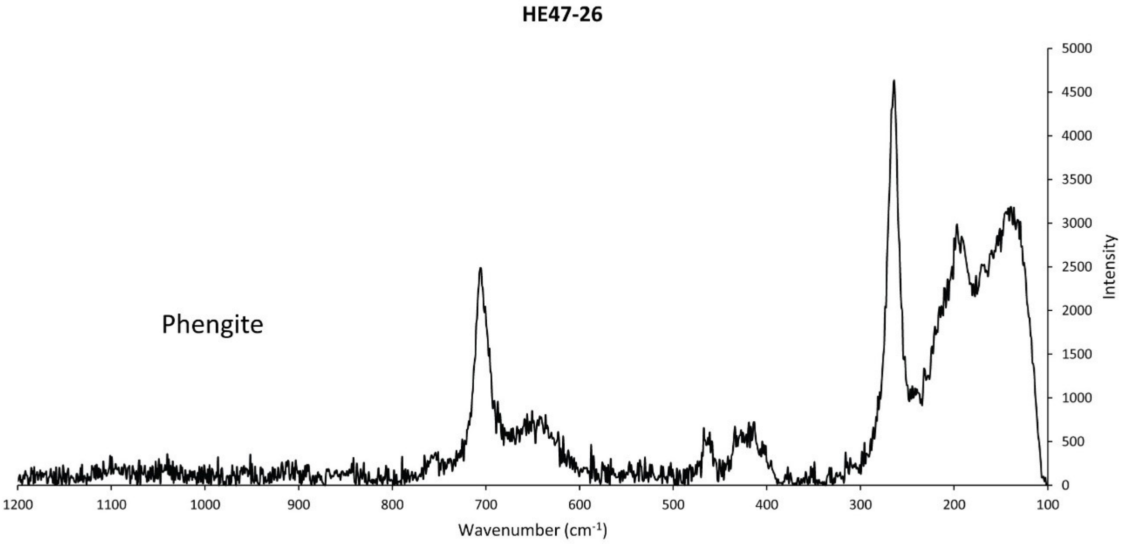
HE47-26
Phengite
Intensity
0
500
1000
1500
2000
2500
3000
3500
4000
4500
5000
1200
1100
1000
900
800
700
600
500
400
300
200
100
Wavenumber (cm^{-1})

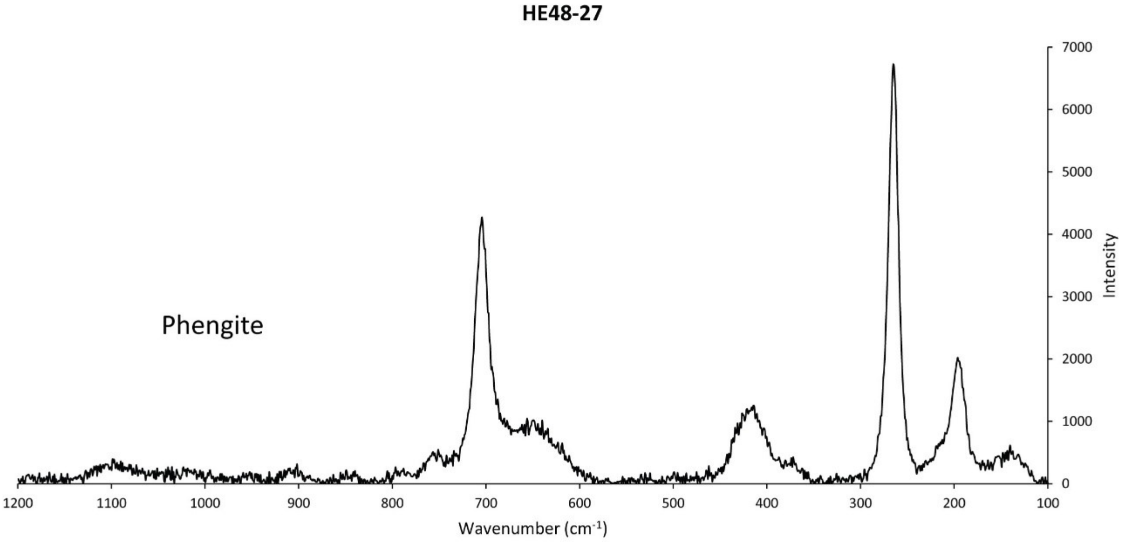
HE48-27
Phengite
Intensity
0
1000
2000
3000
4000
5000
6000
7000
1200
1100
1000
900
800
700
600
500
400
300
200
100
Wavenumber (cm^{-1})

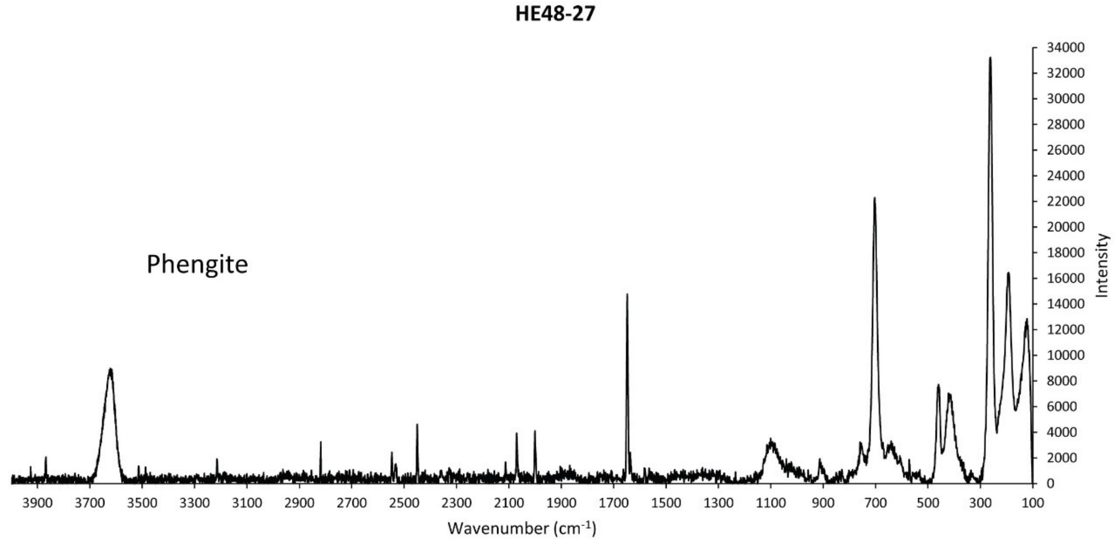
HE48-27
Phengite
Intensity
0
2000
4000
6000
8000
10000
12000
14000
16000
18000
20000
22000
24000
26000
28000
30000
32000
34000
3900
3700
3500
3300
3100
2900
2700
2500
2300
2100
1900
1700
1500
1300
1100
900
700
500
300
100
Wavenumber (cm^{-1})

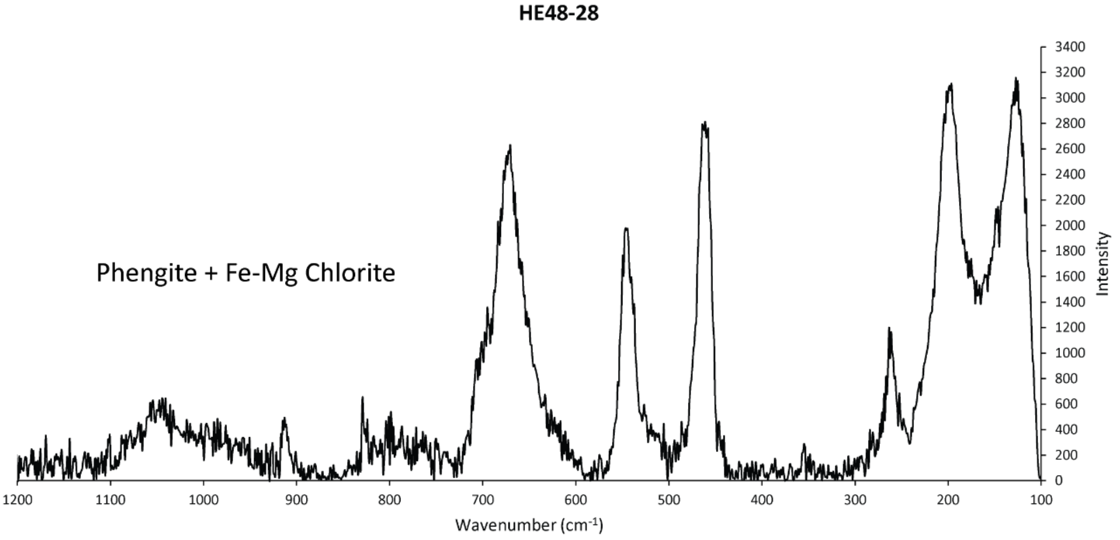
HE48-28
Phengite + Fe-Mg Chlorite
Intensity
3400
3200
3000
2800
2600
2400
2200
2000
1800
1600
1400
1200
1000
800
600
400
200
0
1200
1100
1000
900
800
700
600
500
400
300
200
100
Wavenumber (cm-1)

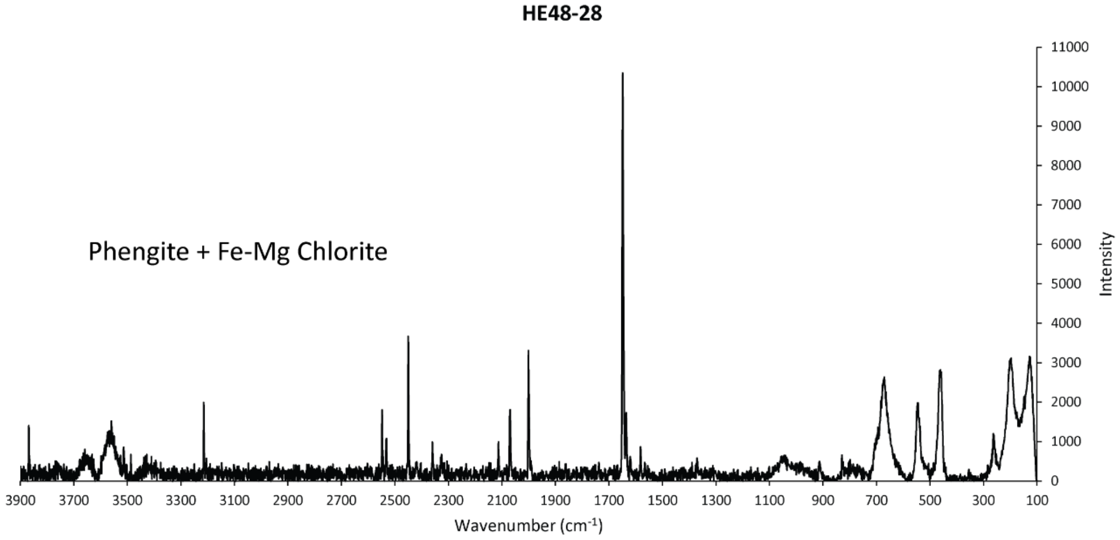
HE48-28
Phengite + Fe-Mg Chlorite
Intensity
11000
10000
9000
8000
7000
6000
5000
4000
3000
2000
1000
0
3900
3700
3500
3300
3100
2900
2700
2500
2300
2100
1900
1700
1500
1300
1100
900
700
500
300
100
Wavenumber (cm-1)

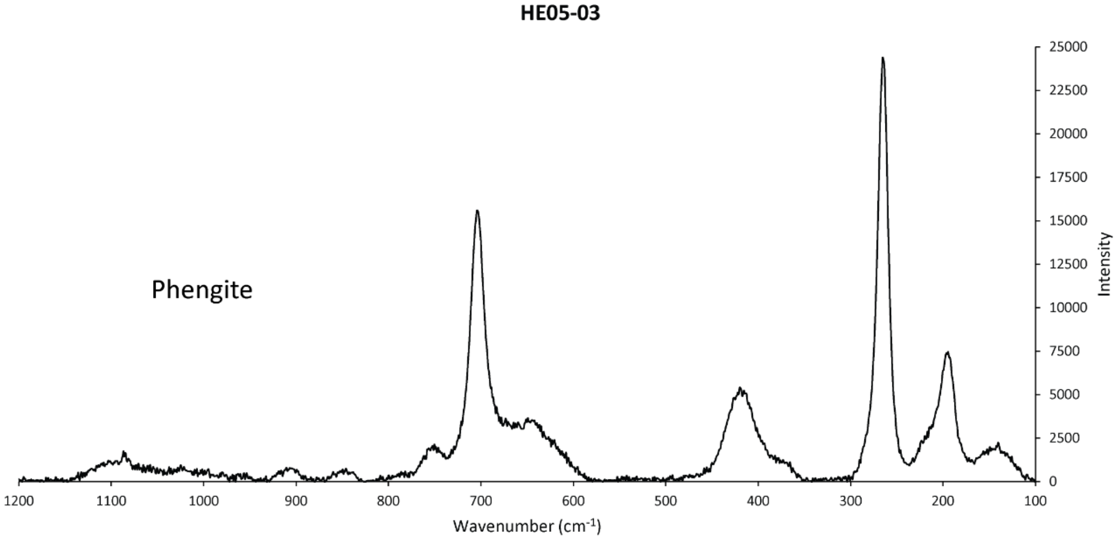
HE05-03
Phengite
Intensity
25000
22500
20000
17500
15000
12500
10000
7500
5000
2500
0
1200
1100
1000
900
800
700
600
500
400
300
200
100
Wavenumber (cm-1)

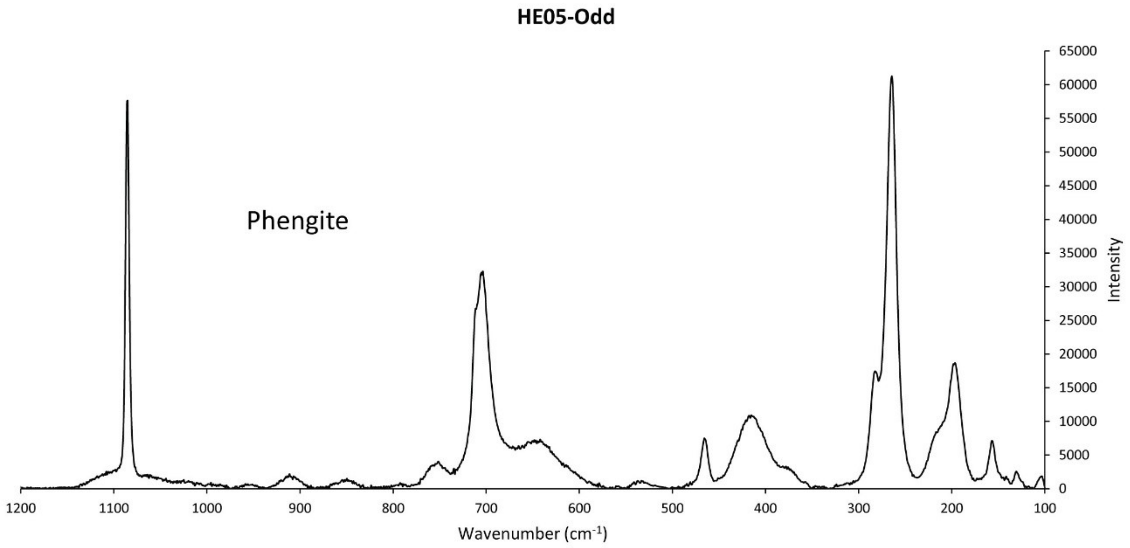
HE05-Odd
Phengite
65000
60000
55000
50000
45000
40000
35000
30000
25000
20000
15000
10000
5000
0
Intensity
1200
1100
1000
900
800
700
600
500
400
300
200
100
Wavenumber (cm-1)

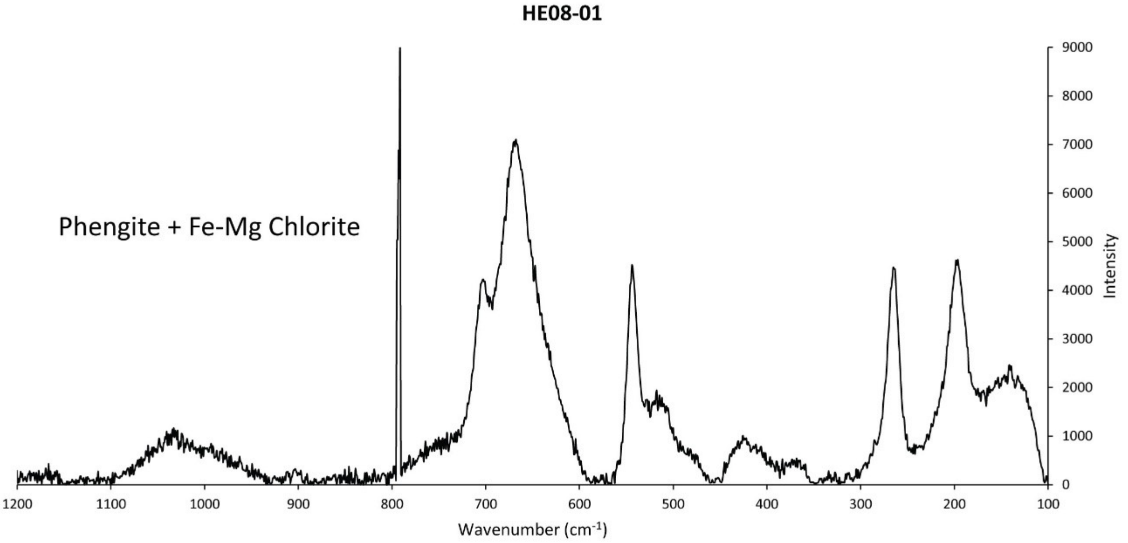
HE08-01
Phengite + Fe-Mg Chlorite
9000
8000
7000
6000
5000
4000
3000
2000
1000
0
Intensity
1200
1100
1000
900
800
700
600
500
400
300
200
100
Wavenumber (cm-1)

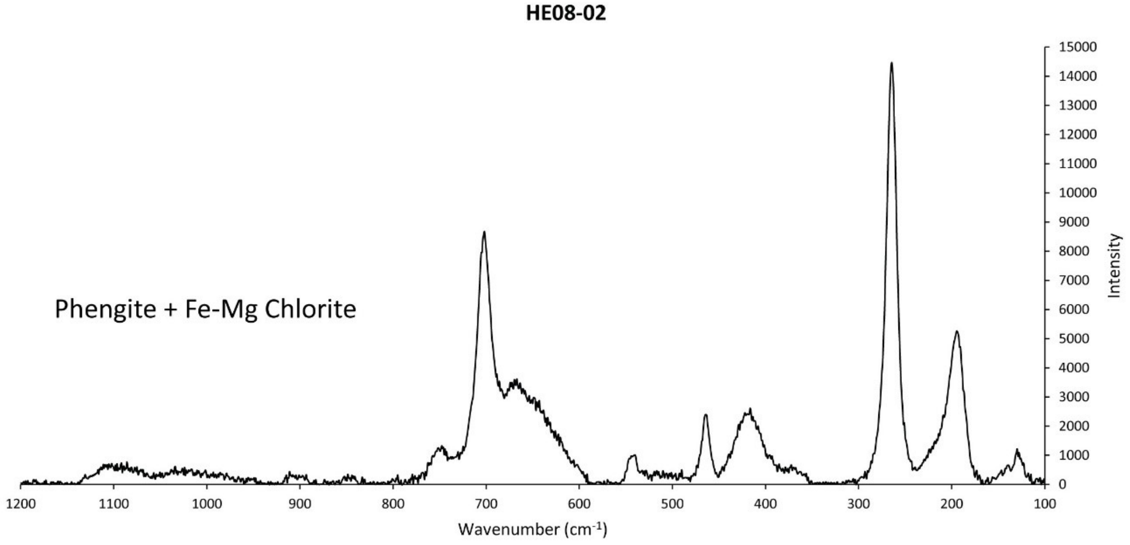
HE08-02
Phengite + Fe-Mg Chlorite
15000
14000
13000
12000
11000
10000
9000
8000
7000
6000
5000
4000
3000
2000
1000
0
Intensity
1200
1100
1000
900
800
700
600
500
400
300
200
100
Wavenumber (cm-1)

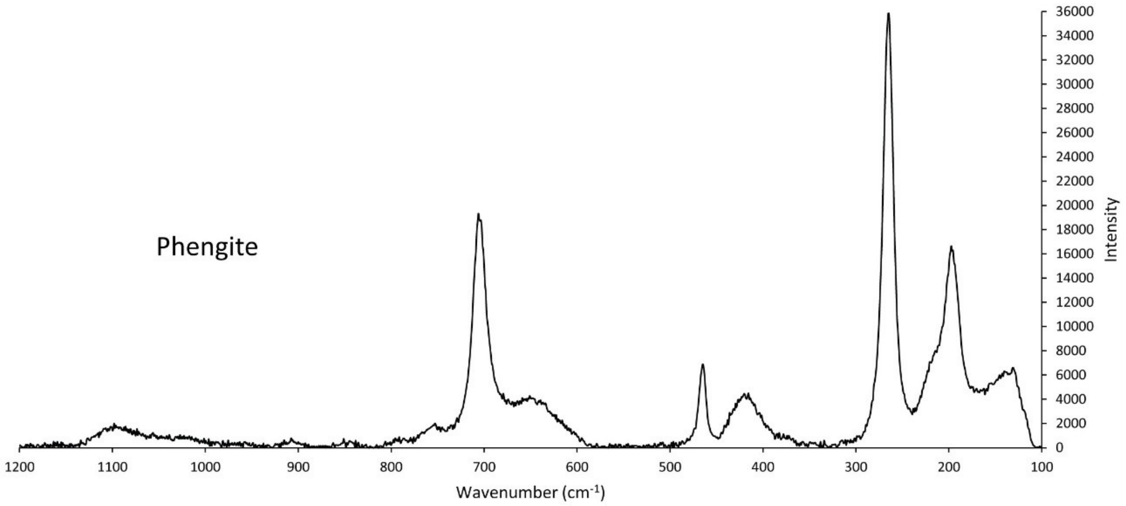
HE08-03

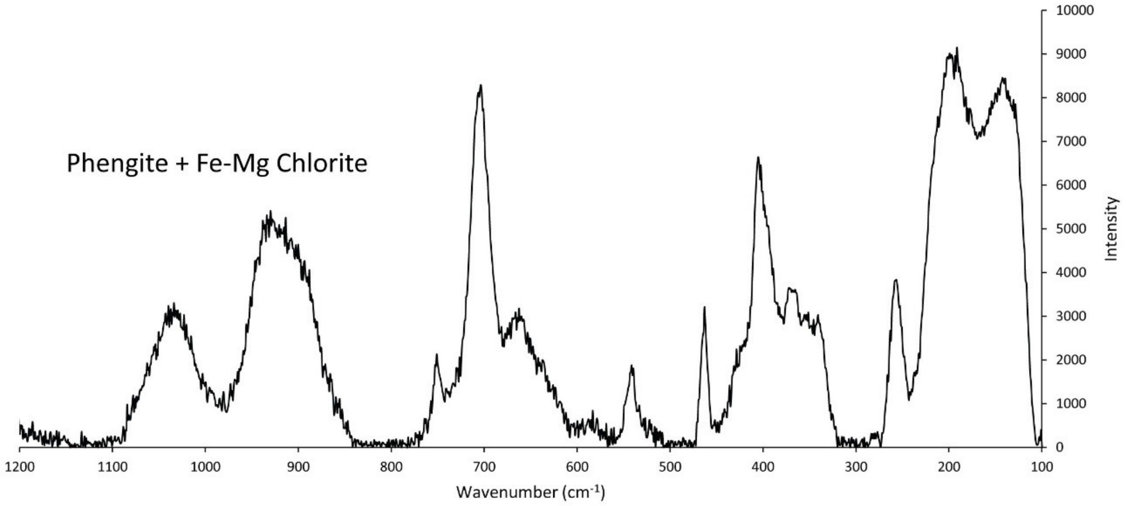
HE09-01

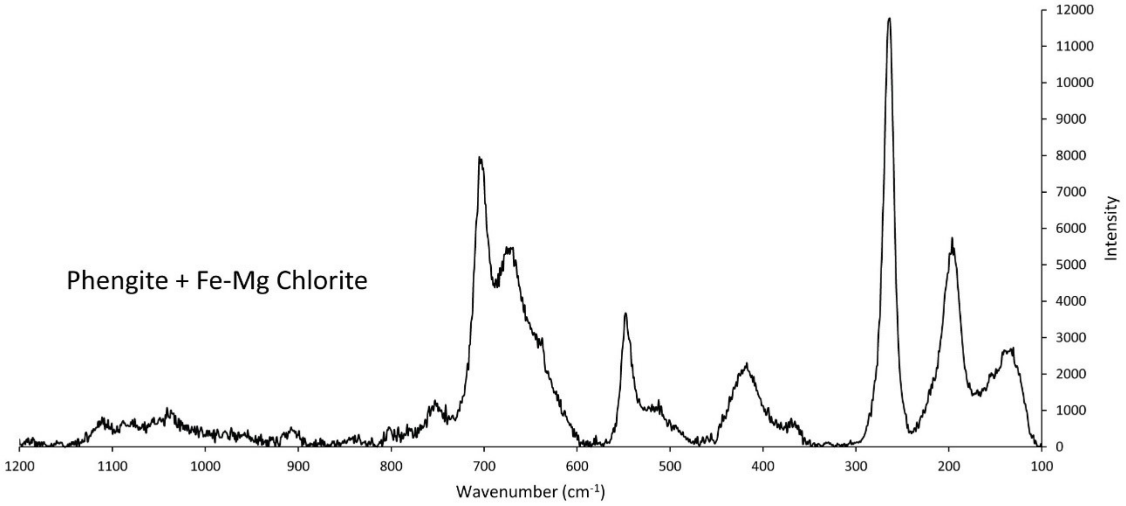
HE09-02

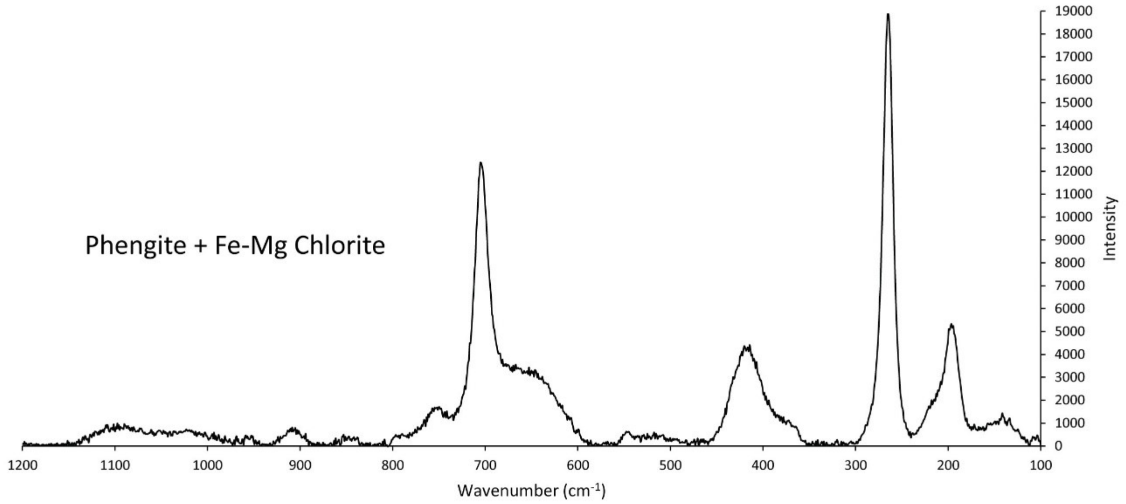
HE22-1R

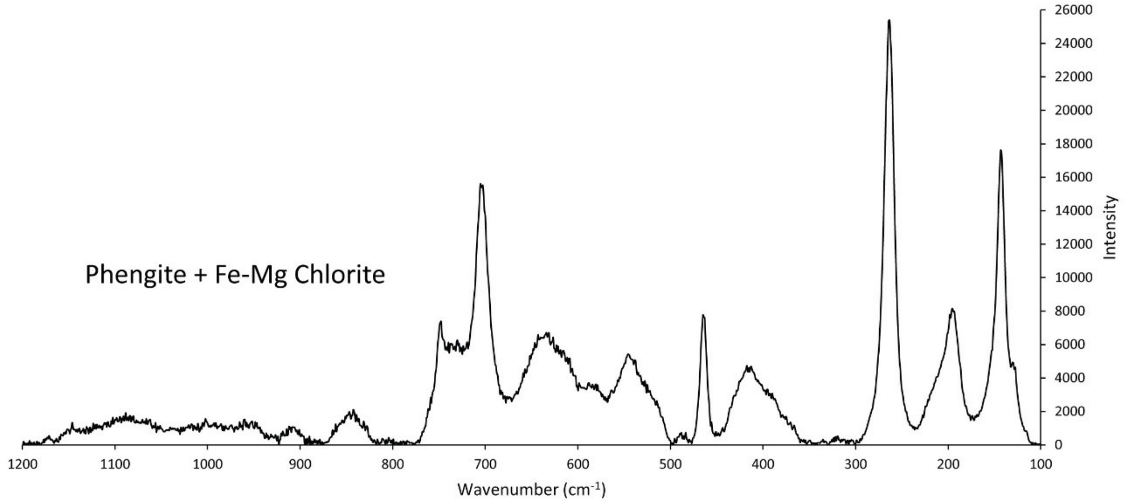
HE23-1R

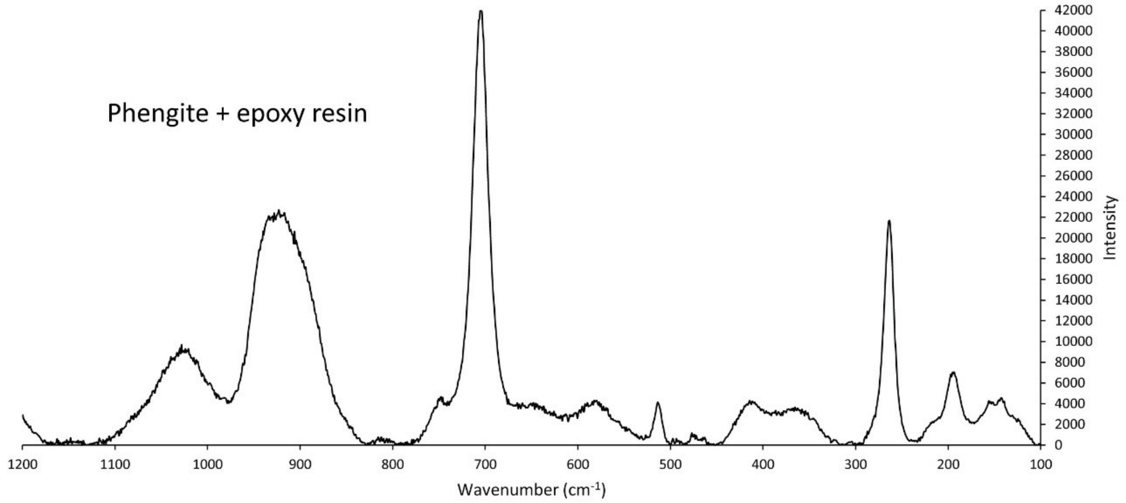
HE23-2R

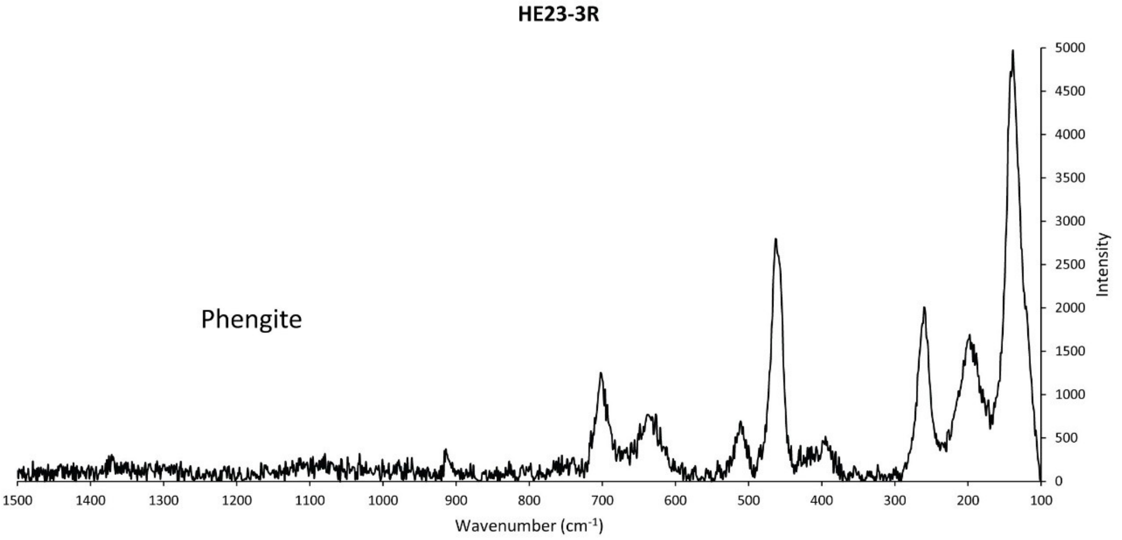
HE23-3R
Phengite
5000
4500
4000
3500
3000
2500
2000
1500
1000
500
0
Intensity
1500
1400
1300
1200
1100
1000
900
800
700
600
500
400
300
200
100
Wavenumber (cm^{-1})

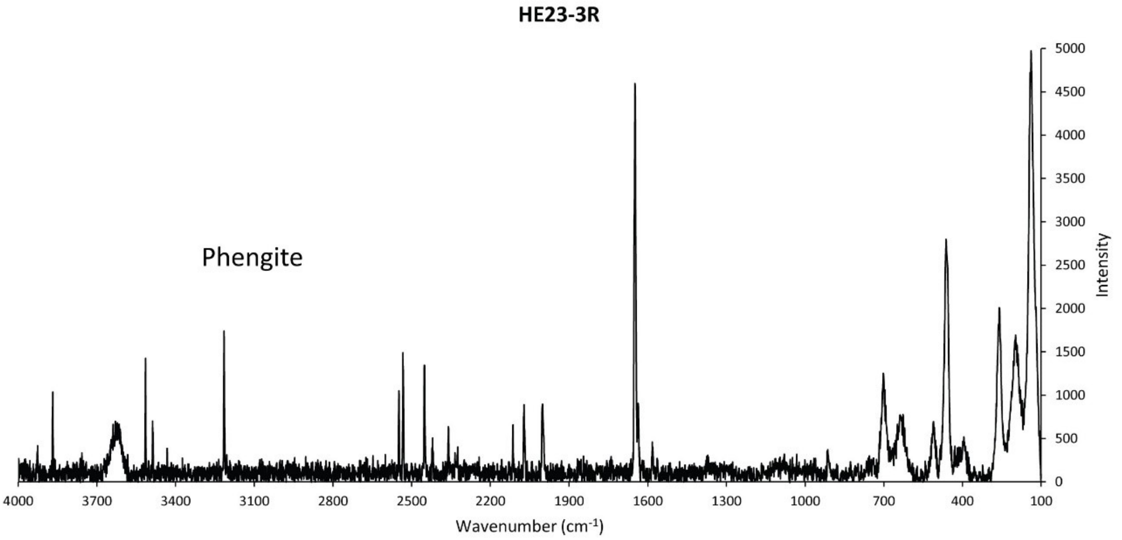
HE23-3R
Phengite
5000
4500
4000
3500
3000
2500
2000
1500
1000
500
0
Intensity
4000
3700
3400
3100
2800
2500
2200
1900
1600
1300
1000
700
400
100
Wavenumber (cm^{-1})

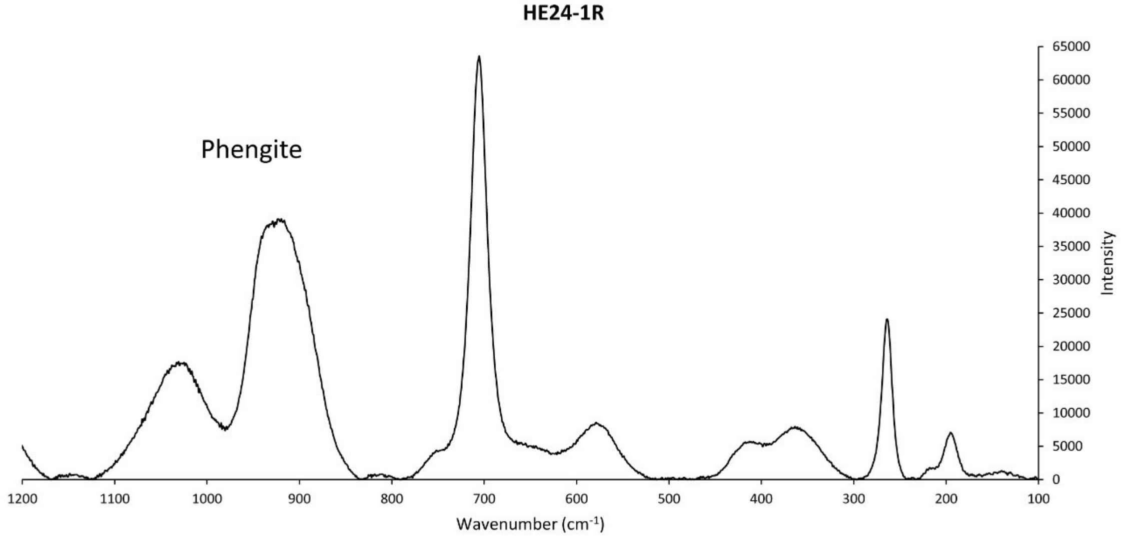
HE24-1R
Phengite
65000
60000
55000
50000
45000
40000
35000
30000
25000
20000
15000
10000
5000
0
Intensity
1200
1100
1000
900
800
700
600
500
400
300
200
100
Wavenumber (cm^{-1})

Appendix 6. Secondary ion inductively coupled mass spectrometry results and standard errors of rutile analyses from orogenic gold occurrences. 2SE is two times the standard error of the mean for all cycles accumulated in each analysis and it is an estimate of the 2σ internal precision for each analysis. Abbreviations: OGO = orogenic gold occurrence; AP = Animal Pond; BN = Stog’er Tight; AE = Argyle.

OGO	AP	AP	AP	AP	AP	AP	AP	AP	AP	AP	AP	AP	AP
Sample	AP-722	AP-722	AP-722	AP-722	AP-722	AP-722	AP-722	AP-722	AP-722	AP-722	AP-722	AP-722	AP-722
#	5	7	8	9	11	18	19	6	5	9	10	8	1
Al	9131	316	242	328	3635	492	4646	4450	937	5015	1917	317	528
2SE	306	12	10	5	86	8	205	208	39	296	39	36	24
Si	10750	986	720	952	5585	1272	21656	16358	8268	7742	7043	1467	1610
2SE	326	17	22	30	91	30	243	786	158	547	217	40	22
P	3	0	0	0	1	0	1	2	2	1	1	0	0
2SE	0.14	0.03	0.02	0.02	0.07	0.02	0.04	0.17	0.12	0.09	0.04	0.03	0.07
Ca	952	2106	1405	7329	1168	2334	8363	2031	9117	15106	644	1295	927
2SE	18	63	62	268	12	84	534	226	360	165	10	24	35
Sc	40	69	219	206	47	457	85	65	46	65	432	52	50
2SE	0.2	1.6	6.5	2.3	1.2	8.4	3.6	8.1	0.2	0.7	4.6	0.5	0.6
V	650	545	868	963	366	1157	819	598	588	513	1572	476	730
2SE	3	24	6	18	5	28	4	30	6	3	46	3	4
Cr	31	2	2	1	1	1	3	2	2	6	2	4	3
2SE	3.85	0.26	1.01	0.05	0.15	0.03	0.27	0.06	0.05	0.62	0.08	0.48	0.40
Mn	559	184	156	344	362	268	1290	401	375	625	255	949	383
2SE	14.9	4.8	1.7	11.2	19.1	18.8	26.4	15.1	7.6	31.4	2.7	15.6	19.4
Fe	70956	40805	27955	29266	39347	28230	67989	50504	45699	71209	38707	60563	41623
2SE	1446	1120	671	176	1483	726	1707	1348	837	922	974	420	740
As	38	20	18	22	31	22	33	39	31	52	36	29	38
2SE	1.6	0.6	1.1	1.6	2.1	1.0	1.8	3.7	2.4	3.2	1.9	1.6	4.5

Y	50	50	34	35	64	46	54	81	232	76	86	56	81
2SE	1.3	1.3	0.6	1.3	0.8	0.4	1.0	3.7	13.1	0.6	0.6	0.7	1.0
Zr	917	1248	1162	1339	1167	1303	938	1244	1377	1305	1616	1269	889
2SE	29	16	31	32	46	36	103	28	23	26	48	53	28
Nb	210	273	380	294	429	564	392	873	487	309	754	214	185
2SE	3	2	2	5	3	3	4	72	9	4	7	2	4
Sn	6	12	15	16	6	48	13	8	5	9	41	6	5
2SE	0.4	1.6	1.1	1.2	0.9	1.8	1.1	1.6	1.2	0.7	2.8	0.8	1.1
Sb	37	54	57	66	46	47	43	42	43	46	51	43	34
2SE	1.9	3.9	9.2	4.1	4.5	4.4	1.6	3.4	2.9	3.0	3.7	3.7	4.0
Ta	15	14	18	14	32	43	26	70	42	19	23	16	18
2SE	0.6	0.7	0.6	0.6	0.9	3.3	1.2	4.1	3.9	0.5	0.6	0.8	2.1
W	7	10	952	827	14	308	46	36	15	11	196	10	13
2SE	0.6	0.8	21.0	40.4	1.3	14.5	9.3	6.6	2.2	1.0	8.3	0.8	2.4

OGO	BN	BN	BN	BN	BN	BN	BN	BN	BN	BN	BN	BN	BN	BN	BN	BN	BN	BN	BN
Sample	BN-748	BN-748	BN-748	BN-748	BN-748	BN-748	BN-748	BN-748	BN-748	BN-748	BN-748	BN-748	BN-748	BN-748	BN-748	BN-748	BN-748	BN-748	BN-748
#	F1-1	F1-2	F1-3	F1-4	F1-5	F1-8	F2-1	F2-2	2	5	6	8	10	14	11	7	8	9	2
Al	13003	1322	933	3386	294	372	1933	5138	11213	1385	11171	332	7028	1296	17229	9426	5871	4449	2628
2SE	801	62	41	42	14	7	366	318	483	91	271	36	751	17	548	159	362	180	242
Si	14745	1558	1084	3440	483	422	1562	5393	13264	1456	11803	718	7666	1505	17215	12473	7824	3825	2731
2SE	981	95	47	248	34	23	385	369	597	273	264	147	796	38	503	353	554	159	381
P	2	1	0	1	0	0	0	1	2	1	1	0	1	0	2	2	3	1	1
2SE	0.14	0.08	0.03	0.18	0.11	0.15	0.11	0.11	0.10	0.04	0.04	0.04	0.04	0.04	0.09	0.14	0.11	0.13	0.06
Ca	83	105	40	57	220	2781	4645	1475	120	187	85	5803	9030	963	154	73	439	375	4360
2SE	28	11	8	14	19	213	183	81	42	30	8	268	928	104	20	10	30	38	1075
Sc	24	18	13	29	21	21	30	39	25	27	25	19	21	38	28	114	52	21	36
2SE	0.3	0.3	0.2	12.3	0.9	0.7	2.7	0.5	1.6	2.7	0.9	0.7	0.5	0.2	1.9	20.6	10.6	1.1	1.9
V	1424	1359	1401	1346	1357	1325	1485	1269	1680	1434	1491	1410	1622	1448	1372	1555	1354	1407	1725
2SE	4	5	5	7	8	3	16	6	11	6	4	4	5	3	4	5	6	7	40
Cr	4	3	3	3	2	2	3	2	7	4	3	3	3	1	4	7	5	4	8
2SE	0.11	0.14	0.09	0.18	0.12	0.12	0.68	0.11	0.24	0.82	0.09	0.77	0.57	0.07	0.15	2.01	0.54	0.26	0.33
Mn	7	5	3	22	5	90	47	23	13	8	30	159	230	22	73	7	27	48	48
2SE	0.4	0.2	0.2	0.4	0.2	2.5	1.0	1.0	1.6	0.5	3.3	14.7	8.2	0.8	3.8	0.8	1.0	1.5	5.3
Fe	5383	5052	5364	12017	4981	6227	7222	5585	7341	7543	11771	9760	11460	5710	28032	6742	9126	17568	9326
2SE	75	150	144	328	40	169	148	114	63	1350	1355	463	257	26	792	67	385	319	371
As	14	9	7	10	7	5	17	33	16	16	37	8	30	5	40	18	16	20	10
2SE	1.7	1.1	1.0	1.3	1.2	0.3	2.9	5.9	1.3	1.4	2.1	1.5	4.0	0.5	4.3	1.8	2.2	4.0	2.2
Y	3	1	1	5	6	2	1	4	7	9	2	3	3	1	5	15	44	3	9
2SE	0.3	0.1	0.0	3.4	0.5	0.1	0.1	0.3	0.3	1.0	0.3	0.2	0.2	0.1	0.5	3.3	3.3	0.7	1.7
Zr	206	456	254	1492	1006	257	530	451	844	1360	608	215	265	769	971	5717	5621	620	695
2SE	11	30	6	1103	120	10	25	16	103	161	87	25	4	24	73	1228	974	103	90

Nb	864	781	1143	1194	1301	1331	1020	821	2067	1164	1588	1307	1243	743	1158	1111	959	1294	1366
2SE	63	10	37	15	6	13	19	10	27	9	12	25	18	2	13	20	15	15	51
Sn	92	26	50	59	58	72	129	117	392	85	115	75	167	34	100	179	74	100	180
2SE	13.9	1.8	5.9	6.9	3.8	3.5	6.8	6.6	13.1	4.2	4.1	2.9	4.1	2.5	4.3	8.4	4.5	3.0	10.1
Sb	117	249	256	101	290	141	205	219	400	180	452	385	582	144	229	274	346	186	284
2SE	6.6	15.8	11.1	9.4	10.5	8.4	14.9	9.0	16.2	6.5	16.7	22.3	13.4	5.5	10.6	9.2	9.8	17.3	27.3
Ta	55	54	72	79	89	94	73	56	123	73	96	77	85	44	76	61	64	77	89
2SE	4.2	1.8	3.9	2.1	2.2	2.5	1.9	5.2	5.7	3.0	2.5	2.8	2.9	1.0	2.3	1.6	1.7	2.2	7.2
W	505	98	272	199	267	43	2887	1185	2701	351	496	40	4804	117	549	1660	299	465	2269
2SE	69.4	5.7	46.1	8.0	16.4	4.9	205.2	56.8	106.0	19.7	19.6	5.9	100.1	16.2	38.4	14.0	13.0	23.6	306.3

OGO	AE	AE	AE	AE	AE	AE	AE	AE	AE	AE	AE	AE	AE	AE	AE	AE	AE	AE	AE	AE	AE	AE	AE	AE	AE
Sample	AE-660	AE-660	AE-660	AE-660	AE-660	AE-660	AE-660	AE-660	AE-660	AE-660	AE-660	AE-679	AE-679	AE-679	AE-679	AE-679	AE-679	AE-679	AE-679	AE-679	AE-679	AE-679	AE-679	AE-679	AE-679
#	F1-4	F1-5	F1-7	F1-2	F1-12	F3-1	F3-5	F3---5	F4-1	F4-2	F4-3	F1-3b	F1-6b	F2-1	F2-4	F2-6	F2-7	3	7	8	11	7	8	9	11
Al	722	1755	1308	843	1513	903	4233	6712	761	830	703	556	658	1412	1207	660	3055	850	657	1997	514	1292	768	591	938
2SE	66	36	24	46	52	39	256	98	15	38	28	33	30	55	37	25	98	44	15	204	27	29	53	18	124
Si	15551	2505	14709	6525	14239	43595	4842	10905	2590	12379	34695	5087	7425	6554	3895	1153	8107	1801	5508	883	567	4923	16922	5434	46951
2SE	897	86	243	387	328	756	434	262	164	184	783	215	83	269	226	43	292	297	158	66	30	719	181	152	1234
P	2	1	2	1	2	9	2	3	1	1	2	1	1	1	1	0	1	1	1	0	0	1	3	1	3
2SE	0.14	0.16	0.17	0.06	0.09	0.34	0.11	0.15	0.11	0.04	0.04	0.03	0.04	0.08	0.06	0.10	0.03	0.05	0.11	0.04	0.04	0.10	0.12	0.04	0.16
Ca	148	205	3143	356	418	2856	1787	9266	430	354	340	116	216	61	46	237	69	1188	322	83	311	120	228	185	301
2SE	9	11	87	20	35	216	174	318	22	29	31	17	16	19	15	15	10	132	55	25	183	16	29	14	14
Sc	112	128	100	153	174	117	111	97	198	173	156	17	32	10	22	23	4	4	16	11	11	3	24	15	46
2SE	0.9	1.7	1.2	3.7	5.2	0.4	11.2	2.7	14.6	0.5	2.4	1.0	0.5	0.1	0.2	0.8	0.2	0.2	0.3	0.4	0.1	0.0	0.4	0.8	1.0
V	3544	4311	3017	7169	5675	3215	3320	3449	6077	6792	5572	636	1174	838	796	1665	633	628	783	879	747	771	1726	697	1395
2SE	10	7	11	43	22	29	12	7	77	7	28	2	19	2	2	7	6	28	4	10	2	9	9	10	13
Cr	13	15	9	27	16	24	12	18	14	16	12	1	3	2	3	5	2	2	2	3	2	4	8	2	4
2SE	0.48	0.43	0.23	0.89	0.49	4.34	0.28	0.45	0.90	1.06	1.08	0.05	0.14	0.13	0.26	0.15	0.06	0.16	0.09	0.22	0.09	0.90	0.84	0.08	0.21
Mn	7	8	51	8	6	52	20	114	10	8	6	5	5	3	6	9	14	74	23	5	8	22	9	6	11
2SE	0.4	0.8	1.7	0.9	0.6	0.9	0.5	1.5	0.7	0.5	0.8	1.9	0.3	0.3	0.4	0.4	0.9	5.1	3.2	0.9	0.9	0.9	0.6	0.8	1.9
Fe	2898	5518	5727	2629	2354	3375	2770	6318	2904	2399	2905	2981	2849	4128	17205	3644	8718	13988	7824	6050	4438	13266	4749	4145	4533
2SE	90	124	75	44	72	56	40	39	103	48	121	111	67	85	234	68	172	583	193	51	34	778	30	55	50
As	41	60	57	85	60	68	32	32	94	100	103	16	42	10	13	32	14	20	31	38	25	30	42	35	64
2SE	2.9	2.0	3.5	9.8	6.9	5.8	2.9	2.2	3.7	3.1	7.8	1.2	2.4	0.8	2.0	2.8	1.9	1.8	1.9	1.3	2.2	7.1	3.1	4.2	5.8
Y	65	124	114	188	139	174	50	74	147	186	160	8	81	2	6	67	2	0	23	1	8	2	53	8	92
2SE	1.5	9.6	3.3	2.3	3.0	6.3	1.5	1.7	4.0	1.4	7.9	0.4	1.9	0.1	0.6	1.2	0.1	0.0	1.2	0.0	0.8	0.3	0.5	0.2	10.2
Zr	465	1166	1006	396	375	1272	1487	915	429	198	427	465	521	86	1734	265	155	609	934	104	406	130	209	520	786
2SE	21	306	56	11	7	147	416	150	30	8	13	4	6	3	15	2	13	36	19	1	23	13	2	9	138

Nb	440	411	446	347	675	492	220	243	648	530	380	650	923	1798	9215	3553	2460	6680	3724	1932	534	1727	3358	756	679
2SE	16	5	12	7	7	7	2	2	32	13	10	12	31	20	82	42	142	380	64	28	17	34	27	9	15
Sn	30	22	22	37	57	37	19	16	57	42	34	29	118	16	41	60	15	22	17	11	19	10	50	38	213
2SE	2.6	1.7	1.3	3.0	4.3	3.5	2.6	0.9	3.4	3.0	3.7	2.4	3.0	1.4	2.1	3.3	2.2	2.2	1.2	1.6	1.6	1.5	3.2	2.4	7.3
Sb	158	133	133	183	233	183	87	68	215	192	163	102	105	54	225	108	69	127	98	65	116	50	67	132	91
2SE	9.1	6.0	8.5	11.4	17.9	19.6	9.8	4.8	16.3	8.4	6.8	7.2	5.9	3.3	7.1	3.7	5.8	10.5	4.7	4.7	6.3	4.2	7.0	8.9	8.3
Ta	20	25	33	17	36	24	16	17	32	38	20	33	55	74	232	127	91	209	143	86	37	82	114	41	36
2SE	0.9	1.0	2.1	0.8	1.5	1.5	1.0	0.7	0.9	1.8	1.0	2.0	9.4	1.7	5.7	2.9	5.8	15.7	7.8	2.2	2.5	6.0	2.5	1.3	2.5
W	342	190	27	920	1442	45	116	82	1363	1293	1068	63	177	4	30	540	15	5	45	8	50	4	111	114	385
2SE	19.2	6.7	4.0	51.5	49.7	6.1	6.6	3.8	142.4	39.1	22.9	2.9	8.8	0.9	2.8	6.5	2.2	1.4	3.2	1.5	6.2	1.2	4.9	4.6	15.9

Appendix 7. Principal component analysis (PCA) matrix tables for the different runs performed on EPMA and SIMS analyses.

EPMA PCA run #1 (Fig. 4.4a): Mn, Fe, V, Al, Ca, Nb, Si, Zr

Deposit / Prospect	Sample	Alteration Intensity	PC1	PC2	PC3	PC4	PC5	PC6	PC7	PC8
Animal Pond	AP-704_test_1	Distal	0.50	-0.37	-1.33	0.80	-0.33	-0.66	0.54	0.00
Animal Pond	AP-704_test_2	Distal	-0.99	-2.82	-1.38	1.17	-0.79	0.03	0.29	0.00
Animal Pond	AP-704_test_3	Distal	1.28	-1.17	-1.18	-1.98	-1.36	0.32	-0.24	0.00
Animal Pond	AP-704_test_5	Distal	1.20	-3.18	1.00	-3.88	-1.03	-0.25	1.31	0.00
Animal Pond	AP-714_1	Intermediate	0.59	1.10	-1.43	-0.30	-1.00	-0.61	-0.46	0.00
Animal Pond	AP-714_2	Intermediate	1.31	1.61	-2.52	-0.48	-0.81	0.13	-1.01	0.00
Animal Pond	AP-714_4	Intermediate	0.17	1.22	-2.53	0.28	-0.91	-0.28	-0.12	0.00
Animal Pond	AP-714_5	Intermediate	0.19	0.84	-1.96	1.06	-1.75	-0.78	-0.17	0.00
Animal Pond	AP-714_7	Intermediate	0.17	1.53	-2.52	0.22	-0.71	-0.28	-0.18	0.00
Animal Pond	AP-714_8	Intermediate	-1.29	0.13	-2.07	1.25	-0.81	-0.49	-0.06	0.00
Animal Pond	AP-714_9	Intermediate	-0.55	1.43	-2.22	0.46	-0.52	-0.79	0.27	0.00
Animal Pond	AP-714_10	Intermediate	-0.83	-1.00	-0.93	-0.28	-0.44	-1.42	-0.33	0.00
Animal Pond	AP-714_11	Intermediate	0.67	0.31	-1.32	-0.13	0.32	-0.15	-1.09	0.00
Animal Pond	AP-714_12	Intermediate	2.75	-1.65	1.04	0.20	-1.06	-2.11	-2.41	0.00
Animal Pond	AP-714_13	Intermediate	-0.62	-1.01	-1.30	1.33	0.18	0.47	-0.52	0.00
Animal Pond	AP-714_14	Intermediate	-0.35	-2.25	-0.71	-1.22	0.83	1.15	-0.26	0.00
Animal Pond	AP-714_15	Intermediate	-0.70	-2.61	-0.50	-1.47	1.15	0.58	0.06	0.00
Animal Pond	AP-714_16	Intermediate	2.61	-1.59	0.00	0.95	-0.48	-1.44	-0.61	0.00
Animal Pond	AP-714_17	Intermediate	-0.18	-0.89	-1.28	0.12	0.97	-0.12	0.08	0.00
Animal Pond	AP-714_18	Intermediate	-1.12	-1.08	-1.75	1.15	0.26	0.12	-0.04	0.00
Animal Pond	AP-714_19	Intermediate	-0.48	-0.81	-1.84	0.10	-0.06	0.37	-0.10	0.00
Animal Pond	AP-714_21	Intermediate	0.35	0.34	-2.36	0.37	-0.06	0.24	-0.63	0.00
Animal Pond	AP-714_22	Intermediate	0.58	-0.16	-0.97	-0.73	-0.36	-1.13	-1.17	0.00
Animal Pond	AP-714_23	Intermediate	-0.05	-0.12	-2.02	0.44	0.22	-0.60	-0.32	0.00
Animal Pond	AP-714_24	Intermediate	2.97	0.68	-2.74	-2.97	-3.38	2.16	-0.56	0.00
Animal Pond	AP-714_25	Intermediate	0.11	-0.50	-1.68	-1.52	1.39	-0.62	0.68	0.00
Animal Pond	AP-714_26	Intermediate	0.25	-1.50	-1.48	0.73	1.52	1.18	-0.87	0.00
Animal Pond	AP-714_27	Intermediate	2.73	1.46	-2.81	-2.12	-2.73	2.69	-0.03	0.00
Animal Pond	AP-714_28	Intermediate	-0.45	-0.16	-1.29	-0.55	0.74	-0.13	-0.47	0.00
Animal Pond	AP-714_29	Intermediate	1.56	-1.68	-1.18	0.92	0.45	0.66	-1.04	0.00
Animal Pond	AP-714_30	Intermediate	-0.72	-0.98	-1.64	0.79	0.24	0.01	-0.22	0.00
Animal Pond	AP-714_31	Intermediate	-0.53	-0.85	-1.40	1.28	0.37	0.36	-0.45	0.00
Animal Pond	AP-722_1	Proximal	2.00	-2.36	0.59	1.81	0.27	0.80	1.42	0.00
Animal Pond	AP-722_2	Proximal	1.96	-1.81	0.59	1.51	0.67	1.36	1.42	0.00
Animal Pond	AP-722_3	Proximal	1.99	-1.76	1.07	0.63	-0.28	0.26	0.86	0.00
Animal Pond	AP-722_4	Proximal	0.73	-3.41	0.99	-1.23	-1.59	-2.93	-0.90	0.00
Animal Pond	AP-722_5	Proximal	-0.52	-3.12	0.21	-2.24	-0.20	-1.14	-1.06	0.00
Animal Pond	AP-722_6	Proximal	1.61	-1.49	0.54	0.72	0.01	0.55	1.38	0.00
Animal Pond	AP-722_7	Proximal	1.76	-2.34	1.53	0.37	0.34	0.49	0.75	0.00
Animal Pond	AP-722_8	Proximal	1.71	-2.33	0.99	1.52	0.26	1.44	1.21	0.00
Animal Pond	AP-722_9	Proximal	2.18	-1.50	1.85	0.25	-0.47	0.01	-0.13	0.00
Animal Pond	AP-722_10	Proximal	1.61	-2.16	1.67	-0.29	0.20	0.81	0.68	0.00
Animal Pond	AP-722_11	Proximal	2.45	-2.06	1.22	0.44	-0.40	1.10	0.89	0.00
Animal Pond	AP-722_12	Proximal	2.91	-1.91	1.89	0.03	-1.05	0.04	0.84	0.00

Animal Pond	AP-722_13	Proximal	1.32	0.23	0.16	1.77	-0.31	-0.38	1.29	0.00
Animal Pond	AP-722_14	Proximal	2.72	-0.47	-1.14	1.13	-1.16	0.64	1.30	0.00
Animal Pond	AP-722_15	Proximal	1.76	-1.21	0.04	0.52	-0.91	-0.78	0.71	0.00
Animal Pond	AP-722_16	Proximal	1.22	0.18	0.08	1.11	-0.48	-1.03	1.27	0.00
Animal Pond	AP-722_17	Proximal	1.23	-0.62	-0.24	1.74	-0.85	-0.31	1.51	0.00
Animal Pond	AP-722_18	Proximal	2.05	-1.24	1.08	1.25	-0.96	-1.21	0.29	0.00
Animal Pond	AP-722_19	Proximal	1.71	-0.01	1.31	1.08	-1.15	-0.61	0.21	0.00
Animal Pond	AP-722_20	Proximal	1.29	-0.57	-0.13	2.37	-0.62	-0.16	0.90	0.00
Animal Pond	AP-722_21	Proximal	0.99	-0.67	0.89	0.65	-1.04	-0.76	0.79	0.00
Animal Pond	AP-722_22	Proximal	2.06	-1.27	1.01	0.95	-0.97	-0.69	0.49	0.00
Animal Pond	AP-722_23	Proximal	2.14	-1.49	0.96	0.85	-0.56	-0.12	-0.85	0.00
Animal Pond	AP-722_24	Proximal	1.01	0.14	-0.15	1.45	-0.52	-0.49	1.08	0.00
Animal Pond	AP-722_25	Proximal	2.60	-0.61	0.21	-0.90	-1.67	-1.20	0.18	0.00
Animal Pond	AP-722_26	Proximal	1.34	0.53	0.42	1.65	-0.74	-0.59	0.61	0.00
Animal Pond	AP-722_27	Proximal	1.68	-1.53	1.23	0.73	-0.23	-0.57	0.71	0.00
Animal Pond	AP-722_28	Proximal	1.58	-0.97	1.38	-0.22	-0.13	0.19	0.56	0.00
Animal Pond	AP-722_29	Proximal	1.99	-1.93	0.51	0.48	-0.41	-0.83	0.71	0.00
Animal Pond	AP-722_30	Proximal	0.45	-2.12	0.06	-0.42	1.43	0.09	1.30	0.00
Animal Pond	AP-722_31	Proximal	2.90	-2.17	1.42	0.41	0.34	1.22	0.55	0.00
Animal Pond	AP-722_32	Proximal	1.35	-1.61	0.48	0.89	0.11	0.55	0.65	0.00
Animal Pond	AP-722_33	Proximal	1.54	-1.33	1.04	0.91	0.04	0.41	1.04	0.00
Animal Pond	AP-722_34	Proximal	2.19	-2.18	1.34	-0.25	-0.22	0.67	0.00	0.00
Animal Pond	AP-722_35	Proximal	1.55	-2.83	1.15	-0.38	0.06	0.45	-0.04	0.00
Stog'er Tight	BN-730_1	Proximal	-0.32	0.61	-0.70	0.35	-0.71	0.15	-0.04	0.00
Stog'er Tight	BN-730_2	Proximal	-0.70	0.96	-0.61	0.90	-0.60	0.35	-0.61	0.00
Stog'er Tight	BN-730_3	Proximal	-0.53	0.84	0.99	-0.82	-0.57	1.14	-1.46	0.00
Stog'er Tight	BN-730_4	Proximal	-1.19	0.28	0.38	-0.21	-0.43	0.80	0.63	0.00
Stog'er Tight	BN-730_5	Proximal	-1.86	-2.25	1.14	-0.45	-2.05	1.00	-0.03	0.00
Stog'er Tight	BN-730_6	Proximal	-1.07	-0.88	-0.06	0.34	0.47	0.29	-1.39	0.00
Stog'er Tight	BN-730_7	Proximal	-1.66	-0.81	1.52	-1.50	0.10	-0.60	-1.36	0.00
Stog'er Tight	BN-730_8	Proximal	-2.43	-0.42	0.89	-0.74	0.11	-0.09	0.34	0.00
Stog'er Tight	BN-730_9	Proximal	0.96	-0.30	-2.80	-1.70	-0.30	1.42	0.96	0.00
Stog'er Tight	BN-730_10	Proximal	0.27	0.93	-0.61	-0.77	1.77	-0.44	0.19	0.00
Stog'er Tight	BN-730_11	Proximal	-0.05	0.33	-0.39	0.43	0.49	-0.37	-0.16	0.00
Stog'er Tight	BN-730_12	Proximal	0.08	-0.39	-0.61	-0.06	0.58	-0.24	-0.68	0.00
Stog'er Tight	BN-730_13	Proximal	-0.34	0.14	-0.47	0.12	0.88	0.44	-0.06	0.00
Stog'er Tight	BN-730_14	Proximal	0.87	0.60	-0.32	-0.63	-0.74	0.56	-0.83	0.00
Stog'er Tight	BN-730_15	Proximal	-0.43	0.19	-0.83	0.83	0.15	0.06	-0.43	0.00
Stog'er Tight	BN-730_16	Proximal	0.77	-1.54	-0.40	-2.63	0.81	-1.66	0.16	0.00
Stog'er Tight	BN-730_17	Proximal	0.13	-1.17	-0.83	-1.73	-1.19	0.54	-0.66	0.00
Stog'er Tight	BN-730_18	Proximal	-0.94	-1.87	-0.01	-1.11	-0.69	0.16	0.67	0.00
Stog'er Tight	BN-730_19	Proximal	-0.65	-0.83	-0.89	-0.33	-0.79	-0.33	0.62	0.00
Stog'er Tight	BN-730_20	Proximal	-1.18	-1.46	-0.08	-1.49	0.02	0.46	0.51	0.00
Stog'er Tight	BN-730_21	Proximal	-0.19	1.24	0.88	-1.74	-1.08	0.57	-0.16	0.00
Stog'er Tight	BN-730_22	Proximal	-0.88	1.32	2.16	0.40	-0.53	1.04	-0.06	0.00
Stog'er Tight	BN-730_23	Proximal	0.19	-0.29	-0.60	0.92	-0.06	0.14	-0.42	0.00
Stog'er Tight	BN-730_24	Proximal	-0.03	-0.26	-0.31	0.83	0.07	-0.04	-0.19	0.00
Stog'er Tight	BN-730_25	Proximal	-0.36	0.01	1.11	-0.80	-0.04	-0.39	-0.59	0.00
Stog'er Tight	BN-730_26	Proximal	1.39	1.09	-1.50	-2.79	-3.99	1.60	1.58	0.00
Stog'er Tight	BN-730_27	Proximal	-1.40	0.22	1.32	-0.64	-0.34	0.23	0.93	0.00
Stog'er Tight	BN-730_28	Proximal	-0.13	-1.14	-0.03	0.66	0.59	1.68	-0.77	0.00
Stog'er Tight	BN-730_29	Proximal	0.38	-1.16	-0.58	0.49	0.76	1.56	-0.66	0.00

Stog'er Tight	BN-730_30	Proximal	0.16	0.22	-0.68	0.36	-0.15	-0.49	-0.05	0.00
Stog'er Tight	BN-730_31	Proximal	-1.25	-0.34	0.55	-0.30	0.18	-0.45	1.23	0.00
Stog'er Tight	BN-730_32	Proximal	-0.90	0.86	2.23	-1.26	-0.13	-0.11	0.17	0.00
Stog'er Tight	BN-730_33	Proximal	-0.70	1.60	1.07	0.21	0.32	-0.18	0.19	0.00
Stog'er Tight	BN-730_34	Proximal	-0.72	1.65	0.26	0.62	-0.21	-0.06	0.01	0.00
Stog'er Tight	BN-730_35	Proximal	-0.18	1.75	0.56	-0.20	-0.71	0.26	0.39	0.00
Stog'er Tight	BN-739_1	Distal	-0.70	1.81	1.21	0.07	-0.97	1.19	0.56	0.00
Stog'er Tight	BN-739_2	Distal	-0.03	1.29	1.66	-1.28	-0.31	0.43	-0.95	0.00
Stog'er Tight	BN-739_3	Distal	-1.05	2.15	1.96	0.05	-0.30	1.10	0.68	0.00
Stog'er Tight	BN-739_4	Distal	-2.66	0.13	1.87	0.22	0.26	0.04	1.59	0.00
Stog'er Tight	BN-739_5	Distal	-0.80	2.56	1.84	0.29	-0.39	1.18	0.52	0.00
Stog'er Tight	BN-739_6	Distal	-0.42	1.49	1.71	-0.55	-0.05	0.20	-0.45	0.00
Stog'er Tight	BN-739_7	Distal	-1.72	1.99	2.50	0.96	-0.35	0.30	0.03	0.00
Stog'er Tight	BN-739_8	Distal	-1.05	2.96	1.94	0.78	-0.06	0.48	0.18	0.00
Stog'er Tight	BN-739_9	Distal	-1.06	3.00	1.84	0.48	-0.48	0.32	0.37	0.00
Stog'er Tight	BN-739_10	Distal	-1.63	1.26	0.63	-0.85	-0.59	-0.46	1.60	0.00
Stog'er Tight	BN-739_11	Distal	-0.86	2.49	0.98	0.39	-0.41	0.64	0.15	0.00
Stog'er Tight	BN-739_12	Distal	0.29	1.93	-0.09	0.79	-0.50	0.31	-0.31	0.00
Stog'er Tight	BN-739_14	Distal	1.70	-0.50	0.82	-1.26	2.49	0.74	-0.77	0.00
Stog'er Tight	BN-739_15	Distal	0.42	-0.05	0.20	-1.78	0.78	-0.61	1.28	0.00
Stog'er Tight	BN-739_16	Distal	1.04	0.08	-1.63	-0.17	0.58	0.35	0.26	0.00
Stog'er Tight	BN-739_17	Distal	1.33	1.10	0.20	0.09	0.86	2.21	-0.06	0.00
Stog'er Tight	BN-739_18	Distal	0.70	0.77	-0.38	-0.50	2.24	0.07	0.75	0.00
Stog'er Tight	BN-739_19	Distal	1.63	1.13	0.09	-0.04	1.63	-0.35	-0.58	0.00
Stog'er Tight	BN-739_21	Distal	0.57	1.30	0.81	-1.93	1.84	0.02	-0.01	0.00
Stog'er Tight	BN-739_22	Distal	0.86	-1.35	0.07	-1.25	2.67	0.40	0.14	0.00
Stog'er Tight	BN-739_23	Distal	0.41	0.46	0.33	-1.12	0.46	0.22	-0.59	0.00
Stog'er Tight	BN-739_24	Distal	0.96	1.27	-0.99	0.41	1.33	0.34	-0.29	0.00
Stog'er Tight	BN-739_25	Distal	1.17	1.14	0.11	-0.35	0.82	0.17	-0.25	0.00
Stog'er Tight	BN-739_26	Distal	-0.31	0.15	-1.18	0.00	0.90	-0.13	0.28	0.00
Stog'er Tight	BN-739_27	Distal	1.04	0.77	0.37	-1.07	0.25	0.07	-1.85	0.00
Stog'er Tight	BN-739_28	Distal	0.12	0.31	-0.97	0.51	1.14	0.53	-0.54	0.00
Stog'er Tight	BN-739_29	Distal	-0.06	-0.54	0.16	-0.94	0.71	0.68	-0.93	0.00
Stog'er Tight	BN-739_30	Distal	0.51	-0.37	-0.26	-1.44	0.64	-0.14	-1.27	0.00
Stog'er Tight	BN-739_31	Distal	0.58	-0.29	0.73	-1.25	0.38	-0.07	-1.25	0.00
Stog'er Tight	BN-748_1	Intermediate	0.06	0.93	-1.31	-1.06	1.54	-2.31	1.54	0.00
Stog'er Tight	BN-748_2	Intermediate	0.47	1.75	-1.24	-0.20	0.95	-0.50	0.30	0.00
Stog'er Tight	BN-748_3	Intermediate	-0.84	0.45	-0.76	-0.72	0.72	-1.58	1.54	0.00
Stog'er Tight	BN-748_4	Intermediate	-1.52	-0.25	-0.33	1.34	0.06	-1.36	0.34	0.00
Stog'er Tight	BN-748_5	Intermediate	2.32	0.52	-0.87	0.19	0.71	-1.97	0.07	0.00
Stog'er Tight	BN-748_6	Intermediate	0.37	1.52	-1.57	-0.92	1.30	-1.45	0.93	0.00
Stog'er Tight	BN-748_7	Intermediate	1.01	0.93	-0.16	-0.59	0.31	-1.28	-0.95	0.00
Stog'er Tight	BN-748_8	Intermediate	0.36	0.65	-0.41	0.41	0.11	-1.05	0.15	0.00
Stog'er Tight	BN-748_9	Intermediate	0.72	1.20	-1.44	-0.39	1.82	-0.60	0.26	0.00
Stog'er Tight	BN-748_10	Intermediate	1.07	1.00	-1.51	-0.46	1.57	-0.90	0.37	0.00
Stog'er Tight	BN-748_11	Intermediate	-0.28	1.23	1.90	-3.20	0.11	-1.03	0.47	0.00
Stog'er Tight	BN-748_12	Intermediate	-1.51	0.92	1.22	-0.73	0.74	-0.22	1.23	0.00
Stog'er Tight	BN-748_13	Intermediate	0.78	1.93	-0.49	0.43	1.61	-0.97	-0.12	0.00
Stog'er Tight	BN-748_14	Intermediate	0.85	1.79	-1.21	-0.36	0.15	0.20	0.16	0.00
Stog'er Tight	BN-748_15	Intermediate	1.28	1.42	-1.19	0.14	1.41	-1.22	0.14	0.00
Stog'er Tight	BN-748_16	Intermediate	0.59	1.76	-0.79	-1.41	1.15	-1.16	0.29	0.00
Stog'er Tight	BN-748_17	Intermediate	-0.12	1.44	0.41	0.83	0.94	0.62	-0.73	0.00

Stog'er Tight	BN-748_18	Intermediate	0.79	1.33	0.29	0.01	-0.80	0.16	-0.75	0.00
Stog'er Tight	BN-748_19	Intermediate	0.19	2.13	1.20	0.84	0.34	0.82	-0.47	0.00
Stog'er Tight	BN-748_20	Intermediate	0.31	1.73	1.93	0.64	0.66	-0.04	-0.18	0.00
Stog'er Tight	BN-748_21	Intermediate	1.17	0.22	0.91	-0.53	1.20	-1.04	-0.83	0.00
Stog'er Tight	BN-748_22	Intermediate	1.05	0.83	0.75	-0.63	-0.51	-0.80	-1.41	0.00
Stog'er Tight	BN-748_23	Intermediate	1.00	1.05	-0.31	0.51	0.91	0.30	-0.52	0.00
Stog'er Tight	BN-748_24	Intermediate	0.77	0.99	0.34	0.30	2.22	0.37	-0.54	0.00
Stog'er Tight	BN-748_25	Intermediate	0.55	1.35	0.18	-0.27	1.59	-0.45	0.14	0.00
Stog'er Tight	BN-748_26	Intermediate	-0.24	0.46	1.02	-1.09	0.51	-0.27	-1.02	0.00
Stog'er Tight	BN-748_27	Intermediate	1.12	0.92	-1.54	0.12	-0.32	-0.34	0.17	0.00
Stog'er Tight	BN-748_28	Intermediate	1.49	0.84	-0.46	-0.90	1.57	-1.10	-0.59	0.00
Stog'er Tight	BN-748_29	Intermediate	0.98	0.97	-0.96	0.45	0.55	-0.53	-0.17	0.00
Stog'er Tight	BN-748_30	Intermediate	1.16	1.30	-1.44	0.61	0.29	-0.30	-0.45	0.00
Argyle	AE-660_1	Proximal	-2.85	-0.31	0.41	-0.50	0.27	0.55	0.58	0.00
Argyle	AE-660_2	Proximal	-2.47	-0.86	-1.17	0.14	0.58	0.36	-0.10	0.00
Argyle	AE-660_3	Proximal	-2.39	-0.46	-0.63	-0.54	0.94	-0.09	0.65	0.00
Argyle	AE-660_4	Proximal	-1.93	-2.08	1.06	-1.00	1.12	0.96	-0.15	0.00
Argyle	AE-660_5	Proximal	-1.34	-0.06	-0.60	-0.15	0.01	0.05	-1.10	0.00
Argyle	AE-660_6	Proximal	-2.60	-1.10	0.11	0.85	0.70	1.24	-0.01	0.00
Argyle	AE-660_7	Proximal	-3.66	-2.15	-0.09	0.24	-1.01	-0.20	0.36	0.00
Argyle	AE-660_8	Proximal	-2.67	-0.97	-1.03	-0.33	0.43	-0.06	0.78	0.00
Argyle	AE-660_9	Proximal	-2.69	-0.63	0.36	-1.63	0.36	0.09	0.05	0.00
Argyle	AE-660_10	Proximal	-2.54	-0.86	-0.72	-0.54	0.91	0.37	0.81	0.00
Argyle	AE-660_11	Proximal	-1.26	-1.03	0.21	-0.76	0.82	0.93	-1.53	0.00
Argyle	AE-660_12	Proximal	-1.67	-0.37	-0.74	0.94	0.45	0.85	-0.62	0.00
Argyle	AE-660_13	Proximal	-0.83	-0.41	-1.08	-1.73	-0.11	1.26	0.95	0.00
Argyle	AE-660_14	Proximal	-1.54	-0.68	0.32	-1.07	0.24	0.71	-1.28	0.00
Argyle	AE-660_15	Proximal	-2.11	0.42	0.36	1.48	-0.02	1.02	-0.91	0.00
Argyle	AE-660_16	Proximal	-1.66	-0.53	-0.71	1.38	0.44	-0.55	0.05	0.00
Argyle	AE-660_17	Proximal	-1.95	-0.91	-0.97	0.75	0.36	0.03	0.10	0.00
Argyle	AE-660_19	Proximal	-1.78	-1.74	-0.06	0.92	1.09	1.80	-0.35	0.00
Argyle	AE-660_21	Proximal	-1.35	0.03	-0.39	1.63	0.03	0.21	-0.89	0.00
Argyle	AE-660_22	Proximal	-2.87	-0.61	0.13	-0.05	-0.09	-0.23	0.18	0.00
Argyle	AE-660_23	Proximal	0.27	1.14	1.57	-2.91	1.75	0.88	-1.47	0.00
Argyle	AE-660_24	Proximal	-0.75	0.32	-0.85	-0.05	1.42	0.56	-0.34	0.00
Argyle	AE-660_25	Proximal	-1.27	-0.96	0.34	-0.27	-0.17	-0.03	-1.89	0.00
Argyle	AE-660_26	Proximal	0.95	-0.26	-0.07	-1.18	1.03	-0.60	-1.62	0.00
Argyle	AE-660_27	Proximal	-1.10	-0.25	-1.04	0.25	0.67	0.75	-0.18	0.00
Argyle	AE-660_28	Proximal	-3.11	-0.93	-0.04	-0.12	0.68	0.48	0.68	0.00
Argyle	AE-660_29	Proximal	-2.23	0.47	0.14	0.37	0.19	1.56	-0.38	0.00
Argyle	AE-660_30	Proximal	-2.69	-0.27	-0.36	0.74	0.45	1.18	-0.34	0.00
Argyle	AE-659_1	Distal	2.82	1.12	0.61	0.00	0.34	1.11	2.98	0.00
Argyle	AE-659_2	Distal	1.43	0.58	-0.49	0.32	0.97	0.91	0.42	0.00
Argyle	AE-659_3	Distal	-0.27	-1.12	0.61	0.60	0.39	-0.06	-0.35	0.00
Argyle	AE-659_5	Distal	1.22	0.86	-0.03	0.76	1.33	0.70	1.00	0.00
Argyle	AE-659_6	Distal	2.25	0.43	-0.76	0.44	1.75	0.42	0.83	0.00
Argyle	AE-659_7	Distal	1.79	1.13	-0.04	1.05	1.50	0.42	1.52	0.00
Argyle	AE-659_8	Distal	0.42	0.11	0.81	-0.07	-0.40	1.00	-1.01	0.00
Argyle	AE-659_9	Distal	1.78	0.05	0.79	-0.90	-0.36	0.68	0.04	0.00
Argyle	AE-659_10	Distal	1.05	-0.35	0.84	0.60	-0.17	-0.47	-1.17	0.00
Argyle	AE-659_11	Distal	1.01	0.25	-0.76	0.96	0.96	0.67	-0.07	0.00
Argyle	AE-659_12	Distal	1.90	0.50	-0.02	0.48	0.23	0.50	-0.74	0.00

Argyle	AE-659_13	Distal	1.90	0.02	0.72	-0.53	0.95	0.59	-0.08	0.00
Argyle	AE-659_14	Distal	1.84	0.97	1.08	-1.24	0.21	0.43	0.01	0.00
Argyle	AE-659_15	Distal	2.00	2.63	0.09	0.47	1.37	0.02	1.16	0.00
Argyle	AE-659_17	Distal	-0.71	1.47	0.05	0.11	-0.15	0.74	1.25	0.00
Argyle	AE-659_18	Distal	1.41	1.31	0.59	-1.51	-0.12	0.74	0.47	0.00
Argyle	AE-659_19	Distal	1.62	0.67	1.89	-1.12	-0.72	-0.56	0.54	0.00
Argyle	AE-659_20	Distal	-1.42	-1.02	-0.36	1.98	-2.28	-0.30	0.77	0.00
Argyle	AE-659_21	Distal	2.69	1.27	1.98	-0.44	0.54	-2.26	-0.73	0.00
Argyle	AE-659_22	Distal	0.42	2.62	1.91	1.13	0.12	-0.03	0.67	0.00
Argyle	AE-659_23	Distal	1.36	1.78	-0.46	0.18	-0.12	0.79	0.79	0.00
Argyle	AE-659_25	Distal	0.75	0.68	0.16	1.20	0.32	0.42	-0.07	0.00
Argyle	AE-659_26	Distal	1.13	-1.01	0.69	-0.30	0.83	0.92	-1.00	0.00
Argyle	AE-659_27	Distal	1.74	-1.14	0.45	2.07	0.65	0.90	-0.97	0.00
Argyle	AE-659_28	Distal	1.72	0.40	0.23	2.04	-0.60	-0.79	-0.84	0.00
Argyle	AE-659_29	Distal	-0.09	-0.01	-0.18	0.31	0.20	0.47	0.67	0.00
Argyle	AE-659_30	Distal	2.51	1.66	-0.50	0.72	1.56	0.72	-0.29	0.00
Argyle	AE-672_test_1	Intermediate	-0.83	-2.95	-1.60	0.62	-0.57	0.85	-0.10	0.00
Argyle	AE-672_test_2	Intermediate	0.66	-0.28	-1.60	0.82	0.06	-0.66	-0.36	0.00
Argyle	AE-672_test_3	Intermediate	-0.59	-0.46	-1.72	0.71	-0.32	-0.54	0.37	0.00
Argyle	AE-672_test_4	Intermediate	0.31	-1.60	-1.42	1.24	-0.53	-0.70	-0.28	0.00
Argyle	AE-679_1	Intermediate	-1.90	0.70	1.18	-0.25	-0.71	-0.88	1.21	0.00
Argyle	AE-679_2	Intermediate	-0.10	2.40	2.27	1.94	-0.90	-0.05	-1.04	0.00
Argyle	AE-679_3	Intermediate	-2.23	1.86	2.05	0.50	-0.99	-0.28	0.52	0.00
Argyle	AE-679_4	Intermediate	-2.99	0.81	0.25	0.78	-0.29	-0.02	-0.02	0.00
Argyle	AE-679_5	Intermediate	-3.15	0.00	0.11	0.62	-0.65	-1.73	1.45	0.00
Argyle	AE-679_6	Intermediate	-0.94	-0.12	1.35	-0.40	0.73	0.55	-0.62	0.00
Argyle	AE-679_7	Intermediate	-1.91	-0.43	-0.09	1.99	-0.10	0.02	-0.61	0.00
Argyle	AE-679_8	Intermediate	-2.44	-0.73	0.13	0.92	0.22	0.31	-0.15	0.00
Argyle	AE-679_9	Intermediate	-0.78	0.07	1.51	-0.14	-0.10	0.60	-0.83	0.00
Argyle	AE-679_10	Intermediate	-0.90	-0.79	-0.34	-0.69	1.31	-0.11	1.02	0.00
Argyle	AE-679_11	Intermediate	-0.32	0.21	0.65	1.15	0.33	0.51	-0.11	0.00
Argyle	AE-679_12	Intermediate	-0.46	-0.79	2.46	-0.29	0.18	0.98	-0.71	0.00
Argyle	AE-679_13	Intermediate	0.39	0.17	1.84	1.02	-0.62	-1.90	-1.17	0.00
Argyle	AE-679_14	Intermediate	-0.78	-0.46	1.01	-0.14	0.67	-1.19	0.78	0.00
Argyle	AE-679_15	Intermediate	0.64	0.71	1.45	1.47	-1.23	-0.21	-0.80	0.00
Argyle	AE-679_16	Intermediate	1.04	-1.05	0.22	-1.31	-0.26	-0.22	-0.91	0.00
Argyle	AE-679_17	Intermediate	-1.19	0.12	0.32	1.28	-0.43	-0.06	-0.61	0.00
Argyle	AE-679_18	Intermediate	-1.46	-0.26	0.64	0.95	0.38	0.86	-0.36	0.00
Argyle	AE-679_19	Intermediate	0.13	-1.40	-0.13	0.64	1.38	0.91	-0.49	0.00
Argyle	AE-679_20	Intermediate	0.20	0.12	0.64	2.00	-1.00	-1.80	-0.59	0.00
Argyle	AE-679_21	Intermediate	-0.76	-0.29	-0.31	-1.93	0.33	-1.25	0.10	0.00
Argyle	AE-679_22	Intermediate	-1.42	-0.87	-0.65	0.00	0.04	-1.71	0.81	0.00
Argyle	AE-679_23	Intermediate	0.29	-0.11	-1.48	-0.66	0.63	-1.77	-0.27	0.00
Argyle	AE-679_24	Intermediate	-1.21	-1.09	-0.62	0.36	-3.32	-1.18	-0.68	0.00
Argyle	AE-679_25	Intermediate	-0.26	0.40	-0.83	0.51	-0.33	-0.75	-0.38	0.00
Argyle	AE-679_26	Intermediate	-1.41	-0.99	0.80	0.03	-0.64	-1.53	-0.82	0.00
Argyle	AE-679_27	Intermediate	-1.83	-1.36	0.56	0.26	-0.10	-0.67	0.60	0.00
Argyle	AE-679_28	Intermediate	-1.45	-1.47	1.23	-0.14	0.45	0.77	0.76	0.00
Argyle	AE-679_29	Intermediate	-1.16	-0.18	0.51	-0.08	0.02	-0.09	0.78	0.00
Argyle	AE-679_30	Intermediate	-1.18	-0.39	0.84	-0.36	0.32	-0.25	1.25	0.00

Argyle	AE-684_1	Intermediate	-0.44	0.33	-1.08	0.73	-0.16	-0.29	-0.31	0.00
Argyle	AE-684_2	Intermediate	-0.91	0.72	-0.96	0.54	-0.83	0.31	-0.46	0.00
Argyle	AE-684_3	Intermediate	-2.18	-0.21	-0.91	0.61	-0.26	0.08	-0.66	0.00
Argyle	AE-684_4	Intermediate	-1.07	-1.05	-1.13	0.60	0.12	0.64	-0.32	0.00
Argyle	AE-684_5	Intermediate	-1.01	0.25	-1.21	0.99	0.08	0.47	-0.81	0.00
Argyle	AE-684_6	Intermediate	-1.62	-0.29	0.29	-1.21	0.31	0.02	-0.24	0.00
Argyle	AE-684_7	Intermediate	-0.85	0.45	-0.44	-0.59	0.11	-0.74	0.82	0.00
Argyle	AE-684_8	Intermediate	-1.51	-0.07	0.76	-2.27	-0.33	-0.50	-0.14	0.00
Argyle	AE-684_9	Intermediate	-0.94	0.44	-0.89	-0.94	-0.70	-1.19	1.24	0.00
Argyle	AE-684_10	Intermediate	-0.97	0.37	-0.37	0.82	0.18	0.24	-0.47	0.00
Argyle	AE-684_11	Intermediate	-1.33	0.56	-0.05	-0.25	-0.23	-0.05	0.64	0.00
Argyle	AE-684_12	Intermediate	-0.84	1.42	-0.03	-0.25	-0.73	0.19	0.10	0.00
Argyle	AE-684_13	Intermediate	0.46	1.53	-1.52	-0.38	-1.71	0.18	0.08	0.00
Argyle	AE-684_14	Intermediate	1.50	2.05	-1.91	-1.98	-4.24	2.49	0.27	0.00
Argyle	AE-684_15	Intermediate	-0.91	1.16	-1.07	1.52	-0.27	0.43	-0.70	0.00
Argyle	AE-684_16	Intermediate	0.62	0.44	-0.33	0.63	-0.71	-0.40	-0.42	0.00
Argyle	AE-684_17	Intermediate	0.13	0.58	0.39	0.37	-0.85	-0.30	-1.01	0.00
Argyle	AE-684_18	Intermediate	-0.34	-0.84	0.65	-0.34	-1.16	-0.95	-0.99	0.00
Argyle	AE-684_19	Intermediate	-0.70	0.90	0.23	0.57	-0.66	0.25	-0.40	0.00
Argyle	AE-684_20	Intermediate	-0.63	0.43	0.20	0.96	-0.96	-1.07	-0.05	0.00
Argyle	AE-684_21	Intermediate	0.60	0.43	0.96	-0.22	-0.85	-1.26	-1.48	0.00
Argyle	AE-684_22	Intermediate	-0.19	0.79	2.05	0.43	-0.68	-1.52	-0.94	0.00
Argyle	AE-684_23	Intermediate	-0.70	-0.06	0.86	-0.07	-0.11	-0.47	0.60	0.00
Argyle	AE-684_24	Intermediate	0.22	0.79	0.71	0.15	-0.66	1.08	-0.41	0.00
Argyle	AE-684_26	Intermediate	-1.57	0.81	-0.41	-0.64	-0.03	-0.01	1.03	0.00
Argyle	AE-684_27	Intermediate	-0.59	0.55	-0.57	0.36	-0.34	-0.70	-0.07	0.00
Argyle	AE-684_28	Intermediate	-2.32	0.20	0.46	-1.06	-0.47	-0.20	0.52	0.00
Argyle	AE-684_29	Intermediate	-1.56	0.39	-0.87	-0.73	-0.31	-1.17	1.03	0.00
Argyle	AE-684_30	Intermediate	-1.38	-0.19	-0.84	-0.91	-0.21	-0.34	1.08	0.00
Argyle	AE-684_31	Intermediate	0.03	1.53	-0.85	-0.94	-2.02	1.12	0.35	0.00
Argyle	AE-684_32	Intermediate	-0.83	0.32	0.61	0.85	-0.42	-0.34	-1.05	0.00
Argyle	AE-684_33	Intermediate	-0.85	0.91	0.63	-1.19	-0.54	-1.64	1.03	0.00
Argyle	AE-684_34	Intermediate	-1.43	0.27	0.17	-0.19	-1.48	0.02	0.56	0.00
Argyle	AE-684_35	Intermediate	-0.74	0.68	1.19	-0.14	-2.35	0.71	-1.00	0.00

	Eigenvalues	**Percent**	**Cumulative %**
PC1	1.93	24.17	24.17
PC2	1.51	18.88	43.06
PC3	1.22	15.22	58.28
PC4	1.05	13.08	71.36
PC5	0.93	11.62	82.98
PC6	0.73	9.14	92.12
PC7	0.63	7.88	100.00
PC8	0.00	0.00	100.00

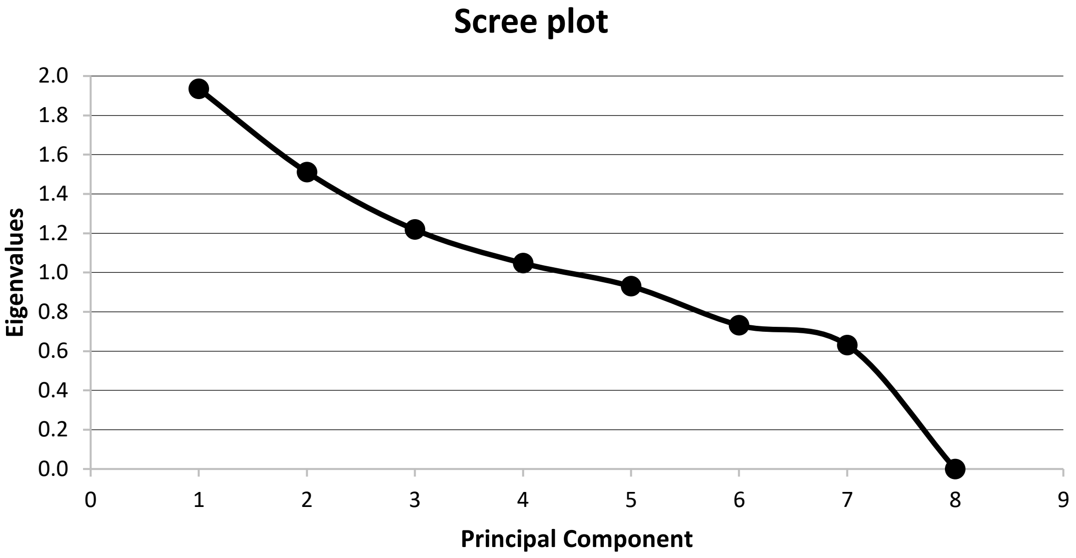

EPMA PCA run #2 (Fig. 4.4b): Fe, V, Al, Ca, Nb, Si, Zr

Deposit/Prospect	Sample	Alteration Intensity	PC1	PC2	PC3	PC4	PC5	PC6	PC7
Animal Pond	AP-704_test_1	Distal	0.73	-0.72	-0.69	-0.40	-0.77	0.27	0.00
Animal Pond	AP-704_test_2	Distal	-0.85	-3.14	-0.49	-0.86	-0.27	-0.30	0.00
Animal Pond	AP-704_test_3	Distal	1.09	-1.03	-1.94	-1.29	0.70	0.26	0.00
Animal Pond	AP-704_test_5	Distal	0.36	-2.44	-0.92	-0.87	1.43	2.82	0.00
Animal Pond	AP-714_1	Intermediate	0.80	0.93	-1.44	-1.01	-0.78	-0.27	0.00
Animal Pond	AP-714_2	Intermediate	1.66	1.29	-2.46	-0.81	-0.35	-1.14	0.00
Animal Pond	AP-714_4	Intermediate	0.62	0.79	-2.09	-0.96	-0.67	-0.52	0.00
Animal Pond	AP-714_5	Intermediate	0.63	0.40	-1.20	-1.83	-1.24	-0.50	0.00
Animal Pond	AP-714_7	Intermediate	0.63	1.11	-2.13	-0.76	-0.68	-0.56	0.00
Animal Pond	AP-714_8	Intermediate	-0.84	-0.32	-1.21	-0.91	-1.05	-0.64	0.00
Animal Pond	AP-714_9	Intermediate	-0.09	1.02	-1.76	-0.59	-1.06	-0.04	0.00
Animal Pond	AP-714_10	Intermediate	-0.81	-1.01	-0.96	-0.47	-1.41	0.27	0.00
Animal Pond	AP-714_11	Intermediate	0.82	0.15	-1.22	0.32	-0.58	-0.99	0.00
Animal Pond	AP-714_12	Intermediate	2.43	-1.44	1.08	-1.07	-2.43	-0.85	0.00
Animal Pond	AP-714_13	Intermediate	-0.36	-1.37	-0.42	0.12	-0.21	-1.25	0.00
Animal Pond	AP-714_14	Intermediate	-0.56	-2.13	-1.13	0.90	1.25	-0.31	0.00
Animal Pond	AP-714_15	Intermediate	-1.00	-2.41	-1.07	1.21	0.90	0.31	0.00
Animal Pond	AP-714_16	Intermediate	2.55	-1.75	0.63	-0.53	-1.62	-0.07	0.00
Animal Pond	AP-714_17	Intermediate	-0.06	-1.09	-0.99	0.95	-0.27	-0.11	0.00
Animal Pond	AP-714_18	Intermediate	-0.81	-1.47	-0.90	0.19	-0.41	-0.74	0.00
Animal Pond	AP-714_19	Intermediate	-0.28	-1.07	-1.51	-0.08	0.08	-0.54	0.00
Animal Pond	AP-714_21	Intermediate	0.71	-0.07	-1.85	-0.09	-0.34	-1.11	0.00
Animal Pond	AP-714_22	Intermediate	0.57	-0.13	-1.23	-0.36	-1.28	-0.38	0.00
Animal Pond	AP-714_23	Intermediate	0.25	-0.47	-1.52	0.18	-1.00	-0.49	0.00
Animal Pond	AP-714_24	Intermediate	2.98	0.66	-3.81	-3.25	2.41	-0.67	0.00
Animal Pond	AP-714_25	Intermediate	0.09	-0.55	-2.17	1.43	-0.19	1.07	0.00
Animal Pond	AP-714_26	Intermediate	0.41	-1.82	-0.80	1.52	0.47	-1.61	0.00
Animal Pond	AP-714_27	Intermediate	2.92	1.24	-3.46	-2.62	2.77	-0.79	0.00

Animal Pond	AP-714_28	Intermediate	-0.36	-0.23	-1.40	0.75	-0.29	-0.37	0.00
Animal Pond	AP-714_29	Intermediate	1.66	-1.99	-0.41	0.43	0.00	-1.50	0.00
Animal Pond	AP-714_30	Intermediate	-0.47	-1.30	-0.99	0.19	-0.45	-0.70	0.00
Animal Pond	AP-714_31	Intermediate	-0.25	-1.21	-0.53	0.31	-0.30	-1.16	0.00
Animal Pond	AP-722_1	Proximal	1.95	-2.67	1.66	0.23	0.87	0.50	0.00
Animal Pond	AP-722_2	Proximal	1.92	-2.09	1.50	0.65	1.43	0.34	0.00
Animal Pond	AP-722_3	Proximal	1.78	-1.78	1.43	-0.28	0.57	0.71	0.00
Animal Pond	AP-722_4	Proximal	0.16	-2.94	0.33	-1.59	-2.35	1.21	0.00
Animal Pond	AP-722_5	Proximal	-1.05	-2.60	-0.89	-0.13	-0.67	0.50	0.00
Animal Pond	AP-722_6	Proximal	1.51	-1.62	1.01	-0.01	0.88	0.88	0.00
Animal Pond	AP-722_7	Proximal	1.42	-2.23	1.70	0.36	0.87	0.70	0.00
Animal Pond	AP-722_8	Proximal	1.59	-2.52	1.85	0.25	1.51	0.22	0.00
Animal Pond	AP-722_9	Proximal	1.83	-1.30	1.87	-0.45	0.24	0.24	0.00
Animal Pond	AP-722_10	Proximal	1.18	-1.93	1.47	0.25	1.31	0.74	0.00
Animal Pond	AP-722_11	Proximal	2.17	-2.05	1.50	-0.38	1.43	0.51	0.00
Animal Pond	AP-722_12	Proximal	2.50	-1.73	1.85	-1.02	0.66	1.16	0.00
Animal Pond	AP-722_13	Proximal	1.52	-0.13	1.11	-0.39	-0.37	0.69	0.00
Animal Pond	AP-722_14	Proximal	2.94	-0.96	-0.24	-1.20	0.66	0.38	0.00
Animal Pond	AP-722_15	Proximal	1.71	-1.34	0.42	-0.95	-0.53	0.85	0.00
Animal Pond	AP-722_16	Proximal	1.35	-0.07	0.69	-0.55	-0.80	1.14	0.00
Animal Pond	AP-722_17	Proximal	1.43	-1.02	0.79	-0.94	-0.24	0.83	0.00
Animal Pond	AP-722_18	Proximal	1.93	-1.31	1.69	-1.01	-1.10	0.61	0.00
Animal Pond	AP-722_19	Proximal	1.64	-0.03	1.73	-1.19	-0.55	0.34	0.00
Animal Pond	AP-722_20	Proximal	1.54	-1.03	1.20	-0.72	-0.44	0.06	0.00
Animal Pond	AP-722_21	Proximal	0.90	-0.68	1.17	-1.08	-0.46	0.96	0.00
Animal Pond	AP-722_22	Proximal	1.92	-1.32	1.48	-1.00	-0.50	0.66	0.00
Animal Pond	AP-722_23	Proximal	1.97	-1.48	1.38	-0.57	-0.36	-0.63	0.00
Animal Pond	AP-722_24	Proximal	1.21	-0.19	0.66	-0.59	-0.49	0.61	0.00
Animal Pond	AP-722_25	Proximal	2.37	-0.49	-0.18	-1.65	-0.66	1.11	0.00
Animal Pond	AP-722_26	Proximal	1.51	0.26	1.23	-0.81	-0.70	0.28	0.00
Animal Pond	AP-722_27	Proximal	1.47	-1.51	1.57	-0.26	-0.26	0.89	0.00
Animal Pond	AP-722_28	Proximal	1.28	-0.80	1.19	-0.09	0.62	0.77	0.00
Animal Pond	AP-722_29	Proximal	1.81	-1.98	0.85	-0.44	-0.50	1.00	0.00
Animal Pond	AP-722_30	Proximal	0.24	-2.10	0.00	1.45	0.62	1.28	0.00
Animal Pond	AP-722_31	Proximal	2.57	-2.13	1.68	0.38	1.47	0.24	0.00
Animal Pond	AP-722_32	Proximal	1.26	-1.74	1.02	0.10	0.60	0.21	0.00
Animal Pond	AP-722_33	Proximal	1.41	-1.40	1.51	0.02	0.64	0.66	0.00
Animal Pond	AP-722_34	Proximal	1.79	-1.98	1.22	-0.17	0.96	0.20	0.00
Animal Pond	AP-722_35	Proximal	1.12	-2.61	0.99	0.11	0.75	0.27	0.00
Stog'er Tight	BN-730_1	Proximal	-0.13	0.46	-0.47	-0.74	-0.05	-0.35	0.00
Stog'er Tight	BN-730_2	Proximal	-0.43	0.76	-0.15	-0.64	-0.20	-1.11	0.00
Stog'er Tight	BN-730_3	Proximal	-0.69	1.18	0.35	-0.50	0.91	-1.29	0.00
Stog'er Tight	BN-730_4	Proximal	-1.21	0.36	0.18	-0.41	0.99	0.27	0.00
Stog'er Tight	BN-730_5	Proximal	-2.16	-1.90	0.77	-2.02	1.24	-0.05	0.00
Stog'er Tight	BN-730_6	Proximal	-1.08	-0.84	0.10	0.46	-0.25	-1.39	0.00
Stog'er Tight	BN-730_7	Proximal	-2.08	-0.21	0.47	0.17	-0.41	-0.16	0.00
Stog'er Tight	BN-730_8	Proximal	-2.61	-0.10	0.32	0.13	0.27	0.63	0.00
Stog'er Tight	BN-730_9	Proximal	1.10	-0.54	-3.18	-0.24	1.75	0.39	0.00
Stog'er Tight	BN-730_10	Proximal	0.30	0.92	-0.93	1.80	-0.29	0.46	0.00
Stog'er Tight	BN-730_11	Proximal	0.07	0.21	-0.14	0.47	-0.57	-0.21	0.00
Stog'er Tight	BN-730_12	Proximal	0.11	-0.44	-0.55	0.58	-0.47	-0.52	0.00
Stog'er Tight	BN-730_13	Proximal	-0.25	0.05	-0.35	0.89	0.26	-0.37	0.00

Stog'er Tight	BN-730_14	Proximal	0.86	0.65	-0.61	-0.70	0.41	-0.74	0.00
Stog'er Tight	BN-730_15	Proximal	-0.20	-0.04	-0.32	0.11	-0.40	-0.82	0.00
Stog'er Tight	BN-730_16	Proximal	0.36	-1.18	-1.60	0.89	-0.79	1.72	0.00
Stog'er Tight	BN-730_17	Proximal	-0.06	-0.97	-1.56	-1.12	0.73	-0.25	0.00
Stog'er Tight	BN-730_18	Proximal	-1.18	-1.66	-0.52	-0.65	0.68	0.91	0.00
Stog'er Tight	BN-730_19	Proximal	-0.62	-0.89	-0.92	-0.80	-0.11	0.63	0.00
Stog'er Tight	BN-730_20	Proximal	-1.42	-1.20	-0.79	0.08	0.96	0.74	0.00
Stog'er Tight	BN-730_21	Proximal	-0.42	1.64	-0.21	-1.00	1.02	0.31	0.00
Stog'er Tight	BN-730_22	Proximal	-0.98	1.58	1.97	-0.51	1.04	-0.35	0.00
Stog'er Tight	BN-730_23	Proximal	0.35	-0.51	-0.03	-0.10	-0.29	-0.79	0.00
Stog'er Tight	BN-730_24	Proximal	0.09	-0.42	0.16	0.04	-0.34	-0.46	0.00
Stog'er Tight	BN-730_25	Proximal	-0.60	0.35	0.51	-0.01	-0.21	0.10	0.00
Stog'er Tight	BN-730_26	Proximal	1.35	1.18	-2.70	-3.89	2.59	1.39	0.00
Stog'er Tight	BN-730_27	Proximal	-1.59	0.53	0.77	-0.32	0.78	1.04	0.00
Stog'er Tight	BN-730_28	Proximal	-0.12	-1.21	0.37	0.61	1.15	-1.50	0.00
Stog'er Tight	BN-730_29	Proximal	0.42	-1.31	-0.16	0.78	1.06	-1.38	0.00
Stog'er Tight	BN-730_30	Proximal	0.30	0.06	-0.41	-0.19	-0.63	-0.07	0.00
Stog'er Tight	BN-730_31	Proximal	-1.35	-0.21	0.31	0.17	0.07	1.35	0.00
Stog'er Tight	BN-730_32	Proximal	-1.26	1.41	1.19	-0.07	0.49	0.89	0.00
Stog'er Tight	BN-730_33	Proximal	-0.69	1.71	0.93	0.31	-0.11	0.23	0.00
Stog'er Tight	BN-730_34	Proximal	-0.55	1.59	0.43	-0.24	-0.25	-0.23	0.00
Stog'er Tight	BN-730_35	Proximal	-0.13	1.83	0.30	-0.70	0.43	0.30	0.00
Stog'er Tight	BN-739_1	Distal	-0.68	1.94	0.98	-0.95	1.34	0.05	0.00
Stog'er Tight	BN-739_2	Distal	-0.31	1.76	0.69	-0.22	0.61	-0.32	0.00
Stog'er Tight	BN-739_3	Distal	-1.10	2.39	1.59	-0.27	1.35	0.28	0.00
Stog'er Tight	BN-739_4	Distal	-2.80	0.39	1.65	0.24	0.59	1.41	0.00
Stog'er Tight	BN-739_5	Distal	-0.78	2.74	1.61	-0.37	1.28	0.01	0.00
Stog'er Tight	BN-739_6	Distal	-0.60	1.84	1.09	-0.01	0.34	-0.07	0.00
Stog'er Tight	BN-739_7	Distal	-1.74	2.23	2.48	-0.37	0.23	-0.16	0.00
Stog'er Tight	BN-739_8	Distal	-0.96	3.10	1.90	-0.07	0.40	-0.17	0.00
Stog'er Tight	BN-739_9	Distal	-0.99	3.17	1.66	-0.49	0.38	0.14	0.00
Stog'er Tight	BN-739_10	Distal	-1.67	1.46	0.01	-0.59	0.29	1.78	0.00
Stog'er Tight	BN-739_11	Distal	-0.73	2.55	0.90	-0.42	0.55	-0.25	0.00
Stog'er Tight	BN-739_12	Distal	0.53	1.77	0.24	-0.52	-0.07	-0.73	0.00
Stog'er Tight	BN-739_14	Distal	1.35	-0.22	0.16	2.60	0.86	-0.32	0.00
Stog'er Tight	BN-739_15	Distal	0.17	0.19	-0.69	0.84	0.30	1.94	0.00
Stog'er Tight	BN-739_16	Distal	1.22	-0.19	-1.44	0.58	0.26	-0.11	0.00
Stog'er Tight	BN-739_17	Distal	1.38	1.02	0.26	0.92	1.98	-0.95	0.00
Stog'er Tight	BN-739_18	Distal	0.72	0.70	-0.55	2.27	0.30	0.67	0.00
Stog'er Tight	BN-739_19	Distal	1.64	1.09	0.06	1.66	-0.51	-0.31	0.00
Stog'er Tight	BN-739_21	Distal	0.30	1.67	-0.32	1.94	0.53	0.71	0.00
Stog'er Tight	BN-739_22	Distal	0.57	-1.18	-0.45	2.75	0.73	0.46	0.00
Stog'er Tight	BN-739_23	Distal	0.24	0.69	-0.31	0.52	0.33	-0.15	0.00
Stog'er Tight	BN-739_24	Distal	1.20	0.99	-0.65	1.33	-0.05	-0.70	0.00
Stog'er Tight	BN-739_25	Distal	1.17	1.16	-0.09	0.86	0.16	-0.16	0.00
Stog'er Tight	BN-739_26	Distal	-0.15	-0.04	-1.02	0.89	-0.20	0.07	0.00
Stog'er Tight	BN-739_27	Distal	0.88	1.03	-0.27	0.32	-0.17	-1.13	0.00
Stog'er Tight	BN-739_28	Distal	0.32	0.08	-0.57	1.13	0.05	-1.00	0.00
Stog'er Tight	BN-739_29	Distal	-0.24	-0.33	-0.33	0.77	0.60	-0.68	0.00
Stog'er Tight	BN-739_30	Distal	0.31	-0.13	-0.95	0.70	-0.16	-0.51	0.00
Stog'er Tight	BN-739_31	Distal	0.28	0.06	0.00	0.45	-0.01	-0.44	0.00
Stog'er Tight	BN-748_1	Intermediate	0.15	0.83	-1.69	1.52	-1.61	2.31	0.00

Stog'er Tight	BN-748_2	Intermediate	0.72	1.54	-1.22	0.94	-0.53	0.26	0.00
Stog'er Tight	BN-748_3	Intermediate	-0.78	0.42	-1.05	0.69	-0.95	1.97	0.00
Stog'er Tight	BN-748_4	Intermediate	-1.30	-0.45	0.35	-0.04	-1.56	0.28	0.00
Stog'er Tight	BN-748_5	Intermediate	2.43	0.29	-0.60	0.67	-1.91	0.71	0.00
Stog'er Tight	BN-748_6	Intermediate	0.55	1.36	-1.86	1.29	-1.07	1.36	0.00
Stog'er Tight	BN-748_7	Intermediate	0.98	1.01	-0.48	0.32	-1.33	-0.09	0.00
Stog'er Tight	BN-748_8	Intermediate	0.49	0.51	-0.17	0.07	-1.08	0.33	0.00
Stog'er Tight	BN-748_9	Intermediate	0.91	0.99	-1.44	1.82	-0.61	0.32	0.00
Stog'er Tight	BN-748_10	Intermediate	1.24	0.78	-1.53	1.57	-0.82	0.57	0.00
Stog'er Tight	BN-748_11	Intermediate	-0.83	2.01	-0.08	0.23	0.20	2.12	0.00
Stog'er Tight	BN-748_12	Intermediate	-1.65	1.20	0.60	0.77	0.41	1.44	0.00
Stog'er Tight	BN-748_13	Intermediate	1.00	1.74	-0.26	1.59	-1.18	0.01	0.00
Stog'er Tight	BN-748_14	Intermediate	1.08	1.59	-1.27	0.16	0.14	-0.06	0.00
Stog'er Tight	BN-748_15	Intermediate	1.51	1.15	-0.96	1.38	-1.30	0.35	0.00
Stog'er Tight	BN-748_16	Intermediate	0.62	1.80	-1.46	1.18	-0.77	1.00	0.00
Stog'er Tight	BN-748_17	Intermediate	0.03	1.36	0.71	0.94	0.11	-1.14	0.00
Stog'er Tight	BN-748_18	Intermediate	0.83	1.36	0.20	-0.79	-0.05	-0.66	0.00
Stog'er Tight	BN-748_19	Intermediate	0.29	2.14	1.38	0.34	0.46	-0.90	0.00
Stog'er Tight	BN-748_20	Intermediate	0.25	1.88	1.92	0.66	-0.10	-0.11	0.00
Stog'er Tight	BN-748_21	Intermediate	0.95	0.44	0.52	1.23	-0.96	0.08	0.00
Stog'er Tight	BN-748_22	Intermediate	0.90	1.07	0.27	-0.47	-0.88	-0.50	0.00
Stog'er Tight	BN-748_23	Intermediate	1.15	0.88	-0.01	0.91	-0.08	-0.78	0.00
Stog'er Tight	BN-748_24	Intermediate	0.80	0.95	0.44	2.24	0.07	-0.67	0.00
Stog'er Tight	BN-748_25	Intermediate	0.57	1.37	-0.01	1.61	-0.35	0.37	0.00
Stog'er Tight	BN-748_26	Intermediate	-0.48	0.83	0.26	0.56	-0.18	-0.24	0.00
Stog'er Tight	BN-748_27	Intermediate	1.38	0.62	-1.26	-0.34	-0.46	0.00	0.00
Stog'er Tight	BN-748_28	Intermediate	1.44	0.87	-0.85	1.61	-1.03	0.20	0.00
Stog'er Tight	BN-748_29	Intermediate	1.20	0.72	-0.61	0.52	-0.78	-0.24	0.00
Stog'er Tight	BN-748_30	Intermediate	1.48	0.95	-0.96	0.26	-0.75	-0.70	0.00
Argyle	AE-660_1	Proximal	-2.92	-0.10	0.02	0.28	0.78	0.40	0.00
Argyle	AE-660_2	Proximal	-2.32	-0.97	-0.98	0.55	0.07	-0.52	0.00
Argyle	AE-660_3	Proximal	-2.36	-0.42	-0.86	0.93	0.11	0.58	0.00
Argyle	AE-660_4	Proximal	-2.30	-1.68	0.44	1.18	1.20	0.00	0.00
Argyle	AE-660_5	Proximal	-1.28	-0.03	-0.67	0.01	-0.34	-1.02	0.00
Argyle	AE-660_6	Proximal	-2.53	-1.14	0.50	0.68	0.87	-0.84	0.00
Argyle	AE-660_7	Proximal	-3.69	-2.04	0.00	-1.06	-0.15	0.25	0.00
Argyle	AE-660_8	Proximal	-2.59	-1.00	-1.09	0.41	0.10	0.55	0.00
Argyle	AE-660_9	Proximal	-2.93	-0.22	-0.59	0.42	0.51	0.53	0.00
Argyle	AE-660_10	Proximal	-2.52	-0.83	-0.92	0.92	0.58	0.52	0.00
Argyle	AE-660_11	Proximal	-1.45	-0.77	-0.23	0.88	0.59	-1.36	0.00
Argyle	AE-660_12	Proximal	-1.46	-0.56	-0.20	0.42	0.22	-1.33	0.00
Argyle	AE-660_13	Proximal	-0.90	-0.33	-1.79	-0.04	1.76	0.66	0.00
Argyle	AE-660_14	Proximal	-1.74	-0.35	-0.32	0.30	0.56	-0.96	0.00
Argyle	AE-660_15	Proximal	-1.90	0.33	0.96	-0.06	0.26	-1.70	0.00
Argyle	AE-660_16	Proximal	-1.41	-0.79	0.06	0.35	-0.97	-0.35	0.00
Argyle	AE-660_17	Proximal	-1.76	-1.10	-0.47	0.31	-0.28	-0.37	0.00
Argyle	AE-660_19	Proximal	-1.75	-1.83	0.46	1.09	1.27	-1.34	0.00
Argyle	AE-660_21	Proximal	-1.07	-0.21	0.43	-0.04	-0.58	-1.48	0.00
Argyle	AE-660_22	Proximal	-2.88	-0.47	0.00	-0.11	-0.18	0.20	0.00
Argyle	AE-660_23	Proximal	-0.23	1.84	-0.19	1.92	1.23	-0.40	0.00
Argyle	AE-660_24	Proximal	-0.62	0.21	-0.79	1.43	0.25	-0.68	0.00
Argyle	AE-660_25	Proximal	-1.42	-0.72	0.10	-0.15	-0.48	-1.40	0.00

Argyle	AE-660_26	Proximal	0.75	-0.03	-0.65	1.09	-0.73	-0.66	0.00
Argyle	AE-660_27	Proximal	-0.93	-0.41	-0.79	0.66	0.41	-0.73	0.00
Argyle	AE-660_28	Proximal	-3.11	-0.84	-0.15	0.68	0.60	0.32	0.00
Argyle	AE-660_29	Proximal	-2.11	0.50	0.21	0.20	1.16	-1.15	0.00
Argyle	AE-660_30	Proximal	-2.51	-0.35	-0.01	0.43	0.68	-1.16	0.00
Argyle	AE-659_1	Distal	2.81	0.95	0.67	0.36	2.01	2.15	0.00
Argyle	AE-659_2	Distal	1.55	0.36	-0.20	0.98	0.81	-0.19	0.00
Argyle	AE-659_3	Distal	-0.35	-1.08	0.87	0.37	-0.23	-0.34	0.00
Argyle	AE-659_5	Distal	1.36	0.62	0.42	1.32	0.70	0.28	0.00
Argyle	AE-659_6	Distal	2.39	0.11	-0.32	1.75	0.43	0.29	0.00
Argyle	AE-659_7	Distal	1.98	0.79	0.58	1.48	0.53	0.73	0.00
Argyle	AE-659_8	Distal	0.31	0.26	0.65	-0.36	0.74	-1.07	0.00
Argyle	AE-659_9	Distal	1.54	0.24	0.29	-0.29	1.01	0.25	0.00
Argyle	AE-659_10	Distal	0.96	-0.28	1.04	-0.18	-0.80	-0.79	0.00
Argyle	AE-659_11	Distal	1.22	-0.07	-0.11	0.94	0.25	-0.75	0.00
Argyle	AE-659_12	Distal	1.96	0.37	0.27	0.24	0.14	-0.93	0.00
Argyle	AE-659_13	Distal	1.70	0.14	0.43	1.01	0.76	0.05	0.00
Argyle	AE-659_14	Distal	1.58	1.24	0.32	0.29	0.86	0.44	0.00
Argyle	AE-659_15	Distal	2.20	2.39	0.32	1.36	0.19	0.76	0.00
Argyle	AE-659_17	Distal	-0.56	1.39	0.05	-0.15	0.97	0.61	0.00
Argyle	AE-659_18	Distal	1.23	1.54	-0.25	-0.04	1.27	0.69	0.00
Argyle	AE-659_19	Distal	1.26	1.05	1.08	-0.66	0.20	1.38	0.00
Argyle	AE-659_20	Distal	-1.15	-1.33	0.69	-2.40	-0.54	0.04	0.00
Argyle	AE-659_21	Distal	2.39	1.59	1.47	0.56	-1.93	0.82	0.00
Argyle	AE-659_22	Distal	0.50	2.64	2.13	0.10	0.03	0.39	0.00
Argyle	AE-659_23	Distal	1.56	1.56	-0.30	-0.11	0.84	0.17	0.00
Argyle	AE-659_25	Distal	0.91	0.47	0.76	0.29	0.06	-0.61	0.00
Argyle	AE-659_26	Distal	0.90	-0.85	0.53	0.89	0.74	-0.91	0.00
Argyle	AE-659_27	Distal	1.81	-1.41	1.56	0.61	0.11	-1.68	0.00
Argyle	AE-659_28	Distal	1.93	0.10	1.25	-0.68	-1.43	-0.97	0.00
Argyle	AE-659_29	Distal	-0.01	-0.12	0.02	0.19	0.52	0.22	0.00
Argyle	AE-659_30	Distal	2.73	1.35	-0.02	1.57	0.29	-0.84	0.00
Argyle	AE-672_test_1	Intermediate	-0.73	-3.22	-0.94	-0.61	0.48	-0.79	0.00
Argyle	AE-672_test_2	Intermediate	0.92	-0.64	-0.93	0.00	-1.09	-0.53	0.00
Argyle	AE-672_test_3	Intermediate	-0.31	-0.81	-1.12	-0.38	-0.76	0.01	0.00
Argyle	AE-672_test_4	Intermediate	0.52	-1.96	-0.52	-0.61	-1.14	-0.51	0.00
Argyle	AE-679_1	Intermediate	-1.98	0.93	0.79	-0.73	-0.29	1.53	0.00
Argyle	AE-679_2	Intermediate	0.02	2.45	2.80	-0.95	-0.64	-1.23	0.00
Argyle	AE-679_3	Intermediate	-2.24	2.12	1.85	-1.02	-0.08	0.55	0.00
Argyle	AE-679_4	Intermediate	-2.80	0.81	0.46	-0.34	-0.29	-0.37	0.00
Argyle	AE-679_5	Intermediate	-3.02	-0.01	0.30	-0.74	-1.36	1.60	0.00
Argyle	AE-679_6	Intermediate	-1.16	0.19	0.93	0.77	0.54	-0.42	0.00
Argyle	AE-679_7	Intermediate	-1.65	-0.66	0.87	-0.19	-0.72	-1.24	0.00
Argyle	AE-679_8	Intermediate	-2.35	-0.76	0.53	0.17	-0.03	-0.60	0.00
Argyle	AE-679_9	Intermediate	-0.98	0.37	1.18	-0.06	0.50	-0.67	0.00
Argyle	AE-679_10	Intermediate	-0.98	-0.74	-0.60	1.33	0.31	1.05	0.00
Argyle	AE-679_11	Intermediate	-0.24	0.13	1.14	0.30	0.19	-0.60	0.00
Argyle	AE-679_12	Intermediate	-0.86	-0.33	1.98	0.24	1.06	-0.49	0.00
Argyle	AE-679_13	Intermediate	0.25	0.35	2.05	-0.67	-2.12	-0.22	0.00
Argyle	AE-679_14	Intermediate	-0.95	-0.28	0.79	0.66	-0.73	1.32	0.00
Argyle	AE-679_15	Intermediate	0.67	0.71	1.96	-1.28	-0.62	-0.83	0.00
Argyle	AE-679_16	Intermediate	0.74	-0.78	-0.42	-0.20	-0.04	-0.10	0.00

Argyle	AE-679_17	Intermediate	-1.04	0.03	0.86	-0.48	-0.55	-0.90	0.00
Argyle	AE-679_18	Intermediate	-1.41	-0.26	1.00	0.36	0.47	-0.91	0.00
Argyle	AE-679_19	Intermediate	0.11	-1.51	0.30	1.38	0.51	-0.96	0.00
Argyle	AE-679_20	Intermediate	0.35	-0.05	1.53	-1.11	-2.24	-0.31	0.00
Argyle	AE-679_21	Intermediate	-0.97	0.01	-1.28	0.37	-0.67	1.17	0.00
Argyle	AE-679_22	Intermediate	-1.38	-0.92	-0.57	-0.01	-1.41	1.24	0.00
Argyle	AE-679_23	Intermediate	0.37	-0.21	-1.61	0.62	-1.71	0.50	0.00
Argyle	AE-679_24	Intermediate	-1.13	-1.11	-0.41	-3.39	-1.36	-0.27	0.00
Argyle	AE-679_25	Intermediate	-0.06	0.23	-0.50	-0.37	-1.04	-0.33	0.00
Argyle	AE-679_26	Intermediate	-1.57	-0.74	0.65	-0.67	-1.55	0.07	0.00
Argyle	AE-679_27	Intermediate	-1.93	-1.24	0.61	-0.14	-0.44	0.76	0.00
Argyle	AE-679_28	Intermediate	-1.69	-1.24	1.03	0.48	1.11	0.56	0.00
Argyle	AE-679_29	Intermediate	-1.22	-0.08	0.38	0.02	0.20	0.75	0.00
Argyle	AE-679_30	Intermediate	-1.33	-0.22	0.54	0.32	0.31	1.35	0.00
Argyle	AE-684_1	Intermediate	-0.18	0.08	-0.60	-0.21	-0.69	-0.58	0.00
Argyle	AE-684_2	Intermediate	-0.64	0.53	-0.63	-0.86	-0.13	-0.90	0.00
Argyle	AE-684_3	Intermediate	-1.97	-0.33	-0.56	-0.30	-0.43	-0.99	0.00
Argyle	AE-684_4	Intermediate	-0.91	-1.25	-0.66	0.09	0.20	-0.90	0.00
Argyle	AE-684_5	Intermediate	-0.70	-0.03	-0.60	0.04	-0.24	-1.43	0.00
Argyle	AE-684_6	Intermediate	-1.80	0.02	-0.42	0.36	0.25	0.20	0.00
Argyle	AE-684_7	Intermediate	-0.81	0.47	-0.72	0.10	-0.37	1.05	0.00
Argyle	AE-684_8	Intermediate	-1.86	0.47	-0.58	-0.25	0.15	0.92	0.00
Argyle	AE-684_9	Intermediate	-0.88	0.45	-1.29	-0.72	-0.60	1.63	0.00
Argyle	AE-684_10	Intermediate	-0.78	0.23	0.04	0.15	-0.21	-0.87	0.00
Argyle	AE-684_11	Intermediate	-1.28	0.60	-0.23	-0.24	0.16	0.55	0.00
Argyle	AE-684_12	Intermediate	-0.74	1.46	-0.25	-0.73	0.22	0.00	0.00
Argyle	AE-684_13	Intermediate	0.72	1.33	-1.56	-1.71	0.12	-0.16	0.00
Argyle	AE-684_14	Intermediate	1.67	1.98	-2.69	-4.15	2.74	-0.43	0.00
Argyle	AE-684_15	Intermediate	-0.49	0.79	-0.25	-0.34	-0.38	-1.52	0.00
Argyle	AE-684_16	Intermediate	0.75	0.29	0.02	-0.74	-0.68	-0.44	0.00
Argyle	AE-684_17	Intermediate	0.16	0.62	0.46	-0.86	-0.62	-0.78	0.00
Argyle	AE-684_18	Intermediate	-0.54	-0.60	0.36	-1.16	-0.95	-0.18	0.00
Argyle	AE-684_19	Intermediate	-0.58	0.88	0.40	-0.68	-0.03	-0.65	0.00
Argyle	AE-684_20	Intermediate	-0.50	0.35	0.60	-1.03	-1.22	0.07	0.00
Argyle	AE-684_21	Intermediate	0.45	0.67	0.65	-0.84	-1.40	-0.47	0.00
Argyle	AE-684_22	Intermediate	-0.36	1.09	1.89	-0.70	-1.55	-0.01	0.00
Argyle	AE-684_23	Intermediate	-0.80	0.09	0.68	-0.11	-0.15	0.82	0.00
Argyle	AE-684_24	Intermediate	0.21	0.86	0.66	-0.64	0.91	-0.74	0.00
Argyle	AE-684_26	Intermediate	-1.49	0.84	-0.75	-0.03	0.36	0.91	0.00
Argyle	AE-684_27	Intermediate	-0.43	0.44	-0.36	-0.39	-0.84	-0.03	0.00
Argyle	AE-684_28	Intermediate	-2.44	0.50	-0.24	-0.45	0.25	0.85	0.00
Argyle	AE-684_29	Intermediate	-1.47	0.39	-1.19	-0.33	-0.71	1.36	0.00
Argyle	AE-684_30	Intermediate	-1.36	-0.17	-1.21	-0.21	0.13	1.16	0.00
Argyle	AE-684_31	Intermediate	0.16	1.51	-1.28	-1.98	1.28	-0.04	0.00
Argyle	AE-684_32	Intermediate	-0.77	0.36	0.88	-0.46	-0.80	-0.96	0.00
Argyle	AE-684_33	Intermediate	-0.99	1.19	-0.14	-0.53	-0.84	1.94	0.00
Argyle	AE-684_34	Intermediate	-1.41	0.35	-0.02	-1.49	0.25	0.49	0.00
Argyle	AE-684_35	Intermediate	-0.83	0.95	0.85	-2.32	0.55	-0.92	0.00

	Eigenvalues	Percent	Cumulative %
PC1	1.90	27.15	27.15
PC2	1.52	21.68	48.82
PC3	1.18	16.84	65.66
PC4	0.94	13.47	79.14
PC5	0.76	10.84	89.98
PC6	0.70	10.02	100.00
PC7	0.00	0.00	100.00

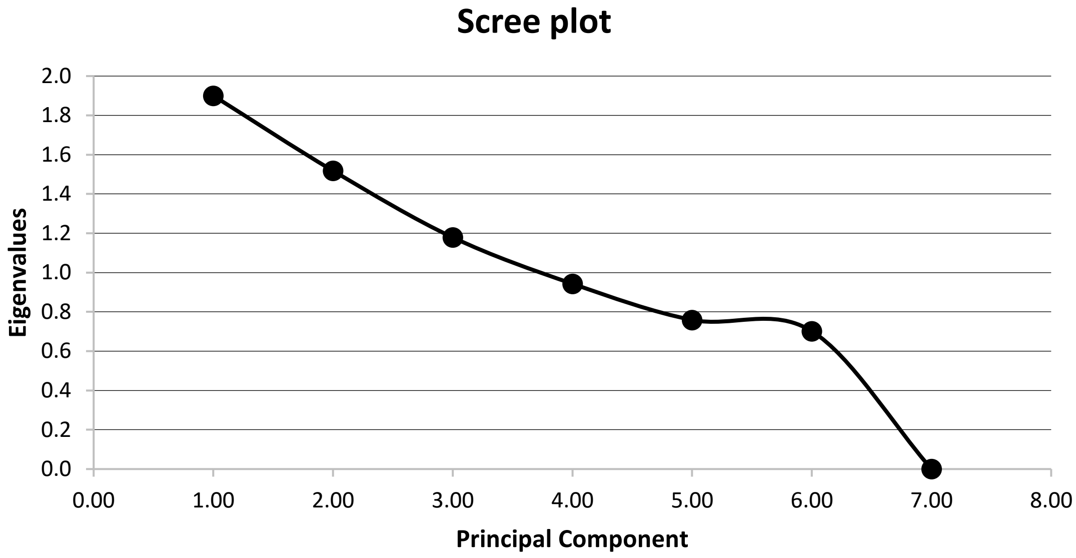

EPMA PCA run #3 (Fig. 4.4c): Mn, Fe, V, Al, Ca, Nb, Si, Zr

Deposit/Prospect	Sample	Alteration Intensity	PC1	PC2	PC3	PC4	PC5	PC6	PC7	PC8
Animal Pond	AP-704_test_2	Distal	-2.43	-3.58	1.71	0.27	-0.35	-0.69	0.01	0.00
Animal Pond	AP-704_test_3	Distal	-0.92	0.38	1.91	-2.18	2.07	0.62	-0.04	0.00
Animal Pond	AP-714_1	Intermediate	0.36	0.96	2.82	0.77	0.46	-0.26	0.30	0.00
Animal Pond	AP-714_2	Intermediate	0.32	2.31	3.97	0.03	0.24	-1.19	-0.15	0.00
Animal Pond	AP-714_10	Intermediate	-0.15	-2.08	1.70	0.37	-0.19	1.27	0.27	0.00
Animal Pond	AP-714_11	Intermediate	0.19	0.77	2.07	-0.16	-1.09	-0.45	-0.29	0.00
Animal Pond	AP-714_22	Intermediate	0.20	0.33	1.80	-0.17	-0.13	1.03	-0.53	0.00
Animal Pond	AP-714_28	Intermediate	0.50	-0.93	1.90	-0.61	-1.16	0.00	0.63	0.00
Animal Pond	AP-722_3	Proximal	-2.37	0.21	-0.79	0.01	-0.16	-0.26	0.38	0.00
Animal Pond	AP-722_6	Proximal	-2.31	-0.21	-0.12	0.02	-0.44	-0.71	1.14	0.00
Animal Pond	AP-722_7	Proximal	-2.25	-0.33	-1.63	-0.69	-0.59	-0.02	0.35	0.00
Animal Pond	AP-722_9	Proximal	-1.58	0.99	-1.70	-0.03	0.14	0.17	-0.58	0.00
Animal Pond	AP-722_10	Proximal	-1.71	-0.23	-1.79	-1.25	0.01	0.02	0.44	0.00
Animal Pond	AP-722_11	Proximal	-2.74	0.63	-1.12	-0.71	0.25	-0.87	0.21	0.00
Animal Pond	AP-722_12	Proximal	-2.58	1.15	-1.57	-0.26	1.08	0.45	0.02	0.00
Animal Pond	AP-722_15	Proximal	-2.18	0.20	0.78	0.68	0.25	0.45	0.36	0.00

Animal Pond	AP-722_16	Proximal	-1.29	0.26	1.13	2.02	-0.49	-0.02	1.42	0.00
Animal Pond	AP-722_18	Proximal	-2.22	0.58	-0.41	1.64	-0.15	0.54	-0.33	0.00
Animal Pond	AP-722_19	Proximal	-1.06	1.20	-0.42	1.95	0.28	-0.35	-0.02	0.00
Animal Pond	AP-722_21	Proximal	-1.27	-0.22	-0.04	1.41	0.45	0.25	0.66	0.00
Animal Pond	AP-722_22	Proximal	-2.21	0.60	-0.37	1.13	0.16	0.22	-0.08	0.00
Animal Pond	AP-722_23	Proximal	-1.84	1.11	-0.75	0.34	-0.39	-0.28	-1.39	0.00
Animal Pond	AP-722_25	Proximal	-1.46	1.74	0.86	-0.06	1.76	1.56	-0.07	0.00
Animal Pond	AP-722_27	Proximal	-1.97	-0.04	-0.82	0.65	-0.41	0.45	0.36	0.00
Animal Pond	AP-722_28	Proximal	-1.00	0.47	-1.01	-0.29	0.15	0.15	0.59	0.00
Animal Pond	AP-722_29	Proximal	-2.54	-0.05	-0.03	0.22	-0.21	0.91	0.23	0.00
Animal Pond	AP-722_32	Proximal	-2.08	-0.31	-0.23	0.03	-0.79	-0.85	0.41	0.00
Animal Pond	AP-722_33	Proximal	-1.97	-0.05	-0.69	0.39	-0.61	-0.70	0.80	0.00
Animal Pond	AP-722_34	Proximal	-1.98	0.59	-1.42	-1.28	0.24	0.01	-0.46	0.00
Animal Pond	AP-722_35	Proximal	-2.04	-0.54	-1.42	-1.61	-0.06	0.49	-0.44	0.00
Stog'er Tight	BN-730_3	Proximal	2.09	0.43	-0.55	-0.21	0.74	-1.39	-0.47	0.00
Stog'er Tight	BN-730_5	Proximal	-0.29	-3.51	-1.01	-0.35	2.40	-0.71	-0.07	0.00
Stog'er Tight	BN-730_6	Proximal	0.54	-1.61	0.15	-0.02	-1.32	-0.78	-0.68	0.00
Stog'er Tight	BN-730_7	Proximal	2.11	-2.10	-1.46	-0.67	0.21	1.46	-0.27	0.00
Stog'er Tight	BN-730_12	Proximal	0.10	-0.45	1.10	-0.17	-1.25	-0.06	0.07	0.00
Stog'er Tight	BN-730_14	Proximal	0.49	1.32	1.14	-0.27	0.65	-0.92	-0.22	0.00
Stog'er Tight	BN-730_17	Proximal	-0.16	-0.62	1.35	-1.89	1.76	0.19	-0.24	0.00
Stog'er Tight	BN-730_21	Proximal	2.03	0.55	0.07	-0.35	1.96	-0.29	0.96	0.00
Stog'er Tight	BN-730_25	Proximal	1.29	-0.52	-0.63	0.07	0.07	0.59	0.29	0.00
Stog'er Tight	BN-730_32	Proximal	2.41	-0.66	-1.60	0.36	0.78	0.52	1.43	0.00
Stog'er Tight	BN-739_2	Distal	2.44	1.01	-1.05	-0.06	0.78	-0.30	0.22	0.00
Stog'er Tight	BN-739_6	Distal	2.35	0.45	-0.99	0.85	0.14	-0.53	0.77	0.00
Stog'er Tight	BN-739_23	Distal	1.21	0.62	0.22	-0.76	-0.29	0.06	0.48	0.00
Stog'er Tight	BN-739_25	Distal	0.83	1.65	0.67	0.02	-1.12	-0.52	0.78	0.00
Stog'er Tight	BN-739_27	Distal	1.49	1.95	0.12	-0.68	-0.35	-0.02	-0.91	0.00
Stog'er Tight	BN-739_29	Distal	0.77	-0.36	-0.02	-1.36	-0.66	-0.28	-0.03	0.00
Stog'er Tight	BN-739_30	Distal	0.83	0.36	0.58	-1.54	-0.56	0.78	-0.32	0.00
Stog'er Tight	BN-739_31	Distal	1.00	0.54	-0.49	-1.10	-0.24	0.66	-0.45	0.00
Stog'er Tight	BN-748_7	Intermediate	0.97	1.40	1.10	0.44	-0.83	1.02	0.02	0.00
Stog'er Tight	BN-748_18	Intermediate	0.91	1.62	0.73	1.00	0.36	-1.07	-0.07	0.00
Stog'er Tight	BN-748_21	Intermediate	0.81	1.11	-0.48	-0.05	-1.62	1.24	0.06	0.00
Stog'er Tight	BN-748_22	Intermediate	1.15	1.72	0.05	0.51	0.19	0.55	-0.73	0.00
Stog'er Tight	BN-748_26	Intermediate	1.90	0.08	-0.60	-0.31	-0.43	0.56	0.16	0.00
Argyle	AE-660_5	Proximal	1.12	-1.48	1.14	0.17	-0.60	-0.59	-0.08	0.00
Argyle	AE-660_11	Proximal	1.21	-1.68	-0.39	-1.41	-0.93	-0.60	-0.53	0.00
Argyle	AE-660_14	Proximal	1.57	-1.80	-0.25	-1.13	-0.11	-0.35	-0.20	0.00
Argyle	AE-660_22	Proximal	1.25	-3.91	0.39	0.75	-0.24	-0.10	1.29	0.00
Argyle	AE-660_25	Proximal	1.04	-1.64	-0.25	-0.18	-0.37	-0.12	-1.21	0.00
Argyle	AE-660_26	Proximal	0.83	0.93	0.34	-1.25	-1.25	1.13	-0.69	0.00
Argyle	AE-659_3	Distal	-0.33	-1.36	-0.42	0.41	-1.18	-0.31	0.03	0.00
Argyle	AE-659_8	Distal	0.59	0.68	-0.43	-0.03	0.14	-1.42	-0.52	0.00

Argyle	AE-659_9	Distal	-0.14	1.65	-0.19	-0.80	0.71	-0.37	0.42	0.00
Argyle	AE-659_10	Distal	-0.22	0.81	-0.41	0.84	-0.78	-0.16	-1.00	0.00
Argyle	AE-659_12	Distal	-0.35	2.18	0.66	0.27	-1.02	-1.30	-0.36	0.00
Argyle	AE-659_13	Distal	-0.10	1.71	-0.36	-0.91	-0.97	-0.33	0.52	0.00
Argyle	AE-659_14	Distal	0.84	2.31	-0.36	-0.69	0.28	-0.04	0.84	0.00
Argyle	AE-659_18	Distal	1.05	1.98	0.36	-0.77	0.88	-0.38	1.48	0.00
Argyle	AE-659_19	Distal	0.58	1.61	-0.97	0.30	1.25	1.00	1.05	0.00
Argyle	AE-659_26	Distal	-0.24	0.61	-0.79	-1.27	-1.09	-0.65	-0.61	0.00
Argyle	AE-672_test_1	Intermediate	-2.27	-3.20	1.70	-0.86	-0.23	-1.16	-0.28	0.00
Argyle	AE-679_6	Proximal	1.53	-1.10	-1.23	-0.17	-0.81	-0.49	0.44	0.00
Argyle	AE-679_9	Proximal	1.42	-0.70	-1.24	0.37	-0.08	-0.87	-0.02	0.00
Argyle	AE-679_12	Proximal	1.01	-0.86	-2.63	-0.30	-0.08	-0.71	-0.17	0.00
Argyle	AE-679_13	Proximal	0.53	0.28	-1.15	2.60	-0.66	0.92	-0.92	0.00
Argyle	AE-679_16	Proximal	-0.14	0.36	0.10	-1.38	0.45	0.98	-0.54	0.00
Argyle	AE-679_23	Proximal	0.09	-0.46	2.44	-0.03	-1.26	1.76	0.72	0.00
Argyle	AE-679_24	Proximal	-0.68	-2.26	1.76	1.81	2.57	0.21	-0.92	0.00
Argyle	AE-679_26	Proximal	0.65	-2.42	-0.31	1.17	-0.03	1.32	-0.28	0.00
Argyle	AE-684_6	Intermediate	1.61	-2.13	0.13	-0.64	-0.02	0.42	1.03	0.00
Argyle	AE-684_17	Intermediate	0.68	0.45	0.44	1.31	0.09	-0.66	-0.49	0.00
Argyle	AE-684_18	Intermediate	0.27	-1.03	-0.09	0.55	0.78	0.87	-0.70	0.00
Argyle	AE-684_21	Intermediate	0.95	0.93	-0.19	1.13	0.25	0.82	-0.99	0.00
Argyle	AE-684_22	Intermediate	1.49	0.12	-1.26	2.38	-0.10	0.73	-0.31	0.00
Argyle	AE-684_32	Intermediate	0.94	-0.74	0.03	1.73	-0.63	-0.83	-0.40	0.00
Argyle	AE-684_35	Intermediate	1.34	-0.08	-0.34	1.23	2.30	-1.55	-0.60	0.00

	Eigenvalues	**Percent**	**Cumulative %**
PC1	2.05	25.62	25.62
PC2	1.89	23.59	49.21
PC3	1.35	16.87	66.08
PC4	0.96	12.02	78.11
PC5	0.78	9.78	87.88
PC6	0.57	7.12	95.00
PC7	0.40	5.00	100.00
PC8	0.00	0.00	100.00

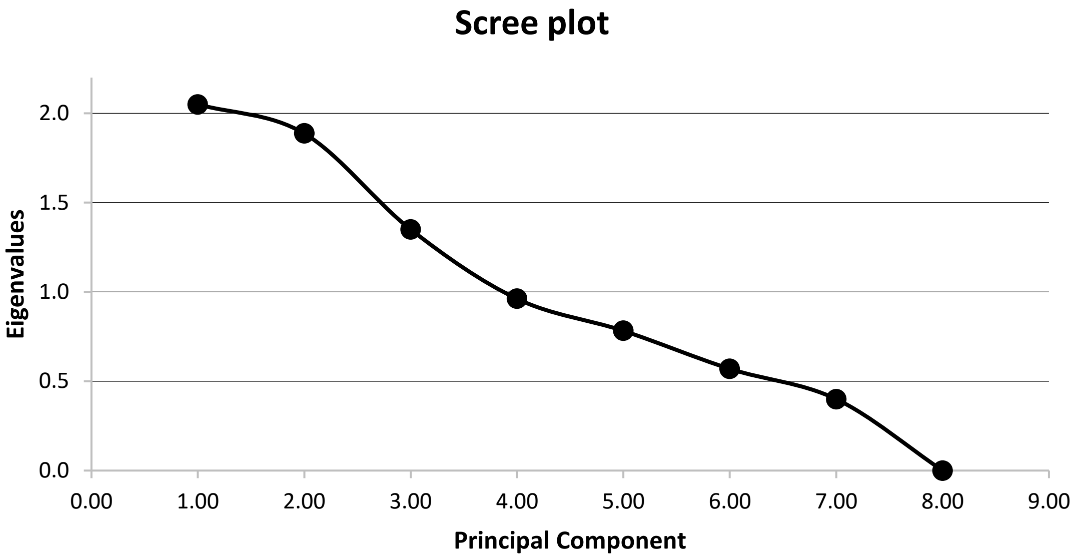

EPMA PCA run #4 (Fig. 4.4d): Fe, V, Al, Ca, Nb, Si, Zr

Deposit/Prospect	Sample	Alteration Intensity	PC1	PC2	PC3	PC4	PC5	PC6	PC7
Animal Pond	AP-704_test_1	Distal	0.37	-1.02	1.05	0.56	0.46	0.51	0.00
Animal Pond	AP-704_test_2	Distal	-2.36	-3.23	0.88	0.41	-0.09	-0.34	0.00
Animal Pond	AP-704_test_3	Distal	0.82	-1.57	2.50	0.92	-1.50	-0.35	0.00
Animal Pond	AP-714_1	Intermediate	1.29	0.84	1.74	1.27	0.24	-0.22	0.00
Animal Pond	AP-714_2	Intermediate	2.61	1.16	2.80	0.59	0.07	-1.29	0.00
Animal Pond	AP-714_4	Intermediate	1.10	0.79	2.46	1.09	0.12	-0.44	0.00
Animal Pond	AP-714_5	Intermediate	0.90	0.26	1.50	2.14	0.51	-0.73	0.00
Animal Pond	AP-714_7	Intermediate	1.24	1.16	2.47	0.91	0.21	-0.36	0.00
Animal Pond	AP-714_8	Intermediate	-1.10	-0.01	1.47	1.04	0.59	-0.28	0.00
Animal Pond	AP-714_9	Intermediate	0.27	1.20	2.10	1.09	0.48	0.52	0.00
Animal Pond	AP-714_10	Intermediate	-1.52	-0.89	1.37	0.93	0.90	0.96	0.00
Animal Pond	AP-714_11	Intermediate	1.01	0.20	1.41	-0.61	0.82	-0.54	0.00
Animal Pond	AP-714_13	Intermediate	-0.97	-1.16	0.53	-0.79	0.50	-0.95	0.00
Animal Pond	AP-714_17	Intermediate	-0.67	-1.03	1.31	-1.18	0.46	0.71	0.00
Animal Pond	AP-714_18	Intermediate	-1.58	-1.21	1.16	-0.57	0.46	-0.18	0.00
Animal Pond	AP-714_19	Intermediate	-0.76	-0.97	1.85	-0.34	-0.25	-0.26	0.00
Animal Pond	AP-714_21	Intermediate	0.88	-0.03	2.15	-0.31	0.37	-0.88	0.00
Animal Pond	AP-714_22	Intermediate	0.54	-0.19	1.57	0.57	1.08	0.05	0.00
Animal Pond	AP-714_23	Intermediate	0.05	-0.41	1.88	-0.16	0.96	0.15	0.00
Animal Pond	AP-714_28	Intermediate	-0.58	0.04	1.68	-0.90	0.36	0.48	0.00
Animal Pond	AP-714_30	Intermediate	-1.12	-1.12	1.26	-0.54	0.50	-0.17	0.00
Animal Pond	AP-714_31	Intermediate	-0.81	-1.02	0.66	-0.90	0.62	-0.73	0.00
Animal Pond	AP-722_3	Proximal	0.97	-2.64	-1.29	-0.17	-0.58	0.24	0.00
Animal Pond	AP-722_6	Proximal	0.73	-2.39	-0.82	-0.45	-0.93	0.56	0.00
Animal Pond	AP-722_7	Proximal	0.33	-3.00	-1.61	-1.01	-0.62	0.46	0.00

Animal Pond	AP-722_9	Proximal	1.25	-2.07	-1.88	0.01	-0.11	-0.26	0.00
Animal Pond	AP-722_10	Proximal	0.22	-2.62	-1.39	-0.97	-1.20	0.41	0.00
Animal Pond	AP-722_11	Proximal	1.36	-3.06	-1.39	-0.52	-1.38	-0.37	0.00
Animal Pond	AP-722_12	Proximal	1.76	-2.94	-1.69	0.70	-0.97	0.21	0.00
Animal Pond	AP-722_13	Proximal	1.37	-0.71	-1.03	0.55	0.21	0.63	0.00
Animal Pond	AP-722_14	Proximal	2.84	-2.06	0.60	0.72	-1.06	-0.64	0.00
Animal Pond	AP-722_15	Proximal	1.11	-2.17	-0.08	1.08	0.09	0.52	0.00
Animal Pond	AP-722_16	Proximal	1.15	-0.66	-0.47	1.07	0.38	1.25	0.00
Animal Pond	AP-722_17	Proximal	0.91	-1.74	-0.57	1.01	-0.18	0.47	0.00
Animal Pond	AP-722_18	Proximal	1.31	-2.18	-1.55	1.22	0.92	0.27	0.00
Animal Pond	AP-722_19	Proximal	1.57	-0.66	-1.77	1.32	0.30	-0.12	0.00
Animal Pond	AP-722_20	Proximal	1.09	-1.65	-1.12	0.55	0.41	-0.26	0.00
Animal Pond	AP-722_21	Proximal	0.41	-1.25	-1.02	1.37	-0.07	0.72	0.00
Animal Pond	AP-722_22	Proximal	1.33	-2.20	-1.33	1.02	0.26	0.17	0.00
Animal Pond	AP-722_23	Proximal	1.47	-2.15	-1.37	0.00	0.68	-1.12	0.00
Animal Pond	AP-722_24	Proximal	1.02	-0.68	-0.51	0.80	0.20	0.57	0.00
Animal Pond	AP-722_25	Proximal	2.26	-1.50	0.63	2.06	-0.17	0.48	0.00
Animal Pond	AP-722_26	Proximal	1.56	-0.24	-1.23	1.02	0.52	0.11	0.00
Animal Pond	AP-722_27	Proximal	0.67	-2.27	-1.43	0.23	0.20	0.76	0.00
Animal Pond	AP-722_28	Proximal	0.81	-1.40	-1.11	-0.18	-0.71	0.57	0.00
Animal Pond	AP-722_29	Proximal	0.89	-2.89	-0.51	0.47	0.30	0.81	0.00
Animal Pond	AP-722_32	Proximal	0.47	-2.33	-0.91	-0.71	-0.42	-0.02	0.00
Animal Pond	AP-722_33	Proximal	0.70	-2.08	-1.45	-0.46	-0.57	0.40	0.00
Animal Pond	AP-722_34	Proximal	0.99	-2.78	-1.11	-0.65	-0.80	-0.39	0.00
Animal Pond	AP-722_35	Proximal	-0.06	-3.27	-0.81	-0.88	-0.58	-0.02	0.00
Stog'er Tight	BN-730_1	Proximal	-0.02	0.57	0.57	0.65	-0.33	-0.29	0.00
Stog'er Tight	BN-730_2	Proximal	-0.17	1.12	0.07	0.38	0.10	-0.98	0.00
Stog'er Tight	BN-730_3	Proximal	-0.28	1.65	-0.62	-0.16	-0.91	-1.37	0.00
Stog'er Tight	BN-730_4	Proximal	-1.40	0.65	-0.19	0.22	-1.48	0.42	0.00
Stog'er Tight	BN-730_5	Proximal	-3.38	-1.71	-0.74	1.42	-2.16	-0.74	0.00
Stog'er Tight	BN-730_6	Proximal	-1.61	-0.33	-0.16	-1.07	0.69	-0.78	0.00
Stog'er Tight	BN-730_7	Proximal	-2.68	0.42	-0.51	-0.08	0.28	0.72	0.00
Stog'er Tight	BN-730_9	Proximal	1.09	-0.95	3.86	-0.42	-2.41	0.09	0.00
Stog'er Tight	BN-730_11	Proximal	0.00	0.34	0.23	-0.44	0.69	0.47	0.00
Stog'er Tight	BN-730_12	Proximal	-0.16	-0.33	0.71	-0.80	0.71	0.12	0.00
Stog'er Tight	BN-730_13	Proximal	-0.39	0.29	0.41	-1.24	-0.01	0.32	0.00
Stog'er Tight	BN-730_14	Proximal	1.26	0.55	0.68	0.27	-0.60	-1.02	0.00
Stog'er Tight	BN-730_15	Proximal	-0.31	0.20	0.37	-0.36	0.53	-0.36	0.00
Stog'er Tight	BN-730_17	Proximal	-0.44	-1.09	1.95	0.63	-1.38	-0.62	0.00
Stog'er Tight	BN-730_19	Proximal	-1.24	-0.94	1.31	0.96	-0.65	0.81	0.00
Stog'er Tight	BN-730_21	Proximal	0.09	1.79	0.20	0.98	-1.77	0.15	0.00
Stog'er Tight	BN-730_23	Proximal	0.12	-0.52	0.10	-0.29	0.44	-0.62	0.00
Stog'er Tight	BN-730_24	Proximal	-0.21	-0.39	-0.10	-0.26	0.44	-0.13	0.00
Stog'er Tight	BN-730_25	Proximal	-0.77	0.56	-0.54	0.10	0.06	0.61	0.00
Stog'er Tight	BN-730_30	Proximal	0.22	0.03	0.59	0.29	0.46	0.31	0.00

Stog'er Tight	BN-730_32	Proximal	-1.20	1.75	-1.36	0.39	-0.94	1.43	0.00
Stog'er Tight	BN-730_33	Proximal	-0.35	2.09	-1.13	-0.02	0.04	0.96	0.00
Stog'er Tight	BN-730_34	Proximal	-0.13	1.96	-0.57	0.42	0.07	0.24	0.00
Stog'er Tight	BN-730_35	Proximal	0.43	1.96	-0.38	0.86	-0.95	0.36	0.00
Stog'er Tight	BN-739_1	Distal	-0.13	2.20	-1.26	0.75	-1.87	-0.20	0.00
Stog'er Tight	BN-739_2	Distal	0.24	2.06	-0.93	0.06	-0.73	-0.15	0.00
Stog'er Tight	BN-739_6	Distal	-0.14	2.21	-1.37	0.04	-0.43	0.34	0.00
Stog'er Tight	BN-739_11	Distal	0.06	3.03	-1.24	0.45	-0.81	-0.01	0.00
Stog'er Tight	BN-739_12	Distal	1.28	1.90	-0.40	0.43	0.00	-0.69	0.00
Stog'er Tight	BN-739_16	Distal	1.24	-0.44	1.78	-0.93	-0.20	0.22	0.00
Stog'er Tight	BN-739_17	Distal	1.97	0.93	-0.46	-2.09	-1.38	-1.10	0.00
Stog'er Tight	BN-739_23	Distal	0.43	0.79	0.36	-0.74	-0.26	0.32	0.00
Stog'er Tight	BN-739_24	Distal	1.71	1.04	0.70	-1.67	0.64	0.03	0.00
Stog'er Tight	BN-739_25	Distal	1.65	1.08	0.10	-1.03	0.15	0.35	0.00
Stog'er Tight	BN-739_26	Distal	-0.34	0.12	1.27	-0.91	0.26	0.95	0.00
Stog'er Tight	BN-739_27	Distal	1.42	1.14	0.21	-0.70	0.55	-0.82	0.00
Stog'er Tight	BN-739_28	Distal	0.35	0.30	0.61	-1.69	0.53	-0.31	0.00
Stog'er Tight	BN-739_29	Distal	-0.49	-0.11	0.37	-1.42	-0.29	-0.21	0.00
Stog'er Tight	BN-739_30	Distal	0.23	-0.04	1.15	-1.00	0.38	0.10	0.00
Stog'er Tight	BN-739_31	Distal	0.21	0.12	0.04	-0.75	0.23	-0.01	0.00
Stog'er Tight	BN-748_2	Intermediate	1.29	1.62	1.44	-0.60	0.55	1.23	0.00
Stog'er Tight	BN-748_4	Intermediate	-1.96	-0.12	-0.22	0.63	1.33	1.27	0.00
Stog'er Tight	BN-748_7	Intermediate	1.37	0.96	0.64	0.10	1.39	0.65	0.00
Stog'er Tight	BN-748_8	Intermediate	0.54	0.44	0.34	0.38	0.93	0.98	0.00
Stog'er Tight	BN-748_14	Intermediate	1.83	1.54	1.46	-0.16	-0.30	0.26	0.00
Stog'er Tight	BN-748_17	Intermediate	0.50	1.78	-1.00	-1.37	0.52	-0.49	0.00
Stog'er Tight	BN-748_18	Intermediate	1.46	1.33	-0.28	0.64	-0.10	-0.83	0.00
Stog'er Tight	BN-748_19	Intermediate	1.08	2.45	-1.82	-0.70	-0.05	-0.64	0.00
Stog'er Tight	BN-748_20	Intermediate	0.77	2.08	-2.31	-0.59	0.48	0.50	0.00
Stog'er Tight	BN-748_21	Intermediate	0.99	0.36	-0.49	-1.03	1.46	1.05	0.00
Stog'er Tight	BN-748_22	Intermediate	1.35	1.02	-0.30	0.62	0.85	-0.31	0.00
Stog'er Tight	BN-748_23	Intermediate	1.59	0.89	-0.04	-1.27	0.63	-0.28	0.00
Stog'er Tight	BN-748_26	Intermediate	-0.39	1.17	-0.33	-0.57	0.32	0.51	0.00
Stog'er Tight	BN-748_27	Intermediate	1.76	0.33	1.58	0.45	0.18	0.14	0.00
Stog'er Tight	BN-748_29	Intermediate	1.54	0.61	0.77	-0.42	0.97	0.36	0.00
Stog'er Tight	BN-748_30	Intermediate	2.05	0.83	1.12	-0.30	0.95	-0.29	0.00
Argyle	AE-660_2	Proximal	-3.12	-0.24	1.15	-0.86	-0.15	0.44	0.00
Argyle	AE-660_5	Proximal	-1.48	0.54	0.71	-0.27	0.34	-0.40	0.00
Argyle	AE-660_6	Proximal	-3.48	-0.36	-0.64	-1.44	-0.64	-0.14	0.00
Argyle	AE-660_11	Proximal	-1.98	-0.14	0.16	-1.75	-0.12	-0.69	0.00
Argyle	AE-660_12	Proximal	-1.91	0.07	0.13	-1.09	0.08	-0.75	0.00
Argyle	AE-660_14	Proximal	-2.16	0.30	0.28	-0.90	-0.48	-0.41	0.00
Argyle	AE-660_15	Proximal	-2.05	1.17	-1.34	-0.60	0.05	-1.30	0.00
Argyle	AE-660_16	Proximal	-2.12	-0.33	0.03	-0.27	1.02	0.60	0.00
Argyle	AE-660_17	Proximal	-2.60	-0.59	0.63	-0.50	0.21	0.44	0.00

Argyle	AE-660_21	Proximal	-1.35	0.34	-0.59	-0.36	0.88	-0.99	0.00
Argyle	AE-660_22	Proximal	-3.70	0.28	0.06	0.29	-0.30	1.10	0.00
Argyle	AE-660_24	Proximal	-0.70	0.69	0.84	-1.86	0.20	0.33	0.00
Argyle	AE-660_25	Proximal	-1.93	-0.15	-0.17	-0.29	0.65	-0.93	0.00
Argyle	AE-660_26	Proximal	0.74	0.02	0.81	-1.27	1.24	0.17	0.00
Argyle	AE-660_27	Proximal	-1.28	0.01	0.88	-1.20	-0.24	-0.10	0.00
Argyle	AE-660_29	Proximal	-2.23	1.34	-0.46	-0.94	-1.08	-0.73	0.00
Argyle	AE-660_30	Proximal	-3.05	0.55	-0.14	-1.10	-0.53	-0.47	0.00
Argyle	AE-659_1	Distal	3.18	-0.11	-0.49	-0.49	-2.36	1.75	0.00
Argyle	AE-659_2	Distal	1.78	0.08	0.27	-1.55	-0.40	0.05	0.00
Argyle	AE-659_3	Distal	-1.07	-1.00	-0.88	-0.69	0.49	0.12	0.00
Argyle	AE-659_5	Distal	1.56	0.37	-0.42	-1.66	-0.26	0.77	0.00
Argyle	AE-659_6	Distal	2.54	-0.42	0.52	-2.14	0.21	0.86	0.00
Argyle	AE-659_7	Distal	2.27	0.34	-0.54	-1.62	-0.08	1.26	0.00
Argyle	AE-659_8	Distal	0.42	0.33	-0.84	-0.38	-0.58	-1.31	0.00
Argyle	AE-659_9	Distal	1.69	-0.25	-0.21	-0.14	-1.16	-0.13	0.00
Argyle	AE-659_10	Distal	0.83	-0.45	-1.13	-0.05	1.13	-0.68	0.00
Argyle	AE-659_11	Distal	1.28	-0.19	0.15	-1.55	0.33	-0.40	0.00
Argyle	AE-659_12	Distal	2.33	0.05	-0.31	-0.83	0.34	-1.02	0.00
Argyle	AE-659_13	Distal	1.79	-0.25	-0.41	-1.53	-0.31	0.25	0.00
Argyle	AE-659_14	Distal	2.10	0.87	-0.32	-0.49	-0.86	0.45	0.00
Argyle	AE-659_17	Distal	-0.27	1.58	-0.06	0.18	-1.45	0.87	0.00
Argyle	AE-659_18	Distal	1.86	1.24	0.33	-0.12	-1.62	0.59	0.00
Argyle	AE-659_19	Distal	1.51	0.52	-1.03	1.08	-0.76	1.25	0.00
Argyle	AE-659_20	Distal	-2.02	-1.36	-0.57	2.52	-0.44	-0.46	0.00
Argyle	AE-659_22	Distal	1.31	2.71	-2.53	0.24	0.01	0.76	0.00
Argyle	AE-659_23	Distal	2.31	1.26	0.36	-0.09	-1.02	0.04	0.00
Argyle	AE-659_25	Distal	1.09	0.39	-0.88	-0.67	0.29	-0.43	0.00
Argyle	AE-659_26	Distal	0.57	-0.98	-0.58	-1.85	-0.06	-0.76	0.00
Argyle	AE-659_28	Distal	2.11	-0.30	-1.36	0.63	1.75	-1.11	0.00
Argyle	AE-659_29	Distal	-0.26	-0.14	0.08	-0.42	-0.64	0.50	0.00
Argyle	AE-672_test_1	Intermediate	-2.16	-3.26	1.32	-0.33	-0.67	-0.98	0.00
Argyle	AE-672_test_2	Intermediate	0.71	-0.81	1.24	-0.05	1.16	-0.13	0.00
Argyle	AE-672_test_3	Intermediate	-0.80	-0.78	1.49	0.51	0.37	0.45	0.00
Argyle	AE-672_test_4	Intermediate	-0.31	-2.23	0.87	0.45	1.04	-0.40	0.00
Argyle	AE-679_4	Proximal	-3.03	1.75	-0.64	0.53	-0.08	0.44	0.00
Argyle	AE-679_6	Proximal	-1.45	0.67	-1.14	-1.18	-0.25	0.25	0.00
Argyle	AE-679_7	Proximal	-2.25	-0.06	-1.05	-0.10	0.92	-0.70	0.00
Argyle	AE-679_8	Proximal	-3.15	-0.06	-0.62	-0.45	0.03	0.14	0.00
Argyle	AE-679_9	Proximal	-1.11	0.77	-1.45	-0.37	-0.39	-0.43	0.00
Argyle	AE-679_11	Proximal	-0.40	0.32	-1.34	-0.71	0.12	-0.27	0.00
Argyle	AE-679_12	Proximal	-1.34	-0.07	-2.33	-0.95	-0.76	-0.37	0.00
Argyle	AE-679_13	Proximal	0.12	0.34	-2.24	1.27	2.17	0.22	0.00
Argyle	AE-679_15	Proximal	0.91	0.61	-2.27	1.17	0.60	-1.20	0.00
Argyle	AE-679_16	Proximal	0.40	-1.04	0.67	-0.07	-0.07	-0.04	0.00

Argyle	AE-679_17	Proximal	-1.29	0.45	-1.03	0.33	0.55	-0.57	0.00
Argyle	AE-679_18	Proximal	-1.85	0.28	-1.24	-0.95	-0.17	-0.44	0.00
Argyle	AE-679_20	Proximal	0.13	-0.15	-1.59	1.70	2.11	-0.06	0.00
Argyle	AE-679_23	Proximal	0.13	-0.24	2.12	0.03	1.55	1.65	0.00
Argyle	AE-679_24	Proximal	-1.78	-1.10	0.71	3.80	-0.03	-0.94	0.00
Argyle	AE-679_25	Proximal	-0.09	0.36	0.66	0.59	0.84	0.15	0.00
Argyle	AE-679_26	Proximal	-2.36	-0.40	-0.57	1.18	1.16	0.76	0.00
Argyle	AE-679_29	Proximal	-1.72	0.15	-0.30	0.15	-0.61	1.32	0.00
Argyle	AE-684_1	Intermediate	-0.24	0.28	0.74	0.19	0.60	-0.14	0.00
Argyle	AE-684_2	Intermediate	-0.50	0.88	0.67	0.66	-0.20	-0.81	0.00
Argyle	AE-684_3	Intermediate	-2.40	0.37	0.60	0.11	0.26	-0.38	0.00
Argyle	AE-684_4	Intermediate	-1.58	-0.95	0.80	-0.71	-0.14	-0.55	0.00
Argyle	AE-684_5	Intermediate	-0.77	0.44	0.60	-0.52	0.44	-0.99	0.00
Argyle	AE-684_6	Intermediate	-2.23	0.56	0.53	-0.36	-0.54	1.02	0.00
Argyle	AE-684_7	Intermediate	-1.00	0.64	1.01	0.46	-0.22	1.88	0.00
Argyle	AE-684_10	Intermediate	-0.88	0.66	-0.11	-0.42	0.35	-0.34	0.00
Argyle	AE-684_11	Intermediate	-1.43	0.94	0.33	0.48	-0.72	1.10	0.00
Argyle	AE-684_12	Intermediate	-0.36	1.79	0.25	0.87	-0.77	0.21	0.00
Argyle	AE-684_13	Intermediate	1.41	1.19	1.84	1.79	-1.02	-0.60	0.00
Argyle	AE-684_15	Intermediate	-0.18	1.27	0.13	-0.01	0.51	-1.22	0.00
Argyle	AE-684_16	Intermediate	0.88	0.15	0.05	0.75	0.50	-0.44	0.00
Argyle	AE-684_17	Intermediate	0.36	0.72	-0.54	0.81	0.49	-0.76	0.00
Argyle	AE-684_18	Intermediate	-1.02	-0.55	-0.25	1.34	0.50	-0.08	0.00
Argyle	AE-684_19	Intermediate	-0.39	1.19	-0.54	0.55	-0.17	-0.53	0.00
Argyle	AE-684_20	Intermediate	-0.64	0.47	-0.57	1.52	0.75	0.37	0.00
Argyle	AE-684_21	Intermediate	0.63	0.67	-0.69	1.17	1.26	-0.26	0.00
Argyle	AE-684_22	Intermediate	-0.27	1.28	-2.13	1.34	1.39	0.48	0.00
Argyle	AE-684_23	Intermediate	-1.20	0.20	-0.63	0.43	-0.25	1.35	0.00
Argyle	AE-684_24	Intermediate	0.54	0.94	-0.86	0.07	-0.98	-1.05	0.00
Argyle	AE-684_26	Intermediate	-1.59	1.23	0.95	0.39	-1.05	1.63	0.00
Argyle	AE-684_27	Intermediate	-0.46	0.63	0.50	0.70	0.51	0.50	0.00
Argyle	AE-684_31	Intermediate	0.85	1.46	1.44	1.76	-2.38	-0.81	0.00
Argyle	AE-684_32	Intermediate	-0.85	0.75	-1.06	0.40	0.86	-0.58	0.00
Argyle	AE-684_34	Intermediate	-1.64	0.59	0.11	1.72	-1.24	0.44	0.00
Argyle	AE-684_35	Intermediate	-0.56	1.21	-1.09	1.99	-1.28	-1.70	0.00

	Eigenvalues	Percent	Cumulative %
PC1	2.02	28.82	28.82
PC2	1.64	23.40	52.21
PC3	1.28	18.34	70.55
PC4	0.91	13.03	83.58
PC5	0.66	9.45	93.03
PC6	0.49	6.97	100.00
PC7	0.00	0.00	100.00

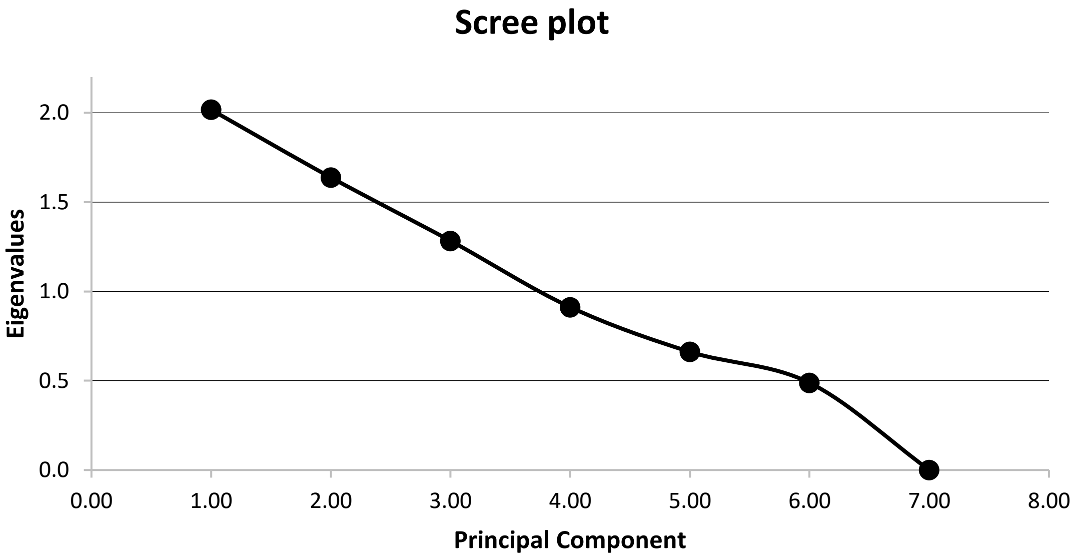

SIMS PCA run #1 (Fig. 4.5a): Al, Si, P, Ca, Sc, V, Cr, Mn, Fe, As, Y, Zr, Nb, Sn, Sb, Ta, W.

Deposit / Prospect	Sample	Alteration Intensity	PC1	PC2	PC3	PC4	PC5	PC6	PC7	PC8	PC9	PC10	PC11	PC12
Animal Pond	AP-722-1	Proximal	-3.60	-0.22	3.40	0.48	0.65	1.80	1.52	0.09	-1.38	-0.19	0.14	-0.08
Animal Pond	AP-722-2	Proximal	-3.59	1.45	-1.20	-0.94	-0.84	0.37	0.07	0.33	-0.12	-0.55	0.35	0.44
Animal Pond	AP-722-3	Proximal	-3.03	1.06	-3.59	-0.15	-0.71	-0.60	0.65	-0.37	-0.43	-0.26	-0.26	-0.69
Animal Pond	AP-722-4	Proximal	-3.66	1.37	-3.42	0.18	0.06	-0.70	0.10	0.04	0.22	-0.14	-0.22	-0.52
Animal Pond	AP-722-5	Proximal	-3.34	1.81	1.78	0.67	-0.57	-0.59	0.17	0.18	0.32	0.38	-0.42	0.56
Animal Pond	AP-722-6	Proximal	-2.94	1.48	-3.11	0.17	-0.70	-1.15	0.01	-1.24	0.25	0.00	0.73	0.11
Animal Pond	AP-722-7	Proximal	-3.97	1.42	1.30	1.15	1.16	-0.75	0.11	-0.53	0.18	-0.21	-0.15	-0.13
Animal Pond	AP-722-8	Proximal	-3.12	1.58	2.17	0.72	-0.27	-1.02	-0.21	-0.53	0.24	0.56	-0.57	-0.07
Animal Pond	AP-722-9	Proximal	-4.12	1.36	1.66	-0.01	-0.17	-0.51	-1.63	-0.01	0.33	0.56	-0.84	0.24
Animal Pond	AP-722-10	Proximal	-4.50	1.20	1.80	0.37	0.80	0.20	0.36	0.65	-0.03	0.33	0.30	0.14
Animal Pond	AP-722-11	Proximal	-2.84	0.45	-1.02	1.14	-1.04	-1.15	0.42	-1.31	0.40	-0.38	0.52	0.22
Animal Pond	AP-722-12	Proximal	-4.41	1.34	-0.36	-1.32	-0.65	0.46	0.67	0.55	-0.85	-0.86	-0.04	-0.09
Animal Pond	AP-722-13	Proximal	-3.94	0.54	-0.02	-1.19	-0.60	0.05	0.92	0.37	-0.42	-0.28	-0.06	0.19
Stog'er Tight	BN-748-1	Intermediate	2.77	-0.41	1.54	2.06	0.94	-0.31	0.73	-0.90	-0.02	0.01	0.14	0.22
Stog'er Tight	BN-748-2	Intermediate	2.59	0.53	-0.18	-0.10	-0.30	1.44	0.37	-0.03	0.67	-0.52	-0.40	-0.03
Stog'er Tight	BN-748-3	Intermediate	3.60	0.67	-0.97	-0.41	-0.26	0.75	0.69	-0.31	-0.12	-0.60	-0.44	0.08
Stog'er Tight	BN-748-4	Intermediate	1.45	1.29	0.05	1.17	-1.32	0.74	0.42	-0.71	-0.26	0.04	0.11	-0.12
Stog'er Tight	BN-748-5	Intermediate	2.24	1.26	-2.42	-0.73	-1.21	1.08	-0.84	0.20	-0.11	0.08	-0.42	0.17
Stog'er Tight	BN-748-6	Intermediate	1.11	2.30	-1.90	-1.35	1.40	0.82	-1.21	-0.89	0.12	0.10	0.39	0.62
Stog'er Tight	BN-748-7	Intermediate	1.42	1.65	-2.20	0.47	1.83	-0.14	0.12	0.50	0.02	0.32	0.43	-0.84
Stog'er Tight	BN-748-8	Intermediate	1.31	0.74	-0.86	1.17	1.18	-1.22	0.42	0.71	0.73	0.25	0.36	0.04
Stog'er Tight	BN-748-9	Intermediate	3.39	0.57	0.22	2.30	0.29	-0.02	-0.10	-0.03	-0.96	-0.01	0.01	0.20
Stog'er Tight	BN-748-10	Intermediate	1.68	0.65	-1.13	0.18	-1.09	0.74	0.04	0.37	-0.45	0.34	0.25	-0.03
Stog'er Tight	BN-748-11	Intermediate	2.62	0.95	0.73	1.11	0.10	-0.72	1.22	0.60	0.34	-0.70	-0.17	0.35
Stog'er Tight	BN-748-12	Intermediate	0.95	2.08	-1.95	-1.89	2.12	0.96	-1.01	-0.12	-0.17	-0.74	-0.10	0.71
Stog'er Tight	BN-748-13	Intermediate	1.42	1.91	-1.22	1.04	3.30	-1.46	0.17	0.97	0.10	-0.10	-0.62	0.05
Stog'er Tight	BN-748-14	Intermediate	0.96	1.79	-1.83	0.53	0.19	1.09	-0.08	-0.73	1.17	-0.10	-0.12	-0.23
Stog'er Tight	BN-748-15	Intermediate	1.31	1.08	1.52	1.78	0.19	-0.50	1.11	0.40	-0.17	-0.48	0.04	0.09
Stog'er Tight	BN-748-16	Intermediate	1.70	-0.01	-0.36	3.10	-2.05	0.95	0.05	0.10	-0.14	0.07	0.32	-0.31
Stog'er Tight	BN-748-17	Intermediate	0.50	0.80	0.06	2.14	-1.43	1.37	-0.87	0.65	0.04	0.39	-0.40	0.30
Stog'er Tight	BN-748-18	Intermediate	1.53	1.29	0.24	0.74	0.61	0.10	0.39	0.08	-0.47	-0.10	0.17	0.05
Stog'er Tight	BN-748-19	Intermediate	1.36	1.24	-1.67	1.05	1.72	0.77	-0.83	-0.19	-1.02	0.52	-0.13	-0.20
Argyle	AE-660-1	Proximal	0.36	-3.54	-0.19	0.09	-0.38	0.18	0.03	-0.27	0.06	-0.73	-0.35	-0.24

Argyle	AE-660-2	Proximal	-0.44	-2.75	-0.79	-0.50	-1.20	1.02	1.21	0.24	0.11	0.55	0.00	0.24
Argyle	AE-660-3	Proximal	-1.57	-1.90	0.65	-0.40	0.17	0.53	-0.76	0.16	0.93	0.01	0.07	0.23
Argyle	AE-660-4	Proximal	0.00	-4.55	-1.21	-0.63	0.24	0.28	0.74	0.17	-0.27	-0.04	-0.20	-0.02
Argyle	AE-660-5	Proximal	0.78	-3.72	-0.87	0.18	0.36	-0.35	0.09	-0.37	0.06	0.11	-0.43	0.06
Argyle	AE-660-6	Proximal	-1.29	-3.25	1.42	0.11	0.30	1.07	-1.83	0.37	0.29	-0.52	0.21	-0.18
Argyle	AE-660-7	Proximal	-1.19	-2.25	-0.18	0.89	0.08	1.73	0.43	0.21	0.87	0.98	0.36	-0.14
Argyle	AE-660-8	Proximal	-2.07	-2.60	0.76	-0.74	1.68	1.44	-1.53	-0.26	-0.45	-0.45	0.27	-0.11
Argyle	AE-660-9	Proximal	-2.24	-1.87	0.82	0.95	1.61	1.63	0.09	-0.29	0.45	0.93	0.13	-0.17
Argyle	AE-660-10	Proximal	0.27	-3.40	-2.22	-1.05	-0.04	-0.41	0.80	0.18	-0.09	0.35	0.04	0.23
Argyle	AE-660-11	Proximal	0.47	-4.29	-1.17	-0.87	0.60	-1.09	0.66	-0.30	0.00	-0.07	-0.46	0.07
Argyle	AE-660-12	Proximal	-0.04	-4.49	-0.24	0.10	-0.07	-0.96	-0.11	0.09	0.46	-0.59	-0.44	-0.38
Argyle	AE-679-1	Intermediate	1.24	-0.25	0.54	0.23	-0.97	-0.44	-0.86	0.43	0.43	-0.37	0.00	0.05
Argyle	AE-679-2	Intermediate	1.06	-1.35	0.03	0.01	-0.85	-1.33	-1.12	0.49	-0.35	0.25	0.65	0.49
Argyle	AE-679-3	Intermediate	2.46	-0.10	2.71	-1.08	0.15	0.00	0.04	-1.46	0.58	-0.25	0.19	0.22
Argyle	AE-679-4	Intermediate	2.35	2.05	0.82	-0.79	-2.61	0.47	-0.45	-0.50	-0.25	-0.11	-0.31	-0.21
Argyle	AE-679-5	Intermediate	1.66	-0.36	-1.29	-1.67	-0.23	-1.20	0.01	-0.19	-1.19	1.38	-0.15	0.16
Argyle	AE-679-6	Intermediate	2.20	1.27	3.04	-0.59	0.29	-0.53	0.35	-0.46	-0.06	0.03	-0.48	-0.08
Argyle	AE-679-7	Intermediate	1.60	3.46	1.61	-2.54	0.19	0.43	-0.45	0.60	0.54	-0.01	0.51	-0.91
Argyle	AE-679-8	Intermediate	0.49	1.09	1.12	-1.11	-1.34	-0.90	-1.13	0.16	0.16	0.56	-0.47	-0.41
Argyle	AE-679-9	Intermediate	1.99	0.42	1.36	-2.65	-0.03	-0.41	2.20	-0.05	0.74	0.50	0.63	0.05
Argyle	AE-679-10	Intermediate	0.71	0.41	-0.74	-1.47	-0.55	-0.03	0.41	1.36	0.20	0.44	0.06	0.35
Argyle	AE-679-11	Intermediate	1.39	0.58	3.63	-2.11	0.48	-0.15	0.47	0.00	-0.18	-0.20	0.06	-0.26
Argyle	AE-679-12	Intermediate	1.36	-1.63	1.72	-1.10	0.11	-1.17	-0.99	-0.91	-0.96	0.37	0.12	-0.35
Argyle	AE-679-13	Intermediate	1.19	-0.26	0.65	-0.16	-0.78	-0.93	-0.70	1.17	0.34	-0.36	0.14	-0.09
Argyle	AE-679-14	Intermediate	0.43	-1.94	0.94	1.26	-0.55	-1.76	-1.56	0.49	-0.41	-0.53	0.97	-0.02

	Eigenvalues	**Percent**	**Cumulative %**
PC1	5.23	30.74	30.74
PC2	3.75	22.06	52.80
PC3	2.70	15.89	68.69
PC4	1.45	8.50	77.19
PC5	1.11	6.52	83.71
PC6	0.84	4.95	88.66
PC7	0.68	3.99	92.65
PC8	0.33	1.97	94.61
PC9	0.27	1.58	96.20
PC10	0.21	1.25	97.45
PC11	0.14	0.82	98.26
PC12	0.10	0.60	98.86
PC13	0.08	0.49	99.35
PC14	0.06	0.35	99.70
PC15	0.04	0.21	99.90
PC16	0.02	0.10	100.00
PC17	0.00	0.00	100.00

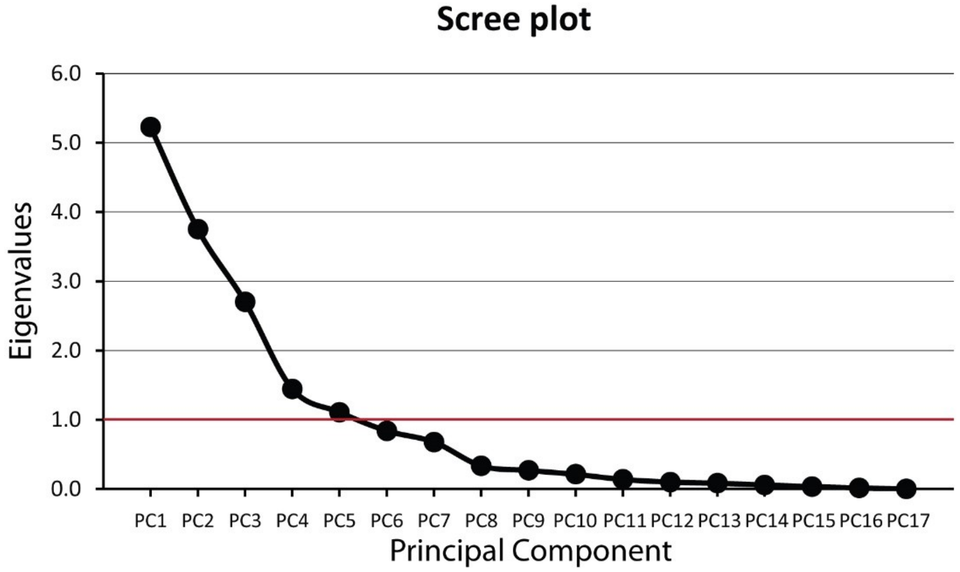

SIMS PCA run #2 (Fig. 4.5b): Sc, V, Cr, Mn, Fe, As, Y, Zr, Nb, Sn, Sb, Ta, W.

Deposit / Prospect	Sample	Alteration Intensity	PC1	PC2	PC3	PC4	PC5	PC6	PC7	PC8	PC9	PC10	PC11	PC12
Animal Pond	AP-722-1	Proximal	4.23	-0.56	-1.79	-0.55	-2.16	-0.82	-0.41	1.16	-0.25	0.19	0.26	0.10
Animal Pond	AP-722-2	Proximal	3.03	-1.25	0.29	0.95	-0.14	0.48	-0.37	-0.13	-0.30	0.82	0.23	-0.25
Animal Pond	AP-722-3	Proximal	2.29	-0.24	2.08	0.22	0.50	1.24	-0.20	0.80	-0.37	-0.29	-0.02	0.35
Animal Pond	AP-722-4	Proximal	2.70	-0.54	2.35	-0.26	0.62	1.08	-0.40	0.13	-0.09	-0.36	-0.14	0.18
Animal Pond	AP-722-5	Proximal	3.49	-2.28	-0.13	-0.04	0.77	-0.32	-0.05	-0.49	-0.14	-0.29	0.30	0.08
Animal Pond	AP-722-6	Proximal	2.25	-0.79	2.27	0.08	1.21	1.47	0.82	0.28	0.41	0.56	-0.06	0.14
Animal Pond	AP-722-7	Proximal	3.75	-1.74	0.32	-1.41	-0.05	0.03	0.35	-0.03	0.23	-0.17	0.05	-0.19
Animal Pond	AP-722-8	Proximal	3.25	-2.25	-0.28	-0.42	0.93	-0.28	0.62	-0.06	0.03	-0.75	0.17	0.06
Animal Pond	AP-722-9	Proximal	3.83	-2.11	-0.23	-0.07	0.79	-0.54	0.60	-0.73	-0.35	-0.76	0.11	-0.44
Animal Pond	AP-722-10	Proximal	4.32	-1.50	-0.68	-0.56	-0.27	-0.68	-0.41	0.13	0.11	0.17	0.47	0.05
Animal Pond	AP-722-11	Proximal	2.86	-0.42	1.74	0.03	1.09	1.08	0.64	0.20	0.58	0.46	0.06	-0.03
Animal Pond	AP-722-12	Proximal	4.02	-1.43	-0.59	0.50	-0.69	0.37	-0.78	0.23	-0.66	0.49	-0.26	0.16
Animal Pond	AP-722-13	Proximal	3.78	-0.66	-0.83	0.35	-0.06	0.48	-0.60	0.10	-0.41	0.19	-0.41	-0.34
Stog'er Tight	BN-748-1	Intermediate	-2.06	0.28	0.41	-1.33	-0.17	-0.16	0.40	0.54	0.48	-0.06	0.43	-0.33
Stog'er Tight	BN-748-2	Intermediate	-2.43	-0.32	0.15	0.85	-1.09	0.73	-0.57	-0.17	0.15	-0.40	0.34	-0.10
Stog'er Tight	BN-748-3	Intermediate	-3.48	-0.22	0.19	0.42	-0.75	0.87	-0.33	0.27	-0.33	-0.16	0.28	-0.32
Stog'er Tight	BN-748-4	Intermediate	-1.03	-1.23	1.06	0.93	-0.50	-0.03	0.41	0.52	0.24	-0.10	-0.49	-0.35
Stog'er Tight	BN-748-5	Intermediate	-2.64	-0.62	1.16	1.60	-0.35	0.22	0.06	-0.27	-0.60	-0.14	-0.08	-0.25
Stog'er Tight	BN-748-6	Intermediate	-1.99	-1.55	0.44	-0.52	-0.82	1.08	1.12	-0.73	-0.03	0.59	-0.37	-0.10
Stog'er Tight	BN-748-7	Intermediate	-2.17	-0.60	1.45	-1.30	-0.24	0.15	-0.54	0.47	0.41	-0.23	-0.40	0.30
Stog'er Tight	BN-748-8	Intermediate	-1.55	-0.12	1.11	-1.19	0.92	-0.11	-0.70	-0.28	0.51	0.04	0.14	0.16
Stog'er Tight	BN-748-9	Intermediate	-2.94	-0.41	1.49	-0.81	-0.36	-1.16	0.21	0.44	-0.27	0.21	0.11	-0.03
Stog'er Tight	BN-748-10	Intermediate	-1.65	-0.25	0.80	1.13	-0.19	-0.43	-0.16	0.43	-0.13	0.13	-0.24	-0.23
Stog'er Tight	BN-748-11	Intermediate	-2.14	-0.86	0.23	-0.63	0.27	0.03	-1.11	-0.31	0.07	0.11	0.22	0.09
Stog'er Tight	BN-748-12	Intermediate	-2.01	-1.29	-0.13	-0.93	-1.48	0.99	0.33	-1.01	-0.71	0.78	0.16	0.12
Stog'er Tight	BN-748-13	Intermediate	-2.12	-1.01	1.14	-3.10	0.17	-0.12	-0.81	-0.71	-0.42	-0.36	-0.04	0.19
Stog'er Tight	BN-748-14	Intermediate	-1.46	-1.01	1.64	0.72	-0.99	1.00	0.44	-0.47	0.53	-0.34	-0.06	-0.16
Stog'er Tight	BN-748-15	Intermediate	-0.71	-1.26	0.40	-0.95	0.04	-0.41	-0.93	0.32	0.22	0.01	-0.02	-0.21
Stog'er Tight	BN-748-16	Intermediate	-1.04	0.08	2.67	1.57	-0.36	-1.21	-0.10	0.60	0.42	0.03	0.21	0.34
Stog'er Tight	BN-748-17	Intermediate	-0.22	-0.81	1.91	1.48	-0.64	-1.47	0.00	-0.53	-0.24	-0.25	0.07	0.04
Stog'er Tight	BN-748-18	Intermediate	-1.41	-1.10	0.44	-0.84	-0.33	-0.13	-0.33	0.42	0.03	0.08	-0.17	-0.24
Stog'er Tight	BN-748-19	Intermediate	-1.91	-0.47	1.71	-1.18	-1.13	-0.64	0.70	0.44	-0.51	-0.13	0.02	0.08
Argyle	AE-660-1	Proximal	0.04	3.17	-0.11	0.33	-0.32	0.23	-0.08	0.02	-0.07	-0.12	0.24	0.09
Argyle	AE-660-2	Proximal	0.85	2.93	-0.39	1.44	-0.22	0.25	-0.36	0.20	-0.04	-0.18	-0.14	-0.26

Argyle	AE-660-3	Proximal	1.53	1.51	-0.68	0.51	-0.29	-0.12	0.18	-0.95	0.36	0.08	-0.04	-0.08
Argyle	AE-660-4	Proximal	0.25	4.64	-0.50	-0.02	-0.27	0.31	-0.34	0.17	-0.30	-0.10	-0.10	-0.07
Argyle	AE-660-5	Proximal	-0.54	3.75	0.12	-0.33	0.22	0.17	0.35	-0.07	-0.22	-0.30	0.30	0.12
Argyle	AE-660-6	Proximal	1.45	2.33	-0.61	0.33	-0.95	-0.97	0.16	-0.74	0.30	0.31	0.04	0.49
Argyle	AE-660-7	Proximal	1.37	2.46	0.41	0.92	-1.02	-0.35	0.04	-0.22	0.78	-0.38	-0.38	0.00
Argyle	AE-660-8	Proximal	1.86	2.03	-0.94	-0.78	-1.70	-0.27	0.60	-0.29	-0.03	0.44	-0.07	0.40
Argyle	AE-660-9	Proximal	2.27	1.86	-0.08	-0.50	-1.56	-0.42	0.58	-0.14	0.58	-0.49	-0.36	-0.12
Argyle	AE-660-10	Proximal	-0.26	3.89	-0.16	0.05	0.64	0.67	-0.25	0.02	-0.27	0.07	-0.12	0.18
Argyle	AE-660-11	Proximal	-0.31	4.36	-0.73	-0.70	0.67	0.70	0.10	-0.05	-0.36	-0.22	0.12	0.01
Argyle	AE-660-12	Proximal	0.37	4.02	-0.18	-0.20	0.72	0.18	-0.39	-0.12	0.10	-0.40	0.13	-0.21
Argyle	AE-679-1	Intermediate	-1.05	-0.14	0.11	0.70	0.70	-0.47	-0.27	-0.43	0.14	0.13	0.22	0.00
Argyle	AE-679-2	Intermediate	-0.90	1.04	-0.05	0.25	1.57	-1.08	0.27	-0.20	-0.06	0.83	-0.07	-0.18
Argyle	AE-679-3	Intermediate	-1.96	-0.58	-2.32	0.06	-0.13	0.71	1.05	0.06	0.53	0.17	0.62	-0.17
Argyle	AE-679-4	Intermediate	-2.05	-2.39	-0.58	2.33	0.18	-0.18	0.59	0.37	-0.35	-0.05	0.58	0.34
Argyle	AE-679-5	Intermediate	-1.80	0.79	-0.91	-0.15	1.34	-0.25	0.98	0.41	-0.90	-0.08	-0.46	0.23
Argyle	AE-679-6	Intermediate	-1.70	-1.91	-2.18	-0.52	0.09	-0.15	0.37	0.06	-0.07	-0.43	-0.05	-0.22
Argyle	AE-679-7	Intermediate	-2.03	-3.62	-2.45	0.62	-0.29	0.16	-0.41	-0.17	0.59	-0.01	-0.60	0.61
Argyle	AE-679-8	Intermediate	-0.48	-1.63	-1.07	0.95	1.31	-0.52	0.44	-0.33	-0.18	-0.60	-0.29	0.38
Argyle	AE-679-9	Intermediate	-1.69	-0.31	-3.26	0.34	0.71	1.29	-0.56	0.43	0.62	0.10	0.24	0.28
Argyle	AE-679-10	Intermediate	-0.91	-0.03	-0.85	0.82	0.63	-0.09	-1.03	-0.37	-0.29	0.08	-0.17	-0.17
Argyle	AE-679-11	Intermediate	-0.93	-1.49	-3.66	-0.47	-0.10	0.14	-0.30	0.35	0.18	-0.14	-0.33	-0.37
Argyle	AE-679-12	Intermediate	-1.06	0.84	-1.90	-0.60	0.85	-0.56	1.34	0.66	-0.19	0.07	-0.10	0.13
Argyle	AE-679-13	Intermediate	-1.05	-0.14	-0.32	0.37	1.17	-0.65	-0.98	-0.33	0.14	0.14	0.08	0.04
Argyle	AE-679-14	Intermediate	-0.11	1.14	0.51	-0.46	1.49	-1.50	0.00	0.09	0.42	1.01	-0.21	-0.31

	Eigenvalues	Percent	Cumulative %
PC1	4.77	36.72	36.72
PC2	3.44	26.47	63.19
PC3	1.76	13.56	76.75
PC4	0.86	6.59	83.34
PC5	0.71	5.47	88.81
PC6	0.49	3.78	92.59
PC7	0.33	2.53	95.13
PC8	0.20	1.52	96.65
PC9	0.15	1.12	97.77
PC10	0.14	1.09	98.86
PC11	0.07	0.55	99.41
PC12	0.06	0.44	99.85
PC13	0.02	0.15	100.00